U.S. DEPARTMENT OF COMMERCE
National Technical Information Service

PB-295 226

Symposium on the Transfer and Utilization of Particulate Control Technology: Volume 1 Electrostatic Precipitators

Denver Research Inst., CO

Prepared for

Industrial Environmental Research Lab., Research Triangle Park, NC

Feb 79

PB 295226

United States
Environmental Protection
Agency

Industrial Environmental Research
Laboratory
Research Triangle Park NC 27711

EPA-600/7-79-044a
February 1979

EPA

Symposium on the Transfer and Utilization of Particulate Control Technology:
Volume I.
Electrostatic Precipitators

Interagency
Energy/Environment
R&D Program Report

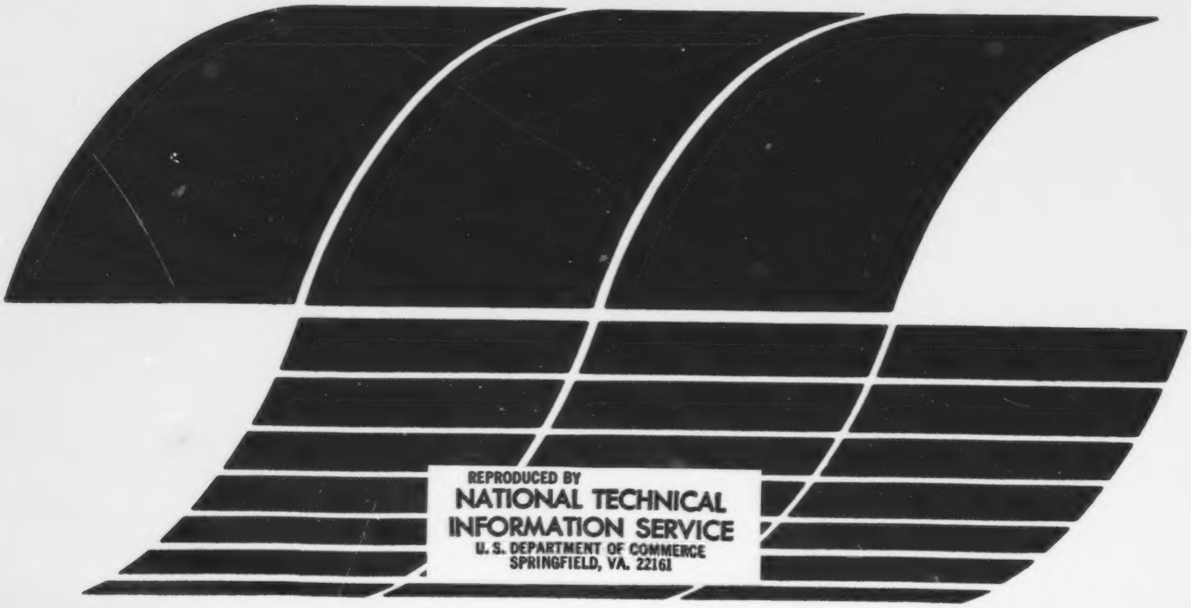

REPRODUCED BY
NATIONAL TECHNICAL
INFORMATION SERVICE
U. S. DEPARTMENT OF COMMERCE
SPRINGFIELD, VA. 22161

RESEARCH REPORTING SERIES

Research reports of the Office of Research and Development, U.S. Environmental Protection Agency, have been grouped into nine series. These nine broad categories were established to facilitate further development and application of environmental technology. Elimination of traditional grouping was consciously planned to foster technology transfer and a maximum interface in related fields. The nine series are:

1. Environmental Health Effects Research
2. Environmental Protection Technology
3. Ecological Research
4. Environmental Monitoring
5. Socioeconomic Environmental Studies
6. Scientific and Technical Assessment Reports (STAR)
7. Interagency Energy-Environment Research and Development
8. "Special" Reports
9. Miscellaneous Reports

This report has been assigned to the INTERAGENCY ENERGY-ENVIRONMENT RESEARCH AND DEVELOPMENT series. Reports in this series result from the effort funded under the 17-agency Federal Energy/Environment Research and Development Program. These studies relate to EPA's mission to protect the public health and welfare from adverse effects of pollutants associated with energy systems. The goal of the Program is to assure the rapid development of domestic energy supplies in an environmentally-compatible manner by providing the necessary environmental data and control technology. Investigations include analyses of the transport of energy-related pollutants and their health and ecological effects; assessments of, and development of, control technologies for energy systems; and integrated assessments of a wide range of energy-related environmental issues.

EPA REVIEW NOTICE

This report has been reviewed by the participating Federal Agencies, and approved for publication. Approval does not signify that the contents necessarily reflect the views and policies of the Government, nor does mention of trade names or commercial products constitute endorsement or recommendation for use.

This document is available to the public through the National Technical Information Service, Springfield, Virginia 22161.

TECHNICAL REPORT DATA
(Please read Instructions on the reverse before completing)

1. REPORT NO.
EPA-600/7-79-044a

2.

3. R
PB295226

4. TITLE AND SUBTITLE
Symposium on the Transfer and Utilization of Particulate Control Technology: Vol. 1 Electrostatic Precipitators

5. REPORT DATE
February 1979

6. PERFORMING ORGANIZATION CODE

7. AUTHOR(S)
F.P. Venditti, J.A. Armstrong, and Michael Durham

8. PERFORMING ORGANIZATION REPORT NO.

9. PERFORMING ORGANIZATION NAME AND ADDRESS
Denver Research Institute
P.O. Box 10127
Denver, Colorado 80208

10. PROGRAM ELEMENT NO.
EHE624

11. CONTRACT/GRANT NO.
Grant R805725

12. SPONSORING AGENCY NAME AND ADDRESS
EPA, Office of Research and Development
Industrial Environmental Research Laboratory
Research Triangle Park, NC 27711

13. TYPE OF REPORT AND PERIOD COVERED
Proceedings: 10/77-10/78

14. SPONSORING AGENCY CODE
EPA/600/13

15. SUPPLEMENTARY NOTES
IERL-RTP project officer is Dennis C. Drehmel, Mail Drop 61, 919/541-2925.

→ during the symposium

16. ABSTRACT

Papers in the proceedings were presented at the Symposium on the Transfer and Utilization of Particulate Control Technology, in Denver, Colorado, July 24 through 28, 1978. The symposium was sponsored by the Particulate Technology Branch of EPA's Industrial Environmental Research Laboratory--Research Triangle Park, and was hosted by the University of Denver's Denver Research Institute. The symposium brought together researchers, manufacturers, users, government agencies, educators, and students to discuss new technology and to provide an effective means for the transfer of this technology out of the laboratories and into the hands of the users. The three major categories of control technologies--electrostatic precipitators, scrubbers, and fabric filters--were of major concern. These technologies were discussed from the perspectives of economics; new technical advances in science and engineering; and applications. Several papers dealt with combinations of devices and technologies, leading to a concept of using a systems approach to particulate control, rather than device control.

[illegible]
the following topics → in grid

17. KEY WORDS AND DOCUMENT ANALYSIS

a. DESCRIPTORS		b. IDENTIFIERS/OPEN ENDED TERMS	c. COSATI Field/Group	
Pollution	Fabrics	Pollution Control	13B	11E
Dust	Economics	Stationary Sources	11G	05C
Aerosols	Sampling	Particulate	07D	14B
Electrostatic Precipitators		Fabric Filters	13I	
Scrubbers		Fugitive Dust	07A	
Filtration				

18. DISTRIBUTION STATEMENT
Unlimited

19. SECURITY CLASS *(This Report)*
Unclassified

20. SECURITY CLASS *(This page)*
Unclassified

21. NO. OF PAGES
524

22. PRICE
A22- A01

EPA Form 2220-1 (9-73)

☆U.S. GOVERNMENT PRINTING OFFICE: 1979-640-013/4203

EPA-600/7-79-044a
February 1979

Symposium on the Transfer and Utilization of Particulate Control Technology:

Volume 1. Electrostatic Precipitators

by

F.P. Venditti, J.A. Armstrong, and Michael Durham

Denver Research Institute
P.O. Box 10127
Denver, Colorado 80208

Grant No. R805725
Program Element No. EHE624

EPA Project Officer: Dennis C. Drehmel

Industrial Environmental Research Laboratory
Office of Energy, Minerals, and Industry
Research Triangle Park, NC 27711

Prepared for

U.S. ENVIRONMENTAL PROTECTION AGENCY
Office of Research and Development
Washington, DC 20460

i.a

ABSTRACT

The papers in these four volumes of Proceedings were presented at the Symposium on the Transfer and Utilization of Particulate Control Technology, held in Denver, Colorado during 24 July through 28 July 1978 sponsored by the Particulate Technology Branch of the Industrial Environmental Research Laboratory of the Environmental Protection Agency and hosted by the Denver Research Institute of the University of Denver.

The purpose of the symposium was to bring together researchers, manufacturers, users, government agencies, educators and students to discuss new technology and to provide an effective means for the transfer of this technology out of the laboratories and into the hands of the users.

The three major categories of control technologies, electrostatic precipitators, scrubbers, and fabric filters were the major concern of the symposium. These technologies were discussed from the perspectives of economics; new technical advancements in science and engineering; and applications. Several papers dealt with combinations of devices and technologies, leading to a concept of using a systems approach to particulate control rather than device control.

These proceedings are divided into four volumes, each volume containing a set of related session topics to provide easy access to a unified technology area.

TABLE OF CONTENTS

Volumes 1 through 4

VOLUME I

ELECTROSTATIC PRECIPITATORS (ESP's)

Section A - ESP's for Coal Fired Boilers

Page

ELECTROSTATIC PRECIPITATOR PERFORMANCE
J. P. Gooch 1

SPECIFICATIONS OF A RELIABLE PRECIPITATOR
R. L. Williams 19

EXPERIENCE WITH COLD SIDE PRECIPITATORS ON LOW SULFUR COALS
S. Maartmann 25

A PERFORMANCE ANALYSIS OF A HOT-SIDE ELECTROSTATIC PRECIPITATOR
G. H. Marchant, J. P. Gooch, L. E. Sparks 39

AIR FLOW MODEL STUDIES FOR ELECTROSTATIC PRECIPITATORS
H. L. Engelbrecht 57

Section B - Flue Gas Conditioning for ESP'S

CHEMICAL CONDITIONING OF FLY ASH FOR HOT-SIDE PRECIPITATION
P. B. Lederman, P. B. Bibbo, J. Bush 79

CONDITIONING OF DUST WITH WATER-SOLUBLE ALKALI COMPOUNDS
H. H. Petersen 99

CHEMICAL ENHANCEMENT OF ELECTROSTATIC PRECIPITATOR EFFICIENCY
R. P. Bennett, A. E. Kober 113

METHOD AND COST ANALYSIS OF ALTERNATIVE COLLECTORS FOR LOW SULFUR COAL FLY ASH
E. W. Breisch 121

Page

BENCH-SCALE EVALUATION OF DRY ALKALIS FOR REMOVING SO_2 FROM BOILER FLUE GASES
N. D. Shah, D. P. Teixeira and L. J. Muzio 131

ANALYSIS OF THERMAL DECOMPOSITION PRODUCTS OF FLUE GAS CONDITIONING AGENTS
H. K. Dillon and E B. Dismukes 155

FLUE GAS CONDITIONING EFFECTS ON ELECTROSTATIC PRECIPITATORS
R. Patterson, R. Riersgard, R. Parker and L. E. Sparks 169

FLUE GAS CONDITIONING AT ARIZONA PUBLIC SERVICE COMPANY FOUR CORNERS UNIT NO. 4
R. E. Pressey, D. Osborn and E. Cole 179

SODIUM CONDITIONING TEST WITH EPA MOBILE ESP
S. P. Schliesser 205

Section C - Novel Electrostatic Precipitators

NOVEL ELECTRODE CONSTRUCTION FOR PULSE CHARGING
S. Masuda 241

PULSED ENERGIZATION FOR ENHANCED ELECTROSTATIC PRECIPITATION IN HIGH-RESISTIVITY APPLICATIONS
P. L. Feldman and H. I. Milde 253

A NEW PRECHARGER FOR TWO-STAGE ELECTROSTATIC PRECIPITATION OF HIGH RESISTIVITY DUST
D. H. Pontius, P. V. Bush and L. E. Sparks 275

ELECTRON BEAM IONIZATION FOR COAL FLY ASH PRECIPITATORS
R. H. Davis and W. C. Finney 287

WIDE SPACING E.P. IS AVAILABLE IN CLEANING EXHAUST GASES FROM INDUSTRIAL SOURCES
R. Ito and K. Takimoto 297

Section D - Fundamentals--Electrical and Particle Characteristics

Page

DESCRIPTION OF A MATHEMATICAL MODEL OF ELECTROSTATIC PRECIPITATION
J. R. McDonald and L. E. Sparks 307

BACK DISCHARGE PHENOMENA IN ELECTROSTATIC PRECIPITATION
S. Masuda 321

MEASUREMENT OF EFFECTIVE ION MOBILITIES IN A CORONA DISCHARGE IN INDUSTRIAL FLUE GASES
J. R. McDonald, S. M. Banks and L. E. Sparks 335

PILOT SCALE ELECTROSTATIC PRECIPITATORS AND THE ELECTRICAL PERFORMANCE DIAGRAM
K. J. McLean and R. B. Kahane 349

THEORETICAL STUDY OF PARTICLE CHARGING BY UNIPOLAR IONS
D. H. Pontius, W. B. Smith and J. H. Abbott 361

AGING CAUSED INCREASE OF RESISTIVITY OF A BARRIER FILM AROUND GLASSY FLY ASH PARTICLES
W. J. Culbertson 373

ELECTROSTATIC PRECIPITATORS: THE RELATIONSHIP OF ASH RESISTIVITY AND PRECIPITATOR ELECTRICAL OPERATING PARAMETERS
H. W. Spencer, III 381

A TECHNIQUE FOR PREDICTING FLY ASH RESISTIVITY
R. E. Bickelhaupt 395

ELECTRICAL PROPERTIES OF THE DEPOSITED DUST LAYER WHICH ARISE BECAUSE OF ITS PARTICULATE STRUCTURE
K. J. McLean 409

VOLTAGE AND CURRENT RELATIONSHIPS IN HOT SIDE ELECTROSTATIC PRECIPITATORS
D. E. Rugg and W. Patten 421

PRECIPITATOR EFFICIENCY FOR LOG-NORMAL DISTRIBUTIONS
P. Cooperman and G. D. Cooperman 433

Section E - Industrial Applications of ESP's

Page

ELECTROSTATIC PRECIPITATION USING IONIC WIND FOR VERY LOW RESISTIVITY DUSTS FROM HIGH TEMPERATURE FLUE GAS OF PETROLEUM-COKES CALCINING KILN
F. Isahaya 453

THE USE OF ELECTROSTATIC PRECIPITATORS FOR COLLECTION OF PARTICULATE MATTER FROM BARK AND WASTE WOOD FIRED BOILERS IN THE PAPER INDUSTRY
R. L. Bump 467

ROOF-MOUNTED ELECTROSTATIC PRECIPITATOR
S. Ito, S. Noso, M. Sakai and K. Sakai 485

POM EMISSIONS FROM COKE OVEN DOOR LEAKAGE AND THEIR CONTROL BY A WET ELECTROSTATIC PRECIPITATOR
R. E. Barrett, P. R. Webb, C. E. Riley and A. R. Trenholm 497

VOLUME II

FABRIC FILTERS AND CURRENT TRENDS IN CONTROL EQUIPMENT

Section A - Fabric Filters

Page

FABRIC FILTER USAGE IN JAPAN
K. Iinoya 1

PERFORMANCE OF A PULSE-JET FILTER AT HIGH FILTRATION VELOCITIES
D. Leith, M. W. First, M. Ellenbecker and D. D. Gibson 11

ELECTROSTATIC EFFECTS IN FABRIC FILTRATION
E. R. Frederick 27

EPA IN-HOUSE FABRIC FILTRATION R&D
J. H. Turner 45

ENVIRONMENTAL PROTECTION AGENCY MOBILE FABRIC FILTER PROGRAM - A COMPARISON STUDY OF UTILITY BOILERS FIRING EASTERN AND WESTERN COAL
B. Lipscomb 53

EVALUATION OF FELTED GLASS FILTER MEDIA UNDER SIMULATED PULSE JET OPERATING CONDITIONS
L. R. Lefkowitz 75

INFLUENCE OF FIBER DIAMETER ON PRESSURE DROP AND FILTRATION EFFICIENCY OF GLASS FIBER MATS
J. Goldfield and K. D. Gandhi 89

FUNDAMENTAL EXPERIMENTS OF FABRIC FILTERS
K. Iinoya and Y. Mori 99

A DUAL PURPOSE BAGHOUSE FOR PARTICLE CONTROL AND FLUE GAS DESULFURIZATION
S. J. Lutz 111

SIMULTANEOUS ACID GAS AND PARTICULATE RECOVERY
A. J. Teller 119

Page

TECHNOLOGY OF FIBER GLASS FILTER FABRIC DESIGN
C. E. Knox, J. Murray and V. Schoeck 133

VERIFICATION OF PROJECTED FILTER SYSTEM DESIGN AND OPERATION
R. Dennis and H. A. Klemm 143

PRECIPITATORS? SCRUBBERS? OR BAGHOUSES? FOR SHAWNEE (WHY TVA IS INSTALLING BAGHOUSES)
J. A. Hudson 161

HIGH RATIO FABRIC FILTERS FOR UTILITY BOILERS
B. L. Arnold and B. Melville 183

RETRO-FITTING BAGHOUSES ON COAL-FIRED BOILERS - A CASE STUDY
J. M. Osborne and L. R. Cramer 197

MATCHING A BAGHOUSE TO A FOSSIL FUEL FIRED BOILER
D. W. Rolschau 211

START-UP, OPERATION AND PERFORMANCE TESTING OF FABRIC FILTER SYSTEM-HARRINGTON STATION, UNIT #2
G. Faulkner and K. L. Ladd 219

APPLYING HIGH VELOCITY FABRIC FILTERS TO COAL FIRED INDUSTRIAL BOILERS
J. D. McKenna, G. P. Greiner and K. D. Brandt 233

FABRIC FILTER RESEARCH AND DEVELOPMENT FOR PC BOILERS USING WESTERN COAL
D. A. Furlong, R. L. Ostop and P. Gelfand 247

A PILOT PLANT STUDY OF VARIOUS FILTER MEDIA APPLIED TO A PULVERIZED COAL-FIRED BOILER
J. C. Mycock 263

APPLICATION OF SLIP-STREAMED AIR POLLUTION CONTROL DEVICES ON WASTE-AS-FUEL PROCESSES
J. M. Bruck, C. J. Sawyer, F. D. Hall and T. W. Devitt 287

Section B - Current Trends in Control Equipment

ASSESSMENT OF THE COST AND PERFORMANCE OF PARTICULATE CONTROL DEVICES ON LOW-SULFUR WESTERN COALS
R. A. Chapman, T. F. Edgar and L. E. Sparks 297

ELECTROSTATIC PRECIPITATION IN JAPANESE STEEL INDUSTRIES
S. Masuda 309

INSTALLED COST PROJECTIONS OF AIR POLLUTION CONTROL EQUIPMENT IN THE U. S.
R. W. McIlvaine 319

DUST EMISSION CONTROL FOR STATIONARY SOURCES IN THE FEDERAL REPUBLIC OF GERMANY: STANDARDS OR PERFORMANCE, BEST AVAILABLE CONTROL TECHNOLOGY AND ADVANCED APPLICATIONS
G. Guthner 333

ENGINEERING MANAGEMENT TRENDS IN THE DESIGN OF PRECIPITATORS AND BAGHOUSES
S. Negrea 361

CONTROL OF PARTICULATES FROM COMBUSTION
J. H. Abbott and D. C. Drehmel 383

VOLUME III

SCRUBBERS, ADVANCED TECHNOLOGY, AND HTHP APPLICATIONS

Section A - Scrubbers

Page

ENTRAINMENT SEPARATORS FOR SLURRY SCRUBBERS
S. Calvert, H. F. Barbarika and L. E. Sparks 1

SCRUBBER DEMISTER TECHNOLOGY FOR CONTROL OF SOLIDS EMISSIONS FROM SO_2 ABSORBERS
W. Ellison 13

IMPROVED MIST ELIMINATOR PERFORMANCE THROUGH ADVANCED DESIGN CONCEPTS
R. P. Tennyson, S. F. Roe, and R. H. Lace 35

FINE PARTICLE COLLECTION IN A MOBILE BED SCRUBBER
S. Yung, R. Chmielewski, S. Calvert and D. Harmon 47

CONTROL OF PARTICULATE EMISSIONS WITH U.W. ELECTROSTATIC SPRAY SCRUBBER
M. J. Pilat and G. A. Raemhild 61

UNION CARBIDE'S HIGH INTENSITY IONIZER APPLIED TO ENHANCE A VENTURI SCRUBBER SYSTEM
M. T. Kearns and C. M. Chang 73

PERFORMANCE TESTS OF THE MONTANA POWER COMPANY COLSTRIP STATION FLUE GAS CLEANING SYSTEM
J. D. McCain 85

RESULTS OF THE TEST PROGRAM OF THE WEIR HORIZONTAL SCRUBBER AT FOUR CORNERS STEAM ELECTRIC STATION UNIT NO. FIVE
G. Bratzler, G. T. Gutierrez and C. F. Turton 99

MATERIALS PERFORMANCE PROBLEMS ASSOCIATED WITH THE SCRUBBING OF COKE OVEN WASTE HEAT FLUE GAS
M. P. Bianchi and L. A. Rosales 113

VENTURI SCRUBBER DESIGN MODEL
S. C. Yung, H. Barbarika, S. Calvert and L. E. Sparks 149

EXPERIMENTAL STUDY OF PARTICLE COLLECTION BY A VENTURI SCRUBBER DOWNSTREAM FROM AN ELECTROSTATIC PRECIPITATOR
G. H. Ramsey, L. E. Sparks and B. E. Daniels 161

Page

EFFECTS OF SURFACE TENSION ON PARTICLE REMOVAL
G. J. Woffinden, G. R. Markowski and D. S. Ensor 179

CONCLUSIONS FROM EPA SCRUBBER R&D
D. L. Harmon and L. E. Sparks 193

Section B - Advanced Technology

FINE PARTICLE EMISSION CONTROL BY HIGH GRADIENT MAGNETIC SEPARATION
C. H. Gooding and D. C. Drehmel 219

THE USE OF ACOUSTIC AGGLOMERATORS FOR PARTICULATE CONTROL
J. Wegrzyn, D. T. Shaw and G. Rudinger 233

ANALYTICAL AND EXPERIMENTAL STUDIES ON GRANULAR BED FILTRATION
C. Gutfinger, G. I. Tardos and N. Abuaf 243

THE EFFECTS OF ELECTRIC AND ACOUSTIC FIELDS ON THE COLLISION RATES OF SUBMICRON SIZED DOP AEROSOL PARTICLES
P. D. Scholz, L. W. Byrd and P. H. Paul 279

ELECTROSTATIC SEPARATION IN CYCLONES
W. B. Giles 291

EVALUATION OF THE ELECTRIFIED BED PROTOTYPE COLLECTOR ON AN ASPHALT ROOFING PLANT
R. M. Bradway, W. Piispanen, and V. Shortell 303

EVALUATION OF AN APITRON ELECTROSTATICALLY AUGMENTED FABRIC FILTER
J. D. McCain, P. R. Cavenaugh, L. G. Felix and R. L. Merritt 311

CORONA ELECTRODE FAILURE ANALYSIS
R. E. Bickelhaupt and W. V. Piulle 323

HIGH TEMPERATURE AND HIGH VELOCITY POROUS METAL GAS FILTRATION MEDIA
L. J. Ortino and R. M. Bethea 341

DRY DUST COLLECTION OF BLAST FURNACE EXHAUST GAS BY MOVING GRANULAR BED FILTER
H. Kohama, K. Sasaki, S. Watanabe and K. Sato 351

Page

CERAMIC FILTER, SCRUBBER AND ESP
R. A. Clyde 361

Section C - High Temperature High Pressure Applications

FUNDAMENTAL PARTICLE COLLECTION AT HIGH TEMPERATURE AND PRESSURE
R. Parker, S. Calvert and D. Drehmel 367

PARTICULATE CONTROL FOR FLUIDIZED BED COMBUSTION
D. F. Becker and M. G. Klett 379

HIGH TEMPERATURE GLASS ENTRAINMENT OF FLY ASH
W. Fedarko, A. Gatti and L. R. McCreight 395

A.P.T. DRY SCRUBBER FOR PARTICLE COLLECTION AT HIGH TEMPERATURE AND PRESSURE
R. Patterson, S. Calvert, S. Yung and D. Drehmel 405

ELECTROSTATIC PRECIPITATION AT HIGH TEMPERATURE AND PRESSURE: CAPABILITIES, CURIOUSITIES AND QUESTIONS
M. Robinson 415

HIGH TEMPERATURE, HIGH PRESSURE ELECTROSTATIC PRECIPITATION
J. R. Bush, P. L. Feldman and M. Robinson 417

BARRIER FILTRATION FOR HTHP PARTICULATE CONTROL
M. A. Shackleton and D. C. Drehmel 441

AEROSOL FILTRATION BY GRANULAR BEDS
S. L. Goren 459

PERFORMANCE CHARACTERISTICS OF MOVING-BED GRANULAR FILTERS
J. Geffken, J. L. Guillory and K. E. Phillips 471

VOLUME IV

FUGITIVE DUSTS AND SAMPLING, ANALYSIS AND CHARACTERIZATION OF AEROSOLS

Section A - Fugitive Dusts

Page

FUGITIVE SULFUR IN COAL-FIRED POWERPLANT PLUMES
R. F. Pueschel 1

RESEARCH IN WIND-GENERATED FUGITIVE DUST
D. A. Gillette and E. M. Patterson 11

DEVELOPING CONTROL STRATEGIES FOR FUGITIVE DUST SOURCES
G. Richard and D. Safriet 25

STATE OF CONTROL TECHNOLOGY FOR INDUSTRIAL FUGITIVE PROCESS PARTICULATE EMISSIONS
D. C. Drehmel, D. P. Daugherty and C. H. Gooding 47

FUGITIVE DUST EMISSIONS AND CONTROL
B. H. Carpenter and G. E. Weant 63

SETTING PRIORITIES FOR THE CONTROL OF PARTICULATE EMISSIONS FROM OPEN SOURCES
J. S. Evans, D. W. Cooper, M. Quinn and M. Schneider 85

USE OF ELECTROSTATICALLY CHARGED FOG FOR CONTROL OF FUGITIVE DUST, SMOKE AND FUME
S. A. Hoenig 105

COLLECTION AND CONTROL OF MOISTURE LADEN FUGITIVE DUST
C. D. Turley 131

Section B - Sampling, Analysis, and Characterization of Aerosols

THE VISIBILITY IMPACT OF SMOKE PLUMES
D. S. Ensor 141

MUTAGENICITY OF COAL FLY ASH
C. E. Chrisp 153

Page

BIO-ASSESSMENT OF CHRONIC MANGANESE INGESTION IN RATS
G. L. Rehnberg, D. F. Cahill, J. A. Elder, E. Gray and J. W. Laskey 159

THE USE OF SHORT TERM BIOASSAY SYSTEMS IN THE EVALUATION OF ENVIRONMENTAL PARTICULATES
N. E. Garrett, J. A. Campbell, J. L. Huisingh and M. D. Waters 175

A KINETIC AEROSOL MODEL FOR THE FORMATION AND GROWTH OF SECONDARY SULFURIC ACID PARTICLES
P. Middleton and C. S. Kiang 187

PARTICLE GROWTH BY CONDENSATION AND BY COAGULATION--BASIC RESEARCH OF ITS APPLICATION TO DUST COLLECTION
T. Yoshida, Y. Kousaka, K. Okuyama and K. Sumi 195

TRANSIENT CHEMISORPTION OF A SOLID PARTICLE IN A REACTIVE ATMOSPHERE OF RECEDING GAS CONCENTRATION
R. Wang 213

STABILITY OF FINE WATER DROPLET CLOUDS
Y. Kousaka, K. Okuyama, K. Sumi and T. Yoshida 231

PARTICLE SIZE ANALYSIS OF AEROSOLS INCLUDING DROPLET CLOUDS BY SEDIMENTATION METHOD
Y. Kousaka, K. Okuyama and T. Yoshida 249

PARTICLE MASS DISTRIBUTION AND VISIBILITY CONSIDERATIONS FOR LARGE POWER PLANTS
T. L. Montgomery and J. C. Burdick III 261

AN OPTICAL INSTRUMENT FOR DILUTE PARTICLE FIELD MEASUREMENTS
W. D. Bachalo 275

IMPACT OF SULFURIC ACID EMISSIONS ON PLUME OPACITY
J. S. Nader and W. D. Conner 289

PARTICLE CHARGE EFFECTS ON CASCADE IMPACTOR MEASUREMENTS
R. Patterson, P. Riersgard and D. Harmon 307

A HIGH-TEMPERATURE HIGH-PRESSURE, ISOKINETIC-ISOTHERMAL SAMPLING SYSTEM FOR FOSSIL FUEL COMBUSTION APPLICATIONS
J. C. F. Wang, R. R. Boericke and R. A. Fuller 319

Page

A PROTOTYPE OPTICAL SCATTERING INSTRUMENT FOR PARTICULATE SIZING IN STACKS
A. L. Wertheimer, W. H. Hart and M. N. Trainer 337

UTILIZATION OF THE OMEGA-1 LIDAR IN EPA ENFORCEMENT ACTIVITIES
A. W. Dybdahl and M. J. Cunningham 347

THE MONITORING OF PARTICULATES USING A BALLOON-BORNE SAMPLER
J. A. Armstrong and P. A. Russell 357

A STUDY OF PHILADELPHIA PARTICULATES USING MODELING AND MEASUREMENT TECHNIQUES
F. A. Record, R. M. Bradway and W. E. Belanger 377

DECISION-TREE ANALYSIS OF THE RELATIONSHIP BETWEEN TSP CONCENTRATION AND METEOROLOGY
J. Trijonis and Y. Horie 391

DESIGNING A SYSTEMATIC REGIONAL PARTICULATE ANALYSIS
J. A. Throgmorton, K. Axetell and T. G. Pace 403

IMPORTANCE OF PARTICLE SIZE DISTRIBUTION
L. E. Sparks 417

THE MORPHOGENESIS OF COAL FLY ASH
G. L. Fisher 433

THE EFFECT OF TEMPERATURE, PARTICLE SIZE AND TIME EXPOSURE ON COAL-ASH AGGLOMERATION
K. C. Tsao, J. F. Bradley and K. T. Yung 441

TEST PROGRAM TO UPDATE EQUIPMENT SPECIFICATIONS AND DESIGN CRITERIA FOR STOKER FIRED BOILERS
S. C. Schaeffer 457

TRACE ELEMENT EMISSIONS FROM COPPER SMELTERS
R. L. Meek and G. B. Nichols 465

AUTHOR NAME	PAGE
Abbott, James H.	I-361, II-383
Abuaf, Nesim	III-243
Armstrong, James A.	IV-357
Arnold, B. L.	II-183
Axetell, Kenneth W.	IV-403
Bachalo, William D.	IV-275
Banks, Sherman M.	I-335
Barbarika, Harry F.	III-1, III-149
Barrett, Richard E.	I-497
Becker, David F.	III-379
Belanger, William E.	IV-377
Bennett, Robert P.	I-113
Bethea, Robert M.	III-341
Bianchi, M. P.	III-113
Bibbo, P. B.	I-79
Bickelhaupt, Roy E.	I-395, III-323
Boericke, Ralph R.	IV-319
Bradley, Jeffrey F.	IV-441
Bradway, Robert M.	III-303, IV-377
Brandt, Kathryn D.	II-233
Bratzler, Gene E.	III-99
Breisch, Edgar W.	I-121
Bruck, John M.	II-287

AUTHOR NAME	PAGE
Bump, Robert L.	I-467
Burdick, J. Clement	IV-261
Bush, John R.	I-79, III-417
Bush, P. V.	I-275
Byrd, Larry W.	III-279
Cahill, D. F.	IV-159
Calvert, Seymour	III-1, III-47, III-149 III-367 III-405
Campbell, James A.	IV-175
Carpenter, B. H.	IV-63
Cavenaugh, Paul R.	III-311
Chang, C. M.	III-73
Chapman, Richard A.	II-297
Chmielewski, Richard D.	III-47
Chrisp, Clarence E.	IV-153
Clyde, Robert A.	III-361
Cole, Edward A.	I-179
Conner, William D.	IV-289
Cooper, Douglas W.	IV-85
Cooperman, Gene D.	I-433
Cooperman, Phillip	I-433
Cramer, Larry R.	II-197
Culbertson, William J.	I-373
Cunningham, Michael J.	IV-347

AUTHOR NAME	PAGE
Daniels, B. E.	III-161
Daugherty, David P.	IV-47
Davis, Robert H.	I-287
Dennis, Richard	II-143
Devitt, Timothy W.	II-287
Dillon, H. Kenneth	I-155
Dismukes, Edward B.	I-155
Drehmel, Dennis C.	II-383, III-219, III-367 III-405, III-441, IV-47
Dybdahl, Arthur W.	IV-347
Edgar, Thomas F.	II-297
Elder, J. A.	IV-159
Ellenbecker, Michael	II-11
Engelbrecht, Heinz L.	I-57
Ensor, David S.	III-179, IV-141
Evans, John S.	IV-85
Faulkner, George	II-219
Fedarko, William	III-395
Feldman, Paul L.	I-253, III-417
Felix, Larry G.	III-311
Finney, Wright C.	I-287
First, Melvin W.	II-11
Fisher, Gerald L.	IV-433
Frederick, Edward R.	II-27

AUTHOR NAME	PAGE
Fuller, R. A.	IV-319
Furlong, Dale A.	II-247
Gandhi, Kumud	II-89
Garrett, Neil E.	IV-175
Gatti, Arno	III-395
Geffken, John	III-471
Gelfand, Peter	II-247
Gibson, Dwight D.	II-11
Giles, Walter B.	III-291
Gillette, Dale A.	IV-11
Goldfield, Joseph	II-89
Gooch, John P.	I-1, I-39
Gooding, Charles H.	III-219, IV-47
Goren, Simon L.	III-459
Gray, E.	IV-159
Greiner, Gary P.	II-233
Guthner, Gerhard O.	II-333
Guillory, J. L.	III-471
Gutfinger, Chaim	III-243
Gutierrez, Gilbert T.	III-99
Hall, Fred D.	II-287
Harmon, D. L.	III-47, III-193, IV-307
Hart, W. H.	IV-337

AUTHOR NAME	PAGE
Hoenig, Stuart A.	IV-105
Horie, Yuji	IV-391
Hudson, J. A.	II-161
Huisingh, Joellen L.	IV-175
Iinoya, Koichi	II-1, II-99
Isahaya, Fumio	I-453
Ito, Shijo	I-485
Ito, Ryozo	I-297
Kahane, Ronald B.	I-349
Kearns, Michael T.	III-73
Kiang, C. S.	IV-187
Klemm, Hans A.	II-143
Klett, Michael G.	III-379
Knox, Charles	II-133
Kober, Alfred E.	I-113
Kohama, Hiroyuki	III-351
Kousaka, Yasuo	IV-195, IV-231, IV-249
Lace, Robert H.	III-35
Ladd, Kenneth L.	II-219
Laskey, J. W.	IV-159
Lederman, Peter B.	I-79
Lefkowitz, Leonard R.	II-75
Leith, David	II-11

AUTHOR NAME	PAGE
Liscomb, Bill	II-53
Lutz, Stephen J.	II-111
Maartmann, Sten	I-25
Marchant, G. H.	I-39
Markowski, Gregory R.	III-179
Masuda, Senichi	I-241, I-321, II-309
McCain, Joseph D.	III-85, III-311
McCreight, Louis R.	III-395
McDonald, Jack R.	I-307, I-335
McIlvanine, Robert W.	II-319
McKenna, John D.	II-233
McLean, Kenneth J.	I-349, I-409
Meek, Richard L.	IV-465
Melville, B.	II-183
Merritt, Randy L.	III-311
Middleton, Paulette	IV-187
Milde, Helmut I.	I-253
Montgomery, Thomas L.	IV-261
Mori, Yasushige	II-99
Murray, Joel	II-133
Muzio, L. J.	I-131
Mycock, John C.	II-263
Nader, John S.	IV-289

AUTHOR NAME	PAGE
Negrea, Stefan	II-361
Nichols, Grady B.	IV-465
Noso, Shigeyuki	I-485
Okuyama, K.	IV-195, IV-231, IV-249
Ortino, Leonard J.	III-341
Osborn, D. A.	I-179
Osborne, J. Michael	II-197
Ostop, Ronald L.	II-247
Pace, Thompson G.	IV-403
Parker, Richard D.	I-169, III-367
Patten, Whitney	I-421
Patterson, Edward M.	IV-11
Patterson, Ronald G.	I-169, III-405, IV-307
Paul, Phillip H.	III-279
Petersen, Hoegh H.	I-99
Phillips, K. E.	III-471
Piispanen, William	III-303
Pilat, Michael J.	III-61
Piulle, Walter V.	III-323
Pontius, D. H.	I-275, I-361
Pressey, Robert E.	I-179
Pueschel, Rudolf F.	IV-1
Quinn, Margaret	IV-85

AUTHOR NAME	PAGE
Raemhild, Gary A.	III-61
Ramsey, Geddes H.	III-161
Record, Frank A.	IV-377
Rehnberg, Georgia L.	IV-159
Richard, George	IV-25
Riersgard, Phillip	I-169, IV-307
Riley, Clyde E.	I-497
Robinson, Myron	III-415, III-417
Roe, Sheldon F.	III-35
Rolschau, David W.	II-211
Rosales, L. A.	III-113
Rudinger, G.	III-233
Rugg, Don	I-421
Russell, Phillip A.	IV-357
Safriet, Dallas W.	IV-25
Sakai, Kiyoshi	I-485
Sakai, Masakazy	I-485
Sasaki, K.	III-351
Sato, K.	III-351
Sawyer, Charles J.	II-287
Schaeffer, Stratton C.	IV-457
Schliesser, Steven P.	I-205
Schneider, Maria	IV-85

AUTHOR NAME	PAGE
Schoeck, Vincent	II-133
Scholz, Paul D.	III-279
Shackleton, Michael A.	III-441
Shah, N. D.	I-131
Shaw, David T.	III-233
Shortell, Verne	III-303
Smith, Wallace B.	I-361
Sparks, Leslie E.	I-39, I-169, I-275 I-307, I-335 II-297 III-1, III-149, III-162 III-193, IV-417
Spencer, Herbert W.	I-381
Sumi, K.	IV-195, IV-231
Takimoto, Ken	I-297
Tardos, Gabriel I.	III-243
Teixeira, D. P.	I-131
Teller, Aaron J.	II-119
Tennyson, Richard P.	III-35
Throgmorton, James A.	IV-403
Trainer, M. N.	IV-337
Trenholm, Andrew R.	I-497
Trijonis, John C.	IV-391
Turner, James H.	II-45
Tsao, Keh C.	IV-441
Turley, C. David	IV-131

AUTHOR NAME	PAGE
Turton, C. F.	III-99
Wang, James	IV-319
Wang, Roa-Ling	IV-213
Watanabe, S.	III-351
Waters, Michael D.	IV-175
Weant, George E.	IV-63
Webb, Paul R.	I-497
Wegrzyn, J.	III-233
Wertheimer, Alan L.	IV-337
Williams, Roger L.	I-19
Woffinden, George J.	III-179
Yoshida, T.	IV-195, IV-231, IV-249
Yung, Kuang T.	IV-441
Yung, Shui-Chow	III-47, III-149, III-405

ELECTROSTATIC PRECIPITATOR PERFORMANCE

John P. Gooch
Southern Research Institute
2000 Ninth Avenue South
Birmingham, Alabama 35205
U. S. A.

ABSTRACT

Studies of the performance of electrostatic precipitators were conducted at six coal-fired power plant sites. Overall collection efficiency and collection efficiency as a function of particle size were measured with the collecting electrode rappers energized and de-energized. Chemical analyses were obtained on samples of coal, fly ash, and flue gas. In situ and/or laboratory measurements of dust resistivity were performed, and secondary voltage-current relationships were obtained from the precipitator transformer-rectifier sets. The measurements of fractional efficiency with and without electrode rapping indicated that rapping efficiency losses occur primarily for particle diameters greater than 2.0 μm diameter. The performance of the electrostatic precipitators was analyzed using a mathematical model based on the physical principles of the electrostatic precipitation process.

INTRODUCTION

As emission control requirements become more stringent, the detailed analysis of existing particulate control device installations assumes more importance in developing more accurate design techniques and in improving the performance capabilities of existing designs. This paper summarizes the techniques employed and the results obtained from studies of the performance of electrostatic precipitators at six coal-fired power plant sites.[1] The basic objectives of the study were threefold: (1) determination of fractional and overall collection efficiency with and without collection electrode rapping for electrostatic precipitators collecting fly ash under various conditions

(2) utilization of the data in an existing mathematical model of the electrostatic precipitation process (3) enlargement of the data base concerning electrostatic precipitator usage on coal-fired boilers.

The test programs were designed to provide the data necessary to differentiate between previously collected but reentrained particles resulting from electrode rapping and uncollected particles. Measurements with and without electrode rapping were performed with mass trains, inertial impactor systems, an ultrafine extractive system for particle diameters less than 0.20 μm, and a large particle sizing system based on a size selective diluter and an optical particle counter. The installations selected for study were in relatively good mechanical condition and were characterized by high collection efficiencies (at least 99%). Boilers using fuels producing high and low resistivity dusts were selected so that the effect of widely varying dust properties could be examined. Two hot-side units were tested to examine the variations in performance that may occur for precipitators located upstream of the air preheater.

MEASUREMENT TECHNIQUES

Figure 1 illustrates the measurements performed at the six installations. The major portion of the effort was directed toward particulate characterization at the precipitator inlet and outlet using cascade impactors for in situ size determination and mass trains with in-stack filters for total mass loading measurements. A point to plane resistivity probe was used for in situ resistivity measurement at the inlet sampling locations. Since SO_x concentrations in flue gases influence dust resistivity, emphasis was placed on obtaining SO_3-SO_2 concentrations at the operating conditions of the precipitators. The accurate determination of SO_3 concentration requires extreme care because of the potential interference of the relatively large concentrations of SO_2 which accompany the SO_3. The technique employed for this determination is similar to one described by Lisle and Sensenbaugh[2], and it involves the use of a condenser maintained below the sulfuric acid dewpoint, but above the water dewpoint.

Cascade impactor sampling procedures as outlined by Harris[3] were followed during the measurement programs to obtain size distribution data from 0.2 to 10 μm particle diameter. Glass fiber substrates, which were preconditioned in the flue using filtered flue gas to minimize weight gains caused by chemical reaction with the gas, were employed for all outlet impactor runs. Blank impactor runs were conducted using the preconditioned substrate material simultaneously with the real runs to determine a correction factor for weight gain attributable to reaction between the flue gas and the preconditioned substrate material.

Data reduction procedures for the impactor stage weights consisted of the following steps:

(1) Stage weights were corrected for blank weight gains.

MEASUREMENTS	PLANT 1	PLANT 2	PLANT 3	PLANT 4	PLANT 5	PLANT 6
MASS TRAIN	▲	▲	▲[1]	▲	▲	▲
IMPACTORS	▲	▲	▲	▲	▲	▲
ULTRAFINE SYSTEM	▲	▲	▲	▲	▲	▲
LARGE PARTICLE SYSTEM	▲	▲	▲	▲	▲	▲
V-I CURVES	▲	▲	▲	▲[2]	▲	▲
ACCELEROMETER		▲	▲		▲	
IN SITU RESISTIVITY	▲	▲	▲	▲	▲	
GAS ANALYSIS	▲	▲	▲	▲	▲	▲
VELOCITY DISTRIBUTION		▲	▲		▲[3]	▲[4]
LEAR SIEGLER	▲	▲	▲	▲	▲	
COAL ANALYSIS	▲	▲	▲	▲	▲	▲
ASH ANALYSIS	▲	▲	▲	▲	▲	▲

1. Mass train measurement at outlet only.
2. V-I curves obtained one month prior to EPRI test.
3. Obtained by vendor before start up.
4. Obtained by utility personnel.

Figure 1. Types of data obtained.

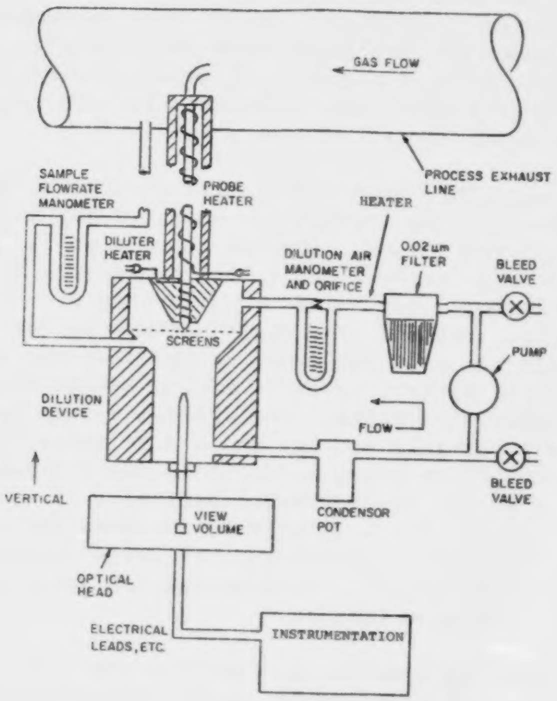
GAS FLOW
PROCESS EXHAUST LINE
SAMPLE FLOWRATE MANOMETER
PROBE HEATER
HEATER
DILUTER HEATER
DILUTION AIR MANOMETER AND ORIFICE
0.02 um FILTER
BLEED VALVE
SCREENS
PUMP
DILUTION DEVICE
FLOW
BLEED VALVE
VERTICAL
VIEW VOLUME
CONDENSOR POT
OPTICAL HEAD
ELECTRICAL LEADS, ETC.
INSTRUMENTATION

Figure 2. Large particle sizing system.

(2) Cut points for the individual stages for each impactor were based on calibration studies conducted in the laboratory using polystyrene latex beads for sizes smaller than 2.0 μm diameter and ammonium flourescein particles for particle diameters from 2.0 to 8.0 μm diameter. Glass fiber substrates were in place for the calibration studies.

(3) Impactor runs are arranged in groups in an appropriate manner for the individual test series.

(4) The data are supplied as input to a computer program which calculates size distributions and fractional efficiencies. (see reference 4)

A Thermo-Systems, Inc. Model 3030 Electrical Aerosol Analyzer (EAA) was used sequentially at single sampling points at the inlet and outlet sampling location to determine concentration vs size information in the diameter range of 0.01 to 0.30 μm. The operating principle of the EAA is based on placing a known charge on the particles and then precipitating the particles under closely controlled conditions. Size selectivity is obtained by varying the electric field in the precipitator section of the instrument. Charged particle mobility is monotonically related to particle size in the operating regime of the mobility analyzer. A dilution system is required because the instrumentation cannot tolerate raw flue gases as sampling streams nor cope with particle concentrations encountered in flue gases. A detailed discussion of the dilution system and data reduction techniques for the mobility analyzer-dilution system is available in reference 5.

Conventional sampling methods with mass trains and impactor systems require long integration times which are unsuited for examining 1 to 5 second duration transient events, such as rapping puffs, on a real time basis. In order to more clearly define the mechanisms by which reentrained dust emissions occur, time resolved data are required on the particulate concentrations and size distributions across typical portions of precipitator exit planes. Therefore, a decision was made to construct and employ a real-time optical particle sizing system to obtain supporting data for the inertial systems. The optical system consists of a modified ambient air particle counter and a size selective diluter. The diluter, as a result of the steep gradient in the fly ash size distributions on a number basis, dilutes small particles in the sample gas streams by large factors, but a relatively confined and undiluted stream containing the lower concentration of large particles is passed directly to the particle sensor. This system has been designated the Large Particle Sizing System (LPSS).[1]

Under ideal sampling conditions, the LPSS would be used as illustrated in Figure 2, with the aerosol sample extracted through a vertical probe from below the outlet duct with a single 90° bend between the sampling point and the particle sensor. In this configuration, the system could conceivably be calibrated to give absolute concentrations. For most of the plant locations discussed in this paper, the ideal configuration was not practical, and a secondary extractive system as illustrated in Figure 3 was constructed. This sampling system provided information on relative concentrations of various particle sizes between and during rapping puffs, but it did not provide quantitative concentration data because of the uncertainties in the probe losses and in the degree to which the secondary sample represented the average concentration in the high flow rate probe.

The use of inertial sampling systems (mass trains and impactors) for the measurement of rapping reentrainment requires a sampling strategy which will differentiate between steady-state particulate emissions and those which result from electrode rapping. At the first installation tested in this research program, the strategy employed consisted of sampling on subsequent days with the rapping system energized and subsequently deenergized while an attempt was made to maintain boiler operating parameters as constant as was practical. The precipitator was characterized by high collection efficiency (99.9%), which required extended sampling times to obtain meaningful mass measurements. However, it was found that the sensitivity of the electrostatic precipitator to changes in resistivity and other process variables could mask the differences in total emissions caused by energizing and deenergizing the rappers.

In order to minimize this difficulty, a revised sampling strategy was adopted for the remaining installations. The revised strategy consisted of sampling with mass trains and impactors dedicated to designated "rap" and"no-rap" periods. Data with a rapping system energized and deenergized were obtained by traversing selected ports with dedicated sampling systems in subsequent periods on the same day. This procedure, while necessarily distorting the frequency of the rapping program being examined, minimized the effects of resistivity and other process variable changes.

The use of the alternating sampling strategy leads to at least three possible procedures for calculating the fraction of losses attributable to rapping reentrainment. The first procedure consists of the calculation of the ratio of emissions obtained with rappers off to rappers on and subtracting from unity. The emissions data utilized in this procedure were obtained during the time in which alternating sampling periods for rap and no rap sampling trains were employed. The second procedure consists of subtracting the mass emissions obtained with the rappers deenergized from those of the previous day with normal rapping, and dividing by the emissions obtained with the rappers operating normally. The data obtained from the "rap" period will be approximately equal to that obtained during other test periods in which the rappers are operating in a normal fashion if: (1) the distortion of the rapping frequency does not significantly influence emissions during the "rap" period and (2) there are no other variations in parameters affecting the precipitator performance.

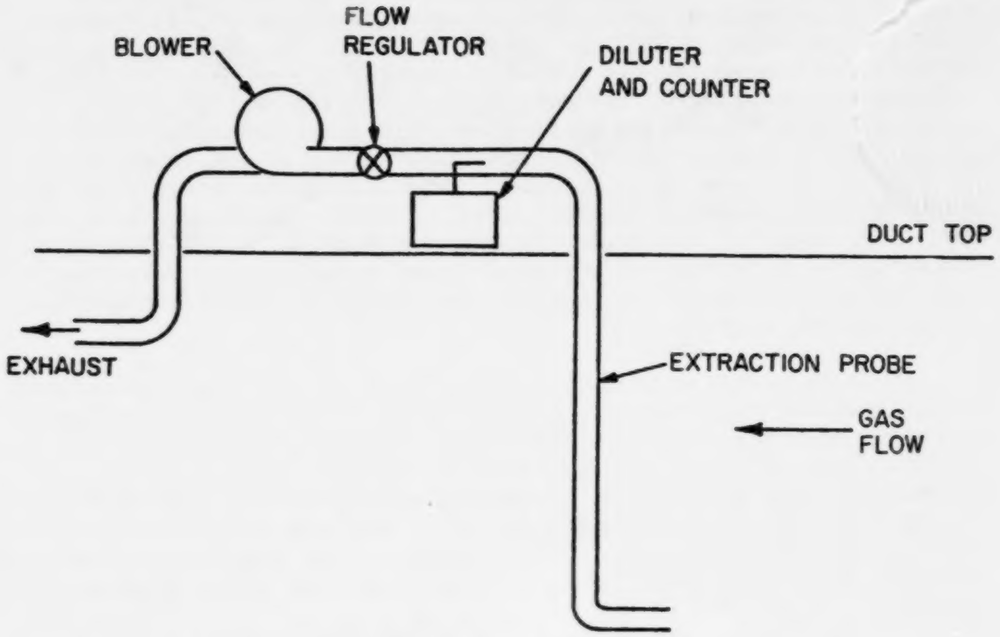
FLOW REGULATOR
BLOWER
DILUTER AND COUNTER
DUCT TOP
EXHAUST
EXTRACTION PROBE
GAS FLOW

Figure 3. Extractive Sampling System.

A third possible procedure consists of the use of a weighted time average emission during the rap-no rap periods as an approximation to the normal emission rates, subtracting the no rap emission from the weighted time average, and dividing the difference by the weighted time average to obtain the fraction of emissions attributable to rapping. This procedure provides an estimate of rapping reentrainment with the effective intervals which result from the alternating sampling periods. All of the above calculation procedures are used when applicable to analyze emissions data from the six installations tested.

RESULTS

In terms of location in the power plant system and type of fuel burned in the boiler, the installations studied in this program may be classified as follows:

Plants 1 and 5 -	Cold-side ESP's collecting ash from low-sulfur Western coals
Plant 6	Hot-side ESP collecting ash from low sulfur Western coal
Plant 4	Hot-side ESP collecting ash from low sulfur Eastern coal
Plant 2 and 3 -	Cold-side ESP's collecting ash from high sulfur Eastern coals

Table 1 summarizes the important design parameters and the results obtained for the six installations. A mechanical collector precedes the precipitator at Plant 1 and Plant 3. The installations were characterized by relatively high overall mass efficiency. Rapping losses as a percentage of total mass emission ranged from over 80% for one of the hot-side units to 30% for the cold-side units. The high rapping losses at Plant 4 are probably due both to reduced dust adhesivity at high temperatures and the relatively short rapping intervals.

Table 2 lists the rapping intervals for each field at the various installations. Also shown are the effective rapping intervals resulting from the alternating sampling schedules which were used to obtain the rap-no rap data. To the extent allowed by process variations, the range of emissions attributable to rapping should be established by the calculations using (rap-no rap) and (normal-no rap) data sets. However, the time weighted average (TWA) calculation is of interest in that it indicates the change in rapping emissions caused by the effective increase in time intervals between raps. With the exception of the normal current density data set at Plant 2, the time weighted average calculation gives the lowest percentage emissions due to rapping of the three calculation methods. Table 3 provides typical flue gas and fly ash compositions obtained at the test sites.

Table 1. SUMMARY OF RESULTS FROM EPRI TESTS

Plant	1	2	3	4	5	6
Number of Electrical Fields in Direction of Gas Flow	6	3	4	4	5	6
Plate-to-Plate Spacing, cm	30.48	27.94	25.4	22.86	24.76	22.86
Emitting Electrode Design	Mast with Square Twisted Wires	Mast with Square Twisted Wires	Rigid Barbed Wires	Hanging Round Wires	Electrode Frame With Spiral Wires	Hanging Round Wires
Rapper Design	Drop Hammer	Drop Hammer	Tumbling Hammers	Magnetic Drop Hammer	Tumbling Hammers	Magnetic Impulse Hammers
Portion of ESP Tested	Total	1/2	1/2	1/2	1/6	1/16
Boiler Load During Test, MW	128	160	122	271	508	800
Gas Flow During Test, am^3/sec	330.2	155.2	117.2	203.9	149.4	126.8
Temperature During Test, °C	152.2	155	157.2	321.1	186.1	358.9
SCA During Test, m^2/(m^3/sec)	113.5	47.6	50.4	76.8	117.9	55.4
Measured Efficiency,%	99.92	99.55	99.83	99.64	99.85	98.98
Dust Resistivity at Operating Temp,Ω-cm	1.4×10^{11}	1.7×10^{10}	2×10^{10}	3.2×10^{10}	4.6×10^{11}	1.5×10^{9}[b]
% of Mass Emissions Attributed to Rapping[a]	31	65-33	30	85	36-29	63-44

[a] Indicating range of values from two methods of calculation.

[b] Laboratory measurement.

Table 2. SUMMARY OF REENTRAINMENT RESULTS

Plant	1	2			3		4		5		6	
		Raps/Hr										
			Rap - No-Rap									
				One-Half	Raps/Hr		Raps/Hr		Raps/Hr		Raps /73	
Field	Raps/Hr Normal	Normal	Normal Current Density	Normal Current Density	Normal	Rap-No-Rap	Normal	Rap-No-Rap	Normal	Rap-No-Rap	Min Normal	Raps/Hr Rap-No-Rap
1	8	10	4.29	3.75	10	1.67	30-60	12.5-25	10	4.17	8	2.74
2	6	6	2.57	2.25	10	1.67	30-60	12.5-25	5	2.08	8	2.74
3	3	1	0.43	0.38	5	0.83	30	12.5	5	2.08	3	1.03
4	3	-			5	0.83	30	12.5	2	0.83	3	1.03
5	1	-			-		-	-	1	0.42	1	0.34
6	1	-			-		-	-	-	-	1	0.34
Rapping Losses, % of Emissions												
Rap-No Rap/Rap	-		65	55	30		85		29		44	
Normal-No Rap/ Normal	31		33	62	-		85		36		63	
T.W.A.-No Rap/ T.W.A.	-		45	38	16		71		18		24	

Figure 4 shows the time variations over the test period at Plant 1 in boiler load, precipitator power, dust resistivity and relative particle concentrations in two size bands (0.6 to 1.8 μm and 1.5 to 3 μm). August 5 and 6 were "normal" rapper operation test periods, whereas August 7 and 8 were "no-rap" test periods. It is readily apparent that, on August 7, changes in variables other than rapper energization caused exit particulate concentration changes which masked the effect of rapping system deenergization. The LPSS system, however, was able to detect rapping puffs, as described below.

Figures 5 and 6 show the number of 6-12 and 12-24 μm diameter particles counted in 10 minute intervals through one day of testing with rapping and one day of testing without rapping, respectively. Cyclic concentration variations with a period of one hour were expected when the rappers were on and are fairly apparent in the data shown in Figure 5. No such cyclic pattern is apparent in the data shown in Figure 6 which were obtained with the rappers deenergized. Note the obvious effect of losing power to one of the T.R. sets. The average counting rate was much reduced in the 6-12 and 12-24 μm channels with the rappers turned off as can be seen by comparison of Figures 5 and 6.

As indicated previously, the attempt to determine rapping losses at Plant 1 by comparison of mass train and impactor data sets from normal and no rap periods was not successful due to other factors influencing outlet emissions. However, an estimate of the contribution of rapping losses to total mass emissions was made from data from the LPSS and outlet impactor systems. The estimate is that 30% of total outlet mass emission during normal rapper operation can be attributed to rapping reentrainment. Figure 7 shows the rap-no rap data for the EAA system and the rap and no-rap impactor derived efficiencies. The estimated no-rap efficiencies are based on the data from the LPSS system and these are subject to large uncertainties because of the poor counting statistics for the larger particles coupled with the limited time span over which the data were taken. Fifty percent confidence intervals are shown for the impactor and EAA data. Even with the existence of the indicated uncertainties, it is apparent that very high collection efficiencies are achieved in the particle diameter range 0.05 to 20.0 μm. The minimum collection efficiency is approximately 99.2% at 0.20 μm diameter.

The alternating sampling strategy with impactors and mass trains was successfully employed at Plant 2 and subsequent test sites to differentiate between reentrainment resulting from rapping and steady-state emissions. Figure 8 presents rap and no rap data from Plant 2 from the EAA and the impactor sampling system. The large error bars (50% confidence intervals) on data obtained from the ultrafine particle system are a reflection of difficulties encountered with condensation of sulfuric acid, which created an interferring aerosol in the ultrafine size range. The data were screened and those results which were felt to be non-representative were discarded. It is apparent that

Table 3. TYPICAL FLUE GAS AND ASH COMPOSITIONS

Plant	1	2	3	4	5	6
Date	8/7/75	1/16/76	2/25/76	4/28/76	10/6/76	1/31/77
Flue Gas						
Temp., °C	164	154	155	333	106	346
SO_2, ppm by vol.	282	3200	2430	750	470	355
SO_3, ppm by vol.	6.5	12	8.3	2.7	<0.5	<0.5
H_2O, vol. %	8.2	7.2	8.2	7.4	8.7	9.6
Fly Ash						
Ash Source	Hopper 1	High Vol. Sample	High Vol. Sample	High Vol. Sample	High Vol. Sample	High Vol. Sample
Date	8/7/75	1/15/76	3/2/76	4/27/76	10/5 & 10/6/76	1/31/77
Wt. % of[1]						
Li_2O	0.02	0.02	0.03	0.04	0.02	0.013
Na_2O	0.[illegible]	0.54	0.67	0.43	1.38	1.52
K_2O	1.7[illegible]	2.49	2.12	3.5	0.54	1.4
MgO	3.61	0.95	1.00	1.3	1.1	1.8
CaO	8.71	4.73	4.95	1.1	5.8	6.0
Fe_2O_3	5.49	22.72	13.13	7.2	6.1	5.0
Al_2O_3	24.64	18.52	21.76	28.4	13.2	24.3
SiO_2	50.55	45.69	50.23	53.8	70.8	57.6
TiO_2	1.22	1.45	1.96	1.8	0.87	2.1
P_2O_5	0.5[illegible]	0.30	0.78	0.23	0.05	0.32
SO_3	0.[illegible]	2.77	2.29	0.50	0.50	0.54
LOI[2]	0.61	5.72	10.92	3.5	1.0	0.11

[1] Chemical analyses obtained from ignited samples

[2] Loss on ignition

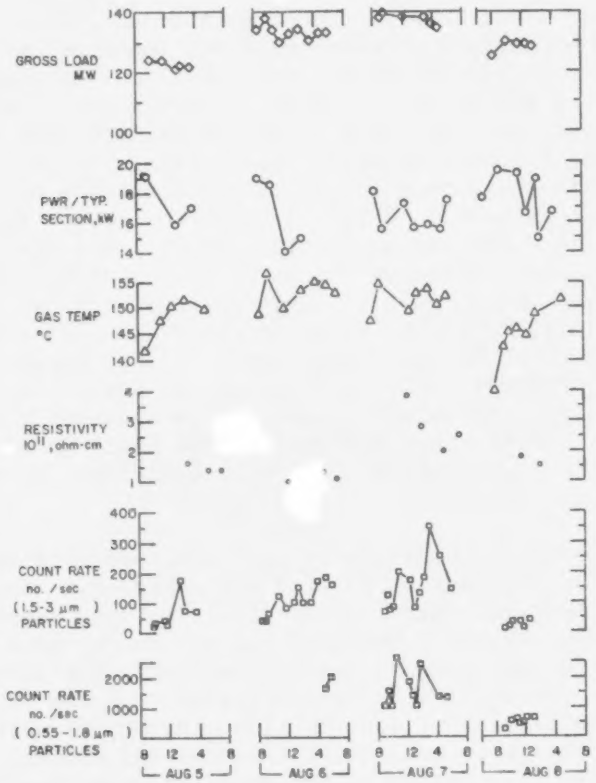

Figure 4. Events for test period Plant 1.

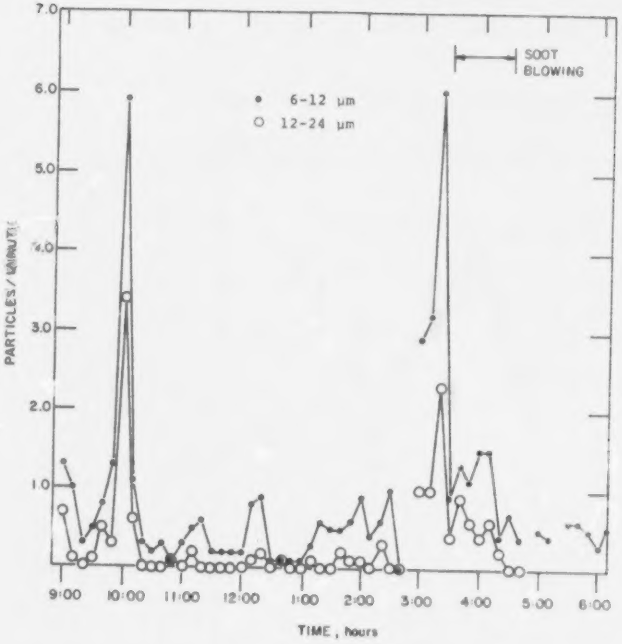

Figure 5. Particles per minute vs. time for large particle system on August 6, 1975 - rappers on (Plant 1).

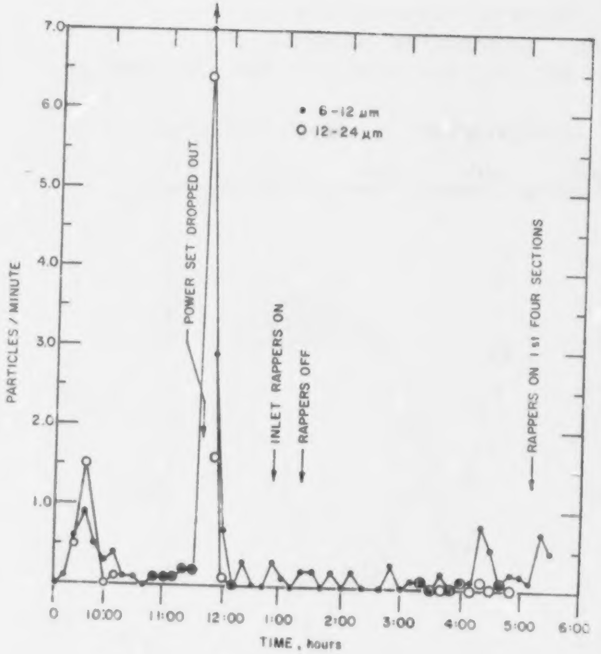

Figure 6. Particles per minute vs. time for large particle system on August 7, 1975 - rappers off (Plant 1).

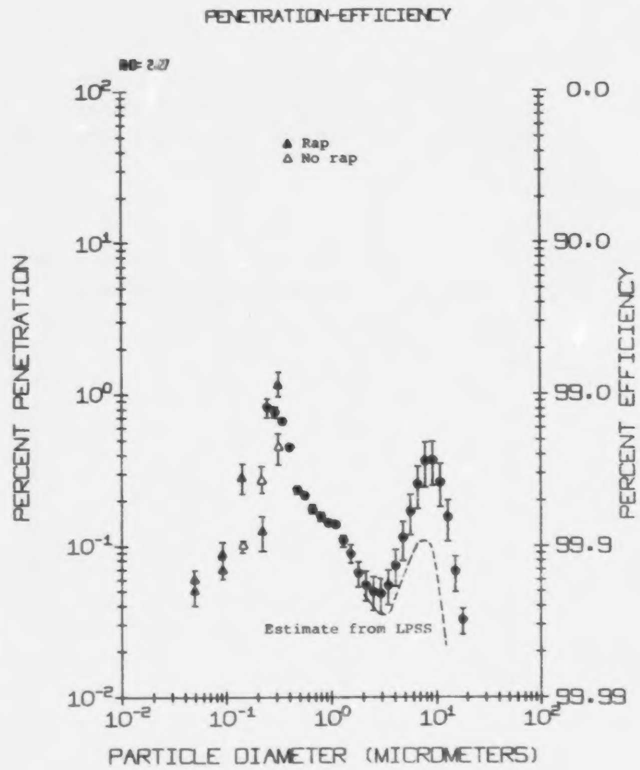

Figure 7. Plant 1 rap-no rap fractional efficiency including ultrafine and impactor measurements.

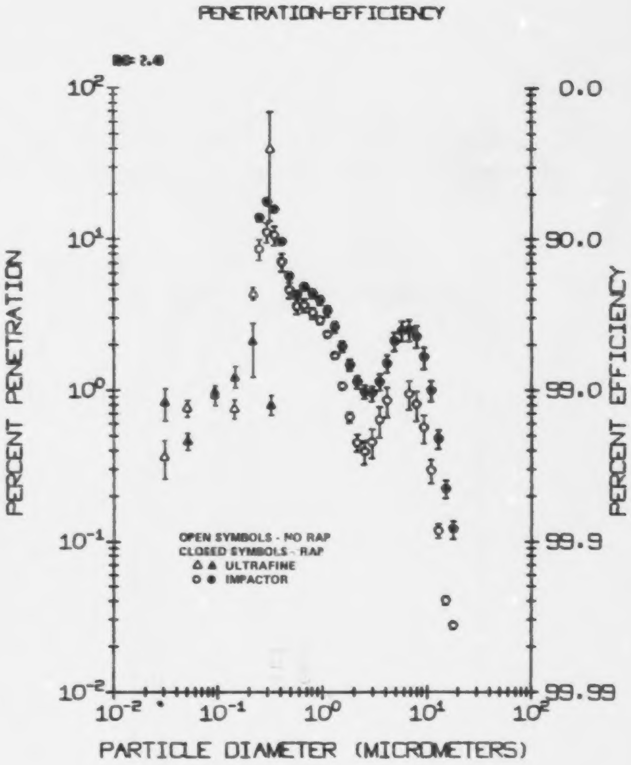

Figure 8. Rap-no rap ultrafine and impactor fractional efficiency. Normal current density, Plant 2.

rapping losses become significant only for particle diameters larger than 1 to 2 µm. The presence of significant large particle emissions in the absence of rapping is also indicated by Figure 8, and was confirmed by data obtained from the LPSS. These emissions apparently resulted from sparking or voluntary reentrainment. Plant 2 was operating with a high sulfur Eastern coal which produced a fly ash with low electrical resistivity.

Figure 9 illustrates the large particle losses (on a relative basis) measured at Plant 4, which is a hot-side installation, using the impactor and ultrafine sampling systems with the rap-no rap sampling sequence. The data obtained with normal rapper operation (not shown) show reasonable agreement for sizes greather than 1.0 µm diameter, indicating the alternating sampling strategy did not significantly distort the results obtained. As with the previously discussed data, the results indicate that rapping reentrainment does not cause a significant change in fine particle emissions.

Comparisons were made between measured collection efficiencies as a function of particle size and those obtained from a mathematical simulation of the precipitators using a model developed at Southern Research Institute under the sponsorship of the Environmental Protection Agency.[6] The model predicted with reasonable accuracy the relative changes in fine particle collection efficiency resulting from resistivity changes and the resultant input power variations. The comparisons indicated that the theoretically calculated collection efficiencies in the fine particle size range were lower than the measured values as a result of certain unmodeled effects. Significant large particle penetrations resulting from sporadic events in the absence of rapping which exceeded theoretical predictions of penetration were also observed. Empirical correction factors were incorporated into the model to account for the under-prediction of fine particle collection efficiencies and to increase the value of the model for design purposes until adequate theoretical modeling of fine particle collection efficiencies under field conditions is accomplished.

Rapping reentrainment losses were represented in the model using an average apparent size distribution of a rapping puff and an empirical relationship between the dust removal rate in the last field and emissions attributable to rapping. Figure 10 contains rapping emissions for the six installations as a function of the dust calculated to have been removed in the last field of the precipitator. Note the effect of current reduction at Plant 2. These data suggest a correlation between rapping losses and dust removal rate in the last field. Data for the two hot-side installations tested show higher rapping losses, which is consistent with the reduced dust adhesivity which is expected at higher temperatures. Obviously, additional data under various conditions are required to determine if this approach or a variation thereof may be used to estimate rapping losses under a range of operating conditions.[1]

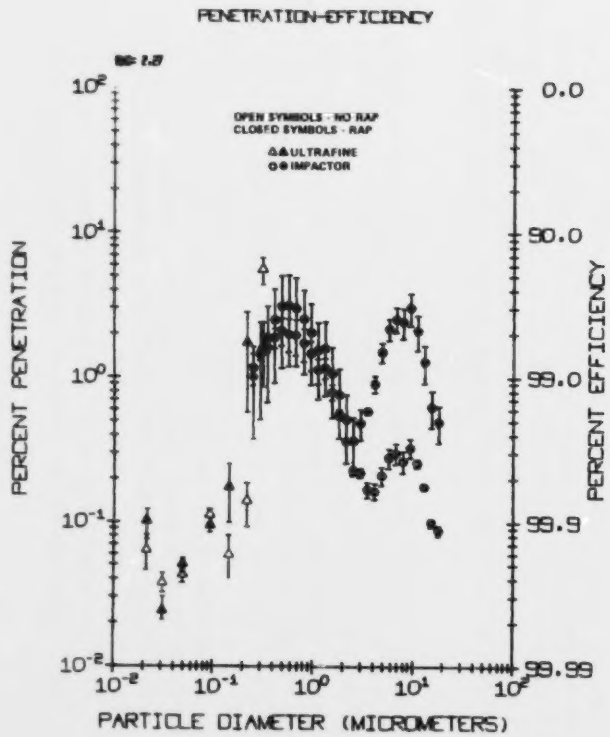

Figure 9. Ultrafine and impactor rap-no rap fractional efficiencies, Duct B1., Plant No. 4, with 50% confidence intervals.

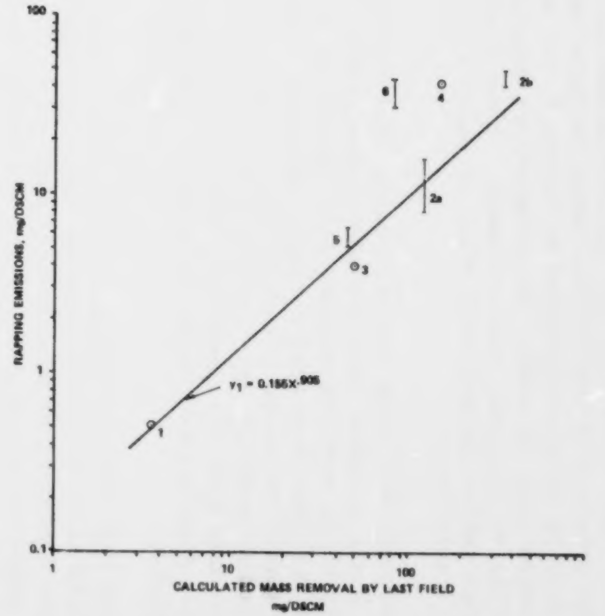

Figure 10. Rapping emissions vs. dust removal by last field (Plant 6 and Plant 4 are hot-side installations).

Figure 11 illustrates the manner in which the empirical correction factors and the representation of rapping change the fractional efficiency prediction of the model for the normal current density test series at Plant 2. The solid line illustrates the model's prediction of efficiency as a function of particle size using only theoretical relationships, the operating parameters for the test conditions, and the precipitator geometry as input data. The open circles give the model prediction with the same input data, but with the inclusion of empirical relationships concerning fine particle collection, gas velocity non uniformity, gas by-passage, and rapping reentrainment. It is apparent that the agreement between measured and predicted results under field conditions is improved by the use of the empirical relationships. In general, it is expected that the rapping puff correlation will tend to under predict large particle emission because the correlation does not represent the large particle penetrations which were observed due to sporadic events other than rapping.

CONCLUSION

Measurements of fractional efficiency with and without electrode rapping at full scale precipitator installations show that rapping efficiency losses occur primarily for particle diameters greater than 2.0 μm diameter. The largest rapping losses were measured on hot-side installations. Mass emission data suggest a correlation, for the installations tested in this research program, between the dust removal rate in the last field of the precipitator and the emissions due to rapping. The electrostatic precipitator with the highest overall mass efficiency exhibited a minimum collection efficiency of 99.2% at 0.20 μm diameter.

Comparisons were made between measured and calculated fractional and overall collection efficiencies using a theoretical model augmented by empirical relationships based on the field test data. The comparisons indicated that the empirical factors improved the capability of the model to simulate the operation of full-scale electrostatic precipitators under field conditions.

ACKNOWLEDGMENTS

The principal financial support for the work discussed in this paper was provided by the Electric Power Research Institute. The cooperation and financial assistance of the Industrial Environmental Research Laboratory, Research Triangle Park, N.C., of the Environmental Protection Agency is also gratefully acknowledged.

The field measurements were performed by members of the Environmental Engineering Group at Southern Research Institute.

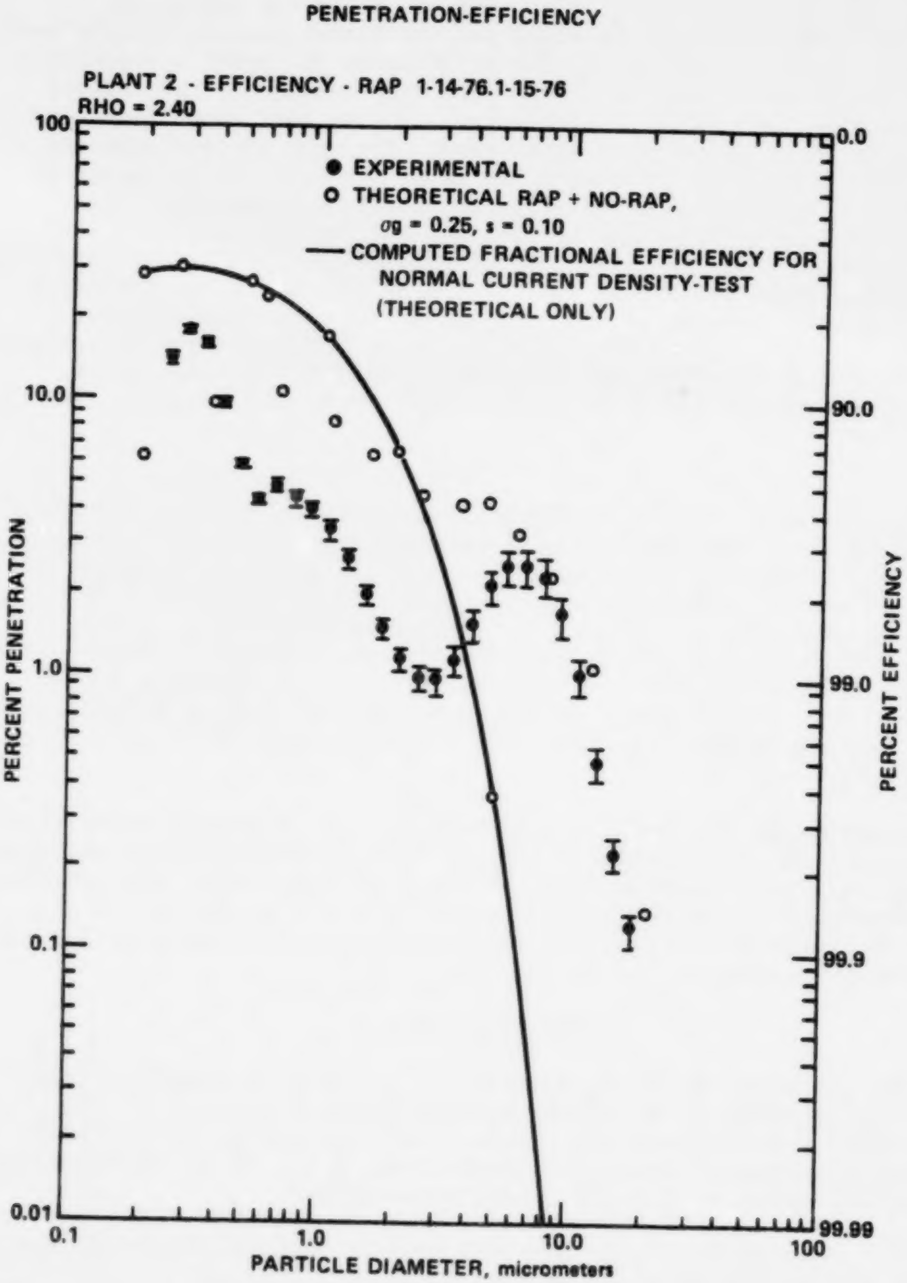

Figure 11. Comparison of measured and computed efficiencies from Plant 2 normal current density series.

REFERENCES

1. Gooch, John P., and Guillaume H. Marchant, Jr. "Electrostatic Precipitator Rapping Reentrainment and Computer Model Studies." Final Draft Report by Southern Research Institute to the Electric Power Research Institute under EPRI Contract RP413-1. August 1977.

2. Lisle, E. S., and J. D. Sensenbaugh. Combustion 36(1), 12 (1965).

3. Harris, D. Bruce. "Procedures for Cascade Impactor Calibration and Operation in Process Streams." Environmental Protection Technology Series, EPA-600/2-77-004. January 1977.

4. Johnson, J., G. I. Clinard, L. G. Felix, and J. D. McCain. "A Computer-Based Cascade Impactor Data Reduction System." U. S. Environmental Protection Agency, Research Triangle Park, N. C. February 1978.

5. Smith, W. B., K. M. Cushing, and J. D. McCain. "Procedures Manual for Electrostatic Precipitator Evaluation." EPA-600/7-77-059. June 1977.

6. Gooch, John P., J. R. McDonald, and S. Oglesby, Jr. "A Mathematical Model of Electrostatic Precipitation." EPA-650/2-75-037, U. S. Environmental Protection Agency, Research Triangle Park, N. C. 1975.

SPECIFICATIONS OF A RELIABLE PRECIPITATOR

Roger L. Williams
Manager Pre-Contract Engineering
Utility Division
P.O. Box 1500
Somerville, New Jersey 08876

Precipitators have conservatism built in by a variety of methods. Excess is added onto operating parameters for many reasons.

This excess reflects in the design and may cause conditions that do not give the desired operation. It may create difficulities during normal and low boiler loads.

There are more intelligent ways of adding conservatism. These will provide a more cost conscious and reliable precipitator.

Let us look at emission requirements and how they affect the efficiency size and cost of the precipitator. The Federal and State, present and future requirements, are as follows:

For particulate, Emission Weight Regulations
Federal: 0.1 Pounds per Million BTU
State: 0.05? Pounds per Million BTU
with a possible future Federal requirement of 0.03#/MBTU

For Particulate, Opacity Regulations
Federal: 20%
State: 10-30 to 40%
with a possible future Federal requirement of 10% opacity

Fine Particulate Regulations
Federal: None at Present
State: New Mexico - 0.02 pounds per million BTU
For particles less than 2 microns diameter
There are some possible future changes although unidentified at this time.

To relate these requirements into efficiency, we take a typical proximate analysis and select the minimum heating value and the maximum ash.

Proximate Analysis	
Fixed Carbon	24.67%
Volatile Matter	29.44
Ash	14.19
Moisture	31.41
Heating Value	6,635 BTU/LB

From this we can calculate the input heating value, using 80% carryover of boiler ash.

Efficiency Calculations For Emission Weight Requirement

Ash Content	14.19%
Heating Value	6,635 BTU/LB

$$\frac{1\text{x}10^6 \text{ BTU } (.14 \text{ lb of Ash/lb. of Coal } (0.8)}{6{,}635 \text{ BTU/lb. of Coal}}$$

$$=17.1 \text{ lb. of Ash/Million BTU}$$

Using the input heating value, and the required output of 0.1#/MBTU, we see that a maximum efficiency of 99.42% is required to meet 0.1#/MBTU

Efficiency Calculation For Emission Weight Regulation

To achieve 0.1 lbs. per million BTU

$$\text{Efficiency} = \frac{\text{Inlet - Outlet}}{\text{Inlet}}$$

$$= \frac{17.1 - 0.1}{17.1}$$

$$= 99.42\%$$

For an opacity we can calculate the outlet particulate required with this equation:

Opacity Equation - $W = \frac{-K p \ln (1/1_o)}{L}$

W = particulate concentration

L = diameter of plume

$1/1_o$ = light transmittance

p = average particle density

K = specific particulate volume/extinction coefficient ratio

To calculate an outlet for 20% opacity using a stack diamter of 25 ft. a particulate density of 2.2 gr/cc and K=0.5 based on data from similar ashes, we calculate 0.014 gr/ACF is needed.

Opacity Calculation Example

Given: 20% opacity required
stack diameter - 7.62 meters (25 feet)
density - 2.2 grams/cc
$K = 0.5$

$$W = \frac{-\ 2.2\ (0.5)\ (\mathrm{LN}(1-0.2))}{7.62}$$

= 0.032 grams/cubic meter
= 0.014 grains/cubic foot

Now using a gas volume of 2,363,000 ACFM our inlet concentration is 5.84 gr/ACF, and using 0.014 gr/ACF outlet, we see that an efficiency of 99.76% is required to meet 20% opacity with beforementioned conditions.

Efficiency Calculations for 20% Opacity

Gas Volume - 2,363,000 ACFM

Inlet Concentration - 5.84 Grains/ACF

$$\text{Efficiency} = \frac{\text{Inlet-Outlet}}{\text{Inlet}}$$

$$\frac{5.84-0.014}{5.84}$$

$$= 99.76\%$$

Particle size plays a major role in determining the size of the precipitator. Small particles encountered on existing precipitator, scrubber and mechanical collector backfits, from cyclone boilers and from some western coals. These are more difficult to collect and cause higher opacity readings.

A typical fractional efficiency curve shows as the particle size decrease from 10μ to 0.5μ, the efficiency of the precipitator drops off drastically, requiring more plate area to maintain an efficiency.

A typical precipitator particle size distribution curve shows that for an outlet of 2μ or less, will include 70% of a typical outlet by weight.

Thus we can calculate the allowable outlet from the following values which gives us a total allowable emission required less than 2μ in diameter of 0.286#/MBTU.

Efficiency Calculation for Fine Particulate Regulation

Given: 70% by Weight of Particles Less Than 2 Microns in Diameter

Allowable Emissions of Fine Particles
0.02 lbs./million BTU

0.7 x Total Allowable Emission = 0.02

Total Allowable Emissions
= 0.0286 lbs./million BTU

From this we can calculate the efficiency required to meet this fine particulate regulation and see that 99.83% is required.

Efficiency Calculation For Fine Particulate Regulation

$$\text{Efficiency} = \frac{\text{Inlet-Outlet}}{\text{Inlet}}$$

$$\frac{17.1-0.029}{17.1}$$

$$= 99.83\%$$

Thus the relative efficiency requirements for an 0.03#/MBTU requires a 99.83% efficiency, and is the same as the fine particulate regulation. A 10% opacity requires a 99.89% efficiency.

Relative Efficiency Requirements

Goal	Efficiency
0.1 lbs/million BTU	99.42%
20% Opacity	99.76%
Fine Particulate	99.83%
5% Opacity (clear stack)	99.94%

The relative costs or plate area to meet these regulations with 0.1#/MBTU as the base of 1.0, shows us that an increase of 50% is required to meet 20% opacity, 75% for fine particulate and 0.03#/MBTU and 120% for a clear stack. Thus what may look like a small change in regulation, affects the size and cost drastically.

Another way of adding conservatism is by a safety factor in the ash carryover.

Safety Factors - Ash Carryover

Assuming 100% Carryover

$$\text{Required Efficiency} = \frac{21.4-0.1}{21.14} = 99.53\%$$

Typical Ash Carryover in lieu of a typical 80%

Given: 14.19% Ash
6,635 BTU/LB

$$\text{Required Efficiency} = \frac{17.1-0.1}{17.1} = 99.42\%$$

100% carryover in lieu of a typical 80% we see an equivalent excess area of 8.3% is added.

The excess area added by these methods creates an overdesign and is costly, but will not create any operating difficulities.

Other methods of overdesign are overspecifying critical parameters. These may cause operating difficulities.

One of these is a safety factor on the gas volume. It is not uncommon to have 20% or even 40% added to the rated volume. A small factor should be added for inleakage and pitot tube correction where necessary. With this excess volume, dust dropout is a major factor for flue structural integrity and for ash handling problems. Another factor is poor gas distribution.

These factors are important in a precipitator that is not base loaded or is cycled. Precipitator and flue design velocities are based on spec. volumes and are designed to minimize dropout down to 75% volume. If 20% was added to the volume, the normal load would be near where dropout occurs. At lower loads dropout would be a certainty. When coming up to normal loads ash is swept into the hoppers and may build up to a point to short out discharge electrodes.

Another overdesign is the safety factor added on the fuel specification.

The effect of changing the fuel specification to adopt to future fuel changes can add excess area as can the ash carryover, but is not nearly as predictable. A few years ago when everyone was using an eastern or mid-western bituminous coal, reducing the sulfur content could provide a reasonable prediction of future fuel changes.

With the advent of Western, Eastern Kentucky, Texas and foreign low sulfur coals and lignites and with the hot precipitator coming along, critical elements like ash constituents play a major role in determining the collectibility of the ash. Identifying ash constituents has become a complex problem that most purchasers cannot address. It requires extensive core samples of a mine to find the range of elements and test burns to find the range of ash constituents. As a precipitator manufacturer, we are able to address this problem. When a fuel spec. is provided to design a precipitator, we should know how this spec was compiled. If the raw fuel data were supplied with the specifications, a more reliable precipitator can be designed.

A more precise way to build in conservatism is to quantify you needs, then determine the amount of conservatism required and incorporate this as a percent of the required size.

The design, purchase and operation of a precipitator is a joint venture. Increasing the level of communication between the owner, the engineer and the precipitator supplier, before the specification is released, will provide a more reliable precipitator.

EXPERIENCE WITH COLD SIDE PRECIPITATORS ON LOW SULFUR COALS

Sten Maartmann
AB Svenska Fläktfabriken
Industrial Division
S-351 87 Växjö, Sweden

ABSTRACT

Dust from low-sulfur coals is generally considered difficult to collect in electrostatic precipitators. Fläkt experience with pilot and full-scale cold side installations on low sulfur coal boilers in U.S., Australia and Canada is reviewed. This experience demonstrates that dust from low sulfur coal is less difficult to collect on the cold side than present common knowledge indicates. Several design parameters are discussed including ash composition and gas temperature.

INTRODUCTION

Low sulfur coals, i.e. coals with sulfur contents below about 1 % are used for power generation in many parts of the world. Australia, Canada and the U.S. have major deposits which are mainly used locally but in part exported.

The energy crisis, the competitive price of coal compared to oil and the interest in limiting SO_2 emissions have resulted in an increased use of low sulfur coals in both Europe and Japan. Coals from the above mentioned countries as well as others already have been or will be fired in existing or new units.

Dust from low sulfur coals is considered diffucult to collect in ESP's particularly on the cold side. One purpose of this paper is to show that this general statement is debateable.

Fläkt, a manufacturer of ESP's for more than 35 years, became involved in the collection of dust from low-sulfur coals at an early date. It has been actively engaged in such projects on pilot and full-scale plants in Australia since the mid-1950s. During the 1970s Fläkt installed a number of plants for the collection of this type of dust in Canada and the U.S.

DEFINITIONS AND CLARIFICATIONS

Efficiency tests have been performed using equipment comparable to the EPA dry train. Most of the pilot test results have been made available to ESP suppliers in test reports issued together with specifications for full-scale plants. Tests have been performed mainly by the end user or an independent testing institution appointed by the end user. Fläkt has performed some of the full-scale tests.

Resistivity values refer to measurements performed in the Fläkt laboratory in Växjö, Sweden on dust samples obtained through collection in an ESP or by isokinetic sampling. A plane to plane apparatus is used with moist air adjusted to the actual water dew point at the plant.

w_k is defined through the generalized Deutsch formula

$$\text{Efficiency} = 1 - e^{-\left(\frac{w_k \cdot SCA}{100}\right)^{0.5}}$$

Where w_k = total migration veloctiy in cm/sec

SCA = specific collecting area in $m^2/(m^3/sec)$

This formula, originally presented by Matts and Öhnfeldt[1] has since been recognized as describing the relationship between SCA and efficiency better than the Deutsch formula. When using an exponent of 1 instead of 0.5 the Deutsch formula appears and w_k is changed to w. It should be observed that there are distinct similarities in the trend curves in diagrams based on the Southern Research Institute (SRI) computer program and curves derived by using the w_k formula.

When the w_k formula is used to calculate total fractional migration velocities for particles of certain characteristics w_{kf} is obtained.

THE FLÄKT ESP DESIGN AND PHYSICAL ARRANGEMENTS FOR PLANTS

The discharge frame is rigid using a box like structure. Discharge electrodes are of spiralized 0.25 cm (0.098 in.) or 0.27 cm (0.106 in.) stainless steel wire. Collecting electrodes are strips 40 cm (1.31 ft.) wide, generally cold-rolled. Tumbling hammer rapping mechanisms are used both for discharge electrodes and collecting surfaces. The Fläkt three field pilot ESP's used around the world are all of the same size.

The nominal dimensions are length 4.8 m (15.75 ft.), width 1 m (3.28 ft.) and height 2 m (6.75). Each field has its own rectifier.

The nominal dimensions of the full scale ESP's reviewed are

Height	9 - 12.5 m (29.53 - 41.02 ft.)
Length	12 - 16 m (38.38 - 52.50 ft.)
Length/height ratio	1 - 1.3
Plate spacing	25 cm (9.84 in.) or 24.77 cm (9 3/4 in.)
Gas velocity	1 - 1.6 m/s (3.3 - 5.2 ft./s)
No. of fields in series	3 - 5
Approx. collecting area connected to one rectifier	1500 - 3600 m^2 (16,000 - 39,000 sq.ft.)

In a few cases the above limits have been influenced by the end user's specification.

FULL SCALE EXPERIENCE

All of these full scale ESP's have been sized based on tests with pilot ESP's. In one case the pilot was not of Fläkt design. Figure 1 shows measured efficiencies against SCA. Each test point covers one complete test on the ESP plant for one boiler. The number of boilers at each site is between three and four. In one case results from both A and B tests have been included.

The spread in results is due mainly to the coal and ash characteristics as well as the operating gas temperature. These factors mainly determine the resistivity level of the dust, whether back corona will occur and to what extent. Typical coal and ash characteristics are shown in table 1.

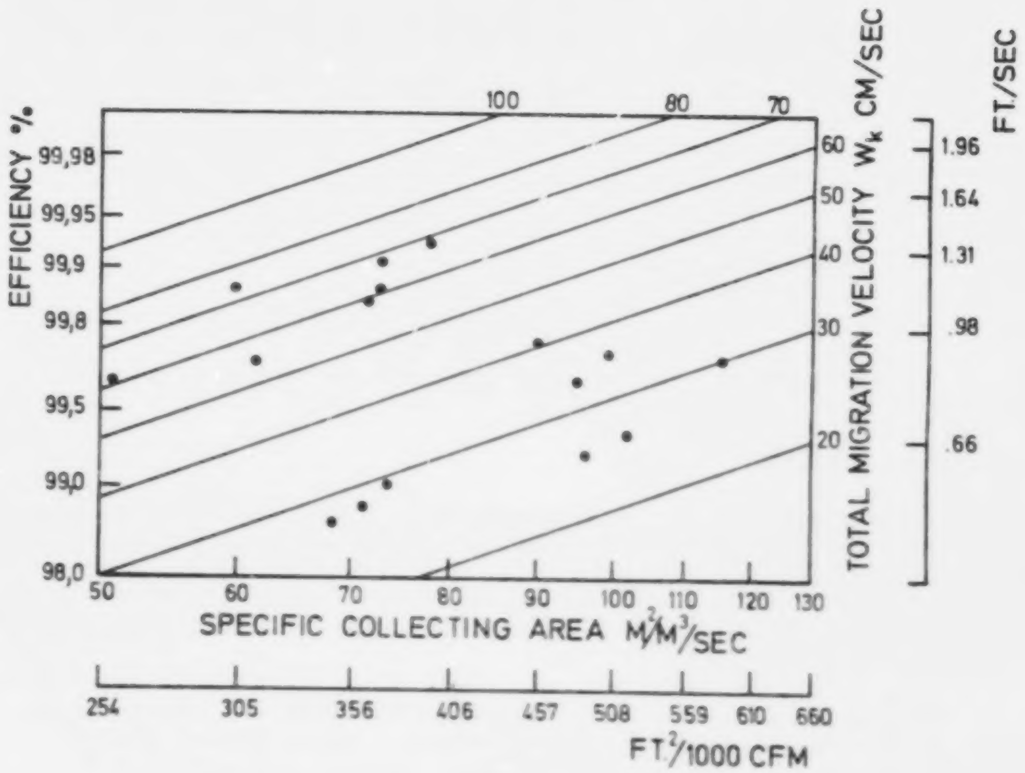

Figure 1. Efficiencies of full-scale plants.

Table 1. TYPICAL COAL AND ASH CHARACTERISTICS
(percent)

Plant Coal Analysis	A	B	C	D	E
Energy MJ/kg	25.68	21.50	22.85	19.67	19.02
Btu/lb	11040	9243	9823	8458	8179
Volatile Matter	29.10	25.10	32.84	28.54	30.66
Fixed Carbon	45.90	41.20	40.55	40.89	35.88
Moisture	7.00	7.60	17.57	18.96	24.97
Ash	17.90	26.10	9.05	11.55	8.49
Sulfur	0.58	0.45	0.53	0.18	0.41
Mineral Analysis					
P_2O_5	NA	0.20	0.26	0.04	0.71
SiO_2	63.10	56.50	61.94	47.38	45.60
Fe_2O_3	0.59	6.32	3.75	4.10	6.92
Al_2O_3	26.80	30.20	16.53	24.98	18.98
TiO_2	0.88	0.95	0.89	0.58	0.37
CaO	0.51	1.33	5.72	14.50	12.14
MgO	0.30	1.08	1.83	1.04	1.92
SO_3	0.30	1.04	5.71	3.51	9.38
K_2O	2.52	0.71	0.59	0.50	0.66
Na_2O	0.12	0.23	2.26	2.07	2.50
Undetermined	4.6	NA	0.52	NA	0.82

The data are averages for respective plants. The mineral analysis for plant A is based on fly ash. At plant B ash analysis are typical only since samples from the efficiency tests are not available. At plant C there have been considerable variations in the ash analysis.

The sulfur contents vary between 0.18 and 0.58 %. This variation is disregarded in the following since the test results confirm the Australian experience that, in this range of sulfur contents, the influence of other components predominate.

The moisture content of the coal and its content of hydrogen results in water contents between about 7 and 12 % by volume, corresponding to water dew points between about 40 and 50 °C (104 - 122 °F). The water content of the gas aids in increasing the performance level of plants D and E in particular but also plant C.

Resistivities and Ash Indexes

Figure 2 shows typical resistivity curves for plants A to E. As expected plant A with the lowest sodium content has the highest resistivity value whereas plant E with the highest sodium content has the lowest resistivity.

The fact that these plants either are designed for or operate at efficiencies above 98.5 % tends to demonstrate that so called critical value of 2 x 10^{10} ohm cm should be revised at least one order of magnitude in the 100 - 200 °C (200 - 400 °F) range. In Fläkt's experience back corona has not occured in ESP plants at a resistivity below 2 x 10^{11} ohm cm. It will occur with certainty about one order of magnitude higher and occassionally between these two levels. At increasing gas temperatures, and particularly in the operating range for so called hot ESP's, the critical value above which back corona can be expected must be considerably lower.

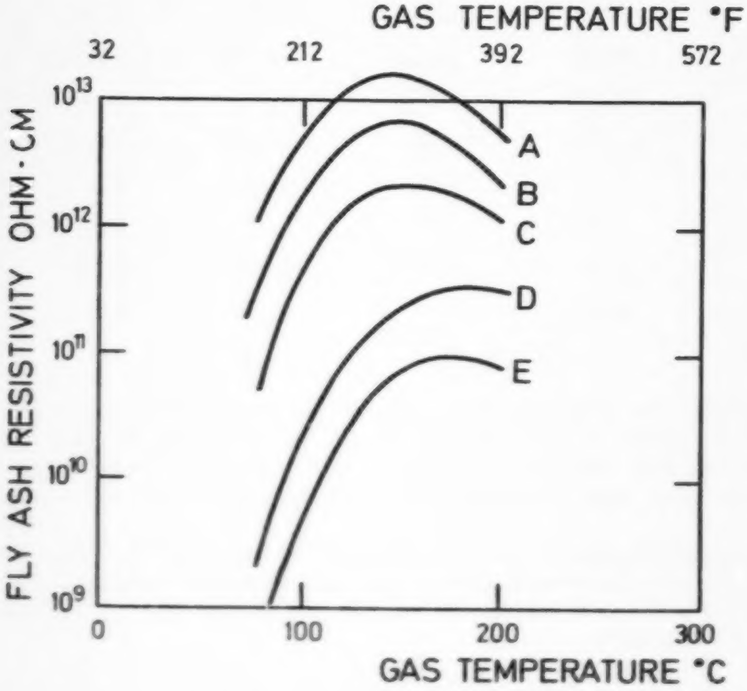

Fgure 2. Resistivities of fly ash

During the seventies a number of ash indexes have been evolved with the purpose of predicting dust resistivity after the composition of the coal ash or the dust. Fläkt developped the ASI (Alkali Sulfate Index) which takes into consideration mainly the oxides of phosphor, potassium and sodium. More known is the work by Bickelhaupt.[2] According to his latest paper the fly ash resistivity is defined by the metal concentrations of sodium, lithium, iron and potassium. The influence of the latter depends on the concentration of iron in the ash. Based on Bickelhaupt's diagrams Fläkt has derived a matematical expression called the Bickelhaupt index, BI. The BI values range between 7.18 for plant A and 2.6 for plant E.

It is worth noting that this index does not take into consideration the contents of components known to form particles with high resistivity, i.e. silicium, aluminium etc.. Neither does it take into consideration that the fly ash may contain smaller or higher concentrations of carbonous material defined as loss on ignition (LOI).

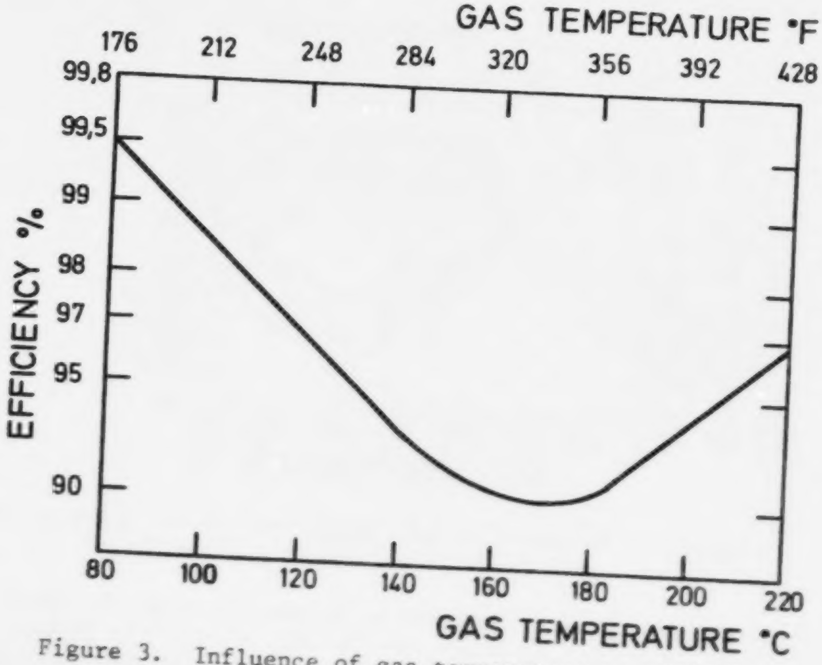

Figure 3. Influence of gas temperature on efficiency from pilot plant tests at plant A

Based on this background the dust from coal A should be the most difficult to collect of the five. Figure 3 shows efficiency obtained during pilot plant tests[3] at temperatures between 80 - 220 °C (176 - 420 °F) with SCA around 70 $m^2/(m^3/sec)$(350 $ft^2/1000$ cfm) (test results from the full scale plant are not yet available). Between 80 120 °C (176 - 248 °F) w_k decreases according to the following formula:

$$w_{kt} = w_{k80} \times 1.0226^{-t}$$

where t is gas temperature in °C

Thus, for each °C increasing gas temperature the SCA value has to be increased with a little more than 2 %. An ESP designed for 150 °C (300 °F) should have to be about 100 % larger than for 115 °C (240 °F). The full-scale plant is designed to operate at the latter temperature.

The dust at plant B should be less difficult to collect. Figure 4 shows both results from full scale tests and the temperature trend according to the pilot tests.[4] According to the latter trend the SCA value should in the temperature range between 100 and 140 °C (212 - 284 °F) have to be increased about 1.4 % for each °C increase in the gas temperature.

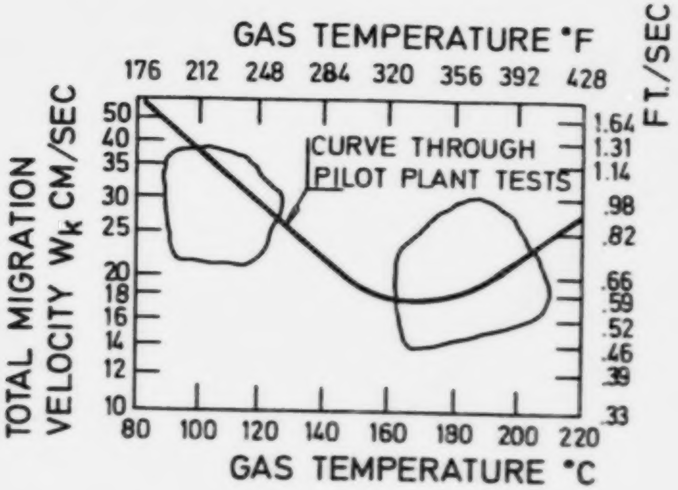

Figure 4. Influence of gas temperature on w_k from pilot and full-scale tests att plant B

Full scale experience is available in two temperature ranges 90 - 120 °C (194 - 248 °F) and 165 - 205 °C (329 - 401 °F). Figure 4 shows good agreement between w_k values obtained in pilot and full-scale. As for plant A the pilot results show a more correct relationship between w_k and gas temperature as its variation was obtained through indirect means and the gas velocity was kept as constant as possible. In full scale the ESP's for the two temperature ranges differ both in size and gas velocity. This might explain the tendency for the results in the lower temperature range to fall below the trend line obtained with the pilot.

The results from plant C falls in the lower range in figure 1. This is considered to be due to several factors including a low content of LOI in the fly ash and a high location. The ambient pressure is only 590 mm (23.23 in.) Hg.

A lower ambient pressure than at sea level will not only result in a lower high voltage (all other factors being equal) but the electrical strength of the gas is lower. Consequently a flash over through the gas will occur at a lower voltage than at sea level. The effect of a resistivity level measured in the laboratory will vary with ambient pressure. The lower this is the higher the resistivity will appear to be in the actual plant, i.e. back corona will start earlier.

Unburnt defined as LOI when dust is heated to about 800°C is considered difficult to collect in ESP's. During tests in Australia on a full scale ESP firing a coal with sulfur content of about 0.5%, the content of LOI decreased in the gas direction. Thus the fractional efficiency on LOI was higher than the total.

As a consequence the LOI content in the dust to the ESP is of importance also when collecting such with high resistivity. It is furthermore probable that if a concentration of 5% is considered normal, dusts with lower concentrations will have a higher resistivity and be more difficult to collect. This fact has to be considered when judging resistivity levels of dusts based on the chemical composition of the ash and using the metal contents only.

As expected test results from plants D and E all fall in the upper range of figure 1. Judged against the other published data the performance level resembles that of ESP's for boilers fired with eastern US coals and with sulfur contents above 1%.

HOT OR COLD ESP

It has been Fläkt policy for some time to quote hot ESP's only when it is required for process reasons. A recent example: Units in Japan where the use of a hot ESP was required ahead of a NO_x collecting system which had to operate in virtually clean gas and at high temperature.

It is not the intention of this paper to give a complete review of the reasons for this attitude towards hot ESP's. A comparison between test results in diagram 1 and such with hot ESP's for low sulfur coals given by Walker[5] could be made. In order to make such a comparison an adjustment has to be made for the difference in operating gas temperature. This can be assumed to be 400 °C (750 °F) for hot ESP's and a maximum of 175 °C (350 °F) for cold ESP's. Thus, in order to have the same total collecting area for a specific boiler project, the w_k values obtainable with the hot ESP's has to be at least 50% higher than with the cold. Or the SCA value for the same efficiency has to be about 35% lower.

The results in figure 1 are grouped in two cathegories. One includes the easy or good dusts where a minimum w_k of 55 has been obtained. The other includes the difficult dusts where the minimum w_k is about 25. In the latter the advantages of low temperature cold operation has been utilized. Let us consider a third performance level 50% lower than the second where the gas temperature is chosen to be in the unfavourable range of 160 °C (320 °F).

With an SCA of 59 $m^2/m^3/sec$ (300 $ft^2/1000$ cfm) efficiencies of 99.6, 98 and 93.7 respectively are obtained if the w_k levels are adjusted to 52, 26 and 13. A hot ESP would have to obtain these at an SCA of 39.3 $m^2/m^3/sec$ (200 $ft^2/1000$ cfm), however. This appears doubtful if the influence of ash composition also on the performance of hot ESP's is considered.

A comparison therefore indicates that the cold ESP data tend to exceed those from hot ESP's both in the upper (easy) and in the lower (difficult) range. Based on this comparison only the use of hot ESP's does not appear warranted except for process reasons. This conclusion becomes even more justified when factors such as increased costs for insulation, ductwork and specific collecting area are taken into consideration. Other factors are longer shut off times for maintenance (it takes long to cool off a hot ESP) and the knowledge that some trace metals will be in vapour form to a larger extent at the higher temperature.

FRACTIONAL EFFICIENCIES

The fractional efficiency on fine particulate and the related efficiencies on trace metals are of considerable interest, particularly when the performance of ESP's is compared with that of fabric filters. Of interest is not only the efficiency on one particular size of particle under given conditions, but also the efficiency variation with grain size and with the conditions under which it is being collected, for instance with size of ESP and power input.

Figure 5 shows a diagram published by Kirkwood[6] based on Bahco sifting of inlet and outlet dust during pilot plant testing on low sulfur coals in Australia. The main feature of this diagram is that the fractional migration velocities w_f decrease with increasing SCA and total collecting efficiency.

The decrease of migration velocity with total efficiency is a known feature of the w_k formula as:

$$w_k = w \times k$$

$$\text{Where } k = \ln\left(\frac{1}{1 - \text{efficiency}}\right)$$

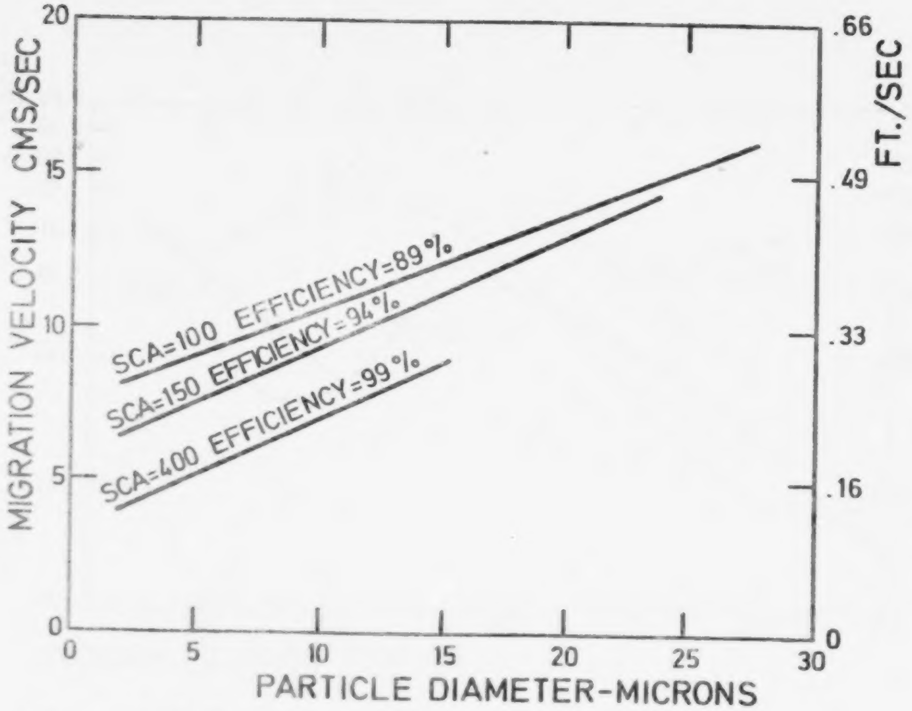

Figure 5. Influence of SCA on fractional migration velocity

Figure 5 indicates, that the decrease of migration velocity with increasing efficiency is not due to the fact that finer particles are collected with lower (constant) fractional migration velocities than coarser. Instead fractional migration velocities for all particle sizes decrease with an increase in total collecting efficiency or SCA.

Investigations made by the Central Electricity Generating Board (CEGB)[7] in pilot scale after a coal fired boiler gives the same indications. w_f for a certain grain size varies with gas velocity, i.e. with SCA. Not only does it increase with gas velocity, i.e. with lower SCA but becomes about constant and then decreases for still higher gas velocities. When the variation of w with SCA is studied a similar decrease is usually considered to be due to so called reentrainement.

w_{kf} values have been calculated and averaged for the Kirkwood data for the grain sizes 5, 10 and 15 micron. If an exponential formula is assumed this follows

$$w_{kf} = 4.75 \, D^{0.8}$$

very closely, i.e. close to direct proportionality between w_{kf} and grain size in the grain size range studied. The trend is similar to that of other investigations available to Fläkt.

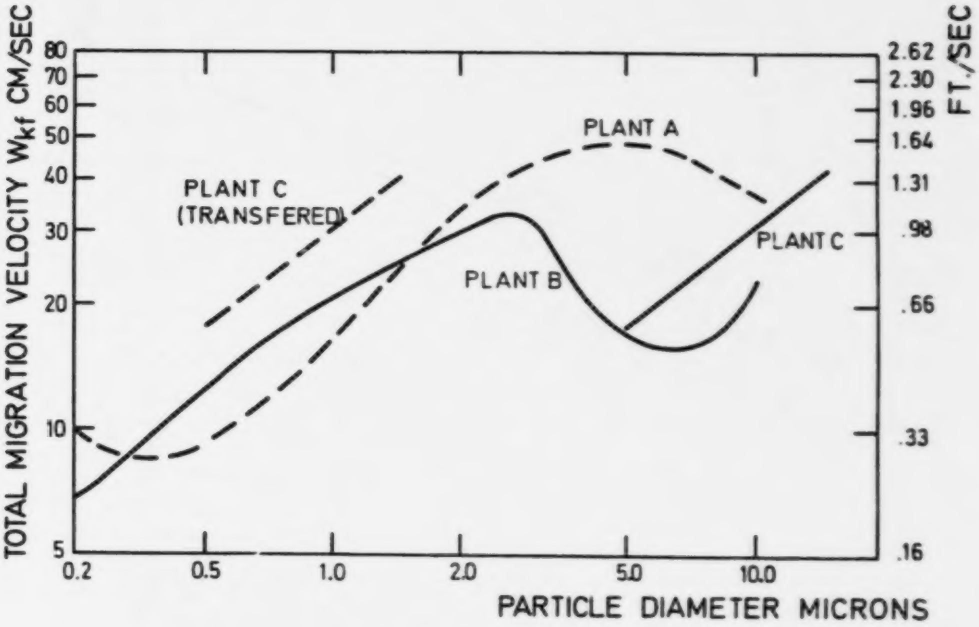

Figure 6. Total fractional migration velocities for pilot and full-scale plants

Diagram 6 shows w_{kf} curves (both based on SRI measurements) against particle diameter for two Fläkt ESP's, one pilot[8] and one full-scale plant.[9] In the diagram the line calculated from diagram 5 is shown both in its correct position and shifted one order of magnitude (as a dotted line). A comparison with the curves show that in the range from about 0.5 up to the maximum in the 3 to 5 micron range the w_{kf} values increase approximately according to the same trend. This fact should indicate that further work on the w_{kf} is warranted.

CONCLUSIONS

Experience with cold precipitators on low sulfur coals shows that the size required for a desired removal efficiency is sensitive to coal ash composition and to the operating gas temperature for ashes with low contents of alkalis, particularly sodium.

When the ash composition is favourable the performance level is comparable to that on high sulfur eastern coals. In less favourable situations the choice of operating gas temperature is of major importance. Not even in a situation where this has to be in the 160 °C (320 °F) range does the choice of the hot alternative appear to be a technically better solution.

REFERENCES

1. Matts, S. and P.O. Öhnfeldt. Efficient gas Cleaning with SF Electrostatic Precipitators. Fläkten, 1963-1964.

2. Bickelhaupt, R.E. Effect of Chemical Composition on Surface Resistivity of Fly Ash. EPA - 600/2 - 75 - 017, August 1975.

3. Mc Lean, K.J. Survey of Australian Experience in Collecting High Resistivity Fly Ash with Electrostatic Precipitators. Prepared for E.P.A. under Contract No. 68 - 02 -0245, September 1972.

4. Lamb, A.N. and K.S. Watson. Electrostatic Precipitation of Fly Ash from Low-Sulphur Coal in Power Stations. Proc. Institute of Fuel Symposium, Adelaide, November 1974.

5. Walker, A.B. Operating Experience with Hot Precipitators on Western Low Sulphur Coals. American Power Conference, April 1977.

6. Kirkwood, J.B. Electrostatic Precipitators for the Collection of Fly Ash from Large Pulverized Fuel Fired Boilers. Clean Air Conference, Sydney, 1962.

7. Dalmon, J. and H.I. Lowe. Experimental Investigations into the Performance of Electrostatic Precipitators for P.F. Power Stations. Colloques Internationaux du Centre National de la Recherche Scientifique, Grenoble, 1960.

8. Nichols, G.B. Theroretical and Practical Aspects of Fine Particle Collection by Electrostatic Precipitators. Symposium on Control of Fine Particular Emissions from Industrial Sources for the Joint US - USSR Working Group Stationary Source Air Pollution Control Technology, San Francisco, 1974.

9. Cau, R., Piulle, W. and J.P. Gosch. Fabric Filter and Electrostatic Precipitator Fine Particle Emission Comparison. American Power Conference, April 1977.

A PERFORMANCE ANALYSIS OF A HOT-SIDE ELECTROSTATIC PRECIPITATOR

G. H. Marchant, Jr.
John P. Gooch
Southern Research Institute
2000 Ninth Avenue South
Birmingham, Alabama 35205

Leslie E. Sparks
Industrial Environmental Research Laboratory
Environmental Protection Agency
Research Triangle Park, N.C. 27711

ABSTRACT

A determination and an analysis of performance were conducted on a hot-side electrostatic precipitator installed on a large power plant boiler. Overall mass and fractional efficiency measurements were conducted across one chamber of the sixteen-chambered unit, and fractional efficiency measurements were conducted across the entire precipitator. *In situ* and laboratory measurements were performed, and voltage-current characteristics of the power supplies were obtained. The chemical compositions of the flue gas and fly ash were determined at the precipitator inlet and outlet. An engineering analysis was conducted for the installation which included an estimate of the specific collecting area required for a cold-side precipitator installed on the same boiler. A theoretical analysis of the performance of the precipitator was also performed.

INTRODUCTION

This paper describes a performance analysis of a hot-side electrostatic precipitator installed on a coal-fired utility boiler. The study was funded by the Industrial Environmental Research Laboratory of the Environmental Protection Agency at Research Triangle Park, N. C., and was conducted with the assistance of the Salt River Project.

Preceding page blank

The major objectives of this evaluation were:

1. To determine the performance of a hot-side ESP.
2. To conduct an engineering analysis of the installation.
3. To compare the hot-side unit with cold-side designs.

A limited survey of the utilities using hot-side electrostatic precipitators was conducted, and the Navajo Generating Station of the Salt River Project in Page, Arizona, was selected for the study.

DESCRIPTION OF FACILITY

The Navajo Generating Station is located approximately 4 miles east of Page, Arizona, on the Navajo Indian Reservation and consists of three 750 MW generating units. The test program was conducted on the precipitator installed on Unit 3.

Units 1, 2, and 3 at the Navajo Generating Station are C-E supercritical, combined circulation, radiant, reheat steam generators with a center water wall dividing the furnace in half.

The electrostatic precipitators installed on the three units were designed by the Western Precipitation Division of Joy Manufacturing Company. Each precipitator consists of two levels (Figure 1) with eight chambers per level (Figure 2). The total unit was designed to operate with a volume flow rate of 1860 m^3/sec (3,940,000 acfm) at 350°C (662°F) with 99.5 percent collection efficiency.

Each of the 16 isolable chambers consists of 6 electrical fields in the direction of gas flow and 35 gas passages spaced 22.9 cm (9 in.) apart. There are a total of 48 transformer rectifier sets, each of which powers parallel fields in parallel chambers. The collection electrodes in each of the six fields are 1.83 m (6 ft) in depth and 9.14 m (30 ft) high. The discharge electrodes have a diameter of 2.68 cm (0.1055 in.) and the average spacing between each wire per field is 22.9 cm (9 in.). Each precipitator has a total collecting area of 112372 m^2 (1,209,600 ft^2) which results in a design specific collection area (SCA) of 60.4 $m^2/(m^3/sec)$, or 307 ft^2/1000 acfm.

TEST PROGRAM

The test program was designed to evaluate the precipitator as a whole and one of the 16 isolable chambers. The test program was conducted during July and August of 1977, and all testing was done at night due to the extreme temperatures at the sampling locations during daylight hours.

Phase I

Phase I of the test program was conducted from July 10 through July 23, 1977, and consisted of an evaluation of Chamber No. 8. Particle

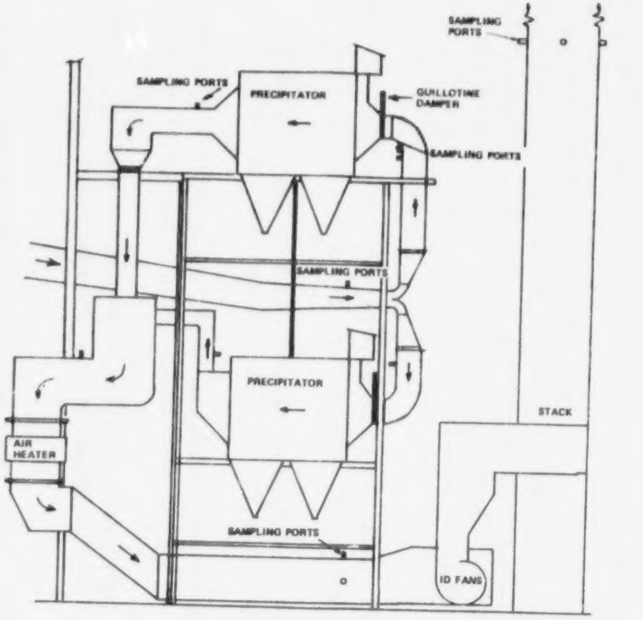
SAMPLING PORTS
SAMPLING PORTS
PRECIPITATOR
GUILLOTINE DAMPER
SAMPLING PORTS
SAMPLING PORTS
PRECIPITATOR
SAMPLING PORTS
AIR HEATER
STACK
ID FANS

Figure 1. Ductwork and precipitator arrangement for Navajo Station, Unit 3.

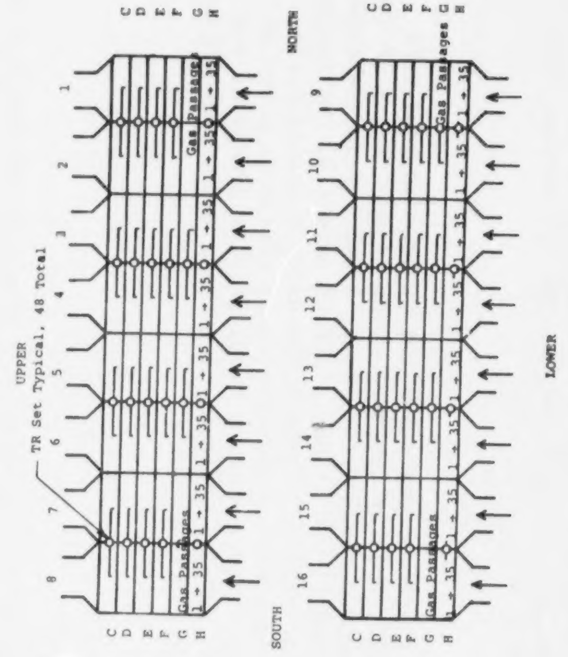
UPPER
TR Set Typical, 48 Total
LOWER
NORTH
SOUTH
Gas Passages
1 + 35
C D E F G H
1 2 3 4 5 6 7 8
9 10 11 12 13 14 15 16

Figure 2. Precipitator chamber arrangement.

size measurements, total mass measurements, gas analyses, ultrafine particle size data, cyclone samples, boiler operating data, hourly secondary voltages and current readings, and coal samples and ash samples were obtained during the Phase I test.

Phase II

Phase II of the test program was scheduled to be conducted from July 31 to August 14, 1977, and was designed to be an evaluation of the entire precipitator. Tests scheduled for August 5 and 6 were cancelled due to operational problems with Unit No. 3 and on August 8, the remainder of the test program was cancelled. Tests which were scheduled during Phase II included particle size measurements, mass train measurements, resistivity measurements, voltage-current readings, gas analyses, and cyclone samples. Due to the plant outage, no overall efficiency measurements with mass trains were obtained.

TEST RESULTS

Mass Train Measurements

Since the test program was conducted on a hot-side precipitator upstream from the air heater, there was concern that boiler soot blowing operations could significantly influence the particulate concentration. Therefore, mass train and impactor runs were scheduled to occur in soot blowing and non-soot blowing periods. Table 1 contains the mass concentration data obtained with the mass trains and impactors during Phase I.

The mass concentration data were analyzed to determine whether soot blowing operations in the boiler significantly increased total particulate loadings. Average particulate concentrations and sample standard deviations were computed for the with and without soot blowing data sets for both the mass train and impactor sampling systems. From these calculations, it was concluded that:

- The mass train data indicate significant mass loading increases during the soot blowing periods at the 90% confidence level.
- Similarly, the impactor-derived mass concentrations show an increase during soot blowing at the 80% confidence interval.
- No significant differences were observed as a result of soot-blowing by either sampling system at the precipitator outlet.

The data in Table 1 indicate that the impactors obtained 77 and 73% of the total mass sampled by the mass trains at the inlet and outlet, respectively.

Overall mass efficiency data for the entire precipitator were not obtained during Phase II as a result of the plant outage. However, impactors were operated at the stack and at the main inlet sampling locations. Table 2 presents the average inlet and stack parameters from the

TABLE 1

AVERAGE INLET AND OUTLET PARAMETERS, CHAMBER 8

	Inlet	Outlet	Eff., %
Temp., °C	361	330	
Vol Flow, dsm^3/sec	44.4	51.5	
Mass Loading, g/dsm^3			
Impactor	5.19	0.0384	99.26
Mass Train	6.77	0.0529	99.22
Number of Runs			
Impactor	27	32	
Mass Train	16	16	

TABLE 2

PHASE II, AVERAGE INLET AND STACK PARAMETERS

	Inlet	Stack
Temperature, °C	368	161
Vol. flow, dsm^3/sec	-	860
O_2, % dry basis	3.90	5.55
Mass Loading, g/dsm^3	5.40	0.0776
No. of runs	12	10
Apparent Collection Eff., %	98.56	

impactor sampling systems during Phase II. A comparison of the data in Tables 1 and 2 indicate that the precipitator as a whole was not performing as well as Chamber 8 (98.56 vs. 99.24%). The volume flow at the stack is consistent with the outlet from Chamber 8, and the simultaneous oxygen determination at the inlet and the stack indicates that total inleakage across the entire precipitator and the air preheater is approximately 10.7%.

Fractional Efficiency Measurements

Figure 3 illustrates the particle size distributions obtained by the modified Brink impactors at the inlet to Chamber 8 with and without soot blowing. The data are presented on a differential basis to illustrate the particulate mass as a function of particle diameter. Since the area under the DM/DLOGD vs. diameter curve is directly proportional to particulate concentration, the relative mass in various size bands can be qualitatively determined by examination of the curve. The majority of the difference in mass concentration between the with and without soot blowing data sets occurs for sizes greater than 8.0 μm.

The size distribution shown in Figure 3 is typical of the bi-modal distributions produced by pulverized coal-fired boilers, with one mode occurring at about 2.0 μm, and the other occurring at a diameter greater than 10.0 μm. The mass median diameter of the entire distribution, based on the impactor determinations of cumulative and total mass loading, is approximately 13 μm. If it is assumed that the difference in mass loadings between the impactor and mass train sampling systems results from under sampling of >20 μm particles by the impactors, the mass median diameter of the distribution increases to 16 μm. This value is based on the extrapclated cumulative mass loadings obtained from the impactor data reduction program and the total particulate concentration obtained with the mass train.

In view of the relatively small differences indicated in Figure 3 between the with and without soot blowing data sets in the size ranges of interest, the results from the two sampling periods were combined. Figure 4 provides the grand average differential size distributions obtained during Phase I and II at the Chamber 8 and at the main inlets, respectively.

In contrast to the similarity observed with the inlet data sets, significantly different results were obtained at the stack location compared to those of the previous test series at the Chamber 8 outlet. The outlet differential size distributions are illustrated in Figure 5. Although the distributions tend to merge at approximately 0.8 μm diameter, the stack outlet data exhibit substantially higher loadings from 0.8 to >10 μm. These differences are also reflected in the fractional efficiency results given in Figure 6. The apparent fractional efficiency data representing the entire precipitator necessarily include the influence

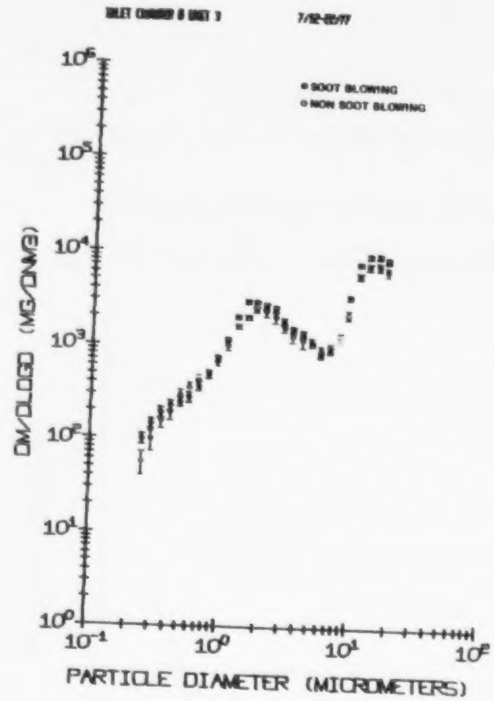

Figure 3. Differential size distributions, Chamber 8 inlet.

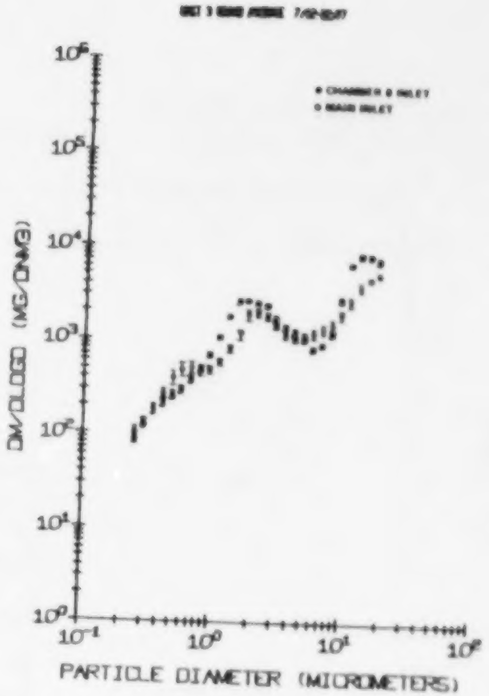

Figure 4. Average inlet differential size distribution.

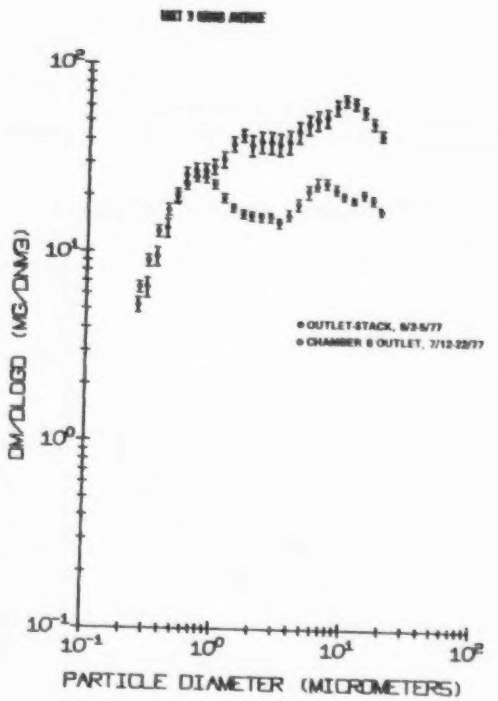

Figure 5. Outlet differential size distribution.

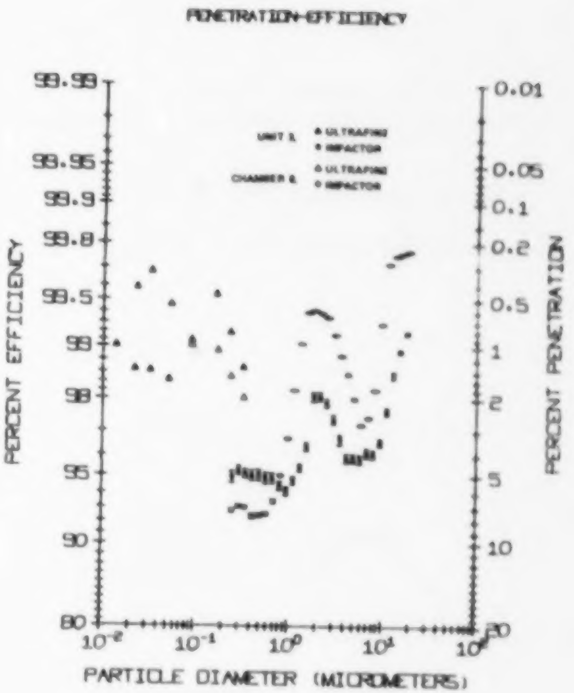

Figure 6. Fractional efficiency for Chamber 8 and total ESP.

of any size distribution changes which result from cooling the flue gas and passing it through the air preheater. There is some disagreement between the impactor and ultrafine results in the overlap region; however, the overlap region is outside the range of maximum accuracy of both sampling systems.

Resistivity Measurements

In situ resistivity measurements were obtained at the main inlet of Unit 3 and laboratory resistivity measurements were conducted on ash samples obtained during the test program. Figure 7 contains the *in situ* and laboratory measurements, and predicted resistivity.

Method 1 is a predicted resistivity from a report published by SRI[1] in 1974 and the predicted resistivity referred to as Method 2 is a result of ongoing research at SRI sponsored by the EPA.

Figure 8 contains predicted resistivity using an analysis of coal ash from a Utah coal source which has been used at Navajo, but which was not in use during the EPA-sponsored test series. These data are included to indicate the range of dust resistivities which may be encountered at the Navajo Generating Station.

The following conclusions have been derived from the resistivity data:

- The measured and predicted laboratory and *in situ* data at 350°C show reasonable agreement.
- The resistivity was relatively constant during the series.

Coal, Ash and Gas Analyses

Coal and ash samples were taken daily. The coal and ash analyses indicated that the coal supply during the tests was fairly constant. None of the analyses indicated that the sodium oxide content of the ash was in the low range.

The SO_x determinations indicated that SO_3 concentrations were never above the detection limit of ~ 0.5 ppm at the inlet or either of the two outlet sampling locations.

Voltage-Current Measurements

The voltage-current characteristics of the precipitator were monitored during the test program. Voltage divider resistor assemblies were attached to the high voltage bus-bars feeding Chambers 7 and 8 during Phase I and corrected secondary voltages and voltage waveform photos from an oscilloscope were obtained. Voltage-current curves were also obtained for each electrical field of Chambers 7 and 8 during Phase I.

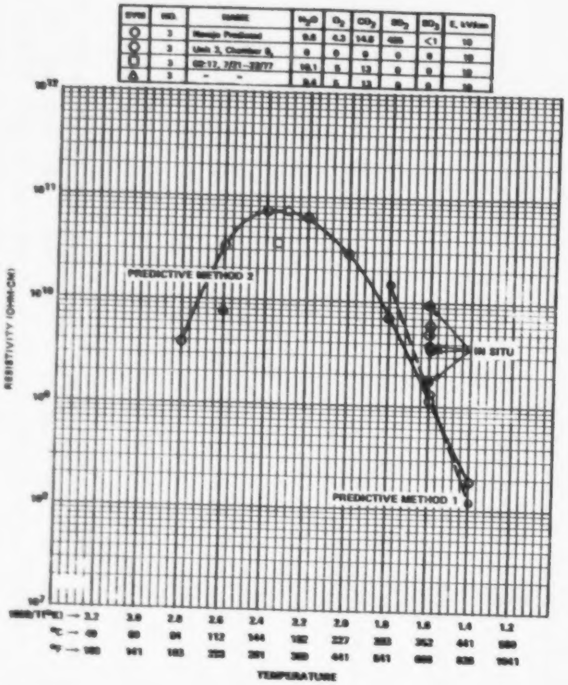

Figure 7. Resistivity vs. temperature, 7/21/77-7/22/77.

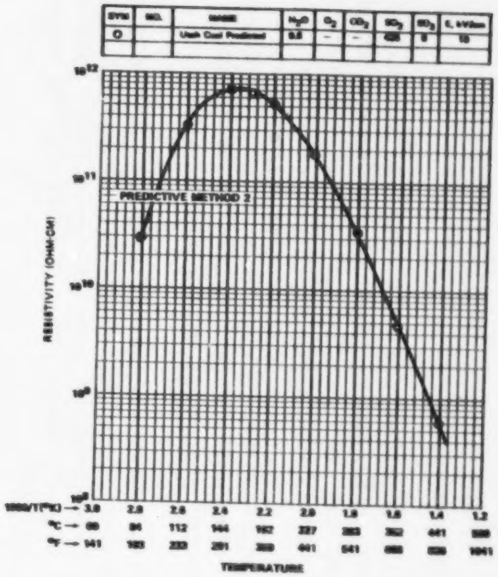

Figure 8. Resistivity vs. temperature, Utah coal.

Figure 9 presents the voltage-current curves obtained from Chambers 7 and 8 on July 13, 1977 (secondary voltages are corrected).

The operating voltages are lower than anticipated, especially for the outlet fields. The following observations indicated that dust deposits influenced the functional relationship between applied voltage and corona current.

- The voltage-current relationships do not respond to changes in electrode diameter in accordance with theoretical predictions.
- Photographs of voltage-current waveforms suggest a back corona discharge at high current levels.
- There is some evidence of hysteresis in the V-I curves from the outlet field.
- The V-I curves are influenced by electrode cleanliness.
- Precipitator performance is influenced by dust resistivity changes in a range of resistivity values below that which would be expected to limit performance.

Figure 10 compares theoretical and actual V-I curves for various wire sizes. The data for C field of Chambers 1 and 2 were obtained after 0.457 cm (0.18 in.) diameter wires had been installed in an effort to improve operating voltages. Although the voltage required for a given current does appear to have been increased by the larger wires, the degree of increase is much less than theoretically predicted. These data suggest that factors other than discharge electrode geometry are limiting the attainable voltages for given current levels.

Figure 11 illustrates voltage waveforms obtained from C field of Chambers 7 and 8, at corona start, the "knee" of the V-I curve, and at the maximum operating point under automatic control. These waveforms illustrate that the voltage between the discharge and collecting electrodes drops below the corona onset voltage at high current densities, indicating that the energy stored in the capacitance of the precipitator is being drained by a discharge process which continues down to voltages as low as approximately 10 kV. Normally, the discharge process stops when the applied voltage drops to the corona onset value. Electrical breakdown in the dust layers on the collecting electrodes is a possible explanation.

Further evidence of dust layer effects is observed by a comparison of V-I curves obtained from C field Chambers 7 and 8. Immediately following start-up from an outage during which the chambers were washed and new wires were installed in the C field, V-I curves were recorded and comparisons were made with those obtained after considerable operating time had elapsed. Figure 12 illustrates the change in the voltage-current curves from May to August of 1977. Although some of this change may be

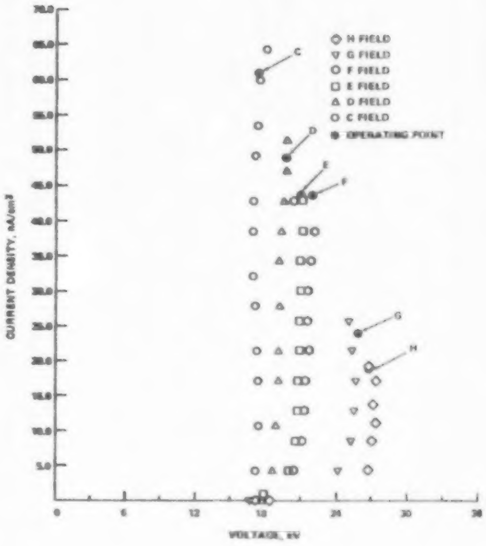

Figure 9. Voltage-current curves for Chamber 7 and 8, July 12-13, 1977.

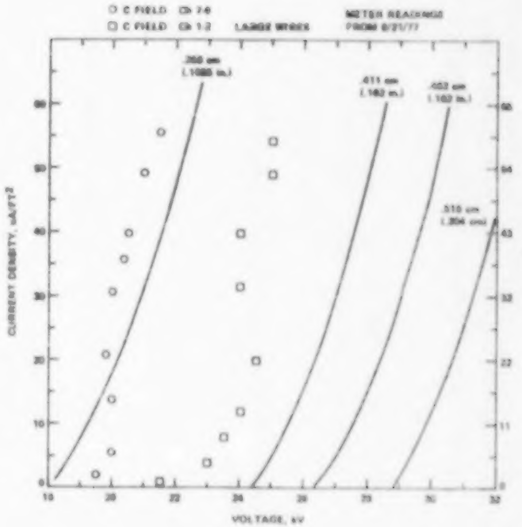

Figure 10. Theoretical and experimental voltage-current relationships for various wire diameters.

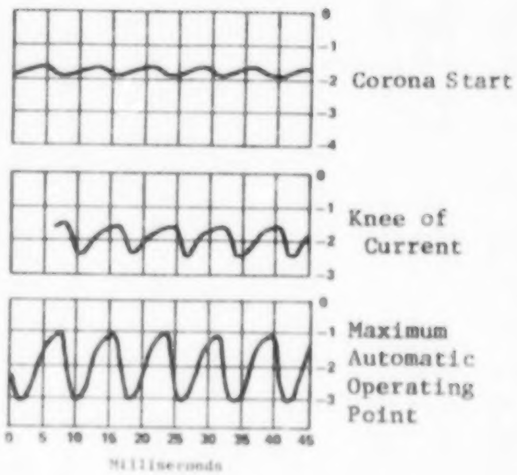

Figure 11. Voltage waveforms for C field, Chambers 7 and 8.

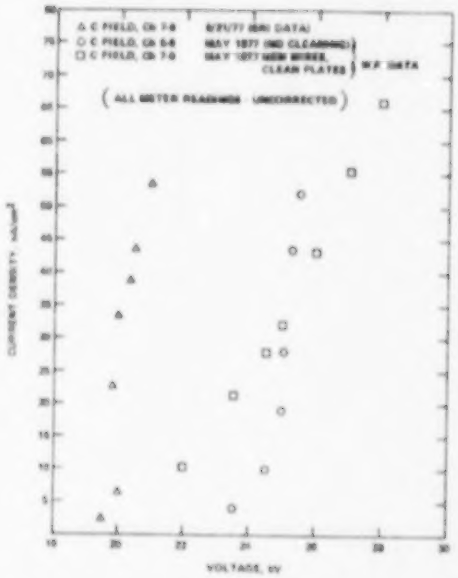

Figure 12. Voltage-current relationships for C fields, Chambers 7 and 8 and Chambers 5 and 6.

due to changes in ash characteristics, a comparison with the data from C field of Chambers 5 and 6, which were taken at the same time, clearly shows the effect of electrode cleaning on the shape of the voltage-current relationship.

ENGINEERING ANALYSIS

Capital and Operating Costs of Existing Unit

Table 3 presents the cost of Unit 3 precipitator in 1977 dollars. The 1977 costs were arrived at by taking the actual contracted dollars assigned to Unit 3 precipitator, adding a 20% distributable cost to each, then adding 9% of the contracted and distributable cost for engineering costs, and finally escalating each cost element to 1977 at 7.5% per year.

The precipitator and ductwork were purchased from Joy-Western in 1973 and erection labor and subcontracts and equipment insulation were assumed to be 1975 charges. The ash collection and storage system was purchased in 1971 for all three units at Navajo and the cost in Table 3 reflects one third of that total purchase. The installation of the ash collection and storage system was assumed to have been completed in 1973. The charges associated with accessory electrical equipment and miscellaneous items were reported by the Bechtel Corporation and were assumed to have been 1975 charges.

The cost of the precipitator for Unit 3 in 1977 dollars is \$46.58/kW, based on the total of \$34,940,000 and the design generating capacity of 750 MW (\$43.67/kW for the 800 MW operating point). The unit area cost of the entire precipitator installation is \$312/m^2 or \$29/ft^2.

Table 4 presents the operating and maintenance costs charged to Unit 3 precipitator from July 1, 1976 to July 1, 1977. These costs include amortization of the estimated capital cost of \$35 million in 1977 dollars.

Based on an extrapolation of the apparent collection efficiency of the entire precipitator [98.6% at an SCA of 53.15 m^2/(m^3/sec) or 270 ft^2/1000 acfm], the SCA required for 99.5% collection efficiency is 78.74 m^2/(m^3/sec) or 400 ft^2/1000 acfm. The recommended design SCA to reliably obtain 99.5% collection efficiency in the presence of the unfavorable electrical operating conditions is 93.90 m^2/(m^3/sec) or 477 ft^2/1000 acfm which includes a safety margin of approximately 20%.

Description and Estimated Costs of an Improved Precipitator

The estimated cost of this design results in a toal estimated capital cost of \$60,440,000, or \$75.5/kW, based on 800 MW generating capacity. No retrofit charges are included in the estimating procedure, since the objective is to estimate the cost of the improved designs in 1977 dollars for a new installation.

TABLE 3

ESTIMATED 1977 COST OF PRESENT INSTALLATION

Item	1977 Cost	\$/kW[a]	\$/ft^2	\$/m^2
ESP and labor	9,863,673	12.33	8.15	87.73
ESP ductwork and insulation	5,460,345	6.83	4.51	48.55
Ash collection system	8,915,691	11.14	7.37	79.33
Accessory electrical equipment	7,637,144	9.55	6.31	67.92
Misc.	3,059,186	3.82	2.53	27.23
TOTAL	\$34,940,000	\$43.67	\$28.87	\$310.76

a. Based on 800 MW.

TABLE 4

SUMMARY OF OPERATING COSTS

	\$/yr	mills/kWh	% of Total Annual Operating Costs
Energy Cost[a]	534,300	0.0953	8.2
Normal Operating & Maintenance Cost	276,000	0.0492	4.2
Ash Handling Cost	460,900	0.0822	7.07
Sub-total	1,271,200	0.227	19.5
Capital Charges \$34,940,000x0.15 =	5,240,000	0.935	80.5
TOTAL	6,511,000	1.162	100.0

a. Based on 7008 hr/yr at full load (800 MW) - 80% load factor

Comparison of Hot and Cold Side Designs

A comparison of hot- vs. cold-side designs for the Navajo Station precipitators is necessarily based on certain assumptions regarding the required plate area and the design details of the installation. The estimated plate area requirements were generated with a mathematical model and the basic geometrical configurations of the recommended designs were arbitrarily chosen to be the same as the existing installation. Table 5 contains the recommended design parameters for one hot-side and two cold-side conditions at Navajo. The enlarged hot-side unit represents an increase in plate area of 83% over the existing unit. The added collecting surface is expected to provide an adequate safety margin to allow the design efficiency to be achieved in the presence of the dust layer effects that limit operating voltages which were observed during the test program.

CONCLUSIONS

The following conclusions have been obtained from this study.

(1) The overall mass collection efficiency of an isolated chamber of the electrostatic precipitator system was 99.22%. The fractional efficiency curve showed a minimum value of 92% at a particle diameter of 0.50 μm. These results were obtained with an average secondary voltage of 22 kV, an average secondary current density of 40 nA/cm^2, a specific collection area of 52.6 $m^2/(m^3/sec)$, and a dust resistivity (*in situ* determination) of approximately $5x10^9$ ohm-cm at 350°C.

(2) The apparent collection efficiency of the entire precipitator, based on a limited Brink impactor traverse of the main inlet and an Andersen impactor traverse of the stack sampling location, was 98.56%. The stack location measurements indicated a total particulate mass emission rate of 31 ng/J (0.0716 $lb/10^6$ Btu) of which 9 ng/J (0.021 $lb/10^6$ Btu) consisted of particles with diameters less than 2.0 μm.

(3) Measured values of dust resistivity at 350°C (both *in situ* and laboratory) are in reasonable agreement with those obtained from predictions based on ash composition.

(4) Voltage waveforms and secondary voltage-current relationships obtained during the test period exhibit certain characteristics similar to back corona from highly resistive dust layers at 150°C.

TABLE 5

RECOMMENDED DESIGN PARAMETERS FOR IMPROVED PERFORMANCE [a]

Condition	Hot-Side Peabody Coal	Cold-Side Peabody Coal	Cold-Side Utah Coal
Gas flow, acfm	4,649,000	3,329,000	3,329,000
m^2/sec	2,194	1,571	1,571
Temperature, °C	350	150	150
Electrical fields in direction of gas flow	8	8	8
No. of chambers	22	22	28
Total collection area, m^2	$2.062x10^5$	$2.062x10^5$	$2.623x10^5$
Specific collecting area,			
ft^2/1000 acfm	477	666	848
$m^2/(m^3/sec)$	93.9	131.1	166.9
Collection efficiency, %			
Design minimum	99.50	99.50	99.50
Expected	99.70	99.77	99.75
Dust resistivity, ohm-cm	$5x10^9$	$8.5x10^{10}$	$7.0x10^{11}$

a. Based on indicated dust resistivity values.

(5) The two principal causes of lower than desired performance of the unit are the relatively low operating voltages and the relatively low values of specific collecting area. The recommended value of specific collecting area to achieve the design collection efficiency of 99.5% is 93.9 $m^2/(m^3/sec)$ or 477 $ft^2/1000$ acfm, based on the results during the test period. An alternative approach to the large increase in plate area, which could not be quantified, is to determine the relationship between dust deposits, voltage-current curves, and collection efficiency. Pilot-scale experiments at the plant site are recommended to determine if it is practical to consistently achieve the "clean plate" values of performance which have been observed.

(6) The installed cost of the electrostatic precipitator system, including the ash handling system, ductwork, and auxiliaries, was estimated as $34,940,000, or $44/kW in 1977 dollars (based on an 800 MW generating unit).

(7) The annual operating costs for the electrostatic precipitator system from June 1976 to June 1977 were $1,271,000, or 0.23 mills/kWh. If the amortized capital costs are included (from 6 above), the operating costs are 1.16 mills/kWh, based on 7000 hr/year.

(8) Although the precipitator has not operated reliably with respect to design efficiency, it has been reliable from a mechanical standpoint. The most significant maintenance problems were air infiltration and ash build-up in hoppers.

(9) The estimated cost of an improved precipitator system, based on the plate area requirements indicated by performance during the test period, is $60,440,000, or $75.4/kW (1977 dollars). The estimated costs of cold-side designs for 99.5% minimum collection efficiency were 52.4 and 65.1 $/kW, based on fly ash resistivities of 9×10^{10} and 7×10^{11} ohm-cm, respectively.

REFERENCES

1. Bickelhaupt, R. E. Influence of Fly Ash Compositional Factors on Electrical Volume Resistivity. Environmental Protection Agency, Control Systems Laboratory, Research Triangle Park, N. C. Environmental Protection Technology Series, EPA-650/2-74-074. July 1974.

AIR FLOW MODEL STUDIES
FOR
ELECTROSTATIC PRECIPITATORS

Heinz L. Engelbrecht
Air Pollution Control Division
Wheelabrator-Frye Inc.
Pittsburgh, Pennsylvania 15219

ABSTRACT

The collecting efficiency of electrostatic precipitators depends, among other requirements, upon acceptable levels of:

--- gas velocity distribution
--- gas temperature distribution
--- dust loading distribution

through the electrode system of the precipitator. Air flow model studies are used to simulate prototype conditions. They are based on the similarity of the fluid flow between the model and the full scale system.

Various devices to maintain and correct flow velocity distribution patterns are used in the industry; their use is becoming increasingly important as a means to reduce pressure losses in ductwork leading to and from precipitators, especially in difficult retrofit applications.

Specifications for the design and fabrication of the model are given.

A description of the test equipment and procedures used in the model work is followed by a review of a model study.

Presently used criteria for acceptable air velocity distributions in the model are reviewed.

Although no exact methods exist at the present time to correlate precipitator collecting efficiency with gas velocity distribution, an attempt is made to examine possible correlations.

INTRODUCTION

The performance; i.e., collecting efficiency of an electrostatic precipitator depends among other requirements upon acceptable levels of ---

gas velocity distribution
gas temperature distribution
dust loading distribution

through the electrode system of the precipitator.

Criteria for acceptable levels of gas velocity distributions in electrostatic precipitators have been specified in general terms and measurable quantities. Expressions, such as "even gas flow", "absence of turbulence and eddy-currents" were used as general terms.

To protect their interest in precipitator collecting efficiency and operating cost, i.e., minimum down-time for repairs, maximum equipment life; power companies, their consultants and engineers started to specify criteria for gas distribution in measurable quantities.

One of the earlier criteria for gas flow distribution was a calculated root-mean-square (RMS) deviation of the finite gas velocities in each test point used as an over-all figure of merit of the gas velocity pattern and the spread of the data, with the R.M.S. deviation to be zero for a perfect gas distribution.

Although the RMS Deviation is still in use as a criteria for the velocity distribution in a given cross-section, in 1965 a definition of an acceptable deviation from an ideal gas distribution was introduced by the Industrial Gas Cleaning Institute (IGCI), which states:

> "Uniform gas distribution shall mean that a velocity pattern five feet or less ahead of the precipitator inlet flange shall have a minimum of 85% of the readings within ± 25% of the average velocity in the area with no reading varying more than ± 40% from the average.[1]

These criteria are specified for a gas flow model of the electrostatic precipitator, as well as for the prototype, although the testing of the model is done very carefully, similar techniques for field testing have not been developed to the same degree of efficiency and accuracy.

Gas temperature distributions in electrostatic precipitators have not been modelled extensively, but only as part of thermal stratification tests to evaluate the influence of thermal stratification, originating in the air preheater, on the liners of large utility stacks.

It is generally assumed that the temperature distribution at the inlet of the precipitator is equalized enough by mixing in the preceeding ductwork not to cause any operational difficulties in a precipitator normally divided in several electrical sections in parallel, each operating at its maximum power level.

Dust loading distributions in electrostatic precipitators are not modelled at the present state-of-the-art. Rather, it is assumed, as a simplification, that the dust is evenly distributed in the gas, and that a gas distribution of a certain quality across the inlet of the precipitator will suffice. Existing differences in the dust loading distribution in various precipitator sections are equally dealt with by electrical sectionalization cross-wise and parallel to the direction of the gas flow.

Thus, the gas velocity distribution in the electrode system of the electrostatic precipitator becomes the main concern and is carefully analyzed.

Designers of electrostatic precipitators and the associated ductwork have gained much experience in the design of gas distribution devices over the years, and this knowledge is applicable to any installation provided the design is within the state-of-the-art. Two basic devices are used for flow control. These are turning vanes in various configurations and diffuser elements, such as grids and perforated plates. Specific requirements of the precipitator are taken care of by pre-tested and pre-engineered designs of the inlet and outlet nozzles. All these designs and devices have certain limitations, which influence the duct design, but within their limitations they are reliable and generally no further model study work is required.

Although the first precipitator flow model studies were performed in the early Fifties, a widespread use of flow modeling techniques was not made until the late Sixties. With the ever increasing size of thermal power stations, uniformity of gas flow, dust distribution, and the gas temperature profile at the inlet of the precipitator become of prime importance. With prior attention focused primarily on structural and space problems, negligence of proper ductwork design resulted in poor performance of the equipment, excessive pressure losses, large dust accumulations, and corrosion due to uneven gas temperature distribution. In larger boiler units for modern thermal power plants, one inch w.g. of pressure drop can be evaluated as an annual operating cost of $40,000 or more.

SIMILARITY OF FLUID FLOWS

The gas velocity distribution in the electrode system of the electrostatic precipitator is analyzed using accepted procedures based on similarities of fluid flows in the three-dimensional scale model and the full-size system (prototype).

The similarity of the fluid flow conditions between the model and the prototype are dependent on matching of some or all of a series of dimensionless parameters, which describe the characteristics of the prototype and model, as well as those of the flows, as ratios of the fluid forces.

In general, three similarities must be satisfied to obtain valid results with the fluid flow models. These similarities are:

1. Geometric Similarity
2. Kinematic Similarity
3. Dynamic Similarity

Any of two flow systems satisfy geometric similarity, if all dimensions have the same scale factor,

$$\ell_1/\ell_2 = \text{constant} \qquad (1)$$

with ℓ = typical length (indices 1 and 2 distinguish between the two flow systems)

Kinematic similarity requires, in addition, that any two flow systems have the same relative velocities and accelerations throughout.

$$v_1/v_2 = \text{constant} \qquad (2)$$

$$b_1/b_2 = \text{constant} \qquad (3)$$

with v = typical velocity

b = typical acceleration

It is normally not too difficult to match all of these requirements in a precipitator model.

The third requirement of a dynamic similarity requires, in addition, the similarity of pressures at corresponding points of model and prototype.

$$p_1/p_2 = \text{constant} \qquad (4)$$

p = typical dynamic pressure

To completely satisfy the similarity of dynamic pressures, a number of ratios of forces in both fluid systems, such as Reynolds, Froude, Weber, Euler, and Mach Number have to be identical, Gilbert[2]. Most of the time, this condition cannot be met in model study work.

A different approach would be to maintain equality of Reynolds and Froude numbers only. Scales for the model can be developed based on gas viscosities and densities of both systems, resulting in a length scale of:

Scales for model and prototype can be developed by using Reynolds and Froude Numbers of both systems, resulting in a length scale of:

$$\lambda = \frac{l_1}{l_2} = \left(\frac{\nu_1}{\nu_2}\right)^{2/3} \qquad (5)$$

a time scale of:

$$\tau = \frac{t_1}{t_2} = \left(\frac{\nu_1}{\nu_2}\right)^{1/3} \qquad (6)$$

and a general force scale of:

$$\varkappa = \frac{P_1}{P_2} = \frac{\rho_1}{\rho_2}\left(\frac{\nu_1}{\nu_2}\right)^{2} \qquad (7)$$

The general force scale can be extended to cover scales for inertial, frictional, and gravitational forces with ν representing gas kinematic viscosity and ρ gas density.

Scale factors for other units of measurements can be calculated from these basic scales; for example, for gas velocity:

$$\frac{v_1}{v_2} = \frac{\lambda}{\tau} = \left(\frac{\nu_1}{\nu_2}\right)^{1/3} \qquad (8)$$

and for gas volume:

$$\frac{Q_1}{Q_2} = \frac{\lambda^3}{\tau} = \left(\frac{\nu_1}{\nu_2}\right)^{5/3} \qquad (9)$$

The general use of these ratios in flow model studies of electrostatic precipitators would require rather large models. For example, for flue gas with a temperature of 180°C. in the prototype and air of 20°C. in the model, the length scale would be 1 to 1.6; the velocity scale 1 to 1.3; and the volume scale 1 to 3.2.

A different approach for model studies, where a significant decrease in size of the model is intended, would be to arbitrarily select a scale factor for a typical length; for example, 1 to 16, and to match the Reynolds number of the prototype by increasing the fluid velocity in the model or changing the fluid properties.

Increasing the system velocity creates significantly larger pressure losses and requires higher head fans. The gas velocity of the prototype system mentioned earlier may be 1.2 m/sec. To match the Reynolds Number using air as model fluid in a 1 to 16 scale model would require an air velocity of 9.6 m/sec., an increase by a factor of eight. The system pressure loss would, thus, increase by a factor of 64; for example, from a design pressure loss of 250mm H_2O to 16,000mm H_2O.

To match the Reynolds Number of the prototype, the model fluid properties could be adjusted by changing the fluid temperature or using a fluid other than air, but neither of these approaches is very practical.

The Reynolds Number is the ratio of inertial to viscous forces. When the inertial forces predominate, flow separation from the critical surfaces occurs and is principally a function of the geometry of the system. If the value of the Reynolds Number is well within the turbulent range ($Re > 3 \times 10^3$, for example), the behavior of the fluid can be successfully modelled at a Reynolds Number other than that of the prototype system.

The model flow pattern observed at reduced Reynolds Number levels will be identical to the full size system, and the model pressure drop will be only slightly higher due to the influence of the Reynolds Number on frictional pressure losses.

In industrial flue systems, which are usually designed to connect major pieces of equipment, many conditions will establish flow separation and induce turbulence. Therefore, the calculated value of Re is no indication of the quality of flow or the state of turbulence. Once the condition of flow separation is established (inertial forces predominating) the flow pattern tends to remain the same over a wide range of calculated Re values. That is, kinematic similarity is established in industrial flues substantially independent of variations in average velocity or model factors.

Therefore, the model study does not have to match the full size Re value, it suffices that:

$$\frac{v_1 \ell_1}{\nu_1} \geqslant 3 \times 10^3 \qquad (10)$$

and

$$\frac{v_2 \ell_2}{\nu_2} \geqslant 3 \times 10^3 \qquad (11)$$

However, Reynolds Number must be considered when the conditions of pressure drop and dust drop-out are studied in the model. It has been shown that the boundary-layer thickness of gas on any surface is an inverse function of Re. In the usual industrial scale model study, Re will be proportionately low due to the scale factor, and the boundary-layer will be too thick. This condition tends to give a conservative estimate of pressure drop and dust drop-out.

Model studies involving two-phase fluid systems or airborne particulates influenced by gravitational forces, require the adherence to a constant Froude Number, i.e.:

$$\frac{v_1^2}{\ell_1 g} = \frac{v_2^2}{\ell_2 g} \qquad (12)$$

Another approach, which is frequently used, consists of using a 1:16 scale model with the collecting surface plates installed in a 1:8 scale, and, thus, test at a flow condition characterized by a Reynolds number in the turbulent range, closer to the Reynolds number of the prototype.

The fluid velocity level in a model should be selected to be in a range which can be easily and accurately measured (velocity head above 10mm H_2O) but low enough to be incompressible (Mach Number below 0.2). As a result, the fluid velocity in a duct will normally range from 10 to 20 m/sec., and in the precipitator model itself, from 0.5 to 3.0 m/sec.; the latter being measured with a hot wire anemometer.

If smoke is used to visualize the flow pattern, the fluid velocity should not exceed 10 m/sec. to maintain visibility of the smoke pattern.

It is recommended to use a fan with a variable speed drive or to have air dampers between flow model and fan to be able to reduce the air flow through the model to one-half or one-third of the design flow volume during the test program.

FLOW CONTROL DEVICES

Flow control devices to maintain and/or improve an existing velocity distribution pattern are used throughout the system at each point where either velocity and/or direction of the fluid change. These devices are mostly:

Diffusers
Turning Vanes
And Perforated Plates

Together, for example, they can be used in a gas distribution system upstream of an electrostatic precipitator with an opening ratio of up to 1 to 22.5 (Figure 1). Other examples of flow control devices in ductworks have been published by Bragg[3], Vath[4], Burton[5], and others.

FLOW MODEL CONSTRUCTION

Three-dimensional scale models have become the most widely used means for a fluid velocity distribution analysis. For purpose of convenience, some of the models made in early gas flow studies were constructed in a scale of 3/4 in. in the model being equivalent to one foot in the prototype; that is, the model was 1/16 of actual size. This scale became common and is widely used in the industry, although for more demanding work, especially for predictions of pressure drop and dust fallout, a scale of 1 to 12 or even 1 to 10 could become increasingly more necessary.

The model is a precise replica of the entire gas cleaning system and includes items, such as air preheaters, flues, precipitators, fans, stacks, etc. All of the model or parts of it are made of transparent plastic to make it possible to observe flow indicators, such as cotton tufts or smoke and dust fallout. Internal parts of the ductwork, such as flow control devices, may be constructed of light gauge sheet metal.

The precipitator model has sidewalls, hoppers, box girders, and roof made out of transparent plastic. Collecting surface plates are made out of flat sheets of plastic or metal and are hung between the box girders or plate supports. Normally, only the first and last electrical fields need to be equipped with collecting surface plates. Walkways, horizontal and vertical baffles are included in the model, as well as hopper partitions. The discharge system is normally not included in the model.

Inlet and outlet nozzles are also made out of transparent plastic. Perforated plates or similar devices used for gas distribution are selected with equal opening ratios as those to be used in the prototype.

The air preheater is modelled as exact as possible, complete with transitions between the round arc of the wheel and the rectangular outlet flanges, as well as the wash-out hopper underneath the air preheater outlet duct.

The model is set up on the suction or pressure side of a fan with a suitable gas volume, normally following the configuration used in the prototype.

Larger models need a separate support structure and access platforms next to the test ports.

INSTRUMENTATION

Air velocity distributions in the ductwork of the model are measured with a calibrated standard pitot tube; for example, Dwyer 1/8 inch diameter, with an inclined water manometer; for example, Meriam

Model M-173-FB with a range of 0-6 inches and minor graduations of 0.01 inch.

Static pressures in ductwork are measured with a calibrated standard pitot tube connected to an inclined water manometer; for example, Meriam Model HE 35 WM with a range of 0-14 inches and minor graduations of 0.01 inch.

The air velocity distribution in the model of the precipitator chamber is measured with a hot-wire linear flow flowmeter; for example, Datametrics (Gould) model 800-LV with a model U-25 probe.

MODEL STUDY

The main purposes of a model study are to determine the location and configuration of gas flow control devices, such as vanes, baffles, perforated plates, to satisfy the contractural requirements on gas velocity distribution in the inlet and outlet of the electrostatic precipitator, and to minimize the pressure drop through the complete system (Figure 2)[6].

In a typical model study, the requirements may be to satisfy that the gas velocity distribution meets the requirements of I.G.C.I. Publication EP-7 at the inlet and outlet of the precipitator, to have an R.M.S. velocity deviation of less than 17 percent, and that the gas velocities in the lower portion of the precipitator are less than the gas velocities in the middle and upper regions.

Also, a prediction has to be made for possible areas and magnitude of dust fallout during normal and reduced flow rates.

Air velocity measurements within the precipitator were taken at discrete locations using the equipment described earlier. Traverses of 13 vertical measurements were taken in 11 gas passages evenly distributed across the inlet and outlet of the precipitator; thus, 143 measurements were used for the determination of the average velocity and the R.M.S. deviations. Each individual velocity was considered to be representative for the mean velocity through an 8.1 sq. ft. area of the prototype.

The model study results (Figure 3) indicated that the gas flow distribution in the precipitator inlet would meet the first requirement with ---

No. of Readings within 10% of Mean Vel. = 72 -- % of TOT. RDGS = 50
No. of Readings within 15% of Mean Vel. =104 -- % of TOT. RDGS = 72
No. of Readings within 20% of Mean Vel. =124 -- % of TOT. RDGS = 86
No. of Readings within 25% of Mean Vel. =137 -- % of TOT. RDGS = 95
No. of Readings within 30% of Mean Vel. =142 -- % of TOT. RDGS = 99
No. of Readings within 40% of Mean Vel. =143 -- % of TOT. RDGS =100

The gas flow distribution in the precipitator outlet was:

No. of Readings within 10% of Mean Vel. = 99 -- % of TOT. RDGS = 69
No. of Readings within 15% of Mean Vel. =122 -- % of TOT. RDGS = 85
No. of Readings within 20% of Mean Vel. =131 -- % of TOT. RDGS = 91
No. of Readings within 25% of Mean Vel. =136 -- % of TOT. RDGS = 95
No. of Readings within 30% of Mean Vel. =137 -- % of TOT. RDGS = 95
No. of Readings within 40% of Mean Vel. =142 -- % of TOT. RDGS = 99

with one reading below the limit of $0.6\bar{V}$. The R.M.S. velocity deviations were 13.3 percent in the inlet and 12.3 percent in the outlet of the precipitator. The gas velocity profile of the inlet of the precipitator is shown (Figure 4), also, as a histogram (Figure 5) and a log-probability graph (Figure 6).

The dust deposition tests were done by covering all horizontal inside surfaces with a 50/50 mixture of granulated cork and sawdust, graded through a No. 12 mesh screen. The original depth of this deposit was 3/4 in. in the model. Testing was started by operating the fan at it's lowest possible setting and gradually increasing the volume to 10 percent and higher. The inlet and outlet ducts cleaned out at a flow rate of 38 percent; the elbow sections cleared at a flow rate of approximately 50 percent.

REVIEW OF PRESENTLY USED CRITERIA

With electrostatic precipitators in the 90-95% collecting efficiency range, a R.M.S. deviation of 20 to 25% was considered representative of an adequate gas distribution pattern. The increase in collecting efficiency requirements of the electrostatic precipitator to the +99% range shifted this requirement to lower R.M.S. percentages, with 10-15% R.M.S. considered to be representative of an excellent to good gas distribution.

The earlier mentioned I.G.C.I, Publications EP-3 and EP-7 are most widely used at the present time.

Some power companies have specified even more stringent criteria for gas distribution in the inlet of the precipitator; for example:

> "A minimum of 85% of the readings within ± 10% of the
> average velocity and no reading varying more than
> ± 20% from the average."

As a comparison, an R.M.S. deviation of approximately 28% equals the worst case of the I.G.C.I. criteria, whereas the second criteria equals an R.M.S. deviation of approximately 12% in the worst case. These percentages are considerably lower, if instead of the worst possible case, a Gaussian distribution of individual inlet velocities is used.

I.G.C.I. has also prepared a new more detailed set of criteria for an acceptable gas velocity distribution, which is presently in the approval process by its member companies. These criteria include a re-stated velocity distribution pattern, an R.M.S. deviation criteria, and limitations on gas velocity deviations between individual chambers of large precipitator installations.

CORRELATION TO PRECIPITATOR COLLECTING EFFICIENCY

The ultimate objective of an air velocity distribution model study would be to correlate the results of the study with the collecting efficiency of the prototype electrostatic precipitator.

It is generally assumed that a reduced gas flow in a finite section of the precipitator results in an increased collecting efficiency in this same section and that an increase in gas flow will result in a decrease of the collecting efficiency.

Using the Deutsch formula for precipitator collecting efficiency and the R.M.S. percentage deviation, curves can be calculated, which show the overall theoretical effect of gas mal-distribution on the precipitator, Bragg[3]. For example, a precipitator with a design collecting efficiency of 99 percent at a perfect gas distribution (R.M.S.= zero) would degrade to --

E = 98.90 percent at R.M.S. of 10 percent
E = 98.55 percent at R.M.S. of 20 percent
E = 98.00 percent at R.M.S. of 30 percent

This calculation assumes no variation of the precipitation rate parameter as a function of the change in gas velocity.

A different approach is to calculate a second precipitation rate parameter w, which has to be achieved under otherwise unchanged operating conditions to make up for the losses/gains in collecting efficiencies in finite portions of the electrostatic precipitator; i.e., to maintain the original design collecting efficiency. The correlation is --

$$W_o = \frac{Q}{A_c} \ln \left(\frac{\sum_{i=1}^{n} v_i}{\sum_{i=1}^{n} v_i \exp. - \left(w' \frac{A_c \bar{v}}{Q \, v_i} \right)} \right) \quad (13)$$

with W_o = original precipitation rate parameter

W' = adjusted precipitation rate parameter

A_c = collecting surface area

Q = gas volume/unit time

v_i = local gas velocity

$\bar{v}$ = average gas velocity

A perfect gas distribution would be characterized by $W' = W_o$, and a lesser quality distribution by $W' > W_o$. A numerical value K for the quality of the gas velocity distribution can be formed by ---

$$K = \frac{W' - W_o}{W_o} \qquad (14)$$

The quality of the distribution can also be represented by a graph (Figure 7).

A correction factor to calculate the degradation of the precipitator performance based upon the gas velocity distribution has been suggested by Gooch, et al[7] to provide an estimating technique for a mathematical model of an electrostatic precipitator. This correction factor F is described as the ratio of the original migration velocity to reduced "apparent" migration velocity. This factor can also be used to describe the quality of a gas velocity distribution with --

$$F = -\frac{k}{\bar{v} \ln p} \qquad (15)$$

$$k = W_o \frac{A_c}{A_x} \qquad (16)$$

$$p = \frac{1}{n\bar{v}} \sum_{i=1}^{n} v_i (1 - E_i) \qquad (17)$$

W_o = original migration velocity

A_C = collecting surface area

A_X = cross-sectional area

$\bar{v}$ = average gas velocity

p = average penetration due to uneven gas distribution

n = number of test points

E_i = fraction collecting efficiency

A fourth approach is presented in this paper, which is based on the use of an exponent k on the exponent of the original Deutsch equation. Thus,

$$E = 1 - e^{-wf} = 1 - e^{-(w^* f)^k} \qquad (18)$$

with $w \neq w^*$ and $f = Ac/Q$

This allows to compare the penetration

$$\varepsilon = 1 - E \qquad (19)$$

of two precipitator sections, one representing the complete precipitator under ideal gas distribution, and the other, an imaginary precipitator section corresponding to the traverse point of the gas velocity measurements.

$$\frac{\ln \varepsilon_1}{\ln \varepsilon_2} = \left(\frac{f_1}{f_2}\right)^k \qquad (20)$$

To suit the gas velocity measurements taken in the model or the prototype precipitator, equation (19) can be re-written as ---

$$\ln \varepsilon_2 = \ln \varepsilon_1 \left(\frac{v_1}{v_2}\right)^k \qquad (21)$$

with $\varepsilon_1 = \bar{\varepsilon}$ = average penetration at ideal conditions

$\varepsilon_2 = \varepsilon_i$ = typical penetration at Test Point i

$v_1 = \bar{v}$ = average gas velocity at ideal conditions

$v_2 = v_i$ = typical gas velocity at Test Point i

Equation (21) can be written as

$$\ln \varepsilon_i = \ln \bar{\varepsilon} \left(\frac{\bar{v}}{v_i}\right)^k \qquad (22)$$

The exponent k is expected to be in a range from 0.4 to 0.6.

A review of data presented by Nichols et al[8] resulted in the following comparison:

Table 1

Gas Velocity	Ft/Sec	4.4	5.4	6.7	8	10	12
Reported Collecting Efficiency	%	97.76	96.9	95.5	94.0	91.81	89.45
Calculated Collecting Efficiency	%	---	96.8	95.4	94.0	92.0	90.0

The calculated collecting efficiencies are based on = 4.4 ft/sec., ln = -3.8, and k = 0.5.

The good agreement between the reported and the calculated collecting efficiencies confirm the aforementioned range of k. Using the inlet dust load as unity, the total penetration becomes ---

$$1 - E_T = \frac{\sum_{i=1}^{n} (\upsilon_i \varepsilon_i)}{\sum_{i=1}^{n} \upsilon_i} \quad (23)$$

and the total collecting efficiency after consideration of the gas distribution ---

$$E_T = 1 - \frac{\sum_{i=1}^{n} (\upsilon_i \varepsilon_i)}{\sum_{i=1}^{n} \upsilon_i} \quad (24)$$

These formulas are presented for estimating purposes only. More work is needed to evaluate the influence of changing parameters, for example gas velocity, on the collecting efficiency of the precipitator. Although the collecting efficiency will decrease with increased gas velocity, the drop in efficiency is softened by an increase in the precipitation rate parameter and the increase in collecting efficiency at a lower gas velocity is reduced by a reduction of the precipitation rate parameter.

The four evaluation methods described in this paper can be compared using the precipitator inlet velocity distribution shown in Figure 5 as an example, assuming that this precipitator would achieve a collecting efficiency of 99.8 percent under ideal conditions of velocity distribution.

Method 1

R.M.S. Deviation: 13.28%
Corrected Collecting Efficiency: 99.73%

Method 2

Original Precipitation Rate Parameter W_o = 9.15 cm/sec
Adjusted Precipitation Rate Parameter W' = 9.6 cm/sec
Quality Factor K = 5.49%

Method 3

Constant k = 33.97
Mean penetration p = 0.0027
Corrected Collecting Efficiency = 99.73%
Correction Factor F = 1.05
Original Precipitation Rate Parameter = 9.1 cm/sec
Reduced Precipitation Rate Parameter = 8.7 cm/sec

Method 4

Original Collecting Efficiency E = 99.8%
Corrected Collecting Efficiency E = 99.78%

Although the results vary according to the methods and criteria used in these evaluations, the results indicate an acceptable velocity distribution pattern in the inlet of the precipitator model described in this paper.

REFERENCES

1. Industrial Gas Cleaning Institute, Inc. Criteria for Performance Guarantee Determinations, Publication No. EP-3. August 1965.

2. Gilbert, Gerald B. Experimental Flow Modeling for Power Plant Equipment. Power Engineering Magazine. May 1974.

3. Bragg, L. G. Gas Flow Model Studies of Flues. Canadian Mining and Metallurgical Bulletin. October 1962.

4. Vath, D. E. and Rabkin S. New Precipitator Layout at Keystone Helps Keep Overall Plant Cost Down. Power Engineering. November 1965.

5. Burton, C. L. and Smith, D. A. Precipitator Gas Flow Distribution Symposium on Electrostatic Precipitators. Pensacola, Florida. October 1974.

6. Industrial Gas Cleaning Institute, Inc. Gas Flow Model Studies. Publication No. EP-7.

7. Gooch, John P., McDonald, Jack R. and Oglesby, Sabert, Jr. A Mathematical Model of Electrostatic Precipitation. Southern Research Institute, Birmingham, Alabama. Contract No. 68-02-0265. U.S. Environmental Protection Agency, Washington, D.C. April 1975.

8. Nichols, Grady B. and Gooch, John P. An Electrostatic Precipitator Performance Model. Southern Research Institute, Birmingham, Alabama. Contract No. CPA70-166. U.S. Environmental Protection Agency, Research Triangle Park, N.C. July 1972.

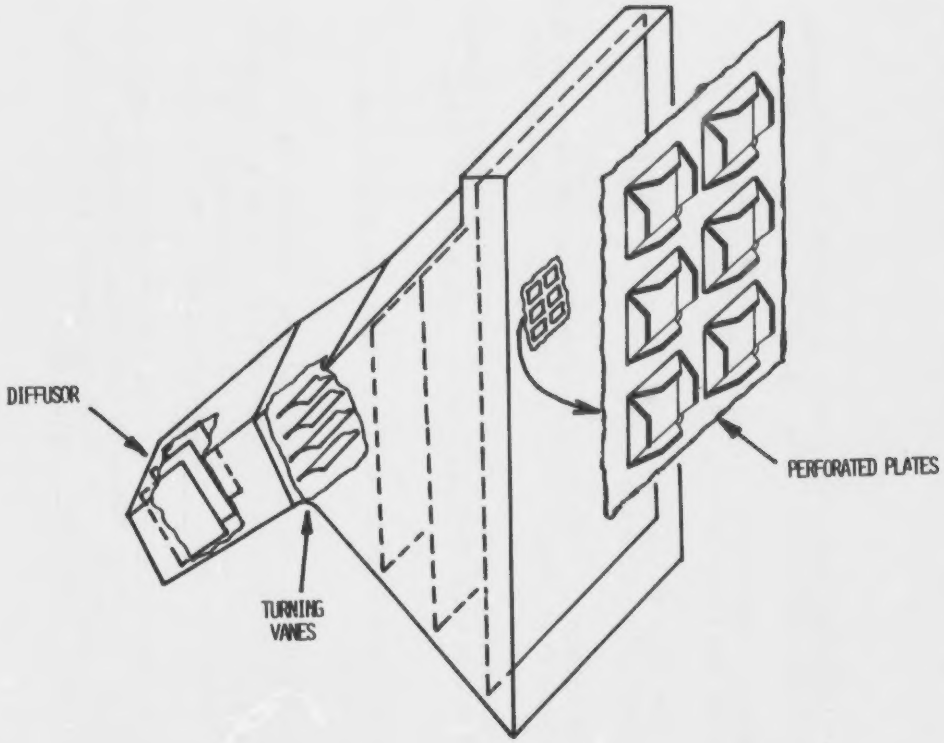
DIFFUSOR
TURNING VANES
PERFORATED PLATES

Figure 1

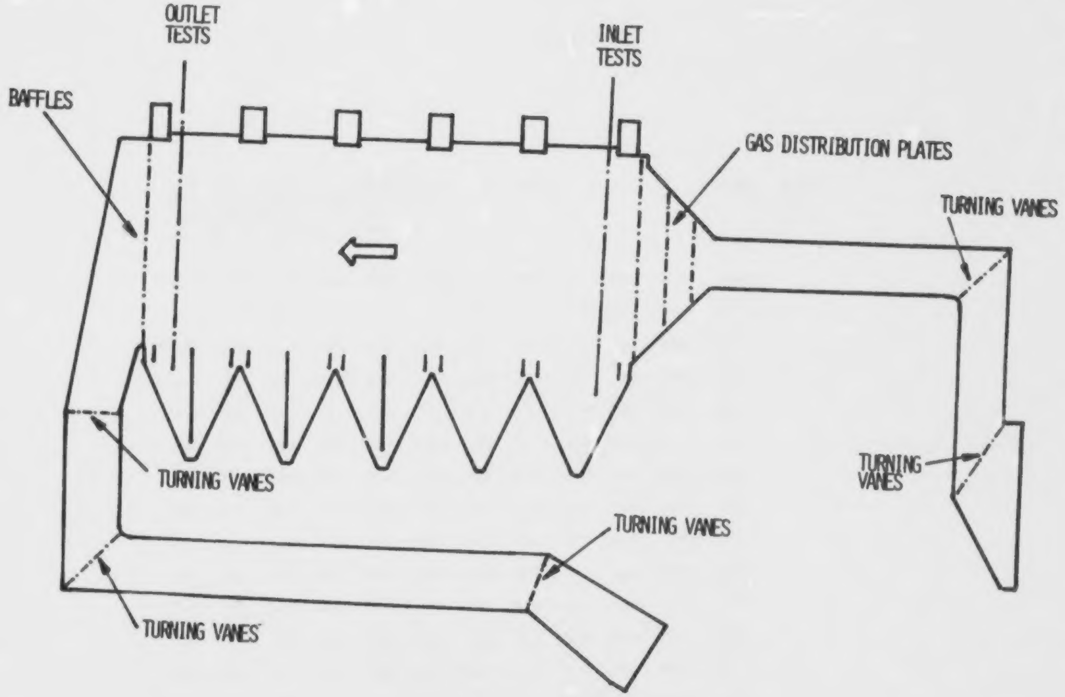
OUTLET
TESTS
INLET
TESTS
BAFFLES
GAS DISTRIBUTION PLATES
TURNING VANES
TURNING
VANES
TURNING VANES
TURNING VANES
TURNING VANES

Figure 2

```
****** GAS VELOCITY DISTRIBUTION ******
              100% FLOW
        14:1RFST *** 05/03/77

 1    2    3    4    5    6    7    8    9    10   11   AVG.
---------------------------------------------------------------------
280  250  295  295  265  250  270  290  290  230  320   276
280  265  300  285  315  215  260  290  320  250  280   278
275  290  315  315  330  255  295  305  330  285  240   294
300  320  345  385  360  355  335  315  340  325  285   333
310  340  370  395  370  345  350  360  350  325  310   3 [illegible]
345  325  395  415  390  370  370  375  375  325  340   366
345  350  395  420  410  380  390  390  385  310  345   375
355  340  400  410  375  365  390  385  385  320  345   370
325  325  390  395  390  385  335  375  390  305  335   359
310  320  365  385  365  350  355  340  360  315  315   344
290  305  360  375  340  335  340  340  335  300  300   329
285  280  300  345  295  290  290  310  300  255  300   295
290  315  300  320  320  320  305  275  275  235  335   299
---------------------------------------------------------------------
307  310  348  365  348  324  330  335  341  291  312   AVG.

NUMBER OF-READINGS= 143
MEAN VELOCITY= 328 FPM
ROOT MEAN VELOCITY= 331 FPM
R O O T  M E A N  S Q U A R E = 13.2891              INLET TEST
```

Figure 3

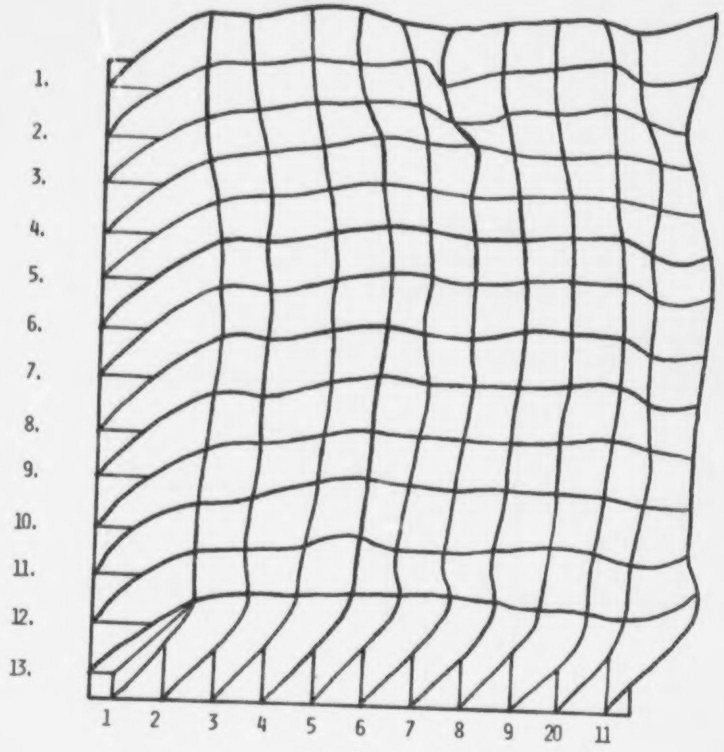

VELOCITY PROFILE
PRECIPITATOR
INLET

Figure 4

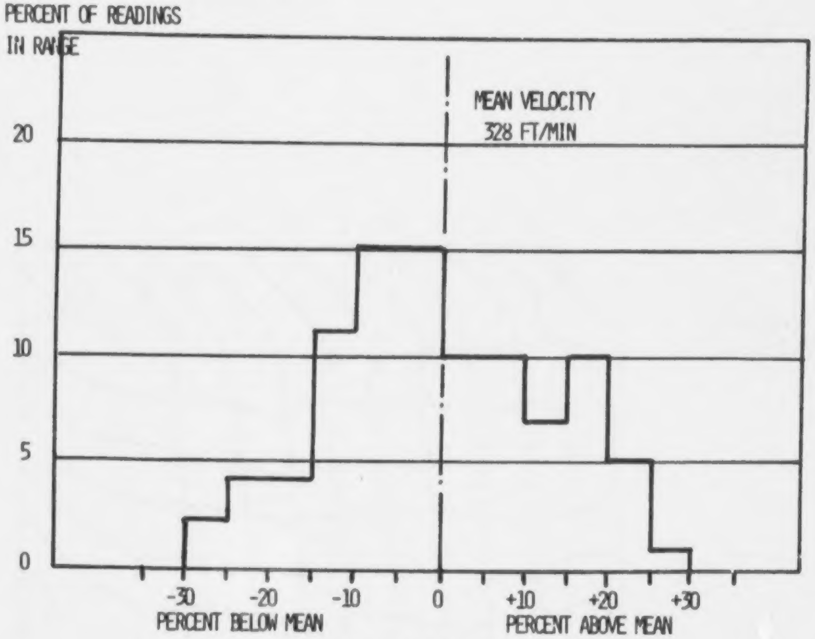

HISTOGRAM OF VELOCITY
DISTRIBUTION
PRECIPITATOR INLET

Figure 5

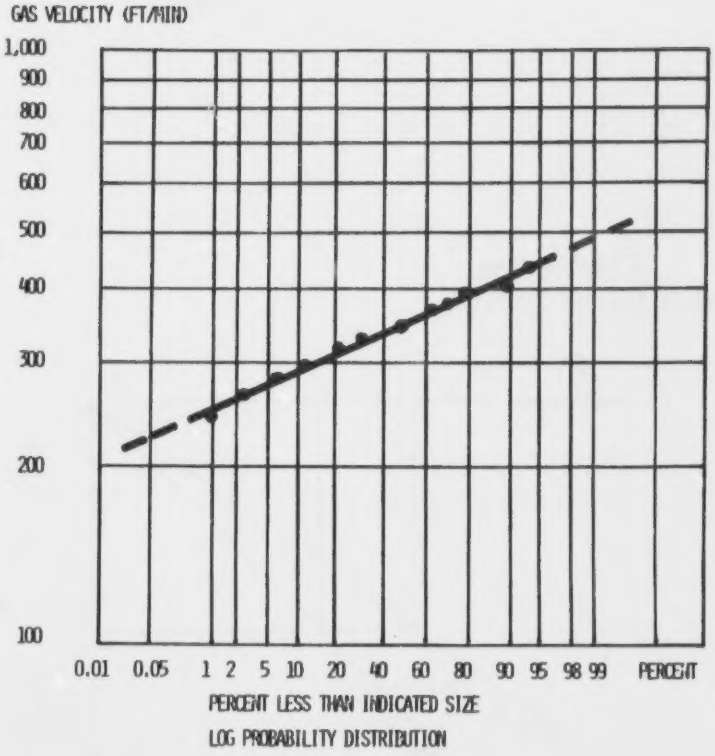
GAS VELOCITY (FT/MIN)
1,000
900
800
700
600
500
400
300
200
100
0.01
0.05
1
2
5
10
20
40
60
80
90
95
98
99
PERCENT
PERCENT LESS THAN INDICATED SIZE
LOG PROBABILITY DISTRIBUTION

Figure 6

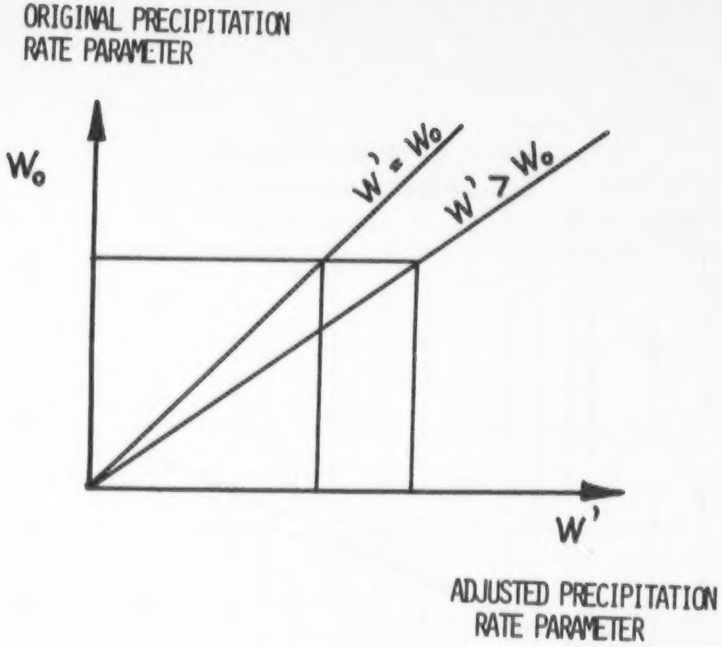
ORIGINAL PRECIPITATION
RATE PARAMETER
W_o
$W' = W_o$
$W' > W_o$
W'
ADJUSTED PRECIPITATION
RATE PARAMETER

Figure 7

CHEMICAL CONDITIONING OF FLY ASH
FOR
HOT SIDE PRECIPITATION

Peter B. Lederman, Ph.D.(1)
Peter B. Bibbo
John Bush
Research-Cottrell
Somerville, New Jersey 08876

Electrostatic precipitation has been and continues to be the primary method used by the utility industry to collect particulate matter generated during combustion. In the last ten years precipitators have been required to perform at increasingly greater collection efficiencies, often on fly ash which is harder to collect. This presents a precipitator manufacturer and the utility with choices

- make the precipitator larger
- modify the operating conditions
- modify the ash

The first option has been used frequently. It often is not attractive because of significantly larger investment requirements, and larger, and often unacceptable real estate demands. Increases in temperature, from 420°K (300°F) to 645°K (700°F), to the hot precipitator concept often result in a decrease in the resistivity to a level, 10^8 ohm-cm, where collection is easier and investments are more acceptable.

These options are not viable where a precipitator is already in place or the resistivity does not decrease sufficiently. In these situations, if an incremental efficiency increase is required (2% to 10% efficiency), ash modification is probably the more economical approach. Ash modification is usually the most economic alternative when switching coal.

---

(1) Current Address: V.P. & G.M. Cottrell Environmental Sciences, P.O. Box 1500, Somerville, NJ 08876

In cold side, low temperature, applications the addition of SO_3 is usually the chemical modifier. It is effective in most situations, economical and easy to produce on site. Its application has been widely discussed previously (1, 2). Its use is limited to situations where the temperature is below 450°K (350°F).

At elevated temperatures, above 475°K (400°F), SO_3 and other gaseous chemical modifiers have not been successfully used. Thus for hot side precipitators, those where the particulate is removed before entering the air preheater, another means of chemical modification is required. The modifiers of choice have been found to come from the alkali metal salts of which sodium salts are the most common. It is fortuitous that sodium is effective, because it is plentiful and relatively inexpensive. This paper presents in some detail the work leading to the choice of sodium and the inital commercial results.

Selection of Sodium Salts as Conditioning Agents

The sodium in fly ash, along with sulfur oxides and other selected components, helps to decrease resistivity. (3) The ions are good electron donors and contribute to electron mobility. Analyses have shown that the difficult-to-collect ashes are very low in alkali metal salts. The availability of these salts should decrease the resistivity and enhance precipitability. Sodium salts were chosen as the prime modifiers because of their availability and relatively low cost. A laboratory program was initiated to confirm the theoretical analysis.

Laboratory Methodology

Chemically modified ash was tested in a laboratory unit at typical operating conditions by comparing current-voltage curves of modified ash to curves of unmodified ash. In addition, resistivity values were compared.

The laboratory apparatus used for conditioning ashes and evaluating precipitator performance consists of five basic sections:

- a humidifier
- a gas heater
- a dust feed system
- a wire-pipe precipitator
- a gas mixing/additive system

The humidifier is designed to disperse gas bubbles through a water bath controlled to a specific temperature (320°K). This saturates the gas and provides a narrow range for water content - usually set at 10%. The temperature of the humidified gas is increased to the required operating temperature of 645°K (700°F) in the heater. The dust feed system adds the fly ash to the gas stream at a steady rate, between 2 and 6 grains per ACF. Any solid conditioning agent can be mixed with the fly ash before addition to the gas stream. The dust laden gas then flows into a small wire pipe precipitator Figure 1, where the ash is deposited on the pipe walls. The collecting pipe is one foot by 2-1/2" I.D. and is electrically isolated from ground. The discharge electrode is 0.030" stainless steel wire. A 30 kV D.C. negative power supply is used for energization and a Mosley X-Y recorder plots the applied voltage and corona current for each test condition.

The test ash samples were prepared using actual fly ash. Samples of Colstrip and Belle Ayre coal fly ash, fired in P.C. boilers, were tested at various times. All fly ash samples were selected from a uniformly mixed five gallon drum of hopper ash. Each sample was then preheated in an oven for 24 hours to remove surface condensables prior to further treatment. Unconditioned ash was stored in an oven at 700°F for 24 hours prior to injection. Each sample consisted of 20 grams of the preheated ash.

Conditioned ashes using 20 gram samples of the preheated ashes were prepared by one of the following methods:

a) The sample was spread out to a thin layer in a large crystallizing dish and sprayed with 10 milliliter of an aqueous solution of the conditioning agent, prepared by adding a specific quantity of the conditioning agent, based on a percentage of the sample weight, to five ml of water. This produced a very wet ash uniformly ceated with the agent. When spraying, the first five ml is used, and five ml of water is added to remove any remaining agent, and again sprayed on the ash. The ash was then dried for two hours at 422°K and for 22 hours or more at 730°K.

b) The conditioning agent was added to 10 ml of water. This solution is then added to the 20 grams of fly ash and mixed well. An additional aliquot of five ml of water is used to wash out any remaining solution, and added to the fly ash sample. This produced a wet slurry of ash, conditioning agent, and water. The slurry was then dried to a stiff paste on a hot plate, while

while continuously being stirred. This semi-dry paste was then placed in an oven at 730°K for drying for a minimum period of 24 hours.

c) A dry quantity of the conditioning agent was added to the fly ash sample and uniformly mixed and interdispersed. This mixture was then placed into the oven at 730°K.

Prior to the use of samples treated by method (a) or (b), it was necessary to pulverize the samples with a mortar and pestle to break up the large lumps that had formed. After pulverizing, the samples were placed back into the oven at 730°K until they were needed for injection.

"Blank" samples of all three methods were prepared in which the fly ash samples were prepared as described above except that conditioning agent was not added. These blanks were used to check that the properties of the unconditioned fly ash samples were unchanged.

Testing was carried out in the special laboratory pipe precipitators discussed above. The pipe precipitator was operated isothermally and voltage-current data taken. Voltage was increased until sparking occurs, or until back corona is indicated. These data were then compared to establish the effect of the conditioning agent.

For the test runs a simulated flue gas was prepared to give a final composition as follows:

Component	% by Volume
CO_2	16
O_2	7
N_2	67
H_2O	10
SO_2	250 ppm

Conditions of 10% moisture, 61 cm/sec (2ft/sec) gas velocity, 2.7 to 3 grains ash/ACF of gas, 645-670°K (700-750°F) gas and wall temperature, and constant gas composition were maintained throughout the test runs. The only variables were the amount of agent added and the methods of mixing. The ash was analyzed for chemical composition, resistivity and particle size distribution (Bahco). Data curves included clean conditions, dust feeding with the gas, and precipitated dust with gas flowing. Each curve is compared to the clean condition and to a reference curve taken for unconditioned ash.

Laboratory Results

The laboratory pipe precipitator simulates the full size unit but cannot provide collection efficiency data. Therefore current-voltage curve comparisons provide the best means of comparison. Typical base line curves, for the clean pipe precipitator are compared to unconditioned and conditioned ash as shown in Figure 2. An ash that will present no precipitation problems will have a voltage-current curve similar to that obtained with no dust in the unit, curve A. A difficult to precipitate ash, will typically have a very steep current-voltage slope at a relatively low voltage, as typified by curves C, depicting untreated, hard to collect ash. The negative slope, exhibited by curve D, is indicative of back corona, often found with high resistivity ash.

Several chemical modifiers were evaluated. Based on the relative slope and break in the current voltage curve, they were rated good, fair, poor. These evaluations are summarized in Table I. Curves that are representative of these semi-quantitive measures are compared to the clean precipitator curve in Figure 3. Sodium and the other alkali metal salte exhibit current-voltage characteristics that are essentially identical to those of the clean pipe precipitator, as shown by curve B-2 and B-3; these agents are considered good. On the other hand, TiO_2 and $FeCl_3$ were poor modifiers based on laboratory evaluations, as shown by curve B-1.

The effect of concentration can be seen in Figure 4 for sodium carbonate addition at typical hot precipitator conditions. This threshhold level is, of course, dependent on the virgin ash characteristics. However, addition rates of between 2% and 5% sodium as Na_2O appear to be reasonable for most applications studied.

The effect of operating temperature on conditionability was also studied in the laboratory. Alkali metal salt conditioning appears to be applicable over the entire range of interest including cold side units operating typically at 420° to 450°K (300-350°F).

A solution system appears to offer the most effective utilization of chemical. The solution would cover the fly ash particles and the sodium salt would adhere to the surface in a molecular layer when the water evaporated. This would provide the highest availability of sodium.

Pilot Unit Evaluation Next Step

Sodium carbonate was chosen for further field evaluation in a pilot precipitator. Although other sodium salts were evaluated in the field, Na_2CO_3 was the prime candidate because of availability and cost.

The pilot precipitator was a 6" diameter pipe unit with its own 45 KV transformer rectifier. Flue gas was removed isokinetically from the main flue using a mini-isolationg duct inside the main duct. Conditioning agent was sprayed into the mini-duct, shown in Figure 5, at a controlled rate as a water solution containing up to 15% sodium carbonate.

The principal evaluation was based on collection efficiency and current-voltage data. These results duplicated the laboratory results, as seen in Figure 6. Addition of conditioning agent increased the W_k, as shown in Figure 7.

Full Scale Commercialization

The success of the pilot program led to immediate installation of a full scale demonstration unit, using solution addition, at Wisconsin Power and Light's Columbia Station.

The full scale system, as depicted in Figure 8, consisted of

- Soda ash receiving system
- Soda ash make up and dissolving tank
- Solution day tank
- Feed pump
- Spray nozzels
- Wash system
- Addition to appropriate instrumentation

The demonstration system, at full scale, on a 525 MW P.C. boiler, was started up in November 1976. Opacities below 20% were achieved. In the full scale demonstration performance test emission levels were reduced by 90% and were well below compliance levels. The unit's efficiency was increased from about 85%, without conditioning, to 99.4% with conditioning with emissions as low as 0.04 lb/MM Btu during tests as shown in Table II. The demonstration unit was operated successfully from December 1976 til May 1978, to keep the unit within compliance.

The permanent system at Colubmia was started up in May 1978. It is based on the demonstration system, spraying sodium carbonate solution into the duct ahead of the precipitator. Residence times of under one second appear adequate. The system is fully automated, including solution, dilution, concentration and flush operations. Automatic start-up and shut-down are provided. Shake-down is basically complete. Opacities continue to be under 30% during normal operation, and can be reduced below 20% when desired. The removal of SO_x is a side, but important, benefit obtained when soda ash is used as the chemical conditioning agent.

Second Generation

A second generation system has been operated as a full scale demonstration, at the Comanche Station of Public Service Company of Colorado. Water is a critical commodity and further testing indicated that direct addition of a commercial grade soda ash could provide adequate conditioning. The permanent system, as outlined in Figure 9, is relatively simple as it eliminates the entire solution step. Solid soda ash, as received, is pulverized, and airveyed into the duct ahead of the precipitator. The system has been operating continuously since December. Opacity levels have been maintained below 20% and emission levels during test have been below 0.02 lb/MM Btu as compared to 0.06 to 0.14 lb/MM Btu prior to conditioning as detailed in Table II.

Economics Are Favorable

Investment for a liquid solution conditioning depends on the degree of duplication and automation. Typically a system will require an investment of $1,500-3,000 per installed MW. Chemical and operating costs will vary depending on the degree of conditioning required. Although no long term numbers are available, it is reasonable to expect that operating costs, exclusive of depreciation and capital costs will be in the neighborhood of 0.03 Mils/KWH. Investment requirements for the solid system will be somewhat lower. As no system has been built, it is premature to provide definitive costs; however, relative costs for conditioned and unconditioned units, detailed in Table III, show a definite advantage for hot, conditioned precipitators.

Conclusion

The concerns over universal application of hot precipitators to certain low alkali, low sulfur western coals, which emerged when performance problems on a few installations in the west were encountered (Columbia, Comanche, Hayden), have now been eliminated with the development of a practical and proven hot precipitator conditioning technology. Sodium conditioning has been proven in the field as the chemical modifier of choice, for hot precipitators. It is economically attractive compared to other means of upgrading marginal precipitators. This technology should be considered for new units to provide conditioned precipitator units capable of operating on difficult ashes, with the added benefit of some SO_x removal, at lower costs than systems not utilizing chemical conditioning.

REFERENCES

(1) White, H. J., Industrial Electrostatic Precipitators, Addison-Wesley, Reading Mass. 1963

(2) Dismukes, E. B., Conditioning of Fly Ash with SO_3 and NH_3, NTIS, P.B. 247231 (1975)

(3) Bickelhaupt, R. E., Effect of Chemical Composition on Surface Resistivity, NTIS, P.B. 244885 (Aug. 1975)

TABLE I

Conditioning Agent Evaluation

Conditioning Agent	% Added (1)	Effectiveness
NH_3	100 ppm (2)	Moderate
SO_3	50 ppm (2)	Poor
NH_3+SO_3	50 ppm (2)	Poor
$(NH_4)_2SO_4$	1.26	Poor
$NaHSO_4$	2.83	Good
Na_2SO_4	1.38	Good
Triethyl Amine	0.177	Moderate to Poor
Ferrous Sulfate	6.74	Moderate to Poor
NaOH	10 (5.9 Na)	Good
NaCl	5.56 (2.2 Na)	Moderate to Poor
Na_2HOP_4	6.14	Good
KOH	2.92	Good
$KHSO_4$	6.97	Good
$NaHCO_3$	4.8 2.135	Good Moderate
Na_2CO_3	6.7 4.5	Good Good
TiO_2	3.26	Poor

---

(1) On solid except as noted
(2) On gas

TABLE II

Sodium Carbonate Conditioning

Full Scale Operating Conditions

	Collection Efficiency, %	Current Density ma/1000 ft^2	Particulate Emissions lb/MM Btu
Solution Conditioning (1)			
Unconditioned (2)	84	13.0	0.85 (0.1-1.9)
Conditioned (3)	99.3	30.8	0.04 (0.031-0.047)
Solid Conditioning (4)			
Unconditioned (5)	98.0	21.1	0.101 (0.06-0.14)
Conditioned (6)	99.8	26.6	0.011 (0.006-0.014)

(1) Unit #1, Columbia Station, Wisconsin Power and Light
(2) Average - 9 tests over 5 days
(3) Average - 5 tests over 3 days
(4) Unit #2, Comanche Station, Public Service Co. of Colorado
(5) Average 5 tests over 2 days
(6) Average 6 tests over 3 days

TABLE III

Relative Costs for Various Electrostatic Precipitator-Conditioning Options

	Investment	Own & Operate Annual
Cold Precipitator (1)	100%	100%
Cold Precipitator with SO_3 Conditioning	74%	86%
Hot Precipitator with Solid Sodium Salt Conditioning	72%	69%

(1) Base Case

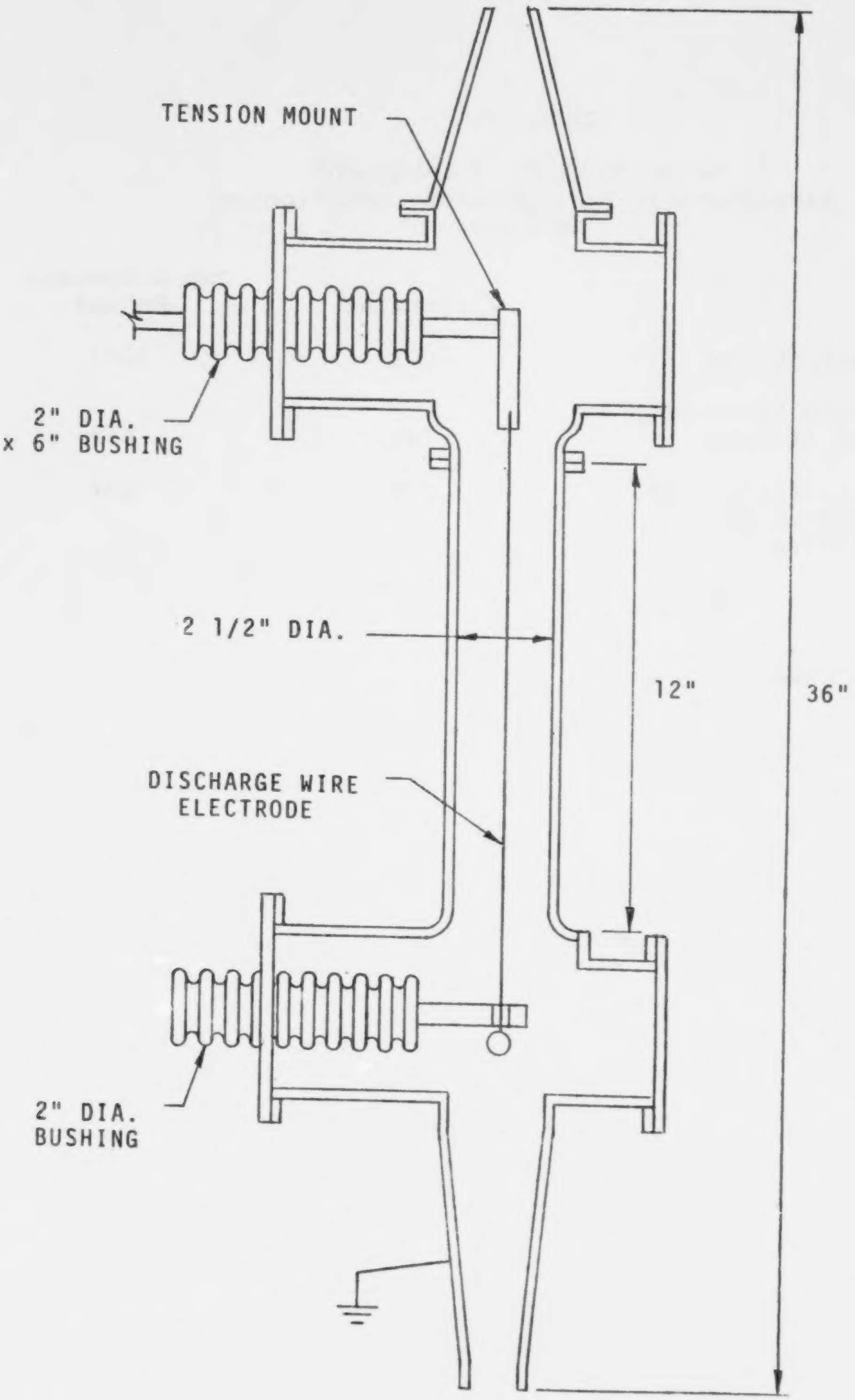
TENSION MOUNT
2" DIA.
x 6" BUSHING
2 1/2" DIA.
12"
36"
DISCHARGE WIRE
ELECTRODE
2" DIA.
BUSHING

FIG. 1
LABORATORY PIPE PRECIPITATOR

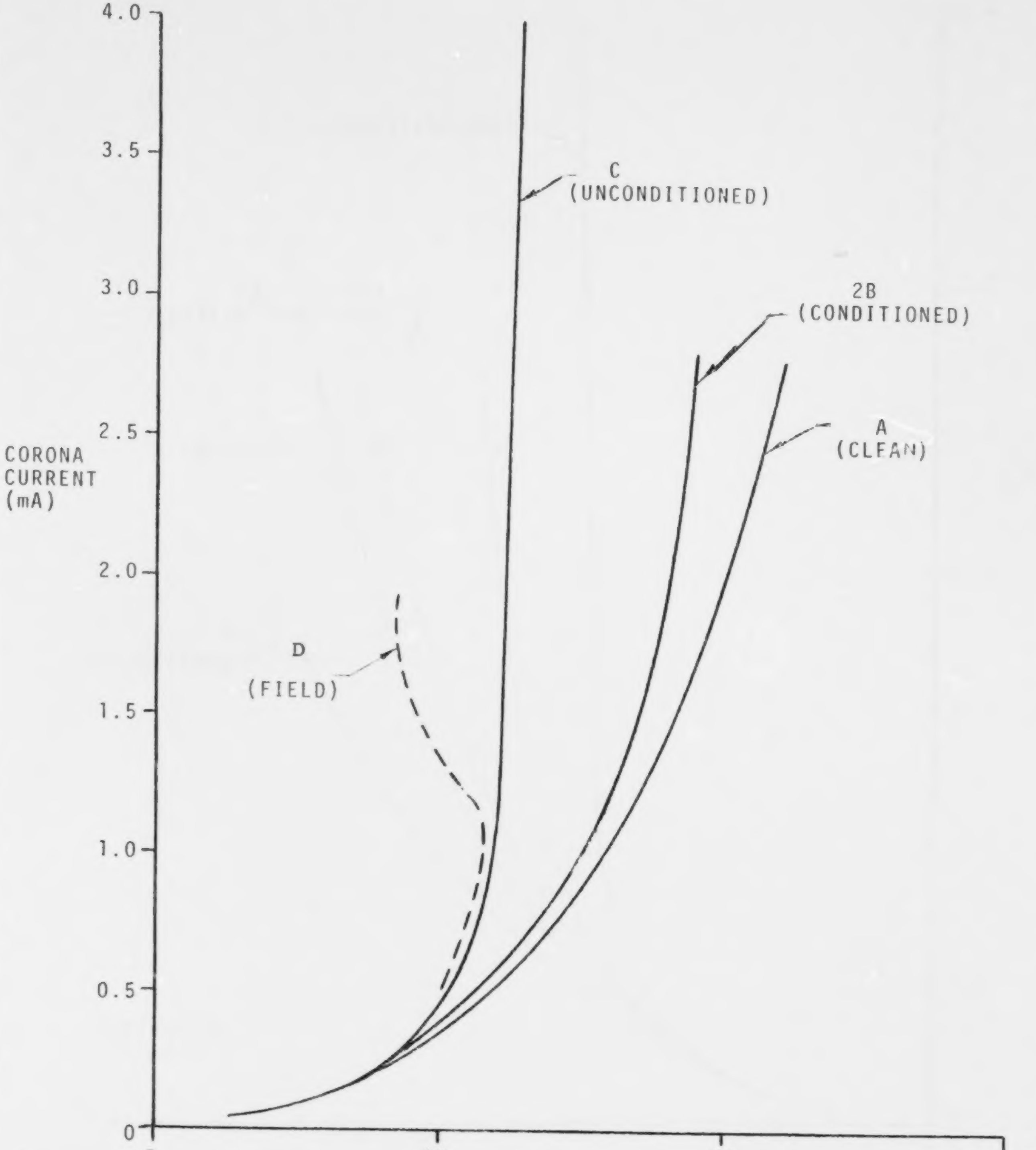

FIG. 2
EFFECT OF CONDITIONING ON CURRENT

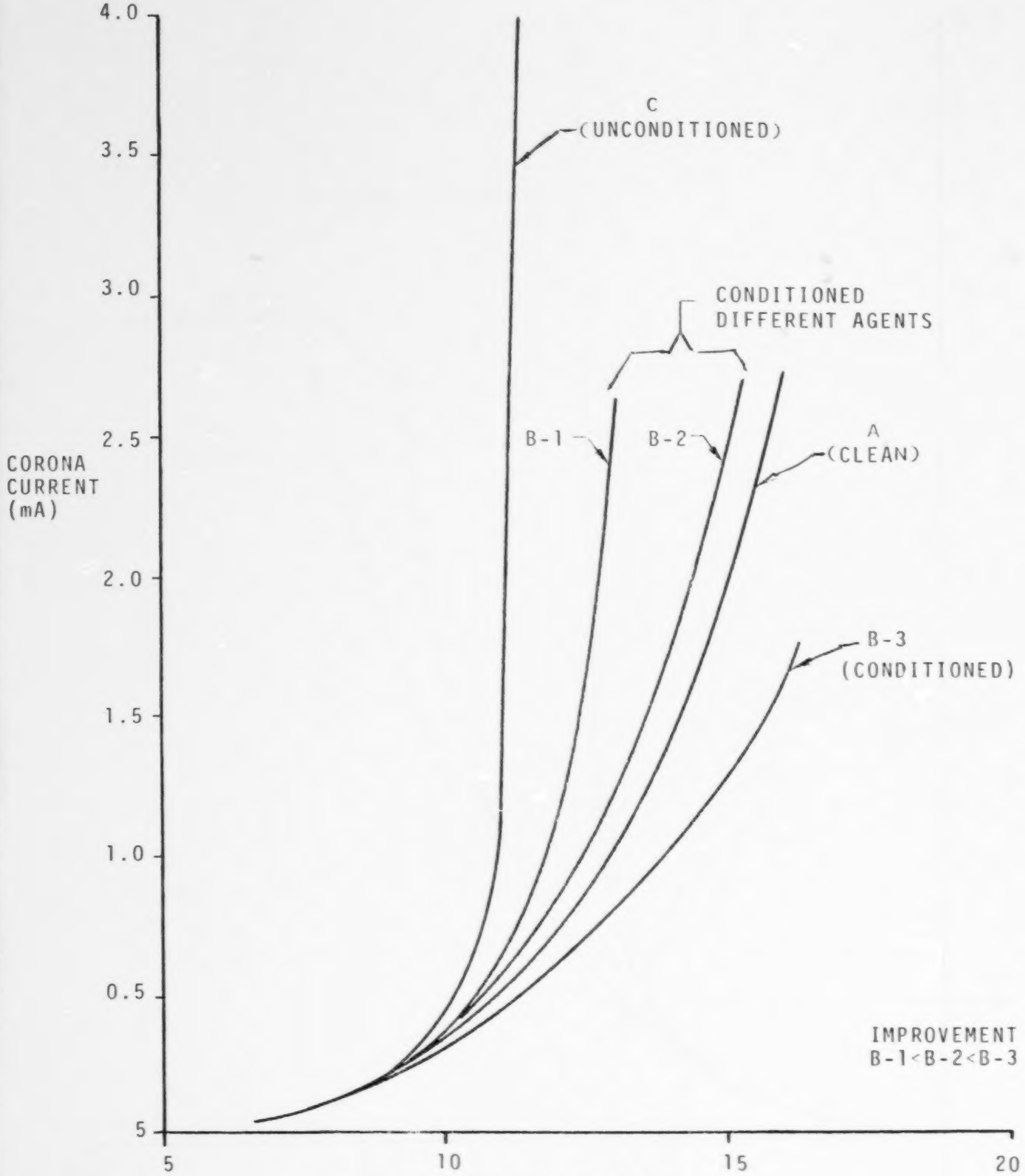

FIG. 3

EFFECT OF CONDITIONING

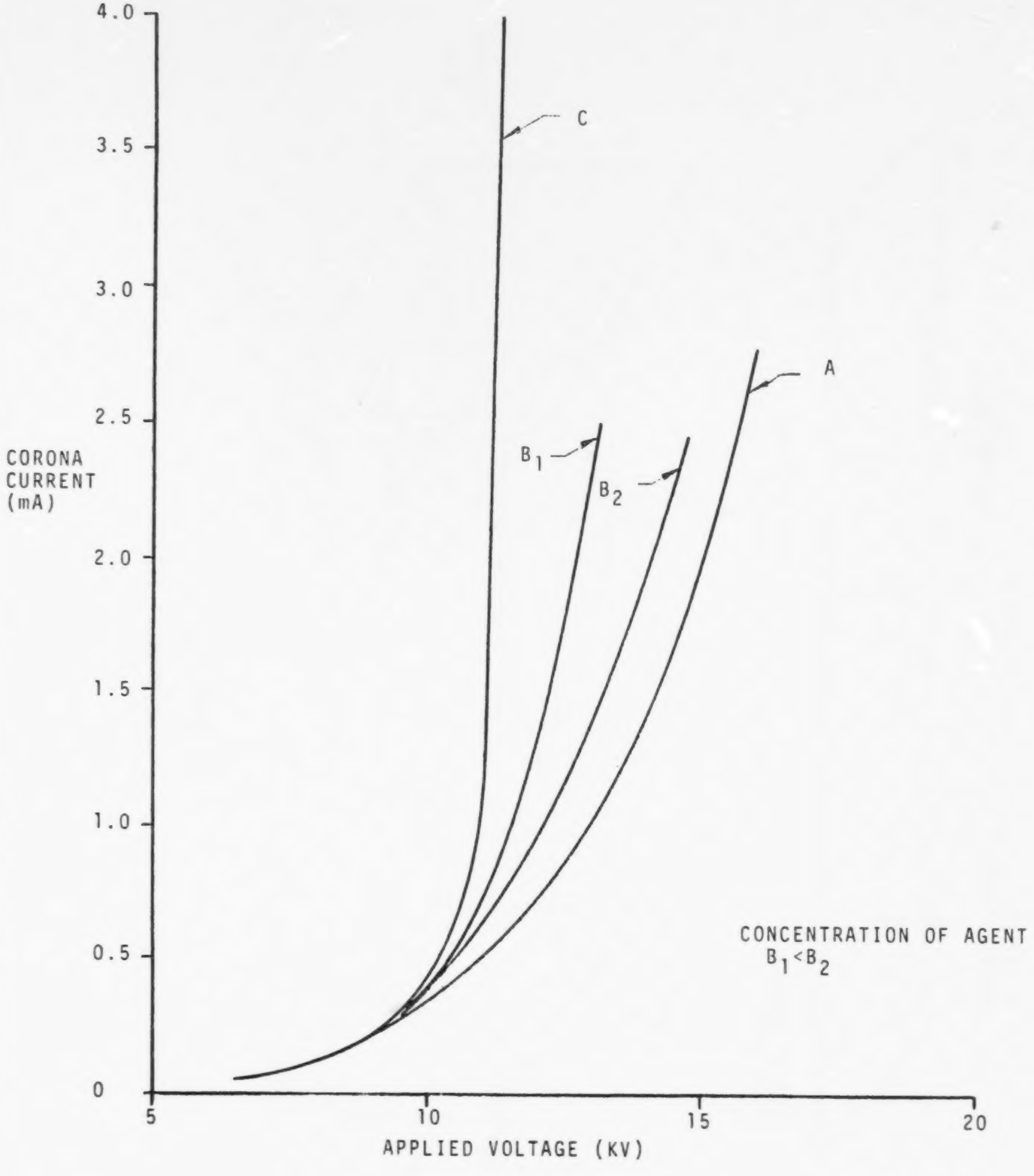

FIG. 4
EFFECT OF CONCENTRATION

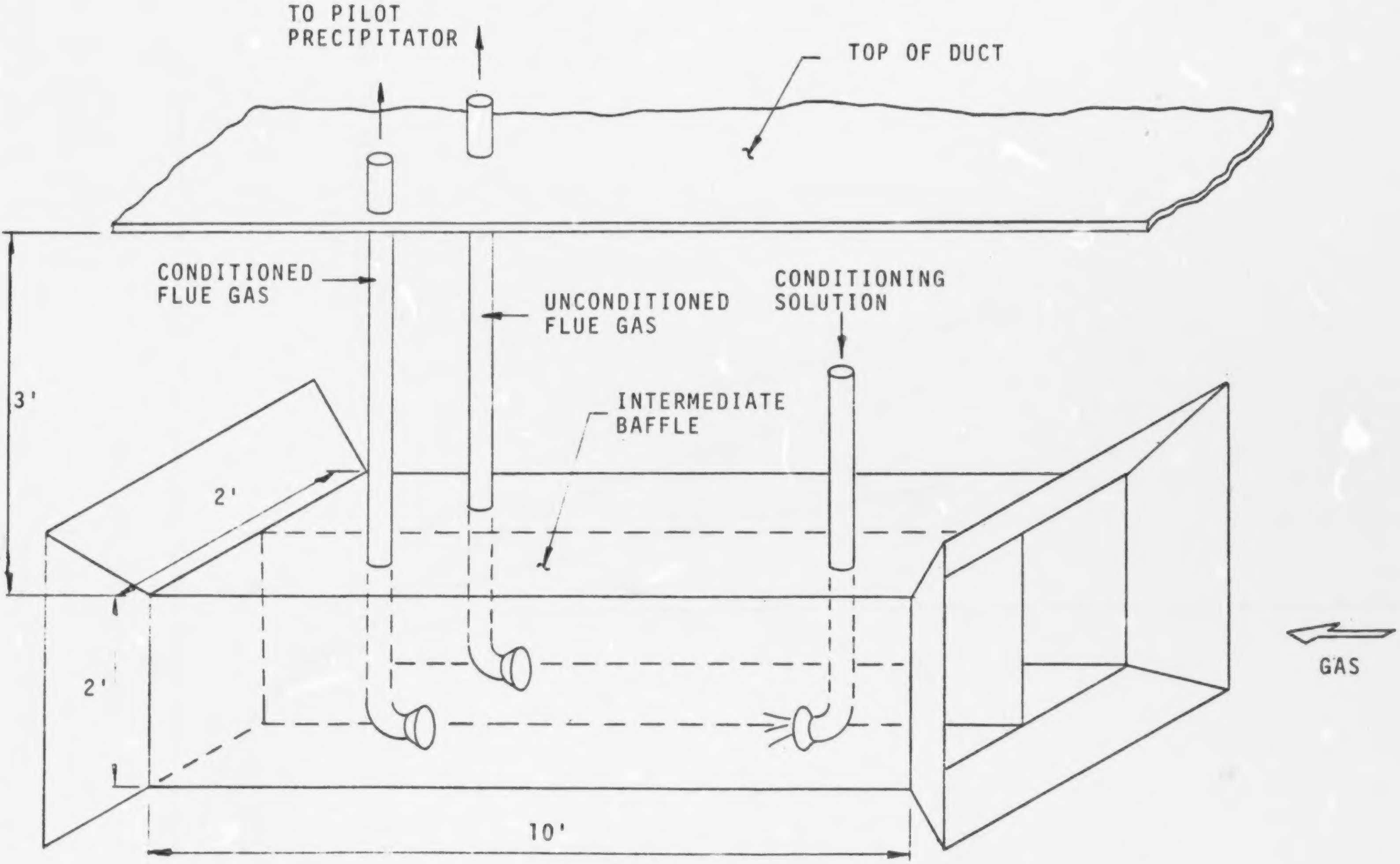
TO PILOT
PRECIPITATOR
TOP OF DUCT
CONDITIONED
FLUE GAS
UNCONDITIONED
FLUE GAS
CONDITIONING
SOLUTION
INTERMEDIATE
BAFFLE
3'
2'
2'
10'
GAS

FIG. 5
PILOT MINI-DUCT

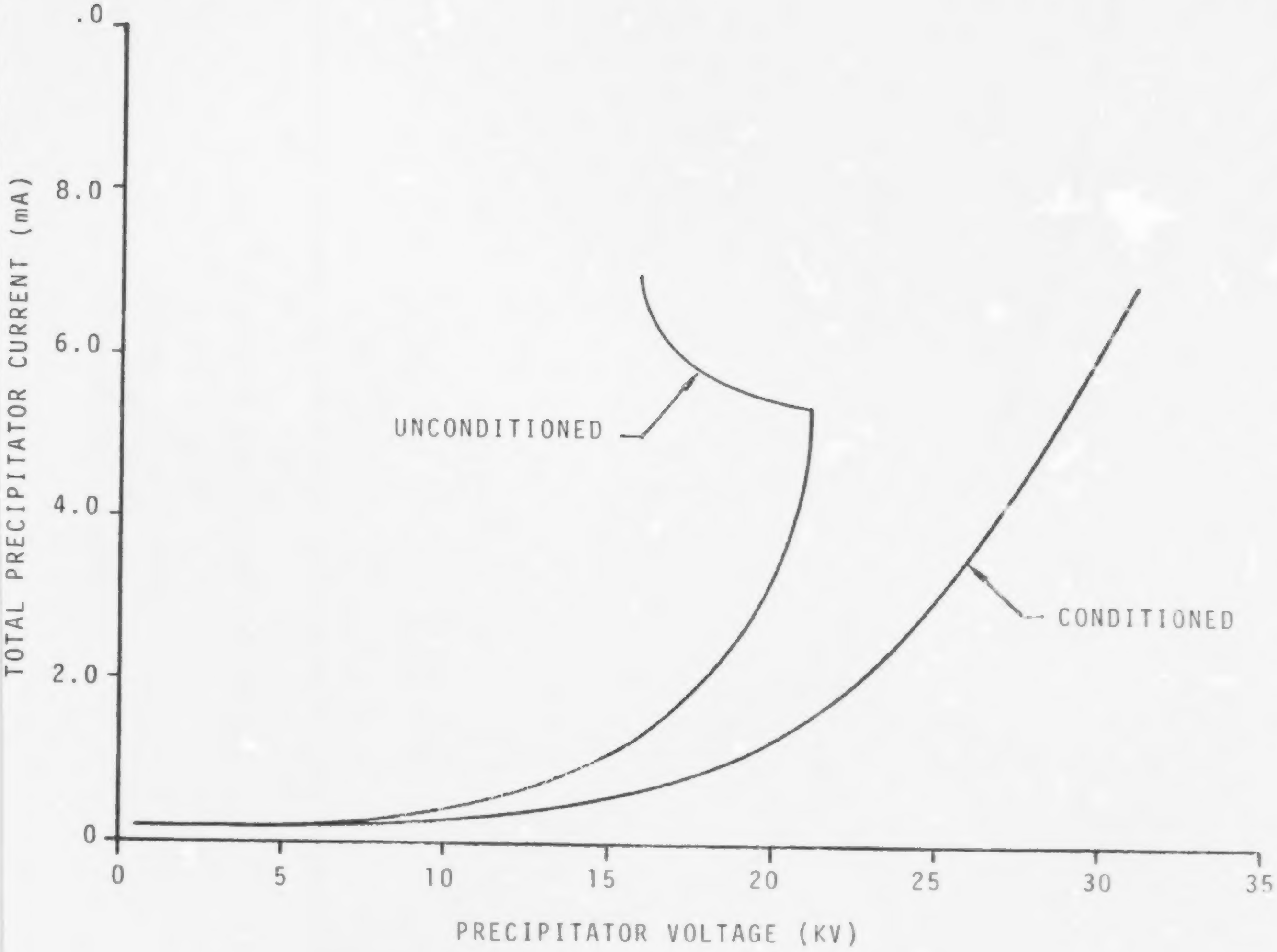

FIG. 6
SODIUM CONDITIONING
PILOT UNIT

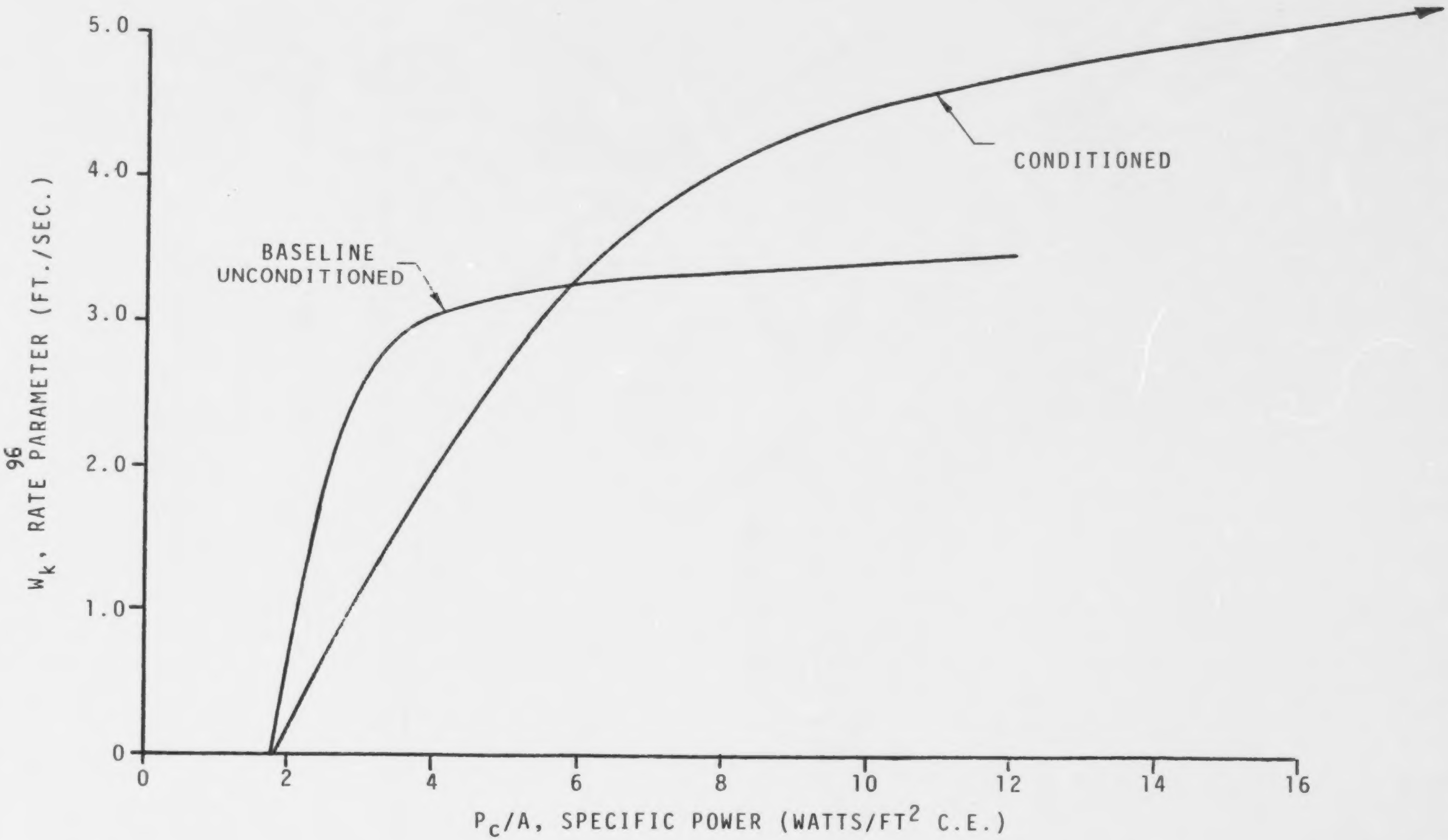

FIG. 7
SODIUM CONDITIONING
PILOT UNIT
PRECIPITATION RATE

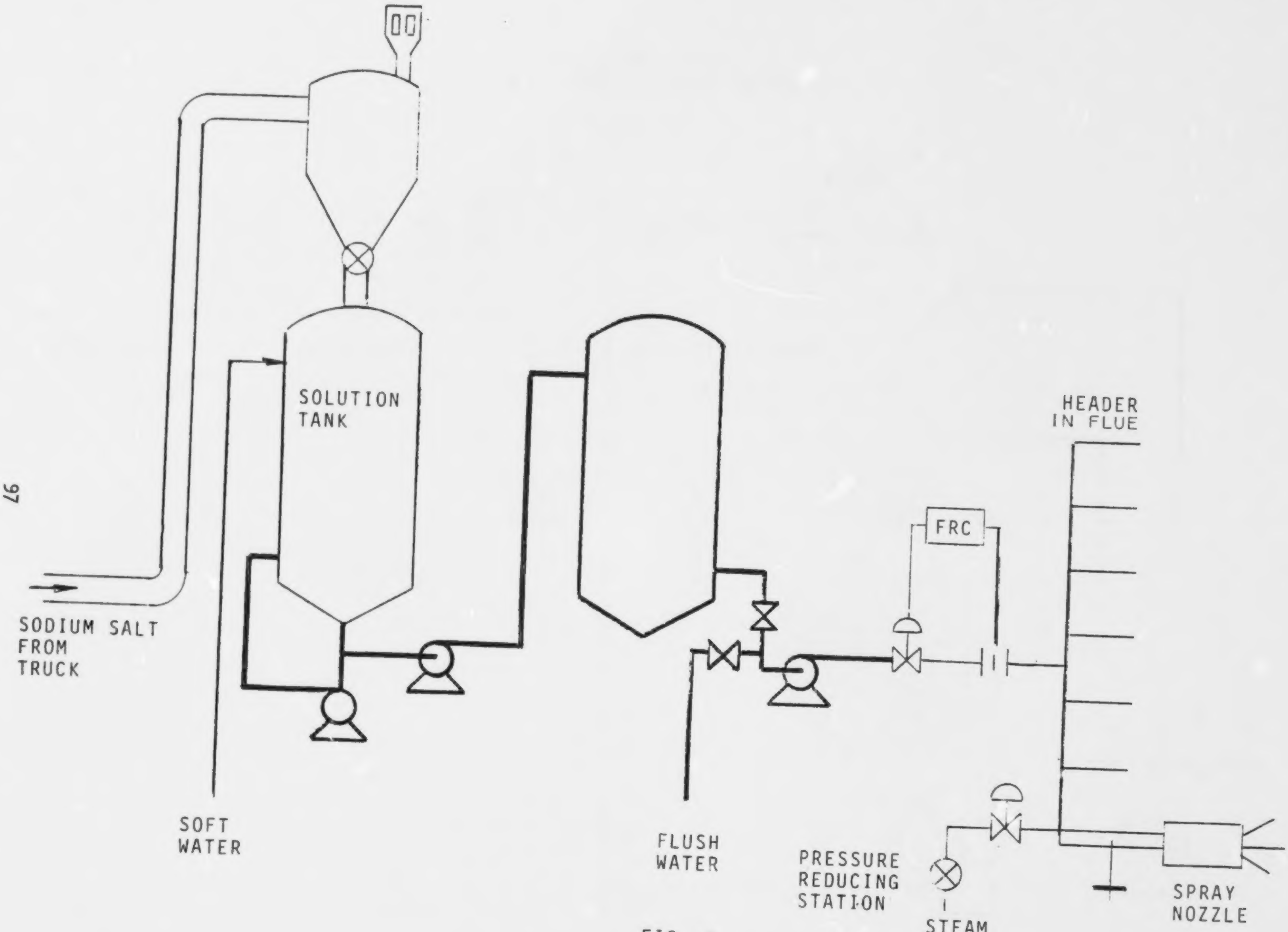
SOLUTION TANK
HEADER IN FLUE
FRC
SODIUM SALT FROM TRUCK
SOFT WATER
FLUSH WATER
PRESSURE REDUCING STATION
STEAM
SPRAY NOZZLE

FIG. 8
FULL SCALE DEMONSTRATION
SODIUM SALT SOLUTION
CONDITIONING SYSTEM

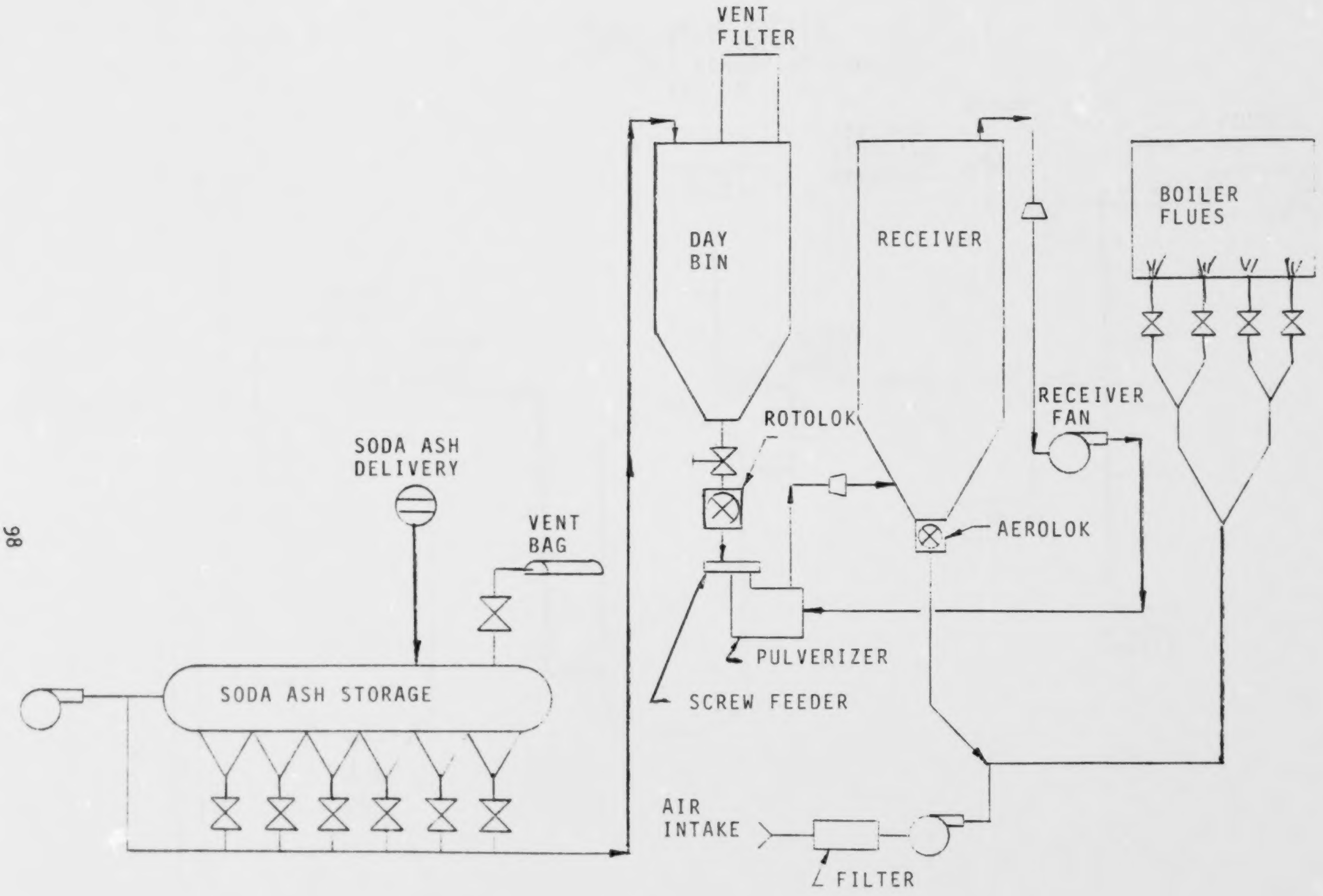
VENT FILTER
DAY BIN
RECEIVER
BOILER FLUES
ROTOLOK
RECEIVER FAN
SODA ASH DELIVERY
VENT BAG
AEROLOK
PULVERIZER
SODA ASH STORAGE
SCREW FEEDER
AIR INTAKE
FILTER

FIG. 9

SOLID CONDITIONING AGENT
ADDITION SYSTEM

CONDITIONING OF DUST WITH WATER-SOLUBLE ALKALI COMPOUNDS

H. Hoegh Petersen
F.L. Smidth & Co.
Copenhagen, Denmark

ABSTRACT

A comparison of resistivity measurements and chemical analyses of dusts from cement rotary kilns has shown a close relationship between resistivity and the content of water-soluble alkali compounds. Laboratory experiments comprising impregnation of high resistivity dust samples with various water-soluble alkali salts confirmed that small quantities of alkali compounds were sufficient to reduce the resistivity considerably. This led to full scale experiments at a precipitator installation treating high resistivity dust from a preheater kiln at a cement plant in Brazil. Here an aqueous solution of potassium sulphate was injected, atomized and evaporated in the gas stream before the precipitator. An 0.4% increase in water soluble K_2O reduced the resistivity of the dust from 10^{13} to 10^{11} ohm·cm and a corresponding improvement in precipitator performance was observed. Recent additional full scale conditioning experiments with potassium sulphate and sodium chloride at a precipitator installation after a coal-fired lime kiln in South Africa yield similar results.

INTRODUCTION

In cement manufacturing raw materials, consisting of limestone or chalk with addition of silica and clay minerals are finely ground and fed to a rotary kiln installation either as raw mix slurry (wet process), or as a dry raw meal (dry process). Here the raw mix is being burnt into cement clinker by firing with pulverized coal, oil or gas through a burner pipe into the outlet end of the kiln.

Wet-process kilns, which formerly were predominant, were succeeded by fuel-saving long dry-process kilns in the early sixties. Later further improvement in fuel economy was obtained by introduction of short dry-process kilns equipped with suspension cyclone preheaters with 1 to 4 stages. The diagrams Figures 1 and 2 show examples of such kiln installations.

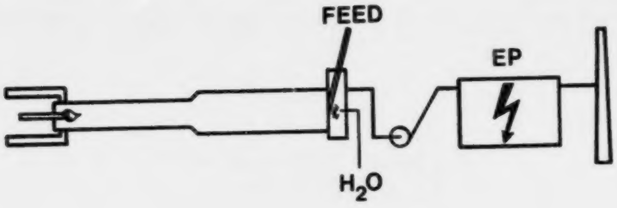

Figure 1. Long dry-process rotary kiln with precipitator. Gas cooling by injection of water in kiln inlet.

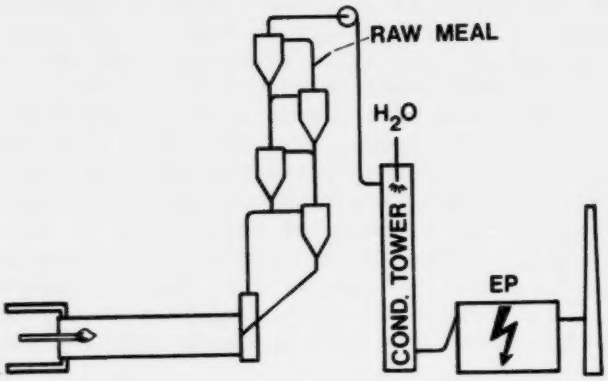

Figure 2. Short dry-process rotary kiln with 4-stage cyclone preheater and precipitator. Gas cooling in evaporative conditioning tower.

In the newest types of dry-process kilns a precalciner, where fuel is added, is inserted between the cyclone preheater and the rotary kiln.

The new fuel-saving kiln systems turned out to be more difficult to dedust. This was due to a general increase in dust resistivity, refer Figure 3, which shows typical resistivity curves for dust from different kiln types. These curves must only be taken as typical examples. There may for same kiln type be large variations in resistivity level from one plant to another, depending on raw materials, fuel, kiln operation etc.

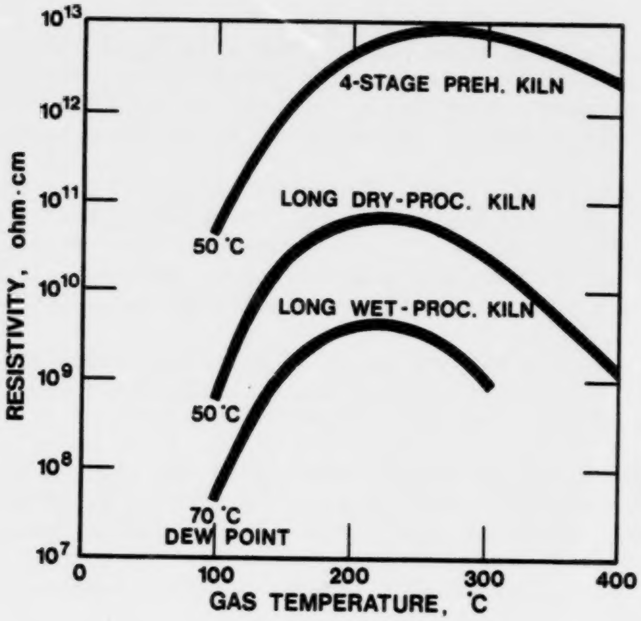

Figure 3. Resistivity of dust from different types of cement kilns.

The resistivity of the dust after a kiln with 4-stage cyclone preheater is usually so high that water conditioning is required, either in an evaporative conditioning tower, or by utilization of the hot gases for drying of raw materials, or by a combination hereof. The reason for this high resistivity will be further discussed in the following.

RESISTIVITY AND ALKALIES

The transition from long wet- or dry-process cement kilns to short dry-process kilns with preheaters carried with it a major change in the alkali circulation pattern of the process.[1,2]

Volatile matters, i.e. potassium, sodium, sulphur, and chlorides contained in small quantities in the raw mix will evaporate in the burning zone of the kiln and condense again when cooled, either on the surface of dust particles or forming small separate particles. Alkalies which have been vaporized and have condensed again in the kiln system form more high volatile compounds than the raw material alkalies do. This repeated evaporation and condensation results in an increasing internal circulation of alkalies in the installation until an equilibrium is reached.

With the long kiln a major part of the evaporated and condensed alkalies are carried with the gases to the precipitator, where they are collected and are fully or partially returned to the kiln system. The precipitator here is a part of the alkali circulation circuit.

In the short kiln with 4-stage cyclone preheater most of the vaporized alkalies carried with the gases from the burning zone condense on the cold raw materials fed into the preheater, and are returned direct to the kiln without reaching the precipitator. The main alkali circulation is here between kiln and preheater, excluding the precipitator.

As a result of this difference in alkali circulation patterns the alkali content of the dust after a preheater kiln is in general substantially lower than after a long kiln without preheater.

Where a lowering of the alkali content in the clinker from a 4-stage preheater kiln is desirable, this may be obtained by letting a part of the kiln gases with their content of alkali-rich dust by-pass the preheater for dedusting in a separate precipitator. Such an arrangement, often termed an "alkali by-pass", allows removal of alkalies from the process.

With a long kiln, removal of alkalies from the process may be obtained by full or partial discarding of the kiln precipitator dust.

Resistivity measurements and chemical analyses of a large number of dust samples from different cement kiln installations under varying operating conditions have pointed towards a close relationship between the resistivity of the dust and its content of water-soluble potassium and sodium compounds, rather than with its total content of alkalies.

Figure 4 shows the result of a regression analysis on data from 38 samples of dust from a precipitator installation at a 300 ts/24 h gas-fired 4-stage preheater cement kiln in Mexico.

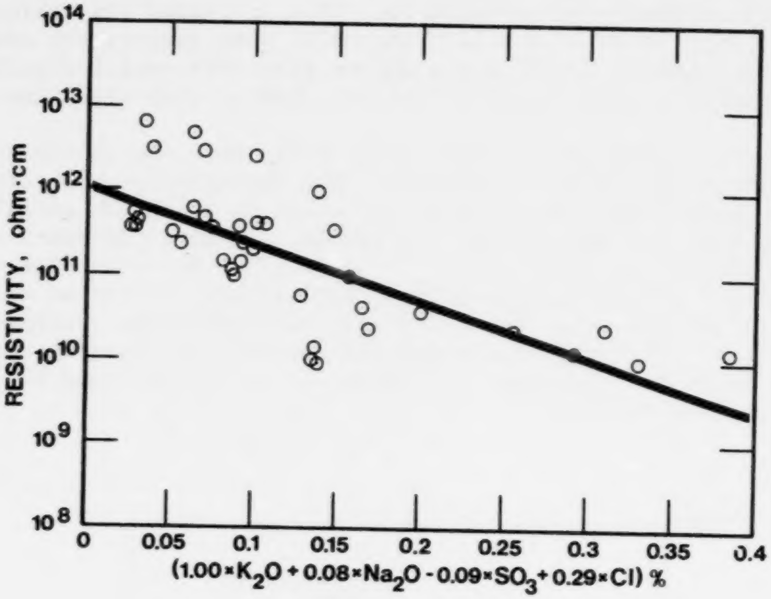

Figure 4. Regression analysis of resistivity (380°C, dew point 40°C) versus water-soluble K_2O and Na_2O and total SO_3 and Cl on dust samples from 4-stage preheater cement kiln in Mexico.

At this installation, where there was no conditioning tower before the precipitator, variations in precipitator performance had been found to be due to resistivity variations. The regression analysis relates the resistivity variations to variations in the content of water-soluble alkali compounds in the dust, particularly potassium.

Regression analyses with samples from other installations have shown similar results except for Na_2O having a considerably greater effect.

LABORATORY EXPERIMENTS

Further proof that the conductivity factor for dust from cement kilns is water-soluble alkali compounds was obtained by a series of laboratory experiments carried out at F.L. Smidth's laboratories in 1969.

The soluble chemical substance was extracted with water from a dust sample with medium level resistivity. This increased its resistivity from 2.5×10^9 ohm·cm to 6×10^{10} ohm·cm at same temperature and dew point. Chemical analyses of the filtrate showed that this mainly contained potassium and sodium sulphates and chlorides together with some lime.

Other dust samples with high resistivity were impregnated with various water-soluble alkali compounds. The impregnation was carried out by mixing equal quantities of dust and water in which the alkali salt had been dissolved, and then drying the sample. These experiments showed that small quantities of alkali salts were sufficient to reduce the resistivity considerably. Among the more promising compounds, as far as resistivity reducing effect and price are concerned, were potassium sulphate and sodium chloride. Figure 5 thus shows the resistivity reducing effect of these two salts in quantities corresponding to 0.1% K_2O and Na_2O in such laboratory experiments.

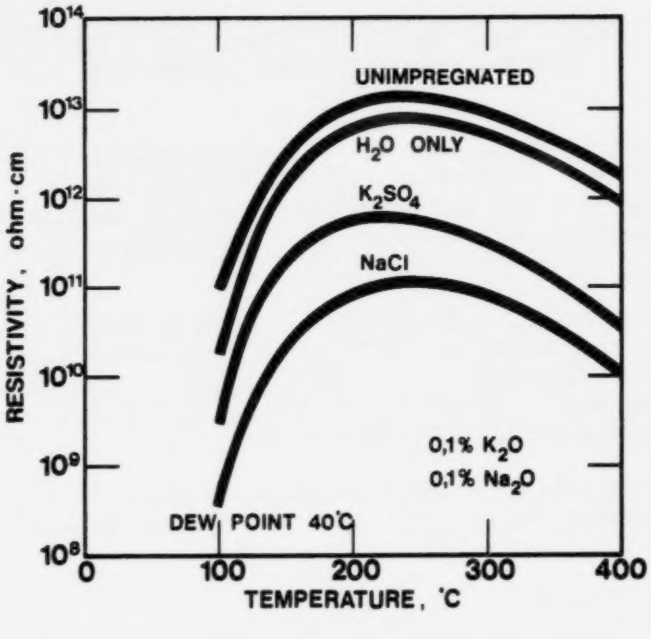

Figure 5. Resistivity reductions by aqueous impregnation of high resistivity dust samples with potassium sulphate and sodium chloride.

It was found that dry admixture of powdered alkali salts to high resistivity dust samples required considerably larger amounts of salts than aqueous impregnation did, in order to produce the same resistivity reductions.

These experimental findings for dust from cement kilns have parallels in earlier discoveries for fly ash, where research described by H.J. White[3] had shown that the conductivity factor for fly ash is water soluble (sulphate) leading to the discovery of SO_3 as the natural conditioning agent for fly ash.

FULL SCALE TESTS AT CEMENT KILN IN BRAZIL

The laboratory experiments were followed by extensive full scale tests at a cement plant in Brazil in 1971. The tests were carried out at the plant's 800 ts/24 h 4-stage preheater kiln with conditioning tower and precipitator, where dust samples had shown high resistivities typical for this type of kiln. The object of the tests was to find out if addition of potassium sulphate to the dust immediately before the precipitator would give a similar drop in the resistivity of the precipitated dust, as found at the laboratory experiments, and to study the effect on precipitator performance.

The potassium sulphate was introduced as an aqueous solution, which was injected, atomized and evaporated in the gas stream before the precipitator in order to obtain a uniform distribution of very fine alkali particles on the dust. The injection facilities of the conditioning tower were used for this purpose. It was only necessary to add a 1 m^3 blending tank for batchwise preparation of a 5% potassium sulphate solution, a 10 m^3 tank for storing the solution, and a pump for adding the solution to and blending it with the clean water fed to the conditioning tower.

Two series of efficiency tests, respectively without and with potassium sulphate conditioning, were carried out with the precipitator at varying gas temperatures. The gas temperature was varied by adjusting the amount of water injected in the conditioning tower from 0 up to 6000 litres per hour. During the test series with conditioning approximately 500 litres per hour of 5% potassium sulphate solution was added to the cooling water, corresponding to approx. 0.4% K_2O of the total amount of dust entering the conditioning tower. An impregnation period of several days was allowed from the start of the conditioning until the beginning of the efficiency tests.

The conditioning resulted in an increase of water-soluble K_2O in the precipitated dust from originally 0.03 - 0.05% in unconditioned state to 0.4 - 0.5% in conditioned state, and a drop in resistivity of approximately 2 decades, refer Figure 6.

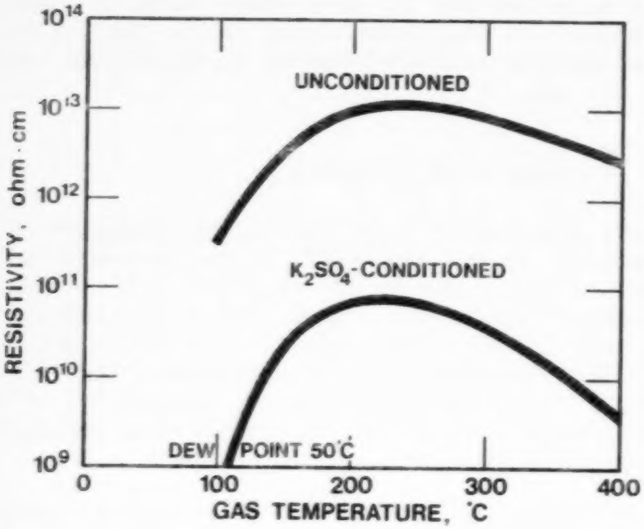

Figure 6. Resistivity reduction by potassium sulphate conditioning at cement preheater kiln.

Figure 7 shows the migration velocity as a function of the gas temperature without and with conditioning.

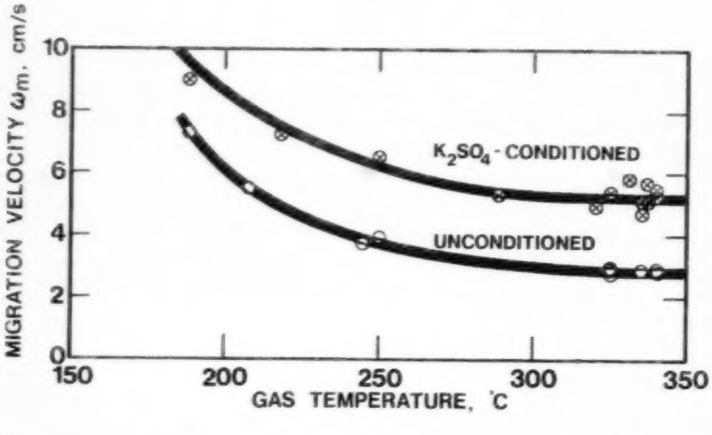

Figure 7. Improvement in migration velocity by potassium sulphate conditioning at cement preheater kiln.

The effect on precipitator performance of the resistivity reduction resulting from the conditioning is evident from the obtained improvements in migration velocities in the temperature range 200°C to 340°C. The generally rather low migration velocities at the higher gas temperatures are partially attributed to reentrainment at the high gas velocities resulting from operating the precipitator at gas temperatures far above the 150°C for which it is designed with the conditioning tower in normal operation.

Table 1 contains further information about precipitator operating conditions during the tests.

Table 1. Precipitator Operating Data.

	Design Data	Conditioning Tests	
		Unconditioned	Conditioned
Kiln Output, ts/24 h	925	785 - 830	825 - 835
Gas Volume, Nm^3/h	66,800	67,200 - 79,000	68,300 - 77,800
Gas Temperature, °C	150	188 - 340	188 - 340
Barometric Pressure, mm Hg	690	675 - 680	673 - 680
Dew Point, °C	60	42 - 55	42.5 - 54.5
Inlet Dust Conc., g/Nm^3	75	21.7 - 28.2	24.0 - 30.5
Outlet Dust Conc., g/Nm^3	1.50	1.85 - 10.73	0.78 - 6.29
Gas Velocity, m/s	1.06	1.39 - 1.60	1.36 - 1.61

Precipitator Data: 1 chamber, 2 sections, 1535 m^2 total collecting area, 250 mm duct width, two 70 kV/400 mA rectifiers.

Alkali conditioning requires only small amounts of water compared with conventional conditioning towers. The price of commercially available potassium sulphate, however, has so far made practical use of alkali conditioning less attractive as an alternative to conditioning towers for cement preheater kilns, even at plants with water shortage. There is, however, the not yet tried out possibility that the necessary quantities of water-soluble alkalies for the conditioning in future could be obtained from the process itself, by leaching of a minor part of the dust extracted directly from the kiln through the "alkali by-pass" and the separate precipitator of same.

The amounts of K_2O and SO_3 introduced in the cement making process with the conditioning are negligible (0.02% K_2O) compared with the normal content of these constituents (0.4% K_2O) in the raw meal.

Sodium chloride, which has the advantage of being comparatively cheap, is not suitable for conditioning purposes in the cement industry due to adverse effect of chlorides, even in very small concentrations, on kiln operation and clinker quality.

Sodium chloride, however, might be an interesting conditioning agent in other industries where process and product are not sensitive to chlorides.

FULL SCALE EXPERIMENTS AT LIME KILN IN SOUTH AFRICA

Early in 1978 full scale conditioning experiments with potassium sulphate and sodium chloride were carried out at a coal-fired lime kiln in South Africa located 1600 m above sea level. The precipitator had not been able to meet the guarantees due to an unexpected high resistivity level of the dust from the kiln, and conditioning was tried out as a method to improve performance. The gases from this long rotary kiln with an output of 700 ts/24 h are cooled to 300-375°C before treatment in the precipitator by injection of 6-10 ts/h of water in the kiln inlet. The precipitator treats approximately 100,000 Nm^3/h with a dust concentration of about 20 g/Nm^3. Microscope-examinations of the dust had shown that this consisted of approximately equal parts of lime dust and fly ash from the coal burning.

The conditioning experiments were carried out by adding potassium sulphate (25 kg/h), respectively sodium chloride (50 kg/h) in solution to the cooling water injected in the kiln inlet. Only 33% of the added potassium sulphate, respectively 17% of the added sodium chloride was refound in the 2000 kg/h of dust precipitated, the balance apparently being lost in the kiln with the feed.

The potassium sulphate conditioning increased the content of water-soluble K_2O in the precipitated dust from 0.02% to 0.25% reducing the resistivity by approximately 2 decades, refer Figure 8.

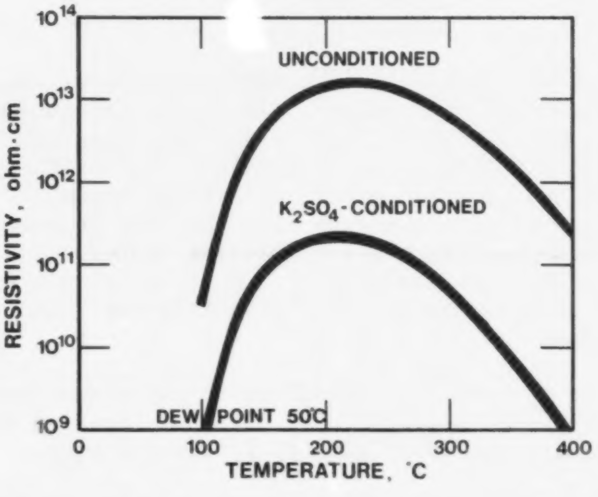

Figure 8. Resistivity reduction by potassium sulphate conditioning at lime kiln.

The result of the sodium chloride conditioning was an increase in water-soluble Na_2O in the precipitated dust from 0.04% to 0.27%, and a resistivity reduction of also approximately 2 decades, refer Figure 9.

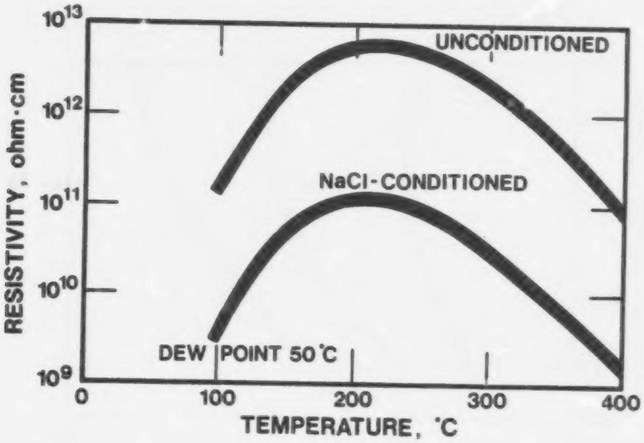

Figure 9. Resistivity reduction by sodium chloride conditioning at lime kiln.

The resistivity reducing effect of the conditioning could be seen shortly after the conditioning had been started, and lasted for some time after it had been stopped, refer Figure 10.

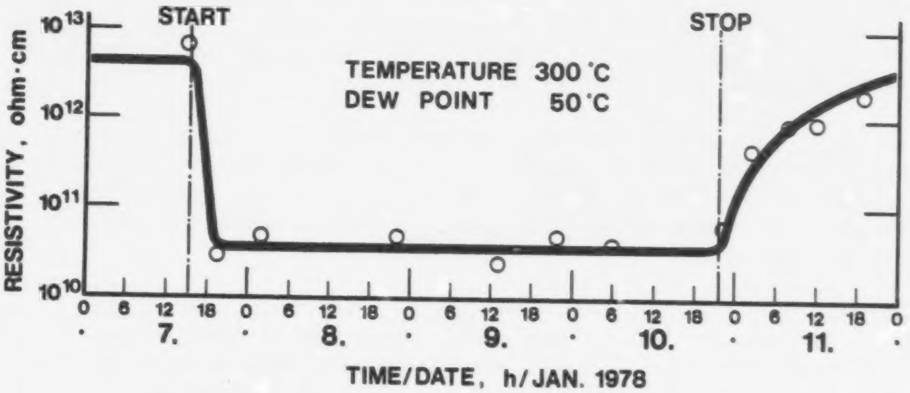

Figure 10. Resistivity reductions during conditioning test with potassium sulphate at lime kiln.

The resistivity reduction obtained by the conditioning reduced "back-corona" and increased precipitator voltage, refer Figure 11, which shows the current-voltage characteristics for the precipitator's three consecutive sections A, B, and C without and with sodium chloride conditioning.

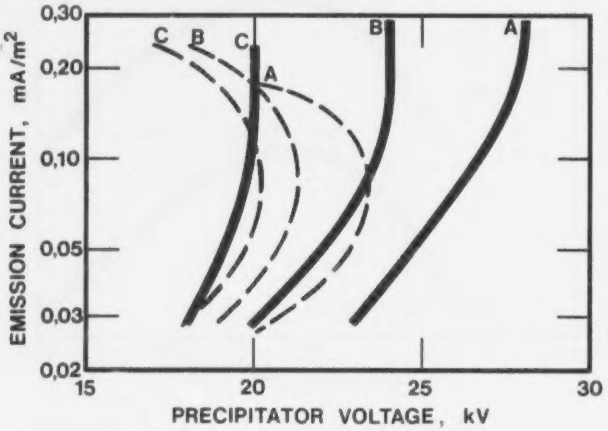

Figure 11. Current-voltage characteristics for
consecutive precipitator sections A, B, and C.
----- without conditioning.
——— with sodium chloride conditioning.

Both the potassium sulphate conditioning and the sodium chloride conditioning reduced the precipitator outlet dust concentration from 650 - 700 mg/m^3 (0°C, 625 mm Hg) without conditioning to approximately 160 mg/m^3 (0°C, 625 mm Hg) with conditioning, bringing the installation within the guarantee of 175 mg/m^3 (0°C, 625 mm Hg).

Additional sodium conditioning tests have been planned at the installation with the aim of reducing salt consumption. At these tests the sodium chloride solution will be injected and evaporated direct in the gas stream before the precipitator, instead of adding it to the cooling water injected in the kiln inlet.

Other tests under consideration comprise dry conditioning by addition of sodium chloride to the coal. Experiments carried out at a Danish lime kiln installation June this year, where small amounts of sodium chloride were added dry at the coal grinding mill, have indicated that considerable improvements in precipitator performance is obtainable by this method.

CONCLUSIONS

Laboratory experiments and full scale tests show that water-soluble alkali compounds, as for example potassium sulphate and sodium chloride are powerful conditioning agents when applied to high resistivity dusts from cement and lime kilns.

Small quantities of alkali compounds can produce substantial resistivity reductions when introduced as an aqueous solution injected, atomized and evaporated in the gas stream before the precipitator. This method[4] results in a uniform distribution of very fine alkali particles on the dust, ensuring effective use of the conditioning agent.

Water-soluble alkali compounds could have similar resistivity reducing effects on other types of dusts, as for example high resistivity fly ash. If this should be the case, conditioning of high resistivity fly ash by injection and evaporation of sea water in the gas stream, which could be accomplished without any substantial cooling of the gases, might be an interesting subject for further investigations.

ACKNOWLEDGEMENTS

The author wishes to acknowledge the cooperation of his colleagues, H. Alsted Nielsen, who conducted the laboratory experiments, and P.F. Carlsen and G. Werner who carried out the major part of the field work upon which this study is based.

REFERENCES

1. Von P. Weber. Alkaliprobleme und Alkalibeseitigung bei wärmesparenden Trockendrehöfen. Zement-Kalk-Gips. Heft 8, August 1964.

2. Von F.W. Locher, S. Sprung und D. Opitz. Reaktionen im Bereich der Ofengase. Zement-Kalk-Gips. Heft 1, Januar 1972.

3. H.J. White, "Industrial Electrostatic Precipitation", Addison -Wesley, Reading, Massachusetts. 1963, pp. 315-316.

4. H. Claudi Westh. Treatment of Hot Dust-Laden Gases. British Patent 1,262,100 (1972).

CHEMICAL ENHANCEMENT OF ELECTROSTATIC PRECIPITATOR EFFICIENCY

R. P. Bennett and A. E. Kober
Apollo Chemical Corp.
35 South Jefferson Road
Whippany, New Jersey 07981

The problem of coal-burning power plants as a major source of fine particulate pollution has become a national concern, especially in relation to the nation's commitment to double coal consumption by 1985. Federal and State environmental protection agencies and many other groups have become increasingly concerned over the effects of fine particulate pollution. The majority of coal-fired power plants today rely on the electrostatic precipitator as the primary means of particulate emission control. Generally, power plants which have switched to lower sulfur coal in order to comply with SO_2 emission regulations have experienced a deterioration in the efficiency of the precipitator. This may result in an increase in particulate emissions and an inability to meet compliance regulations for both particulate emissions and opacity control.

Mechanical solutions to this problem involve the retrofitting or expansion of precipitator capacity or the addition of scrubbers or baghouses to the existing facility. This generally results in large capital expenditures and significant time spans before such solutions can be implemented. Even then, there is no guarantee that the new equipment will be adequate for the fuels available at the time these units become operative.

During the past several years there has been an increased interest in the use of chemical conditioning for the enhancement of precipitator efficiency, generally with the aim toward meeting compliance regulations without the need for the major expenses and the long lead time necessary before the system is operable. We have previously reported[1,2] on the use of blended chemical formulations in utility power plants of up to 750 Mw. These chemical conditioning agents have been used with a variety of low- to medium-sulfur coals, resulting in substantial precipitator efficiency

Preceding page blank

improvement, usually allowing compliance levels for both particulate emissions and opacity. We wish now to report on the further expansion of this technology into new areas. Specifically, we wish to discuss the successful use of chemical conditioning with high-sulfur coal, with a hot precipitator and with a new technique involving a dual injection system.

High Sulfur Coal

In a number of cases, units burning design coal with high sulfur content are still experiencing emissions problems. Assuming that the precipitator is in optimal mechanical condition, there are several reasons possible for excessive emissions levels. One reason can be that of over-conditioning of the flyash. Too low a resistivity results in particles discharging their acquired electrical charge too quickly so that the particles are easily eroded and reentrained in the flue gas stream. A second factor is that of high exit gas temperatures which are maintained in order to prevent condensation of excess SO_3 from the flue gas which could result in corrosion and air heater pluggage. This method of operation not only reduces boiler efficiency, but also increases the gas volume and velocity through the precipitator, thus reducing the precipitator efficiency.

Table 1.
HIGH SULFUR COAL EXAMPLE

Description of Unit	
Boiler Mfr.	Foster-Wheeler, front-fired
Capacity	320 Mw
Precipitator	Buell
SCA	137 ft^2/1000 ACFM
Velocity	5.8 fps
Gas rate	1.1 MM ACFM @ 268°F
Design Coal	3.7% Sulfur; 8.5% Ash; 12,000 BTU/lb
Current Coal	3.2-3.9% Sulfur; 9-13% Ash; approx. 12,000 BTU/lb

Results at 320 Mw

	Emissions			Precipitator Efficiency %
	#/hr	#/MM BTU	% Reduction from Baseline	
For Compliance	350	0.100	–	99.1
Untreated, Baseline	488	0.139	–	98.8
LPA-treated (approx. 0.20 GPT)				
Average of all tests	180	0.055	68	99.5

One relatively new way to combat this situation with high-sulfur coals is by the addition of a properly blended chemical conditioning agent into the flue gas stream in a hot section of the boiler. Chemical conditioning of flyash alters resistivity by means of a surface coating. The resistivity of treated flyash, therefore, approaches the same final value regardless of whether the resistivity of the untreated ash is above or below that required for optimum collectibility. In the case of high-sulfur coal, the resistivity of the ash is actually shifted toward higher values closer to the optimum by chemical treatment. In this case the effects of agglomeration of flyash by the additive cannot be readily distinguished from electrical effects. The unit described in Table 1, burning design coal, was unable to meet particulate emissions compliance levels without additive treatment.* A test program was first performed to optimize precipitator operation. Thereafter, chemical treatment was applied to successfully condition the ash, improving its collectibility and reducing particulate emissions to well within required compliance levels. The approximate treatment cost for this type of process was only $0.52/ton of fuel.

Hotside Precipitators

It is well known that resistivity, which has a major effect on the collectibility of flyash, varies with temperature. An optimum range of resistivity exists in which flyash is most readily collected. At approximately 100°C, flyash resistivity is relatively insensitive to coal sulfur content; however, with increasing temperature the resistivity of flyash from low-sulfur coal increases much more rapidly than that from high-sulfur coal. A maximum occurs at about 165°C, and, thereafter, the resistivity decreases steadily with increasing temperature. One technique which is being used to take advantage of this aspect of low resistivity at high temperature is to build a "hot precipitator" placed ahead of the air heater where the flue gas temperature will be in the 330°-450°C range. In this temperature zone resistivity generally is within the optimum range for collection. Two obvious drawbacks to this design are the increased volume of gas which must go through the precipitator in this temperature range and, secondly, the heat loss realized with the precipitator ahead of the air heater.

One unit firing low-sulfur Western coal and utilizing a hot precipitator is described in Table 2. This unit was unable to consistently meet emissions compliance for particulate matter and was not able to meet opacity requirements due to an excessive amount of fine particulate which was not being collected. The unit load had to be controlled so that the opacity limit was not exceeded. A chemical treatment program was established and several different chemical formulations were evaluated for their ability to reduce opacity since electrical response was not deemed to be the problem. While several formulations were evaluated in this unit, it is interesting that the most effective blend contained no sodium.

---

* LPA and LAC are product series designations of Apollo Chemical Corp. GPT represents gallons of additive per ton of coal fired.

A dramatic reduction in opacity was obtained in a very short response time and at relatively low additive treatment level. Additionally, the particulate emissions were reduced substantially so that this unit can operate with an "emissions buffer" at a minimal annual treatment cost of approximately $120,000 per year.

Table 2.
HOT SIDE PRECIPITATOR AND LOW-SULFUR COAL EXAMPLE

Description of Unit	
Boiler Mfr.	Combustion Engineering
Capacity	280 Mw (1005°F/1950 psig)
Precipitator	Wheelabrator-Frye
SCA	347 ft^2/1000 ACFM
Velocity	5.16 fps
Gas rate	1.664 MM ACFM at 695°F
Design Efficiency	99.5% (=0.01 grain/SCF outlet)
Design Coal	0.5% Sulfur; 11.5% Ash; 10,300 BTU/lb
Current Coal	Approx. 0.5% Sulfur; 8-15% Ash; 10,500 BTU/lb

Results at 280 Mw

	Emissions #/MM BTU	**Opacity %**
For Compliance	0.10	20
Untreated	0.10 - 0.14	22-30
LPA-40 treated (0.07 GPT)	0.02 - 0.03	12

Dual-Additive Injection

Previous papers have discussed the various mechanisms by which chemical conditioning can enhance the collectibility of flyash.[3, 4] It has previously also been noted that not all of these mechanisms are affected equally in each instance of successful chemical conditioning. In addition, the predominant mechanism has been found to vary in some cases with the temperature of injection. For example, it is possible to obtain dramatic, rapid reduction in opacity without necessarily seeing any change in precipitator power or flyash resistivity by careful selection of additive or injection site.

This discovery has led to a new technique of dual injection which takes advantage of the multiplicity of mechanisms of flyash conditioning. This technique involves the application of one additive into a hot section of the boiler, followed by injection of the same or a different additive into a relatively low-temperature zone, usually after the air heater. The combined treatment rate is generally less than that required by the single injection into the hot temperature zone. Additionally, this technique gives greater flexibility for formulation in that different materials may be applied into each injection zone, depending upon the deficiency of the precipitator. The remaining discussion describes units which are currently being successfully treated by this procedure.

Table 3.
DUAL INJECTION FLUE GAS CONDITIONING EXAMPLE

Description of Unit

Boiler Mfr.	Combustion Engineering
Capacity	380 Mw (1005^{o}F/2450 psig)
Precipitator	Buell
SCA	174 ft^2/1000 ACFM
Velocity	6.1 fps
Gas Rate	1.1 MM ACFM @ 260^{o}F
Design Efficiency	Not determined after third field was put in.
Design Coal	0.6% Sulfur; 9.1% Ash; 13,370 BTU/lb
Current Coal	0.8-1.5% (1.0% Av.) Sulfur; 13-17% Ash; 12,500 BTU/lb

Results at 370-385 Mw

Treatment, GPT		Emissions #/MM BTU
For Compliance		0.135
LPA	**LAC**	
0	0	0.375
0.15	0	0.270
0.15	0.10	0.105

The unit described in Table 3 had very low power and had emissions of about three times the particulate compliance level. Application of an LPA formulation produced increased power and reduced the ash resistivity from 2 x 10^{11} to 5 x 10^{10} ohm-cm. Some reduction in particulate emissions was obtained. This unit has a mechanical collector ahead of the precipitator for the removal of large particles. An LAC product was then applied to reduce reentrainment with the result that emissions were reduced significantly below the compliance level.

The unit described in Table 4 was diagnosed as having a reentrainment problem. Resistivity was not considered to be a problem. Even derating the boiler down to 300 Mw still did not produce compliance particulate emissions. Several LPA products were then evaluated. No electrical changes were observed, but one formulation gave compliance emissions at 0.15 GPT. Since there was insufficient leeway for continuous compliance under various operating conditions, an additional LAC feed was applied, allowing significantly reduced emissions, even at higher load.

Table 4.
DUAL INJECTION FLUE GAS CONDITIONING SYSTEM EXAMPLE

Description of Unit

Boiler Mfr.	Babcock & Wilcox
Capacity	480 Mw, dry bottom
Precipitator	Research-Cottrell
SCA	170 ft^2/1000 ACFM
Velocity	7.0 fps
Gas Rate	1.5 MM ACFM @ 272°F
Design Efficiency	98.5%
Design Coal	2% Sulfur; 12% Ash; 12,000 BTU/lb
Current Coal	1.3-1.7% Sulfur; 14-18% Ash; 11,000-13,000 BTU/lb

Results

Gross Load Mw	Precip. Power, Mw	Treatment, GPT LPA	LAC	Particulate Emissions, #/MM BTU	Opacity %
For compliance				0.24 Max.	40 Max.
≃ 300	0.6	0	0	<0.24	40
470-480	0.6	0	0	2.15	>60
410	0.6	0	0.10	0.24	35-40
470-480	0.6	0.075	0.10	0.09	19-28

The unit described in Table 5 burns a lignite fuel and frequently had opacity excursions due to fine particulate. Significant deration would be required to achieve both particulate and opacity compliance consistently. Application of an LPA formulation showed some particulate and opacity reduction, but the addition of an LAC formulation was necessary to control opacity adequately.

Summary

It has been shown previously that chemical conditioning of flyash can offer an immediately available alternative to retrofit precipitators, baghouses, or other methods of mechanical collection and usually provides compliance emissions at relatively low operating costs. The equipment required involves minimum capital investment and can usually be installed in a matter of weeks with no significant unit downtime being involved.

It has now been demonstrated that the technique of chemical conditioning can be expanded into previously untried areas with the successful treatment of high-sulfur coals, of hot precipitators, and of low-sulfur coals utilizing a dual-injection system to provide minimum emissions and minimum opacity. Ready availability and minimum total costs are two advantages of this method. The use of new conditioning agents for these processes is continually being examined for further advances in the state of flue gas chemical conditioning.

Table 5.
DUAL INJECTION FLUE GAS CONDITIONING SYSTEM EXAMPLE

Description of Unit	
Boiler Mfr.	Combustion Engineering
Capacity	575 Mw
Precipitator	Research Cottrell
SCA	186 ft^2/1000 ACFM
Velocity	5.0 fps
Gas Rate	2.1 MM ACFM @ 335°F
Design Efficiency	98.85%
Design Coal	0.6% Sulfur; 14.2% Ash; 6800 BTU/lb
Current Coal	0.6-1.0% Sulfur; 18% Ash; 6000-7500 BTU/lb

Results

Gross Load Mw	**Treatment, GPT LPA**	**LAC**	**Particulate Emissions #/MM BTU**	**Opacity %**
Compliance Requirement			0.30 Max.	30 Max.
<500	0	0	0.30	–
570-580	0	0	0.68	>70
570-580	0.05	0	0.41	47
570-580	0.10	0	0.36	40
570-580	0.10	0.10	0.20	28

REFERENCES

1. Bennett, R. P. Fly Ash Conditioning to Improve Precipitator Efficiency with Low Sulfur Coals. ASME 76-WA/APC-8.

2. Borsheim, R. and Bennett, R. P. Chemical Conditioning of Low-Sulfur Western Coal. (Presented at 39th Annual Meeting, American Power Conference. Chicago, IL. April 1977.)

3. Oglesby, S. Jr. and Nichols, G. B. A Manual of Electrostatic Precipitator Technology. Southern Research Institute, Contract EPA-22-69-73, National Air Pollution Control Administration, 1970, Part I - Fundamentals. NTIS PB 196380. Part II - Application Areas, NTIS PB 196381.

4. Dismukes, E. B. A Study of Resistivity and Conditioning of Fly Ash. Southern Research Institute, Contract EPA 70-149, Environmental Protection Agency, Publication Number EPA-R2-72-087. NTIS PB 212607.

METHOD AND COST ANALYSIS OF ALTERNATIVE COLLECTORS FOR LOW SULFUR COAL FLY ASH

Edgar W. Breisch
Wahlco, Inc.
3600 W. Segerstrom Ave.
Santa Ana, CA 92704

INTRODUCTION

Electrostatic Precipitators have been the traditional and predominant high efficiency fly ash collector for high sulfur coal fired power boilers. Their low pressure drop and location on the relatively low gas volume cold side of the air preheaters provides the most economical collector system for achieving required particulate collection efficiencies. The debate over the most economical collector begins when low sulfur coal is substituted in place of the high sulfur coal.

As a result of the 1970 Clean Air Act many utilities have switched to low sulfur coal as a means of complying with SO_x emission standards. Although this approach achieves the targeted SO_x objective, the collection efficiency of the precipitator is often impaired due to the high resistivity of the fly ash. The reduction in the sulfur content of the coal can increase the resistivity of the fly ash by depriving it of the small but necessary quantities of sulfuric acid necessary to "condition" the dust. Characteristics commonly observed with high resistivity fly ash are excessive sparking and reduced power densities, both of which adversely affect the precipitator's ability in achieving high collection efficiencies.

The electrical resistivity of the fly ash is a critical parameter in the design and operation of the precipitator. To resolve the high resistivity problem, precipitator manufacturers have either drastically increased the size of the precipitator, moved the precipitator to the hot gas side of the air preheaters where volume conductivity prevails over surface conductivity, or installed conditioning systems to lower the resistivity and provide an optimum electrical environment for the precipitation process.

Preceding page blank

The combined precipitator/flue gas conditioning alternative is the most cost-effective means of obtaining compliance on low sulfur coal fly ash. Both Research-Cottrell and Western Precipitation have issued publications indicating this conclusion.[1, 2, 3]

COLD SIDE PRECIPITATOR WITH CONDITIONING

A flue gas conditioning system using either liquid sulfur dioxide or sulfur as the material source for the production of SO_3 is used to reduce the resistivity of the fly ash by injecting trace amounts of SO_3 just downstream of the air preheaters. This enables the precipitator manufacturer to design the precipitator to high sulfur coal parameters even though low sulfur coal will be fired.

The migration velocity of the conditioned precipitator increases from about 4 cm/sec for the cold precipitator without conditioning, and 8 cm/sec for the hot gas side arrangement, to 8.5 cm/sec with conditioning. This permits a substantial reduction in precipitator size and cost, reducing the required SCA (Sq. Ft. of Collecting plate per 1000 ACFM) from 673 and 336 to 317, respectively, to achieve a collection efficiency of 99.5%.

The use of flue gas conditioning to improve precipitator performance has primarily been applied to existing precipitator installations. With the significant savings flue gas conditioning provides and the results achieved, many precipitator manufacturers are now willing to guarantee new precipitator performance with flue gas conditioning systems installed. Wahlco will guarantee that the resistivity of the fly ash will not exceed 4×10^{10} ohm-cm.

COLD SIDE PRECIPITATORS WITHOUT CONDITIONING

In order to achieve required collection efficiencies on low sulfur coal without conditioning, the precipitator must be at least doubled in size. Because of the low migration velocity, a large SCA is required to extend the retention time enabling the precipitator to attain required collection efficiencies.

Due to the tendency of high resistivity ash to ahere tenaciously to the collecting plates, high intensity impact rappers are required (120 - 200 g) to remove the dust from plate to hopper. To withstand these rapping forces, rigid electrode frames are desirable. The intense rapping increases the possibility of dust re-entrainment, structural plate failures, and implies more difficult equipment maintenance. This approach is considered to be the most expensive precipitator system and one of brute force rather than applied science.

HOT SIDE PRECIPITATORS

When the precipitator is designed for service on the hot gas side of the air preheaters, the increase in gas volume dictates that the precipitator be increased in size by almost 70% in comparison to the conditioned precipitator. The cost of a hot side precipitator is considerably more due to the increased size, as well as special expansion provisions, increased insulation, increased draft fan requirements, and additional ductwork in an unconventional configuration.

In addition, the hot precipitator design reduces boiler efficiency due to the heat loss and operates at a lower voltage for a given current density. The reduction in voltage in turn reduces the electrical charge on the particulate being collected as well as the electrical field adjacent to the collecting plate. Both of these considerations dictate an increased plate area to volume flow ratio[4].

Hot side precipitators are also not as impervious to ash constituents as commonly believed. Mr. A. B. Walker of Research-Cottrell stated that when the base to acid ratio of the fly ash is greater than 15%, performance characteristics are marginal. The inclusion of a sodium based conditioning system to sustain acceptable operation may be necessary. Research-Cottrell has installed such a conditioning system with capital costs ranging between \$1.75 to \$2.00 per KW and operating costs between \$1.00 to \$1.20 per ton of coal. In comparison, an SO_3 conditioning system ranges between \$2.00 to \$2.50 per KW in capital expense with operating costs of only \$.03 per ton of coal[6].

BAGHOUSES

Baghouses have not been used extensively for the collection of fly ash from utility boilers, the reasons being their inherent huge size and uncompetitive cost on high sulfur coal applications. As the SCA of the precipitator for low sulfur coal applications reaches 350 to 400, the baghouse appears as a more cost-effective alternative. With the inclusion of flue gas conditioning, the precipitator design regains its competitive edge.

The baghouse comes the closest to the conditioned precipitator being only 11% greater in initial capital expense. However, yearly operating costs are 23% greater rendering the conditioned precipitator the most attractive alternative over the life of the generating plant.

Just as the SCA reflects the size and cost of precipitator systems, the gas to cloth ratio dictates the size and cost of the baghouse installation. Of the existing baghouse installations the filter ratios are between 2:1 and 3:1 with a designed maximum pressure drop between five to six inches of water[7]. In comparison, precipitators display a total pressure drop of less than one-half inch of water. The reduced energy requirements for the precipitator systems are due to the fact that precipitators act only on the particles to be collected and not on the entire flue gas stream.

The greatest operating cost of the baghouse is not, however, the increased power requirements, but the cost of bag replacement. On an 800 MW generating unit, with about 16,000 bags, the replacement cost becomes a significant, recurring expense. At an average of $55.00 per bag, the cost is about $880,000.00 every two to three years.

COST COMPARISON

For the purpose of this economic comparison for alternate fly ash collection systems, a design collection efficiency of 99.5% has been chosen for use with an 800 MW unit fired with low sulfur coal (see Tables 1, 2 and 3). All elements of the alternate systems are included. For the hot side precipitator, this includes all parts from the outlet of the economizer to the inlet of the air heater, and the ductwork from the air heater to the I.D. fan. For the cold precipitator and baghouse, this includes all parts from the outlet of the air heater to the inlet of the I.D. fan.

The following assumptions were made in preparation of this comparison:

1. The gas volume for the cold side precipitator systems and the baghouse includes 9% leakage at the air heater.

2. The flues are sized to provide a gas velocity of 60 feet per second.

3. The necessary expansion joints for thermal motion and dampers for isolation and gas distribution are included.

4. Typical accessories for the precipitator and baghouse include such items as safety interlocks, internal walkways, hopper heaters, hopper level indicators, remote controls, transformer-rectifier removal systems, weather enclosures, gas distribution devices, access facilities, reverse air fan system (baghouse), and typical instrumentation.

5. The power consumption for each system is based on typical usage and includes power for the I.D. fan and hopper heaters (for cold side precipitator systems and baghouse only) as well as power required for T/R operation. For the gas conditioned precipitator the power to operate the sulfur burner is also included. Power cost is calculated at $.015 per KwHr.

6. Pressure drop is calculated at 2.5 in. VWC for the precipitator and flue system and 6 in. VWC for the baghouse.

7. The cost of the fly ash removal system is included.

8. For the hot side precipitator, the heat loss penalty is based on 150 BTU/sq. ft./hr.

9. The evaluation format is a composite from several sources and is believed to be an accurate estimate of costs incurred.

CONCLUSION

Flue gas conditioning in conjunction with a conventionally sized precipitator is shown to be the most cost-effective means of collecting low sulfur coal, high resistivity fly ash. The results obtained with flue gas conditioning are both predictable and dramatic.

A case in point is the experience which Public Service Company of Colorado has had with vendors for their new 99.2% efficient precipitator installation at Arapahoe Station Unit 1. PSCC received bids from a number of vendors for hot side precipitators and for cold side precipitators with and without conditioning. The Specific Collecting Areas proposed ranged from 295 to 334.5 for the hot gas side precipitator. The bids for cold side ranged from an SCA of 688 with no conditioning, down to 279 with conditioning. PSCC chose the conditioned precipitator and after a year's operation of the combined installation, acceptance tests were conducted. The results were even better than the original conformance tests. Emissions in lb/MM BTU's were .0161; well below the statutory limit of .10. Average outlet grain loadings were only .0079 gr/dscf[8].

REFERENCES

1. Bubenick, David V. Economic Comparison of Selected Scenarios for Electrostatic Precipitators and Fabric Filters. In: Session 14 Power Generation 1. Emission Control. (Presented at the 70th Annual Meeting of the Air Pollution Control Association. Toronto, Ontario, Canada June 1977.)

2. Atkins, Richard S. and David V. Bubenick. Keeping Fly Ash Out of The Stack. Environmental Science & Technology. June 1978. p. 657.

3. Harrison, M. E. Economic Evaluation of Precipitator and Baghouse for Typical Power Plant Burning Low Sulfur Coal. (Presented at the American Power Conference. Chicago, IL April 24-27, 1978.)

4. The Electrostatic Precipitator Manual. The McIlvaine Co. Chapter III Section 1 p. 5.0 1976.

5. Walker, A. B. Operating Experience With Hot Precipitators On Western Low Sulfur Coals. (Presented at the American Power Conference. Chicago, IL April 24-27, 1978.)

6. Archer, William E. Flyash Conditioning Update. Power Engineering. Vol 81 June 1977.

7. Szabo, M. F. and R. W. Gerstle. Control of Fine Particulate From Coal-Fired Utility Boilers. In: Session 14 Power Generation 1. Emission Control. (Presented at the 70th Annual Meeting of the Air Pollution Control Association. Toronto, Ontario, Canada June 1977.)

8. Brines, H. G. and R. L. Reveley. Flue Gas Conditioning To Reduce Size and Costs of a New Precipitator at Public Service Company of Colorado Arapahoe Station Unit No. 1. (Presented at the American Power Conference. Chicago, IL April 24-27, 1978.)

Table 1. DESIGN PARAMETERS FOR ALTERNATE COLLECTORS ON AN 800 MW UNIT COLLECTING LOW SULFUR COAL FLY ASH

	Cold Pptr.	Hot Pptr.	Baghouse	Cold Pptr. w/Cond.
Volume (MACFM)	2,800	4,458	2,800	2,800
Temperature	300°F	750°F	300°F	300°F
Efficiency	99.5%	99.5%	99.5%	99.5%
Migration Velocity (cm/sec)	4.0	8	---	8.5
Collecting Surface Area (1,000 ft^2)	1,884	1,500	1,400	887
SCA	673	336	---	317
Filter Ratio	---	---	2:1	---
Area Required excluding flues (1,000 ft^2)	45	35	37	21

Table 2. TOTAL FIXED INVESTMENT

OF ALTERNATE COLLECTORS

FOR AN 800 MW UNIT

PLANNED INSTALLATION

($000)

SYSTEM	Cold Pptr.	Hot Pptr.	Baghouse	Cold Pptr. w/Cond.
Base Equipment	$ 6,258	$ 4,554	$ 5,377	$ 2,565
Accessories	3,071	2,013	1,200	1,332
Plenums	1,396	1,294	inc. above	759
Flues	494	1,261	442	359
Support Structures	1,050	850	785	447
Subtotal	$12,269	$ 9,972	$ 7,804	$ 5,462
Erection	$ 8,751	$ 7,377	$ 3,595	$ 4,209
Insulation	2,805	3,367	1,800	1,358
Gas Cond. (D&E)	---	---	---	1,250
Subtotal	$23,825	$20,716	$13,199	$12,279
Ash Handling @ $5K/Hopper	$ 370	$ 330	$ 350	$ 200
Capacity Charge @ $800/KW	3,715	2,424	2,760	2,261
Land @ $10K/Acre	10	8	8	5
TOTAL INVESTMENT	$27,920	$23,478	$16,317	$14,745
Relative Investment Difference	+90%	+60%	+11%	Base

Table 3. ANNUAL OPERATING & OVERHEAD COST

OF ALTERNATE COLLECTORS

FOR AN 800 MW UNIT

($000)

ITEM	Cold Pptr.	Hot Pptr.	Baghouse	Cold Pptr. w/Cond.
Amortization (inc. interest taxes & insurance @ 18% investment)	$ 5,026	$ 4,226	$ 2,937	$ 2,654
Heat Loss @ $1.75/ Million BTU's	---	572	---	---
Energy Charge @ $.015/KwHr	610	396	430	374
Gas Conditioning (Sulfur)	---	---	---	60
Bag Replacement	---	---	440	---
Maintenance	112	105	85	70
TOTAL ANNUAL COST	$ 5,748	$ 5,299	$ 3,892	$ 3,158
Relative Cost Difference	+82%	+68%	+23%	Base

BENCH-SCALE EVALUATION OF DRY ALKALIS FOR REMOVING SO_2 FROM BOILER FLUE GASES

N. D. Shah and D. P. Teixeira
Electric Power Research Institute, Inc.
Palo Alto, California 94303

L. J. Muzio
KVB, Inc.
Santa Ana, California

ABSTRACT

The use of dry chemical sorbents in conjunction with a conventional baghouse to remove sulfur oxides from flue gases has been examined in several test programs conducted by vendors of baghouses, fabrics, and sorbent materials. However, most of the work conducted to date is confidential and concentrated in specific areas for sales purposes without due consideration to providing the basic design specifications data for the process.

EPRI has initiated a bench-scale study of dry SO_2 scrubbing to investigate the technical feasibility of the process and define the range of operating parameters. The data generated is expected to provide a basis for preparing process and equipment specifications to western utilities interested in this technology.

The test facility was equipped with a heat exchanger between the duct and baghouse to simulate the flue gas temperature profile normally encountered in a full-scale power plant. The effects of the following variables on SO_2 removal efficiency and sorbent utilization were investigated: Sorbent type (commercial $NaHCO_3$, trona and nahcolite), residence time (up to 6 sec), temperature (up to 600°F), particle size (up to -400 mesh) and stoichiometric ratio (up to 2). In addition, the

Preceding page blank

degree of reaction occurring in suspension vs. on the filtercake of the bags was determined. The effect of sorbent injection on NO_x and particulates emissions in the resultant flue gas were also examined.

INTRODUCTION

Increasing interest by Western State utilities in dry SO_2 removal with alkaline materials such nahcolite has led to the formulation of an EPRI program in this area. This paper contains a summary of the Phase I test results conducted by KVB, Inc., under EPRI contract RP982-8.

The primary objective of Phase I was a preliminary evaluation of the feasibility for the dry removal of SO_2 from boiler flue gases with sodium compounds. In particular, the tests sought to determine (1) the extent that sodium compounds would react with SO_2 in suspension and the removal in conjunction with a baghouse, and (2) the sensitivity of the removal and utilization to the process parameters. The sodium compounds were injected into the flue gases upstream of the baghouse and the dry sorbent, along with fly ash, was collected on the bags. The reaction between SO_2 and sorbent occurred during suspension and while particles were coated on the bags. It was desirable to determine the extent to which reaction occurs in suspension for potential application to electrostatic precipitators.

During the study, three dry sorbents were investigated: commercial sodium bicarbonate, nahcolite and trona. In addition, the sensitivity of the SO_2 removal process to the system parameters was also investigated. These parameters are listed in Table 1, along with the range covered during these experiments.

Table 1. EXPERIMENTAL VARIABLES

VARIABLE	NOMINAL RANGE INVESTIGATED
Dry Sorbent Type	Commercial sodium bicarbonate, nahcolite, trona
Initial SO_2 Level	400 ppm at 3% O_2
Sorbent Particle Size	70% through 200 mesh 100% through 400 mesh
Sorbent Stoichiometric Ratio	0 - 1.5
Temperature in Suspension	340°F, 530°F
Baghouse Inlet Temperature	255°F - 290°F
Residence Time in Suspension*	Approx. 1.8 sec, 5.6 sec
Sorbent Injection Location	(1) Duct upstream of baghouse (2) Baghouse inlet
Air/Cloth Ratio	1.3, 2.2

*In the duct upstream of the baghouse

The coal used to generate the combustion products was Energy Coal from Utah. An analysis of a sample of this coal showed a sulfur content of 0.45% and an ash content of 9.27% with moisture determined to be 9.17%.

EXPERIMENTAL APPARATUS AND PROCEDURE

The experiments were carried out in a pulverized coal-fired facility firing at a nominal rate of 2.5×10^6 Btu/hr with a resulting combustion product flow of approximately 600 scfm. An overall schematic of the experimental apparatus is shown in Figure 1. The combustion products exiting the stack could be directed to either baghouse. The experiments were conducted in baghouse No. 2. The duct leading to the baghouse was insulated to provide a near isothermal zone to study the reactions of the sorbent with SO_2 in suspension. At a duct temperature of 600°F, the residence time between the point of sorbent injection and the inlet of the heat exchanger was about 1.8 sec. The heat exchanger was a plate-type heat exchanger which was used to provide independent control of the duct temperature and the baghouse temperature.

The baghouse used for these tests was a Buell "Norblo" Mechanical Shaker Model 4-141-5.5. This particular unit is intended for intermittent service and contains 56 five-inch diameter fiberglass bags, 5'6" long. The effective filter cloth area is 360 square feet. An induced draft fan at the baghouse exit provides the pressure drop and induces the flow through the unit. The dust-laden gases enter the unit through the hopper. This gas then flows upward through the distributor plate through the inside of the bags. The particulate matter is collected on the inside surface of the bags. The clean filtered gas continues through the filter bags and exits the collector. The particulate matter which has collected on the bag surface is removed via mechanical shaker cleaning. During this cleaning process the combustion products from the combustor are diverted to baghouse No. 1 (see Figure 1).

The dry sorbent was metered into a carrier air stream with a calibrated screw feeder; the carrier air then dispersed the sorbent into the combustion products. Experiments were conducted with the sorbent injected into the duct, as indicated in Figure 1, as well as at the baghouse inlet downstream of the heat exchanger. This provided a means to study the "pretreatment" effect of exposing the sorbent to a high-temperature environment prior to deposition on the bags.

Gas samples were withdrawn for analysis at the four points indicated in Figure 1. At points 1 and 4, sintered metal filters located in the duct were used to filter particulate matter prior to transport to the gas analyzers via heated Teflon sample lines. At sample points 2 and 3 samples were withdrawn from the duct with stainless steel probes, with the inlet oriented downstream of the flow to minimize ingestion of the particulate matter.

Continuous gas analyzers were used to determine the concentrations of SO_2, O_2, CO, CO_2, NO in the flue gas.

DISCUSSION OF RESULTS

The experimental program comprised 16 test conditions covering the variables outlined in Table 1. In this section the results obtained during the experiments will be presented in the following sequence:

- Effect of sorbent type and stoichiometric ratio (SR) on SO_2 removal (duct injection)
- Effect of sorbent type on SO_2 removal (baghouse injection)
- Effect of air/cloth ratio
- Effect of particle size on overall SO_2 removal
- Removal in suspension versus on the filter cake
- Effect of baghouse temperature on SO_2 removal

During these experiments the pressure drop across the bags ranged from 0.6 - 1.4 inches H_2O.

Effect of Sorbent Type and Stoichiometric Ratio (Duct Injection)

The overall effect of sorbent type and stoichiometric ratio of the dry sorbent on SO_2 emissions is presented in Figure 2. In these experiments the sorbent was injected into the duct where the combustion product temperature was 530°F (residence time of approximately 1.8 sec). The heat exchanger then cooled the products to approximately 270°F prior to entry into the baghouse. The results in Figure 2 indicate that nahcolite was the most effective sorbent in removing SO_2, followed by commercial sodium bicarbonate and then trona. At SR = 1, 50% removal can be achieved with trona, 70% with commercial $NaHCO_3$, with nahcolite removing over 80% of the SO_2. It should be pointed out that SO_2 removals were determined from the steady-state SO_2 levels that were attained with continuous injection of the sorbent. In an actual application, the average SO_2 removal over the cycle time of the baghouse would have to be determined through an integration of the removal over the cycle time.

The SO_2 removals obtained during this phase of the program are consistent with those reported by other investigators.[1,2,3,4]

Baghouse Injection of Dry Sorbent

In these tests the dry sorbent was injected at the baghouse inlet downstream of the heat exchanger. The temperature at the point of injection ranged from 265°F to 290°F. These test results are plotted in Figure 3. When these results are compared to the results obtained with the previous tests, it is observed that the extent of SO_2 removal is similar for the commercial sodium bicarbonate.

While the ultimate removal was similar, injection in a "hot" region upstream of the baghouse may be desirable from an overall system's operational standpoint. The data reported in Figures 2 and 3 were obtained when the SO_2 level reached a steady-state level and this occurred at different times for the two injection configurations. In an actual application, the pressure drop across the bags will determine the time available for sorbent injection and SO_2 removal. Further, to increase sorbent utilization, it will probably be desirable to stop sorbent injection some time before the bags are cleaned, thus utilizing the sorbent which has accumulated on the bags. The degree to which this is feasible will depend on the integrated average removal of SO_2 over the baghouse cycle. This suggests that it is desirable to have the SO_2 levels respond as radpily as possible upon the start of injection. Figure 9 shows the characteristic time response for the two injection schemes. As can be seen in Figure 9, SO_2 removal occurs more rapidly when injected into the duct, where the combustion products are at about 530°F, rather than directly into the baghouse with an inlet temperature of about 290°F. Thus, sorbent injection upstream of an air preheater may provide more flexibility in terms of system optimization.

The SO_2 removal using trona was actually greater with injection at the inlet to the baghouse than when it was injected into the "hot" products upstream of the heat exchanger. Nahcolite exhibited higher SO_2 removal at 550°F duct injection compared to injection at 280°F at baghouse inlet.

Effect of Air/Cloth Ratio

The overall effect of air/cloth ratio is shown in Figure 4, using sodium bicarbonate as the sorbent. For the results plotted in Figure 4, the sorbent was injected into the duct, the duct temperature was about 340°F for the 1.3 air/cloth ratio and about 520°F for the 2.2 air/cloth ratio. As Figure 4 illustrates, the air-to-cloth ratio does affect the SO_2 removal. However, the quantitative relationship shown in Figure 4 should be taken as preliminary, since the effects of temperature and air-to-cloth ratio is confounded.

Effect of Sorbent Particle Size on SO_2 Removal

The majority of the tests with the commercial sodium bicarbonate were conducted with a sorbent particle size of 31% on 200 mesh. A test was conducted using a finer sorbent particle size (100% through 400 mesh). This test was conducted by injecting $NaHCO_3$ in the duct at 550°F. The result of this test, shown in Figure 2, indicates that sorbent particle size has no effect on the overall SO_2 removal when used in conjunction with a baghouse. However, the finer particle size did produce a greater removal of SO_2 in suspension in the duct: 30% compared to 14% at SR = 0.9 (see Figure 6).

SO_2 Removal in Suspension Versus on the Filter Cake

The relative removal of SO_2 by the dry sorbent (1) in suspension in the duct, (2) in the baghouse prior to deposition on the bags, and (3) on the filter cake was assessed during these tests. Gas samples obtained from the duct upstream of the heat exchanger provided the extent of reaction in suspension in the duct for a residence time of nominally 1.8 sec (530°F duct temperature) and 5.6 sec (300°F duct temperature).

In addition, the extent of suspension reaction could be obtained by monitoring the baghouse exit SO_2 level versus time from the start of sorbent injection. These traces exhibited the general characteristics depicted in Figure 5. The rapid decrease in SO_2 (Region A) was taken to represent the SO_2 removal in suspension (duct and baghouse) with the gradual further reduction of SO_2 in Region B resulting from the buildup of the sorbent on the bags. The total removal in suspension is then $(1-X_2)X_1$.

Figure 6 shows the SO_2 removal that occurred in suspension in the duct as well as the overall reduction obtained through the baghouse. The reductions in the duct were determined from gas samples withdrawn from a point just upstream of the heat exchanger (sample point 2) and prior to sorbent injection. These results indicate that little SO_2 removal occurs in the duct with sodium bicarbonate at duct temperatures up to 600°F. Essentially no removal occurred with a duct temperature of 300°F (5.6 sec residence time in the duct). The two exceptions were the fine particle test with sodium bicarbonate (31% removal at SR = 0.9) and trona (35% removal at SR = 1.12).

The SO_2 versus time traces are shown in Figures 7, 9 and 10 for duct and baghouse sorbent injection of commercial sodium bicarbonate, nahcolite and trona.

Figure 7-a,b,c shows the SO_2 traces for duct injection of commercial sodium bicarbonate at the three stoichiometric ratios. These traces exhibit the general shape sketched in Figure 5, the initial rapid drop in SO_2 is taken to be the result of reactions in suspension which occur in both the duct and the baghouse. From these traces, the relative SO_2 removals in suspension and on the filter cake can be calculated and these are shown in Figure 8. This calculation indicates that approximately half of the SO_2 removal occurs in suspension and half on the bags when the commercial sodium bicarbonate is injected into the duct at a temperature of 540°F.

The SO_2 vs. time traces for nahcolite injection into the duct and baghouse are shown in Figures 9-a and 9-b, respectively. With injection into the duct, the same characteristic as observed with the sodium bicarbonate is observed. However, when injected at the baghouse inlet, a different trend occurs. No rapid reduction in SO_2 occurs, suggesting that when injected at the baghouse inlet at a nominal temperature of 290°F, no removal occurs in suspension. Yet the overall SO_2 removals are comparable. These different characteristics suggest that injection into the duct results in a pretreatment of the sorbent that allows reaction to occur in suspension (at SR = 0.85, 12% removal in the duct, 30% total removal in suspension, 60% overall removal), whereas all of the reaction occurs in the bag surface when injection occurs at the baghouse inlet.

The trona also showed interesting behavior. As shown in Figure 10b, a similar characteristic to the commercial bicarbonate is observed when the trona is injected in the duct -- a somewhat rapid initial SO_2 removal followed by a more gradual removal as the cake builds up. It can be noted that this initial rate of removal is not quite as rapid, suggesting that the removal in suspension is not as large with injection of trona into the duct at 540°F.

Trona exhibited a totally different behavior when injected at the baghouse inlet (downstream of the heat exchanger, T = 262°F). This is shown in Figure 10-a; a rapid reduction in SO_2 occurred to a final steady-state level suggesting that all of the removal occurred in suspension. This was confirmed by terminating sorbent injection and observing the increase in SO_2. If the reaction was occurring in suspension, termination should result in a rapid increase in the SO_2 levels at the exit; this was observed. On the other hand, if the reaction on the filter cake was dominant upon termination of sorbent injection, a more gradual buildup of the SO_2 level at the exit would be expected as the sorbent accumulated on the bags was consumed; this was not the case. This observation with the injection of trona suggests that trona injection may be a viable approach in conjunction with a cold-side precipitator, since most of the reaction appears to occur in suspension. Further testing is needed to characterize this phenomena.

Effect of Baghouse Temperature on SO_2 Removal

The temperature at the entrance to the baghouse was found to affect the SO_2 removal with both sorbent injection in the duct and baghouse.

With injection into the duct (T = 520°F), the SO_2 removal tended to increase as the temperature at the entrance to the baghouse was reduced below 300°F. This is illustrated in Figure 11, where the baghouse inlet temperature is reduced by increasing the water flow through the heat exchanger. This trace shows that reducing the temperature from 282°F to 235°F resulted in an additional 45 ppm removal of SO_2 (14% additional removal). This effect requires further characterization with each of the dry sorbents.

When the commercial sodium bicarbonate was injected at the baghouse inlet (T = 300°F), the SO_2 removal was observed to increase as the temperature at the inlet decreased. An additional 25-35 ppm removal occurred when the temperature was increased from 265°F to 290°F. Again, further characterization is warranted.

Effect of Sorbent Injection on NO Emissions

During the Phase I tests, injection of the various sodium compounds resulted in no measurable change in the emissions of oxides of nitrogen.

CONCLUSIONS

The following specific conclusions can be made from the results of the Phase I testing.

1. Sodium alkalis in conjunction with a baghouse are effective in removing SO_2 from coal-derived combustion products. Nahcolite was the most effective, with over 80% removal at a stoichiometric ratio of 1.0. Commercial sodium bicarbonate removed 68% of the SO_2 at SR = 1.0. Trona was the least effective with a 53% removal at SR = 1.0.

2. With an exposure time of 1.8 sec, sodium bicarbonate and nahcolite exhibited 15% SO_2 removal at SR = 1 in suspension in the duct.

3. Reducing the sodium bicarbonate particle size from a nominal 31% retained on 200 mesh to 100% through 400 mesh produced the same overall removal of SO_2, but the fraction removed in the duct (1.8 sec exposure at 520°F product) increased to 31%.

4. Trona produced the largest removal in suspension, with 35% SO_2 removal (1.8 sec exposure in 520°F products).

5. Essentially no SO_2 removal occurred in suspension with sodium bicarbonate injection into the duct at 300°F (approximately 6 sec exposure time).

6. Analysis of the SO_2 versus time traces with sodium bicarbonate injection indicates that approximately half of the overall removal occurs in suspension (duct plus baghouse), with the balance being removed as the SO_2 passed through the filter cake containing the sorbent.

7. Sodium bicarbonate or nahcolite injection into hot combustion products upstream of the baghouse (approximately 530°F) results in a more rapid removal of SO_2 than injection into the baghouse inlet. This will allow more flexibility in optimizing the duty cycle in a commercial application.

8. Injection of trona at the baghouse inlet (T = 290°F) resulted in 59% removal of SO_2 (SR = 1.0). Analysis of the transient response indicates that essentially all of this removal occurred in suspension. This suggests that trona may be applicable with systems incorporating electrostatic precipitators.

9. Injection of the sodium compounds resulted in no change in the emissions of the oxides of nitrogen.

REFERENCES

1. Estcourt, V. F.. Tests of a Two-Stage Combined Dry Scrubber/SO_2 Absorber Using Sodium or Calcium (Presented at the 40th Annual Meeting, American Power Conference. Chicago, Illinois. April 26, 1978.)

2. Liu, H., and Chaffee, R. Evaluation of Fabric Ilter as Chemical Contactor for Control of Sulfur Dioxide from Flue Gas. Final Report, Public Health Service Contract PH22-68-51. December 1969.

3. Wheelabrator-Frye. Nahcolite Pilot Baghouse Study. Leland Olds Station, nonconfidential test data section. March 1977.

4. Bechtel Corporation. Evaluation of Dry Alkalis for Removing Sulfur Dioxide from Boiler Flue Gases. EPRI FP207. October 1976.

SYSTEM SCHEMATIC

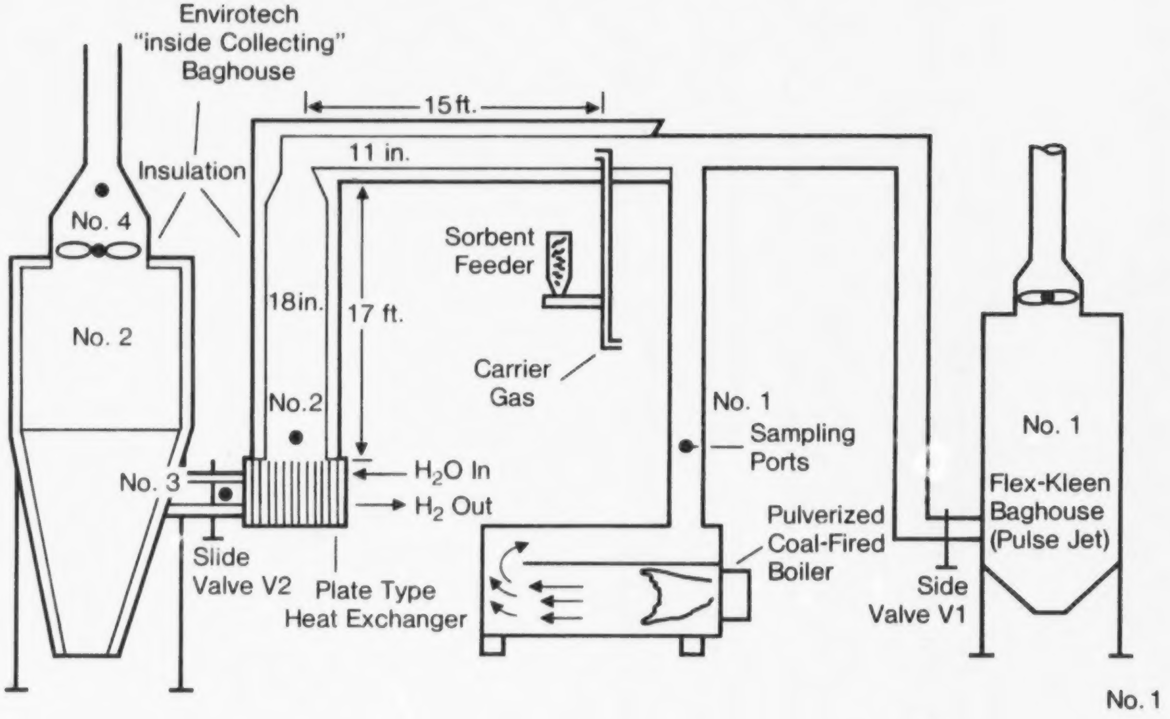
Envirotech
"inside Collecting"
Baghouse
15 ft.
11 in.
Insulation
No. 4
No. 2
18in.
17 ft.
Sorbent
Feeder
Carrier
Gas
No.2
No. 1
Sampling
Ports
No. 1
No. 3
H_2O In
H_2 Out
Pulverized
Coal-Fired
Boiler
Flex-Kleen
Baghouse
(Pulse Jet)
Slide
Valve V2
Plate Type
Heat Exchanger
Side
Valve V1
No. 1

SORBENT INJECTION IN A DUCT AT 530°F FOLLOWED BY BAGHOUSE COLLECTION

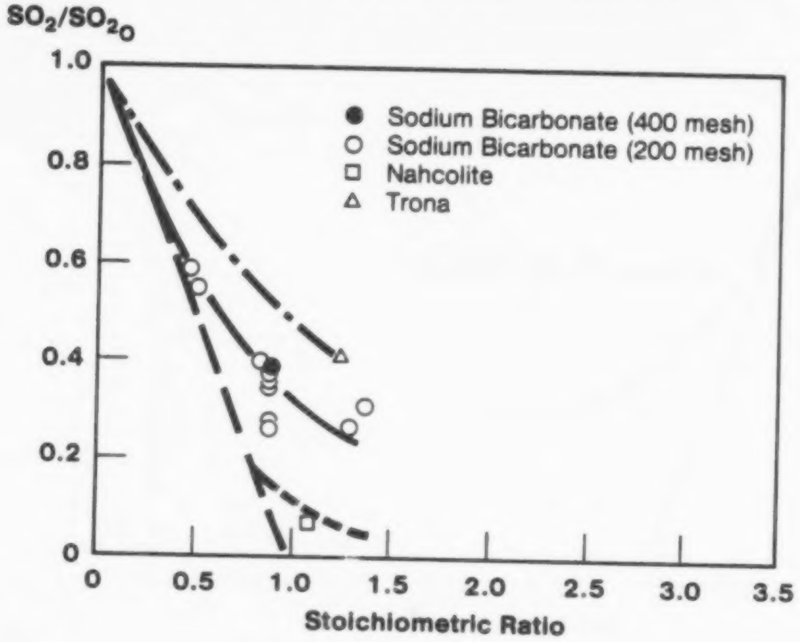

No. 2

SO_2 REMOVAL WITH SORBENT INJECTION AT THE BAGHOUSE INLET

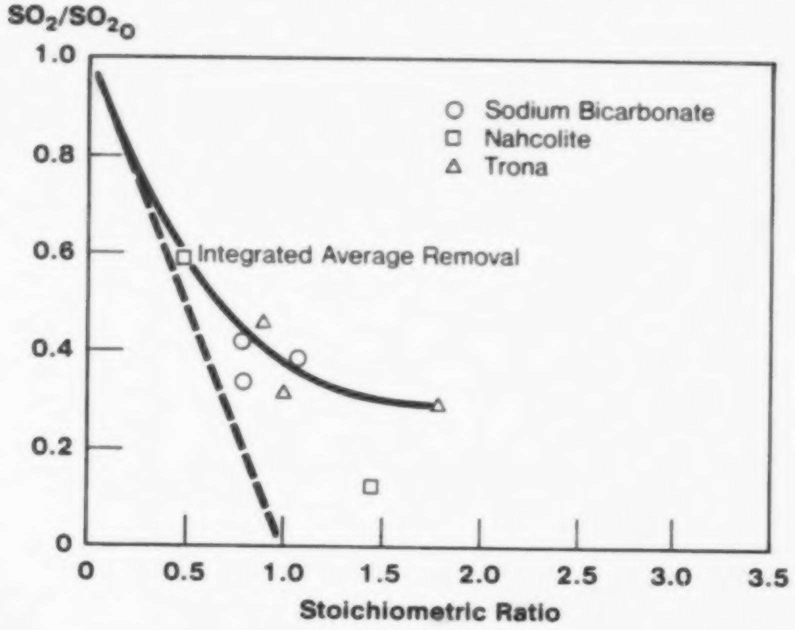

No. 3

EFFECT OF AIR CLOTH RATIO ON SO_2 REMOVAL WITH SODIUM BICARBONATE

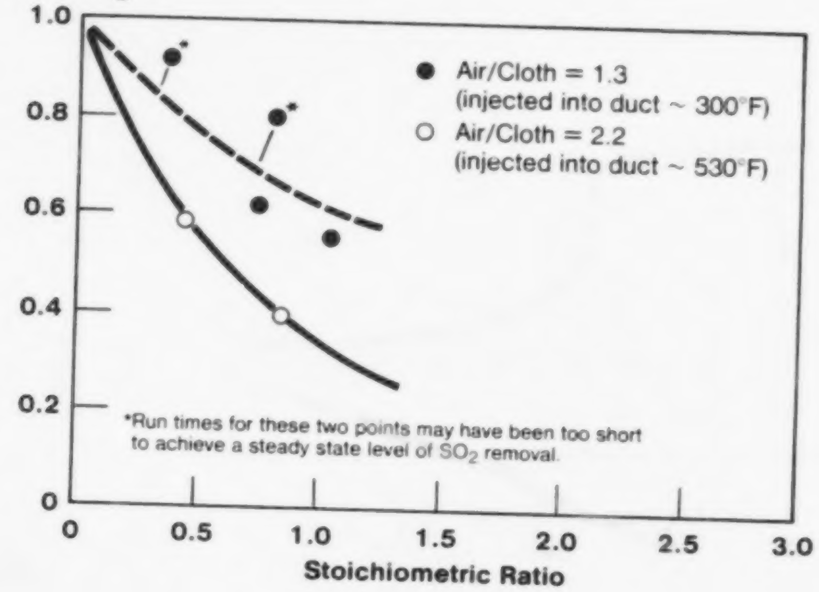

*Run times for these two points may have been too short to achieve a steady state level of SO_2 removal.

No. 4

SO_2 VS TIME CHARACTERISTICS

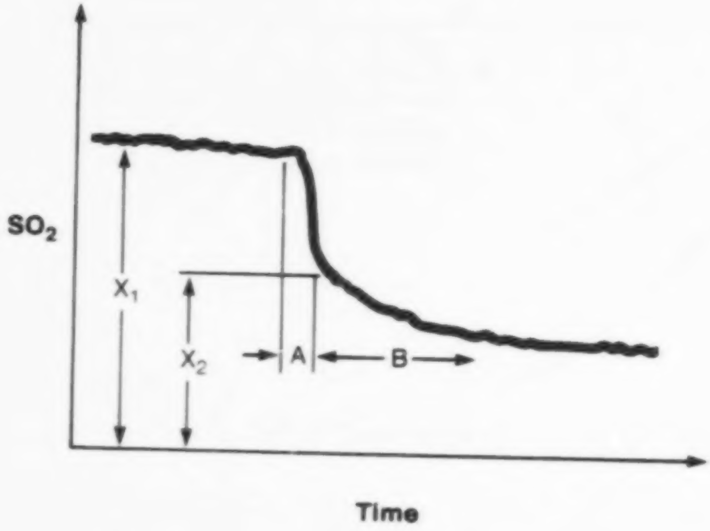

No. 5

SO_2 REMOVAL IN SUSPENSION VS OVERALL SO_2 REMOVAL IN THE DUCT

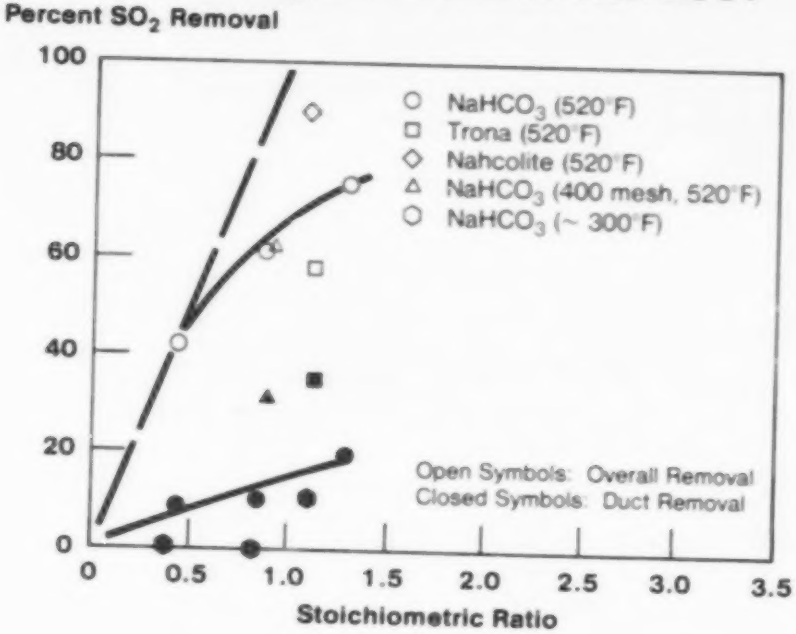

No. 6

SO_2/TIME TRACE FOR DUCT INJECTION OF COMMERCIAL SODIUM BICARBONATE

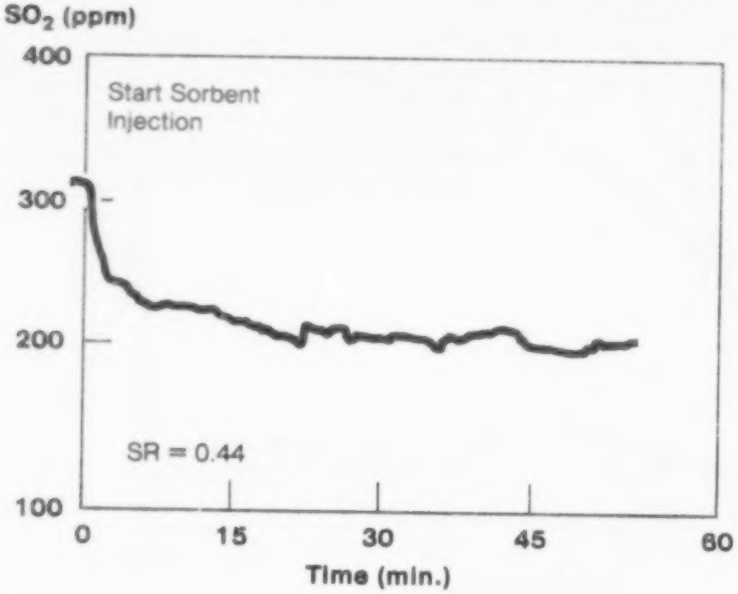

No. 7a

SO_2/TIME TRACE FOR DUCT INJECTION OF COMMERCIAL SODIUM BICARBONATE

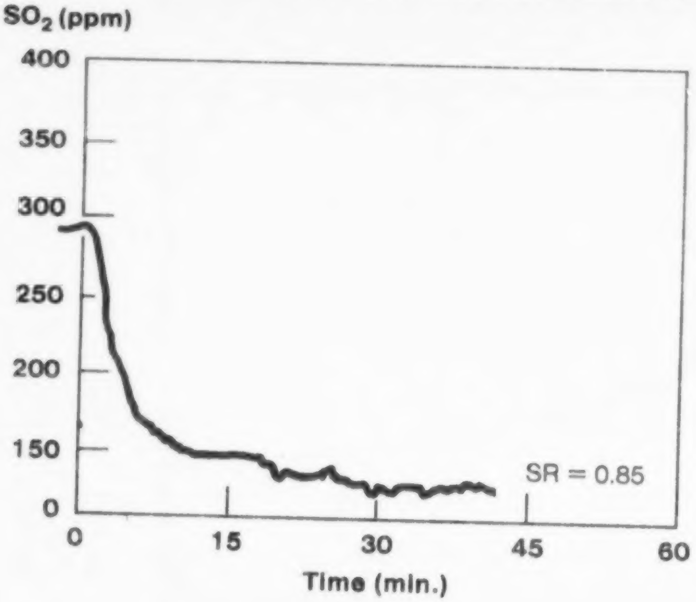

No. 7b

SO$_2$/TIME TRACE FOR DUCT INJECTION OF COMMERCIAL SODIUM BICARBONATE

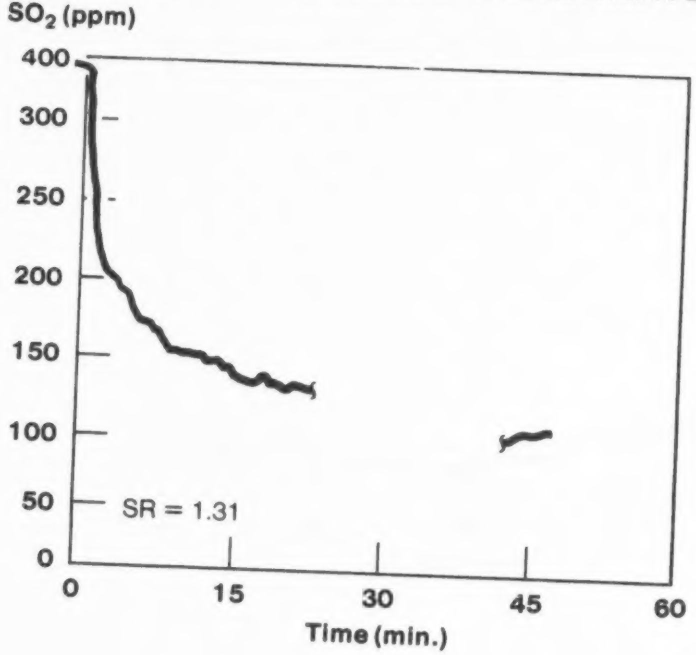

No. 7c

COMPARISON OF THE OVERALL VS SUSPENSION REMOVAL OF SO_2

Duct Injection at 540°F, Commercial Sodium Bicarbonate

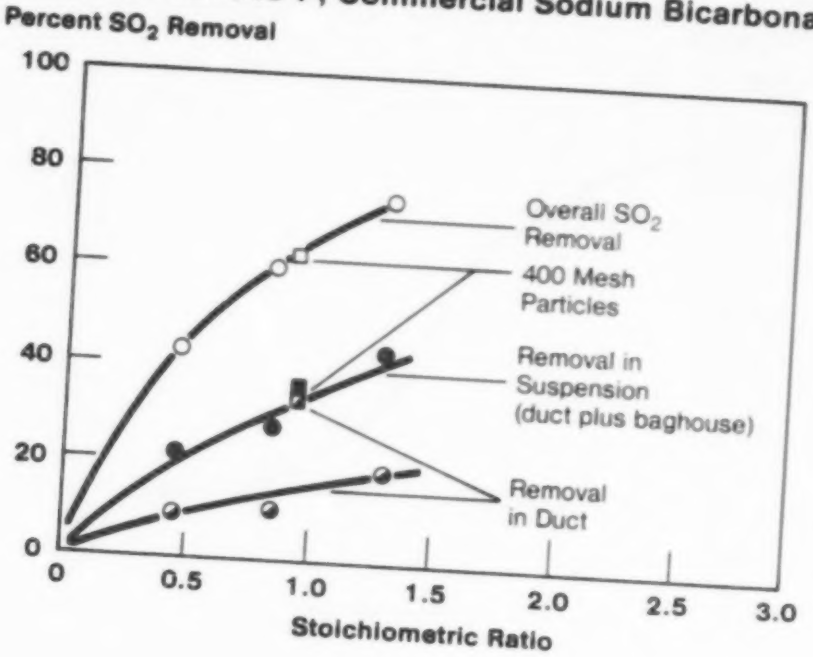

No. 8

SO_2/TIME TRACE FOR NAHCOLITE INJECTION

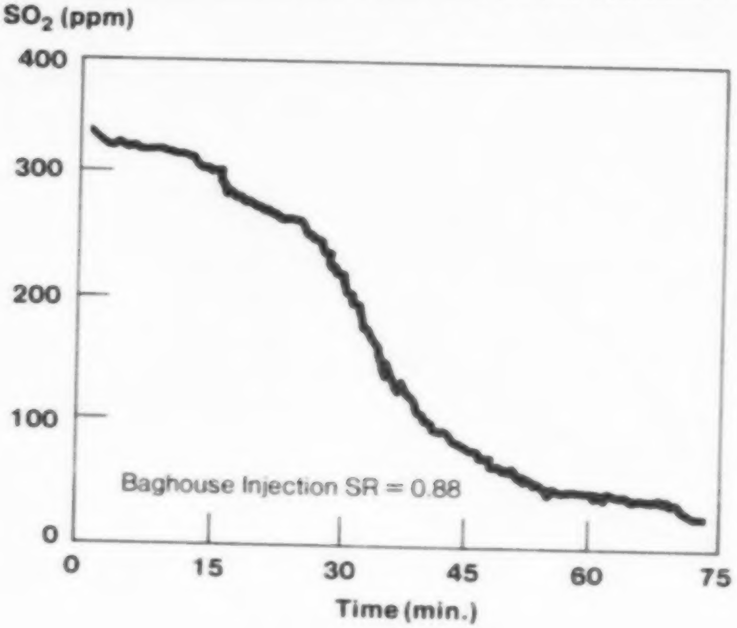

No. 9a

SO_2/TIME TRACE FOR NAHCOLITE INJECTION

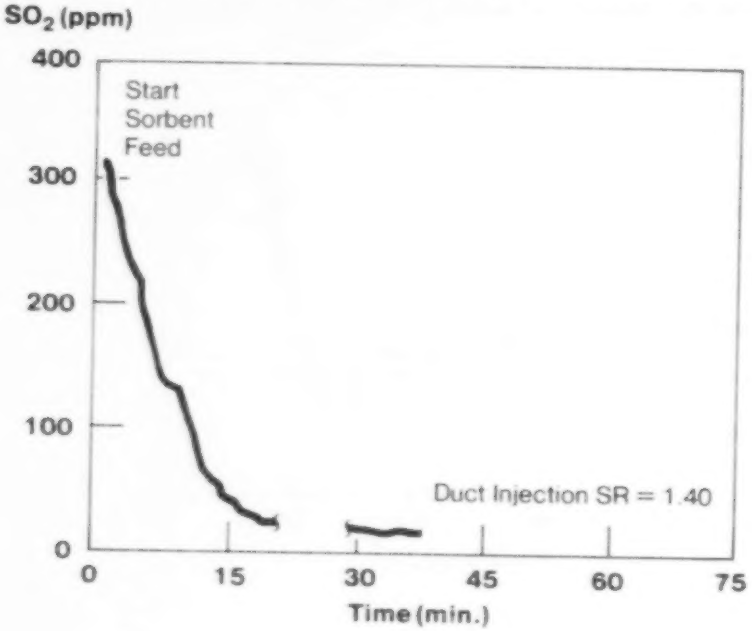

No. 9b

SO_2 TIME TRACES FOR TRONA INJECTION

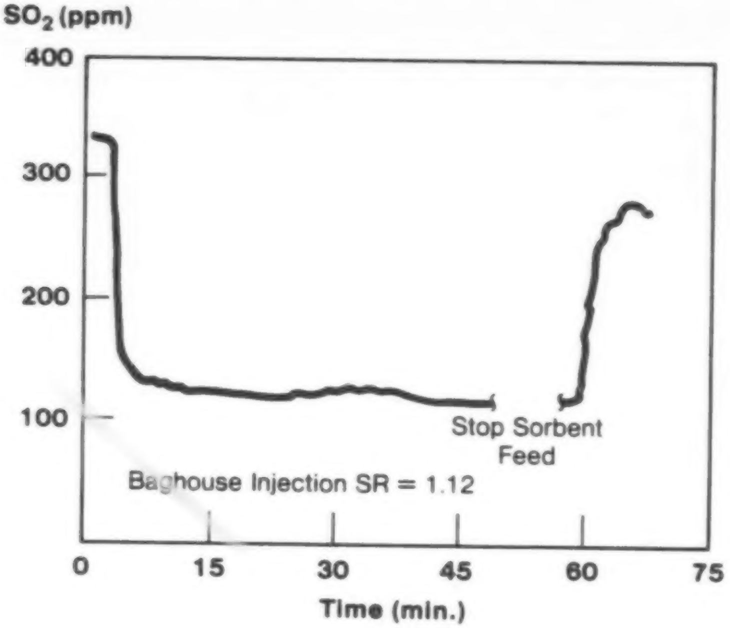

No. 10a

SO_2 TIME TRACES FOR TRONA INJECTION

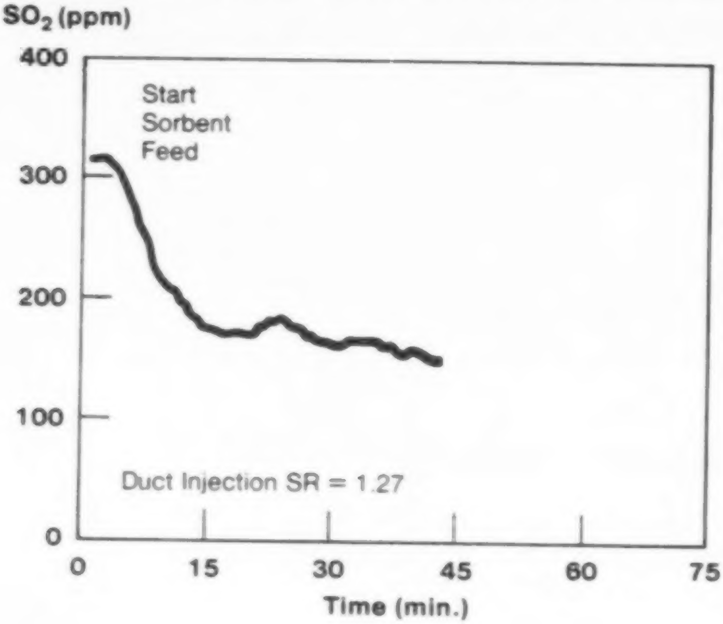

No. 10b

EFFECT OF BAGHOUSE TEMPERATURE ON SO_2 REMOVAL

Duct Injection of Commercial Sodium Bicarbonate

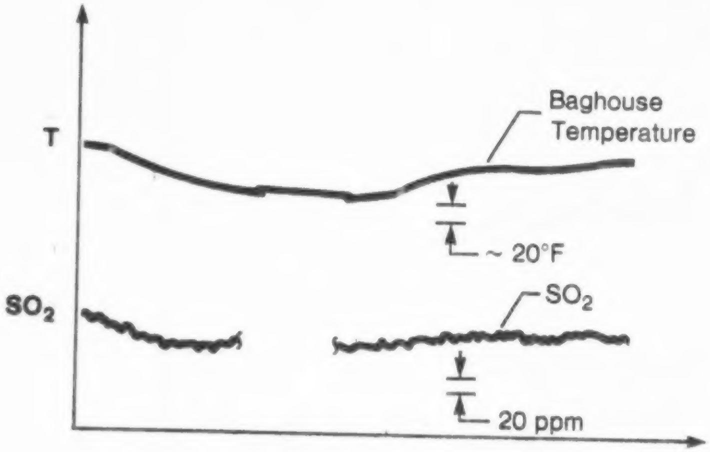

No. 11

ANALYSIS OF THERMAL DECOMPOSITION PRODUCTS OF FLUE GAS CONDITIONING AGENTS

H. Kenneth Dillon
Edward B. Dismukes
Southern Research Institute
Birmingham, Alabama 35205

ABSTRACT

The reactions of several flue gas conditioning agents have been investigated in the laboratory under conditions simulating those in the flue gas train of a coal-burning power plant. The primary emphasis of the study is the identification of reaction products that occur near the exit of the flue gas train. This information will show whether hazardous materials are emitted as the result of conditioning. The compounds investigated to date include ammonia, triethylamine, and sodium carbonate. The most prevalent types of reactions observed are addition or substitution reactions rather than decomposition reactions. Thus, ammonia, triethylamine, and sodium bicarbonate react with sulfur oxides to form sulfates and sulfites as the major products. However, the addition of triethylamine to flue gas leads to the occurrence of small amounts of the carcinogenic compound, N-nitrosodiethylamine. This compound arises through the decomposition of triethylamine to diethylamine or the appearance of diethylamine as an impurity in triethylamine.

INTRODUCTION

One approach that has been taken to improve the performance of an electrostatic precipitator in collecting fly ash from power plant flue gas is the addition of a chemical agent to the gas stream before it enters the precipitator. The overall effects upon stack emissions of the injection of chemicals into power plant flues are a primary concern of the Environmental Protection Agency. Not only is the EPA interested in the beneficial results of flue gas conditioning, but it is also charged with the responsibility of determining whether or not agents employed for conditioning may increase the hazards associated with power plant emissions. It is conceivable that the injection of chemicals into flue gas may result in the release to the environment of noxious compounds consisting of the agents, their thermal degradation products, or their reaction products with the flue gas.

We are currently investigating the reactions of flue gas conditioning agents under laboratory conditions simulating those in the gas train of a coal-burning power plant. Our work is funded under EPA Contract 68-02-2200 and monitored by the Industrial Environmental Research Laboratory of Research Triangle Park, North Carolina. Dr. Leslie E. Sparks is the EPA Project Officer.

DESCRIPTION OF THE LABORATORY FACILITY

For the investigation of flue gas conditioning agents, a laboratory bench-scale facility has been constructed that simulates the composition of the flue gas of a coal-fired power plant and the temperature zones and residence times relevant to the injection of agents. The bulk constituents of the flue gas are furnished by mixing and heating compressed gases and water to produce a gas mixture that is about 76% nitrogen, 12% carbon dioxide, 8% water vapor, and 4% oxygen. The total volume flow rate is 35 l/min as expressed for 25°C. After this gas mixture is heated to 650°C, trace amounts of sulfur dioxide, nitric oxide, and nitrogen dioxide can be added individually or in various combinations to the gas stream. Typical concentrations of these oxides in the gas mixture are 500 ppm sulfur dioxide, 1000 ppm nitric oxide, and 100 ppm nitrogen dioxide. No fly ash has been introduced into the flue gas to date.

The simulated flue gas mixture is introduced into a series of heated cylinders of Pyrex or quartz that represent various parts of the flue gas train of a coal-fired power plant. A diagram of the main components of the train are presented in Figure 1 and are listed as follows in the order of their occurrence in the train:

- A heated quartz cylinder maintaining a portion of the gas stream at 650°C, a representative gas temperature upstream from the economizer in a power plant flue.
- A glass heat exchanger representing the economizer.
- A heated Pyrex cylinder maintaining a portion of the gas stream at about 370°C, the approximate gas temperature between the economizer and the air preheater.
- A glass heat exchanger representing the air preheater.

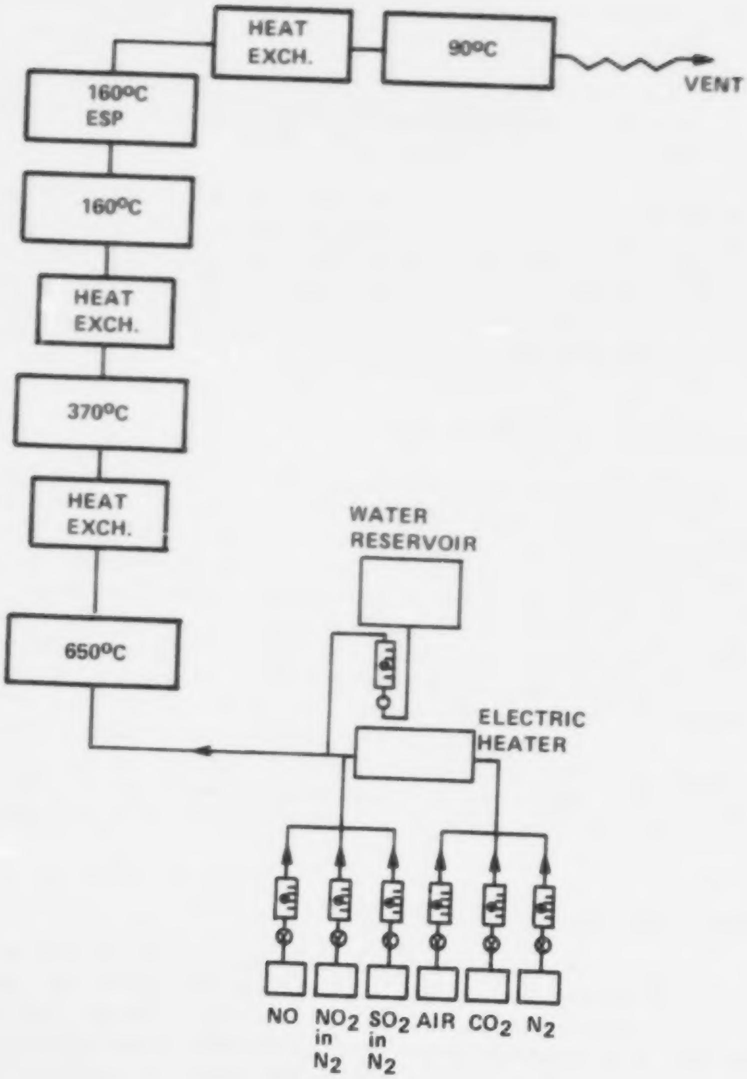
HEAT EXCH.
90°C
VENT
160°C ESP
160°C
HEAT EXCH.
370°C
HEAT EXCH.
WATER RESERVOIR
650°C
ELECTRIC HEATER
NO
NO2 in N2
SO2 in N2
AIR
CO2
N2

Figure 1. Schematic of flue gas train.

- A heated Pyrex cylinder maintaining a portion of the gas stream at 160 ± 15°C, the approximate range of temperature between the air preheater and the electrostatic precipitator.

- A small wire-and-pipe electrostatic precipitator (ESP) with a specific collecting area of 845 $ft^2/(1000\ ft^3/min)$ as calculated for the flue gas flow rate of 51 l/min at 160°C. The ESP is maintained at temperatures in the range of 160 ± 15°C.

- A glass heat exchanger simulating cooling near the stack exit.

- A heated Pyrex cylinder maintaining a portion of the gas stream at about 90°C, a conceivable temperature of the gas stream near the top of the stack.

The dimensions of the cylinders were chosen to provide gas residence times of 2 sec within each cylinder except the heat exchangers and the ESP. The gas residence time within the heat exchangers is a fraction of a second. At 160°C, the gas residence time is about 7 sec within the ESP. Each cylinder enclosing a constant temperature zone is provided with an injection port near its inlet and a sampling port near its outlet.

INVESTIGATION OF TRIETHYLAMINE

This compound, an organic amine, is one of four conditioning agents thus far studied. The study of this compound has been selected for special emphasis in this paper for several reasons. First, the compound is the object of considerable interest in Australia as an alternative to sulfur trioxide and ammonia for conditioning flue gas. Second, the compound is a suspected component of one or more proprietary blends of conditioning agents that have been used in this country. Third, the compound offers several possible routes of thermal decomposition or other reactions at high temperatures. In other words, the investigation of triethylamine is especially challenging in an analytical sense. As will be shown in the discussion to follow, one of the reaction products of the compound is a source of considerable concern as an air pollutant not to be expected in the absence of conditioning by triethylamine.

Postulated Reaction Mechanisms

Some of the possible high temperature reactions of triethylamine are shown in Figure 2. The expected products in the thermal degradation of triethylamine include ethyl and diethyl amines, ammonia, hydrogen cyanide, and hydrocarbons. Fragments may interact or combine with components of the flue gas to yield the types of compounds in the second group. Another possible reaction pathway is the oxidation of triethylamine to carbon dioxide, water vapor, nitrogen, and nitrogen oxides.

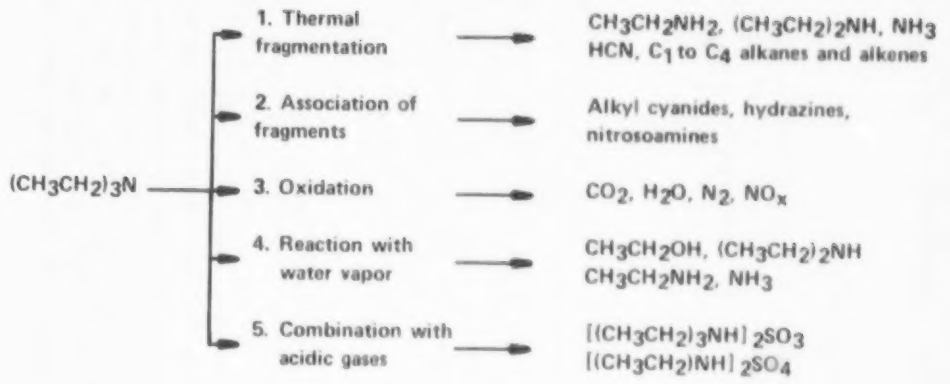
$(CH_3CH_2)_3N$
1. Thermal fragmentation
$CH_3CH_2NH_2$, $(CH_3CH_2)_2NH$, NH_3 HCN, C_1 to C_4 alkanes and alkenes
2. Association of fragments
Alkyl cyanides, hydrazines, nitrosoamines
3. Oxidation
CO_2, H_2O, N_2, NO_x
4. Reaction with water vapor
CH_3CH_2OH, $(CH_3CH_2)_2NH$ $CH_3CH_2NH_2$, NH_3
5. Combination with acidic gases
$[(CH_3CH_2)_3NH]_2SO_3$ $[(CH_3CH_2)NH]_2SO_4$

Figure 2. Possible reaction schemes of triethylamine.

Ammonia and primary and secondary amines may also be formed along with ethanol by the reaction of triethylamine with water vapor. Finally, solid salts may result from the combination of triethylamine with sulfur dioxide, sulfur trioxide, and water.

The oxidation of triethylamine offered little opportunity for identification because of the high background concentrations of carbon dioxide, water vapor, and nitrogen; however, nitric oxide and nitrogen dioxide were identifiable if these compounds were not added to the flue gas. All of the other products in Figure 2 were identifiable in principle because they were not normal components of the flue gas.

Sampling and Analytical Methods

During the investigation of triethylamine, the flue gas was analyzed for a variety of substances including sulfur oxides, nitrogen oxides, ammonia, hydrogen cyanide, aliphatic amines, other organic vapors (specifically including N-nitrosodiethylamine), and salts of protonated amines. The basis for selecting some of these compounds for analysis is indicated by Figure 2.

Sulfur trioxide, as sulfuric acid, was collected by condensation in a jacketed glass coil maintained at about 70°C.[1] Sulfur dioxide was trapped in a bubbler containing 3% hydrogen peroxide downstream from the coil. After a sample was collected, the sulfuric acid was rinsed from the coil with 80% 2-propanol in water, and the amount of sulfate was determined by titration with a 0.005 N barium perchlorate solution with Thorin as the indicator.[2] The sulfur dioxide was determined by titrating the bubbler solution with 0.1 N sodium hydroxide to the bromophenol blue endpoint.

Nitrogen dioxide and total nitrogen oxides were determined independently. Nitric oxide was then determined by difference. Nitrogen dioxide was absorbed from the flue gas stream in the Griess-Saltzman reagent in a bubbler and determined by colorimetry.[3] When the nitric oxide level was expected to be less than about 50 ppm, the compound was oxidized to the dioxide with chromium trioxide impregnated on firebrick and then determined along with the original nitrogen dioxide by the Griess-Saltzman procedure. When the nitric oxide level was expected to be near 1000 ppm, both nitric oxide and nitrogen dioxide were oxidized to nitric acid and the nitrate ion was determined by the phenol-disulfonic acid method.[4]

Ammonia was absorbed from the flue gas in bubblers containing 0.1 N sulfuric acid; ammonium ion was then determined by the indophenol colorimetric procedure.[5] Hydrogen cyanide was collected in 1 N sodium hydroxide, and cyanide ion was determined with a cyanide-specific electrode.

Organic amines were collected from the flue gas in bubblers containing 0.1 N sulfuric acid. An aliquot of an exposed bubbler solution was made alkaline with sodium hydroxide solution to regenerate the free amine; the basic solution was then analyzed by gas chromatography (GC).[6]

In some experiments, a nonspecific sampling and analytical procedure for organic compounds was followed. Two different sampling devices were employed: (1) a cartridge containing Amberlite XAD-2 porous polymer maintained at about 30°C and (2) a cold trap at 0°C followed by a trap at -78°C. The exposed sorbent material and the cold traps were extracted with methylene chloride. The extracts were concentrated and then analyzed by GC.

Although the nonspecific sampling procedures for organics were applicable to the determination of N-nitrosodiethylamine, a separate sampling and analytical procedure was carried out for the compound. Flue gas was sampled through bubblers containing 1 N sodium hydroxide. The alkaline solutions were extracted with methylene chloride and extracts were concentrated prior to analysis by GC.

Salts formed in the flue gas were collected on a heated Teflon filter. The filter was maintained at 160°C except when samples were taken from the 90°C zone; here it was maintained at 90°C. Exposed filters were extracted by vacuum filtration with distilled water. A portion of the extract was analyzed for protonated organic amine cations; in another portion of the extract, sulfate was determined. For the determination of the sum of sulfite and sulfate salts, a third portion of the extract was oxidized with hydrogen peroxide before sulfate was determined.

Injection of Triethylamine Vapor into the Flue Gas

Triethylamine vapor was generated by bubbling dry nitrogen through a reservoir of triethylamine maintained at 0°C in an ice bath. The levels produced were determined by sampling the generator effluent directly. The values observed corresponded to 14 to 36 ppm by volume after dilution in the flue gas. Traces of diethylamine were generated along with triethylamine due to the presence of small amounts of diethylamine in the liquid, reagent-grade triethylamine used in the generator. For instance, diethylamine was added to the flue gas at a concentration of about 80 ppb when the triethylamine level was 21 ppm.

Variation of Experimental Parameters

Experimental parameters that were varied included the composition of the flue gas into which triethylamine was added, the temperature of injection of the amine, and the temperature of removal of gas samples to be analyzed. The specific combinations of experimental conditions that were employed are shown in Table 1. The first series of experiments was conducted with a simplified flue gas mixture containing no oxides of sulfur or nitrogen; the amine was injected at temperatures of 650, 370, and 160°C, and samples were removed at temperatures of 160 and 90°C. In the later series of experiments, the reactive oxides of sulfur and nitrogen were added; here the only injection temperature used was 160°C because it was assumed that the combination reactions expected between these oxides and triethylamine would be likely to occur only at the lower gas temperatures.

Table 1. EXPERIMENTAL CONDITIONS USED IN THE INVESTIGATION OF TRIETHYLAMINE

Gas composition	Injection temperature, °C	Sampling temperature,[a] °C
Without SO_x or NO_x	650	160, 90
	370	160, 90
	160	160, 90
With 500 ppm of SO_2 added[b]	160	160, 90
With 500 ppm of SO_2 and 20 ppm of SO_3 added	160	160, 90
With 500 ppm of SO_2 and 1100 ppm of NO_x added[c]	160	160

a. The 160°C sampling point refers to the outlet of the electrostatic precipitator.

b. The background concentration of sulfur trioxide was 1 to 2 ppm.

c. About 1000 ppm of nitric oxide and 100 ppm of nitrogen dioxide. The background sulfur trioxide concentration was 3 to 6 ppm.

Summary of Experimental Results

Recovery of Triethylamine as a Function of Injection Temperature-

Data showing recoveries of triethylamine with injection at various temperatures, all without sulfur or nitrogen oxides present, are given in Table 2. These data indicate that with injection at 650°C very little of the compound could be detected at the downstream sampling location. On the other hand, with injection at 370 or 160°C, 70 to 80% of the compound was recovered at the sampling location. It seems obvious, therefore, that extensive degradation of the amine occurred in the 650°C zone.

Table 2. RECOVERY OF TRIETHYLAMINE IN FLUE GAS CONTAINING NO OXIDES OF SULFUR OR NITROGEN

Injection temperature, °C	Sampling temperature,[a] °C	Avg. observed TEA, ppm	Avg. expected TEA, ppm
650	160	1.1	25.6
370	160	16.4	20.3
160	160	18.4	25.5
	90	18.2	21.9

---

a. The 160°C sampling point refers to the outlet of the electrostatic precipitator.

Efforts to account for the reaction products occurring at 650°C were not very successful. The principal results in terms of other reaction products were as follows:

- Nitric oxide, 1 ppm
- Nitrogen dioxide, 0.05 ppm
- Hydrogen cyanide, 1 ppm
- Ammonia, 2 ppm

In addition, diethylamine was found at the parts-per-billion level (as expected because of the occurrence of this compound in the injected triethylamine), and another unidentified nitrogen compound was found at an even lower level.

Recovery of Triethylamine as Filterable Solids and Vapor as a Function of the Flue Gas Composition-

The data in Table 3 show another principal finding in the investigation of triethylamine: with the addition of sulfur and nitrogen oxides, a substantial part of the amine was collected on a filter in the sampling train, indicating that combination with acidic gases to form salts had occurred. The data further indicate that the fraction of the amine collected as solids increased as the sampling temperature was reduced from 160 to 90°C or as the concentration of sulfur trioxide was increased. Analysis of the material on the filters confirmed that sulfate or its possible antecedent, sulfite, was present in addition to the amine. When sulfur trioxide was present in the flue gas, the assumed salt present was the sulfate or bisulfate. When sulfur trioxide was not present at a significant concentration, as when sulfur dioxide alone was added to the flue gas, the assumed salt present was the sulfite or bisulfite. In some instances, the relative amounts of amine and sulfate suggested that the bisulfate rather than the sulfate was the more probable salt.

It was expected that the reaction of sulfur trioxide with the amine would produce a fine particulate that would enhance the space charge in the electrostatic precipitator. Voltage-current curves for the precipitator with and without triethylamine addition to the flue gas containing sulfur trioxide are compared in Figure 3. At voltages just above that required for corona initiation, the expected shift in the voltage-current curve occurred; however, at higher voltages, the shift in the location of the curve was opposite to that expected.

As indicated in Table 3 a substantial fraction of the injected triethylamine was not accounted for as either solid or vapor. In the experiments with sulfur trioxide added to the flue gas, however, evidence for other reaction products was obtained. About 3 ppm of diethylamine (much more than was expected from the impurity level in the triethylamine) was found along with the original compound, mainly on the particulate filter. Other products were found in a charred, viscous deposit on the walls of the 160°C zone; these included diethylamine and diethylsulfamic acid.

Table 3. RECOVERY OF TRIETHYLAMINE AS SOLIDS AND VAPOR AS A FUNCTION OF FLUE GAS COMPOSITION[a]

Added components of flue gas	Sampling temperature, °C	Avg. observed TEA, ppm			Avg. expected TEA, ppm
		Filter	Bubbler	Total	
None[b]	90	0.0	18.2	18.2	21.9
SO_2	160	0.6	17.1	17.7	27.9
	90	5.3	15.3	20.6	28.3
$SO_2 + SO_3$	160	9.4	3.5	12.9	23.4
	90	18.1	1.3	19.4	25.0
$SO_2 + NO_x$	160	3.9	9.1	13.0	20.9

---

a. The amine was always injected at 160°C.

b. The flue gas contained only the basic components: N_2, O_2, CO_2, and H_2O.

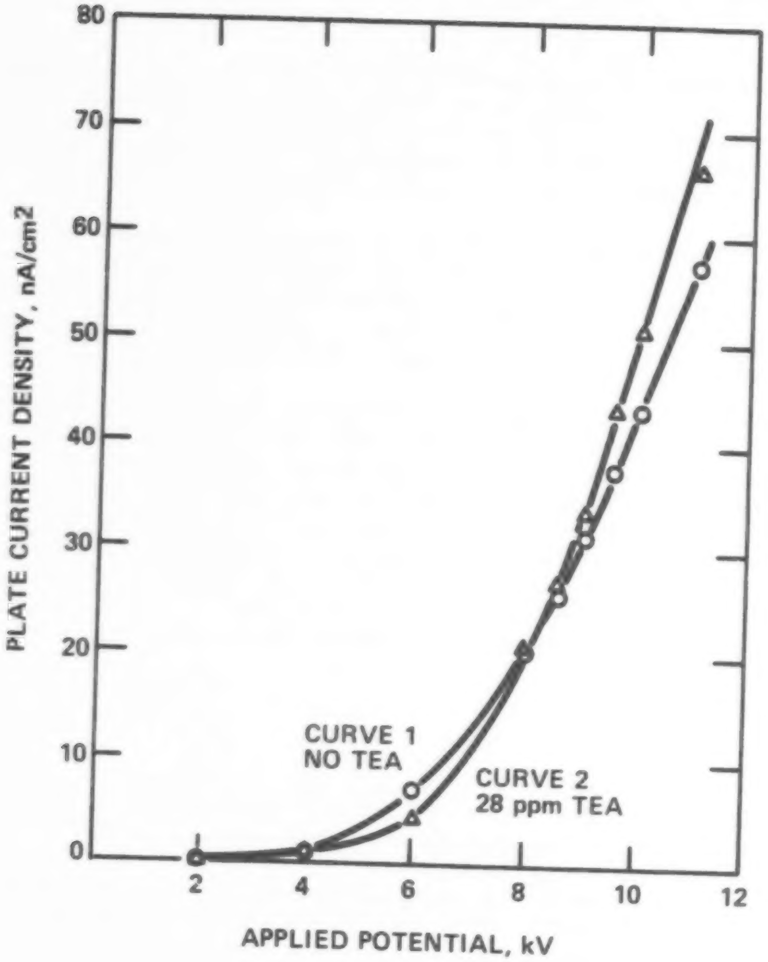

Figure 3. Current-voltage relationship for ESP.

Identification of N-Nitrosodiethylamine as a Reaction Product-

A deliberate effort was made to identify this nitrosoamine as a reaction product because of the concern about other compounds of this type as carcinogenic pollutants. A reasonably conclusive identification of the compound was made successfully during the experiments with nitrogen oxides included in the flue gas composition. Identification was based on retention times on two gas chromatographic columns and on the occurrence of a molecular ion at m/e of 102 in a mass spectrometer.

The occurrence of N-nitrosodiethylamine in the flue gas appeared to be related to the concentration of diethylamine. An increase in the observed concentration of diethylamine vapor in the flue gas from 60 to 110 ppb at comparable levels of triethylamine was accompanied by an increase in the amount of N-nitrosodiethylamine found from 90 to 210 ppb.

It was also observed that the occurrence of N-nitrosodiethylamine did not appear to be related to the concentration of nitric oxide in the flue gas. An amount of N-nitrosodiethylamine corresponding to 67 ppb was found when sampling flue gas containing no nitric oxide, and a comparable amount, 89 ppb, was found with 750 ppm nitric oxide in the flue gas.

It was observed that some, but apparently not all, of the N-nitrosodiethylamine was produced during the sampling of flue gas, rather than during the time of residence of triethylamine in the flue gas train. When bubblers used for sample collection were spiked with triethylamine and diethylamine and then exposed to flue gas containing neither of these amines, some N-nitrosodiethylamine formed in the bubblers. The results indicated, however, that the bubblers had to be spiked with many times the amounts of amine vapors actually sampled from the flue gas to produce amounts of N-nitrosodiethylamine comparable to those found in unspiked bubblers.

CONCLUSIONS

The injection of triethylamine into the flue gas of a coal-fired boiler upstream from the economizer at temperatures near 650°C would result in extensive thermal degradation of the amine. In our laboratory studies the principal products eluded detection. In a past study of the degradation of triethylamine in a closed reactor at 470 to 500°C,[7] methane and nitrogen were the chief products found after the decomposition of chemical intermediates. Methane would not have been trapped in the sampling trains employed in our investigation. The detection of small amounts of nitrogen that would be produced would have been prohibited by the high background concentration in the flue gas.

Our laboratory studies also indicated that the addition of triethylamine at lower temperatures to power plant flue gas containing typical levels of sulfur dioxide would result in the formation of triethylammonium salts. A possible mechanism for the reaction of triethylamine with sulfur dioxide has been proposed in another study of the

Currently, the investigation of other commercial conditioning agents is underway. These studies will continue until March 1979, at which time a report summarizing all of the studies will be prepared for general distribution.

ACKNOWLEDGMENTS

Several staff members in the Analytical and Physical Chemistry Division, Southern Research Institute—especially Don B. Hooks, Assistant Chemist—assisted in the laboratory work.

REFERENCES

1. Lisle, E. S., and J. D. Sensenbaugh. The Determination of Sulfur Trioxide and Acid Dew Point in Flue Gases. Combustion. 37:12-16, January 1965.

2. Fielder, R. S., and C. H. Morgan. An Improved Titrimetric Method for Determining Sulfur Trioxide in Flue Gas. Anal. Chim. Acta. 23:538-540, 1960.

3. Recommended Method of Analysis for Nitrogen Dioxide Content of the Atmosphere (Griess-Saltzman Reaction). In: Methods of Air Sampling and Analysis, Katz, M. (ed.). Washington, D. C., American Public Health Association. 1977. p. 527-534.

4. Standards of Performance for New Stationary Sources. Method 7—Determination of Nitrogen Oxide Emissions from Stationary Sources. Federal Register. 36(247):24891-24893, December 1971.

5. Harwood, J. E., and A. L. Kühn. A Colorimetric Method for Ammonia in Natural Waters. Water Research. 4:805-811, 1970.

6. Aliphatic Amines in Air. In: NIOSH Manual of Analytical Methods, Taylor, D. G. (ed.). Cincinnati, National Institute for Occupational Safety and Health. 1977. Method No. 221.

7. Taylor, H. A., and E. E. Juterbock. The Thermal Decomposition of Triethylamine. J. Phys. Chem. 39:1103-1110, 1935.

8. Bateman, L. C., E. D. Hughes, and C. K. Ingold. Molecular Compounds between Amines and Sulfur Dioxide. A. Comment on Jander's Theory of Ionic Reactions in Sulfur Dioxide. J. Chem. Soc.:243-247, 1944.

reaction with bulk amounts of the reactants.[8] According to this mechanism, sulfur dioxide reacts to form a one-to-one addition product with triethylamine that rapidly absorbs water on exposure to moist air to form triethylammonium bisulfite. The bisulfite slowly absorbs oxygen to produce chiefly the bisulfate salt. If we suppose that the addition product would only exist as an unstable intermediate in the presence of water vapor in power plant flue gas, then the resulting bisulfite would be expected to slowly absorb oxygen to produce the bisulfate. We would then expect that the flue gas would contain the bisulfite, the bisulfate, or a mixture of both.

If the flue gas contains significant concentrations of sulfur trioxide, triethylammonium sulfate or bisulfate appears to form directly. Evidence was also obtained to indicate that sulfur trioxide induces other reactions of the amine to products including diethylamine and diethylsulfamic acid.

The addition of triethylamine at relatively low temperatures to flue gas containing typical levels of sulfur and nitrogen oxides may result in the formation of a highly toxic nitrogen compound, N-nitrosodiethylamine. In our laboratory tests, the observed amounts of the nitrosoamine appeared to correlate with the levels of diethylamine found. Since the nitrosoamine did not appear to be related to the level of nitric oxide, it seems reasonable to conclude that the formation of diethylnitrosoamine occurred by the reaction of nitrogen dioxide with diethylamine. In our tests, there were two potential sources of diethylamine for this reaction. The compound was introduced as a contaminant of triethylamine. There was also evidence that some triethylamine was degraded to diethylamine, especially in flue gas enriched in sulfur trioxide.

SUMMARY OF THE INVESTIGATIONS OF OTHER AGENTS

Other conditioning agents that have been studied are ammonia, sodium carbonate, and COALTROL LPA-40 (Apollo Chemical Corporation). In the investigation of ammonia, it was found that the compound combined with sulfur trioxide to form a bisulfate salt at temperatures around 160°C. There appeared to be no reaction of ammonia with sulfur dioxide. Even at 650°C, no significant thermal degradation of ammonia was observed.

The study of sodium carbonate revealed that the compound reacted extensively with sulfur oxides to produce both sulfates and sulfites at temperatures between 90 and 160°C. Nitrogen oxides did not appear to react with sodium carbonate.

The study of LPA-40 initially involved an analysis of the formulation, which indicated that the material is about 40% (by weight) ammonium sulfate in water containing a few tenths of a percent iron. In the simulated flue gas, it was found that LPA-40 decomposed at 650°C to produce chiefly sulfur trioxide and ammonia. These gases recombined at lower temperatures. At 160°C, the predominant recombination product was ammonium bisulfate; at 90°C, ammonium sulfate.

FLUE GAS CONDITIONING EFFECTS ON ELECTROSTATIC PRECIPITATORS

R. Patterson, P. Riersgard and R. Parker
Air Pollution Technology, Inc.
San Diego, California

L. Sparks
U.S. Environmental Protection Agency
Industrial Environmental Research Laboratory
Research Triangle Park, North Carolina

INTRODUCTION

Flue gas conditioning agents are used primarily for maintaining high particulate collection efficiency in electrostatic precipitators (ESPs) operating on high resistivity fly ash from low sulfur coals. Burning low sulfur coals has been a popular method for meeting sulfur dioxide emission limits. Flue gas conditioning is rarely designed into a new installation; rather, it is normally used as a corrective method for an ailing precipitator.

Many conditioning agents have been investigated for improving the collection efficiency of ESPs. When injected, the conditioning agents mix with the gas to form various gaseous and particulate compounds, depending on the flue gas composition and temperature. Therefore, this program is designed to determine the improvement in ESP performance and the additional gaseous and particulate compounds which penetrate the ESP.

TEST METHODS AND PLANT DESIGN INFORMATION

Field testing of the ESP was completed with and without injection of the flue gas conditioning agent. Variances were obtained from the proper agencies for periods covering the unconditioned tests.

The particulate analyses included size, mass, resistivity and chemical composition. Size distributions were obtained at the inlet and the outlet of the ESP with calibrated cascade impactors. A modified EPA Method 5 train was used for total mass determination.

The resistivity of the particulates entering the ESP was monitored with a point to plane resistivity probe. Plume opacity in the outlet duct of the ESP was recorded continuously.

Samples of particulate matter collected with a cascade impactor at the ESP inlet and outlet were analyzed to determine their elemental composition as a function of particle size. The amount of particulate sulfate collected on the impactor substrates was determined with an acid-base titration using bromophenol blue as the indicator. Ion-excited X-ray emission analysis was used to determine the other elements.

The flue gas velocity and static pressure were measured at the inlet and outlet using calibrated pitot tubes. The molecular weight and density of the gas were determined by measuring the gas composition and temperature. Concentration of H_2O vapor was obtained by measuring the wet and dry bulb temperature of cooled stack gas.

SO_2 entering and leaving the ESP was determined using a Dupont SO_2 stack analyzer (model 459). The output from the SO_2 analyzer was recorded continuously during the field test.

The concentration of SO_3 entering and leaving the ESP was determined with the controlled condensation method as described by Maddelone[1]. This technique is recommended for monitoring the mass emission rate of SO_3 from combustion sources.

Thermal decomposition products in the stack gas depend on the particular flue gas conditioning agent used. Ammonia and organic vapor concentration at the ESP inlet and outlet were determined for the second test reported here. Organic vapors were collected in an absorption column containing Tenax GC as the absorbent. The ammonia concentration of the stack gas was determined with a modified Kjeldahl titrimetric procedure.

Fuel analyses were performed to determine the composition of fixed carbon, volatile carbon, ash, sulfur, moisture and alkali metals. The conditioning agent from the second field test was analyzed for NH_4^+, SO_4^{--} and total organics.

Information on the ESP design, maintenance and operation was obtained from power plant personnel through survey forms and personal conversations. The current-voltage relationships for each section of the ESP were determined for both conditioned and unconditioned tests. Annual operating and maintenance costs were obtained for the ESP, flue gas conditioning equipment and chemicals.

FIELD TEST NO. 1

Field test No. 1 was performed at a plant with five power generating units and a sixth unit under construction. Testing was performed on unit No. 3 which had a boiler rated at 44 MW. Unit No. 3 is normally operated at an average rating of 58 MW producing 10,000 kPa (1,450 psi) steam at 540°C (1,005°F). A typical coal analysis for the plant is given in Table 1. The location of the injection ports, and inlet and outlet sampling ports is shown in Figure 1.

TABLE 1. CHEMICAL ANALYSIS OF COAL FROM TEST NO. 1

Component	Conditioned % Wt.	Unconditioned % Wt.
Sodium	0.013	0.016
Potassium	0.06	0.06
Lithium	0.00019	0.00014
Calcium	0.19	0.18
Magnesium	0.02	0.02
Sulfur	1.09	0.78
Sulfur*	0.88	0.85
Ash*	10.7	11.1
Volatile hydrocarbons*	33.5	33.6
Fixed carbon*	55.8	55.7
Heat content*, BTU/lb	13,100	13,100

*Averaged data received from plant.

The electrostatic precipitator, installed in 1972 after the air preheater, has a design efficiency of 95 percent when burning high sulfur coal. It is preceded by a bank of axial entry cyclones of undetermined efficiency. The ESP consists of two sections in series; i.e., an inlet and an outlet section. Each has a T/R set which can be electrically isolated into a right and left subsection. Design information for the ESP is given in Table 2.

Fly ash is removed from the wires and plates by vibrators which operate on a 5 minute cycle. The collection ash falls into hoppers beneath the ESP. The ash handling system pneumatically transfers the ash from the hoppers to a storage tank.

The Wahlco SO$_3$ injection system converts hot vaporized SO$_2$ and air into SO$_3$ over a vanadium pentoxide (VO$_5$) catalyst. It is injected into the flue gas downstream from the air preheater and cyclone at 490°C (920°F) through five rows of nozzles. The flue gas is approximately 160°C (320°F) at the injection point. The SO$_2$ is consumed at a constant rate of approximately 46 lb/hr at full load of 58 MW. This corresponds to 32 ppm of SO$_3$ in the flue gas stream.

The field test spanned the period January 25 to February 7, 1978. Testing of the conditioned case started on January 25 and ended on February 2. During this time, unit no. 3 was shut down for boiler tube repairs (January 28, 29, 30). After a 3 day deconditioning period, the baseline tests (unconditioned case) started February 5 and lasted through February 7.

Particulate Tests

The results of the cascade impactor tests are given in Table 3. Inlet size distributions are similar for both conditioned and unconditioned tests.

Grade penetration curves were determined from the cascade impactor data. Average particle penetrations with and without SO_3 conditioning are shown in Figure 2. This figure shows that SO_3 conditioning enhanced particle collection in the size range of 0.2 to 5 microns diameter.

Total particulate mass concentrations for the inlet and outlet are given in Table 3. The overall collection efficiency averaged 95.4 percent with a standard deviation of 1.0 percent for SO_3 injection. Without addition of the conditioning agent to the flue gas the overall efficiency averaged 79.2 percent with a standard deviation of 3.4 percent.

Results of the fly ash resistivity tests are given in Table 3. The fly ash resistivity averaged 5×10^{10} ohm-cm with SO_3 injection and 2×10^{11} ohm-cm without injection.

The opacity was measured in the outlet duct with a modified Lear-Siegler instrument. The opacity during conditioned runs averaged approximately 35 percent and increased to approximately 75 percent for the unconditioned tests.

Chemical analysis of the cascade impactor substrates showed that particulate sulfate was below the detection limit of 1 ppm. Results are not yet available for the ion-excited X-ray elemental analysis.

Gas Analysis

Flue gas temperature, velocity and composition are given in Table 3. The oxygen content increased from the inlet to the outlet, indicating that atmospheric air was leaking into the ESP. The outlet SO_2 concentration averaged 670 ppm during the conditioned tests and 620 ppm during the unconditioned tests.

The SO_3 concentration in the flue gas averaged 10.9 ppm at the inlet and 8.1 ppm at the outlet during the conditioned runs. Without SO_3 injection the inlet concentration was 1.6 ppm and the outlet 1 ppm. There are no known thermal decomposition products resulting from injection of SO_3 as a conditioning agent.

FIELD TEST NO. 2

Field test No. 2 was performed at a power plant with four power generating units. Testing was performed on unit No. 3 which had a boiler rated at 840 MW. Unit No. 3 is normally operated at 300 MW, producing 24,820 kPa (3,600 psi) steam at 593°C (1,100°F). The inlet and outlet sampling ports are shown in Figure 3.

Unit No. 3 has two ESPs in parallel. Flue gas enters each ESP from one separate and one common Lungdstrom air preheater. There is no control on the volumetric flow of the split streams. Each ESP has five T/R sets, one for each of its electrically isolatable sections. The inlet section occupies one third of the ESP volume. Two side-by-side center sections and two side-by-side outlet sections make up the remaining volume of each ESP. Design information for the ESP is given in Table 4.

The collected fly ash is removed from the plates by drop-hammer rappers which operate every 2 minutes. A 5-second vibration cleans the wires every 30 minutes. The ash falls into hoppers beneath the precipitator. It is transferred pneumatically to a water sluicing tank and an ash settling pond.

The flue gas conditioning system was provided by Apollo Chemical Corporation. Two conditioning agents were injected: one in the economizer section (flue gas at about 600°C) and one after the preheater (flue gas at about 120°C). The two chemicals injected were LPA 445 and LAC 51B, respectively. The conditioners were automatically controlled to follow the coal feed rate at 0.1 gal./ton coal for LAC 51B, and 0.075 gal./ton for LPA 445.

The field test spanned the period from April 17 through May 18. Testing of the conditioned case started April 17 but was suspended on April 22 because of multiple problems with unit no. 3. Testing of the conditioned case was completed on May 11. After a 2 day deconditioning, the 3 day test of the baseline case started on May 16 and ended on May 18.

Particulate Tests

Grade penetration curves were determined from analysis of the cascade impactor runs. Average particle penetration with and without injection of the conditioning agent is shown in Figure 4. This figure shows that collection of particles in the size range of 0.2 to 3 μm increased during the runs with injection of conditioning agent.

Overall collection efficiency averaged 99.6 percent with a standard deviation of 0.3 percent when the conditioning agent was injected. Without addition of the conditioning agent to the flue gas the overall efficiency averaged 99.6 percent with a standard deviation of 0.4 percent. Overall collection efficiency was not affected by the conditioning agent because greater than 95 percent of the particulate entering the ESP was larger than 3 μm.

Fly ash resistivity averaged 6.9 x 10^{10} ohm-cm for conditioned and baseline tests. Particulate sulfate on the cascade impactor substrates was below the detection limit of 1 ppm. Results are not yet available for the ion-excited X-ray elemental analysis.

Gas Analysis

Flue gas temperature, velocity and composition are given in Table 5. The SO_2 concentration varied over the range of 500 to 1,800 ppm during the period of a day's testing.

The SO_3 concentration in the flue gas averaged 1.2 ppm at the inlet and 2.2 ppm at the outlet during the conditioned tests. This is believed to be a result of the injection location. The second conditioning agent is injected approximately 12 meters upstream of the inlet sampling ports which may not allow adequate time for complete mixing in the flue gas.

Ammonia concentrations were below the detectable limit of 1 ppm. Analysis for the thermal decomposition products are not yet available.

ACKNOWLEDGEMENT

The work described in this publication was performed under Contract No. 68-02-2628 with the U.S. Environmental Protection Agency.

REFERENCE

1. Maddelone, R.F. Guideline for Combustion Source Sulfuric Acid Emission Measurements. TRW Document No. 28055-6005-RU-00. EPA Contract No. 68-02-2165, Task Order 13. February 1977.

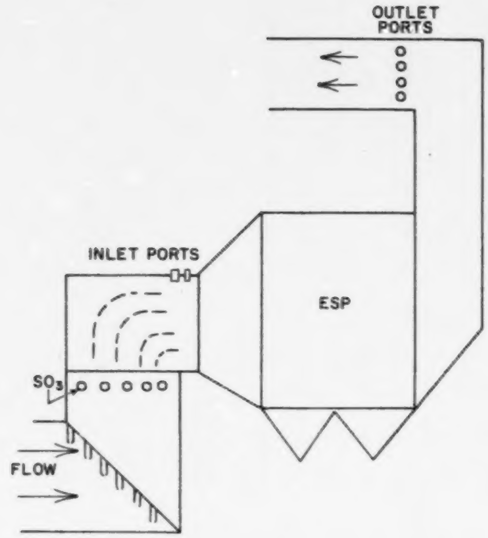
OUTLET PORTS
INLET PORTS
ESP
SO_3
FLOW

FIGURE 1. PLANT LAYOUT FOR TEST NO. 1

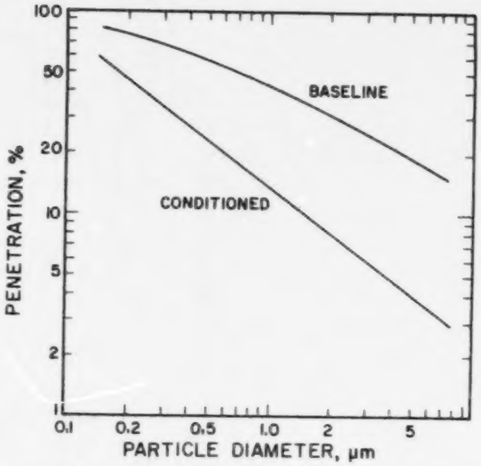

FIGURE 2. GRADE PENETRATION TEST NO. 1

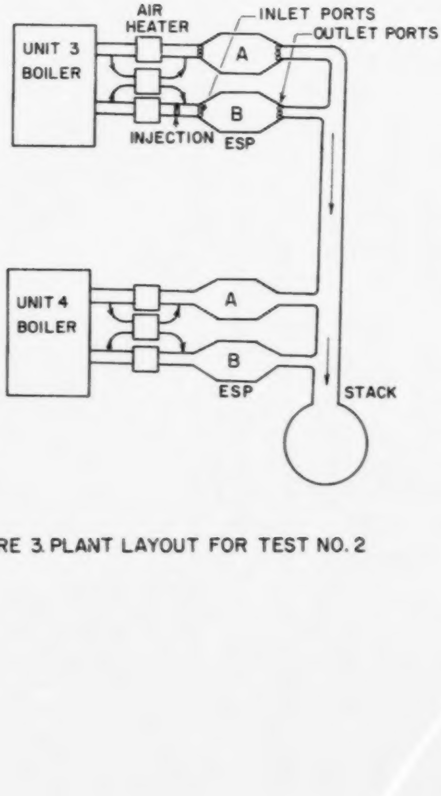
AIR HEATER
INLET PORTS
OUTLET PORTS
UNIT 3 BOILER
A
B
INJECTION
ESP
UNIT 4 BOILER
A
B
ESP
STACK

FIGURE 3. PLANT LAYOUT FOR TEST NO. 2

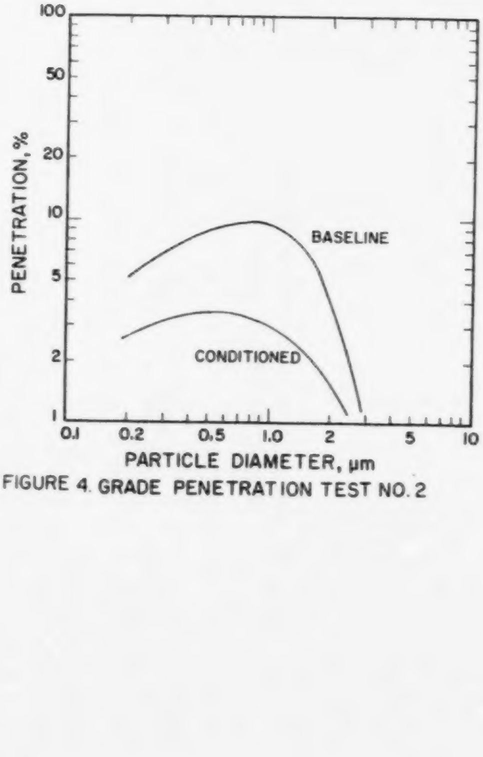

FIGURE 4. GRADE PENETRATION TEST NO. 2

Table 2. ELECTROSTATIC PRECIPITATOR DESIGN INFORMATION FOR FIELD TEST NO. 1

Startup date	1972
Design gas flow	104 actual m³/s (220,000 actual ft³/min)
Design gas velocity	1.05 m/s (3.4 ft/s)
Design specific collector area	36 m² per actual m³/s (182 ft² per 1000 actual ft³/min)
Design efficiency	95%
Overall configuration	2 series chambers 2 electrical sections in parallel per chamber 36 parallel gas passages
Plates	37 plates per chamber (cold rolled steel sheets) plate height is 9.46 m (31 ft) plate length each section is 2.74 m (9 ft) for total length in direction of flow of 5.48 m (18 ft) plate-to-plate spacing is 0.229 m (9 in.) total surface area of plates is 3737 m² (40,176 ft²)
Wires	18 equally spaced wires per gas passage wire diameter is 2.77 mm (0.109 in.) wires are hanging type, placed in the center ±6.35 mm (1/4 in.) of the plate-plate space
Electrical	2 transformer-rectifier sets which were electrically insolatable into 4 subsections maximum power consumption is approximately 50 kW

Table 3. DATA SUMMARY FOR TEST NO. 1

TEST	With SO_3		Without SO_3	
	Inlet	Outlet	Inlet	Outlet
Boiler Load	58 MW	58 MW	58 MW	58 MW
Velocity	5.5 m/s	9.0 m/s	5.4 m/s	8.8 m/s
Temperature	141°C	147°C	141°C	146°C
Composition				
O_2	4.1%	5.3%	4.7%	6.0%
CO_2	14.4%	14.0%	14.1%	13.0%
H_2O	5.3%	4.5%	5.1%	5.4%
SO_2	740 ppm	670 ppm	670 ppm	620 ppm
SO_3	10.9 ppm	8.1 ppm	1.6 ppm	1.0 ppm
Resistivity	5×10^{10} Ω-cm	-	2×10^{11} Ω-cm	-
Mass Loading	2.6 g/DNm³	0.12 g/DNm³	2.4 g/DNm³	0.5 g/DNm³
Overall Efficiency	-	95.4%	-	79.2%
Mass Mean Diam., μm/ Standard Dev.	13.2 /3.5	3.5 /4.2	10.9/3.3	5.5 /4.6

Table 4. ELECTROSTATIC PRECIPITATOR DESIGN INFORMATION FOR FIELD TEST NO. 2

Startup date	1968
Design gas flow	697 actual m^3/s (1,470,000 actual ft^3/min)
Design gas velocity	2.14 m/s (7.0 ft/s)
Design specific collector area	17 m^2 per actual m^3/s (86 ft^2 per 1000 actual ft^3/min)
Design efficiency	98.5%
Overall configuration	2 parallel chambers 5 electrical sections per chamber 39 parallel gas passages per chamber
Plates	40 plates per chamber (cold rolled steel sheets) plate height is 9.15 m (30 ft) plate length each section is 2.74 m (9 ft) for total length in direction of flow of 8.24 m (27 ft) plate-to-plate spacing is 0.229 m (9 in.) total surface area of plates is 11,754 m^2 (126,300 ft^2)
Wires	36 equally spaced wires per gas passage wire diameter is 2.77 mm (0.109 in.) wires are hanging type, placed in the center ±6.35 mm (1/4 in.) of the plate-plate space
Electrical	10 transformer-rectifier sets which were electrically isolated maximum power consumption is approximately 770 kW

Table 5. DATA SUMMARY FOR TEST NO. 2

TEST	With Conditioning		Without Conditioning	
	Inlet	Outlet	Inlet	Outlet
Boiler Load	420 MW		420 MW	
Velocity	16.4 m/s	12.1 m/s	16.4 m/s	10.3 m/s
Temperature	121°C	122°C	115°C	120°C
Composition				
O_2	4.4%	-	5.0%	
CO_2	14.1%	-	13.8%	
H_2O	4.5%	-	5.5%	5.7%
SO_2	880 ppm [1]	850 ppm[1]	890 ppm[1]	850 ppm[1]
SO_3	1.2 ppm	2.6 ppm[2]	-	2.2 ppm
NH_3	<1 ppm [2]	<1 ppm [2]	<1 ppm [2]	<1 ppm [2]
Resistivity	6.9x10^{10} Ω-cm	-	6.9x10^{10} Ω-cm	
Mass Loading	7.0 g/DNm^3	0.02 g/DNm^3	8.3 g/DNm^3	0.03 g/DNm^3
Overall Efficiency	-	99.6 %	-	99.6%

[1] SO_2 concentration varied from 500 to 1,800 ppm during the period of a day's testing.

[2] NH_3 concentration was below the detectable limits.

FLUE GAS CONDITIONING AT ARIZONA PUBLIC SERVICE COMPANY FOUR CORNERS UNIT NO. 4

R. E. Pressey
Denver Research Institute
University of Denver

D. Osborn
Stearns-Roger, Inc.

E. Cole
Arizona Public
Service Company

ABSTRACT

A Flue Gas Conditioning Program was implemented between March 22, 1977 and July 22, 1977. The objective was to evaluate the effects of Apollo Chemical Corporation's LPA-40 on precipitator performance and emissions.

During the test period, the usual operating problems were encountered. Apollo personnel were given the task of using EPA Method 5 to determine emission rates and recommend adjustments and optimization of flow rates. During the time frame of May 17 through 23, the flow rate was increased from 0.10 G/T to 0.15 G/T with a corresponding reduction in emissions. At this point, the unit developed high pressure differential across the preheater. The conditioning agent was changed from LPA-40 to LPA-445. After additional testing and review, it was determined that the differential pressure was increasing again. At this point, the decision was made to test the precipitator's performance with LPA-445 being injected at a rate of 0.10 G/T and follow up with performance testing without additives. Test results by Apollo indicated a steady operation with desirable results.

Preceding page blank

Results of the D.R.I. conditioning tests were determined by measuring mass loading, integrated average and real-time particle size distribution, flue gas composition, temperature, velocity and oxygen profiles and precipitator performance. The test was separated into two phases; one with conditioning and one without. The phases were one month apart.

Chemical and physical analyses were performed to determine the composition of the conditioning agent, its decomposition products and both the coal and ash composition.

CONCLUSIONS

- A comprehensive precipitator performance test program has been designed and implemented. It may be useful to compare these techniques with other methods for future testing.
- Admittedly the disruption of the precipitator performance, due to the loss of a coal mill, introduces some question, but we observed little improvement with the use of the chemical conditioning agent Apollo LPA-445.
- Similar detailed tests are needed to demonstrate the utility of chemical conditioning agents over a longer period of time. Such tests must determine both the positive and the negative aspects of chemical conditioning.
- Use of Apollo's LPA-40 resulted in air preheater plugging.

INTRODUCTION

This paper presents the results of test work conducted at Arizona Public Services Company's Four Corners Generating Facility, located near Fruitland, New Mexico. The test work was performed in two phases: Phase 1, during the period 18-26 June 1977, and Phase 2, during the period 16-21 June 1977. The program was designed to evaluate the beneficial effects of flue gas conditioning on particulate removal capabilities of existing control equipment. This was accomplished during Phase 1, with LPA-445 injection at 0.1 gallons/ton of coal and during Phase 2 without injection. The following tests were included in the program:

- Particulate mass emissions
- Outlet Particle size distribution, both real-time and integrated average condition
- In-situ fly-ash resistivity

- Power supply electrical readings.
- Chemical and physical analysis of particulates and chemical additives.

Particulate Mass Emissions and Electrostatic Precipitator Efficiency

Results indicated that there was marginal improvement in the precipitator efficiency with the chemical conditioning during the test demonstrations. Refer to Table 1 for a summary of results.

Tables 2 and 3 present the particulate mass emission results for Phases 1 and 2.

Particle Size Distribution and Visibility Effects

Direct measurements of the size distribution and the total number concentration of emitted particles are of interest, in addition to mass concentration, to assess the impact of any chemical agent aimed at a shift in size distribution and/or reducing the mass concentration of TSP. Such measurements indeed present a complex problem since the emitted particles range in size from 10^{-3} µm to 100 µm thus covering the size range of five orders of magnitude.

Real-time Outlet Particle Size Distribution Test Approval--

Direct measurement of the particulate size distribution in the diameter range from 0.3 µm to 3.0 µm were carried out by using Climet CI-201 Particle Analyzer, which was operated in conjunciton with the Climet Model 0294-1 Dilution System. The setup is capable of measuring particles whose diameter exceeds 0.3, 0.5, 0.7, 1.0, 1.5, 2.0, 2.5, and 3.0 µm successively and whose number concentrations lie in the range 10^3-10^8 per ft^3. Concentrations exceeding 10^8 ft^{-3} were measured with the help of a mixing-type dilution system that we designed and calibrated. The CI-201 Particle Analyzer photoelectricly registers the particle concentration by sensing the light scattered by a particle in the near forward direction. The total number concentration of particles was monitored with the help of a Small Particle Detector, Type CN, manufactured by the Gardner Associates, Inc. It consists of a small expansion chamber in which a relative humidity of the order of 320% is created so as to initiate condensation on all the submicron particles. The growing water droplets render these submicron particles detectable through a light-extinction technique. By controlling the expansion ratio, the relative humidity resulting from the expansion, the number concentration of particles with diameter exceeding 0.002, 0.003, 0.010, 0.026, and 0.260 µm successively is monitored. It is in order here to emphasize that only an indirect classification of particles with respect to their size is obtained through the Gardner counter insofar as a theoretical relationship exists between the critical value of the relative humidity and the particle diameter based on the nucleation theory.

TABLE 1

SUMMARY OF PARTICULATE EMISSION DATA

Date	Emission Rate lb/hr	ESP Efficiency n%	Penetration (1-n) %
Phase 1 (with Apollo 445 Injection)			
6/22/77	4400	97	3
6/23/77	4400	97	3
6/24/77	4700	96	4
Phase 2 (without Apollo 445)			
7/18/77	5250	96	4
7/19/77	8000	94*	6
7/20/77	6200	95	5

*At 10:30 hours on 7/19/77 one mill went out reducing the net megawatts generated from 745 to 660.

TABLE 2

PARTICULATE MASS EMISSION TESTING

SUMMARY OF RESULTS - PHASE II

	TEST #1		TEST #2		TEST #3		AVERAGE	
	INLET	OUTLET	INLET	OUTLET	INLET	OUTLET	INLET	OUTLET
TEST DATE	07/18/77	07/18/77	07/19/77	07/19/77	07/20/77	07/20/77	07/77	07/77
TEST TIME 1315-1515	1315-1515	1250-1628	1215-1415	1200-1556	0847-1115	0830-1122		
TOTAL TIME	224	120	224	120	224	120	224	120
BAROMETRIC PRESSURE	24.70	24.70	24.80	24.80	24.85	24.85	24.78	24.78
GAS STATIC PRESSURE (in H_2O)	+2.10	+0.10	+2.10	+0.10	+1.60	+0.10	+1.93	+0.10
GAS TEMPERATURE (°F/°R)	230/690	228/688	222/682	218/678	221/681	207/667	224/684	218/678
GAS FLOWRATE (ACFM)	3,011,400	3,262,300	2,930,400	3,116,900	2,939,900	3,203,100	2,960,500	3,194,100
GAS FLOWRATE (SCFM)	1,711,700	1,861,700	1,692,000	1,818,300	1,709,000	1,894,800	1,704,200	1,858,300
GAS SAMPLED (ACF)	149.39	100.17	144.61	97.38	144.20	101.22	146.07	99.59
GAS SAMPLED (SCF)	84.92	57.13	84.70	56.80	83.86	59.88	84.49	57.94
GAS VELOCITY (Ft./Sec.)	59.75	76.15	58.14	77.76	58.33	74.77	58.74	74.56
PARTICULATE COLLECTED (Grains)	46.2555	1.2192	46.2821	1.8903	47.0811	1.4737	46.5396	1.5277
DUST CONCENTRATION (Grains/ACF)	4.778	0.188	4.938	0.300	5.038	0.225	4.918	0.238
DUST CONCENTRATION (Grains/SCF)	8.405	0.329	8.431	0.514	8.663	0.380	8.500	0.408
ISOKINETIC SAMPLING (%)	100.8	101.1	100.2	102.9	99.3	104.1	100.2	102.7
ESP EFFICIENCY (as tested)	96.1		93.9		95.6		95.2	

TABLE 3

PARTICULATE MASS EMISSION TESTING

SUMMARY OF RESULTS - PHASE I

	TEST #1		TEST #2		TEST #3		AVERAGE	
	INLET	OUTLET	INLET	OUTLET	INLET	OUTLET	INLET	OUTLET
TEST DATE	06/22/77	06/22/77	06/23/77	06/23/77	06/24/77	06/24/77	06/77	06/77
TEST TIME	1152-1407	1312-1654	1000-1206	0935-1250	1120-1320	1130-1455		
TOTAL TIME	240	120	224	120	224	120	229	120
BAROMETRIC PRESSURE	24.80	24.80	24.67	24.67	24.70	24.70	24.72	24.72
GAS STATIC PRESSURE (in H_2O)	+1.9	+0.1	+1.95	+0.1	+1.95	+0.10	+1.93	+0.1
GAS TEMPERATURE (°F/°R)	229/689	215/675	262/686	220/680	231/691	227/687	229/689	221/681
GAS FLOWRATE (ACFM)	2,876,800	3,096,900	2,879,900	3,189,900	2,925,200	3,249,400	2,894,000	3,178,700
GAS FLOWRATE (SCFM)	1,682,300	1,822,800	1,701,100	1,843,700	1,698,800	1,852,900	1,694,100	1,839,800
GAS SAMPLED (ACF)	153.49	93.89	137.15	98.42	145.16	100.75	145.27	97.69
GAS SAMPLED (SCF)	89.72	55.25	81.02	56.91	84.31	57.48	85.02	56.55
GAS VELOCITY (Ft./Sec.)	57.08	72.29	57.14	74.47	58.04	75.85	57.42	74.20
PARTICULATE COLLECTED (Grains)	51.7630	1.0179	45.0179	1.0370	42.8782	1.0948	46.5530	1.0499
DUST CONCENTRATION (Grains/ACF)	5.204	0.167	5.065	0.163	4.558	0.168	4.942	0.166
DUST CONCENTRATION (Grains/SCF)	8.902	0.284	8.574	0.281	7.847	0.294	8.441	0.286
ISOKINETIC SAMPLING (%)	101.1	99.9	97.8	101.6	101.9	102.1	100.3	101.7
ESP EFFICIENCY (as tested)	96.8		96.7		96.3		96.6	

Test Data--

- Submicron particles in the stack effluents showed a dramatic increase when the stack was treated with the Apollo chemical agent (Figure 1). A majority of these particles have their diameter in the range from 0.002 to 0.26 μm.
- In the presence of the Apollo LPA-445, unexpectedly large variations, on the order of four orders of magnitude, occurred with the time of the day. Such variations were real and cannot be accounted for by any experimental errors.
- Aerosol particles in the diameter range from 0.2 μm to 3.0 μm had comparable size distribution frequencies with and without the Apollo agent. Two instances show that such particles increased in number in the absence of the Apollo agent.

Conclusion--

- On the basis of our limited observations, it may be concluded that the treatment of the stack effluents with the Apollo agent did produce a considerable increase in the total number concentration of such submicron particles.

Integrated-Average Outlet Particle Size Distribution--

Outlet particle size distribution measurements were performed during each phase of the test using an integrated average method (Andersen Impactor) as well. Size distribution collected on the Anderson impactor plates was checked by electron microscopy.

In Figure 3 there is no significant difference when the averages of the impactor tests are compared.

Ash Resistivity

It has been stated that flue gas conditioning improves electrostatic precipitator performance by reduction of fly-ash resistivity. In order to measure possible benefits from chemical treatment, fly-ash resistivity measurements were performed. (The objective of laboratory resistivity tests were to complement the in-situ tests and determine if the composition of the ash varied from inlet to outlet hoppers.

In-Situ Fly-Ash Resistivity Procedures

In-situ fly-ash resistivity measurements were performed during both phases; the objective was to determine if the in-situ ash resistivity was reduced by injection of LPA-445.

Tests were performed at a test port in the vertical duct inlet to the precipitator, at a point where the velocity and temperature at the sample location were 55 feet/second and 237^{o}F.

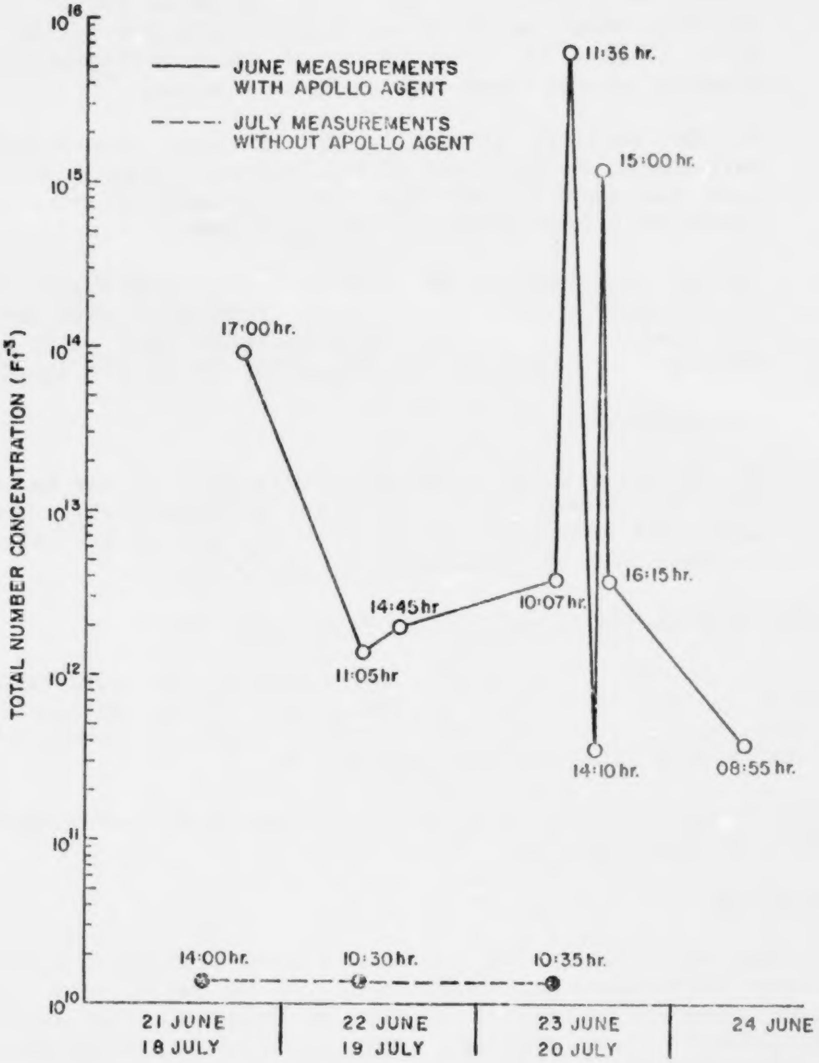

Figure 1. Real-Time Particle Size Distribution (Gardner Counter 0.002-0.26 μm).

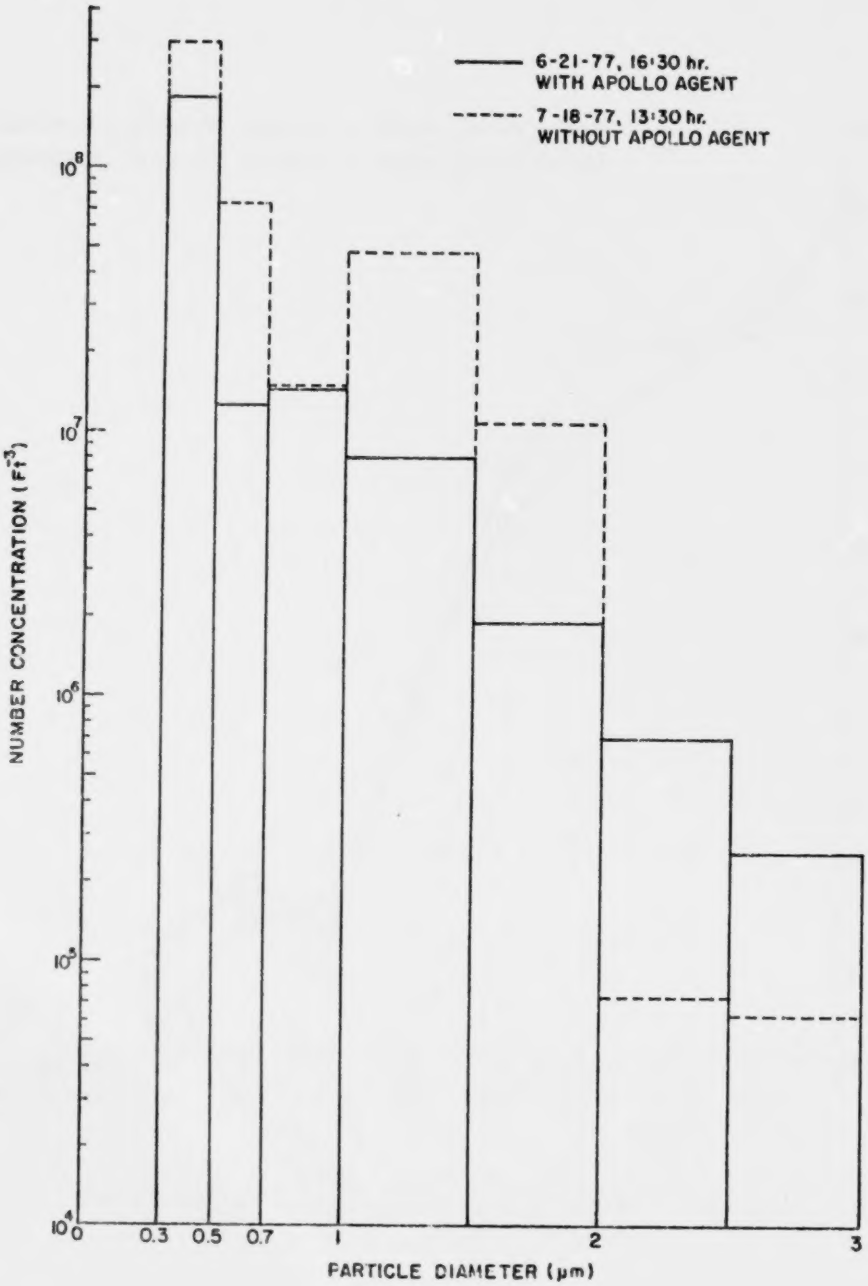

Figure 2. Real-Time Particle Size Distribution (Climet)

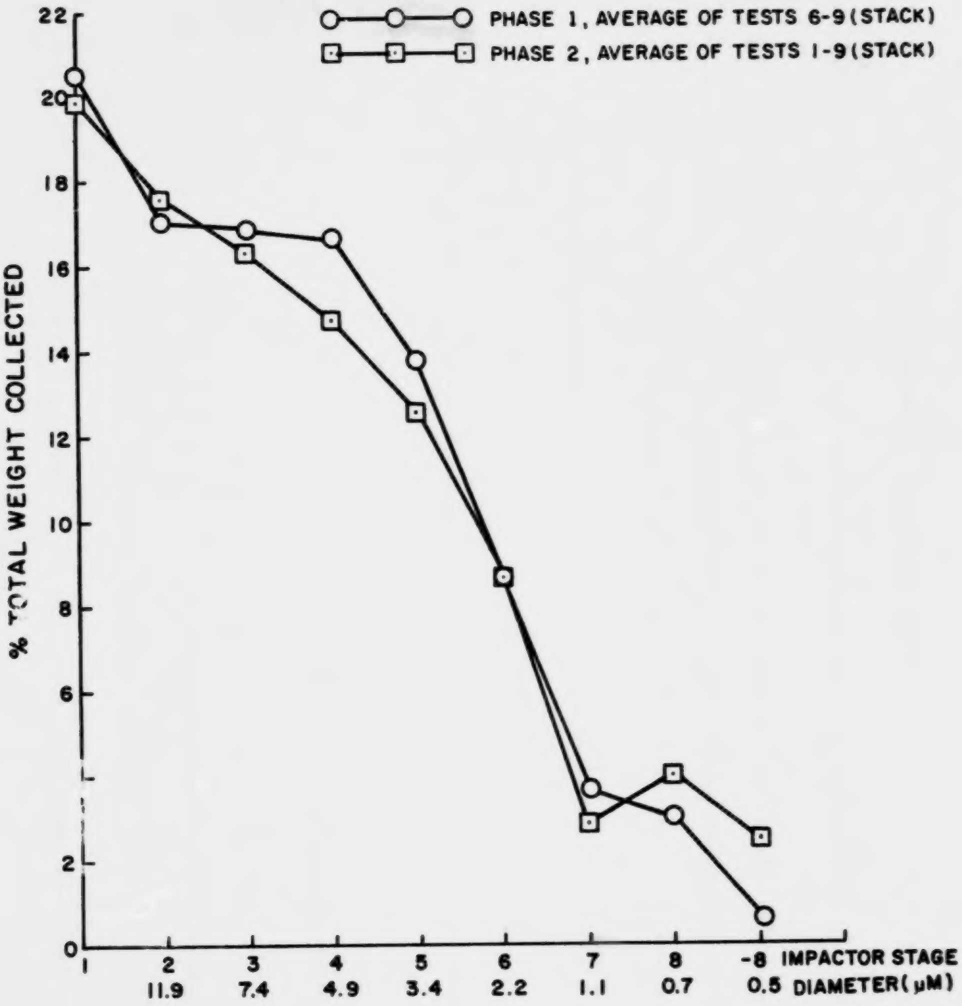

Figure 3. Particle Size Distribution Collected on Impactor Plates

The test procedure followed to measure fly-ash resistivity consists of passing a sample of ash-laden flue gas through a portable electrostatic precipitator-resistivity unit in which the resistivity of a precipitated ash layer is measured. As shown in Figure 4, the flue gas is withdrawn through a sampling probe which extends to the middle of the duct and is turned into the gas stream. A vacuum pump draws the gas sample through the probe, the precipitator-resistivity unit, a cooling and settling tank, and a calibrated orifice flow meter. Isokinetic sampling is achieved by adjusting the gas rate control valve such that the pressure differential across the calibrated orifice corresponds to a sampling velocity at the probe equal to the duct velocity. This precipitator is a point-plane type in which a needle is the negative high voltage corona point and a small disc is the ash collecting electrode. Fly-ash passing through the precipitator is electrically precipitated until a measurable layer accumulates, and it is this layer whose resistivity is measured. This method permits one to obtain a resistivity as a function of temperature curve, an advantage over the probe which must be operated in the duct.

Laboratory Ash Resistivity Procedures--

Ash samples were collected in thimbles during the precipitator inlet mass loading tests, and from the precipitator ash hoppers during each phase.

An automated system designed and fabricated by Denver Research Institute was used to measure ash resistivity of the thimble and hopper samples. Figure 7 is typical of all the samples.

Results--

Resistivity versus temperature curves for each phase are presented in Figures 5 and 6. At the duct temperature of 250^{0}F, the resistivity is nominally 1 x 10^{11} ohm-cm, and there is no significant change between Phase 1 and Phase 2.

Power Supply Electrical Readings and Voltage-Current Curves

It has been suggested that chemical conditioning of the flue gas may:

- Increase precipitator space charge
- Increase ash coagulation and particle size growth in the gas stream
- Increase ash cohesion on the collection plate
- Increase power factors

The Apollo conditioning agent LPA-445 was introduced into the 650^{0}C (1200^{0}F) superheater region of the furnace gases where we presume it

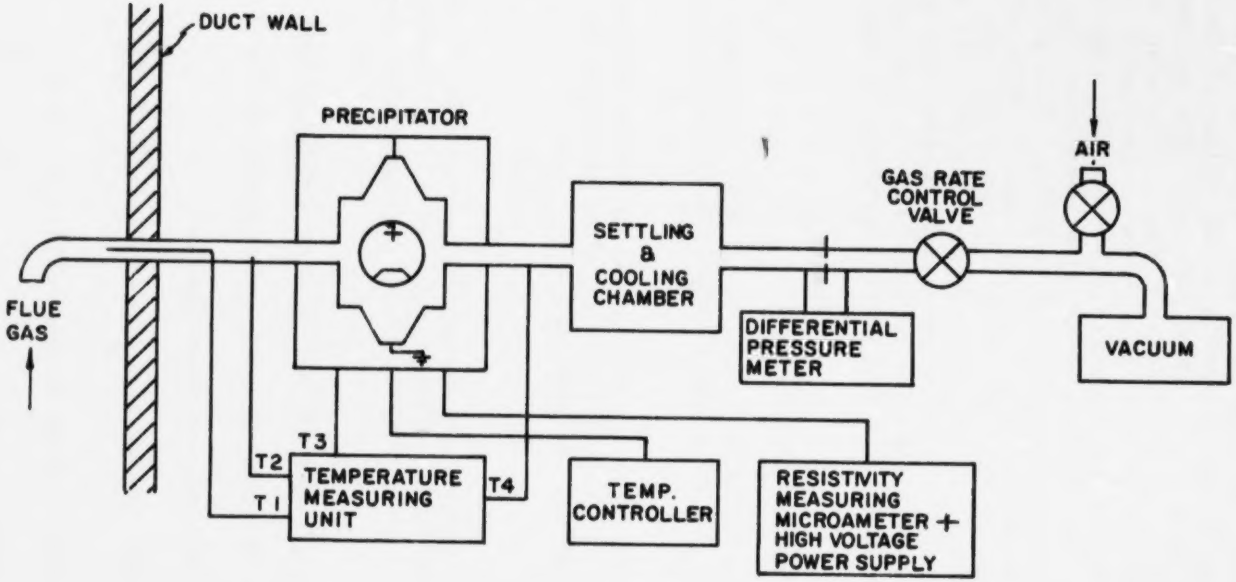
DUCT WALL
PRECIPITATOR
FLUE GAS
SETTLING & COOLING CHAMBER
DIFFERENTIAL PRESSURE METER
GAS RATE CONTROL VALVE
AIR
VACUUM
T1
T2
T3
T4
TEMPERATURE MEASURING UNIT
TEMP. CONTROLLER
RESISTIVITY MEASURING MICROAMETER + HIGH VOLTAGE POWER SUPPLY

Figure 4. Field Resistivity Measurement System

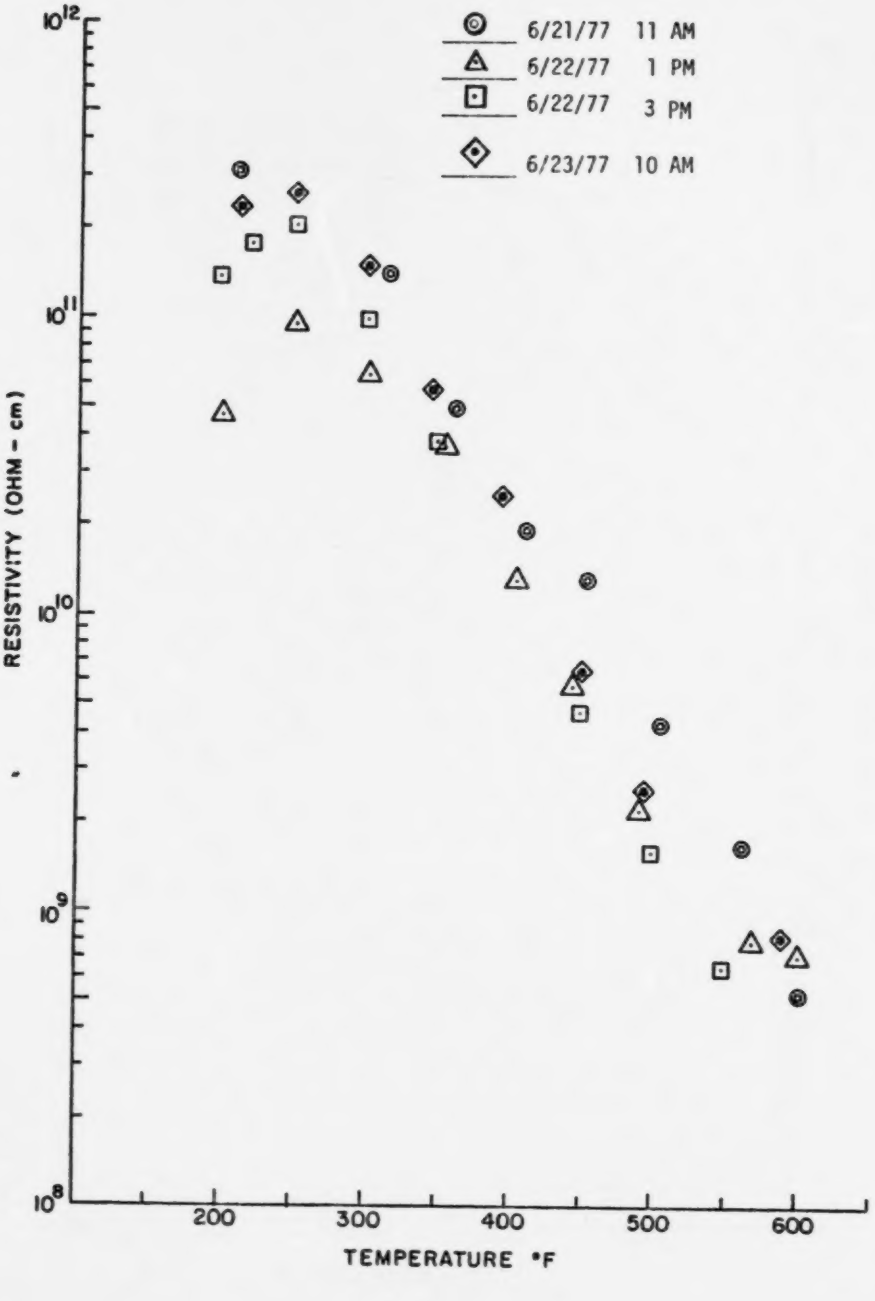

Figure 5. In Situ Resistivity

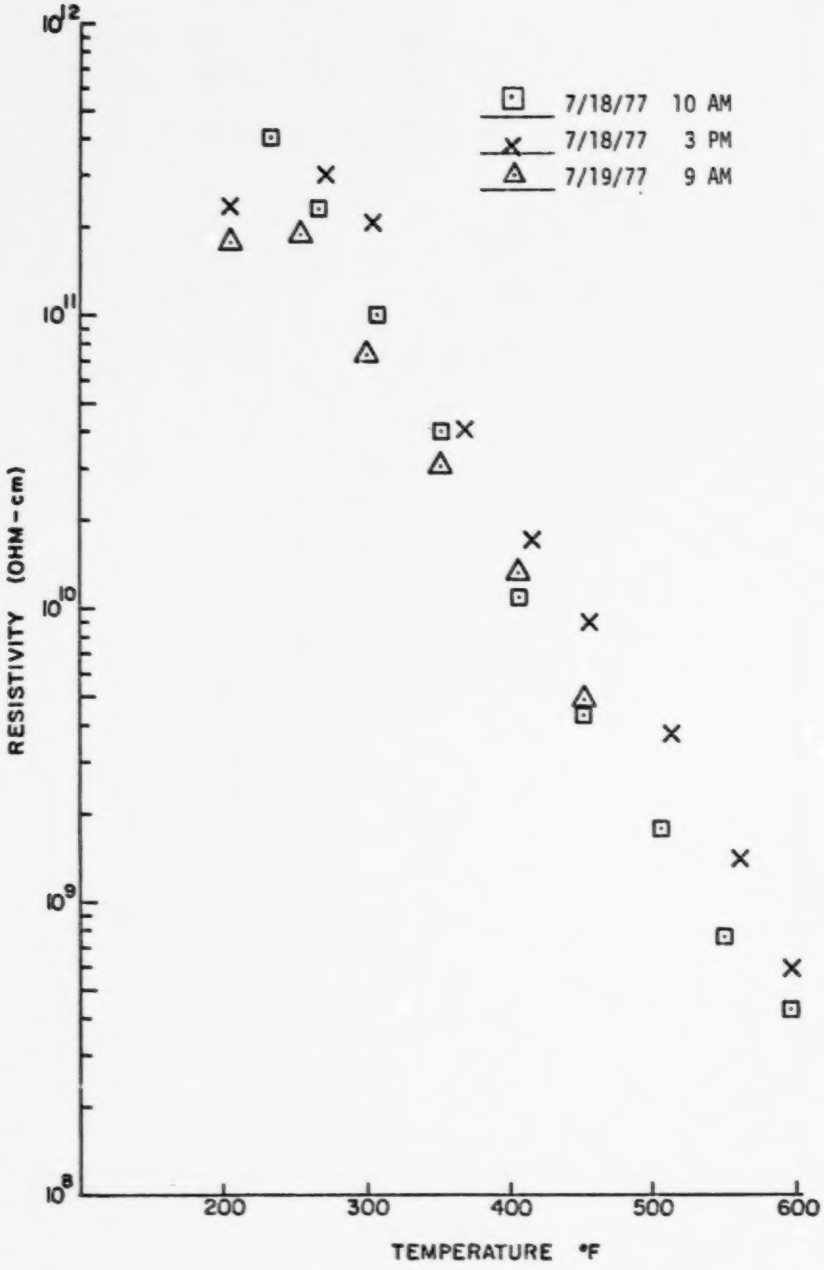

Figure 6. In Situ Resistivity

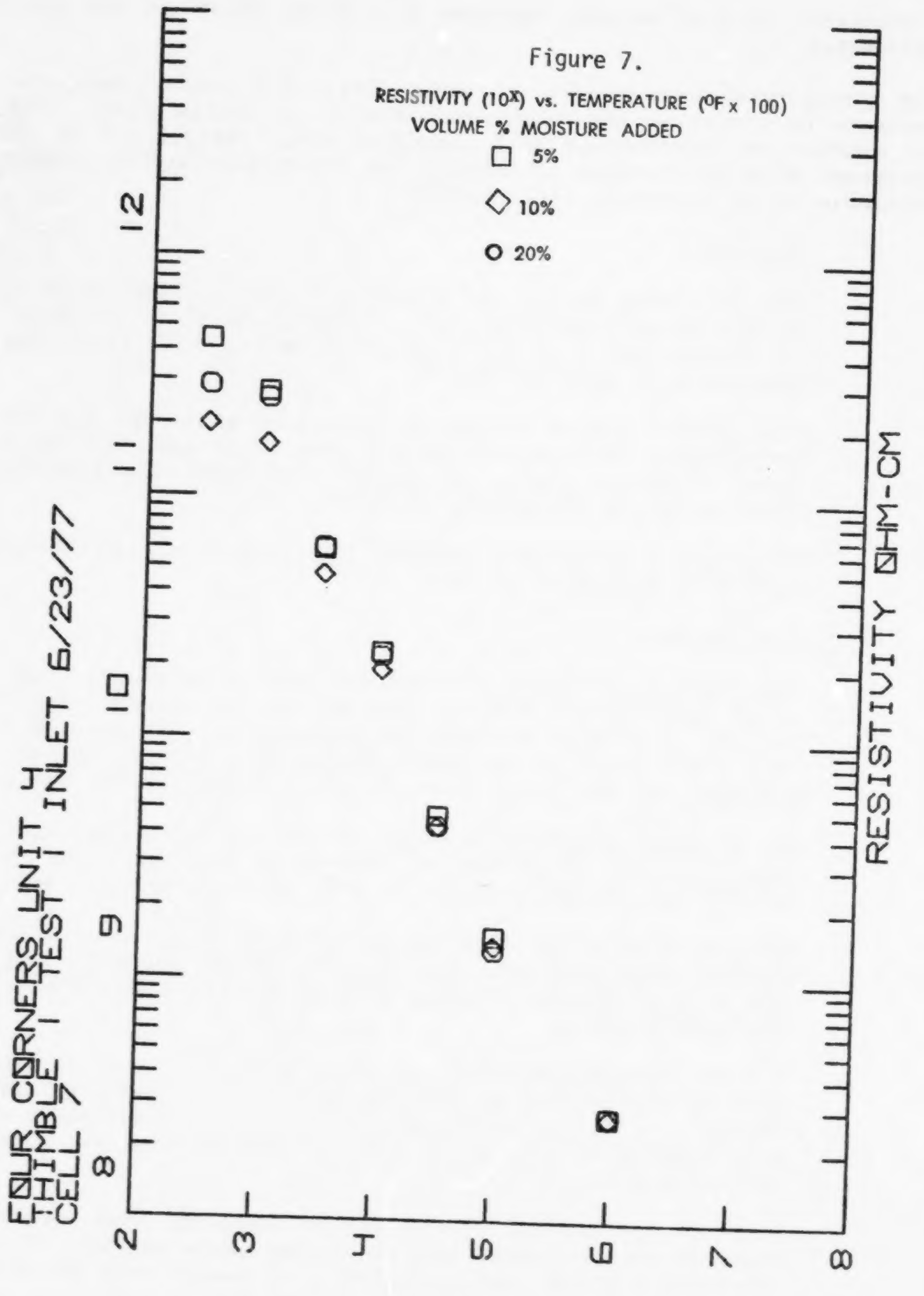

Figure 7.

RESISTIVITY (10^x) vs. TEMPERATURE (°F x 100)

VOLUME % MOISTURE ADDED

dissociates to give ammonia, ammonium di-hydrogen phosphate and pyrophosphates.

The precipitator voltage-current curves (Figures 8 and 9) show some increase in current in the inlet sections with the Apollo agent. This is opposite of expectations with increased space charge, but is in agreement with expectations if reduced ash resistivity and/or reduced thickness on the collection plate occurred.

Results--

- The V-I curves do not indicate back ionization since there is no significant hysteresis loop. Moreover, they are not greatly concave upward at their upper extremity, which is another indication of back ionization.
- Precipitator applied voltage is limited by spark rate, and the precipitator sections are normally run at a rather high spark rate. Slightly higher precipitator voltages were possible when the Apollo LPA-445 was injected.
- There was no appreciable increase in precipitator space charge caused by the Apollo LPA-445.

Conclusions--

- The thinner ash layers on the inlet collection plates, indicated with Apollo LPA-445, may be due to improved rapper action; or it could be caused by increased ash cohesiveness of the outer layer of new ash combined with reduced ash cohesiveness of the inner layer of old ash next to the plate.
- An increased cohesiveness might be due to an enhanced electrical barrier layer due to removal of Na^+ ions from the surface of the ash particle by SO_2, SO_3 or phosphoric acid.
- Reduced cohesiveness might be due to aging of the ash in the reduced concentration of SO_2, SO_3, or LPA-445, but with clamping current present, causing gradual partial destruction of the barrier layers.
- Reduced cohesiveness might be caused by another form of aging where dipole mosaics of the ash particles are gradually discharged. A barrier layer may be conducive to development of such dipoles by the corona and its deterioration may allow their disappearance.
- Part of the LPA-445 effect may be dependent upon ammonia chemisorption to single OH's on the ash glass surface, which increases hydrogen bond conductivity in concert with hydrogen bonded OH pairs. Another part may be due to stickiness of

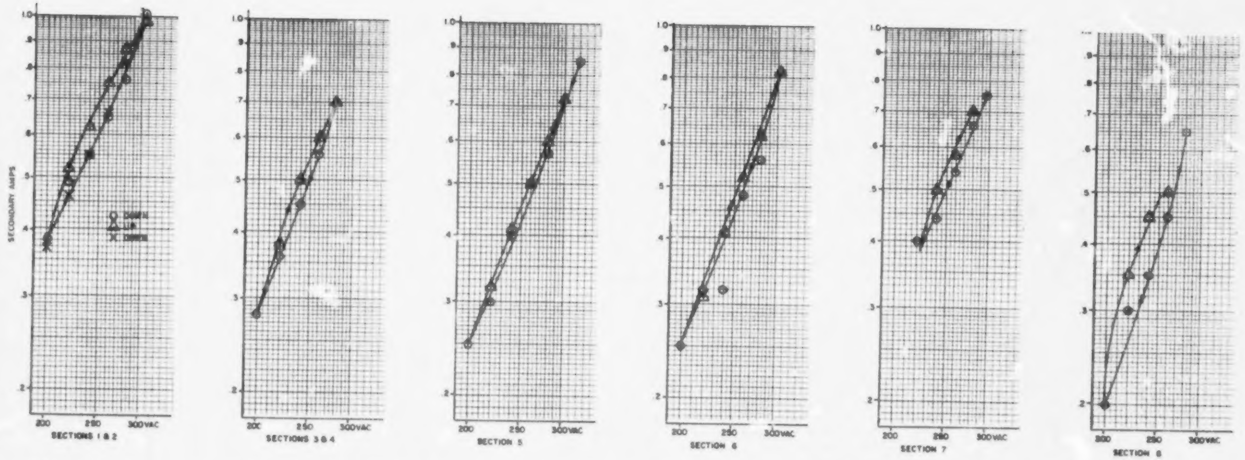

Figure 8. V-I Curves for South Precipitator with Apollo LPA 445 (Phase 1)

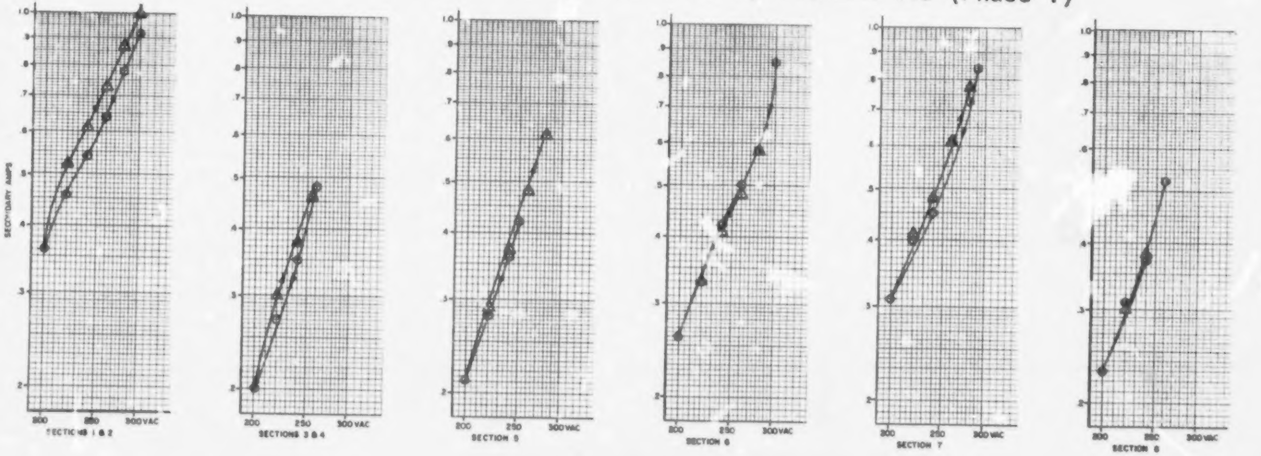

Figure 8. V-I Curves for South Precipitator without Conditioner (Phase 2)

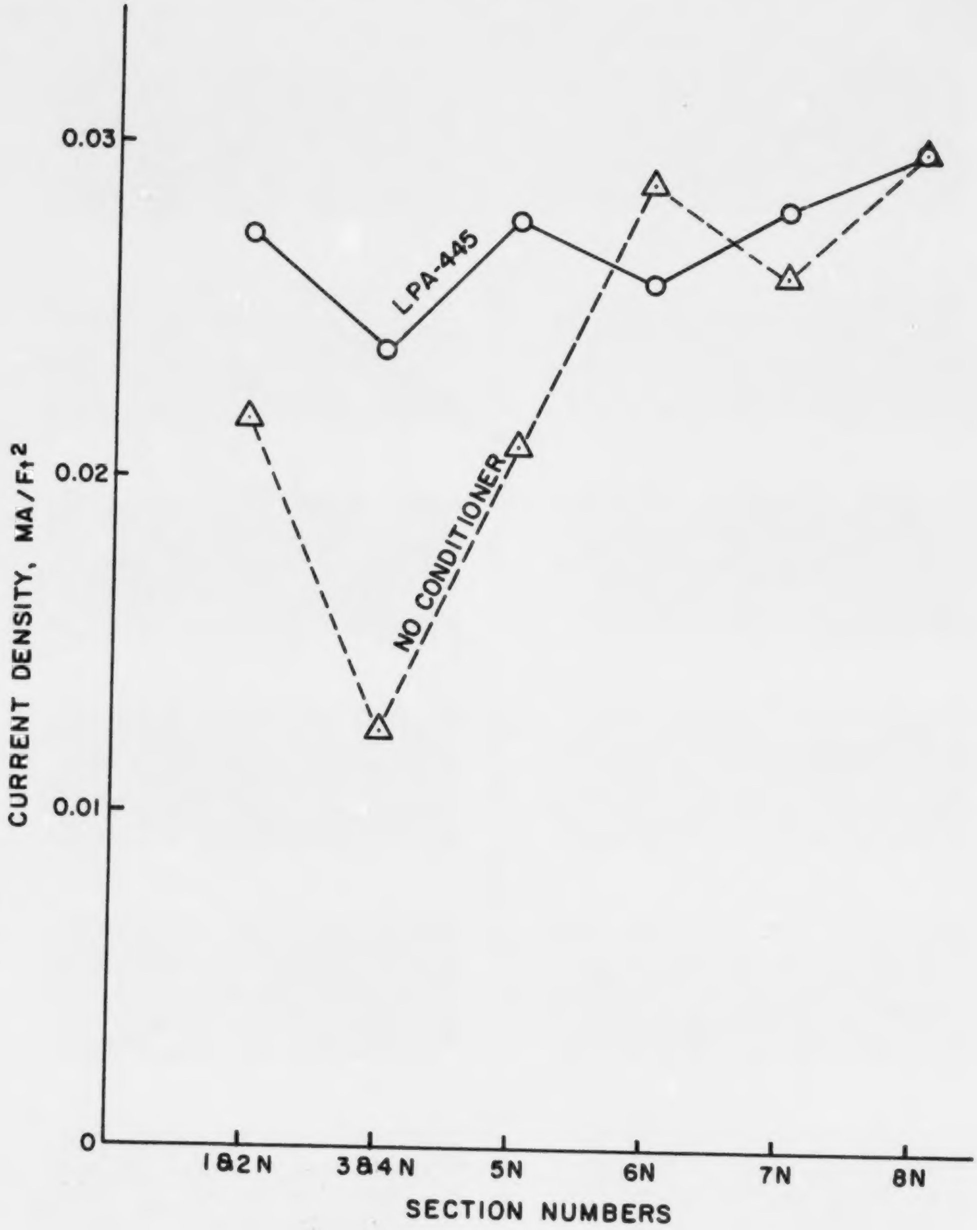

Figure 9. Current Densities in North Precipitator

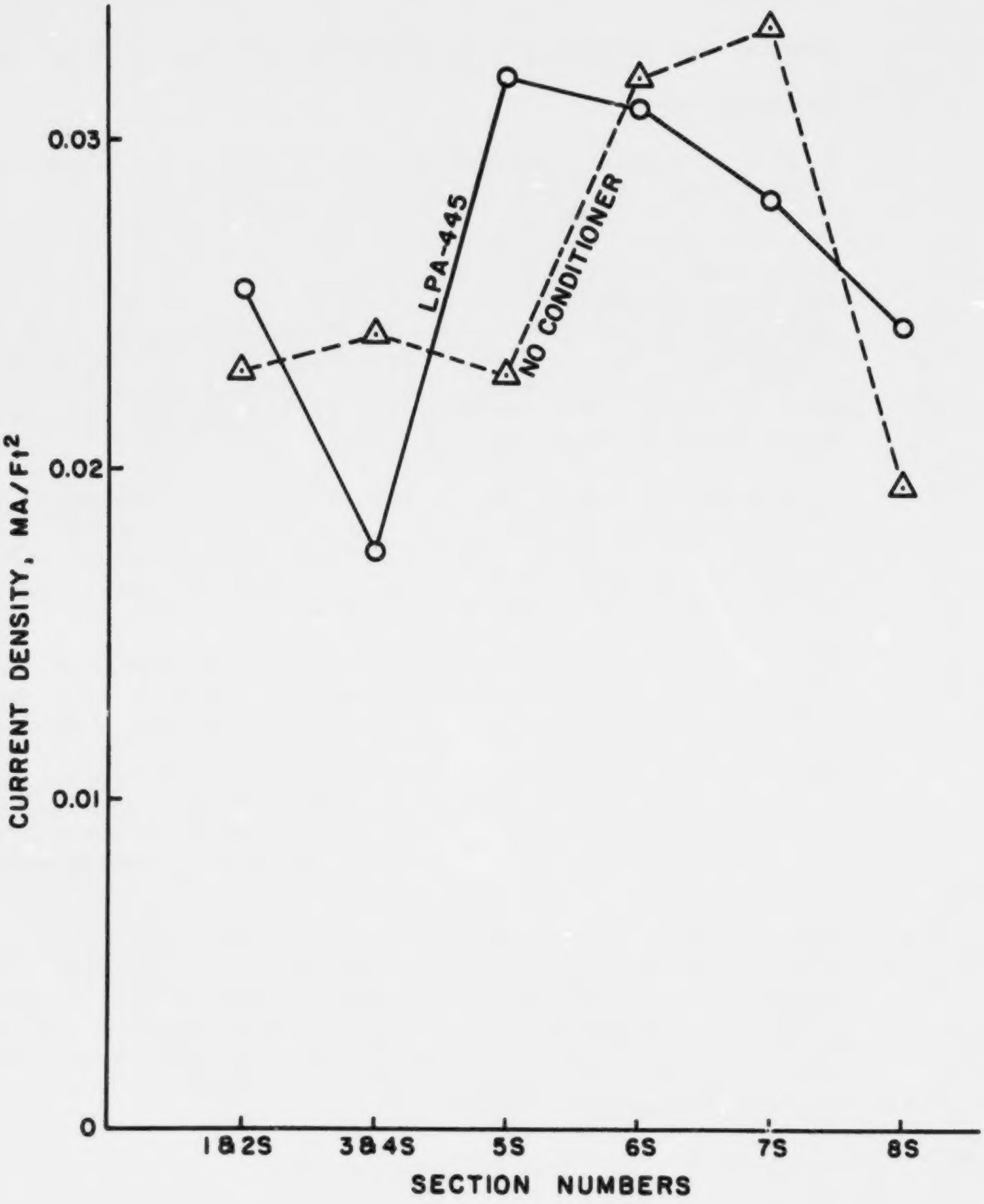

Figure 10. Current Densities in South Precipitator

molten phosphoric and metaphosphoric acid from ammonium phosphate decomposition, which agglomerates some of the fly ash particles.

- Ammonia conditioning may be effective with Four Corners ash.

Recommendations--

- A more reactive conditioning agent should be considered. Ammonia would probably be cheaper; it per se has not been tried at Four Corners. Both SO_3 and NH_3 conditioning should be tried, perhaps on a small slip stream of precipitator inlet gases. Ash resistivity and cohesion could be measured before and after the addition of the conditioners. Steam injection could also be tried to simulate water injection in the boiler. Refinement of the cohesion tester first tried at Four Corners is desirable. The resistivity and cohesion tests would be used to predict efficient rapping of the ash and attainable precipitator voltages and current densities.

- Increasing the rapping period should be tried. Various periods of as long as an hour or so should be tried to see if less coherent old ash next to the plate can improve rapping efficiency and reduce average emissions. Reduced rapper impact force is suggested by recent APS tests.

- The relative contribution of rapping puffs and hopper boil up perhaps should be measured by a series of mass loading measurements, or portable opacity monitors at various heights in the precipitator outlets ducts. If excessive boil up is found, hopper baffling could be increased or the hoppers may be operated at lower ash levels. These measurements could be made for each conditioner tried. Some conditioners may promote hopper boil up while others could promote rapping puffs as side effects.

- Some permanent structural limitation on the maximum voltage that can be applied to some of the sections may exist. If further study confirms this, heavier corona wire weights should be considered and perhaps thicker corona wires to support the weight would be needed. These would also increase the corona onset voltage and operating voltage, but may accumulate more ash on themselves.

Control Circuit Operation

During the Phase 1 test, it was concluded that since precipitator efficiency is intimately related to discharge electrode voltage, the analysis of the precipitator would be incomplete without documentation of the secondary current and voltage waveforms. The necessary equipment was made ready and calibrated, and during the Phase 2 tests the resulting data and observations were made.

Observations--A temporary high-voltage divider was installed on two of the power supply secondaries so that voltage waveforms could be observed on an oscilloscope. Current waveforms were observed on a second scope trace from a point in the existing metering circuit. By triggering the scope on the spark-current pulse, a series of oscillographs were taken, documenting the following observations:

- Following a spark, the high voltage returns immediately to a value near or exceeding the pre-spark voltage. This often results in a second spark on the next power half-cycle.
- Current is generally excessive following a spark, often well above the value necessary to re-charge the discharge wire capacitance.
- Repeated sparking on successive half-cycles causes an over-current condition. The power supply shuts down completely and recovers much slower than appears necessary.

Oscillographs of various current and voltage waveforms were taken for the remaining power supply controls. From these, it was inferred that the above observations apply generally to all the power supplies/controls on Unit 4.

Frequent adjustment of the power supply controls is necessary to maintain optimum operation of the precipitator. Only one instance was noted where control settings were in error, but the fact that the control was operating improperly was not detected until the current waveform was displayed on an oscilloscope.

Precipitator Energization Concepts--

Fly-ash particles above about 0.5 microns in effective diameter are charged by a process which is dependent upon the value of the electric field, which in turn is directly related to the discharge-electrode voltage. In addition, the rate at which the charged particles drift toward the collector plates is dependent upon the average electric field. For a given voltage waveform such as half-wave, the precipitator efficiency is proportional to the square of the voltage. Increasing the voltage increases the precipitator efficiency, at least up to the point where sparking or back corona begins to occur. If there is no back corona, the voltage may be raised well above the sparking threshold. As the voltage is increased above the sparking threshold, efficiency will continue to increase, until the voltage dropout due to sparking causes a decrease in the average value of the high voltage. The spark rate is a non-linear function of voltage; i.e., raising the high voltage from 40 to 41 K might double the sparking rate. In order to obtain maximum efficiency from a given precipitator, the high voltage must be automatically controlled. If the control is derived from a spark rate counter, then there must be a separate means of determining what the optimum spark rate should be. In addition, the automatic circuitry should shut off the primary current to the HV transformer for at least one-half cycle after a spark, and then limit the rate-of-rise of high voltage so the high voltage does not reach the pre-spark value until a few half-cycles have elapsed. Other features which the controls must provide include automatic overcurrent, overvoltage, and undervoltage shutdown, safety interlocks, and sufficient internal impedence to limit the sparking current to a reasonable value.

The choice of half-wave vs. full wave energizations should be viewed from a practical point of view. If both are available, use whichever results in best operation. The most significant difference is probably the fact that sparking, or the short-term residual effects of sparking, is easier to control with half-wave energization.

Conclusions and Recommendations--In the absence of back corona, the average of the discharge electrode voltage should be as high as possible. As voltage is increased above the sparking threshold, a point will be reached at which the average value will begin to decrease because:

- The voltage is close to zero during sparks, and
- There is a necessity to reduce or shut down the voltage following sparks to quench the spark to prevent equipment failure.

An optimum control system should contain features to control the current after a spark, and to limit the rate of voltage following a spark. In addition, the control system should be capable of automatically maintaining the average output voltage at a value close to the optimum. The existing system has circuitry which is apparently intended to limit the current and voltage following spark but does not in fact perform these functions. The existing system has an automatic control feature to adjust the output voltage based on feedback from a spark-rate detector. This circuitry works as intended, but there is no direct method of correlating spark rate with optimum output voltage.

Recommendations for the immediate future are as follows:

- Proceed with in-plant fabrication and installation of new rapper controls, and plan for extensive testing after rapper controls are installed. Obtain outside fabrication and testing consultation as necessary.
- Install permanent voltage dividers in all power supplies and provide oscilloscope jacks in control room.
- Install oscilloscope jacks from existing secondary current metering circuits.

- Replace control modules as necessary so that, following a spark, current is limited, voltage rate-of-rise is controlled, and spark rate metering is accurate.

For the longer term, the recommendations are as follows:

- Investigate the possibility of increasing the number of separate high-voltage sections.

- Replace the control electronics with an automated system which is capable of detecting and maintaining an optimum level of output voltage.

Table 6. m/e RATIOS OF REFERENCE STANDARDS

m/e	Di-ammonium Hydrogen Phosphate	Ammonium Di-hydrogen Phosphate	Ammonium Sulfate	Sulfamic Acid
98	40%	40%	5%	--
97	--	--	--	10%
81	80%	100%	--	--
80	--	10%	100%	100%
64	100%	15%	50%	70%
63	--	40%	--	--
48	50%	10%	70%	80%
47	--	60%	--	--

Precipitator Inlet Velocity, Temperature and Oxygen Profiles

A systematic analysis of the data has not been undertaken but the inhomogeneity of the flow distribution is obvious. This fact was suspected and the data presented as plotted contours provide a clear presentation (Figure 16).

Future planned modification of Unit 4 includes the installation of test ports immediately adjacent to the precipitator. The data shown was collected at the inlet to the chevron flow distributor. If there is a similar flow distribution across the precipitator inlet, the efficiency could be particularly low in the high velocity sections. At present it is only possible to calculate the average flow through each section of the precipitator.

Reproduced from
best available copy.

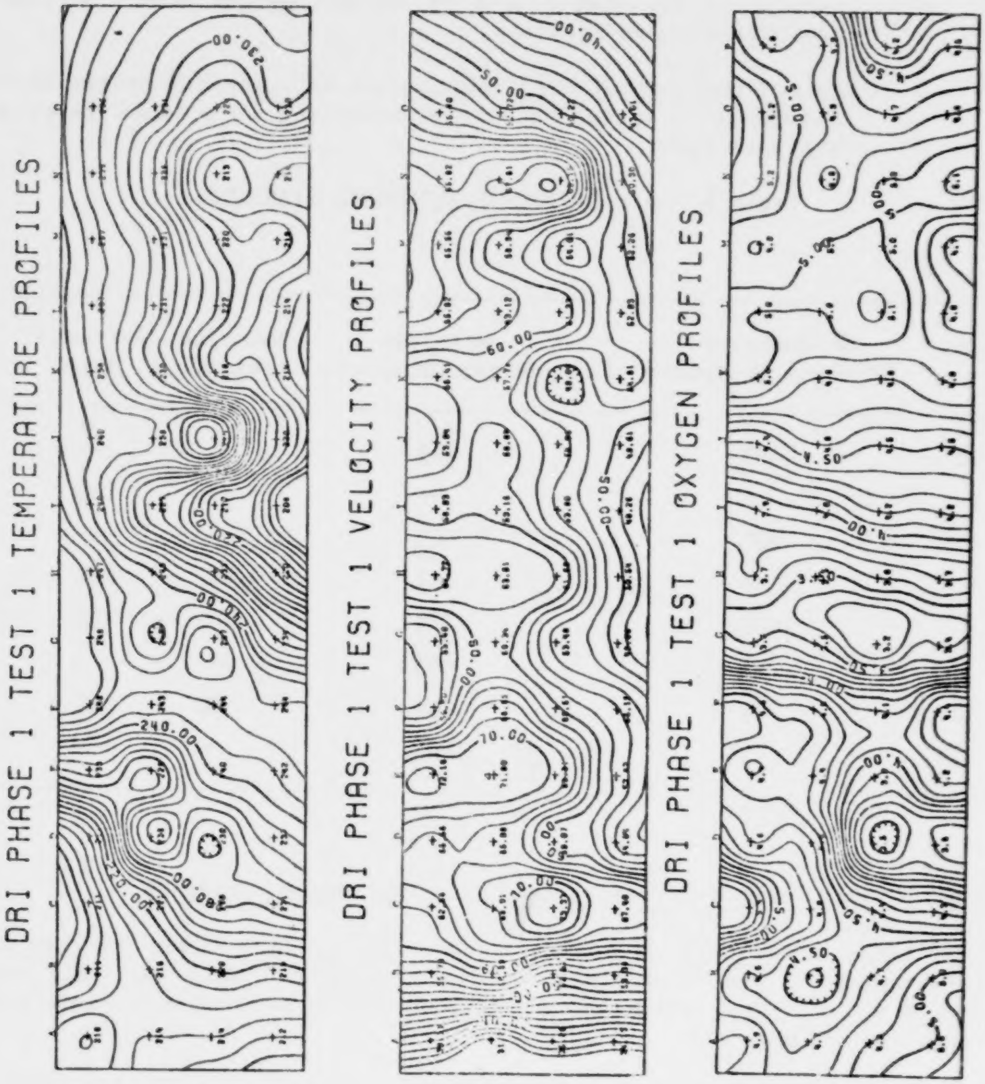

Figure 11.

ACKNOWLEDGEMENT

J. Stant, G. Perkins, E. Jones and E. Schmidt of APS were most helpful in the collection of samples and plant operation data. D. Gourdin, J. Ritter and J. Bratton of Stearns-Roger, Inc. and W. Culbertson, T. Espinoza, C. Habenicht, W. Patten, V. Saxena, F. Bonomo and K. Gala of Denver Research Institute conducted the test program.

SODIUM CONDITIONING TEST
WITH EPA MOBILE ESP

Steven P. Schliesser
Acurex Corporation

1.0 SUMMARY AND CONCLUSIONS

The objective of this pilot program was to determine the conditioning effects of adding anhydrous sodium carbonate into a "cold-side" slipstream with respect to the collection performance of an electrostatic precipitator (ESP). A power plant combusting low sulfur, low sodium western coal generated the high resistivity ash (2.5×10^{12} OHM-CM @270°F) for conditioning evaluation.

A performance evaluation was conducted on a pilot scale precipitator which treated the base and sodium-conditioned flyash. The program, conducted over several weeks, consisted of twenty days of operating and testing. For each ash species, the pilot precipitator treated 28.3 m^3/min (1,000 acfm) of flue gas at an average of 110°C, maintaining a specific collection area equal to 57 m^2/m^3/sec. (290 ft^2/Kcfm).

In situ resistivity measurements, precipitator operating conditions, and particulate concentration and size distribution measurements constitute the data assembled for the comparative demonstration.

The following results reflect the effects of conditioning the base ash with a 1.0-1.5% concentration of sodium carbonate as Na_2O:

1. A sixfold reduction in specific resistivity, suppressing the base ash from 2.1×10^{12} OHM-CM to 3.7×10^{11} OHM-CM.

Preceding page blank

2. Relative improvements in achievable current densities ranging from a factor of two to six. Under steady state conditions, maximum current densities were 1-8 nA/cm^2 for the base ash, and 10-24 nA/cm^2 for the conditioned ash.

3. Enhancement of particulate collection levels, resulting in an improvement in collection efficiency from 98.19 to 99.46 percent, associated with a reduction in outlet loading from 140 to 40 mg/DSm^3.

4. Improvement in fractional efficiency characteristics, particularly in the fine particle range, as demonstrated by the following results:

FRACTIONAL EFFICIENCY@

	0.3μ	0.5μ	1.0μ	3.0μ
Base Ash	69.4	81.2	93.9	98.9
Conditioned Ash	91.8	93.7	97.4	99.7

5. On this pilot scale basis the difference in collection efficiency between the base ash and the sodium-conditioned ash was significant enough to move performance from noncompliance (0.122 lb/10^6 Btu) to compliance (0.0361 lb/10^6 Btu).

Assimilation of the test results prompt the following conclusions:

1. Conditioning by the admixture of conductive material to reduce specific resistivity of the process effluent, in quantities small enough to be potentially economical, has been demonstrated.

2. A material for such conditioning, which has the potential to be economical, commercially available, and environmentally acceptable has been identified.

3. This material can be utilized for flyash treatment without special equipment or extensive maintenance requirements by simply injecting it into a pilot scale process stream.

4. The effects of using sodium carbonate as a conditioning agent coincide with alternative methods:
    a. An increase in the operating corona points for each precipitator field.
    b. An increase in collection performance, primarily in the fine particle size range.

Note:

Federal new source performance standards for coal-fired steam electric plants of 250×10^6 Btu or greater heat input for particulate matter = 0.1 lb/10^6 Btu, 2 hour average.

2.0 INTRODUCTION

The program objective was to determine the effects on precipitator operation and collection performance of adding sodium carbonate into the exhaust of a boiler burning low sulfur low sodium western coal. The specific effects of interest were:

1. particulate resistivity level
2. precipitator operating conditions
3. particulate removal characteristics

The feasibility of utilizing conditioning agents at the test site (Montana Power Station, Colstrip, Mont.) is documented by another power facility (Montana Power/Corrette Station, Billings, Mont.) using coal from the same strip mine. Injection of proprietary conditioning material into the flue gas before it entered the precipitator dramatically affected operating corona points and improved particulate collection performance so that compliance limits were met.[1] In situ resistivity measurements at 135°C at the test site determined the flyash resistivity to be in the lower 10^{12} OHM-CM range, outside the preferred range of 10^8 to 10^{10} OHM-CM. Compositional analyses of the coal and flyash provide the basis of this excessive resistivity, i.e., low sulfur (1.01 percent) and low sodium (0.31 percent) content.

The experimental conditioning agent was anhydrous sodium carbonate (Na_2CO_3), a dry, powdery material with size distribution comparable to flyash (mean size ≐ 15 μ). Charging was achieved by metering the material with a calibrated screwfeeder, and entraining it with a compressed air supply through an injector. Identical test methodology employing a pilot-scale precipitator was implemented for a two phase program:

1. Operation with sodium carbonate addition and a 4 - 5 percent rate relative to flyash concentration.

2. Operation without conditioning additives.

The pilot scale ESP is one of three mobile field units owned by the Utilities and Industrial Power Division, Industrial Environmental Research Laboratory-U. S. Environmental Protection Agency (EPA), Research Triangle Park, North Carolina. A pilot scale scrubber and baghouse complement a fleet of conventional collection systems designed to offer:

- Comparative evaluation of removal and economic performance factors among the three conventional control systems on either traditional sources or process streams, or inadequately documented particulate-laden process streams.
- A parametric evaluation characterizing a given control device/emission source in search for optimum design criteria.
- Feasibility/demonstration programs on novel or modified processes.
- Specific problem-solving programs in control technology.

3.0 DESCRIPTION OF FACILITIES AND INSTALLATION

Power Plant

The test program was conducted at the Montana Power Company Station at Colstrip, Montana. The recently constructed facility represents current design and operating methodology for coal-fired electric-power-generating stations. Modular venturi scrubbers provide emission control for two 350 megawatt (MW) boilers. More pertinent information is available via a performance evaluation program conducted by Southern Research Institute.[2]

Design operating data from the test facility is listed in Table 1, along with power production data for several days during the test program. Table 2 presents coal and flyash analyses, as well as gas composition data.

Table 1. COLSTRIP POWER PLANT DESIGN AND OPERATING DATA

Unit 11 Operating Data As Designed	358	330	282	212
1) Coal Feed Rate, tons/hr. (appr.)	220	185	165	120
2) Steam Production, lb/hr. (design)	2,464,261	2,228,286	1,871,761	1,403,821
3) Output Steam Pressure, PSI (design)	2,520	2,400	2,400	2,400
4) Output Steam Temperture, °F (design)	1,000	1,000	1,000	1,000
5) Generation Rate, MW	358	330	282	212
6) Gas Volume, Kcfm	1,208	1,114	952	716
7) Temperature at Cold-side Air Preheater, °F	300 to 250°F (290°F Normal)			

Table 2. COAL, FLYASH AND FLUE GAS CHARACTERISTICS

Coal Analyses

25.5%	H_2O	37.2%	Moisture-Free Volatile Matter	68.13%	Carbon
27.7	Volatile Matter	51.46	Fixed Carbon	4.51	H_2
38.3	Fixed Carbon	11.3	Ash	14.0	O_2
8.45	Ash	11,745	Btu/lb.	1.0	N_2
8750	Btu/lb.			1.01	S
				11.34	Ash

Flyash Composition

Na_2O	K_2O	MgO	CaO	Fe_2O_3	Al_2O_3	SiO_2	TiO_2	P_2O_5	SO_3	L.O.I.
0.31	0.13	4.95	21.9	5.44	22.4	41.6	0.97	0.41	0	2.05

Gas Composition

CO_2	13.2-13.5 %	
O_2	5.5- 5.6	
H_2O	8-8.4	
SO_2	350 - 450 ppm	(Controlled Condensation Method)*
SO_3	0	

* Improved Chemical Methods for Sampling and Analyses of Gaseous Pollutants from the Combustion of Fossil Fuels. Volume I, Sulfur Dioxide Measurements, June, 1971 (APTD-1106, PB-209 267).

PILOT ESP FACILITY

General Description

The mobile ESP facility consists of two separate units mounted on freight trailers 40 feet in length. Figure 1 is a floor plan of the two units. The first unit is the process trailer which houses a five-section ESP and all auxiliary equipment. This equipment consists of:

- Heat-traced, insulated 10" duct.
- Flow rectification equipment containing vaned turning elbows and diffuser sections.
- An I. D. fan with a cooling system.
- A screw conveyor and gate valve for the removal of the collected material.
- Electromagnetic vibrators for rapping the collection plates.
- Five transformer-rectifiers, with rated capacity of 50 KV and 10 MA. DC.

The system is designed to operate up to 1,000°F over a flow range of 28-35 m^3/min (1,000-3,000 acfm). Figure 2 shows an isometric of the high voltage field design.

The second unit is a control/laboratory trailer containing all process controls, monitors and recorders plus provisions for an analytical laboratory and spare equipment storage.

Pilot ESP design specifications are compared with the specifications typical of full scale precipitators in Table 3. Comparison of each design parameter between the pilot and full scale units shows that:

a. Fixed design parameters on the pilot unit lie midway in the normal range for full scale installations.

b. Operational parameters contain the flexibility to cover the spectrum typical of commercial units.

c. The single exception to conformity with commercial installations is the plate area, the inherent concession of pilot-scale methodology.

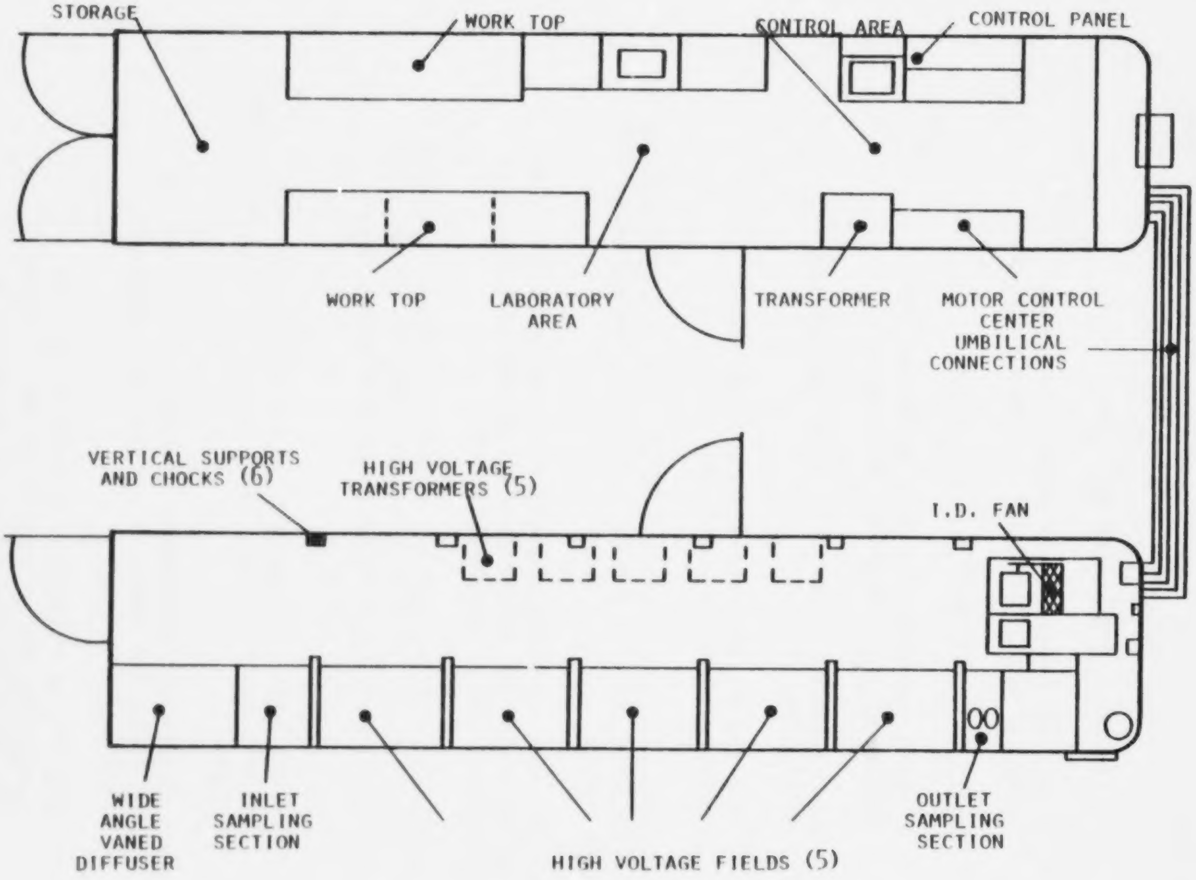
STORAGE
WORK TOP
CONTROL AREA
CONTROL PANEL
WORK TOP
LABORATORY AREA
TRANSFORMER
MOTOR CONTROL CENTER
UMBILICAL CONNECTIONS
VERTICAL SUPPORTS AND CHOCKS (6)
HIGH VOLTAGE TRANSFORMERS (5)
I.D. FAN
WIDE ANGLE VANED DIFFUSER
INLET SAMPLING SECTION
HIGH VOLTAGE FIELDS (5)
OUTLET SAMPLING SECTION

Figure 1. Plan view of mobile ESP facility

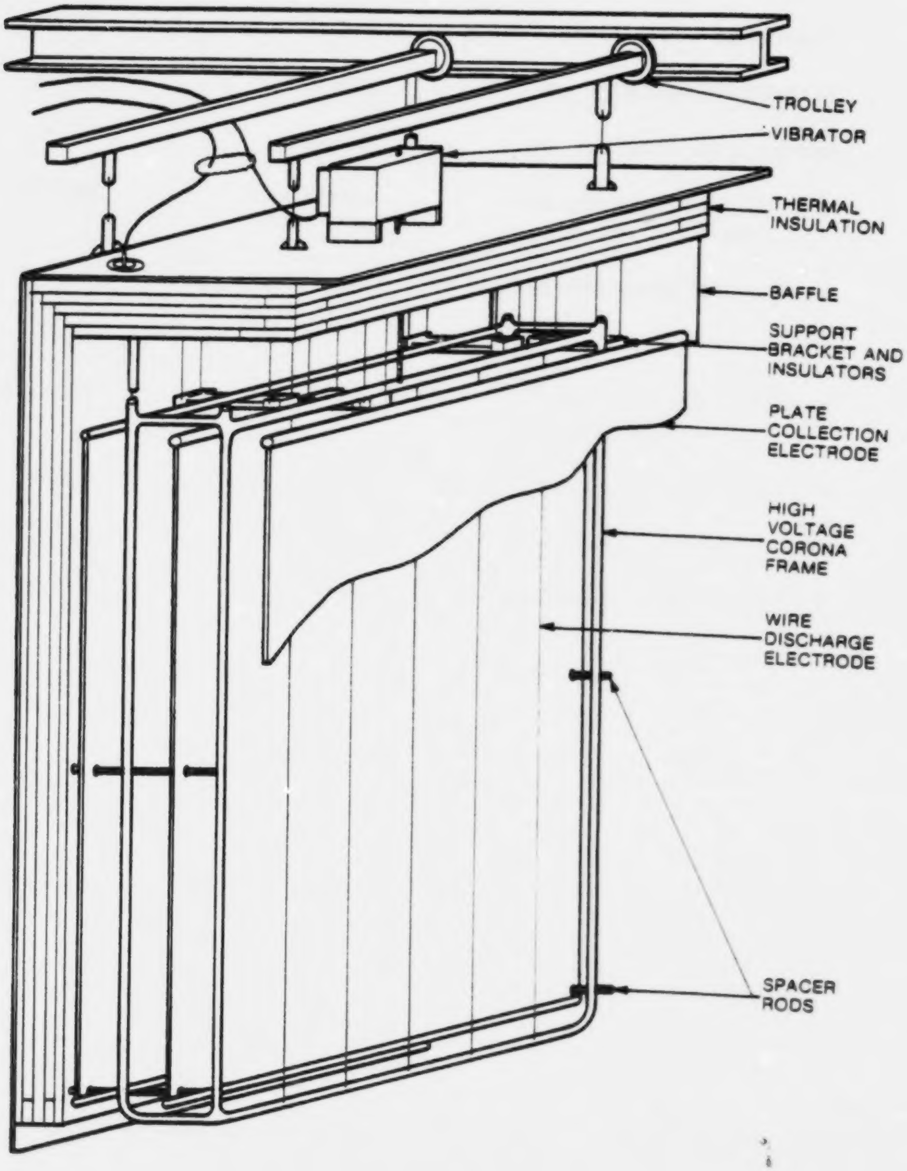
TROLLEY
VIBRATOR
THERMAL INSULATION
BAFFLE
SUPPORT BRACKET AND INSULATORS
PLATE COLLECTION ELECTRODE
HIGH VOLTAGE CORONA FRAME
WIRE DISCHARGE ELECTRODE
SPACER RODS

Figure 2. Removable high voltage field

Table 3. FULL SCALE AND PILOT ESP DESIGN SPECIFICATIONS

	Full Scale[3]	Pilot ESP
Discharge Wire Diameter, cm	0.25	0.25
Wire-Wire Spacing, cm	10-30	18
Wire-Plate Spacing, cm	10-15	13
Specific Collection Area, (m^2/m^3/sec)	20-150	20-100
Collection Area/T-R Set, m^2	50-750	9
Aspect Ratio	0.5-1.5	0.67
Specific Corona Power (watts/m^3/sec)	100-1,000	100-1,000
Current Density, nA/cm^2	5-70	5-100
Gas Velocity, m/sec	1-5	0.5-2
No. of Fields in Series	2-8	2-5

SITE INSTALLATION

A slipstream was withdrawn at a location downstream from the combustion-air preheater and upstream from the pollution control equipment. A 10" pipe located across the midpoint of the process stream served as the means of sample extraction. Sixty feet of heat-traced, insulated 10" pipe transported the slipstream to the pilot precipitator. Ambient air quality standards dictated the need for returning the particulate-abated stream to the access locations for subsequent sulfur dioxide (SO_2) removal. An access door (2½' x 4') was fitted to the stack to accommodate the extraction and return connections, along with a 4" coupling for *in situ* resistivity measurements. Figure 3 illustrates the positioning of the access, ducting, process unit, and sampling and injection locations.

4.0 PROGRAM METHODOLOGY

PILOT PRECIPITATOR OPERATION

To ensure that the test program was conducted on a sound basis with specific guidelines, protocol for installation, preparation, operation and data acquisition was established and is discussed below.

Installation

Considerations for locating the slipstream access point required that:

1. The conditions of the process stream be typical for those of full-scale control unit installation.
2. A representative stream could be withdrawn from the process effluent, i.e., flow disturbances are relatively absent.
3. The location and routing be appropriate for the transport and maintenance of a representative stream.

Operation

The normal operating schedule allowed for one- week test increments, starting at noon Monday and continuing until Friday evening. Operating on a continuous rather than daily start-up/shutdown basis enhanced data credibility and reliability for the following reasons:

1. Steady state conditions would be maintained rather than approached.

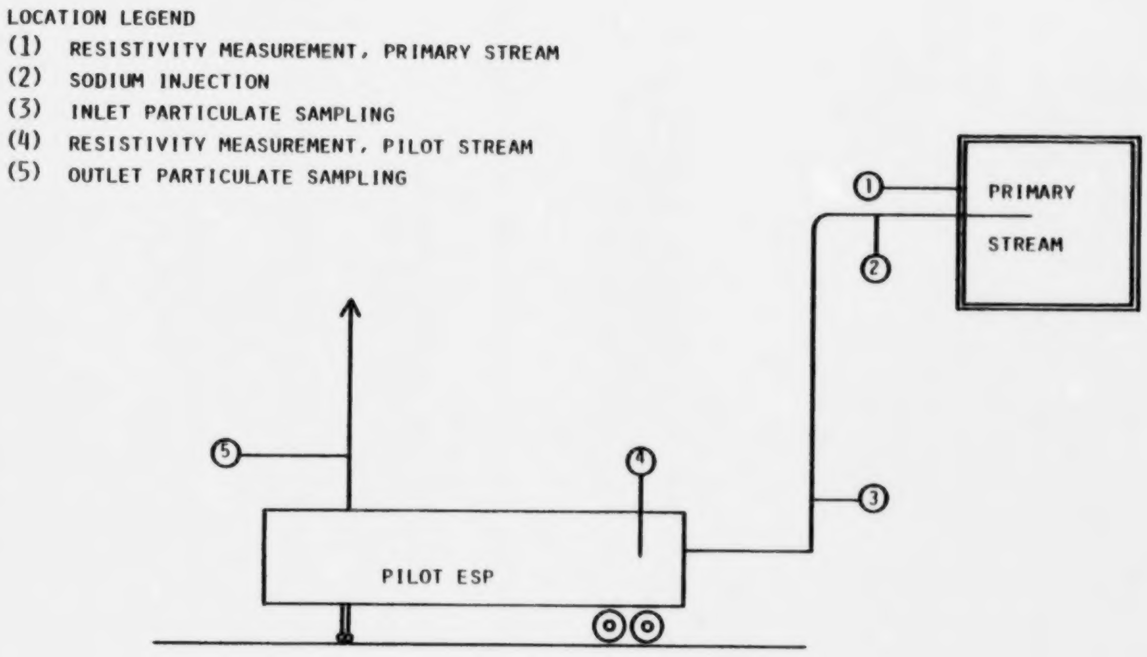
LOCATION LEGEND
(1) RESISTIVITY MEASUREMENT, PRIMARY STREAM
(2) SODIUM INJECTION
(3) INLET PARTICULATE SAMPLING
(4) RESISTIVITY MEASUREMENT, PILOT STREAM
(5) OUTLET PARTICULATE SAMPLING
①
PRIMARY
STREAM
②
⑤
④
③
PILOT ESP

Figure 3. Pilot ESP site installation

2. Extended operating time would permit clearer illustration of time-related characteristics, e.g., flyash accumulation on corona wires and collection plates.

3. Corrosive conditions due to condensation accompanying startup and shutdown periods would be minimized.

4. A uniform daily testing program could be more reliably established and maintained.

Because the reliability of the high voltage cables was limited, approximately half of the test was conducted on an interrupted rather than continuous schedule. Prior to weekly start-up, the precipitator's internal parts were cleaned in order to restore initial conditions. This process consisted of removing flyash from discharge wires and collection plates. Removal of the precipitated flyash between the base ash and sodium test increments was necessary to isolate the causal relationships of the flyash species. Since it has been shown that, due to reentrainment, rapping factors such as frequency and intensity have significant effects on effluent loading, the rapping cycles were terminated during the particulate measurement periods.[5]

Data Acquisition

The following operating data were recorded on a semi-hourly basis:

- inlet gas temperature
- outlet gas temperature
- individual voltage levels
- individual current levels

Additionally, "V-I" data (corona discharge curves) were generated before and after the daily sampling periods, and following the weekly internal cleaning. Sampling activities were conducted during normal working hours, with operating data acquisition and analytical activities being performed during the remainder of the day.

PARTICULATE MEASUREMENTS

Particulate measurements were taken using a sample train, as depicted schematically in Figure 4. Stainless steel filter holders were used with 47mm glass fiber filters to provide mass concentration data. Seven stage Brinks^{R} and U of W Mark III^{R} impactors containing greased substrates were employed to measure the inlet and outlet size distributions, respectively. A common grease mixture (20 percent Apiezon "H" with benzene) was applied to the metallic substrates used with each impactor. Quality assurance measures and procedures for conditioning, greasing, and weighing substrates were conducted in

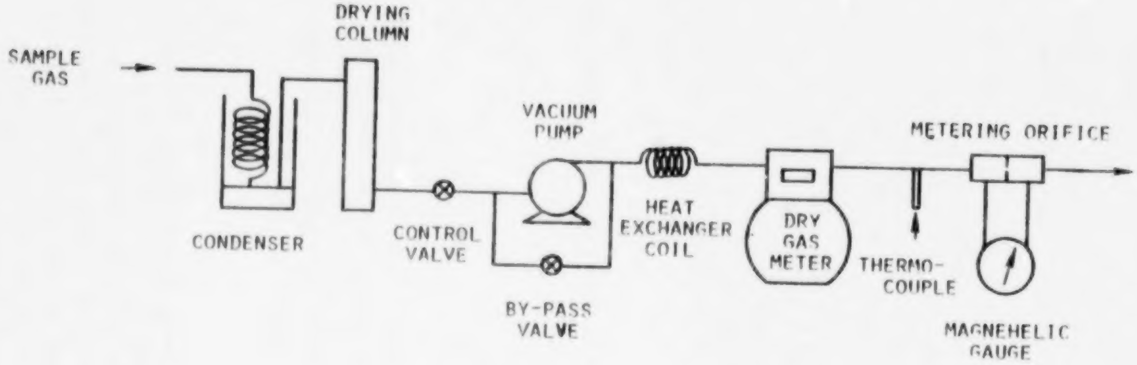
SAMPLE GAS
DRYING COLUMN
CONDENSER
CONTROL VALVE
VACUUM PUMP
BY-PASS VALVE
HEAT EXCHANGER COIL
DRY GAS METER
THERMO-COUPLE
METERING ORIFICE
MAGNEHELIC GAUGE

Figure 4. Sample train schematic

accordance with Reference 6. Sample ports, available at virtual plug-flow locations, consisted of 1" stainless steel couplings welded to the duct, 10.75" I. D.

Extractive probes (1/4" stainless tubing, 12" long) were mounted in the ports and fitted with interchangeable nozzles to allow isokinetic sample removal. The probes were positioned at average velocity locations. Particulate concentrations and size distribution determinations were conducted at inlet and outlet locations. Two determinations of each type at both locations constituted a test unit consisting of eight individual measurements. Substrate and filter weight gains were processed nightly, providing qualitative feedback on precipitator performance and data quality.

RESISTIVITY MEASUREMENTS

A point-to-plane probe was used to measure in situ resistivity. Maintenance and procedural operations were conducted in accordance with the recommended practice for resistivity measurements.[7] The primary location for these determinations was a reduced velocity area (3-5 m/sec.) immediately upstream from the first high voltage field. Longer sampling periods (1-2 hours) were required for the relaxed flow region (1-2 hours) than for the primary process (½-1 hour). Quality assurance tests were conducted in situ at the slipstream access, yielding consistently comparable resistivity levels.

Three values of resistivity are reported for each test unit, and are labeled:

- P_A (Spark Method at Breakdown Strength)
- P_B (Spark Method at Electric Field Strength = 10 kv/cm)
- P_C (Re: V-I Method).

Each resistivity value is calculated as the ratio of the electric field to current density. A complete discussion of the equipment, procedure, and significance of resistivity measurement is contained in Reference 7.

5.0 DISCUSSION OF PERFORMANCE RESULTS

The data base presented in the following sections consists of five measurement categories:

- mass balance of sodium material
- specific resistivity
- operating measurements

- particulate mass measurements
- particulate size distribution measurements

Unavoidable fluctuations in boiler load, gas temperature, and precipitator operation occurred throughout the test program, but these fluctuations did not, in the final analysis, obscure the results of the demonstration test program. The data clearly support the general conclusions that, for sodium carbonate addition:

- specific resistivity of the particulate was reduced,
- precipitator operating levels were improved, and
- particulate collection efficiency (total and fractional) was enhanced.

CONDITIONING BY SODIUM CARBONATE ADDITION

Resistivity conditioning was achieved by metering and pneumatically injecting anhydrous sodium carbonate into the slipstream immediately adjacent to the primary stream (Figure 3). Mixing was achieved by injecting the material into the center of the slipstream, and transporting the mixture through 60 feet of duct, four 90° elbows, and the flow rectification sections at the trailer entrance. A previous in-house program, in which sodium carbonate was injected 35 feet upstream from the flow rectification section, demonstrated, by analyses of samples taken from each field, that equal and consistent distribution could be achieved. Injection was accomplished through use of a screwfeeder, an air injector, and an air compressor. Figure 5 illustrates the configuration of the injection assembly. The material was metered through the calibrated screwfeeder into the injector, where compressed and induced air entrained and delivered it through a gently bending probe into the slipstream.

The amount of sodium carbonate to be injected was calculated as sodium oxide, with conversion being made on the basis of molecular weight ratio:

$$\frac{\text{Mole. Wgt, Na}_2\text{O} \quad = 62}{\text{Mole. Wgt, Na}_2\text{O CO} = 106} = 0.585$$

Thus, under most conditions, 11.5 gm/min of sodium carbonate was added to represent 6.7 gm/min as sodium oxide, reflecting a 5.0 percent injection rate relative to a mean flyash rate of 135 gm/min.

Analysis of the collected ash from the high voltage fields (Table 4) shows an average 1.16 percent differential collection rate in sodium oxide content between the base and conditional ash. These independent determinations reveal an unaccountable portion for a mass balance of sodium material. The discrepancy between the injection and collection rates suggests two possible occurrences:

1. Deposition of the sodium material between injection and electrostatic collection, and

2. Penetration of the sodium through the ESP.

The latter contingency cannot be well supported, since the unaccountable portion of sodium carbonate is ten times the concentration of the penetrating ash. The author suggests that the unaccountable sodium material was deposited during transport to the ESP through a non-optimum injection system.

The beneficial irony of sodium conditioning is that one gram of sodium oxide caused an equal amount of flyash to be collected. Numerical analysis correlating the precipitated amounts of sodium and the causal increase in flyash shows a 1.16/1.0 relationship.

The term "conditioning" in the context of controlling particle resistivity usually implies the addition of moisture or chemicals to the carrier gas. In a broader sense, conditioning includes effectively controlling particle resistivity by any appropriate means, such as temperature or composition control.

Conditioning by sodium carbonate injection, unlike moisture and chemical conditioning, does not change the conductivity of the original flyash particles. The conditioning effect is achieved by simply injecting a conductive material into the stream, which, when collected on the plates with the original high resistivity material, provides ionic carriers or additional electrical paths for the corona current. The insulating effect of the high resistivity flyash is reduced, allowing the precipitator to treat the stream at a lower resistivity level.

The purpose of these tests was to determine the improvement in precipitator performance associated with sodium carbonate addition. To date, this approach to conditioning has several limitations:

- Some applications require large quantities of conductive material.

- Some economically viable conductive materials are unavailable.

- The material is difficult to adequately distribute into the process stream.

- Uncertainties result from selective precipitation of the conductive material.

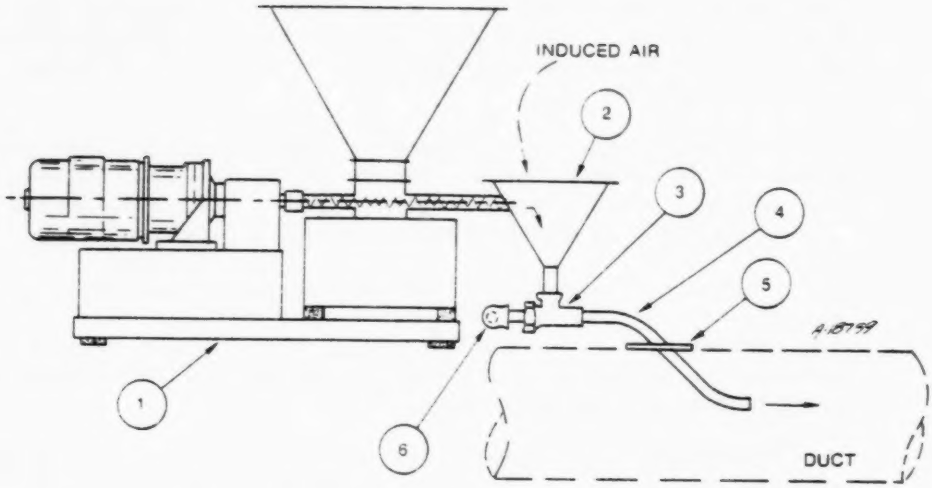

1. VIBRASCREW FEEDER SCR-20, 3/8 SCREW, 0-0.1 CFH
2. FABRICATED CONNECTION BETWEEN FEEDER AND INJECTOR
3. JET INJECTOR, McMASTER-CARR, P.O. BOX 4355, CHICAGO 60680, CAT. 4977K-11
4. FABRICATED PIPE
5. COVER PLATE APPROX. 6" DIAMETER, WELDED TO BENT PIPE
6. COMPRESSED AIR SUPPLY LINE, APPROX. 70 PSIG

Figure 5. Depiction of sodium injection equipment

Table 4A FLYASH CONSTITUENCY DATA

NO Sodium Injection

	6/24 Cell 1	6/24 Cell 2	6/24 Cell 3	6/30 Cell 1	6/30 Cell 2	6/30 Cell 5	8/23 Cell 3	8/23 Cell 4	8/23 Cell 5	8/24 Cell 3	8/24 Cell 4	8/24 Cell 5
Li_2O	0.04	0.05	0.05	0.04	0.04	0.04	0.04	0.04	0.04	0.04	0.04	0.04
Na_2O	0.60	0.58	0.56	0.56	0.74	0.75	0.61	0.61	0.71	0.59	0.59	0.61
K_2O	0.8	0.7	1.0	0.7	0.7	0.9	0.8	0.8	0.8	0.7	0.7	0.8
MgO	7.2	7.5	7.7	5.8	6.4	6.7	6.5	6.8	6.5	6.4	6.8	6.8
CaO	18.5	18.3	19.5	17.0	17.7	17.8	19.6	19.3	18.6	19.3	20.5	19.7
Fe_2O_3	4.0	3.5	3.8	3.7	3.5	3.2	3.9	3.2	3.4	3.3	3.8	3.3
Al_2O_3	23.8	23.8	-	21.4	23.3	24.2	23.7	24.4	25.0	23.3	23.6	-
SiO_2	41.5	41.1	-	44.5	43.2	41.9	41.8	40.7	40.2	42.1	39.3	-
TiO_2	1.0	1.0	0.9	0.9	1.0	0.9	0.7	0.7	0.6	0.6	0.7	-
P_2O_5	0.4	0.4	0.3	0.3	0.3	0.4	0.5	0.9	0.6	0.5	0.6	0.6
SO_3	1.1	-	-	1.3	-	-	1.2	1.4	1.7	1.2	1.5	-
LOI	0.5	0.5	0.7	0.5	0.6	0.6	0.3	0.2	0.6	0.5	0.4	-

Table 48 FLYASH CONSTITUENCY DATA

Sodium Injection

7/14 Cell 1	7/14 Cell 2	7/14 Cell 4	7/19 Cell 1	7/19 Cell 2	7/19 Cell 3	7/19 Cell 4	8/17 Cell 3	8/17 Cell 4
0.04	0.04	0.04	0.04	0.05	0.05	0.05	0.04	0.05
1.6	2.1	1.0	2.2	1.9	1.6	1.4	2.4	1.9
0.8	0.8	0.8	0.7	0.6	0.6	0.5	0.4	0.5
7.0	6.7	5.7	6.2	6.4	6.8	6.8	6.8	6.4
18.1	17.8	18.7	18.0	18.2	19.0	18.3	20.3	20.2
3.2	3.3	5.3	4.1	3.2	3.0	2.9	3.3	3.3
24.0	23.7	22.6	23.0	24.3	23.2	24.6	22.5	23.4
41.4	41.9	43.0	42.7	41.3	39.2	39.7	37.8	38.1
0.8	0.9	0.8	0.9	0.8	0.8	1.1	1.1	1.1
0.4	0.4	0.3	0.3	0.4	0.5	0.4	0.6	0.6
1.5	1.8	-	1.9	1.6	1.7	-	1.8	2.2
1.3	1.6	1.4	1.6	1.3	0.9	1.2	2.0	1.3

Remarks: 1) All analyses done on ignited samples. On some samples, there are insufficient amounts to run a complete analysis.

2) Analyses performed by Southern Research Institute.

RESISTIVITY DATA AND RESULTS

In order to quantify the resistivity suppression of sodium conditioning, resistivity measurements were taken on (1) the primary stream near the pilot stream access location, (2) the slipstream containing the base flyash, and (3) the slipstream containing the base ash plus sodium carbonate.

All determinations were made with an in situ probe designed by Southern Research Institute[7]. The design of the probe and the procedure provide the following data as presented in Table 5:

1. P_A - Resistivity value taken at the breakdown strength of the sample.
2. P_B - Resistivity value for electric field strength = 10 KV/CM.
3. P_C - Resistivity value determined by the comparison of volt-amp relationships before and after precipitation of the sample.
4. E_A - Electric field strength at breakdown.

P_A is the preferred resistivity value, because voltage is applied directly to the electrostatically precipitated sample, and determination is made at the breakdown strength of the sampled ash layer.

The other two resistivity values, P_B and P_C, are less significant to precipitator aPplications, but are offered to support the comparison between the two ash species. The last column in Table 5, EA, represents the breakdown strengths of the individual samples. Compilation of over 35 tests resulted in the following log-averaged resistivity values:

a. 2.5×10^{12} OHM-CM (on the primary stream at 130-135°C).

b. 2.1×10^{12} OHM-CM (on the slipstream at 107-115°C with the base ash).

c. 3.7×10^{11} OHM-CM (on the slipstream at 107-115°C with the base ash and 1.2 percent sodium oxide/base ash addition).

Comparison of these values indicates that:

- The characteristic resistivity of the gas and particulate stream were preserved during transport to the pilot unit.

Table 5. RESISTIVITY DATA*

Run No.	P_A	P_B	P_C	E_A
6/22/77**	2.9 E12	2.1 E12	4.5 E11	41, 22, 24
6/23/77**	2.1 E12	2.7 E12	3.8 E11	10, 17, 12, 17
4	- - -	- - -	3.6 E11	- - -
5	5.9 E11	5.2 E11	2.7 E11	19
6	1.1 E12	2.2 E12	2.1 E12	35
7	1.6 E11	- - -	4.0 E11	4
8	4.1 E11	6.8 E11	7.3 E11	32, 27
9	5.0 E11	1.0 E11	7.6 E11	26, 26, 26
10	3.2 E11	5.6 E11	7.3 E11	10, 25, 27
11	1.0 E12	1.7 E12	2.2 E12	20
12	6.0 E12	1.0 E12	2.5 E12	25
13	2.1 E12	5.0 E12	2.2 E12	8, 50
14	- - -	- - -	1.5 E12	- - -
15	- - -	- - -	6.2 E11	- - -
16	2.0 E11	3.6 E11	1.5 E12	55, 33, 73
17	- - -	- - -	2.2 E12	- - -
18	8.0 E11	1.3 E12	2.5 E12	29, 50, 40
19	4.1 E12	6.5 E12	2.6 E12	39, 26
20	2.5 E12	6.0 E12	2.8 E12	32, 37

2.17 E11 = Log Mean Resistivity for Conditioned Ash @ 107-115°C

3.70 E12 = Log Mean Resistivity for Bash Ash @ 107-115°C

P_A = Resistivity Determined by Spark Method @ Breakdown Field (OHM-CM)

P_B = Resistivity Determined by Spark Method @ Electric Field Strength = 10 KV/CM

P_C = Resistivity Determined by V-I Method

E_A = Electric Field Strength @ Breakdown (KV/CM)

* Data Obtained at Pilot ESP Inlet

** Data Obtained on Primary Stream at the Pilot Stream Access Location

- A sixfold reduction in specific resistivity is attributable to sodium injection.

Research by Bickelhaupt has shown that, for surface resistivity of flyash, the alkali metal constituents, particulary sodium, serve as the principal charge carriers in the conduction process.[9] This observation led to two previous field tests demonstrating that sodium conditioning did reduce specific resistivity, and that the reduction was predictable by the relationship of:

$$P_1/P_2 = (W_2)^2/(W_1)^2$$

P_1 = measured resistivity in OHM-CM for W_2

P_2 = predicted resistivity in OHM-CM for W_2

W_1 = measured weight percent Na_2O in ash

W_2 = added weight percent Na_2O in ash.[10]

Demonstration of the sensitive and predictable relationship between sodium content and resistivity is shown from the test data:

For $W_1 = 0.63$, $W_2 = 1.79$, $P = 2.1 \times 10^{12}$:

$$P_2 = 2.6 \times 10^{11} \text{ OHM-CM}$$

The predicted value correlates with the measured resistivity value of 3.7×10^{11} OHM-CM.

OPERATIONAL DATA

Operating corona points and the associated V-I data over the allowable range were taken regularly during the program. The operating corona data reflect the electrical conditions during the sampling period for a given test. It should be noted that the control of the transformer-rectifier sets was accomplished manually, as the pilot facility was not equipped with automatic controllers customarily included in full-sized precipitators. It should also be pointed out that the operating corona points were set 4 KV lower than the maximum allowed. This was done to prevent frequent high voltage cable breakdowns responsible for delays incurred during the initial testing phase.

Table 6 and Figure 6 depict actual and comparative current densities for the base ash and ash-with-sodium conditioning tests. The above table and figure provide a histogram of the current densities related to on-line time following internal purging. The degradation rates are comparable for each species, but the base ash curves show more severe current reductions as they approach steady

Table 6 PRECIPITATOR ELECTRICAL OPERATING DATA
SECONDARY VOLTAGE (KV), CURRENT DENSITY (nA/cm^2)

Base Flyash

Cell										
1	39,11	40,4.2	40,2.3							
2	39,21	40,3.1	40,1.1							
3				38,18	39,10	40,10	40,27	38,10	36,6.0	36,4.0
4				39,24	37,16	40,21	38,21	38,11	40,7.0	38,3.0
5	41,28	39,9.0	39,6.3	39,22	36,12	40,25	38,35	36,26	32,13	32,8.0
Time[1] (days)	1	1½	2	¼	½	1	¼	1	2	3
Test No.	1	2	3	11	12	13	17	18	19	20

Base Flyash + Sodium

Cell										
1	46,36	46,13	39,8.0	42,7.8						
2	39,27	42,16	36,9.0	41,19	44,9.5					
3			35,14	37,26	40,18	42,10	42,9.0	38,23	40,14	41-19
4			39,28	37,26	40,20	41,13	41,10	40,34	40,23	39-20
5	38,31	38,30	35,41	37,23	39,24	40,21	36,5.0	38,38	40,50	
Time	½	1	1½	2	2½	3	3½	¼	1	2
Test No.	4	5	6	7	8	9	10	14	15	16

---

[1] Elasped time operating since internal purge.

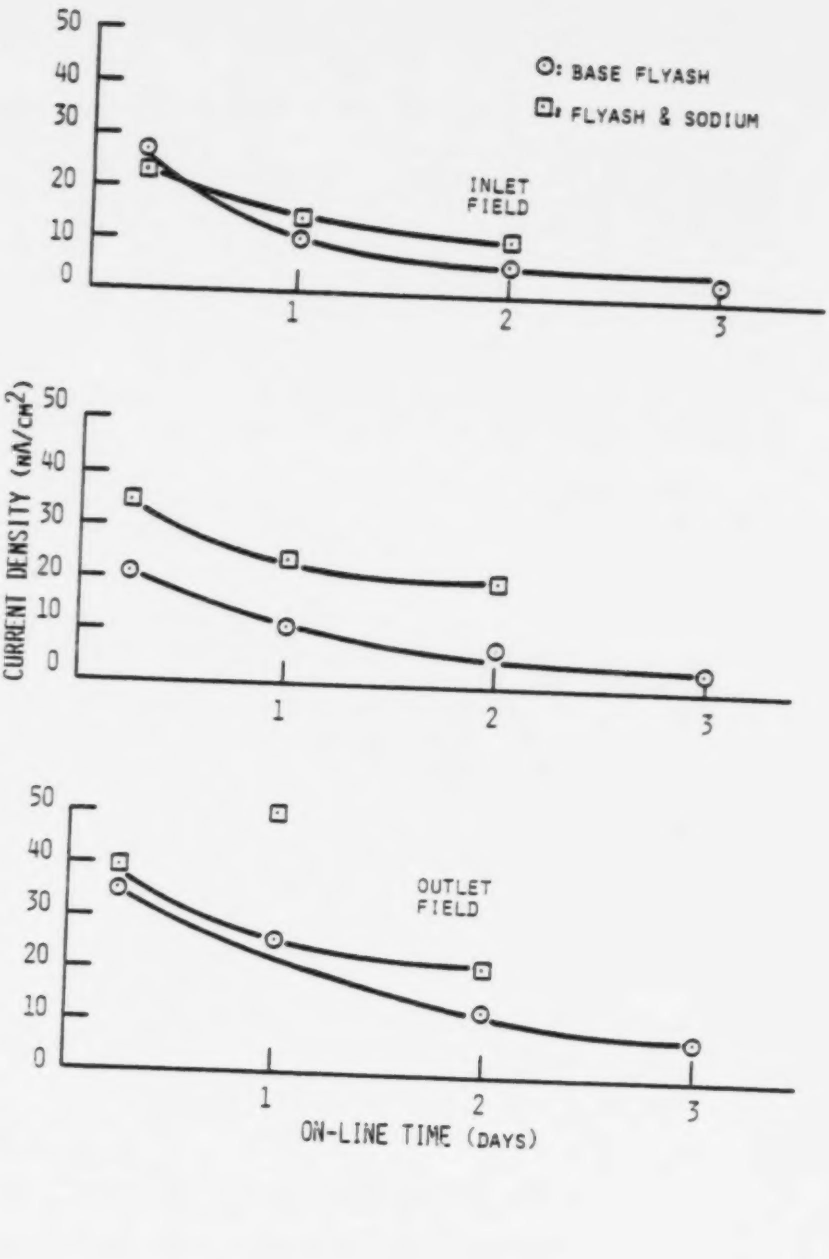

Figure 6. Current density vs. on-line time

state conditions. The inlet field histograms reflect a 2-3 factor improvement in achievable current densities for the sodium conditioning test series, having achieved a 10 nA/cm^2 level compared to a 4 nA/cm^2 level for the base ash series. A consistently comparable relationship exists for the outlet fields, with the sodium series achieving 20 nA/cm^2, relative to 7 nA/cm^2. The second or middle field histogram indicates improvement for the sodium series, achieving 20 nA/cm^2 compared to 4 nA/cm^2 for the base ash.

Reasonable correlation exists between the independent resistivity measurements and the achievable precipitator current densities approaching steady state conditions. The relationship between resistivity (P) and current density (C. D.) is defined by P=E/C. D., where E is the dielectric (breakdown) strength of the collected dust layer. Assigning the limiting breakdown strength of 10 KV/cm for each ash species, one can calculate the achievable current density from the log-averaged resistivity values. For the base ash ($P=2.1 \times 10^{12}$ OHM-CM), the calculated current density is 4.8 nA/cm^2. For sodium-conditioned ash (3.7×10^{11} OHM-CM the calculated value is 27 nA/cm^2. These theoretically calculated values correspond with the empirical values averaged from the operational data (5.0 and 15 nA/cm^2, respectively).

Comparison of the achievable voltage levels shown in Figure 7 for the two ashes are not as dramatic as the current density comparison but higher voltages were consistently obtained for the sodium treated ash.

The relationship of the voltage applied to each precipitation field and the resulting current (corona discharge curves) may be analyzed to gain insight into precipitator operation and performance. Figure 8 portrays the corona discharge curves for the base and conditioned ashes in graphical form. These curves show the characteristic profile of the volt-amp relationships from each field for steady state conditions. Knowledge of the meaning of the V-I curves is a fundamental tool necessary for proper operation of a precipitator. These data can characterize the following parameters/conditions:

- corona current leakage
- corona initiation voltage
- effective corona wire size
- effective wire-to-plate spacing
- alignment effects
- specific resistivity level
- specific collection area

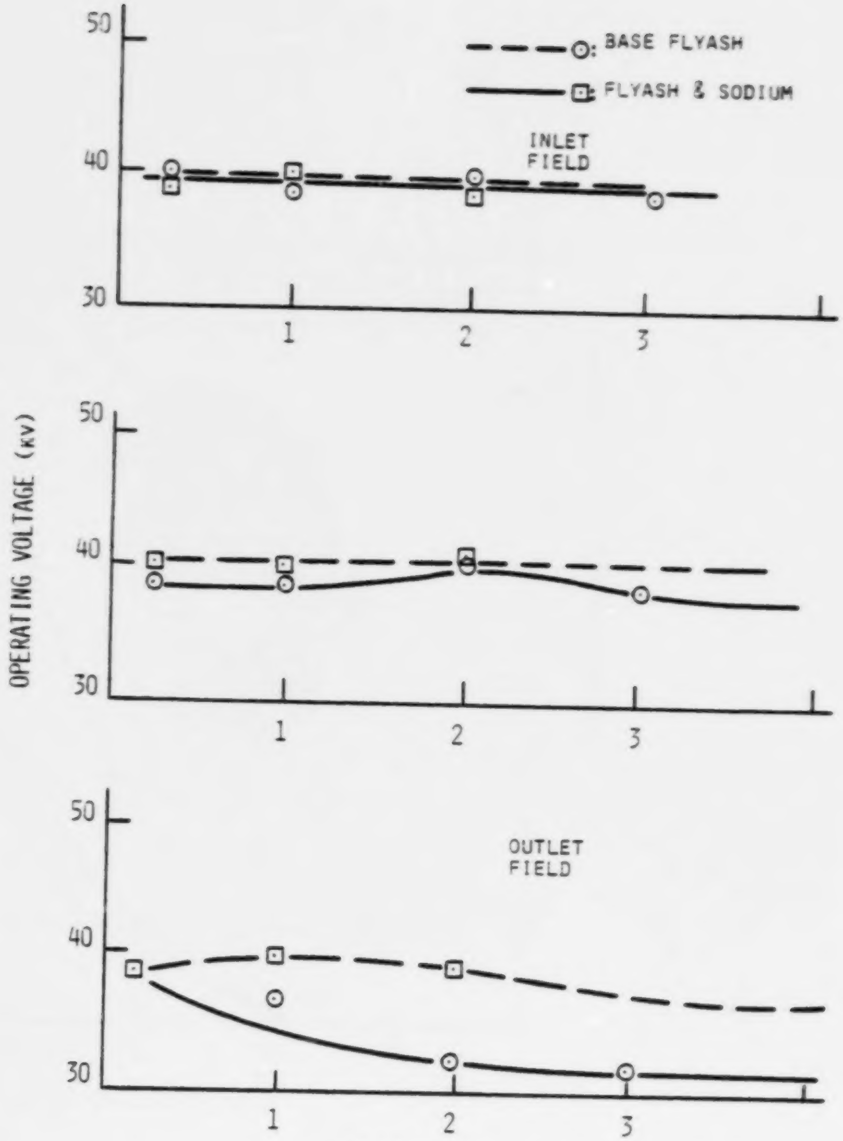

Figure 7. Operating voltage vs. on-line time

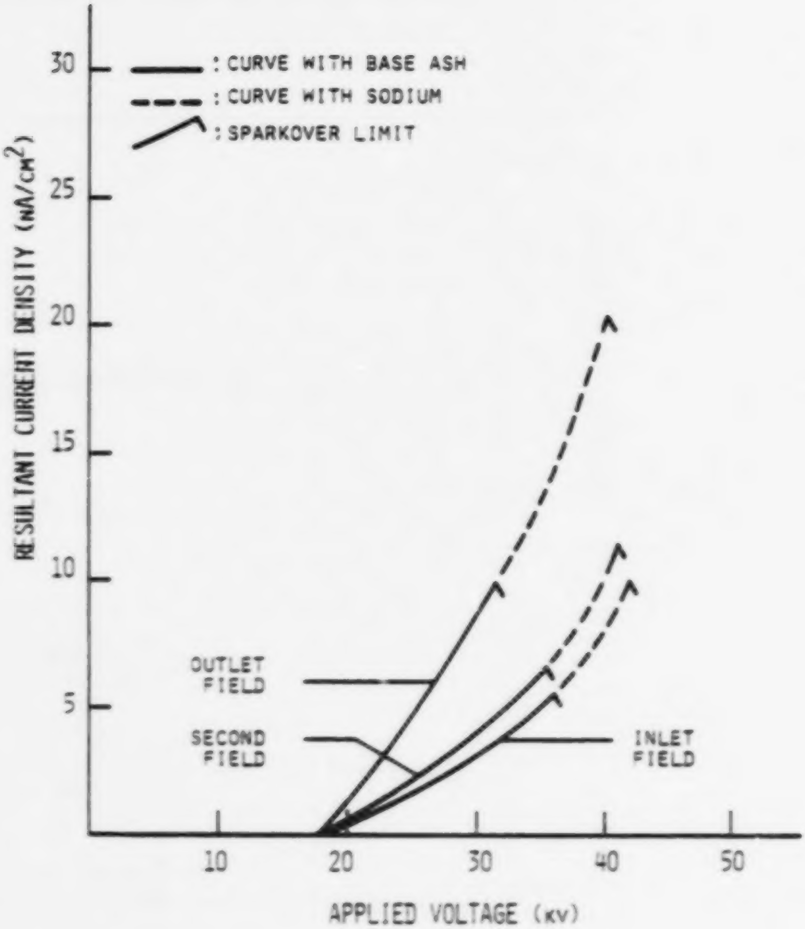

Figure 8. Corona discharge curves

- breakdown voltage
- achievable current density
- concentration of fine particulate
- relative position of each precipitation field (inlet, second ..., outlet)
- variations in emission source process

Analysis and interpretation of these curves provide the basis for the following generalities referenced in other sections of this report:

1. A reduction in specific resistivity between the base ash and sodium-plus-ash test series.
2. An improvement in achievable corona point for the sodium series.
3. An improvement in expected collection performance for the sodium series.
4. The degradation in performance related to elapsed time from internal clean-up.
5. A small increase in effective wire size due to ash build-up.[11]

PARTICULATE COLLECTION RESULTS

Particulate Concentration Results

Table 7 shows the averages of the inlet and outlet concentrations per test used to calculate the average collection efficiency values in Table 9 and Figure 9. The inlet data exhibit considerable scatter resulting from the inconsistent probe catches apparent in the raw data. Due to the reduced flyash concentration and probe catch material, the outlet data offer reasonable agreement and consistency.

The apparent scatter in the particulate data depicts an ordered trend when the elasped operating time from the precipitator "cleaning" is taken into account. As previously noted, the corona wires and collection plates were restored to a clean state between conditioning and nonconditioning test series. The degradation in performance evident particularly for the base ash was caused by the accumulation of high resistivity ash on the collection plate and the discharge electrodes. The marginal differences in performance for the tests after recent cleaning do not reflect the performance levels achievable for steady state operation. According to a best fit approach from Figure 14, sodium conditioning was responsible for reducing outlet loadings from 140 to 40 mg/Ds m^3 (0.122 lb to 0.0361 lb/10^6 Btu), resulting in an improvement in collection efficiency from 98.19 to 99.46 percent.

Table 7
Average of Particulate Data
(mg/SDm^3)

Test	Inlet	Outlet
1	8,657	182
2	11,630	133
3	14,310	394
4	5,198	29.1
5	7,076	45.6
6	19,950	40.1
7	4,259	46.3
8	8,290	47.6
9	3,824	38.2
10	5,977	36.2
11	4,642	33.2
12	4,630	30.5
13	4,649	35.3
14	8,061	17.3
15	8,633	22.9
16	7,282	34.1
17	5,587	50.4
18	3,847	44.6
19	5,908	117
20	8,610	137

Mean: 7,557

Table 8. SUMMARY OF PARTICULATE DATA AND EFFICIENCY RESULTS

Data	Base Flyash	Base Ash with Sodium
Inlet concentration (Mg/DNM^3)	7,550	7,550
Outlet concentration (Mg/DNM^3)	140	40
Inlet mean particle size (μ)	15	15
Outlet Mean particle size (μ)	2.6	2.1
Efficiency		
Total mass (% wt.)	98.2	99.5
Fractional @:		
3.0 μ	98.8	99.7
1.0 μ	94	98
0.5 μ	81	94
0.3 μ	70	92

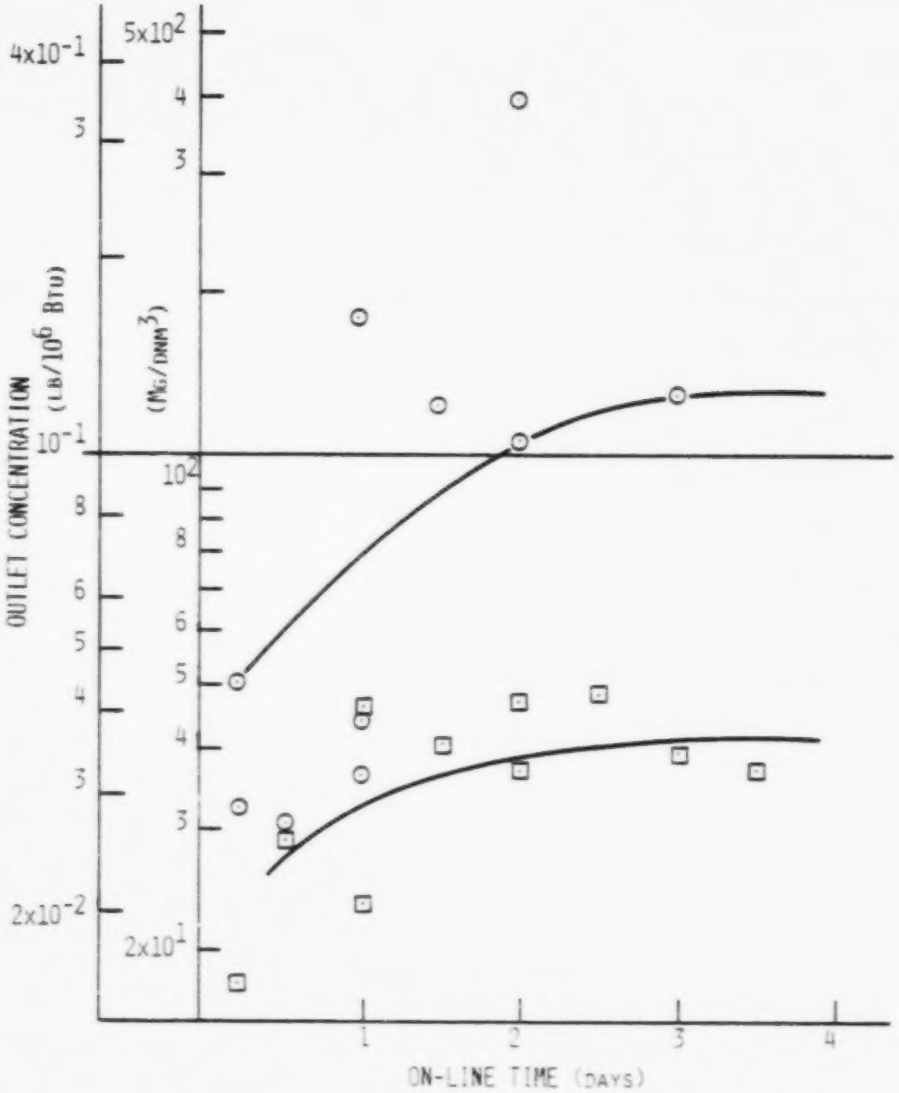

Figure 9. Precipitator collection performance

Table 9 PARTICLE SIZE DATA AND FRACTIONAL EFFICIENCY RESULTS[1]

Test No.	Mass Mean Diameter		Fractional Efficiency @			
	Inlet	Outlet				
1	8.6	1.6	29.3	42.3	90.7	89.7
2	9.7	1.7	89.7	90.9	94.9	99.2
3	26.0	3.5	87.9	90.5	87.2	96.0
4	13.5					
5	13.0	1.6	85.7	88.3	93.5	99.7
6	8.8	1.6	93.3	94.0	97.4	99.5
7	7.4	1.2	93.2	94.6	97.7	99.5
8	7.8	1.4	94.9	96.4	98.7	99.8
9	7.4	1.7	79.6	83.7	94.9	99.8
10	9.9	3.0	93.3	95.6	97.8	99.6
11	11.5	2.1	37.1	71.2	97.7	99.6
12	21.0	1.9	61.1	72.0	97.0	99.4
13	8.0	1.2	92.5	95.9	98.7	99.9
14	23.3	1.4	96.7	98.5	99.1	99.9
15	17.0	2.3	91.5	93.4	98.1	99.9
16	16.0	4.8	98.3	98.4	99.1	99.9
17	12.0	2.1	37.5	78.7	93.2	99.7
18	22.5	1.4	85.0	88.6	97.0	99.7
19	27.0	5.5	90.7	93.5	93.1	99.5
20	29.0	4.7	83.2	88.0	90.0	96.0
Base ash mean:		2.6	69.4	81.2	93.9	98.8
Sodium mean:		2.1	91.8	93.7	97.4	99.7

---

[1] Data obtained from daily averages.

PARTICLE SIZE AND FRACTIONAL EFFICIENCY RESULTS

Brink and the University of Washington (U of W) impactors were employed for obtaining size measurements on the inlet and outlet streams, respectively. Quality assurance measures and proceudres for conditioning and weighing substrates were performed in consistence with EPA/IERL specifications. Due to small weight losses on the greased substrates for the U of W, trial impactor flowrate was reduced for all subsequent tests from 189cc/S to 142cc/S. Evidence of substrate scouring was consequently eliminated with flowrate reduction.

Table 9 presents the particle size data and fractional efficiency results for all test runs. Mass mean diameter on the inlet ranged from 8-29 , with an average M.M.D. of 15 . The outlet stream contained M.M.D's from 1.2—5.5 , with 2.1 and 2.6 being the average mean size for the sodium conditioning and base ash effluents, respectively.

Figure 10 demonstrates the improved fractional collection performance associated with sodium conditioning, particularly in the submicron range.

REFERENCES

1. Private Communication with Bob Olmstead, Plant Superintendent, Montana Power Corrette Station, Billings, Montana.

2. McCain, J.D., CEA Variable Throat Venturi Scrubber Evaluation. EPA-600/7-78-094, U.S. Environmental Protection Agency, Research Triangle Park, N.C., June, 1978.

3. White, H.J., INDUSTRIAL ELECTROSTATIC PRECIPITATION, Reading, Mass., Addison-Wesley, 1963, p. 359.

4. "MOBILE ESP OPERATING MANUAL," Environmental Sciences Group, Naval Surface Weapons Center, Dahlgren, VA., October, 1976.

5. Spencer, H.W., A Study of Rapping Reentrainment in a Nearly Full-Scale Pilot Electrostatic Precipitator. EPA-600/2-76-140, U.S. Environmental Protection Agency, Research Triangle Park, NC, 1976.

6. Harris, D.B., Procedures For Cascade Impactor Calibration & Operation in Process Streams, EPA-600/2-76-144, U.S. Environmental Protection Agency, Research Triangle Park, NC.

7. Nichols, G.N., Test Methods & Apparatus For Conducting Resistivity Measurements, U.S. Environmental Protection Agency, Contract No. 68-02-1083, Final Report No. 3121-III., Sept.,1977.

8. White, H.J., Op. Cit., p. 312.

9. Bickerhaupt. R.E., Surface Resistivity & The Chemical Composition of Flyash, Proceedings From Symposium On Electrostatic Precipitators For The Control of Fine Particles, For National Environmental Research Center, PB 240 440, Jan., 1975, p. 246.

10. Bickelhaupt, R.E., SODIUM CONDITIONING TO REDUCE FLY ASH RESISTIVITY, EPA-650/2-74-092, U.S. Environmental Protection Agency, Research Triangle Park, NC.

11. Banks, S.M., McDonald, J.R., Sparks, L.E., VOLTAGE CURRENT DATA FROM ELECTROSTATIC PRECIPITATORS UNDER NORMAL AND ABNORMAL CONDITIONS,
Proceedings: PARTICULATE COLLECTION PROBLEMS USING EPA'S IN THE METALLURGICAC INDUSTRY, EPA-600/2-77-208, U.S. Environmental Protection Agency, Research Triangle Park, NC, October, 1977.

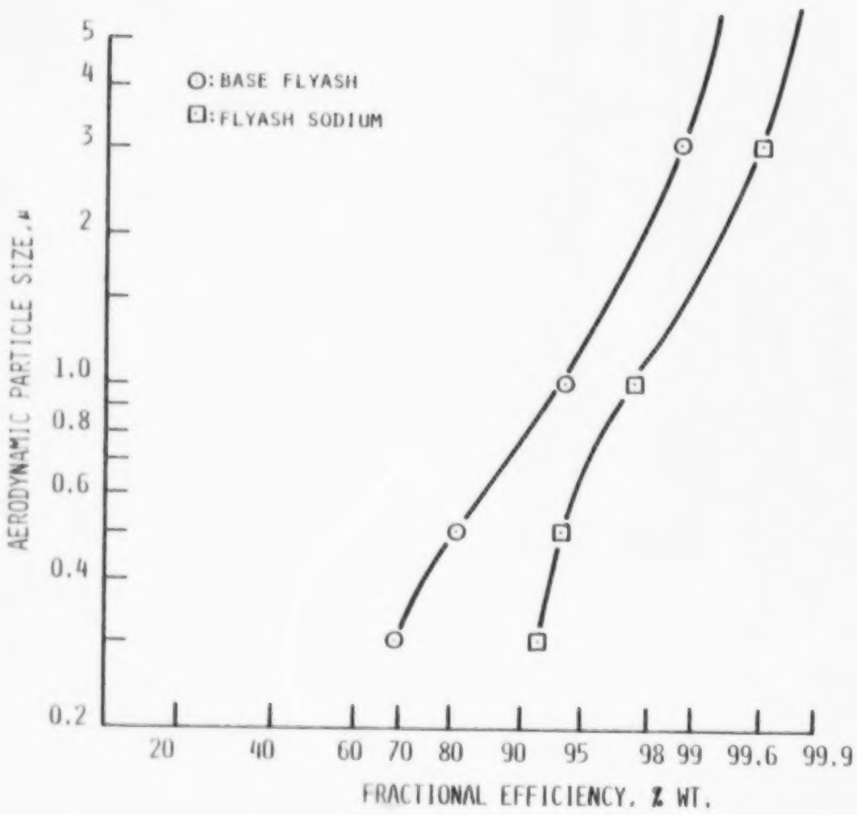

Figure 10. Comparison of mean fractional efficiency results

ACKNOWLEDGEMENTS

This program was sponsored by EPA with participation by Montana Power Company, Southern Research Institute, Monsanto Research Corporation, and Acurex/Aerotherm. The program was initiated under EPA Contract No. 68-02-1816 with Monsanto Research Corporation, and completed under Contract No. 68-02-2646 with Aerotherm.

The author expresses sincere appreciation to the following individuals for their involvement with and contribution toward this program:

Ivan Bonnette, Ray Hoffman, and Bruce Knusten of Montana Power Company, Colstrip, Montana;

Dale Harmon and Les Sparks of EPA, Research Triangle Park, North Carolina;

Grady Nichols and Jerry Sutton of Southern Research Institute, Birmingham, Alabama;

Don Zanders, Billy Bowles, Tony Wojtowicz, and Mark Wherry of Monsanto Research Corporation, Dayton, Ohio;

Hal Buck, Mike Griffin, Randy Page, and Clyde Stanley of Acurex/Aerotherm, based at Research Triangle Park, North Carolina.

NOVEL ELECTRODE CONSTRUCTION FOR PULSE CHARGING

Senichi Masuda
Department of Electrical Engineering
University of Tokyo
7-3-1, Hongo, Bunkyo-ku, Tokyo, Japan

ABSTRACT

The basic concept of pulse charging, its merit and limitation are described. The Bias-Controlled Pulse Charging System equipped with the channel-shaped third electrodes and a dc bias-voltage meets most of the requirements necessary for practical application of pulse charging in large scale precipitators, and has been in successful operation at several practical plants. Its basic characteristics and performance data are presented, and the auxiliary developments including a high voltage pulse source and a pre-charging equipment are also described.

INTRODUCTION

The use of pulse charging for enhancing the collection performance of electrostatic precipitators was firstly proposed by White[1]. Lüthi et al[2] proposed to introduce the third electrodes in the vicinity of the discharge electrode to construct the tri-electrode pulse charging system, as shown in Fig. 1, in order to overcome back discharge problem. Here, the pulse voltage is applied between the discharge and third electrodes whereas a dc voltage is applied between the third and collecting electrodes to maintain the main field where charging and collection of particles are conducted. By changing either the height V_p, duration time τ, or repetition frequency f of the pulse voltage, it is possible to control the ionic current density J with keeping the intensity of the main field E at its maximum. This is impossible with a conventional twin-electrode system energized by a dc high voltage. As a result, the following requirement for extinguishing back discharge can easily be met by reducing the value of J as the resistivity of dust layer ρ_d increases, without lowering the value of E:

$$J_d \times \rho_d = E_{ds} \qquad (1)$$

where Jd = current density in dust layer, and Eds = breakdown field strength of dust layer. The use of pulse voltage also contributes to the increase in uniformity of current density Jd over the layer surface as well as stability and uniformity of corona discharge over the discharge electrode, which become lost at dc corona in case corona current is excessively lowererd. The author and his co-worker introduced a dc bias-voltage in series to the pulse voltage, as illustrated in Fig. 1 (b)[3]. This made a large increase in a gap between the discharge and third electrodes possible without allowing undesirable corona to occur in pulseless periods, and thereby enabled the pulse charging to be practically applied in large scale precipitators. This system is named "Bias-Controlled Pulse Charging System". Penny et al[4] propsed recently to apply pulse voltages in tri-electrode system in a manner as shown in Fig. 1 (c), and obtained a successful result for high resistivity fly ash with resistivities up to 10^{13} ohm-cm. The author and his co-workers further developed a novel pulse voltage source[5] to be used in a precipitator as a capacitive load, and an efficient precharger named "Boxer-Charger"[6] which is based on a concept of bi-directional charging by monopolar ions, and can provide theoretical limit of charge for high resistivity particles up to at least 10^{15} ohm-cm without trouble by back discharge. They also investigated the limitation of the pulse charging system[7], and found that it lies around the resistivity level of ρd = 1013 - 10^{14} ohm-cm. This is because the value of allowable current density J becomes too small beyond this resistivity level so that charging speed becomes too low, and also because entirely new modes of back discharge start to occur when the resistivity exceeds 10^{14} ohm-cm[8].

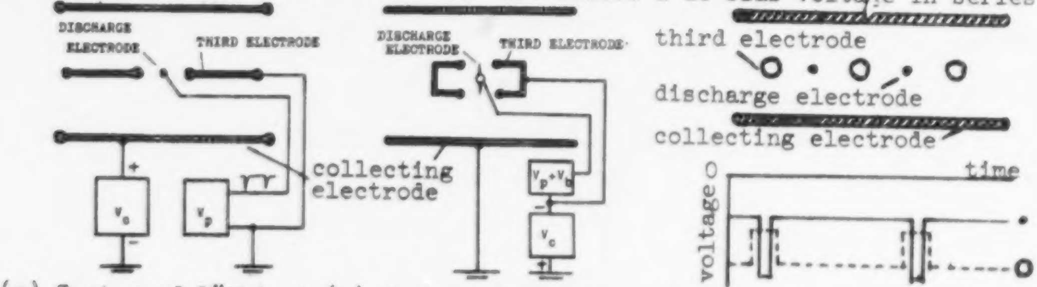

(a) System of Lüthi et al (b) System of Masuda et al (c) System of Penny et al

Fig. 1 Tri-electrode pulse charging system

In this paper are reported on the electrode construction of the bias-controlled pulse charging system used by the authors, its basic characteristics and performance data as well as the pulse voltage sources and the pre-charging device described.

BASIC CONCEPT OF BIAS-CONTROLLED PULSE CHARGING SYSTEM WITH TRI-ELECTRODES

Pulse charging is possible also in the twin-electrode system, as already performed by White, and two different modes of pulse charging exist in this case. One is to set the dc voltage just below sparking voltage, and apply a pulse voltage superposed. The resultant peak voltage can be made higher with the decrease in pulse duration time τ. This provides, in principle, a possibility of raising particle charge in case the dust resistivity ρd is not excessively high as to cause back discharge, but actually its advantage is fairly limited. This is because the increase in the resultant peak voltage remains to be only 10 % of dc sparking voltage even at $\tau = 5$ μs, whereas the decrease in τ results in not only reduction in charging speed but also lowering of the saturation charge itself in twin-electrode system[9]. In case of high resistivity dust, dc voltage is to be set just below the corona starting voltage, which should be raised near to the sparking voltage by appropriate electrode design, and a pulse voltage is applied hereto. This provides an interrupted pulse corona as in the case of pulse charging with tri-electrode system. However, the applicable peak voltage is limited as before, so that the control range of current density J is largely limited in comparison to the pulse charging with tri-electrode system. The operation is also affected much more sensitively by the fluctuation of plant conditions. The advantage of tri-electrode pulse charging system lies in its much larger stability in operation and flexibility of selecting current and main field strength in a wide range at desired, optimum values. This large advantage may more than off-set its increased initial cost in many high resistivity applications.

The prerequisite condition for the tri-electrode pulse charging system to become practically applicable is to increase the gap between the discharge and third electrodes to a level of about 10 cm, necessary for realizing large scale units with an electrode height of more than 10 m. This increase in electrode gap, however, should be realized without losing corona interrupting action in the pulseless period, which was achieved in case of a short electrode gap by screening effect of the third electrodes. The author solved this problem by inserting between the discharge and third electrodes a dc bias-voltage, which keeps the potential of the discharge point in the pulseless periods at a value which originally corresponds to its local potential when only the third and collecting electrodes are existing. At this potential the field intensity at the needle point becomes minimum which shall lie below the breakdown field strength at the point, so that no dc corona occurs in the pulseless periods. This dc bias-voltage is mostly provided from a separate voltage source whereas, in some cases, the auto-biasing effect appears. The use of the bias-voltage also enables half or full-wave ac voltage to be used to provide the economical and reliable "quasi-pulse voltages" to be described later.

As already described, the pulse charging system loses its function as a precipitator or a charger when the value of ρd exceeds $10^{13} - 10^{14}$ ohm-cm. In such an extremely high resistivity range, the two-stage type precipitator with an effective pre-charger and a low voltage collection part may provide one of the few solutions. The field intensity in the collection part should be kept sufficiently low so that the new modes of back discharge do not appear. A minute amount of current, however, has to be supplied to avoid dust reentrainment, whereas its value should not exceed a level of causing back discharge. This current value may be so low that it becomes unstable and non-uniform when dc corona is used. The bias-controlled pulse charging system should be very suited also in this application as a dust collection part, as it can provide the field intensity and current density at any desired values. The pulse charging system with twin-electrodes may also be used in this case.

It should be added that the tri-electrode system can be used also with a dc voltage to be applied instead of a pulse voltage. This mode of operation is not suitable for applications in high resistivity dusts because of less uniformity and large unstability to occur in corona current which has to be lowered to a very small level in this case. In case of medium or low resistivity ρ_d, however, this operation mode provides large advantages. It can provide large corona current in many cases where dust space charge is so large that corona quenching appears in twin-electrode system. It can provide fairly high value of main field strength E under elevated temperature beyond 300 °C with a reasonable current level which may otherwise become too large so that power consumption becomes excessively high. All these effects proved in pilot plant tests as well as in practical precipitators to give very satisfactory results in these applications.

In order to avoid the performance loss due to dust reentrainment to occur on rapping of electrodes in the tri-electrode system, the authors[10] developed an after-collector with a very small size named "ES (Electric Screen)" which utilizes hydrodynamic effect in addition to electrostatic force (EHD-effect) to collect the reentrained particles which possess an increased size due to agglomeration in the tri-electrode system.

ELECTRODE CONSTRUCTION

Fig. 2 illustrates the electrode construction of the Bias-Controlled Pulse Charging System used by the authors. The discharge electrode is the needle-on-rod type which is rigid enough and least affected by dust deposition. The third electrodes are of channel type which is rigid in elongated construction of more than 10 m height under elevated temperature, and low in cost. Pipes are welded to the periferies of the channels to avoid corona discharge to occur there. The distance between the needle points and the channel periferies is 10 cm. The channel-shaped configuration provides an excellent shielding effect to the periferies whereas its hollow space inside allows an easy arrangement of the rod supporting the needles. As a result, a very good control characteristics of the bias-voltage can be obtained, and flashover is avoided to occur between the rod and channels. The appreciable portion of the main field becomes uniform and has an effective component normal to the collecting electrodes. The gas flow is enforced by the channel to turn towards the collecting electrodes, and passes through the field area far from the discharge electrode. All these factors may contribute to an excellent collection performance of this tri-electrode system as described later. The tri-electrode system equipped with the channel type third electrodes is named "PAC System".

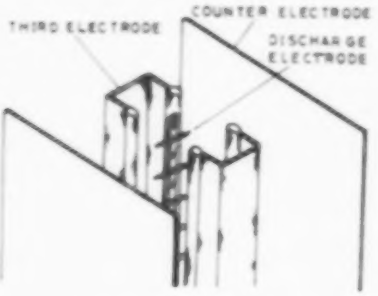

Fig. 2 Electrode construction of PAC System

PULSE VOLTAGE SOURCE

The use of the dc bias-voltage enables not only narrow pulses with a short duration time τ, but also quasi-pulses to be used in the tri-electrode system. Fig. 3 illustrates the static current characteristics of PAC System which explaines how the quasi-pulses can be produced, where V_D represents the dc voltage applied between the discharge and third electrodes, V_T the dc bias-voltage, and I_D, I_C and I_T the current of the discharge, collecting and third electrodes respectively. Owing to a large gap between the discharge and third electrodes, current should flow from the discharge electrode to the collecting electrode at $V_D = 0$ if not the bias-voltage is used. The bias-voltage V_T, positive at the discharge electrode in relation to the third electrode, shifts the origin O to O', and thereby supresses the current to flow at $V_D = 0$. It can be seen that pulsive corona can occur by applying a half-wave or full-wave ac voltage superposed to the dc bias-voltage around its peak to provide the quasi-pulse voltages[4]. This provides a very economical and reliable means of pulse energizing in most of the applications where a sufficiently large pulse duration time is allowed, and enabled an early application of the Bias-Controlled Pulse Charging System in large scale precipitators prior to the development of a more advanced pulse voltage source capable of provinding narrow pulses to the capacitive precipitator load, as illustrated in Fig. 4. The pulse voltage source to be used in the precipitators of both twin-electrode and tri-electrode systems, which have a large static capacity of 0.1 - 1.0 μF connected in parallel to a high corona resistance, has its inherent difficulties. In order to get a sharge pulse, the capacity C should be quickly charged up to the peak voltage Vp with an energy $(1/2)CVp^2$, which then should be quickly dissipated in the next instant through a fairly low additional resistance to be inserted in parallel to the load for the purpose of wave shaping. As a result, an essntial part of the energy supplied from the source is lost uselessly in this resistance in both pulse and pulseless periods, making the initial and running costs of the pulse source prohibitively high. Fig. 4 illustrates the circuit diagram and output voltage wave form of the pulse

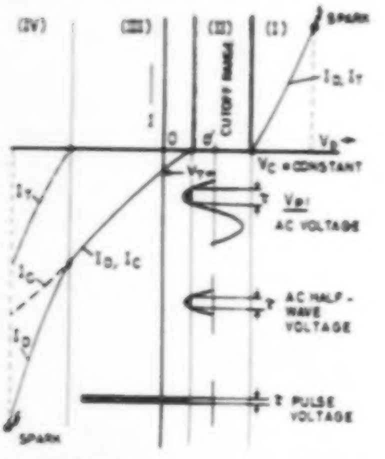

Fig. 3 Static current characteristics of PAC System

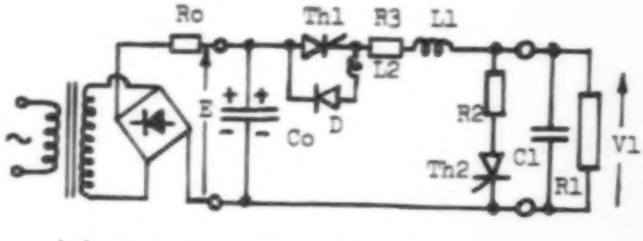

(a) circuit diagram (for positive pulse)

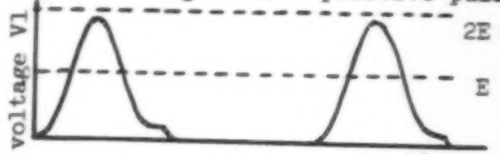

(b) voltage wave form

Fig. 4 Pulse voltage source of energy recovery type

voltage source to be used for capacitive load, which has been developed by the author and his co-workers to solve the difficulties described above[5]. This uses a transient LC-oscillation occurring when Th1 is triggered for a quick charging and discharging of the load capacity C1 where Co>>C1 so that τ is governed by L1 and C1, and the energy stored in C1 in the charging cycle is recovered to the source in the discharging cycle, since C1 is charged up to about 2 E in the charging cycle. The thyrister Th2 is to reset the residual potential to zero so that the LC-oscillation does not fade away. This energy recovery concept enables a narrow pulse voltage to be used for the capacitive load with low initial and running costs. The details of circuit actions are to be reported separately, together with several alternative circuits[5].

CHARACTERISTICS OF PAC SYSTEM

Fig. 5 illustrates the typical control characteristics of bias-voltage V_T against discharge current Ip (aver. val.) in PAC System measured in a pilot plant (20 m^3/min, 0.5 m/s, cement klinker mill) under air load and dust load condition, where a square wave pulse voltage with τ = 10 μs was used. The cutt-off characteristics of Ip by means of V_T are cleary indicated. It was observed that discharge current Ip denpends on τ, pulse height Vp and pulse repetition frequency in the following way:

$$Ip = Ipo + \alpha\tau, \quad Ip = \beta Vp^n \ (n=1\sim2), \quad Ip = \gamma f \qquad (2)$$

where α, β, and γ represent proportional constants[3]. Fig. 6 shows a comparison of current distributions on the collecting electrode between the energizations with a square wave pulse voltage, quasi-pulse voltage with full wave ac, and a dc voltage where Ip = 50 μA in common. It can be seen that a fairly large improvement in current distribution can be obtained with a quasi-pulse voltage.

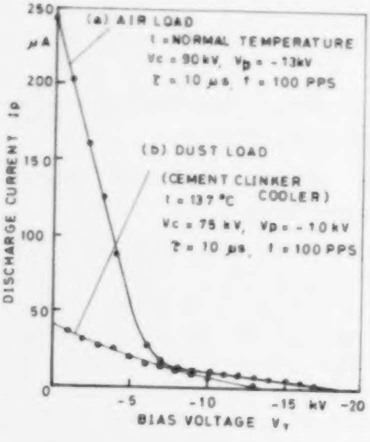

Fig. 5 Bias controll characteristics of PAC System

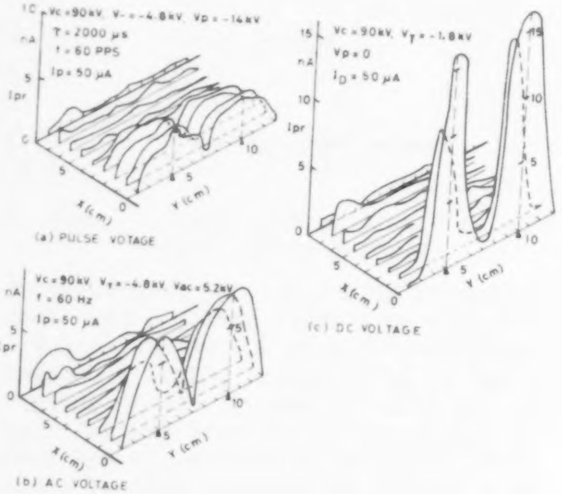

(a) PULSE VOTAGE

(b) AC VOLTAGE

(c) DC VOLTAGE

Fig. 6 Comparison of current distribution in PAC System

PERFORMANCE LIMIT OF BIAS-CONTROLLED PULSE CHARGING SYSTEM

Fig. 7 indicates the critical current density on the collecting electrode, ic, at which visible back discharge starts to occur, versus layer resistivity ρd, where a tissue paper is used as a sample layer, and measurements are made in air at NTP. Vp and τ are varied so that ic becomes maximum at each measuring point under constant main field strength E = 4 kV/cm (aver. val.). The quantity ic governs the upper limit of particle charging speed. It can be seen that PAC System provides a sufficiently large critical current density up to $\rho d \approx 10^{14}$ ohm-cm as far as the third electrodes are kept clean. In the course of a pilot plant test made at an iron-ore sinter furnace where $\rho d \approx 10^{13}$ ohm-cm, it was discovered that occurrence of detrimental effect of back discharge is governed not only by current density i, but also by the magnitude of the main field strength E. This had been expected because the occurence of the most detrimental streamer-mode back discharge is dependent on these two quantitities[11]. This starts to occur in air at NTP when $i > 2 \times 10^{-7}$ A/cm^2 and E > 5 kV/cm. The level of this critical field strength lowers when temperature is raised.

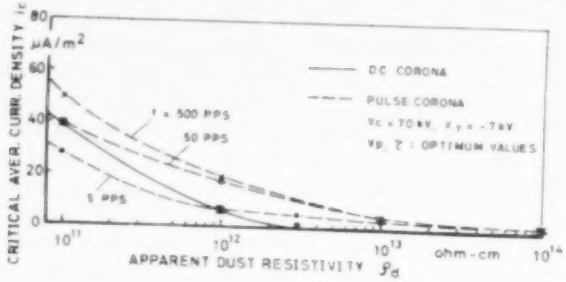

Fig. 7 Critical current density ic of back discharge initiation vs. ρd.

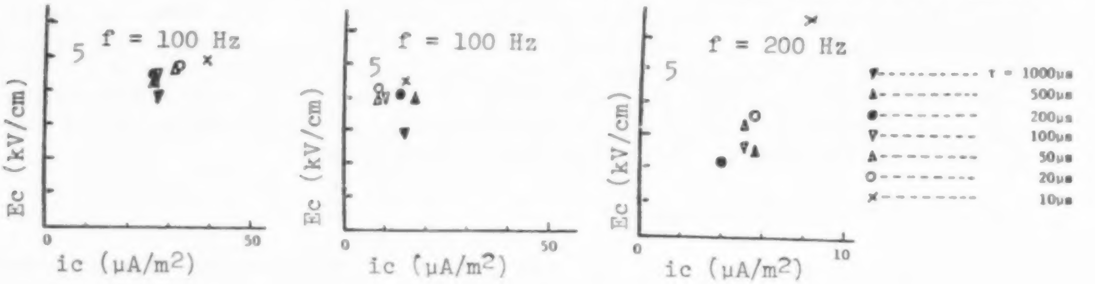

(a) $\rho d \approx 10^{12}$ ohm-cm (b) $\rho d \approx 10^{13}$ ohm-cm (c) $\rho d \approx 10^{14}$ ohm-cm

Fig. 8 Performance limit diagram of PAC System in Ec - ic plane (air at NTP, tissue paper, Vp = - 10 kV, VT = 0)

The quantities, ic and Ec, at which visible back discharge occurs, represent the performance limit of pulse charging system, because ic determines the upper limit of charging speed as described whereas Ec governs the saturation charge of particles and Coulombic force. The values of ic and Ec are primarily governed by ρd, but also by the values of Vp, V_T, f and τ of the pulse voltage used, as indicated in Fig. 8[7]. It can be seen from the figure that the performance limit of pulse charging system may lie in the resistivity level of 10^{13} - 10^{14} ohm-cm where the values of ic and Ec fall down to unacceptable levels. The author and his co-worker discovered recently that, when the value of ρd exceeds about 4×10^{13} ohm-cm, back discharge appears at E > 3 kV/cm in air at NTP also on the third electrodes if they are covered with the dust layer[8]. This back discharge is triggered by the ions emitted from the back discharge points on the collecting electrode opposite to the discharge electrode, and it in turn triggers back discharge at the area of collecting electrode next to the original back discharge zone. As a result, back discharge starts to propagate on both third and collecting electrodes over their entire surfaces. This lateral propagation of back discharge becomes noticeable when ρd exceeds about 3×10^{14} ohm-cm, and the whole surfaces of the both electrodes begin to glow. This lateral propagation does not occur when the value of E is lowered below 3 kV/cm, whereas sparking occurs when E is raised up to 5 kV/cm. When the discharge electrodes are removed with third and collecting electrodes being covered by the layer, neither back discharge nor its propagation appear even at ρd = 4×10^{14} while sparking takes place at E = 8 ~ 9 kV/cm. There is another mode of the lateral propagation which occurs at ρd > 3×10^{14} ohm-cm even if the third electrode is not contaminated[8]. This is the streamer-mode back discharge occuring randomly from the whole layer surface on the collecting electrode. The prerequisite condition for this streamer-mode back discharge to occur is that sparking occurs (at E = 8.5 kV/cm) as a result of a usual back discharge. Once triggered by the sparking, these streamers continue to occur as far as E is kept higher than 5 kV/cm, even if the discharge electrode is removed. It is likely that these streamers triggered by successive breakdown of the layer are maintained by copious positive ions produced by the streamers themselves which will be accumulated on each spot on the layer through electrical migration and also diffusion.

These new modes of back discharge occuring when ρd exceeds about 4×10^{13} ohm-cm and 3×10^{14} ohm-cm lead to a conclusion that even the pulse charging systems will not work beyond 10^{13} - 10^{14} ohm-cm except that they are used only as a collecting part of the two-stage type precipitator to be operated at a sufficiently low level of E. It should be added that these new modes of back discharge might be carefully considered in relation to the abnormal back discharge occuring in hot precipitators.

PERFORMANCE DATA OF PAC SYSTEM

Although PAC System can be used either alone as a single-stage precipitator or in combination to a precharger as a collecting part of the two-stage precipitator, the authors have used it in combination with a new type of dust

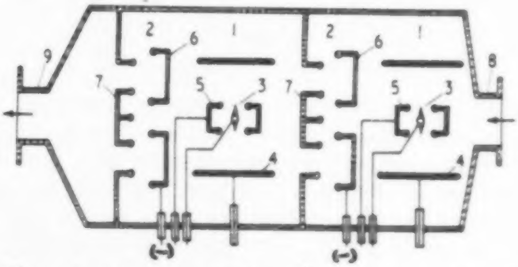

Fig. 9 PAC-ES System (2--- ES collector)

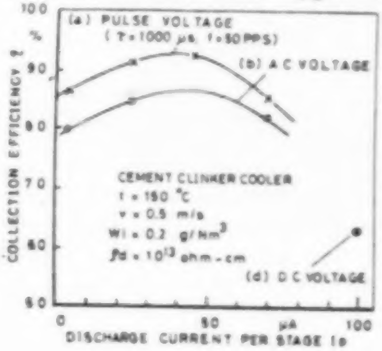

Fig. 10 Performance of a pilot plant →

collecting part named "ES (Electrostatic Screen)" which consists of the zig-zag arranged channel electrodes, as shown in Fig. 9. Some times, the discharge electrodes are attached to the negative channels in the upstream side, and water irrigation is also made at the grounded channels in the downstream side. ES is one of the collecting parts utilizing EHD (electrohydrodynamic)-effects where a fluiddynamic force is used in addition to electrostatic force for particle collection. The nozzle flow produced by the negative channels penetrates deep into the inside of the positive channels, and bring the charged particles near the inner surface of the channels where the particles can be effectively precipitated by electrostatic and innertia forces. ES has a good collection performance for particles larger than 2 μm in diameter, and collects the reentrained particles from PAC System which are mostly aggromerated up to this particle size range. This combination of PAC System and ES is named "PAC-ES System" where PAC collects most of the dust and acts as a pre-charger for ES. The use of the corona discharge and water irrigation in ES result in a marked increase in its collection performance in the smaller particle size range.

Fig. 10 represents the collection performance of PAC-ES System for the pulse and quasi-pulse energizations measured at a pilot plant (PAC-ES-PAC-ES) installed at a cement clinker mill where $\rho d = 10^{13}$ ohm-cm at T = 150 °C. The point (d) represents a performance with dc voltage application where a severe back discharge took place. The improvement of performance by pulse and quasi-pulse operations are quite satisfactory[3]. Fig. 11 shows the relationship between the peak pulse voltage Vp (quasi-pulse) and discharge current I measured at another pilot plant installed at an iron-ore sinter furnace where $\rho d = 10^{13}$ ohm-cm[11]. The main voltage was kept at 40 kV (1.8 kV/cm) in order to avoid the occurrence of detrimental steamer-modes back discharge. It can be seen from the figure that the use of a narrow pulse voltage and strong rapping system give a remarkable effect for solving back discharge, which are indicated by a large lowering of the discharge current when τ_e and dust layer thickness were reduced. PAC-ES System proved to provide an excellent performance also in this application if the correct operating conditions were selected. The improvement of performance due to the strong rapping, by which the dust layer thickness is kept small, seems to originate from the fact that appearance of the streamer-mode back discharge is hindered when the layer thickness is small[12].

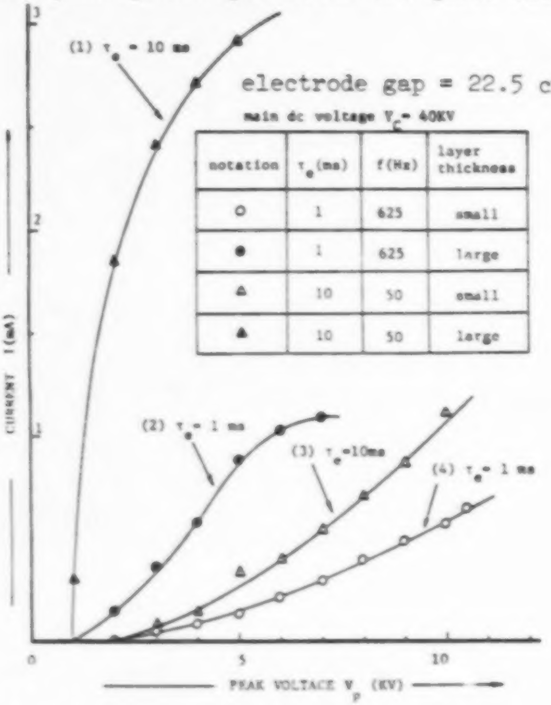

Fig. 11 Discharge current vs. peak pulse voltage in PAC System at a pilot plant. (first PAC-stage, VT = 0)

Fig. 12 shows a photograph of a large scale PAC-ES precipitator installed at a cooler of an iron-ore sintering furnace (Shin Nippon Steel Co., Ltd., Nagoya Plant) where gas volume is 11,000 m^3/min. at 100 - 250 °C.

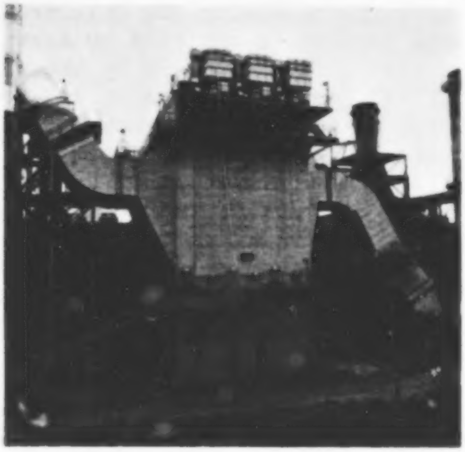

Fig. 12 PAC-ES type ESP with quasi-pulse charging for high resistivity dust.

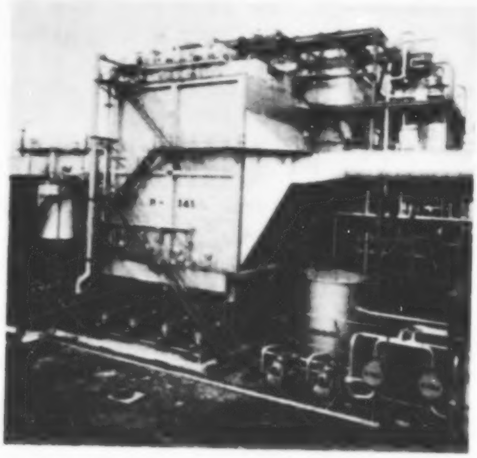

Fig. 13 PAC-ES type ESP with a dc voltage charging for low resistivity carbon dust.

The electrode system is composed of 3 x(PAC-PAC-ES) combinations, and the total treating time in the active PAC zones amounts to 3 s at 1.0 m/s gas velocity, so that the precipitator could be installed in a very limited space. The resistivity of dust lies in the range of 10^{11} - 10^{13} ohm-cm, and a quasi-pulse voltage out of half-wave ac voltage with a commercial frequency is used. The precipitator has been in a very successful operation since 4 months with an excellent performance where the dust concentration could be reduced from 3 g/Nm^3 at the inlet to less than the guaranteed level of 0.05 g/Nm^3 (0.03 - 0.025 g/Nm^3).

Fig. 13 shows a picture of a large scale PAC-ES type precipitator installed at an oil-fired boiler plant (240 t/h boiler, Mitsui Petrochemical Co., - Ukishima Petrochemical Co., Lt.) where gas volume is 6,500 m^3/min. at 140 - 160 °C. The electrode system is out of 3 x(PAC-ES) combinations, and the total treating time in the active PAC zones is 1.5 s at 1.0 m/s gas velocity. The dust is primarily carbon particles with a low resistivity, and the dc voltage charging is used to maintain a high current density. The precipitator has been successful operation since 3 years where dust concentration is lowered from 0.3 g/Nm^3 at the inlet to 0.01 g/Nm^3 at the outlet.

CONCLUSIONS

The bias-controlled pulse charging system with tri-electrodes proved to overcome back discharge troubles in the dust resistivity range up to 10^{13} ohm-cm. The tri-electrode system can also be used for low resistivity dusts with dc charging mode where discharge current can be largely increased even in the case dust space charge is dominating. A large scale

PAC-ES type precipitator has been in very successful operation at an iron-ore sintering furnace with a quasi-pulse voltage applied. Three other practical precipitators of PAC-ES type are also in successful use with the dc charging mode for low resistivity dusts; one in a large scale boiler plant and two in the waste disposal furnaces. The improved type of pulse voltage source based on the energy recovery concept, and a novel pre-charger based on the monopolar bi-directional charging concept have been developed for use in combination with the bias-controlled pulse charging system. The author thanks his co-workers for their assistance.

REFERENCE

1. White, H.J. Industrial Electrostatic Precipitation, Addison-Wesley Pub. Co., 1962. p. 232 - 234.
2. Lüthi, J.E. Grundlagen zur elektrischen Abscheidung von hochohmigen Stäuben. Dissertation ETH-Zürich, No. 3924 (1967).
3. Masuda, S., Doi, I., Aoyama, M. and A. Shibuya. Bias-Controlled Pulse Charging System for Electrostatic Precipitator. Staub-Reinhaltung der Luft, Bd. 36, Nr. 1, p. 19, Januar, 1976.
4. Penny, G.W. and P.C. Gelfand. The Trielectrode Electrostatic Precipitator for Collecting High Resistivity Dust. J. Air Pollution Control Assoc., Vol. 28, No. 1, p. 53, January 1978.
5. Masuda, S., Obata, S. and J. Hirai. A Pulse Voltage Source for Electrostatic Precipitators. to be presented at IEEE/IAS 1978 Annual Meeting, Tronto, Canada, October 1978.
6. Masuda, S., Washizu, A., Mizuno, A. and K. Akutsu. Boxer Charger - A Novel Charging Device for High Resistivity Powders. Proc. CSIRO Conf. on Electrostatic Precipitation. Leura, New South Wales, Australia, August 1978, and to be presented at IEEE/IAS 1978 Annual Meeting, Tronto Canada, October 1978.
7. Masuda, S., Doi, I., Hattori, I. and A. Shibuya. Utility Limit and Mode of Back Discharge in Bias-Controlled Pulse Charging System. Conf. Record of IEEE/IAS 1977 Annual Meeting, p. 875, Los Angels, Oct. 1977.
8. Masuda, S. and S. Obata. Lateral Propagation of Back Discharge. to be submitted to J. of Electrostatics.
9. Masuda, S. and A. Mizuno. Saturation Charge of A Spherical Conductive Particle Imparted by Pulse Charging. to be submitted to J. of Electrostatics.
10. Masuda, S. and Y. Matsumoto. Motion of A Micro-Charged-Particle Within Electrohydrodynamic Field. Electrical Engineering in Japan, Vol. 94, No. 6, 1974 (english).
11. Masuda, S. and A. Mizuno. Initiation Condition and Mode of Back Discharge, J. of Electrostatics, Vol. 4, p. 43, 1977.
12. Masuda, S. and A. Mizuno. Flashover Measurement of Back Discharge. J. of Electrostatics, Vol. 4, p. 220, 1978.

PULSED ENERGIZATION
FOR
ENHANCED ELECTROSTATIC PRECIPITATION
IN
HIGH-RESISTIVITY APPLICATIONS

Paul L. Feldman
Research-Cottrell
Somerville, New Jersey 08876

Helmut I. Milde
Ion Physics Co.
Burlington, Massachusetts 01803

ABSTRACT

A new method of energization for electrostatic precipitators featuring significantly improved particle charging capabilities has been developed and tested in pilot and full scale operations. The technology employs very short duration, high voltage pulses to create intense electrical fields, greatly enhancing particle charging and collection over conventional energization. The paper presents the results of laboratory and full scale verification tests. In addition the technical and economic advantages of pulsed energization are compared with conventional electrostatic precipitation, fabric filtration and other approaches used to handle high resistivity particulate, as generated in the combustion of low sulfur coal for example.

INTRODUCTION

This paper describes a new system for pulsed energization of electrostatic precipitators which has been developed jointly by Research-Cottrell, Inc. and Ion Physics Co. The system has been successfully demonstrated in the laboratory and on a full-scale precipitator serving a PC boiler. It is particularly intended for use in applications requiring the collection of high resistivity dust, such as low sulfur western coal combustion.

Preceding page blank

The concept of pulsed energization for improvement of electrostatic precipitation is not new. In fact there are exampls of very enlightened patents on the subject which issued as long ago as the 1930's. Since then, the concept has been further developed by several of the people well known in electrostatic precipitation including White, Penney, Hall and Masuda. Despite all of this work, commercialization of pulsed energization has been slow because of certain technical and economic problems.[1] The system described in this paper finally allows realization of the benefits of pulsed energization.

CONCEPT AND SYSTEMS

Electrostatic precipitation of high resistivity ash is problematic because of restrictive voltage limitations traceable to dielectric breakdown of the ash layer on the collecting plates. This breakdown appears either as back corona at very high resistivities (10^{12} ohm-cm or greater) or as premature sparking at moderately high resistivities (about 10^{11} ohm-cm). In both cases, electrical energization is at a much lower level than desired, and corona is very poorly distributed along the discharge electrode. These factors adversely affect the precipitation process, and means for improving them can have a significant impact on precipitator performance. For a thorough discussion of the problems of high resistivity precipitation and their causes and effects, the reader is referred to White[1].

The pulsed energization system described here can overcome much of the difficulty in dealing with high resistivity ash. The scheme employed is to superimpose high voltage impulses of very short duration and steep wave front on an underlying, relatively constant potential. This constant "base voltage" is maintained at a level just below the onset of sparking or back corona and provides a field to maintain ion and particle migration toward the collecting plates. In the case of very high resistivity this base voltage may preferrably be below the normal corona starting voltage. The high voltage impulses momentarily raise the total potential well above the sparking or back corona limit.

This pulse voltage can actually be two or three times the base voltage because breakdown of a gas is high with respect to short pulsed potentials[2]. The effect of the high voltage impulses is to initiate strong and uniform corona generation, but by properly adjusting important pulse parameters such as pulse width and frequency, the adverse effects of excessive sparking and back corona can be avoided.

The net result is a significant improvement both in the current density and in the uniformity of its distribution compared to conventional energization. Visual observations in the laboratory and field have spectacularly shown the corona enhancement possible with pulsed energization. An electrode with very spotty corona under conventional energization can literally be made to glow with pulsed energization. The precipitation process benefits directly from the higher and more uniform current density through greater availability of ions for particle charging. Furthermore, the electric field strengths necessary for particle charging and collection are improved by the increased space charge, but the charging field enjoys an additional improvement due to the instantaneously high field strength present during the pulse.

The pulser system has been developed with the guiding consideration of producing a reliable, cost-effective system for immediate use with large industrial and utility precipitators. In doing so, the system design itself had to be adapted so that only components of proven operation and reliability could be used. The resulting first-generation system has been quite successful in meeting the requirements for both effectiveness and reliability, and the planned future development of optional system components makes the prospects for later generation systems even more promising.

The present system consists of a charging supply, the pulse-forming network, a switching device and base voltage isolation. The pulse is generated by charging the pulse-forming network to a predetermined voltage and then activating the switch which initiates the energy transfer from the pulse forming network to the discharge electrode structure of the precipitator. After the pulse has decayed, the switch recovers its electrical hold-off strength and the pulse-forming network can be recharged. The system allows control over a wide range of the critical pulse characteristics of pulse amplitude, pulse width and pulse repetition rate.

The system can be used in both newly designed precipitators and in retrofit applications. In the case of a retrofit, installation is very convenient because all of the changes are external to the precipitator.

LABORATORY STUDY

Pulser system development and component reliability testing has been conducted by Ion Physics Co. and Research-Cottrell for more than five years. During this time all of the pulser variables have been explored over a range of precipitation parameters and dust characteristics and with several precipitator electrode geometries. For purposes of this paper, however, only those results pertaining to the collection of high resistivity dust in conventional geometry will be discussed since this is the area most immediately applicable. The objective of the series of tests reported here was to demonstrate the improvement in performance attainable with pulsed energization as compared to conventional energization at two resistivity levels. Thus in this series of tests all operating parameters of the system such as flow rate, particulate loading, etc. were held constant, and only the mode of energization was varied.

Laboratory Setup

Figure 1 shows the arrangement of the precipitator system used in the laboratory test program. Dust was fed to the system by a weigh feeder in order to accurately control dust loading. The dust was well dispersed in the inlet air stream by means of an ejector-distributor arrangement in the duct. Electric heaters were used to heat the inlet air to its desired operating temperature prior to entraining the dust. Downstream of the dust feed, a low-efficiency mechanical collector was used to remove larger particles and, therefore, present the precipitator with a relatively fine particle size.

In all of the runs, hydrated alumina was used as the high-resistivity dust. Its particle size distribution at the precipitator inlet was characterized by a mean diameter of 4.5 microns and a geometric standard deviation of 2.76. Particulate loading at the precipitator inlet was 3 grains/scfd. Resistivity of the dust was controlled by varying the operating temperature. For the tests reported in this paper the temperature levels were chosen to provide operation at very high resistivity with back-corona limitation, and moderately high resistivity with sparking limitation: at 300°F the resistivity of the dust was 5×10^{12} ohm-cm and at 200°F the resistivity was 2.5×10^{11} ohm-cm.

The precipitator itself was a single-duct precipitator consisting of three energized sections with total collecting plate area of 54 ft^2. Each section was 4.5 feet long with an effective flow height of 2 feet. Collecting plate spacing was 9 inches, and discharge electrodes were .109 inch shrouded wires spaced 5¼ inches apart. The air velocity in the precipitator was 5 feet/sec for all runs. Thus the specific collection area (SCA) was 120 ft^2/1000 acfm.

The precipitator was operated as a two stage precipitator, the inlet section being energized separately from the downstream two sections. During the pulse-energized runs, only the inlet section was pulsed, the downstream sections conventionally energized, serving as the collecting section. Base electrical energization of both sections was provided by 70 kVp full-wave rectified power supplies. Pulses were superimposed on the base voltage in the inlet section from the pulser system.

Prior to the test program outlet particulate concentrations from the precipitator were measured over a range of precipitation efficiencies under the operating conditions described above. These loadings were correlated with optical density as measured at the precipitator outlet using a Lear-Siegler RM4 optical transmissometer. During the test program transmissometer readings were taken and the correlation curve was used to determine the outlet loading during each run for precipitation efficiency calculation.

Laboratory Results

Table I presents the individual test results achieved during the test program. Results are grouped according to resistivity level and mode of operation (pulsed or conventional), not chronologically. Each of the runs was made at its optimum condition of energization; i.e. for the conventional runs, voltage was set at a value yielding maximum efficiency, and for the pulsed runs, the combination of base voltage, pulse voltage, pulse width, and frequency was set to yield best performance. Thus the numbers reported in Table I are optimums so that comparison among modes can be made on the basis of best performance. All of the runs are shown here to provide an indication of the reproducibility of results.

Table I. Laboratory data for pulsed vs. conventional energization

Mode of Operation	Temp (^oK)	Resistivity (ohm-cm)	Precipitation Efficiency (%)	w (m/sec)	w_k (m/se
Conventional	367	2.5×10^{11}	96.3	.140	.286
			98.0	.166	.375
			96.3	.140	.286
			96.3	.140	.286
			95.7	.133	.265
			95.3	.129	.253
			97.5	.156	.342
			97.0	.148	.315
Pulsed	367	2.5×10^{11}	98.0	.166	.375
			98.0	.166	.375
			98.3	.172	.401
			97.3	.153	.330
			99.7	.246	.707
			98.3	.172	.401
			98.0	.166	.375
			98.0	.166	.375
Conventional	422	5×10^{12}	82.7	.0743	.104
			82.7	.0743	.104
			80.3	.0688	.092
			82.3	.0733	.102
			80.0	.0681	.090
			82.7	.0743	.104
Pulsed	422	5×10^{12}	95.3	.129	.253
			96.0	.136	.275
			95.3	.129	.253
			94.3	.121	.228

All runs were conducted with inlet loading = 3 grain/scf and gas velocity 5 feet/sec.
Precipitator electrode geometries were conventional as described in text.
Each test was run at optimum electrical energization.

For each of the cases Table I shows collection efficiency, Deutsch migration velocity, w, and the modified migration velocity, w_k. The modified migration velocity is preferred for use in comparative evaluations of pulsed vs. unpulsed performance because its value in a given case is independent of the efficiency level. Details of the reasoning behind this preference and development of the modified equation are given in an earlier paper by Feldman[3]. The modified efficiency equation is:

$$1 - \eta = \exp\left[-\left(w_k A/V\right)^m\right] \qquad (1)$$

where

η = collection efficiency, fractional

A = collecting area, m^2

V = volumetric flow rate, m^3/sec

w_k = modified migration velocity, m/sec

m = exponent depending on inlet particle size distribution For the laboratory dust m = .635.

Examination of Table I shows the expected trends in the data. Precipitator efficiencies for 5×10^{12} ohm-cm resistivity level are lower than for the 2.5×10^{11} level for both pulsed and conventional operation. However, at each resistivity level the pulsed operation is more efficient than conventional. In order to quantify the improvement in performance attributable to pulsed energization, a single value of w_k was calculated for each mode of operation based on the average penetration $(1-\eta)$ for that mode. A very good quantitative measure of improvement due to pulsing is then the ratio of these w_k values at each resistivity level. This is because w_k is a direct indicator of the level of precipitator energization.[3] Since the w_k ratio represents an enhancement of precipitator energization it is termed the "enhancement factor", H. Table II shows the effective w_k for each operating mode and the enhancement factors at each resistivity level.

Because of the large number of individual runs involved in Table I and their good reproducibility in each mode of operation, it is felt that the values of the enhancement factor and their difference at the two resistivity levels have very significant meaning. The fact that the level of enhancement of w_k increases as resistivity increases

Table II. Averaged laboratory data for each operating mode

Mode of Operation	Temp (^{o}K)	Resistivity (ohm-cm)	Precipitation Efficiency (%)	w_k m/sec	Enhanceme Factor
Conventional	367	2.5×10^{11}	96.55	.295	1.33
Pulsed			98.20	.392	
Conventional	422	5×10^{12}	81.80	.0993	2.53
Pulsed			95.22	.251	

supports the previously described concept of the effect of pulsed energization. The poorer the conventional energization, the greater degree of improvement possible by pulsing. It should be noted, however, that although the enhancement factor increases with resistivity, the value of w_k for both conventional and pulsed energization decreases. This shows that pulse-energized precipitation as well as conventional is subject to resistivity caused limitations although the limitation to the pulsed performance is much less severe. This is reasonable based on theory, because, no matter how precipitator energization is achieved, dielectric breakdown of the dust layer will preclude further useful energization. With pulsed energization, however, greater and more uniform ion densities and higher effective field strengths exist when this limit is reached.

It was mentioned previously that only the inlet section of the laboratory precipitator was pulsed. This is consistent with the expectation that pulsed energization acts primarily to enhance particle charge. Thus, the laboratory setup represents a two-stage precipitator in which enhanced charging is accomplished in the inlet section and the downstream sections act primarily as collecting sections. Indeed it was found in a series of tests, not specifically reported here, that pulsing more than the inlet section results in no significant performance inprovement over pulsing only the inlet section. Thus, use of the pulser actually invites the development of a two-stage precipitator. Discussion of this in detail is beyond the scope of this paper. However, it is realized that significant additional gains in precipitator performance can be made through optimization of electrode configuration and geometry separately for the charging and collection functions. Tests have been run with this objective and further gains in performance have been measured. Work is continuing to take full advantage of this extra degree of freedom in precipitator design.

FULL SCALE RESULTS

Full-scale investigation of pulsed energization was conducted on a Research-Cottrell precipitator following a mechanical collector serving a pulverized coal fired boiler. Each of its two fields was equipped with separate pulsers. Each pulsed field contained a collecting plate area of 8200 ft^2. Plate spacing was 9 inches and discharge electrodes were .109 inch diameter wires spaced 5½" apart. The downstream, unpulsed precipitator consisted of two fields each with collecting area of 10,800 ft^2. The total collecting area of the precipitators was therefore 38,000 ft^2.

In order to characterize pulsed and conventional operation of the precipitator, a full test program was run at the site. During the test program, low-sulfur Eastern Bituminous coal was burned and the boiler was operated steadily at full load. The coal burned during the test program averaged about 1.1% sulfur with 18% ash content. Gas volume flow through the precipitator varied about 110,000 acfm.

Data taken during the test program included in-situ resistivity measurements, particle size distributions, velocity traverses, stack opacity readings using a Lear Siegler transmissometer, precipitator outlet loadings, mechanical collector inlet loadings, and all electrical and boiler operating data. Coal and ash samples were collected during each run. Due to inacceptable flow patterns between the mechanical collector outlet and precipitator inlet it was not possible to measure directly the precipitator inlet loading and size distribution. However, by applying the mechanical collector performance curves to the measured mechanical collector inlet data it was possible to calculate the loading and particle size distribution to the precipitator for purposes of isolating precipitator performance. The size distribution of the ash to the inlet of the precipitator was found to be characterized by a mean diameter of 2.2 microns with a geometric standard deviation of 2.2.

Operation of the precipitator during the test program was typical of the moderately-high resistivity limitation characterized by heavy sparking at very low current levels resulting in poor energization. The in-situ resistivity measurements were compatible with this type of operation. They ranged from 1×10^{11} to 9×10^{11} ohm-cm, averaging about 5×10^{11} ohm-cm.

All of the runs made during the test program were at optimum levels of operation for the mode being tested, i.e. both pulsed and unpulsed operations were set to yield maximum collection efficiency. Pulser variables in all runs were set at levels previously determined to be optimum.

Because it was possible to pulse each of the two inlet fields independently, four modes of operation were tested:

1) All fields energized conventionally.

2) Inlet field (A) pulsed, others conventional.

3) Second field (B) pulsed, others conventional.

4) Both inlet fields (A+B) pulsed, others conventional.

Table III presents data for runs made during the test program. The data are grouped by the mode of operation as described above, not chronologically. The chronological order of the runs is also indicated, showing how operation was switched among the modes of operation. This was done so that the effects of variation in coal and boiler operation could be minimized. As with the laboratory data, precipitator efficiency, w, and w_k are reported for each run. In addition, the average stack opacity and specific collection area for each run are reported; variations in SCA were due to fluctuations in gas volume. Finally the enhancement factor, H, is reported for each pulsed run. It is based on the average value of w_k of .0805 for the unpulsed runs.

For the particle size distribution determined at the inlet to the precipitator, the exponent, m, in the modified Deutsch efficiency equation is essentially the same as found for the laboratory dust, i.e. 0.625. The actual levels of w and w_k are lower for the full-scale tests than for the corresponding laboratory tests. This is a normally expected difference.

Examination of the data in Table III shows consistent improvement in performance creditable to pulsed energization. The best improvement occurred in those runs in which both fields A and B were pulsed; the average enhancement factor for these four runs was 1.5. Pulsing either field A alone or B alone also improved performance in every run but not to the same extent as A and B together.

While the test program was being conducted it was very obvious, just by observing the stack, that the pulsed modes of operation were improving the precipitator performance. Figure 2 illustrates this fact by plotting stack opacity vs. number of sections pulsed. This plot clearly shows the benefits in going from zero to one to two pulsed fields in the precipitator. In fact the plot appears to indicate that further significant benefits can be realized by pulsing additional fields.

The improvement in going from one to two pulsed fields is shown both in the enhancement factors in Table III and in the opacity reduction in Figure 2. At first this appears to contradict the laboratory results which showed essentially no additional improvement in pulsing more than one section.

Table III. Full-scale precipitator data for pulsed vs. conventional energization.

Fields Pulsed	Chronological Number	SCA (ft^2/1000 acfm)	Precipitator Efficiency (%)	Stack Opacity (%)	w (m/sec)	w_k (m/sec)	H
None	4	341	93.84	25.9	.0415	.0768	--
None	7	369	95.70	25.6	.0433	.0861	--
None	10	351	94.58	26.7	.0422	.0802	--
A	1	340	95.29	23.7	.0457	.0893	1.11
A	5	329	98.28	15.6	.0627	.145	1.80
A	9	339	96.05	21.5	.0484	.0978	1.21
B	8	349	95.35	22.8	.0447	.0876	1.09
B	11	371	95.56	20.8	.0426	.0842	1.05
A+B	2	337	97.84	16.3	.0578	.129	1.60
A+B	3	355	97.99	17.0	.0559	.127	1.58
A+B	6	371	98.24	16.3	.0553	.128	1.59
A+B	12	371	97.17	16.7	.0488	.105	1.30

The explanation for this probably lies in the fact that the full scale operation is limited at a lower level of energization than the laboratory for both pulsed and unpulsed operation. It is, therefore, reasonable to expect that a greater pulsed precipitator length is necessary in the full-scale application to accomodate the benefits of enhanced energization. In fact, it may further be expected that enhancement factors greater than those measured in the laboratory are possible in this situation because of the very low energization basis of conventional operation. This is indicated by the data in Table III and Figure 2.

IMPLICATIONS TO NEW AND RETROFIT INSTALLATIONS

Laboratory and full-scale tests have confirmed that the pulsed energization system developed by Ion Physics Co. and Research-Cottrell significantly enhances precipitator performance for the collection of high resistivity dust. Laboratory data showed enhancement factors in the range of 1.33 to 2.53 for moderately high to very high resistivity; field data for a moderately high resistivity ash showed the ratio to be 1.5.

It is now of interest to use this information with equation (1) to assess the impact of pulsed energization in two important classes of application: (1) for a new precipitator, the size reduction creditable to pulsed energization, and (2) for a retrofit application, the improvement in efficiency achievable with pulsed energization.

Figure 3 shows the percent precipitator area reduction possible with pulsed energization, as a function of the enhancement factor. Using conservative value of 1.5, for example, it is seen that a pulse-energized precipitator can be built with 33% less collecting area than a conventional precipitator to achieve the same efficiency level.

For retrofit applications, Figure 4 indicates the efficiency enhancement possible with pulsed energization for a typical pulverized coal boiler application ($m = .5$ in equation (1)) assuming reasonable values of H. For example, with $H = 1.5$, a 96% efficient precipitator can be improved 98.1% by incorporating pulsed energization.

ECONOMICS

From the foregoing, the economic implications of pulsing in high resistivity applications are obvious. Reductions in collection electrode area per unit volume (SCA) are directly related to capital and operating costs.

Table IV. Bases for cost estimates

Efficiencies: 99.5%

Resistivity: 1×10^{12} ohm-cm

Cold precipitator SCA; 729 ft^2/1000

Cold precipitator power: 0.5 watts/ft^2

Cold precipitator
 Pulse energization enhancement factors (a) 1.5
 2.0

Hot precipitator SCA: 365 ft^2/1000

Hot precipitator power: 1.0 watts/ft^2

Fabric filter A/C ratio: 2.5

Fabric filter bag life: 2 years

Comparative cost estimates of several particulate control alternatives using the methods described by Bubenick[8] have been developed. The parameters assumed for these estimates are shown in Table IV.

Figure 5 shows the capital investment in \$/KW versus the power output of the boiler served for each of the options. The cost shown here is the installed cost to the user of the flange-to-flange collector with structural support and typical accessories.

Figure 6 shows the annual cost to own and operate the collector. This includes all direct operating costs such as labor, maintenance and utilities, plus capital charges including interest and depreciation.

Figures 5 and 6 demonstrate the economic viability of pulsed energization compared with other generic options for high resistivity conditions.

CONCLUSIONS

1. The pulsed energization system developed by Research-Cottrell and Ion Physics Co. is effective in enhancing the electrostatic precipitation of high resistivity dust when precipitator energization is limited by premature sparking or back corona.

2. Laboratory measurements indicated that w_k is increased by pulsed energization by a factor of 1.33 for a moderately high resistivity dust to 2.53 for a very high resistivity dust.

3. Tests on a full scale precipitator have shown that w_k is increased by pulsed energization by a factor of 1.5 when collecting ash from a low-sulfur Eastern bituminous coal. Trends in the data strongly indicate even further increase is possible.

4. Economics of the pulsed energization system are favorable comparable with other alternatives for collection of high resistivity dust. Further improvements in pulser system costs are expected in later generations.

5. The pulser system is especially advantageous in retrofit applications because of cost and ease of installation. No internal precipitator or fluework changes are normally necessary, so installation of the system can be done without process shutdown.

NOMENCLATURE

A	Precipitator collecting area, m^2
H	Enhancement factor due to pulsed energization
m	Exponent in modified Deutsch equation
V	Volumetric gas flow rate, m^3/sec
w	Deutsch migration velocity, m/sec
w_k	Modified Deutsch migration velocity, m/sec
η	Precipitator collection efficiency

REFERENCES

1. H. J. White, "Resistivity Problems in Electrostatic Precipitation", JAPCA 24(4): 314 (1974).

2. P. Felsenthal and J. M. Proud, "Nanosecond-Pulsed Breakdown in Gases," Physical Review 139(6A): A1796 (1965).

3. P. L. Feldman, "Effects of Particle Size Distribution on the Performance of Electrostatic Precipitators," Paper 75.02-3 presented at 68th Annual Meeting of the Air Pollution Control Association, Boston, MA, June, 1975.

4. D. V. Bubenick, "Economic Comparison of Selected Scenarios for Electrostatic Precipitators and Fabric Filters," JAPCA 28(3): 279 (1978).

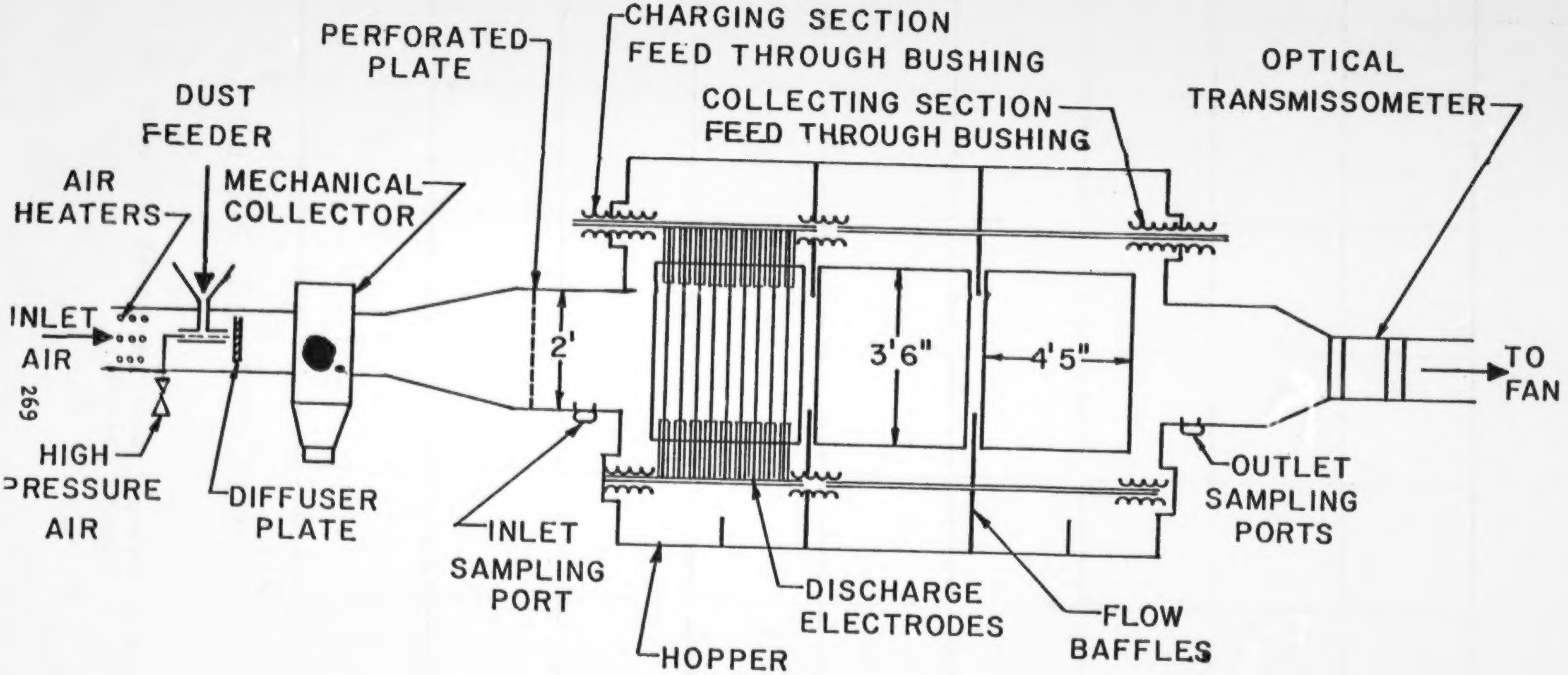
CHARGING SECTION
FEED THROUGH BUSHING
COLLECTING SECTION
FEED THROUGH BUSHING
OPTICAL
TRANSMISSOMETER
PERFORATED
PLATE
DUST
FEEDER
AIR
HEATERS
MECHANICAL
COLLECTOR
INLET
AIR
2'
3'6"
4'5"
TO
FAN
HIGH
PRESSURE
AIR
DIFFUSER
PLATE
INLET
SAMPLING
PORT
OUTLET
SAMPLING
PORTS
DISCHARGE
ELECTRODES
FLOW
BAFFLES
HOPPER

Figure 1 Laboratory Precipitator Arrangement

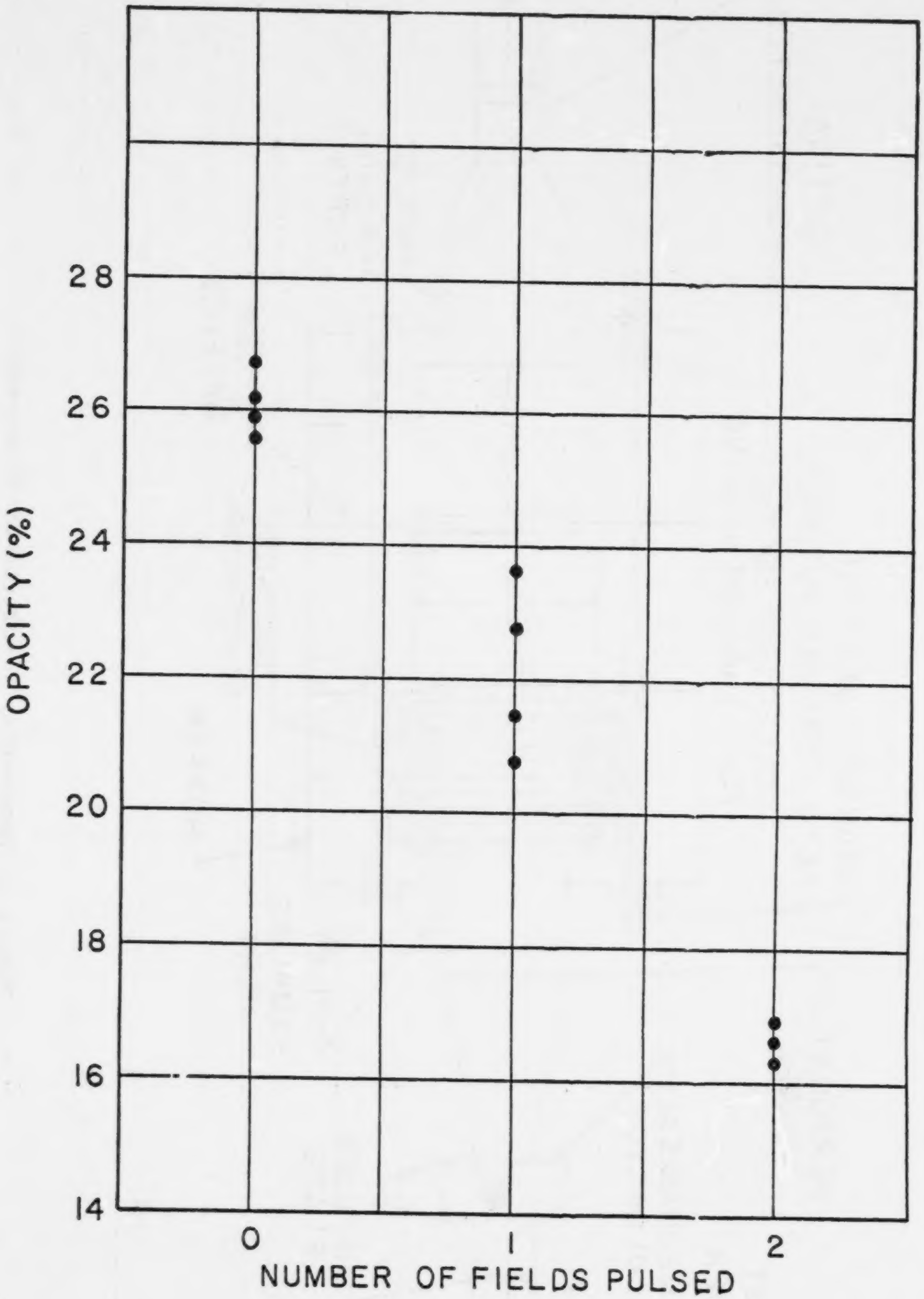

Figure 2 Stack Opacity Response to Number of Fields Pulsed

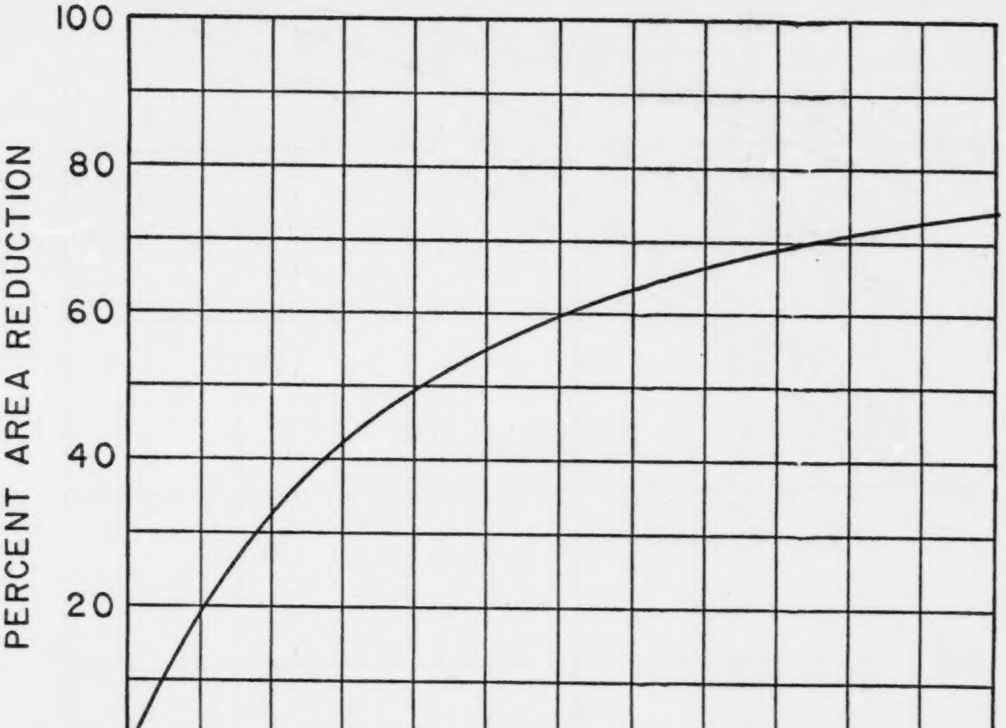

Figure 3 Precipitator Area Reduction Possible With Pulsed Energization

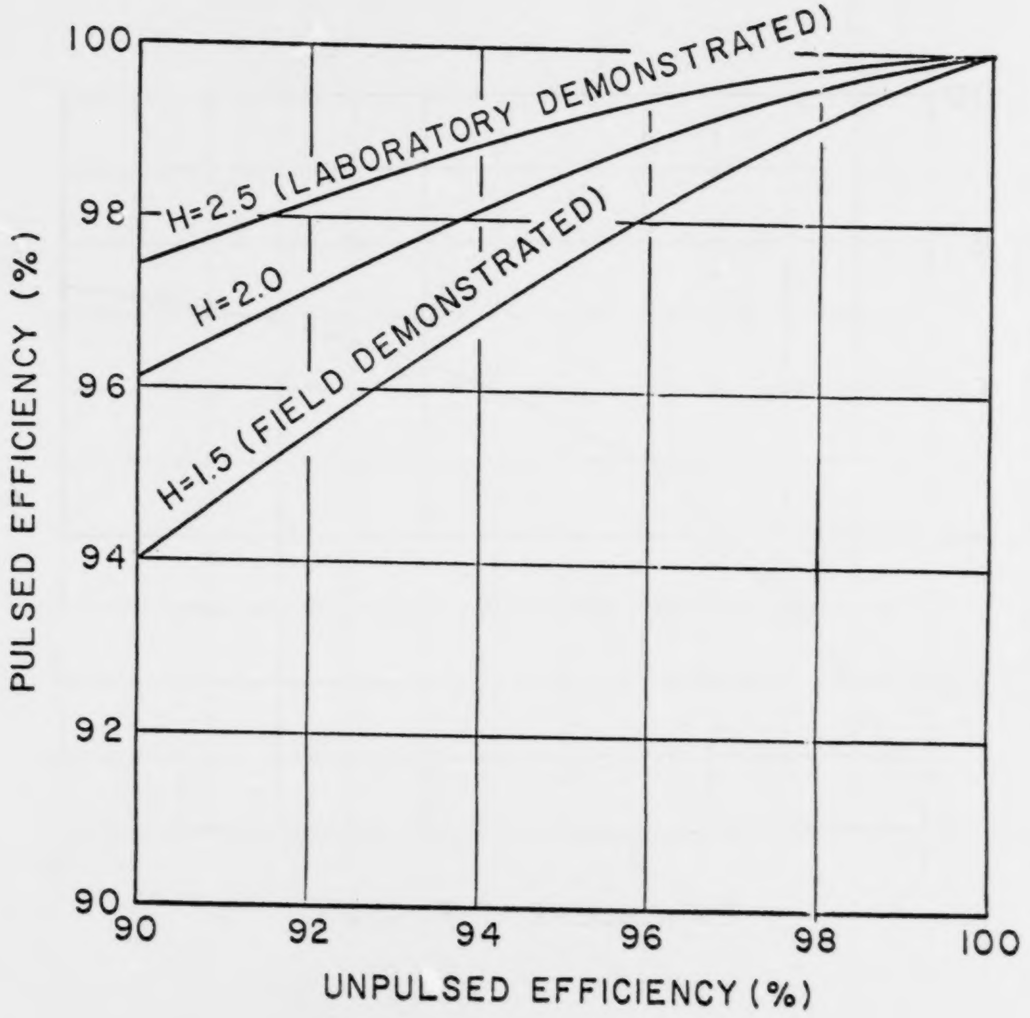

Figure 4 Efficiency Improvement Possible with Pulsod Energization in Retrofit Installations

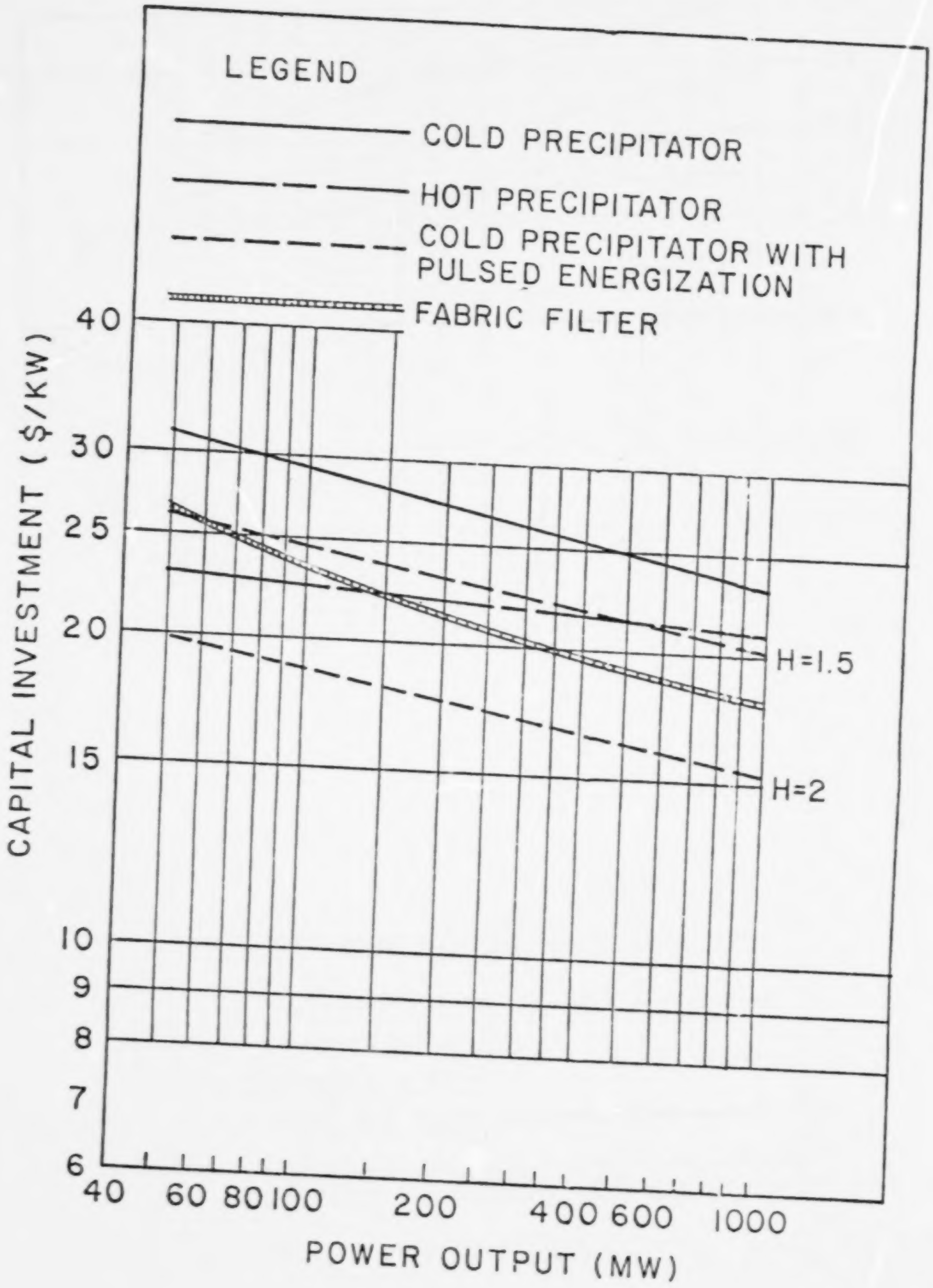

Figure 5 Capital Investment for Various High Resistivity Gas Cleaning Options

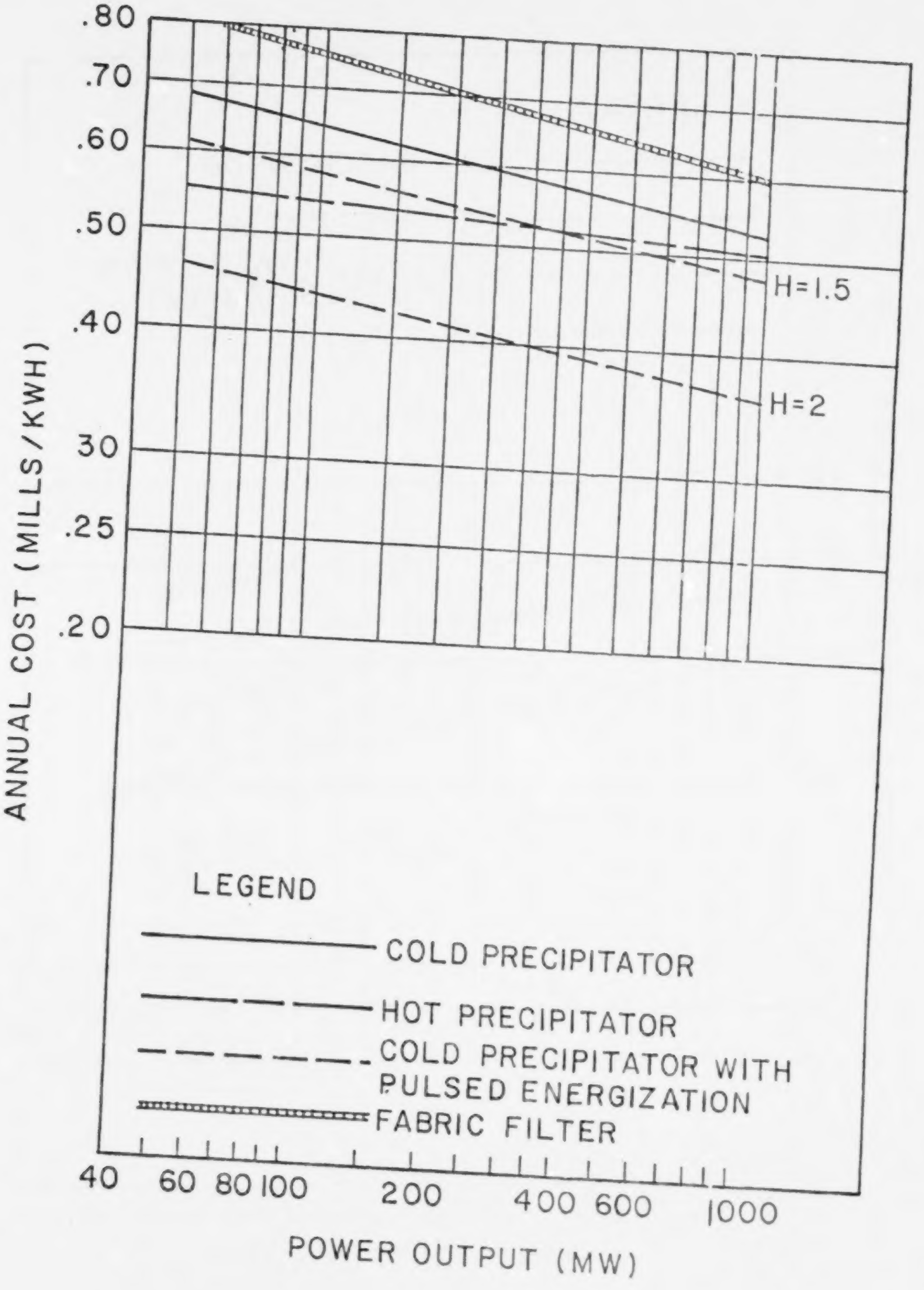

Figure 6 Operating Costs for Various High Resistivity Gas Cleaning Options

A NEW PRECHARGER FOR TWO-STAGE ELECTROSTATIC PRECIPITATION OF HIGH RESISTIVITY DUST

D. H. Pontius
P. V. Bush
Southern Research Institute
Birmingham, Alabama 35205

and

L. E. Sparks
U.S. Environmental Protection Agency
Industrial Environmental Research Laboratory
Research Triangle Park, North Carolina 27711

ABSTRACT

A new particle charging device is described in which the effects of back corona resulting from the presence of high resistivity dust are confined to a narrow region near a planar passive electrode by the action of a properly biased screen electrode. A small pilot scale device has been constructed and tested in the presence of particulate matter having resistivity above 10^{12} ohm-cm.

INTRODUCTION

The degradation of the performance of an electrostatic precipitator resulting from the presence of particulate material having a resistivity of more than approximately 5×10^{10} Ω-cm is due to a reduction in particle charging effectiveness. This is not because particles having high electrical resistivity are intrinsically more difficult to charge, but because back corona, resulting from deposition of the material on the passive electrode, produces a bipolar ion field. When ions of both positive and negative polarity are present in the charging region, the competing effects of the two produce very poor net particle charging results.

The approach taken by Southern Research Institute in dealing with the high resistivity problem is based on a two-stage ESP concept in which a novel technique is employed for control of the problem of high resistivity in the relatively high current density first stage (precharger), and the second stage (collector) is operated at a very low current density and high electric field strength.

THREE-ELECTRODE PRECHARGER CONCEPT

In research sponsored by the Particulate Technology Branch of the Industrial Environmental Research Laboratory, Environmental Protection Agency, Research Triangle Park, North Carolina, Southern Research Institute has devised and investigated the performance of a three-electrode system for controlling the effects of back corona in a particle precharger. In this device two of the three electrodes are the conventional corona discharge and passive electrodes. The third is a screen electrode placed near the passive electrode. Separate power supplies are provided for the corona discharge and screen electrodes. The passive electrode is set at ground potential.

The general principle of operation is based on the use of the screen electrode as a sink for ions generated at the passive electrode as a result of back corona effects. Consider, for example, a two electrode system where the corona discharge electrode is at a high negative potential with respect to the grounded passive electrode. Now, locate an equipotential surface near the passive electrode and insert a conducting screen coincident with that equipotential surface. If the screen voltage is set equal to the original potential on the surface, the electric field will be practically undisturbed in comparison with the original field. Only the non-zero thickness of the wires in the screen will cause very localized modifications to the field. A corona current originating at the discharge electrode will be distributed such that a fraction of the total (equal to the ratio of open area to total surface of the screen) will reach the passive electrode. The remainder of the current will be intercepted by the screen.

Now, if the potential on the screen electrode is made more negative, the field near the screen will become distorted in such a way that negative ions from the discharge electrode will be repelled from the screen wires and forced toward the open area, through which they can proceed to the plate. If we introduce high resistivity particulate material into the system, deposition will occur on both the plate and the screen electrodes. Since negative ions from the discharge electrode are being repelled by the screen, it must have a lower current density than the plate, and hence corona from the screen electrode would probably not occur. If back corona occurs, the positive ions from the passive electrode would be attracted to the screen electrode, where many would be captured and removed from the system. If most of the positive ions resulting from back corona can be captured by the screen electrode, the ion field between the screen and the discharge electrode would be essentially unipolar.

EXPERIMENTAL VERIFICATION

Preliminary experimental tests were run to verify the basic concepts involved in the three-electrode system discussed in the preceding paragraphs. The laboratory apparatus used for the preliminary investigation was a small point-plane corona system with a screen electrode mounted parallel to the plate. The system was operated inside an oven, and fly ash was dispersed between the electrodes by means of an elutriator. Effectiveness of the concept is interpreted in terms of the relative magnitudes of the current measured for each electrode. When back corona occurs the plate current should rise significantly. If the screen grid is effective in removing ions resulting from back corona, there should be a rise in screen current consistent and commensurate with the rise in plate current, and the discharge electrode current should remain nearly constant.

Figure 1 shows the results of an experiment where the behavior was near that predicted. After an overall initial drop in current at all electrodes (cause uncertain, possibly because of development of a space charge) back corona apparently set in rapidly. The plate current and screen current increased quite consistently. The corona discharge current rose also, but by less than 50%, compared with a 7-fold increase in plate current.

Following the preliminary experiments described above, a small laboratory-scale device was designed and constructed in order to test the three-electrode concept in a wire-plate configuration. The precharger, having plates 30 cm high and plate-to-plate separation of approximately 18 cm, was installed in the test section of a pilot scale ESP in order to evaluate its performance under conditions of elevated temperature and dust loading.

Figure 2 shows the results of one test where the charger was subjected to a dust loading of approximately 3.4 g/m^3 at a temperature of 125°C. The charger grids and plates were continually rapped with pulsed solenoids at a rapping frequency of 2 sec^{-1}. Back corona is evident in the sharp increase in the plate current. The grid voltage was adjusted throughout the experiment to maintain the corona current at its initial value. In this case, the grid electrode effectively suppressed the back corona for the duration of the test. The random fluctuations in the grid and plate currents could be a result of uneven dust feeding, an effect related to the rapping of plates and grids, or some combination of the two.

This experiment also included a determination of charging effectiveness. Particle charging measurements were made by collecting fly ash on an isolated silver filter which was placed immediately downstream from the charger. The filter was connected to an electrometer so that the integrated charge could be monitored for a sample of fly ash which was passed through the charger. The collected fly ash was then weighed and

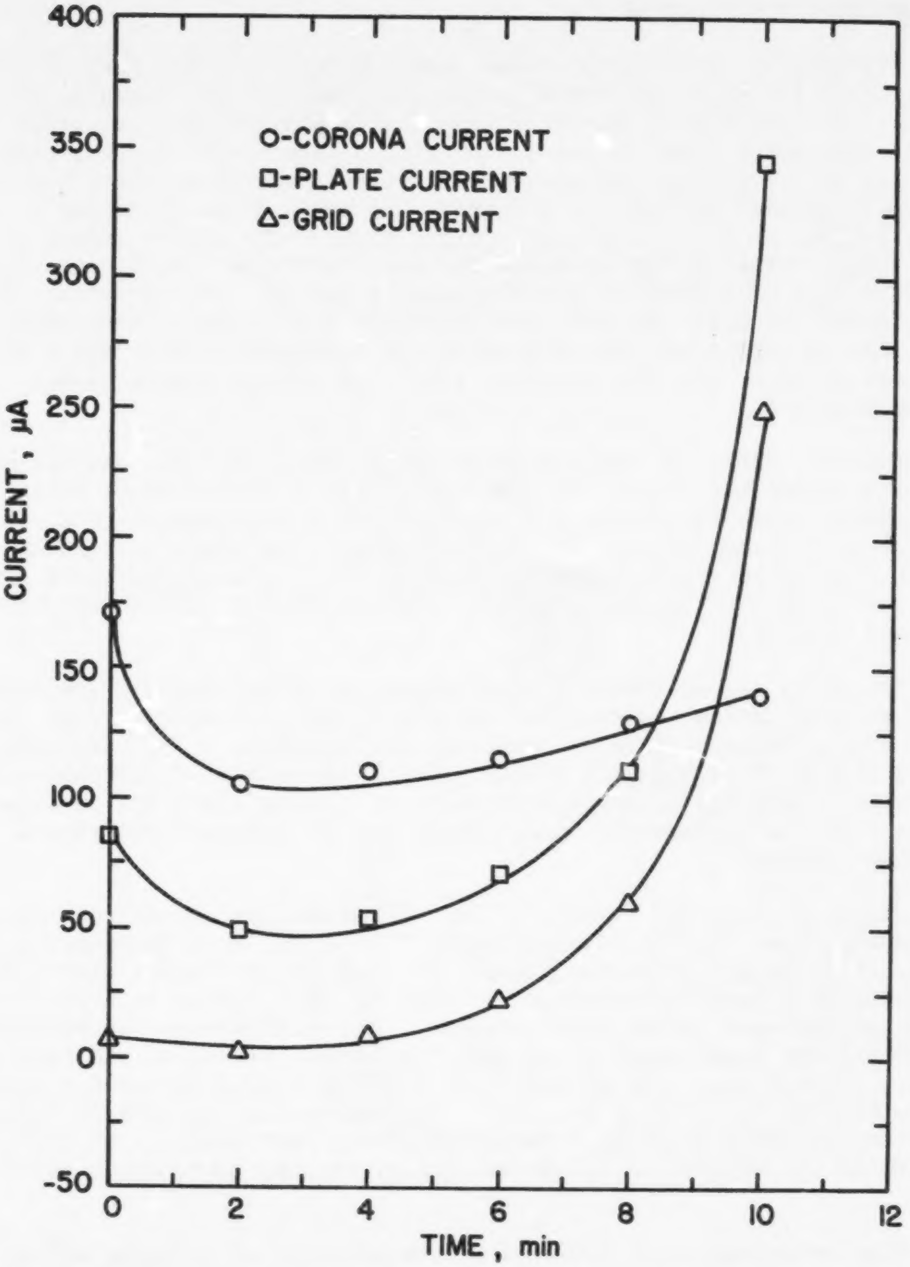

Figure 1. Current as a function of time for each electrode. Corona discharge electrode is at -25 kV, and screen electrode is at -9 kV. Dust laden air is injected at 1.2 l/min.

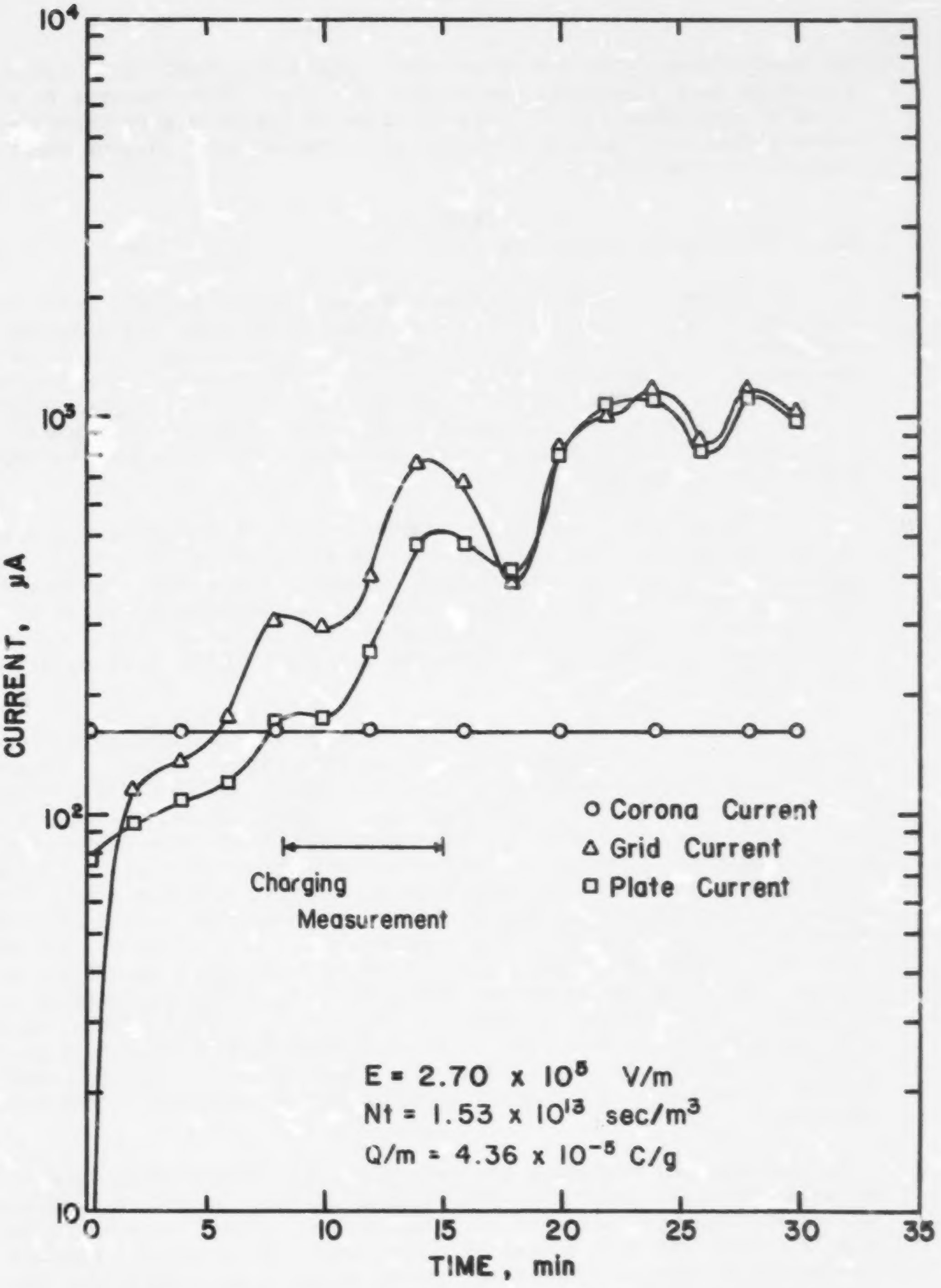

Figure 2. Test Results of a Three-Electrode Charger Used for Back Corona Suppression
Temperature = 125°C
Corona electrode-to-plate spacing = 8.9 cm
Grid electrode-to-plate spacing = 2.6 cm
Dust loading ≈ 3.4 g/m³

the charge/mass ratio was calculated. The charge/mass (Q/m) ratio obtained in this experiment was 4.36×10^{-5} C/g. This compares to a Q/m value of less than 1×10^{-6} C/g obtained in previous experiments with a conventional wire-plate precharger at a similar dust loading where the resistivity was comparable.

SMALL PILOT SCALE INVESTIGATION

Following a series of laboratory scale tests, a small pilot scale charging device, capable of handling about 2000 acfm, was designed and constructed. In the initial testing phase an existing pilot scale ESP was used as the particle collection stage. Experiments were done with fly ash redispersed in air. The aerosol was heated to produce high resistivity particles. Values of resistivity, measured by both an in situ probe and the ASME-28 method, were above 10^{12} Ω-cm for the experimental conditions used.

The pilot scale precharger, shown lying on its side during assembly in the photograph, Figure 3, consists of two parallel sections. The plate and screen electrodes are approximately 1.2 m high and extend 15 cm along the direction of gas flow. Protruding through the top of the housing are spring loaded plate supports and rapping rods. When the device is installed for testing, a pneumatic rapping assembly fits on top of the housing.

Since adjustments in the screen voltage are required to maintain proper operation of the precharger when back corona occurs, a programmable high voltage power supply (Spellman Model RHR15PN225/RVC/TP/FG) was used to provide the screen voltage. A small signal voltage, 0 to 6 Vdc, controls the output of this power supply over the range of 0 to 15 kV. Automatic control of the screen voltage is accomplished by means of the electronic circuit shown schematically in Figure 4. An input signal is taken from the ground return on the primary corona current power supply by means of a 4N25 optoisolator. The signal is then amplified by a factor of 10 and passed on to an integrating amplifier, which smooths out rapid transient voltages. A dc bias voltage, derived from a voltage divider network, is added to the control signal at the input of the integrating circuit. The dc bias is used to set the steady state operating voltage of the screen supply, and variations in the primary corona current are counteracted by automatic adjustments in the screen voltage.

As a general procedure for each test, a primary corona current was established with clean hot air blowing through the system, and the screen voltage was increased until the screen current dropped to zero. The dust feed was then turned on. Typically, after several minutes of operation, a rise in the screen current would occur, signalling the onset of back corona. When the back corona became severe, changes in the primary corona current could be observed; however, these changes could be controlled by manual or automatic adjustments in the screen voltage.

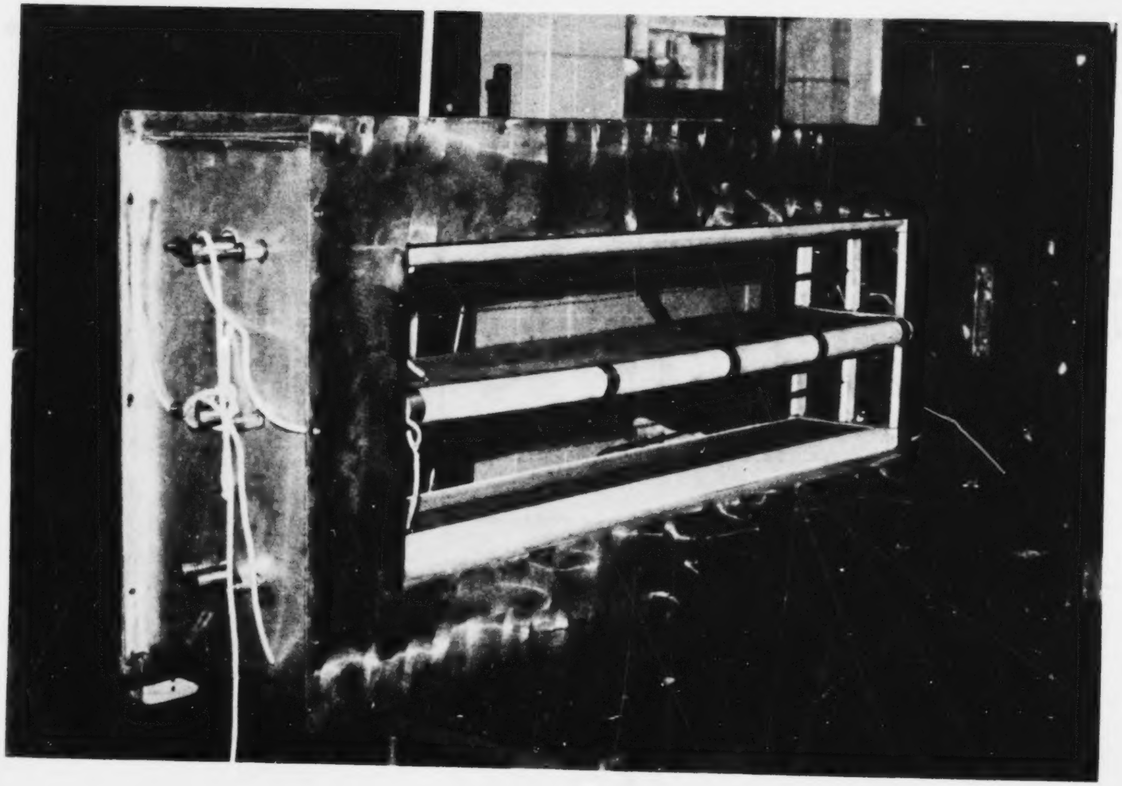

Figure 3. View of the pilot scale precharger on its side.

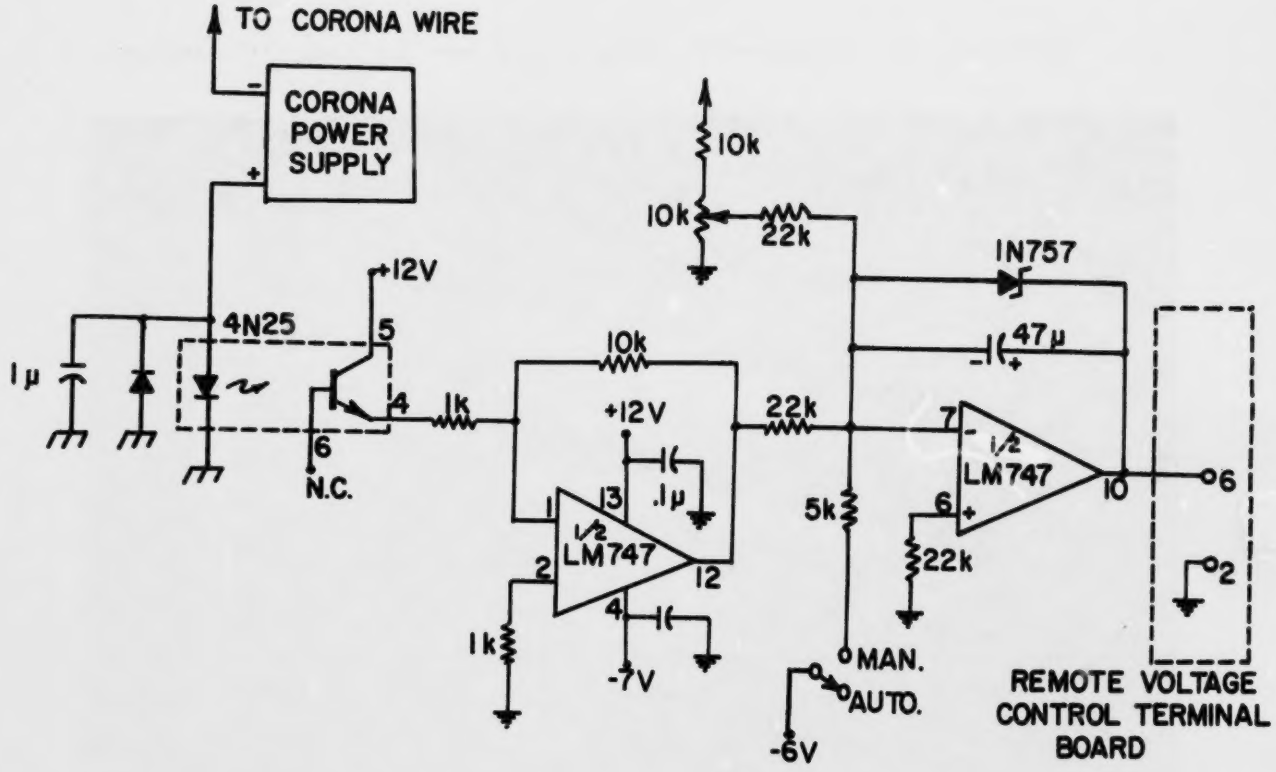
TO CORONA WIRE
CORONA POWER SUPPLY
-
+
1µ
4N25
+12V
5
4
6
N.C.
1k
10k
+12V
13
.1µ
1
2
1/2 LM747
12
4
-7V
1k
10k
10k
22k
22k
IN757
47µ
-
+
7
6
1/2 LM747
10
22k
5k
MAN.
AUTO.
-6V
6
2
REMOTE VOLTAGE CONTROL TERMINAL BOARD

Figure 4. Schematic diagram of the electronic circuit designed to provide automatic adjustment of the precharger screen voltage in response to changes in the primary corona current.

Under proper operating conditions it was possible to maintain the current at the discharge electrode constant even when the back corona current, as observed at the screen electrode, was large in comparison with the primary corona current. Tests up to a few hours duration were carried out where the primary corona current was kept constant in the presence of very large fluctuations in back corona current.

Evaluation of the performance of the precharger was based upon its electrical characteristics, effectiveness in charging particles, and particle collection efficiency in combination with a downstream collector, all in the presence of high resistivity dust. Electrical characteristics of interest were the current density and electric field strength in the region between the discharge electrode and the screens. Particle charging effectiveness was determined by capturing samples of particles downstream from the precharger, on a metallic filter enclosed in an insulating chamber. The filter was connected to the input of an electrometer so that the accumulated charge could be monitored. The charge was then compared with the mass of the sample. Fractional collection efficiency measurements with precharger on and off were made for the two stage system using inertial impactors and optical particle counters.

PILOT SCALE TESTS

The system used for testing the precharger included an air preheater and particulate source upstream of the device and a conventional ESP downstream. Tests were run at 75 and 130°C with fly ash redispersed by a sandblaster. Inertial impactors were used to determine the size distribution of the particles. The mass median diameter is approximately 19 μm. Tests were done with dust loading between 1.9 and 7.6 g/m^3 (0.8 to 3.3 gr/ft^3). Measured values of resistivity were for all tests greater than 10^{12} Ω-cm.

Figure 5 shows the results for a specific test, run over a period of 1 hour. It can be seen that the corona current remained quite constant in spite of extremely large fluctuations in the screen current. During this test the gas temperature was 100°C, and the moisture content was 1.2% by volume. Effects of back corona first occured at about 14 minutes after the beginning of the experiment, as indicated by the first rise in the screen current. A measurement of charge to mass ratio, Q/m, was taken during a 10 minute period of intense back corona activity.

The current density, based on the primary corona current only and normalized to the area of the plate electrode, was 94 nA/cm^2. Using an ion density-residence time product of 9.38×10^{12} sec/m^3 corresponding to that current density, and an electric field strength of 3.15 kV/cm, a theoretical value of Q/m for the particle size distribution was calculated to be 2.9×10^{-6} C/g. The experimental value of Q/m taken during the interval shown in Figure 5 was 2.86×10^{-6} C/g. It may be somewhat fortuitous that the agreement is so close in this particular example; however, it is clear that the charging results agree with the assumption

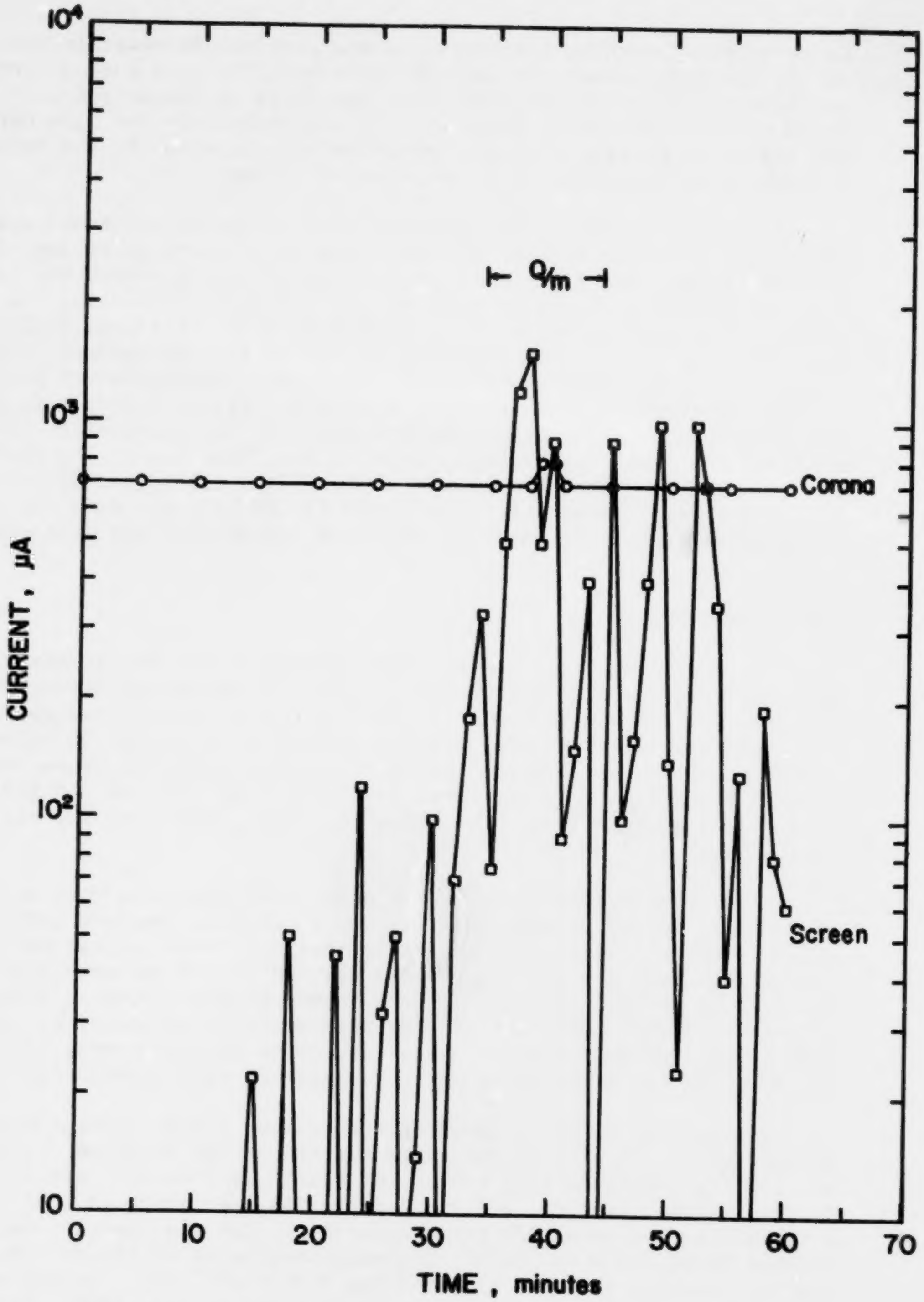

Figure 5. Experimental values of screen and plate current during a test of the pilot scale precharger. The wide variations in grid current indicate a high level of back corona activity.

that the primary corona current produces an essentially unipolar ion field, and that the screen electrode is quite effective in suppressing the effects of back corona.

In comparison with these results, a conventional electrostatic precipitator operated below the condition for onset of back corona with dust resistivity of the order of 10^{12} Ω-cm would be limited to a current density of 0.1 to 1% of the values achieved in these experiments.

A downstream collector for use with the precharger has been designed, and tests will be made in the field to determine overall collection efficiency. The collector was designed with a specific collection area of 33.6 sec/m (171 ft^2/1000 acfm). It is anticipated that a collecting field strength of 5.25×10^5 V/m can be achieved at a low value of current density, so that back corona in the collector can be avoided.

CONCLUSIONS

The precharger concept described in the preceding sections has been shown to be effective in counteracting the effects of back corona on particle charging processes. A two-stage system based on this concept appears to have potential for efficient collection of high resistivity particulate materials without resorting to extremely large values of specific collection area, and without the necessity for injecting chemical additives to reduce resistivity.

ELECTRON BEAM IONIZATION FOR COAL FLY ASH PRECIPITATORS*

R. H. Davis and W. C. Finney
Department of Physics
The Florida State University
Tallahassee, Florida 32306

ABSTRACT

Coal fly ash removal by electrostatic precipitation strongly depends on ion current flux and electric field geometry. In preliminary experiments with accelerated electron beams passing through air, ion current densities have been measured which are 50 times larger than those which can be obtained in a duct type electrostatic precipitator with corona ionization. Theoretical calculations show that even larger values can be obtained with driving voltages higher than the 10 kV available in the preliminary experiments. An additional advantage of the high ion current flux is the enhancement of the electric fields in the vicinity of the collection plate. These results are the basis for a design of an experimental precipitator system with which to test electron beam ionization on reentrained coal fly ash. A comparison of electron beam ionization with the high intensity ionizer developed by EPRI points out both similarities and differences. A further possible application of electron beams lies in the fact that energetic electrons will ionize solid materials as well as gases. Consequently electron irradiation will induce conduction in the fly ash layer deposited on a conduction plate.

REVIEW OF EARLY EXPERIMENTS

Davis and Finney[1] pointed out that the stopping of an energetic electron in air (or stack gas) provides a copious supply of ions. The specific ionization for electrons is approximately 33 eV per ion pair over a wide range of electron energy. Consequently the stopping of a 1 MeV electron produces approximately 3×10^4 ion pair. If these are

Preceding page blank

separated by the presence of an electric field, the incident beam current I_B will produce an ionization current I_A given by

$$I_A = I_B \frac{\Delta T_B}{\Delta T_i} \qquad (1)$$

where ΔT_B is a kinetic energy loss of the primary beam and ΔT_i is the specific ionization. For example, in the case of complete separation, a 1 μA electron beam with an energy loss of 1 MeV will produce 30 mA of ion current.

The electron beam ionization geometry which is analogous to the duct electrostatic precipitator is shown in Fig. 1. In the conventional Cottrell device (Fig. 1a), the plates are at the same potential and a coplanar array of corona wires is maintained at a negative potential.[2] For this choice polarity, the charge on the working ions is negative.

A section of electron beam duct system is shown in Fig. 1b. The corona wires are replaced by a plane of ionization produced by scanning the electron beam parallel to the plates.[3] For purposes of illustration, a "good geometry" electron beam is assumed in that the energy and collimation of the beam are such that the ionization region is approximated by an infinite plane.

The expected ion current density magnification was confirmed by the experiments with the equipment schematic shown in Fig. 2. The current drawn across the center plates (c,c') is plotted as a function of the voltage between the plates as shown in Fig. 3. The current density drawn through the plates was 13 mA/m^2 at 10 kV which is approximately 65 times larger than the space charge limited value for comparable plate separation in a conventional precipitator. Further the comparison was made for the unrealistic assumption of zero on-set voltage for the conventional precipitator.

The nearly ohmic behavior of the curve is itself a point of interest. In the case of space charge limitation across the gap between the plates, the dependence of the current density on voltage is quadratic

$$j \propto V^2 \qquad (2)$$

The observation of a nearly ohmic I-V curve rather than the V^2 dependence expected from space charge limitation may be explained[1] by the establishment of a virtual cathode close to the plate and a resistance determined by the ion mobility.

In practice there would appear to be no advantage in a well collimated "good geometry" although experimentally such geometry permits

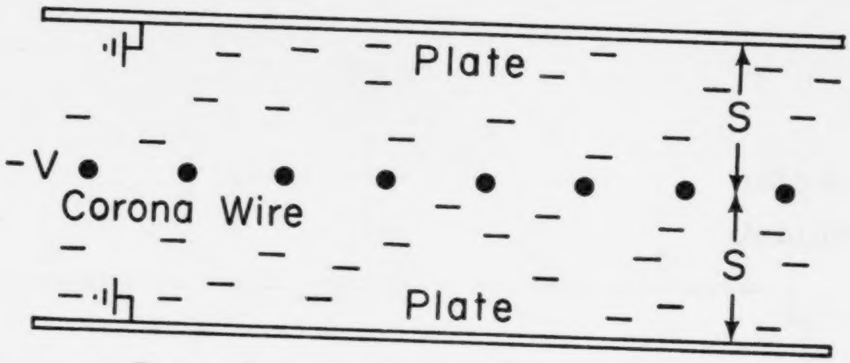

a. Duct Precipitator

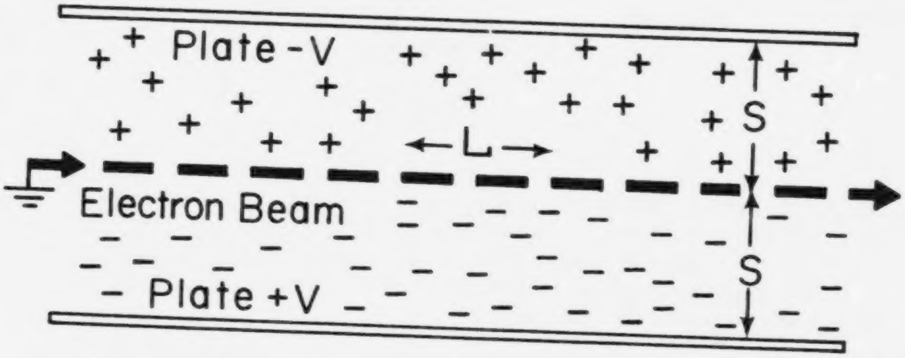

b. Electron Beam Precipitator

Fig. 1. Schematic comparison of corona and electron beam ionization systems. The usual Cottrell geometry is shown in part a. An idealized, high-energy, good-geometry electron beam ionization system is shown in part b. The electron beam is collimated to form an ionization sheet parallel to the collector plates.

control for experimental studies. The angular distribution of the current collected by a plate position at a radius of 10 cm from the beam output window is shown in Fig. 4. The effect of collimation in reducing the ion current density is shown by the lower curve in Fig. 3. The pertinent reason for mentioning collimation in this discussion is to emphasize the flexibility allowed by electron beam ionization with respect to direction of beam (collimation), energy of beam, current, and the possibility of making all of these parameters time dependent. Electron beam ionization is flexible.

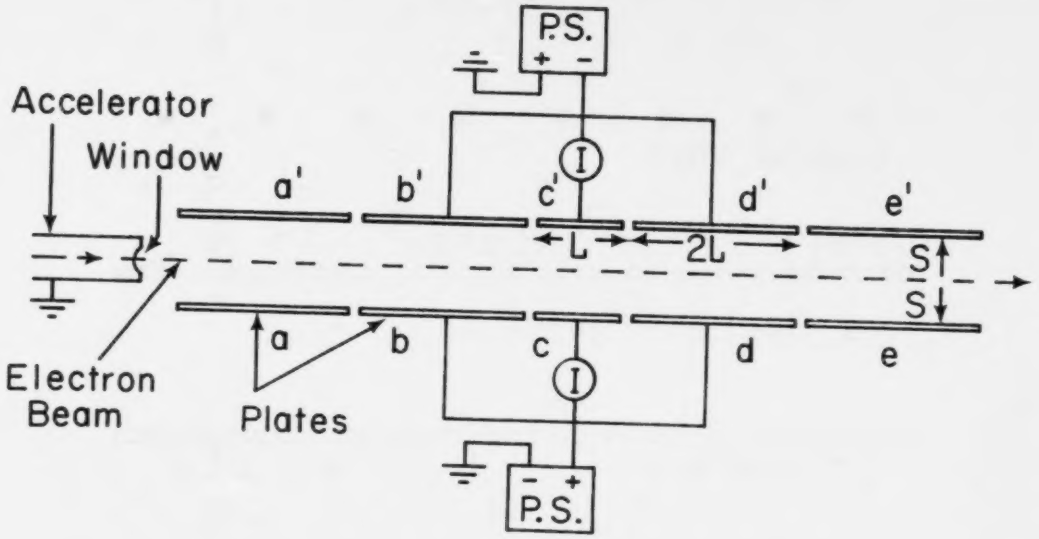

Fig. 2. Schematic for poor geometry measurement of ion current densities produced by electron beam ionization. The geometry is poor in the sense that there is no collimation prior to the plates (c,c') to restrict the beam to an ionization plane parallel to the plates.

MODULAR TEST SYSTEM PLAN

The purpose of the project is the determination of optimum conditions for electron beam ionization in the precipitation of coal fly ash. A laboratory system is planned at the Florida State University. A schematic of the modular design is shown in Fig. 5.

Sample fly ash is resuspended in an air stream, promptly monitored for concentration, and then delivered to the test precipitator unit. After treatment the concentration is again promptly monitored by an optical system and monitored on a time-integrated basis with an impactor. After treatment, the gas is drawn through a filter by an exhaust fan and vented.

Modularity is essential at this stage of development since the purpose of the system is to optimize both the geometry of the components and the irradiation conditions, both beam energy and current. Various window thicknesses can be used to spread the beam and pneumatic sweeping is planned to keep the windows free of dust. Scanning

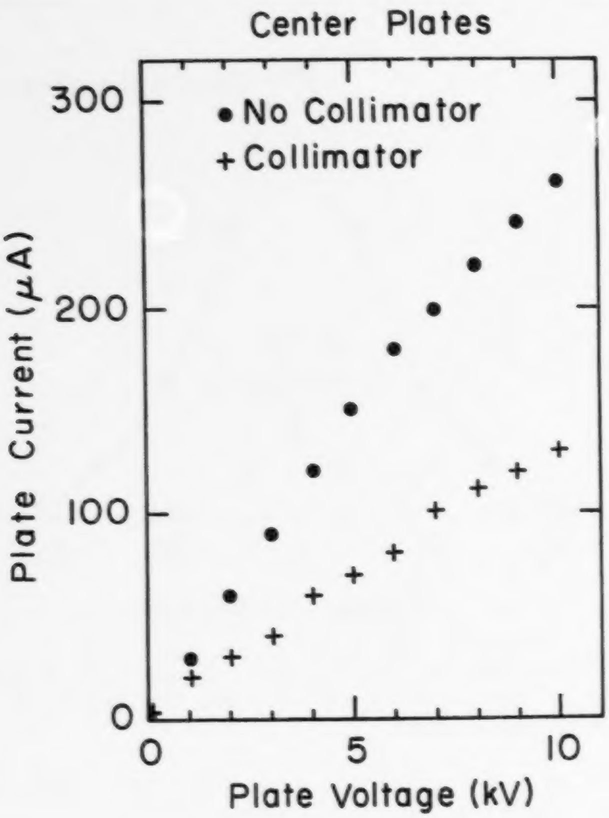

Fig. 3. Plate current vs. plate voltage curve. The current collected by plate c of Fig. 2 is plotted against the positive bias voltage. The same plot holds for plate c' except for change in sign for both current and bias. No collimator data (dots) correspond to the arrangement shown in Fig. 2 while the collimator data (crosses) is obtained by the collimator of Fig. 4.

of the beam over a wide angle is incorporated in another configuration now shown here.

The option to include corona wires in a conventional geometry is shown in Fig. 5 but it is not at all clear that such tests will be necessary since the performance characteristics for conventional precipitators have been studied for many years.

The hazards of scaling are such that the results obtained with a small laboratory system can not be reliably extrapolated to a full scale operating system. The results are expected to provide a design

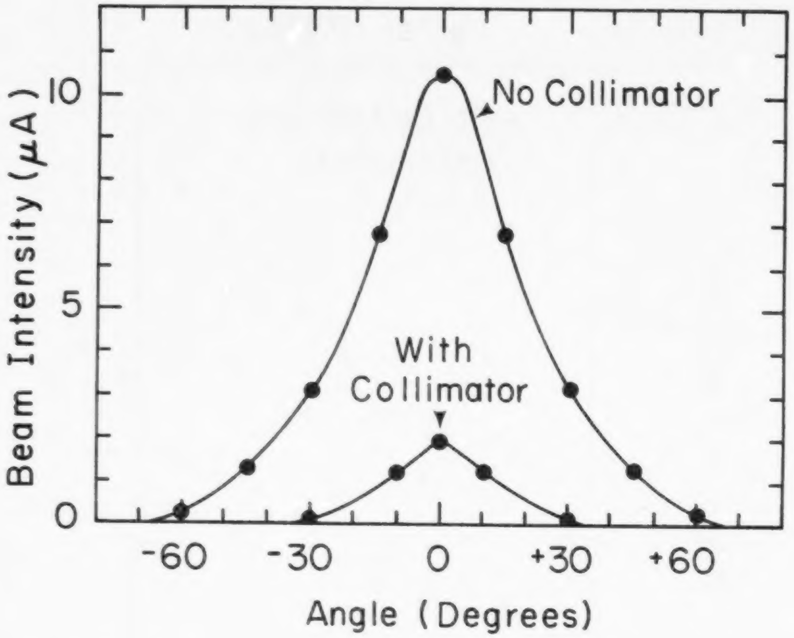

Fig. 4. Angular distribution of current collected by a small grounded plate at a radius of 10 cm with and without ±0.1 radian honey-comb collimator.

basis for a pilot system in which the problems of scaling and more realistic operating conditions are addressed.

Electron beam ionization is similar to the high intensity ionizer developed by EPRI[4] in that both produce larger currents and stronger electric fields than do conventional precipitators. Theoretical estimates suggest that the current and field values for electron beam ionization will exceed those for the EPRI device but this has not been experimentally confirmed. A two stage system is used with the EPRI high intensity ionizer while a one stage system can be used with electron beam ionization and no orifice array is required.

ELECTRON BEAM IRRADIATION OF HIGH RESISTIVITY FLY ASH

While the burning of low sulphur coal has an obvious advantage, the fly ash produced by the combustion of such coal often exhibits a resistivity which is deleteriously high for satisfactory electrostatic precipitator operation ($\rho > 10^{10}$ ohm-cm)[2]. Two adverse effects are reported. First, because of the high resistivity of the layer of ash collected on the plate, a significant fraction of the potential difference between the plate and the corona wire must be established

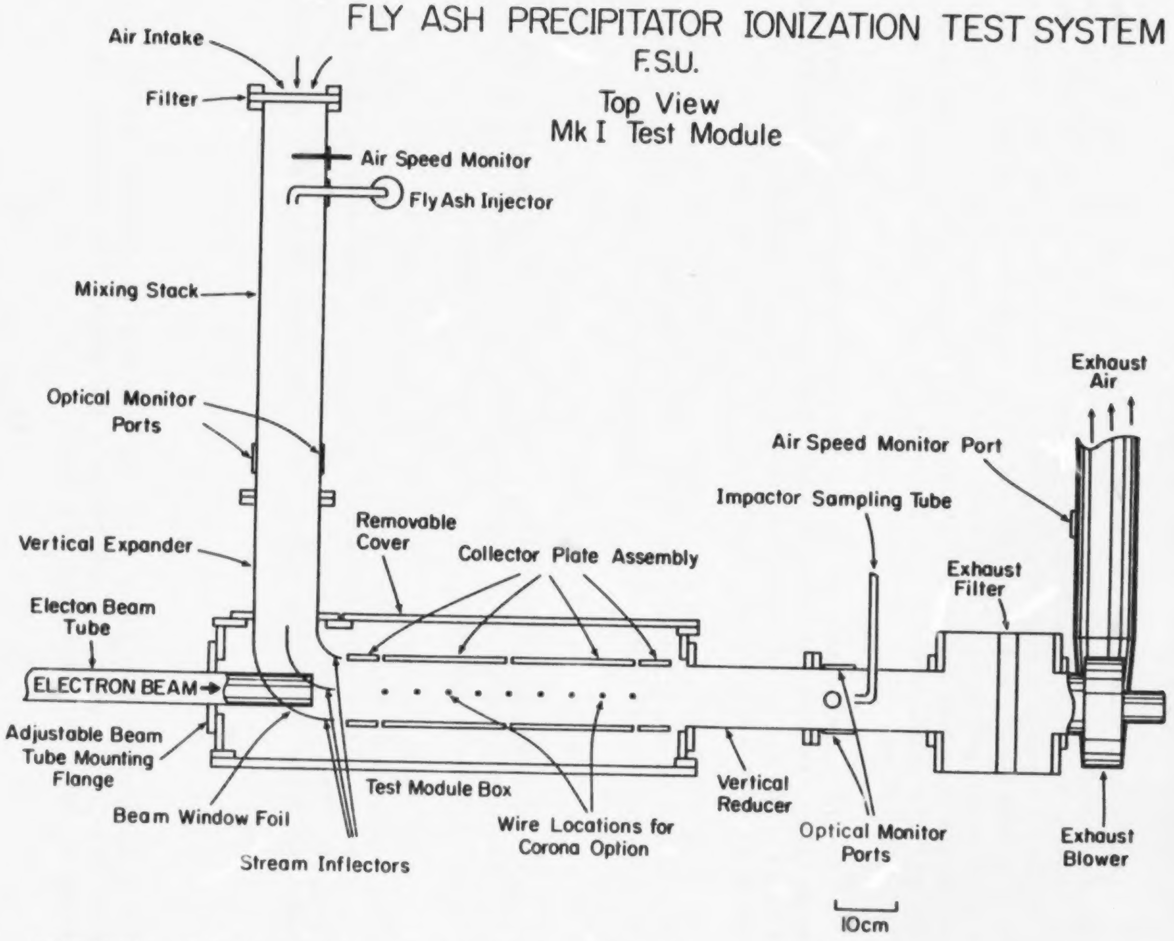
FLY ASH PRECIPITATOR IONIZATION TEST SYSTEM
F.S.U.
Top View
Mk I Test Module
Air Intake
Filter
Air Speed Monitor
Fly Ash Injector
Mixing Stack
Optical Monitor Ports
Vertical Expander
Electon Beam Tube
ELECTRON BEAM
Adjustable Beam Tube Mounting Flange
Beam Window Foil
Stream Inflectors
Removable Cover
Collector Plate Assembly
Test Module Box
Wire Locations for Corona Option
Vertical Reducer
Impactor Sampling Tube
Optical Monitor Ports
Air Speed Monitor Port
Exhaust Filter
Exhaust Air
Exhaust Blower
10cm

Fig. 5. Schematic of test precipitator system utilizing electron beam ionization.

across the ash layer in order to carry the current density required for precipitator operation. Second, discharges initiate at the plate (back corona) which can lead to spark over and at least reentrain ash in the vicinity of the discharge. Since higher current densities are anticipated with the use of electron beams, it would at first appear that this problem will be exacerbated.

Energetic electrons ionize atoms in solids as well as in gases. The fact that the resistivity of very high resistivity materials can be lowered by bombardment with ionizing radiation has been known for a number of years. Such a reduction in resistivity was demonstrated by Van Heerden in the invention of the "conduction counter".[5] The modification and possible control of effective resistivity of the fly ash layer by electron beam bombardment is a new attack on the high resistivity problem which complements electron beam ionization in the duct gas volume.

In the case of the "conduction counter" various single crystal materials have been classified with regard to effective specific ionization, the energy required to produce an electron-hole pair. The value is typically the order of tens of electron volts.[6]

The physical state of a layer of fly ash on a collector plate is, of course, very different from that of a pure single crystal! Nonetheless the resistivity does follow an activation dependence[2] given by

$$\rho = \rho_0 \exp \{a/(kT)\} \qquad (3)$$

where a is the activation energy, k is Boltzmann's constant, and T is the absolute temperature. The functional dependence is that for intrinsic conductivity of a high resistance material.

An effective specific ionization for precipitated fly ash has not been measured at this laboratory as yet, but the interest in the subject can be illustrated by making an order of magnitude estimate in an example. The current density in the condensed fly ash j_f, the average electric field in the fly ash E_f, and the resistivity are related by

$$j_f = \frac{E_f}{\rho} \qquad (4)$$

The relationship between the current density j_f and the radiation current density j_B which is appropriate for conduction counters is assumed to hold for condensed fly ash

$$j_f = j_B \frac{\Delta T_B}{\Delta T_f} \qquad (5)$$

where ΔT_B is the energy loss by the beam electrons and ΔT_f is the effective specific ionization for conduction in fly ash. The expression for the necessary bombarding electron beam current density is given by

$$j_B = \frac{E_f}{\frac{\Delta T_B}{\Delta T_f} \rho} \qquad (6)$$

To complete the numerical example let $E_f = 10^4$ V/cm, $\Delta T_B = 10^6$ eV, $\Delta T_f = 10^2$ eV, and suppose that the desired value for the effective resistivity is $\rho = 10^9\ \Omega$ cm. Substituting in Eq. (6) the required beam current density is $j_B = 10^{-9}$ A/cm^2 $= 10^{-5}$ A/m^2 $= 10\ \mu$A/m^2.

One further remark concerning the conjectured use of energetic electron irradiation to control condensed fly ash resistivity. An observed performance limit for conduction counters is the buildup of polarization in the insulating material to the point where the internal field was not sufficient to collect the ionization charge. Very large fields were produced in the insulator near the electrodes with the hazard of breakdown. A similar situation in condensed fly ash would produce the high fields necessary for back corona. Electron beam irradiation will reduce the polarization by providing charge carriers in the strong field region near the boundaries of the insulator.

*Now supported by the Department of Energy and previously supported by the National Science Foundation.

REFERENCES

1. Davis, R. H. and W. C. Finney. Ionization by Electron Beams for Use in Electrostatic Precipitators. Energy Research. 2:19-27, January - March 1978.

2. White, H. J. Industrial Electrostatic Precipitation. Reading, Massachusetts, Addison-Wesley, 1963.

3. Davis, R. H. Ion Source and Accelerator Applications to Electrostatic Precipitators. In: Conference Record 76CH1122-1-1A, IEEE Industrial Applications Society, Chicago. 1976. p. 328.

4. Spencer, H. W., J. J. Schwab, and O. J. Tassicker. Test Program for an Ionizer - Precipitator Fine Particle Dust Collection System. Electric Power Research Institute, Palo Alto, California. Paper No. 77-2.1.

5. Van Heerden, P. J. The Crystal Counter, A New Instrument in Nuclear Physics. In: N. V. Noord Hollandsche Uitgevers Maatschappij, Amsterdam. 1945.

6. Sharpe, J. Nuclear Radiation Detectors. New York, Methuen and Co. 1955.

WIDE SPACING EP IS AVAILABLE IN CLEANING EXHAUST GASES FROM INDUSTRIAL SOURCES

Ryozo Ito, Ken Takimoto
SUMITOMO METAL MINING COMPANY LIMITED
Tokyo, Japan

INTRODUCTION

As restrictions on air pollution become stronger and stronger, the demand for electrostatic precipitators increases sharply while the techniques for developing and producing electrostatic precipitators have advanced. The wide spacing electrostatic precipitator, the monitor electrostatic precipitator and electrostatic precipitators with conductive FRP are examples of the recently developed electrostatic precipitator techniques. Although these techniques are now getting known quite widely in Japan, we here introduce some of them and hope that they will be of some help for the prevention of air pollution.

1. WHAT IS WIDE SPACING SYSTEM

The wide spacing system has a wider spacing (between collecting plates) than that of the conventional electrostatic precipitator. While the conventional electrostatic precipitator generally has a spacing of about 0.2 to 0.25m, the wide spacing electrostatic precipitator has a spacing of more than 0.4m. Increasing the spacing involves the use of higher collecting voltage, and this requires a transformer-rectifier which withstands higher voltages. Therefore we could say that the wide spacing system was realized by the remarkable advancements of electrical insulating materials and semiconductor materials in late years. With the spacing expanded to twice as great as that of the conventional EP, dust collecting efficiency equivalent to or greater can be derived without changing the overall dimensions from those of the conventional types. On the other hand, the internal construction of the EP is simplified, providing various features as described below.

2. FEATURES OF WIDE SPACING SYSTEM

The wide spacing system has the following advantages.

- Adverse effect to the applied voltage is minimized even if the distance between the high voltage applied unit and grounding unit fluctuates due to a distortion of dust collecting electrode caused by stress such as heat. Thus, the initial performance can be maintained toward a long period of time.
- Because of the same reason as above, permissible range of the discharge electrode and dust collecting electrode centering error can be increased, providing a manufacturing ease.
- The total weight is reduced as number of dust collecting plates is greatly reduced. Thus, not only realizing a cost down but also advantageous in designing a monitor EP mounted on a building.
- Number of discharge electrodes and dust collecting plates is greatly reduced and at the same time, number of the attached devices such as hammering device is reduced. Thus, the overall construction is simplified, minimizing trouble and realizing the maintenance ease.
- The mutual space between the dust collecting plates is so wide that even a worker can enter, and therefore, maintenance services can be conducted easily.
- In the wet EP, spark over due to water drip is hardly to occur. This is extremely advantageous because the operation is stabilized.
- Although it's collection theory has not yet been made clear but the wide spacing EP provides a high collecting performance even for submicron particles of heavy metal oxide. (Conventionally, it has been said that it is difficult to collect heavy metal submicron particle.)
- With the wide spacing systems, various types of dust collecting electrode and discharge electrode which could not be applied previously can be applied, expanding applicabilities of the EP.

While the wide spacing systems have the above described features, the systems have the following disadvantages.

- Price of the power pack increases. Smaller the capacity of EP, greater the occupancy of the power pack cost ratio in the total cost.
- Particular insulation system is required for the high tension supporting equipment. Especially, when using an air purge, a large volume of air is required.

When the air flow is extremely small, the wide spacing system may not be superior to the conventional system. In general, however, the wide spacing system has substantial advantages over the conventional system.

3. THEORY OF WIDE SPACING SYSTEM

Deutsch formula has been used as a formula to estimate dust collecting efficiency of EP for many years.

$$\mathrm{EFF} = (1 - F) \times 100\ (\%) \quad \ldots\ldots\ldots\ldots\ldots\ldots \quad (1)$$

$$F = \exp\,(-w \times \mathrm{SCA}) \quad \ldots\ldots\ldots\ldots\ldots\ldots \quad (2)$$

where,

EFF: Collection Efficiency (%)
F : Fraction of Particles which escape collection
SCA: Specific Collecting Area (sec./M)
w : Particle Migration Velocity (M/sec.)

As a theoretical equation used to obtain migration velocity "w" of the individual size of particles, the follwoing equation has been suggested based on the balance between Coulomb's force and viscosity resistance by Stock's law. (In this suggestion, only Coulomb's force is taken into consideration as a force which acts the dust collection.)

$$w = \frac{qE_p}{6\pi\eta a}\ [\mathrm{m/sec.}] \quad \ldots\ldots\ldots\ldots\ldots\ldots\ldots\ldots \quad (3)$$

where,

q : Charge (C)
E_p: Electric Field Strength of Collecting Area (V/M)
η : Gas Viscosity (N sec./M)
a : Particle Radius (M)

In this suggestion, Cunningham correction factor must be taken into consideration for those particles the diameter of which is less than 1μ.

For the above equation, field charging and diffusion charging are considered for the particle charging q.

When the migration velocity ω is calculated according to the above theory, a relationship between particle diameter and migration velocity as shown in Fig. 1 is obtained.

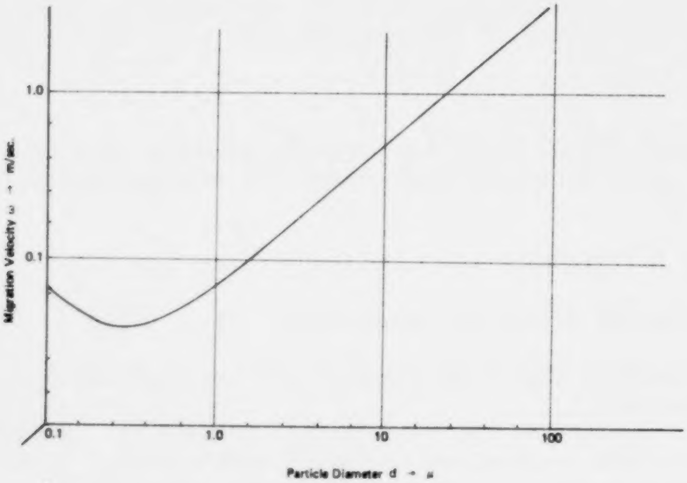

Fig. 1

It has been well known, however, that the result well agrees with the actual values experimentally but does not for those EP practically used in the industrial fields. And, equations which theoretically prove collection efficiency of an industrial EP have not yet been found.

Now, for example, when migration velocity is led out by the method described in the above and when thus obtained migration velocity is applied to the Deutsch formula, the collection efficiency is decided by SCA. When volume of air is constant, greater the collecting area may be, higher the collection efficiency. Next, when cubic volume of the EP is constant, smaller the spacing between electrodes, greater the collecting area. Thus, smaller the spacing, a higher performance can be realized.

If this theory were true, the wide spacing system could not exist. However, when the spacing is increased, the system has been generally recognized to present its efficiency higher than or equal to that of the conventional system even if the total size of its electrostatic precipitator is the same. It is obvious that the wide spacing system has a specific collecting area smaller than that of the conventional system. According to the Deutsch formula, this fact may not be explained unless the wide spacing system produces greater effective migration velocity. We accordingly assume that the effective migration velocity is a function of the spacing b. Most of the EP manufacturers obtain their own effective migration velocities based on their experiences, and are deciding EP sizes. We use our own migration velocity based on the numerous experiments and experiences on the actual EP centered around the wide spacing systems.

The effective migration velocity can be affected by many factors such as gas state, dust state and operating conditions of the electrostatic precipitator. When only the dust particle size and the spacing are considered as such factors for convenience sake,

$$\omega = f(d, b) \quad \ldots\ldots\ldots\ldots\ldots\ldots \quad (4)$$

where d:particle size and b:spacing. If the spacing is defined to a particular value as a standard spacing, the migration velocity ω_0 can be expressed as a function of the particle size alone and we obtain

$$\omega_0 = f(d) \quad \ldots\ldots\ldots\ldots\ldots\ldots \quad (5)$$

If the spacing is different from the standard spacing, the equation (5) can be rewritten by multiplication of a correction coefficient $K_s = g(b)$.

$$\omega_1 = f(d)g(b) = K_s\omega_0 \quad \ldots\ldots\ldots\ldots\ldots\ldots \quad (6)$$

where Ks: spacing correction coefficient ($K_s = g(b)$)

It is apparent that f(d) and g(b) are not theoretical formulas but empirical formulas.

As shown in Fig. 2, the relationship between the spacing b and the spacing correction coefficient K_s varies with the kind of dusts and the dust collecting conditions, but b and K_s are generally in a directly proportional relation.

What brings about such a phenomenon? Unfortunately this phenomenon has not perfectly been explained in a theoretical manner. The following are hypotheses which were introduced so far.

(1) The phenomenon is due to the turbulence of the collecting area.
(2) The phenomenon is due to the field strength of the collecting area.

These are probably reasonable. In addition, the following can be considered as some of the important factors to give a solution.

(3) Ionic wind
(4) Electrostatic agglomeration

Although we have continued studies based upon the above we have not yet had a solution to explain the difficult phenomenon.

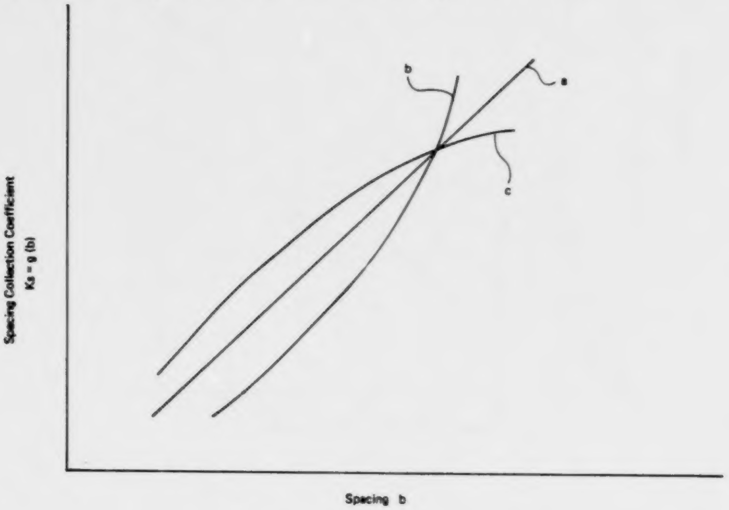

Fig. 2

4. COLLECTION EFFICIENCY OF WIDE SPACING EP

Now, let us try to obtain the collection efficiency from the abovementioned migration velocity multiplied by the correction coefficient. If all dust particles have the same diameter, the Deutsch formula (2) can be used. However, the actual dust particle size has a distribution and also the migration velocity is a function of the particle diameter, so that it is not very easy to obtain the collection efficiency.

In other words, even in case of a particular dust, the effective migration velocity is not constant, because the dust particle size distribution is different between the inlet and outlet of the electrostatic precipitator. Normally, larger particles have higher migration velocity than smaller particles, so that the particle size is smaller in the outlet of the electrostatic precipitator than in the inlet. Therefore, the overall migration velocity has a smaller value in the outlet than in the inlet. As a result, the overall migration velocity is a function of the specific collecting area SCA, as shown in Fig. 3. Accordingly, it is necessary to consider the partial migration velocity rather than the overall migration velocity.

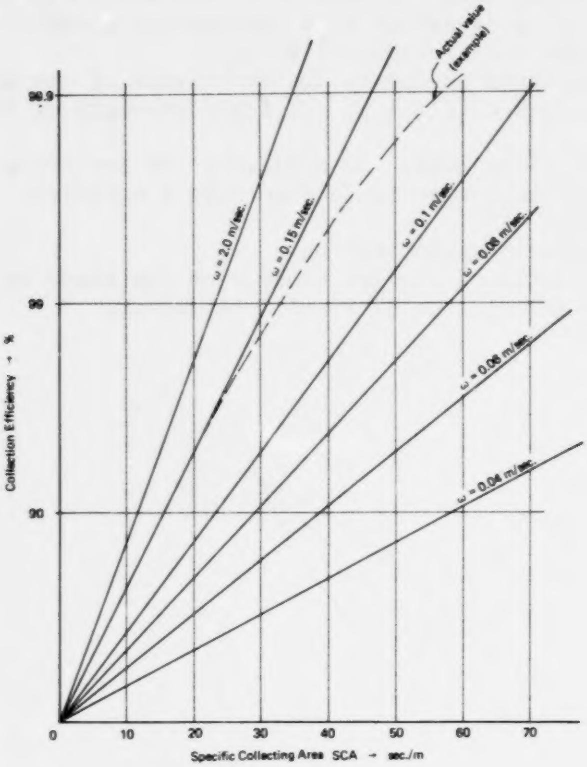

Fig. 3

(1) Particle size distribution

In order to handle the migration velocity for each particle size, it is convenient to use the dust particle size distribution as a formula.

Using the Rosin-Rammler-Sperling Graph for example, cumulative percentage Ri can be expressed as follows:

$$Ri = h(di) = \exp\left(-\ell n2 \times (di/d50)^{n}\right) \;\ldots\ldots\; (7)$$

where, di:particle diameter [μ]
d50:particle diameter with which cumulative percent becomes 50% [μ]
n:Average number (= tan a)

Relative weight ratio of dust in that particle diameter is expressed by the following equation.

$$Di = Ri - R_{i+1} \;\ldots\ldots\ldots\ldots\ldots\ldots\ldots\ldots\ldots\; (8)$$

Fraction of particle which escapes collection by each particle diameter is expressed as follows.

$$Fi = \exp(-\omega_{0i} \times SCA) \quad \ldots\ldots\ldots\ldots\ldots\ldots \quad (9)$$

When total dust containing value at the inlet of the EP is expressed as Dst, dust containing value by each particle diameter is expressed as follows.

$$Dsi = Dst \times Di \quad \ldots\ldots\ldots\ldots\ldots\ldots\ldots\ldots \quad (10)$$

Dust containing value at outlet by each particle diameter Ddi can be obtained by using equations (9) and (10).

$$\begin{aligned} Ddi &= Dsi \times Fi \quad \ldots\ldots\ldots\ldots\ldots\ldots\ldots\ldots \quad (11) \\ &= Dst \times Di \times Fi \end{aligned}$$

Total dust outlet loading Ddt can be obtained by integrating equation (11).

$$Ddt = \Sigma\,[Dst \times Di \times Fi] = Dst\,\Sigma\,[Di \times Fi] \quad \ldots\ldots\ldots\ldots \quad (12)$$

Hence, overall fraction of particles which escape collection FT is obtained as follows.

$$\begin{aligned} Ft &= Ddt/Dst \\ &= \Sigma\,[Di \times Fi] \\ &= \Sigma\,[\{h(di) - h(di+1)\} \times \exp\{-f(b, di) \times SCA\}] \quad .. \quad (13) \end{aligned}$$

When the equations of the particle size distribution and the migration velocity are obtained as above, the collection efficiency in a particular SCA can be obtained. As seen in the equation (13), the collection efficiency is given as a function of the particle size, the spacing and the SCA. In effect, other factors such as characteristics of gases and dusts, and performance data of EP must be considered, so that the migration velocity equation f(b, di) given in (13) becomes more complicated.

5. APPLICATION OF WIDE SPACING EP

(1) Standard type of wide spacing EP

This type of EP has a structure basically similar to that of the conventional EP, and its discharge wires are held vertically by the frame, not by weights. This type can be applied to either the dry type or wet type.

(2) EP with horizontal discharge wire

This type has discharge wires which are horizontally held and realized by the use of the wide spacing system. This type can be designed to have a smaller installation area by overlapping a number of collecting passages of the box type.

(3) EP using conductive FRP

In Japan, the wet type of electrostatic precipitators, which requires anticorrosiveness, is currently composed mostly of conductive FRP. Electrostatic precipitators using lead as collecting plates have already been out of date. For the wet type, the use of the wide spacing system diminishes the occurrence of sparks when droplets fall off the lower end of the collecting plate, thus allowing a collecting plate of honeycomb structure to be adopted. As a result, this type can be more compact than the plate type. Figure 5 shows a structure of a conductive FRP. The conductive material is carbon, which offers sufficient conductivity and anticorrosiveness.

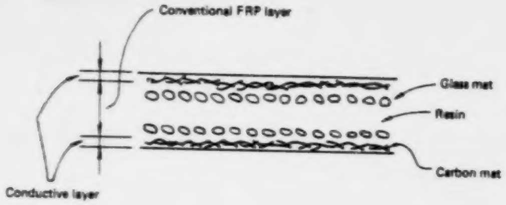

Fig. 4

(4) Monitor EP

Since in Japan regulations strictly restrict the leakage of dust out of factories equipped with open-hearth furnaces of electric furnaces for the iron and steel industry, fugitive dust collection systems in addition to direct evacuation system are installed in most cases. Normally in such cases, the monitor roof is sealed and air is sucked from the monitor roof through a duct to the dust collector on the ground. This requires a long extention of dust in which a great pressure loss occurs. In addition, power for the exhauster is increased because air flow is very large.

The monitor EP is the type of electrostatic precipitator which is mounted on the roof of a factory. Gases ascending under the thermal effect are admitted into the EP and let out by means of an auxiliary ventilation fan. Therefore very little electric power is required and no space for the precipitator is required on the ground. Figure 5 shows a general sketch of the monitor EP.

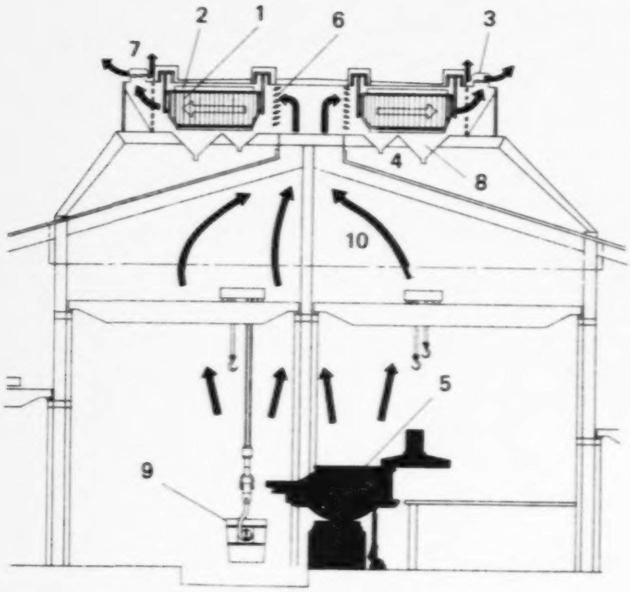

1. Discharge electrode (-)
2. Collecting electrode (+)
3. Roof fan
4. Dust discharge conveyer
5. Electric furnace
6. Control valve
7. Gas outlet
8. Hopper
9. Ladle
10. Exhaust gas

Fig. 5

The monitor EP is required to be as light in weight as possible because it is mounted on the roof. For this purpose, it is preferable to adopt the wide spacing system.

References

1) White, H.J., Industrial Electrostatic Precipitation, Addison-Weslly (1963)
2) Committee of Electrical Technology for Pulution Control, Technical Report II-45, Institute of Electrical Engineers of Japan
3) Cooperman, P., Nondeutshian Phenomena in Electrostatic Precipitation, APCA Annual Meeting
4) Misaka, Electric Field Strength in Wide Spacing Electrostatic Precipitator, 1st National Conference of the Institute of Electrostatics Japan

DESCRIPTION OF A MATHEMATICAL MODEL OF ELECTROSTATIC PRECIPITATION

Jack R. McDonald
Southern Research Institute
2000 Ninth Avenue South
Birmingham, Alabama 35205

Leslie E. Sparks
Industrial Environmental Research Laboratory
Environmental Protection Agency
Research Triangle Park, North Carolina 27711

ABSTRACT

The latest version of a mathematical model of electrostatic precipitation developed under the sponsorship of the Environmental Protection Agency is described. Major improvements to the fundamental basis of the model include the capability of generating theoretical voltage-current characteristics for wire-plate geometries, a new method for describing the effects of rapping reentrainment, and a new procedure for predicting the effects of particles on the electrical conditions. The computer program which performs the calculations in the model has been made more user oriented by making the input data less cumbersome, by making the output data more complete, by making modifications which save computer time, and by providing for the construction of log-normal particle size distributions. The different practical applications of the model are reviewed. These include the examination of the effects of particle size distribution, electrical conditions, specific collection area, resistivity, and nonideal conditions on the performance of a precipitator.

INTRODUCTION

In recent years, increasing emphasis has been placed on developing theoretical relationships which accurately describe the individual physical mechanisms involved in the precipitation process and on incorporating these relationships into a complete mathematical model for electrostatic precipitation. From a practical standpoint, a reliable theoretical model for electrostatic precipitation would offer several valuable applications:

Preceding page blank

(1) precipitators could be easily and completely designed by calculation from fundamental principles;

(2) a theoretical model could be used in conjunction with a pilot-plant study to design a full-scale precipitator;

(3) precipitator bids submitted by various manufacturers could be evaluated by a purchaser with respect to meeting the design efficiency and the costs necessary to obtain the design efficiency;

(4) the optimum operating efficiency of an existing precipitator could be established and the capability to meet particulate emissions standards could be ascertained; and

(5) an existing precipitator performing below its optimum efficiency could be analyzed with respect to the different operating variables in a procedure to troubleshoot and diagnose problem areas.

In addition to its many applications, a mathematical model can be a valuable tool for comparing precipitator performance with its cost and time savings capability. The approach is cost effective because it (1) allows for the analysis and projection of precipitator operation based upon a limited amount of data (extensive field testing is not necessary), (2) can predict trends caused by changing certain precipitator parameters and thus, in many cases, can prevent costly modifications to a precipitator which will not significantly improve the performance, (3) can be used as a tool in sizing precipitators and preventing excessive costs due to undersizing or significant oversizing, and (4) can be used to obtain large amounts of information without extensive use of manpower but, instead, with reasonable use of a computer.

The approach is time effective because (1) large amounts of information can be generated quickly, (2) it does not necessarily depend on time-consuming field tests which involve travel, extensive analysis, and plant and precipitator shutdowns, (3) it can prevent losses in time due to unnecessary or insufficient modifications to a precipitator, and (4) it can prevent losses in time due to the construction of an undersized precipitator.

This paper briefly describes the latest version[1,2] of a mathematical model of electrostatic precipitation developed under the sponsorship of the U.S. Environmental Protection Agency. The capabilities of the model will be stressed rather than mathematical details. In the present version, earlier work[3] has been improved and extended. Major improvements to the fundamental basis of the model include the capability of generating theoretical voltage-current characteristics for wire-plate geometries, a new method for describing the effects of rapping reentrainment, a new procedure for accounting for the effects of particles on the electrical conditions, and the incorporation of experimentally determined correction factors to account for unmodeled effects. The computer program which performs the calculations in the model has been made more user oriented by making the input data less cumbersome, by making the output data more complete, by making modifications which save computer time, and by providing for the construction of log-normal particle size distributions.

CAPABILITIES OF THE MODEL

The present version of the model has the following capabilities:

(1) it predicts collection efficiency as a function of particle diameter, electrical operating conditions, and gas properties;
(2) it can calculate clean-plate, clean-air voltage-current characteristics for wire-plate geometries;
(3) it determines particle charging by unipolar ions as a function of particle diameter, electrical conditions, and residence time;
(4) it can estimate the effects of particles on the electrical conditions under the assumption that effects due to the particulate layer can be ignored;
(5) it accounts for electrical sectionalization;
(6) it predicts particle capture at the collection electrode based on the assumptions of completely random, turbulent flow, uniform gas velocity, and particle migration velocities which are small compared to the gas velocity;
(7) it employs empirical correction factors which adjust the particle migration velocities obtained without rapping losses in order to account for unmodeled effects;
(8) it accounts for the nonideal effects of nonuniform gas velocity distribution, gas bypassage of electrified regions, and particle reentrainment from causes other than rapping by using empirical correction factors to scale down the ideally calculated particle migration velocities; and
(9) it accounts for rapping reentrainment by using empirical relationships for the quantity and size distribution of the reentrained mass.

In its present form, the model has the capability of predicting trends caused by changes in specific collection area, applied voltage, current density, mass loading, and particle size distribution. Comparisons of the predictions of the model with laboratory scale precipitators[2,4] and full-scale precipitators collecting fly ash from coal-fired boilers[5,6] indicate that the model can be used successfully to predict precipitator performance.

BASIC FRAMEWORK OF THE MODEL

The mathematical model is based on an exponential relationship given by

$$\eta = 1 - \exp(-A_p w_p / Q) \quad , \tag{1}$$

where η = collection fraction for a monodisperse aerosol,
A_p = collection area (m^2),
w_p = migration velocity near the collection electrode of the particles in the monodisperse aerosol (m/sec), and
Q = gas volume flow rate (m^3/sec).

White[7] derived the above equation by using probability concepts and the statistical nature of the large number of particles in a precipitator. The equation is based on the following simplifying assumptions:

(1) The gas is flowing in a turbulent pattern at a constant, mean forward-velocity.
(2) Turbulence is small scale (eddies are small compared to the dimensions of the duct), fully developed, and completely random.
(3) The particle migration velocity near the collecting surface is constant for all particles and is small compared with the average gas velocity.
(4) There is an absence of disturbing effects, such as particle reentrainment, back corona, particle agglomeration, and uneven corona.

Experimental data[8] under conditions which are consistent with the above assumptions demonstrate that equation (1) adequately describes the collection of monodisperse aerosols in an electrostatic precipitator under certain idealized conditions. Although the above assumptions are never completely satisfied in an industrial precipitator, they can be closely approached with respect to the treatment of fine particles.

The assumption that the particle migration velocity near the collection surface is constant for all particles has the most significant effect on the structure of the model. This assumption implies two things:

(1) The particles are all of the same diameter.
(2) The electrical conditions are constant.

Because the particles entering a precipitator are not all of the same diameter, the assumption of uniform particle diameters creates a problem. This problem is dealt with in the model by performing all calculations for single diameter particles and then summing the results to determine the effect of the electrostatic precipitation process on the entire particle size distribution.

Because the electrical conditions change along the length of a precipitator, the assumption of constant electrical conditions creates a problem. This problem is dealt with in the model by dividing the precipitator into small length increments. These length increments can be made small enough that the electrical conditions remain essentially constant over the increment. The number of particles of a given diameter which are collected in the different length increments are summed to determine the collection efficiency of particles of a single diameter over the entire length of the precipitator.

In summary, a precipitator is divided essentially into many small precipitators in series. Equation (1) is valid in each of these small precipitators for fine particles of a given diameter.

The collection fraction, $\eta_{i,j}$, for the i-th particle size in the j-th increment of length of the precipitator is mathematically represented in the form

$$\eta_{i,j} = 1 - \exp\,(-w_{i,j}A_j/Q) \quad , \qquad (2)$$

where $w_{i,j}$ (m/sec) is the migration velocity of the i-th particle size in the j-th increment of length and A_j (m^2) is the collection plate area in the j-th increment of length.

The collection fraction (fractional efficiency) η_i for a given particle size over the entire length of the precipitator is determined from

$$\eta_i = \frac{\sum_j \eta_{i,j} N_{i,j}}{N_{i,1}} \quad , \qquad (3)$$

where $N_{i,j}$ is the number of particles of the i-th particle size per cubic meter of gas entering the j-th increment.

Effective or length-averaged migration velocities (w_i^e) are calculated for the different particle diameters from

$$w_i^e = \frac{Q}{A_T} \ln\left(\frac{1}{1-\eta_i}\right) \quad , \qquad (4)$$

where A_T (m^2) is the total collecting area.

The overall mass collection efficiency η for the entire polydisperse aerosol is obtained from

$$\eta = \sum_i \eta_i P_i \quad , \qquad (5)$$

where P_i is the percentage by mass of the i-th particle size in the inlet size distribution.

In order to determine the migration velocities for use in equation (2), the electrical conditions and the particle charging process in a precipitator must be modeled. If the operating voltage and current density are known, then the electric potential and electric field distributions are determined by using a relaxation technique.[3,9] In this numerical technique, the appropriate partial differential equations which describe the electrodynamic field are solved simultaneously under boundary conditions existing in a wire-plate geometry. In order to find the solutions for the electric potential and space charge density distributions, the known boundary conditions on applied voltage and current density are held fixed while the space charge density at the wire is adjusted until all the boundary conditions are satisfied. For each choice of space charge density at the wire, the procedure iterates on a grid of electric potential and space charge density until convergence is obtained and then checks to see if the boundary condition on the current density is met. If the boundary condition on the current density is not met, then the space charge density at the wire is adjusted and the iteration procedure is repeated.

Particle charge is calculated by using a unipolar, ionic-charging theory.[3,10] Particle charge is predicted as a function of particle diameter, exposure time, and electrical conditions. The charging equation is derived based on concepts from kinetic theory and determines the charging rate in terms of the probability of collisions between particles and ions. The theory accounts simultaneously for the effects of field and thermal charging and also accounts for the effect of the applied electric field on the thermal charging process.

The nonideal effects of major importance in a precipitator are (1) nonuniform gas velocity distribution, (2) gas bypassage of electrified regions, and (3) particle reentrainment. These nonideal effects will reduce the ideal collection efficiency that may be achieved by a precipitator operating with a given specific collection area. Since the model is structured around an exponential equation for individual particle diameters, it is convenient to represent certain nonideal effects in the form of correction factors which apply to the exponential argument. The model employs correction factors which are used as divisors for the ideally calculated effective migration velocities in order to account for nonuniform gas velocity distribution, gas bypassage, and particle reentrainment without rapping.[3] The resulting apparent effective migration velocities are empirical.

NEW IMPROVEMENTS TO THE MODEL

Calculation of Voltage-Current Characteristics

A new technique,[11] developed for theoretically calculating electrical conditions in wire-plate geometries, has been incorporated into the model. In this numerical technique, the appropriate partial differential equations which describe the electrodynamic field are solved simultaneously, subject to a suitable choice of boundary conditions. The procedure yields the voltage-current curve for a given wire-plate geometry and determines the electric potential, electric field, and charge density distributions for each point on the curve.

The key element in this technique is the theoretical calculation of the space charge density near the corona wire for a specified current density at the plate. In order to find the solutions for the electric potential and space charge density distributions, the known boundary conditions on space charge density near the wire and current density are held fixed while the electric potential at the wire is adjusted until all the boundary conditions are satisfied. For each choice of electric potential at the wire, the procedure iterates on a grid of electric potential and space charge density until convergence is obtained and then checks to see if the boundary condition on the current density is met. If the boundary condition on the current density is not met, then the electric potential at the wire is adjusted and the iteration procedure is repeated. The entire procedure is repeated for increasing values of current density in order to generate a voltage-current curve. Comparisons[11,12] of the predictions of this technique with experimental data show that the agreement between theory and experiment is within 15 percent.

Method for Predicting Trends Due to Particulate Space Charge

A new method has been incorporated into the model in order to provide a more comprehensive representation of the effects of particulate space charge on the electrical operating conditions in a precipitator. In this method, the precipitator is divided into successive length increments which are equal to the wire-to-wire spacing. Each of these increments is divided into several subincrements. The first calculation in the procedure involves the determination of a clean-gas, voltage-current curve which terminates at some specified applied voltage. At the specified applied voltage, the average electric field and ion density are calculated in each subincrement. This allows for the nonuniformity of the electric field and current density distributions to be taken into account.

As initially uncharged particles enter and proceed through the precipitator, the mechanisms of particle charging and particle collection are considered in each subincrement. In each subincrement, the average ion density, average particulate density, weighted particulate mobility, and effective mobility due to both ions and particles are determined. At the end of each increment, the effective mobilities for the subincrements are averaged in order to obtain an average effective mobility for the increment. Then, for the specified value of applied voltage, the average effective mobility is used to determine the reduced current for the increment by either calculating a new voltage-current curve or using an approximation procedure. Although it is not presently utilized, the method allows for iterations over each length increment so that schemes which ensure self-consistency can be implemented at a future date.

In its present state of development, this method provides good estimates of reduced current due to the presence of particles. The reduced current is a function of mass loading, particle size distribution, gas volume flow, and position along the length of the precipitator. However, this method does not have the capability of predicting the redistribution of the electric field due to the presence of particles. Work is underway to improve the model in this respect.

Method for Estimating Effects Due to Rapping Reentrainment

As part of a program sponsored by the Electric Power Research Institute, an approach to representing losses in collection efficiency due to rapping reentrainment has been developed based upon studies performed on six different full-scale precipitators collecting fly ash.[6] In these studies, outlet mass loadings and particle size distributions were measured both with and without rapping losses. Outlet mass loadings and particle size distributions which can be attributed to rapping were obtained based on the data acquired in these studies. The results of these studies have been incorporated into the model.

The rapping emissions obtained from the measurements are shown in Figure 1 as a function of the amount of dust calculated to have been

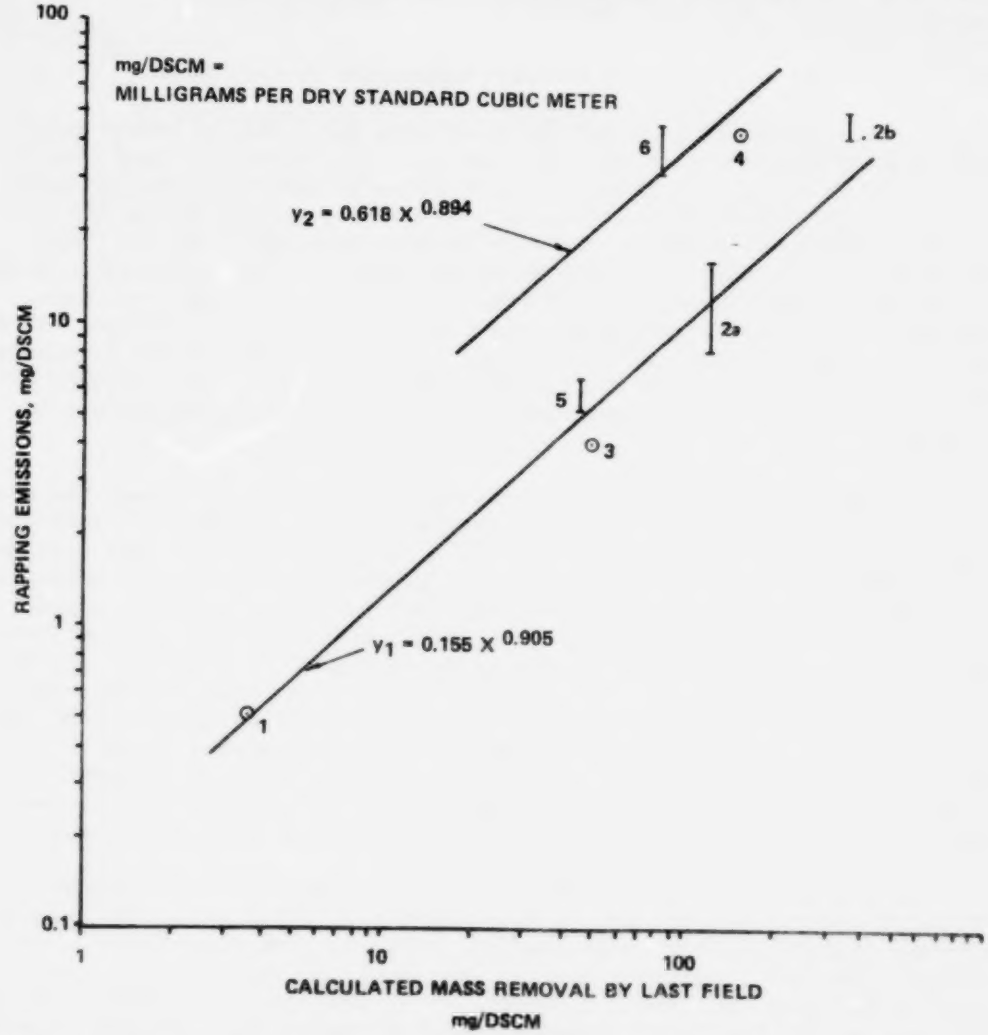

Figure 1. Measured rapping emissions versus calculated particulate removal by last electrical section. These curves are a result of work sponsored by the Electric Power Research Institute.

removed by the last electrical section. The dust removal in the last electrical section was approximated by using an exponential relationship for the collection process and the overall mass collection fraction determined from mass train measurements under normal operating conditions. These data suggest a correlation between rapping losses and particulate collection rate in the last electrical section. Data for the two hot-side installations (4 and 6) which were tested show higher rapping losses than for the cold-side units.

The apparent particle size distribution of emissions attributable to rapping at each installation was obtained by subtracting the cumulative distributions during non-rapping periods from those with rappers in operation and dividing by the total emissions (based on impactor measurements) resulting from rapping in order to obtain a cumulative percent distribution. Although the data indicated considerable scatter, the average particle size distribution shown in Figure 2 has been constructed for use in modeling rapping puffs. In the model, the data are approximated by a log-normal distribution with a mass median diameter of 6.0 μm and a geometric standard deviation of 2.5.

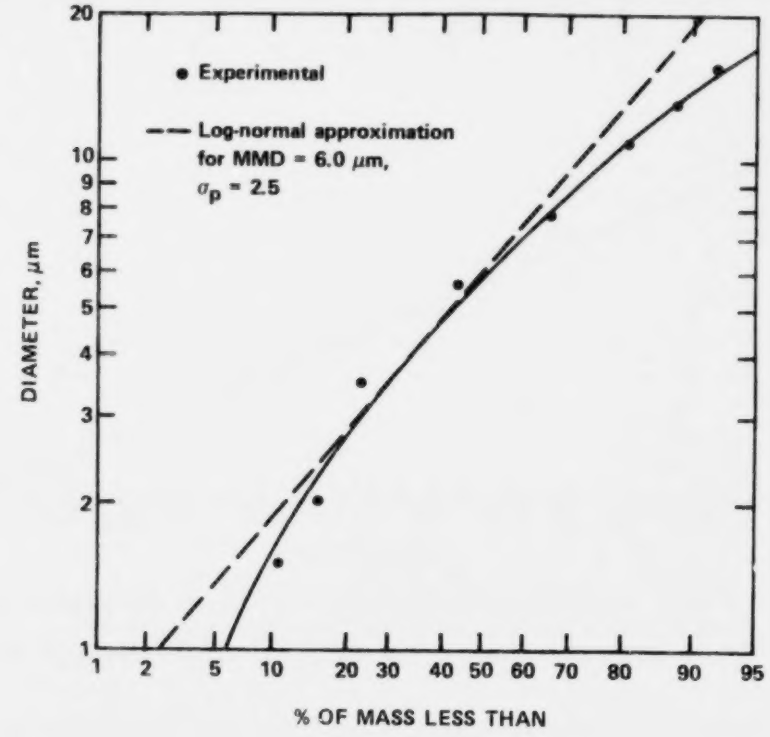

Figure 2. Average rapping puff size distribution for six full-scale precipitators. These data are a result of work sponsored by the Electric Power Research Institute.

In summary, the model determines a rapping puff by using the information in Figure 1 to obtain the outlet mass loading due to rapping and by using a log-normal approximation of the data in Figure 2 to represent the particle size distribution of the outlet mass loading due to rapping. This rapping puff is added to the no-rap outlet emissions to obtain the total outlet emissions as a function of mass loading and particle size distribution.

EMPIRICAL CORRECTIONS TO NO-RAP MIGRATION VELOCITIES

Comparisons of measured apparent effective migration velocities ($\omega_{MEASURED}$) for full-scale precipitators under no-rap conditions with those ($\omega_{CALCULATED}$) predicted by the model indicate that the field-measured values exceed the theoretically projected values (in the absence of back corona, excessive sparking, or severe mechanical problems) in the smaller size range. Based on these comparisons, a size-dependent correction factor has been constructed and incorporated into the model.[6] This correction factor is shown in Figure 3.

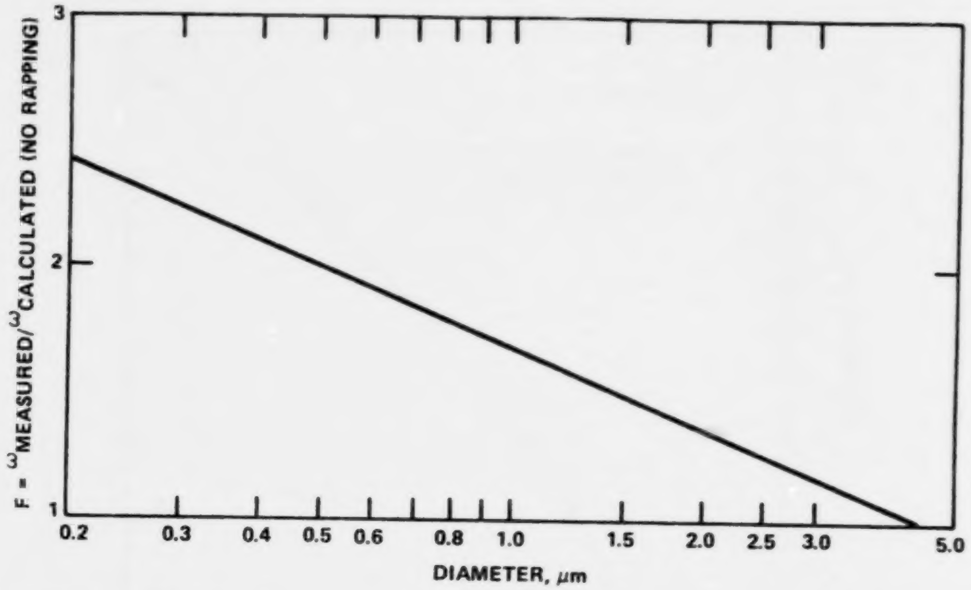

Figure 3. Empirical correction factors for the no-rap migration velocities calculated from the mathematical model. This work was sponsored by the Electric Power Research Institute.

The empirical correction factor accounts for those effects which enhance particle collection efficiency but are not included in the present model. These effects might include particle charging near corona wires, particle concentration gradients, the electric wind, and flow field phenomena. In future work which is planned, efforts will be made to develop appropriate theoretical relationships to describe the above effects and to incorporate them into a more comprehensive model for electrostatic precipitation.

User-Oriented Improvements

The computer program which performs the calculations in the model has been modified to make the input data less cumbersome and the output data more complete. The performance of a precipitator can be analyzed as a function of particle size distribution, current density, specific collection area, and nonideal conditions without repetition of input data which remain fixed. All input data are now printed out in a format which is easily utilized. A summary table of precipitator operating conditions and performance is printed out as the last section of data for a given set of conditions.

Several modifications have been made in order to save computer time. The particle charging algorithm has been modified, decreasing the computer time required for particle charging calculations by approximately 40 percent. In addition, particle charge calculations for a given diameter will terminate whenever the charging rate becomes negligible. The computer program has been modified so that several sets of nonideal conditions can be analyzed in conjunction with the results of one ideal calculation. This allows for the analysis of an extended range of nonideal conditions with only a small increase in computer time. As another means of saving computer time, the computer program now contains an estimation procedure for use in analyzing precipitator performance. This procedure results in considerable savings in computer time since it does not involve numerical techniques. The procedure can be used to good advantage to determine gross trends or to establish a limited range of interest in which to apply the more rigorous calculation.

The computer program now has the capability of constructing log-normal particle size distributions based on specified values of the mass median diameter and geometric standard deviation. This capability can be used to construct inlet and rapping puff particle size distributions. Thus, the effects of different log-normal particle size distributions can be readily obtained. Also, the program can fit any specified particle size distribution to a log-normal distribution.

APPLICATIONS OF THE MODEL

The different practical applications of the model have been discussed previously.[3,5] These include the examination of the effects of particle size distribution, electrical conditions, specific collection area, dust resistivity, and nonideal conditions on the performance of a precipitator. These applications have now been incorporated into procedures for troubleshooting and sizing precipitators.[2] These procedures provide specific guidelines for applying the model to troubleshooting and sizing applications.

SUMMARY

The new version of the mathematical model of electrostatic precipitation offers greater predictive capabilities and is more user oriented than the previous version. Greater predictive capabilities are provided by allowing for the calculation of theoretical voltage-current characteristics for wire-plate geometries, by incorporation of a new method for estimating the effects of particles on the electrical conditions, by use of a new method for determining the effects of rapping reentrainment that is directly related to full-scale precipitators, and by the use of experimentally determined, empirical correction factors for individual particle migration velocities that results in increased agreement between the theory and field test data. The computer program which performs the calculations required by the model is more user oriented than the previous program due to modifications that make the input data less cumbersome, make the output data more complete and useful, result in savings of computer time, and allow for the construction of log-normal particle size distributions.

ACKNOWLEDGMENTS

The development of a mathematical model of electrostatic precipitation has been supported by the Industrial Environmental Research Laboratory, U.S. Environmental Protection Agency, Research Triangle Park, North Carolina, under Contract No. 68-02-2114, Leslie E. Sparks, Project Officer. The work presented on rapping reentrainment was supported by the Electric Power Research Institute, Palo Alto, California, under Contract RP413-1, Walter Piulle, Project Manager.

REFERENCES

1. McDonald, J. R. A Mathematical Model of Electrostatic Precipitation: Revision 1. Volume I, Modeling and Programming. EPA-600/7-78-111a, U.S. Environmental Protection Agency, Research Triangle Park, North Carolina, June 1978.

2. McDonald, J. R. A Mathematical Model of Electrostatic Precipitation: Revision 1. Volume II, User Manual. EPA-600/7-78-111b, U.S. Environmental Protection Agency, Research Triangle Park, North Carolina, June 1978.

3. Gooch, J. P., J. R. McDoanld, and S. Oglesby, Jr. A Mathematical Model of Electrostatic Precipitation. EPA-650/2-75-037 (NTIS No. PB 246188/AS), U.S. Environmental Protection Agency, Research Triangle Park, North Carolina, April 1975.

4. Gooch, J. P., and J. R. McDonald. Mathematical Modelling of Fine Particle Collection by Electrostatic Precipitation. Atmospheric Emissions and Energy-Source Pollution. AIChE Symposium Series, 73(165):146, 1977.

5. Gooch, J. P., and J. R. McDonald. Mathematical Modelling of Fine Particle Collection by Electrostatic Precipitation. Conference on Particulate Collection Problems in Converting to Low Sulfur Coals. EPA-600/7-76-016 (NTIS No. PB 260498/AS), U.S. Environmental Protection Agency, Research Triangle Park, North Carolina, October 1976. pp. 68-106.

6. Gooch, J. P., and G. H. Marchant, Jr. Electrostatic Precipitator Rapping Reentrainment and Computer Model Studies. Final Draft Report prepared for the Electric Power Research Institute, 1977.

7. White, H. J. Industrial Electrostatic Precipitation. Addison-Wesley, Reading, Massachusetts, 1963. pp. 166-170.

8. White, H. J. Reference 7, pp. 185-190.

9. Leutert, G., and B. Böhlen. The Spatial Trend of Electric Field Strength and Space Charge Density in Plate-Type Electrostatic Precipitators. Staub, 32(7):27, 1972.

10. Smith, W. B., and J. R. McDonald. Development of a Theory for the Charging of Particles by Unipolar Ions. J. Aerosol Sci., 7:151-166, 1976.

11. McDonald, J. R., W. B. Smith, H. W. Spencer, and L. E. Sparks. A Mathematical Model for Calculating Electrical Conditions in Wire-Duct Electrostatic Precipitation Devices. J. Appl. Phys., 48(6): 2231-2246, 1977.

12. McDonald, J. R., and D. H. Pontius. Electrostatic Precipitators. AIChE Conference on Theory, Practice and Process Principles for Physical Separations, Pacific Grove, California, November 1977. (To be published in 1978.)

BACK DISCHARGE PHENOMENA IN ELECTROSTATIC PRECIPITATORS

Senichi Masuda
Department of Electrical Engineering
University of Tokyo
7-3-1, Hongo, Bunkyo-ku, Tokyo, Japan

ABSTRACT

The different modes of back discharge, propagation characteristics of the streamer-mode, its flashover characteristics, and the effects of various factors affecting the behaviours of back discharge are described. The mechanism of back discharge is discussed, and the effect on particle charging of different modes of back discharge is presented.

INTRODUCTION

Back discharge is an abnormal gaseous discharge occurring in all of the particle collection processes using corona discharge when the resistivity of particle layer covering the surface of collecting electrode, ρd, becomes excessively high. In this case, the potential drop across the layer exceeds its breakdown threshold so that breakdown occurs at weak points in the layer. This triggers gaseous discharge from the points to proceed towards the discharge electrode or along the surface of the layer, or in both directions, which is called back discharge. It occurs under usual conditions when ρd exceeds about 5×10^{10} ohm-cm, manifesting itself in a form of excessive sparking near this threshold resistivity. When ρd exceeds the range of $10^{12} - 10^{13}$ ohm-cm, it takes a form of surface glow covering the whole layer surface, resulting in an abnormal increase in current. The excessive sparking enforces the lowering of operation voltage, and thereby impairs the collection performance. The surface glow provides the charging zone with copious positive ions which neutralize the useful negative charge of the particles, and can even charge them inversely. Thus, the performance drop becomes more serious in this case. In addition, the layer breakdown causes particle ejection[1], and strong local

Preceding page blank

ionic wind is resulted from the back discharge points[2]. All these phenomena are also likely to contribute the performance loss. In this paper are summarized the results of the latest investigations by the author and his co-workers on the back discharge phenomena occurring in electrostatic precipitators.

INITIATION OF BACK DISCHARGE

Initiation Condition

Back discharge is preceded by the breakdown of the particle layer, which occurs under the usual conditions in precipitators when the following condition is fulfiled[1]:

$$id \times \rho d > Eds \qquad (1)$$

where id and Eds represent the current density and breakdown field strength in the layer respectively. The value of ρd becomes appreciably lower as the field strength in the layer, Ed, approaches Eds[3,4]. In addition, the quantity Eds takes a much higher value in corona field than in a measuring cell out of parallel plate electrodes. Hence, it should be emphasized that the condition (1) holds its meaning only when the values of ρd and Eds measured in a corona field at the instant of layer breakdown are used.

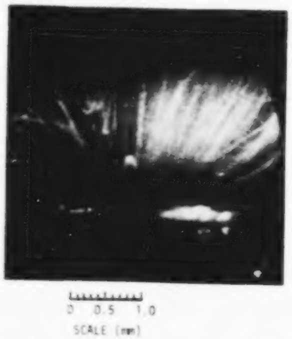

Fig. 1 Crater Formation

The breakdown of the layer occurs in a repetitive manner, ejecting the particles from the breakdown point (Fig. 1) to form a crater where a feeble but continuous glow starts to appear[1]. This glow is considered the initial stage of back discharge, although it is detectable only with the aid of an image intensifier tube. Hence, the layer breakdown condition (1) also represents the initiation condition of back discharge. In case ρd is excessively high, a slight error appears because the formation of a crater does not immediately lead to the appearance of this glow in this case[5]. The diameter of the craters is roughly equal to the layer thickness, and the crater formation takes place even at a very thin layer thickness (50 μm), producing in this case a "micro-crater". The precipitation of particles can continue, even under back discharge condition, until a certain thickness (100 - 200 μm) is reached. The micro-craters produced are successively covered by oncoming particles so that a random motion of glows is observed to occur over the layer surface. Once its thickness reached a level of producing a sufficiently large "macro-crater", it remains uncovered any more. This fact provides a justification for using an insulator plate with a pinhole in the study of back discharge, by which the reproducibility of the results can be greately improved.

Factors Affecting the values of ρd and Eds

Apart from the factors already described, temperature and humidity have the most essential effects on the value of ρd. The value of Eds is also affected by these two factors to some extent[3]. The value of ρd is further affected by impurity components, such as SO_3, Na, K etc, contained in gas and particles. There are many publications on this problem, and its discussions are omitted here.

MODE OF BACK DISCHARGE

The point-like feeble but continuous glow discharge appearing at the crater as decribed represents the initial stage of back discharge, and this mode is named "onset-glow-mode". The onset-glow contains in its current both Trichel pulse and dc components. When the voltage is raised very small surface streamers begin to appear around the crater, accompanied by random appearance of current pulses which are much larger than the Trichel pulse. This mode is named "onset-streamer-mode". When the voltage is further raised, much larger streamer corona appears from the crater to proceed either towards the discharge electrode or along the layer surface, or in both directions. Large current pulses are observed to appear, resulting in a strong non-linear rise in current. This mode is named "streamer-mode" which is subdivided into the "space-streamer-mode", "surface-streamer-mode", and "mixed-streamer-mode" according to the directions of streamer propagation described. The next mode to appear following the streamer-mode is twofold, depending upon the factors governing gaseous discharge. In a region of low gas mean free path, including air at NTP, flashover occurs at a voltage where the space-streamer bridges across the electrode gap. This flashover voltage is much lower than that without back discharge. In a region of higher gas mean free path, corresponding to an elevated temperature and/or reduced pressure, the bridging of the space-streamer only results in a gentle random sparking, or no sparking at all. With the voltage slightly raised, a transition occurs from the streamer-mode to an entirely different glow-mode where the streamers completely disappear to turn into a bright and stable "steady-glow" which has a much higher flashover voltage and no pulse component in current. This new glow-mode is named "steady-glow-mode". It should be added that, in a region of much higher gas mean free path, no streamers appear at all, and the onset-glow-mode is immediately succeeded by this steady-glow-mode, where the Trichel pulse suddenly disappears in current component. Fig. 2 shows the photographs of the different modes of back dis-

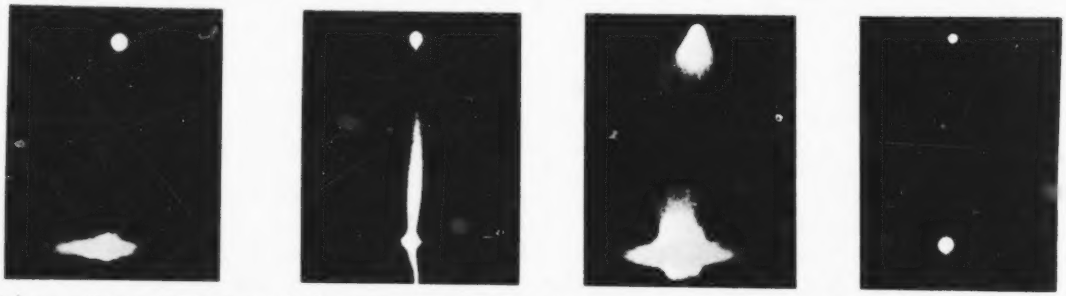
(a) surface-streamer (b) space-streamer (c) mixed-streamer (d) steady-glow

Fig. 2 Different modes of back discharge

charge. The mode of back discharge under positive corona point is completely different, as shown in Fig. 3. The breakdown points are uniformly distributed over the layer surface, and no streamers occur so that, independent of ρd, the glow-mode remains to exist until flashover occurs. The abnormal rise in current is small, and the flashover voltage is approximately 1.5 times higher than with negative corona point. No streamer appears also at the positive corona point. It is considered that Hermstein's glow appears at the corona point due to copious negative ions supplied from back discharge points[6]. Electrons may be detached from these negative ions to form a strong electron sheeth covering the point, so that the development of positive streamers will be hampered.

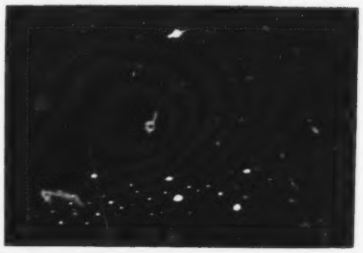

Fig. 3 Back discharge under positive corona point

EFFECTS OF VARIOUS FACTORS ON BACK DISCHARGE

Vertical Field Ea and Current Density J

Use of a grid electrode between the discharge and plane electrodes enables the separate change of the vertical field in gas space, Ea, and the current density, J, in the space charge field above the layer. Fig. 4 represents the mode-diagram of back discharge in air at NTP plotted in an Ea-J plane[5]. The current density J (or current I) plays an essential role in mode transitions. In Region IV where Ea $<$ 5 kV/cm, only the surface-streamer occurs, and current saturates on Curve E limited by ionic space charge. In Region V where Ea $\geq$ 5 kV/cm, the space-streamer appears in addition to the surface streamer to form the mixed-streamer-mode. The space-streamer turns into flashover on Curve F. When Ea exceeds 8.5 kV/cm, the layer breakdown triggers flashover immediately without passing through the back discharge stage.

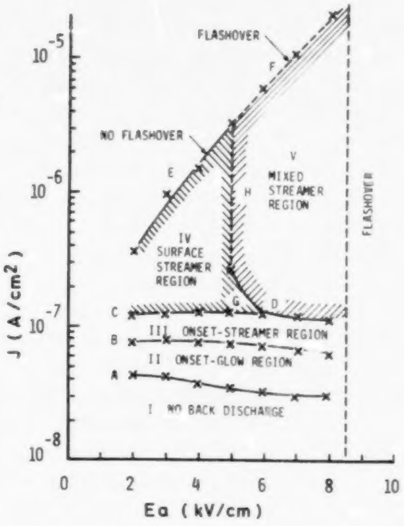

Fig. 4 Mode-diagram in Ea-J domain (glass plates)

Tangential Field Et

The effect of the tangential field at the breakdown point can be studied by using two glass plates, each having a pinhole, on top of one another and changing the distance, d, between the two pinholes[5]. This changes the value of Eds, and hence the value of surface charge density on the layer at the instant of its breakdown, $\sigma o = \varepsilon$ Eds. It is evident that the value of the tangential field, Et, is determined by σo. The tangential field Et has an essential role for the occurence and development of the surface-streamer. The dominant surface-streamer appears in air at NTP when the value of σo exceeds about 5×10^{-9} C/cm^2.

Dust Resistivity ρd

In corona field the value of ρd governs the behaviours of back discharge through its effect on the voltage division between the gas space and particle layer. When ρd is sufficiently low, the voltage drop in gas space becomes high so that the space-streamers are enhanced and the excessive sparking occurs. Whereas, when ρd becomes higher, the voltage drop across the layer is raised so that breakdown occurs at a number of points in the layer before the space-streamers are resulted. This leads to the appearance of many onset-glows or onset-streamers to form a surface glow and an abnormal current rise is resulted. When ρd exceeds the level of about 10^{14} ohm-cm, the propagation of back discharge begins to occur between the layer on the collecting electrode and the high voltage members existing near the discharge electrode. This is more enhanced when the high voltage members are covered by particle layers. This propagation disappears when the discharge electrode is removed or the value of Ea is lowered[7]. When ρd is further raised, back discharge becomes possible to appear by dark current or space charge field inside the layer[1].

Gas mean-free-path λ

Gas mean free path can be changed either by changing temperature or pressure, but its effect on the flashover characteristics of back discharge is the same, except for the temperature range where no back discharge takes place, as shown in Fig. 5 (a)[8]. The gas mean free path λ in the figure is normalized by its value at NTP, λo. There are two different curves for flashover. Curve I represents the flashover voltage from the

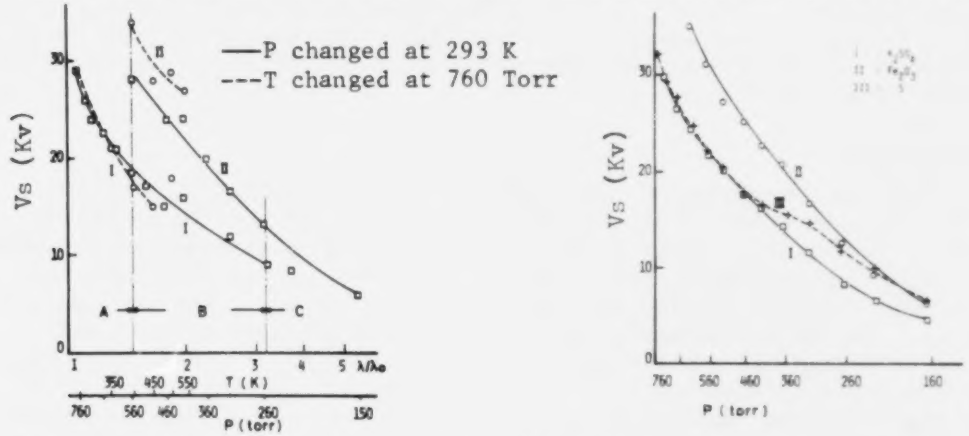

(a) effect of T and P (mica plate with 0.45 mm thickness and a pinhole)

(b) effect of chemical composition (layer thickness: 2 mm, T: 293 K)

Fig. 5 Effects of temperature T, pressure P, and chemical composition of dust on flashover characteristics of back discharge in air.

space-streamer, whereas Curve II that from the steady-glow. In Region A, flashover occuring on Curve I turns into arc. In Region B, the space-streamer bridges across the gap on Curve I, resulting in a random sparking in the lower mean-free-path region. Just beyond this curve, a transition occurs in Region B from the streamer-mode to the steady-glow-mode which lasts until mighty flashover occurs on Curve II. In Region C, the onset-glow turns immediately into the steady-glow which lasts until Curve II is reached and mighty flashover occurs.

Thickness of Dust Layer d

The decrease in the thickness of the layer, d, shifts the boundary between Regions B and C to the left-side, resulting in a dominance of the steady-glow-mode and rise in flashover voltage[8]. In case of a mica-plate with a pinhole in air and a sharp needle electrode with a radius of curvature of 0.005 mm, Region C occupies the whole range of $\lambda/\lambda o$ in Fig. 5 (a) at d = 47 μm so that no streamers occur below this layer thickness. This suggests an effect of stronger electrode rapping, but more detailed investigations are needed to get conclusions on this matter.

Chemical Composition of Dust

The effect of chemical composition of dust is shown in Fig. 5 (b)[8]. In case of dusts out of alkali-metal compounds which have low ionization potential, the propagation of space-streamer is very enhanced, and there is only Curve I for flashover voltage, since the boundary between Regions A and B shifts to the right-side. In case of powders which easily eject particles from back discharge points to form the large conical craters with thin effective layer thickness at their bottoms, there is only Curve II for flashover voltage. In case of dusts which tend to form many pinholes, the flashover voltage is represented by Curve III, since the transition from the streamer-mode to the steady-glow-mode occurs at different points at different values of $\lambda/\lambda o$.

Gas Composition

The streamer propagation and flashover characteristics of back discharge are strongly affected by electron affinity and ionization potential of gaseous components[9]. It is known that initiation of streamer is hampered by electro-negative gaseous molecules, as decribed later. However, once started, the streamer obtains the increased plasma density and propagation tendency. The former enhances its transition to a leader to turn into arc when it bridges across the gap to cause flashover. As a result, the increase in O_2-concentration shifts the boundary between Regions A and B to the right side in Fig. 5 (a), and viceversa. Similarly, once streamer started, its propagation tendency is largely enhanced by the existence of gaseous molecules with low ionization potential, such as NO, since the propagation is governed by photo-emission of electrons from gas molecules. Whereas the plasma density is not necessarily increased in this case, so that the bridging of streamers across the gap mostly does not triggers the mighty flashover. In case of NO which also has some electron affinity, Curve I in Fig. 5 (a) is lowered with the increase in NO-concentration until about 700 ppm in a gas mixture with O_2 = 0.94 %, CO_2 = 21.3 % and N_2 = 77.76 %. Beyond this concentration, the space-streamer begins to diffuse, finally to turn into the surface-streamer at around 2 000 ppm. Curve I rises again in this process, and Region A, which has been absent, appears at 2 000 ppm. The further increase in NO-concentration results in the continued rise of flashover voltage. The initial decrease in the flashovervoltage is evidently resulted by the very low ionization potential of NO (NO: 9.25 eV, O_2: 12.1 eV, CO_2: 13.7 eV, N_2: 15.7 eV). The later rise of flashover voltage, resulted by the transition of space-streamer to surface-streamer, may be caused by the accumulation of NO^- ions with the low ionization potential in the gas space near the layer and onto its surface.

PROPAGATION OF STREAMER-MODE BACK DISCHARGE

Mixed-Streamer-Mode

The time change in light signal of back discharge from a local spot can be measured using a concave mirror and a photo-multiplier-tube. Fig. 6 represents the results obtained for the mixed-mode back discharge in a needle-to-plane electrode system at various points on z- and r-axes[10]. It can be seen that the light wave consists of two parts: the primary wave rising very rapidly and lasting about 20 ns, and the secondary wave rising more slowly and lasting about 200 ns. Fig. 7 (a) shows a streak-photograph of the mixed-mode backdischarge from side view, which clearly indicates that

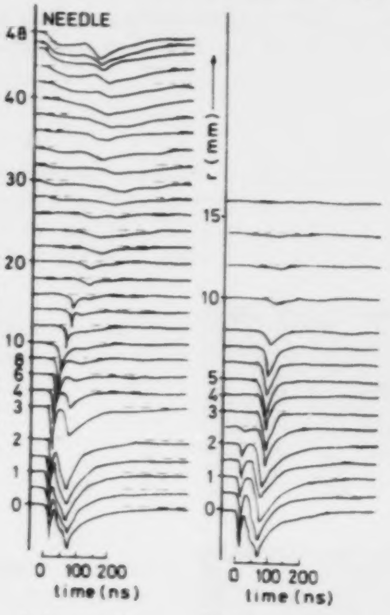

(a) z-AXIS (b) r-AXIS

Fig. 6 Time change in light signal (mixed-streamer-mode).

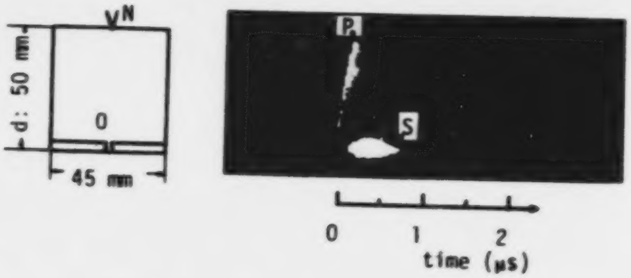

(a) mixed-streamer-mode

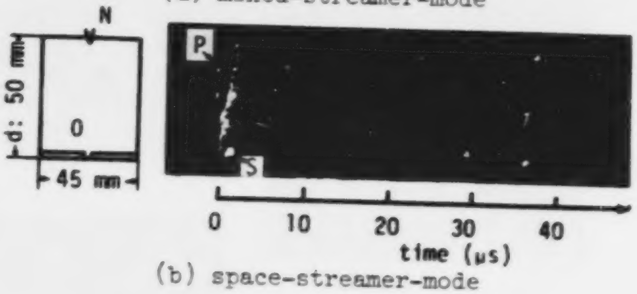

(b) space-streamer-mode

Fig. 7 Streak-photograph of back discharge from side view.

the primary wave corresponds to the space-streamer whereas the secondary wave to the surface-streamer. The primary wave advances towards the needle electrode with a speed of about 4×10^7 cm/s in air at NTP, and its current pulse contains $1 - 2 \times 10^{-9}$ C/pulse. The secondary wave propagates along the layer surface with a speed of about 2.5×10^7 cm/s, and its current pulse has one order of magnitude larger charge content of $2 - 4 \times 10^{-8}$ C/pulse. During two back discharge pulses, a repetitive light pulses corresponding to the Trichel pulse appear at the needle tip, while the continuous glow corresponding to the onset-glow disappears at the layer breakdown point. The pulse repetition period of the mixed-streamer-mode is about two orders of magnitude longer than that of the space-streamer-mode to be described.

Space-Streamer-Mode

The prerequisite condition for the space-streamer to occur is that the vertical field strength in gas space exceeds a certain threshold (5 kV/cm in air at NTP), and that either the surface charge density or surface resistivity of the layer is sufficiently small. Fig. 7 (b) represents the streak-photograph of the space-streamer-mode back discharge from side-view taken in air at P = 410 Torr, which shows three successive streamers. A faint glow denoted by S represents the weak secondary light wave. The glow at the needle tip disappears in this case at the time interval when back discharge glow does not exist.

Flashover from Space-Streamer

Fig. 8 shows the light signal and current wave form at the breakdown point when the space-streamer turns into a mighty flashover. There are two stages A and B, the former corresponding to the streamer pulses at its initial stage, the latter to those at its later stage. The streak-photographs at these stages are shown in Fig. 9 (a) and (b). The first streamer is very luminous owing to the full voltage existing between the two electrodes. The following streamers,

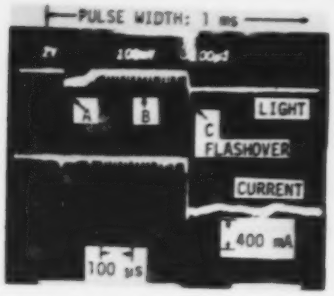

Fig. 8 Light and current signals at flashover from space-streamer

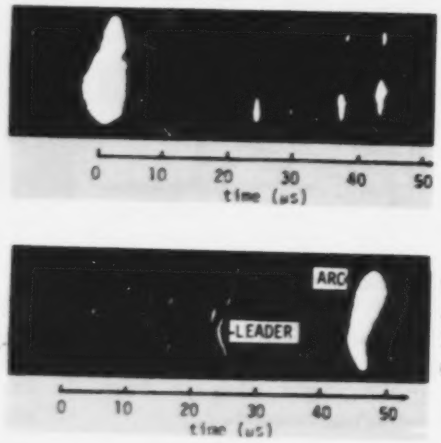

(a) streak-photograph from side-view at initial stage

(b) streak-photograph from side-view at later and flashover stages

Fig. 9 Streak-photograph at flashover from space-streamer

much weaker in its luminosity, repeats itself to heat up the streamer channel and increase its plasma density, and finally turns into a leader. The leader proceeds along the streamer channel towards the both electrodes and finally turns into a flashover at point C (Fig. 8), which takes a form of high voltage arc in this case.

Carriers Triggering Layer Breakdown and Back Discharge

The carriers triggering the breakdown of the layer, and hence the back discharge, are either negative ions or electrons, which can be identified by measuring its transit time across the gap with the use of a pulse voltage. The transit time is obtained by the time interval between the light spot appearing at the needle tip and that appearing at the layer in the streak-photographs, or the time interval between the light spot at the needle and current signals appearing at the plane electrode shielded from the needle electrode with a grid at a fixed potential[10]. Fig. 10 shows the trigger delay time τ_d and carrier transit time τ_t measured in air at room temperature for different pressure P. An abrupt increase in τd, more than two orders of magnitude, occurs at P = 560 Torr, suggesting the change of carriers responsible for triggering back discharge from electrons to ions. The values of τd and τ_t below this pressure agree very well to the transit time of electrons estimated from their mobility[10]. With the increase in pressure, τd and τ_t increase whereas the charge quantity in a current pulse decreases, resulted by the decrease in number of electrons arriving at the plane electrode. As a result, back discharge cannot be triggered by electrons above P = 560 Torr, although they still arrive at the plane electrode. Hence, this transition pressure is strongly affected by electron affinity of gaseous component. For instance, in case of SF_6 gas the transition pressure lies lower than 160 Torr, at which the trigger delay amounts to 4 µs.

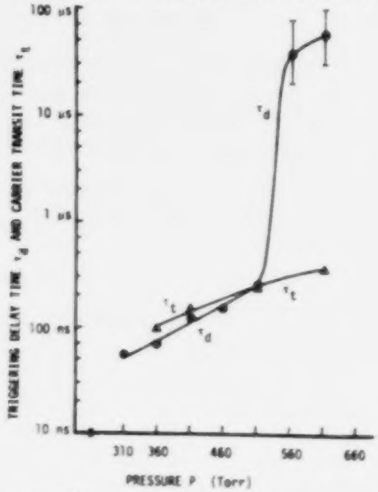

Fig. 10 Trigger delay time τ_d and carrier transit time τ_t in air vs pressure.

CHARGING EFFICIENCY UNDER BACK DISCHARGE CONDITION

Back discharge under negative corona points constitutes a source of positive ions which form a bi-polar atmosphere in corona gap. The effect on particle charging, however, differs depending upon the mode of back discharge. The surface-streamer-mode constitutes the surface-like ion source, whereas in the space- and mixed-modes ion generation in gas space occurs. Fig. 11 represents the saturation charge aquired by a steel ball with 3 mm diameter under different modes where a needle-to-plane electrode system with a grid electrode is used, and the ball is droped through different positions, d, from the plane electrode. The percentage values given in

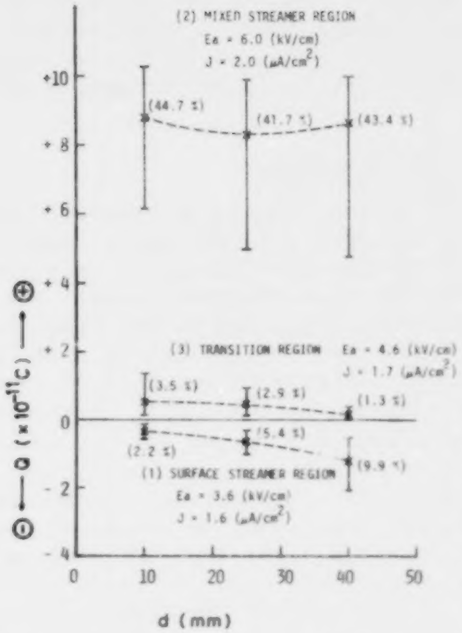

Fig. 11 Saturation charge vs. position d.

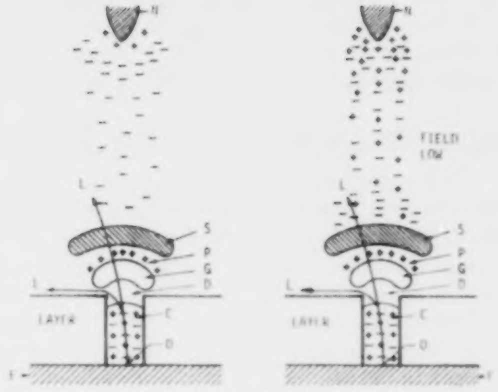

(a) onset-glow (b) steady-glow

S:electron detachment zone, P:accumulate zone of positive ions, G:negative glow, D: dark space, C: positive column, N: needle-electrode, E: plane electrode

Fig.12 Mechanism of back discharge in onset-glow-mode and steady-glow-mode.

the bracket represent the ratio of measured charge to the theoretical value obtainable in a mono-polar ion atmosphere according to Pauthenier's equation[11]. In the surface-streamer region (Curve (1)), the value of charge becomes 90 - 98 % less than the Pauthenier's limit, whereas its sign remains unchanged. The decrease in charge with the decrease in d suggests that the surface-like ion source provides positive ions with their concentration decreasing monotonically towards the discharge electrode. In the mixed-streamer region where the space-streamer is pronounced (Curve (2)), the measured charge scatters largely around its average value which is a fairly high positive value, and remains unchanged regardless of position. This indicates that the space-streamer produces copious positive ions along its channel which play an dominant role as the majority carriers in particle charging. Another experiment indicates that particle charging is strongly affected by whether or not the particle is hit by the streamers. Curve (3) represents the transition region between the foregoing cases. It should be added that the field intensity plays an important role in particle charging in practical precipitators, presumably through its effect on the back discharge mode.

MECHANISM OF BACK DISCHARGE

Onset-Glow and Steady-Glow

Fig. 12 represents the mechanism of back discharge in the onset-glow-mode and steady-glow-mode. The electrons necessary to maintain the glow discharge may be supplied in both modes by electron detachment possible to occur in the high field region S above the space charge region P of positive ions. The difference exists in the negative corona region at the point. In case of the onset-glow-mode where the field at the tip is low, a relaxation phenomena occurs in the discharge due to self-choking resulted by negative ion accumulation outside, so that it takes a form of Trichel pulse. When copious positive ions are supplied to the point to form a dense positive ion sheeth, the self-choking effect may disappear and electrons can be continuously emitted from the tip in a much larger amount, which in turn enhances the glow discharge at the breakdown point in the layer. Hence, Trichel pulse disappears, and the field in gas space is weakened by the appearance of dense bi-polar ions. Such a copious supply of positive ions may be resulted by bridging of the streamers across the gap, who then disappear due to the meakened field to turn into the steady-glow.

Streamers

The initiation of streamers requires the following condition to be fulfiled[12]:

$$\int_0^L (\alpha - \eta)\, dl = K, \quad K = 10 - 20 \qquad (2)$$

where α is the first Townsend's coefficient and η is the attachment coefficient of electrons to neutral molecules. The integration should be performed from the origin O, through the crater, to the position L at which $\alpha = \eta$, along an optimum field line (see Fig. 11). Thus, the streamers may propagate either towards the needle electrode or along the layer surface, or in both directions. In Region A in Fig. 5 (a) where gas mean-free-path is low, the number of collision for unit length is large, while the diffusion of the produced plasma in streamer channel is supressed, so that, when the streamer bridges across the gap, the plasma density can be easily raised in the course of streamer repetition to turn into a leader and arc. In Region B where gas mean-free-path is larger, the plasma density cannot be raised sufficiently in the streamer bridge so that only the random sparking can occur at most. In Region C where gas mean-free-path is very large, the streamer initiation condition (2) cannot be fulfiled owing to the decrease in collision number and increase in diffusion of plasma. Since the essential part in the integration of condition (2) will located inside the pinhole at the layer, the product (pressure) x (layer thickness) may play a major role in streamer initiation. Thus, it can be understood that the decrease in the thickness results in a shift of the boundary between Regions B and C to the left-side. Once the streamer initiated, its behaviors may be governed primarily β_p-effect (photoemission of electrons from netral gas molecules) and the electron attachment to neutral gas molecules to produce negative ions. The former enhances primarily the propagation of streamers. The increase in electron attachment may results in an increase in plasma density and temperature, because it supresses the diffusion of plasma so that the plasma is localized and easily heated up by repetition of streamers. From these considerations the effects of alkali-atom components contained in dust and O_2 and NO contained in gas on the propagation and flashover characteristics of the space-streamers can be understood. It should also be added here that these characteristics are strongly affected by the inter-electrode capacity and output impedance of the voltage source[8].

CONCLUSION

The initiation condition of back discharge, its different modes, propagation characteristics of the streamer-mode back discharge, particle charging efficiency under back discharge condition, and effects of different factors on the behaviors of back discharge are decribed. The discussions are made to clarify the mechanism of back discharge from the aspect of gaseous electronics. It should be noted that careful examinations of the laboratory results and more detailed investigations are needed before the results are correlated to any back discharge phenomenon occuring in practical precipitators. The existence of charged dust particles in gas space, large differences in electrode capacity and output impedance of the source, and the existence of many breakdown points must especially be considered in future. For instance, when the onset- or steady-glows occur at many points closely distributed, the negative glow regions G for each point are connected to each other to form a common glowing film, which should be carefully discriminated from the surface-streamer. It also should be pointed out that, although the marked effects of O_2 and NO concentrations may provide a clue on a delicate difference in performance of precipitators, the effects of other components, such as H_2O, NO_2, Cl_2, etc. have to be studied. The effect of the radius of curvature of point tip should not be neglected[13].

The author expresses his gratitude to Ministry of Education of Japan for her financial support given to this research. Thanks are also due to his co-workers, Dr. A. Mizuno and Mr. K. Akutsu.

REFERENCE

1. Masuda, S., Mizuno, A. and K. Akutsu. Initiation Condition and Mode of Back Discharge for Extremely High Resistivity Powders. Conf. Rec. IEEE/IAS 1977 Annual Meeting. p. 867, October, 1977.
2. Masuda, S. Recent progress in electrostatic precipitation. In: Static Electrification 1975- Inst. Phys. Conf. Ser. No. 27. Inst. Phys. London, 1975. p. 160.
3. Masuda, S. Reverse Ionization Phenomena in Electrostatic Precipitators. J. Inst. Elect. Engrs. Japan, Vol. 35, No. 102, p. 1482, 1960 (japanese).
4. Potter, E.C. J. APCA. Vol. 28, No.1, p.24, Jan. 1978.
5. Masuda, S. and A. Mizuno. Initiation Condition and Mode of Back Discharge. J. Electrostatics, Vol. 4 (1977/1978), p. 35, 1977.
6. Masuda, S. and M. Niioka. Charging of Dust Particles by Means of Hermstein's Glow Corona. Inst. Elect. Engrs. Japan Trans.-B,No.9,p.9,1975.
7. Masuda, S. and S. Obata. Abnormal Propagation of Back Discharge Zone. to be submitted to J. Electrostatics.
8. Masuda, S. and A. Mizuno. Flashover Measurement of Back Discharge. J. Electrostatics, Vol. 4 (1978), p. 215, 1978.
9. Masuda, S., Mizuno, A. and M. Akimoto. Effects of Gas Composition on Sparking Characteristics of Back Discharge. Proc. CSIRO Conf. on Electrostatic precipitation. Leura, New South Wales, Australia, Aug. 1978.

10. Masuda, S. and A. Mizuno. Light Measurement of Back Discharge. J. Electrostatics, Vol. 2 (1976/1977), p. 375, 1977.
11. Pauthenier, M. and M. Moreau-Hanot. La Charge des Particules Sphèrique dans un champ ionisé. J. Physique et le Radium, 3, p. 590, 1932.
12. Takuma T. Discharge Characteristics of Gases, Part 1, Central Research Inst. of Electric Power Industries Japan - Technical Report No. 69015 (1965).
13. Masuda, S. Electrical Principle of Precipitation. In: Proc. of CSIRO Conf. on Electrostatic Precipitation. Leura, New South Wales, Australia, Aug. 1978.

MEASUREMENT OF EFFECTIVE ION MOBILITIES IN A CORONA DISCHARGE IN INDUSTRIAL FLUE GASES

Jack R. McDonald
Sherman M. Banks
Southern Research Institute
2000 Ninth Avenue South
Birmingham, Alabama 35205

Leslie E. Sparks
Industrial Environmental Research Laboratory
Environmental Protection Agency
Research Triangle Park, North Carolina 27711

ABSTRACT

A technique for making in situ measurements of effective ion mobilities in a corona discharge in industrial flue gases is described. This technique is based on a measured voltage-current curve obtained for corona discharge in a wire-cylinder geometry. The measured voltage-current curve is fit to an analytical expression relating voltage and current for wire-cylinder geometry using the effective ion mobility as an adjustable parameter. An instrument referred to as an "ion mobility probe" has been developed and utilized for making the measurements. The operation of this probe is discussed. Measurements made at three different installations where the flue gas was generated in the combustion of coal are presented. These measurements include effective ion mobilities for positive and negative corona in ambient air outside the flue and positive and negative corona in the flue gas. Depending on the flue gas composition, reduced effective ion mobilities for positive corona were found to be approximately 1.5 to 2.5 times as large as those for negative corona.

INTRODUCTION

The effective mobility of ions which are created in a corona discharge is an important parameter associated with the electrostatic precipitation process. This parameter influences the voltage-current characteristic of the corona discharge device, the electric field distribution in the gaseous interelectrode region, and the particle charging

Preceding page blank

process. Thus the effective ion mobility can have a significant effect on particle collection efficiencies in an electrostatic precipitator. In general, the effective ion mobility depends on the temperature, pressure, and composition of the gas and the electric field strength.

Although measurements of effective negative ion mobilities have been made for simulated flue gases in a laboratory,[1] measurements of effective ion mobilities in an actual flue gas environment have not been previously made. In this paper, a technique for making in situ measurements of effective ion mobilities in a corona discharge in industrial flue gases is described. An instrument referred to as an "ion mobility probe" has been developed and utilized for making the measurements. Measurements have been made at three different installations where the flue gas was generated in the combustion of coal. These measurements include effective ion mobilities for positive and negative corona in ambient air outside the flue and in the flue gas. Approximate effective charge carrier mobilities due to both ions and particles were also obtained.

MEASUREMENT TECHNIQUE AND APPARATUS

The technique for determining the effective ion mobility is based on fitting the theoretical voltage-current characteristic of a wire-cylinder corona discharge to the experimental voltage-current characteristic. This technique has been used previously by Spencer[1] and Tassicker[2] in laboratory applications. The theoretical voltage-current relationship for a wire-cylinder corona discharge is given by

$$V = r_0E_0 \left[\ln\frac{b}{a} - 1 + \sqrt{1 + \frac{i}{2\pi\varepsilon_0 K} \bullet \frac{b^2}{(r_0E_0)^2}} - \ln\left\{ \frac{1 + \sqrt{1 + \frac{i}{2\pi\varepsilon_0 K} \bullet \frac{b^2}{(r_0E_0)^2}}}{2} \right\} \right], \qquad (1)$$

where

a = radius of the corona wire (m),
b = radius of the cylinder (m),
i = current per unit length of corona wire (A/m),
K = effective mobility of the charge carriers (m^2/V-sec),
E_0 = electric field strength at the outer radius of the region of ionization (V/m),
r_0 = outer radius of the region of ionization (m),
V = applied voltage (V), and
ε_0 = permittivity of free space (coul/V-m).

The theoretical voltage-current characteristic predicted by equation (1) depends on the values of the parameters r_0E_0 and K. The values of r_0E_0 and K can be determined by fitting equation (1) to an experimental voltage-current characteristic. In the work presented here, equation (1) was fitted to experimental data by means of Marquardt's[3] nonlinear least-squares algorithm with r_0E_0 and K used as adjustable parameters. In previous laboratory work,[1] this method of fitting the experimental data and of determining r_0E_0 and K was found to work quite well.

An instrument referred to as an "ion mobility probe" has been designed and developed for making measurements of wire-cylinder, voltage-current characteristics in a flue gas environment. Figure 1 shows a schematic diagram of the ion mobility probe. The probe which is made of stainless steel was designed to be inserted through a standard 10.16 cm test port into a flue gas environment at temperatures up to 400°C. A wire-cylinder discharge system with its supportive and protective devices and connections for measuring voltage, current, and temperature is contained inside the probe. The ends of the discharge system fit into grooved ceramic glass insulating rings, and this isolates the cylinder from ground. An inner support tube machined as a contrahelically wound spring provides the force necessary to maintain electrode alignment and allows for thermal expansion and contraction through the necessary temperature excursions. The high voltage, current, and thermocouple wires are enclosed in alumina tubing. The high voltage wire is spring loaded at both the corona wire and high voltage lead connections. The end of the probe which is inserted into the flue has provisions for mounting either an Alundum thimble holder or glass fiber filter holder in order to remove the particles from the gas before it enters the discharge system. An Alundum thimble with a nominal 0.3 μm cut point has been used in obtaining the data contained in this paper. The end of the probe which remains outside the flue has feed-throughs for high voltage, cylinder electrode current, and thermocouple wires. This end also has openings for a suction pump and pressure gauge.

Certain steps were taken when using the probe to ensure that reliable data would be obtained. All electrical wiring was checked for proper contact and isolation. It is especially important that the current lead and the cylinder of the discharge system be isolated from ground. Since the voltage-current characteristics of the discharge system could be affected to some extent by the gas flow rate, adequate measurement of this quantity was obtained. This means that the probe had to be checked for leaks. When the probe was inserted into the flue, it was sealed off from outside air and allowed to come to thermal equilibrium before any flue gas was pumped through the system. This measure was taken to help prevent condensation from occurring inside the probe due to hot flue gas coming in contact with cool surfaces. Once thermal equilibrium was obtained with no pumping, the pump was turned on and the probe was allowed to again come to thermal equilibrium before any measurements were made.

The probe has proven to be reliable, and only minor operational

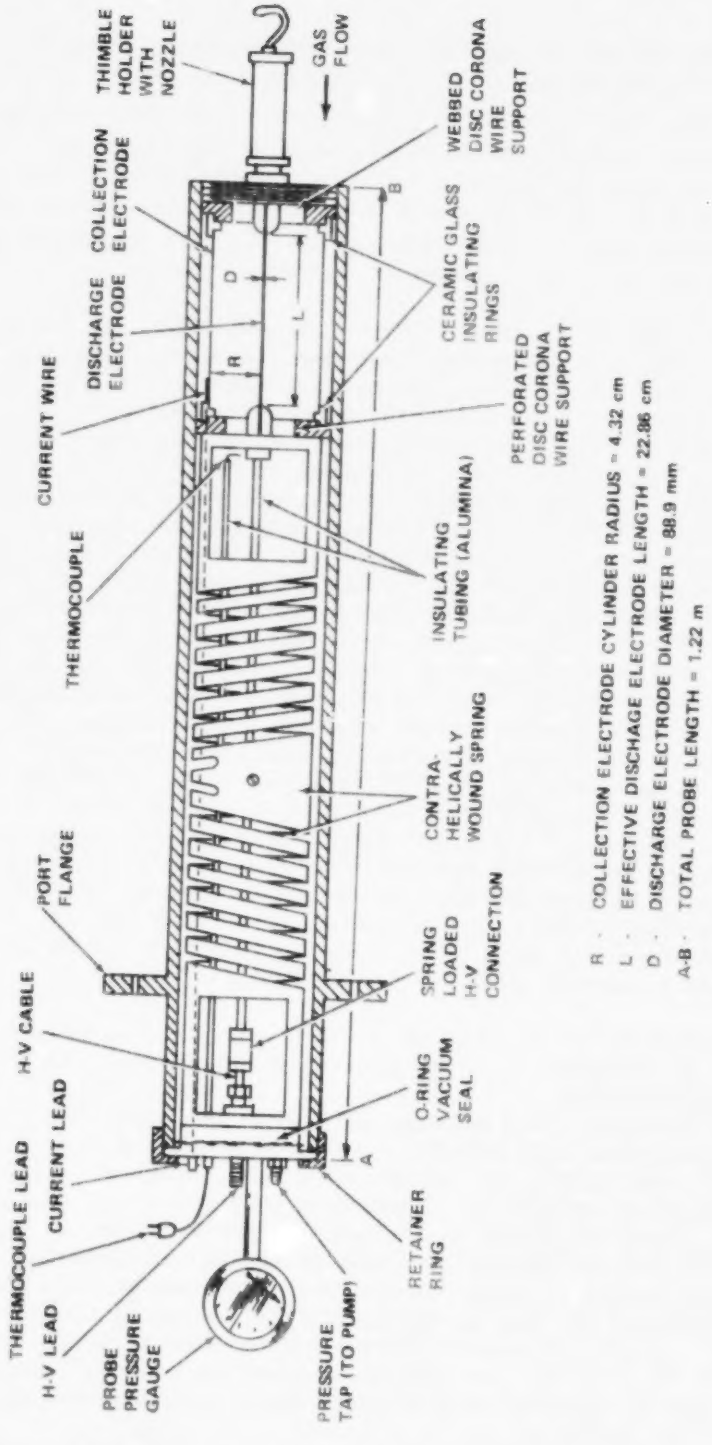
THIMBLE HOLDER WITH NOZZLE
GAS FLOW
COLLECTION ELECTRODE
WEBBED DISC CORONA WIRE SUPPORT
B
DISCHARGE ELECTRODE
D
CERAMIC GLASS INSULATING RINGS
L
R
CURRENT WIRE
PERFORATED DISC CORONA WIRE SUPPORT
THERMOCOUPLE
INSULATING TUBING (ALUMINA)
CONTRA-HELICALLY WOUND SPRING
PORT FLANGE
SPRING LOADED H-V CONNECTION
H-V CABLE
CURRENT LEAD
O-RING VACUUM SEAL
A
THERMOCOUPLE LEAD
RETAINER RING
H-V LEAD
PROBE PRESSURE GAUGE
PRESSURE TAP (TO PUMP)
R - COLLECTION ELECTRODE CYLINDER RADIUS = 4.32 cm
L - EFFECTIVE DISCHAGE ELECTRODE LENGTH = 22.86 cm
D - DISCHARGE ELECTRODE DIAMETER = 88.9 mm
A-B - TOTAL PROBE LENGTH = 1.22 m

Figure 1. Schematic diagram of the ion mobility probe.

problems have been encountered with the design described in this paper. One problem with the design is that it is difficult to get the probe into and out of 10.16 cm sampling ports, especially when the ports contain rough welds or are not completely circular. Future designs should allow for a larger clearance. Another problem encountered was that of attaining the temperature of the flue gas in the measurement chamber. Typically, the temperature in the measurement chamber could only be brought up to approximately 85-90 percent of the flue gas temperature. This problem can be alleviated by heating the end of the probe which remains outside the flue, using heating tape and insulation. A further problem encountered was due to the use of a short piece of RG8U coaxial cable to connect the high voltage lead to the spring-loaded high voltage connection. The insulation on the cable would melt when the probe was used for prolonged periods at temperatures of approximately 150°C. This problem can be avoided by using a different type of cable that can withstand higher temperatures or by devising a different type of high voltage connection.

Experimental Measurements and Results

In order to obtain reliable measurements of effective ion mobilities with the measurement technique described earlier, it is important to ensure that (1) particulate space charge effects are negligible, (2) free electron currents are negligible, and (3) ion mobility is not a function of electric field strength. Calculations of particulate charge densities based on measured mass loadings, particle size distributions, voltages, current densities, and residence times indicate that particulate space charge effects for particles less than 0.3 μm in diameter are negligible for the applications presented in this paper. Although indications are that free electrons can contribute a non-negligible component to the current at voltages greater than approximately 30 kV, the measurement technique can be applied at voltages below this value where the effect of free electrons can be ignored. If the ratio of the electric field strength (E) to the pressure (p) is in a certain range, the effective ion mobility will be independent of E. For positive and negative ions in air, the effective ion mobility is constant for ranges of E/p from 10^{-3} to 20 V/cm-Torr. In the results presented here, E/p ranged from 6.0 to 17.0 V/cm-Torr, and it has been assumed that the ion mobility is independent of E.

The measurement capabilities and operational characteristics of the ion mobility probe were analyzed in the laboratory with ambient air. Measurements of negative and positive effective ion mobilities in ambient air at approximately 25°C and 760 Torr were made with the probe under static conditions. Five measurements in negative corona and six in positive corona resulted in effective ion mobilities of 2.76 ± 0.17 and 1.75 ± 0.11 cm^2/V-sec, respectively. These values were obtained by using the entire voltage-current characteristic up to sparkover, which occurred at approximately 37 and 33 kV for negative and positive corona, respectively. Due to the higher than anticipated value of the negative effective ion mobility, both negative and positive mobilities were determined by using portions of the voltage-current characteristic up to various voltages before sparkover in order to determine if free electrons were contributing to the negative corona current at the higher voltages. For voltages less than 31 kV, the ranges for negative and positive mobilities were 2.1-2.3 and 1.6-1.7 cm^2/V-sec, respectively. These values of mobility are in agreement with those reported in the literature.[5,6] Since the positive mobility remained independent of applied voltage within the scatter of data but the negative mobility showed a dependence on applied voltage at higher voltages, this indicates that free electrons contribute a non-negligible component to the negative corona current at the higher voltages. Thus, for negative corona and applied voltages greater than approximately 31 kV, the higher values of electric field strength lead to a non-negligible contribution of free electron current due to the high energies acquired by electrons between collisions with neutral molecules.

The effects of gas flow and pressure on the measurement of effective ion mobilities were also analyzed in the laboratory. In these studies, both effective and reduced effective ion mobilities were determined. The reduced effective ion mobility (K_0) is defined as

$$K_0 = K \frac{p}{760} \frac{273}{T + 273} , \qquad (2)$$

where p (Torr) and T (°C) are the pressure and temperature at which the measurement was made.

Measurements of negative and positive effective ion mobilities in ambient air as a function of gas flow rate from 0.00012 m^3/sec (0.25 cfm) to 0.00083 m^3/sec (1.75 cfm) showed no dependence of flow rate on the measured mobilities within the scatter of the data. All these measurements were made at approximately 25°C and 760 Torr.

Measurements with no flow of negative and positive effective ion mobilities in ambient air as a function of gas pressure from 244 to 760 Torr showed the anticipated strong pressure dependence on both types of mobility. However, the reduced effective ion mobility for positive corona was essentially independent of pressure whereas the reduced effective ion mobility for negative corona increased significantly with decreasing pressure. Since the applied voltages at reduced pressures less than 625 Torr did not exceed 30 kV for negative corona, the dependence of the negative reduced effective ion mobility on pressure can not be attributed to a free electron contribution to the current due to high electric fields. The effect is one which is entirely pressure-dependent where large free electron currents are obtained at reduced pressures due to the increased mean free path of the electrons. Thus, measurements of effective ion mobilities of flue gases should be made at pressures which are as close as possible to that in the flue in order to minimize the undesired effect due to pressure and to simulate better the conditions in the precipitator. The data showed that the negative reduced effective ion mobility did not vary significantly between 625 and 760 Torr.

The ion mobility probe was used to obtain data at three different installations where the flue gas was generated in the combustion of coal. These installations will be referred to as Plants A, B, and C. At all three installations, measurements of both positive and negative effective ion mobilities were obtained under three different conditions. These conditions were (1) ambient air outside the flue without the thimble and with the pump on, (2) ambient air outside the flue with the thimble in and the pump on, and (3) inside the flue with the thimble in and the pump on. At Plants A and B, measurements of both positive and negative, approximate effective charge carrier mobilities due to both ions and particles were obtained by using the probe inside the flue without the thimble and with the pump on. Although this type of mobility will be a function of applied voltage and current to some extent due to the particle charging process, the value of mobility obtained by fitting the entire voltage-current curve with a constant mobility should provide a good estimate of the effective charge carrier mobility due to both ions and particles. The value of this type of mobility will depend on the mass per cubic meter of gas and the particle size distribution of the particles entering the measurement chamber. It should be emphasized that, if back corona occurs during this type of measurement, the measurement will not be meaningful.

Figures 2, 3, and 4 show representative voltage-current curves obtained under different conditions at the three different installations. Table 1 contains the results of the measurements. The multiple correlation coefficient provides a measure of how well the experimental data were fit by equation (1). A value of 1 would represent a perfect fit. O_2 and CO_2 concentrations were measured with an Orsat apparatus.[7] H_2O concentrations were measured by a solid absorbent technique[8] modified by Southern Research Institute. SO_2 and SO_3 concentrations were measured using a condensation method.[9]

The in situ effective ion mobilities given in Table 1 were obtained at reduced pressures. Therefore, the conditions under which the measurements were made are not representative of those in the precipitator and are very susceptible to significant free electron contribution to the negative corona current. Due to time constraints, the field test data had to be acquired before the laboratory study was completed, and the extent to which free electrons might contribute to the negative corona current at low pressures was underestimated. Thus, the philosophy used during the field test period was to pull enough gas flow (~0.00024 m^3/sec) through the measurement chamber to ensure a continuous, representative gas sample and to make the measurements at the lower pressures introduced by the pressure drop across the filter media. In future applications, it is anticipated that the pressure in the flue can be closely approximated in the measurement chamber by using a glass fiber filter and, if necessary, lower gas flow rates.

SUMMARY AND CONCLUSIONS

The following list summarizes the results obtained from using the ion mobility probe.

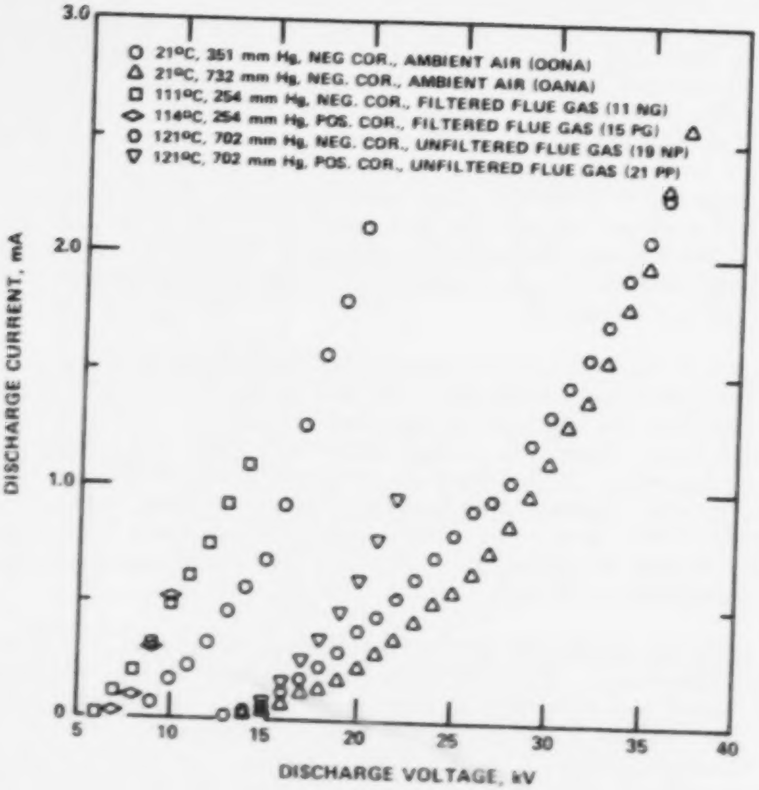

Figure 2. Typical voltage-current characteristics obtained with the probe at Plant A.

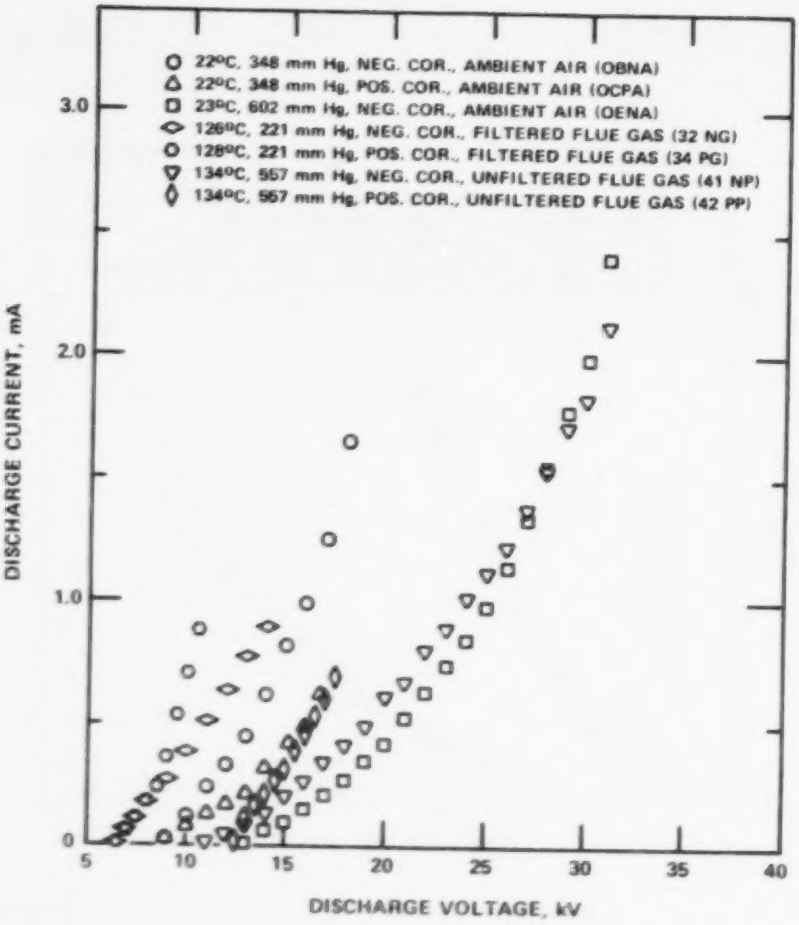

Figure 3. Typical voltage-current characteristics obtained with the probe at Plant B.

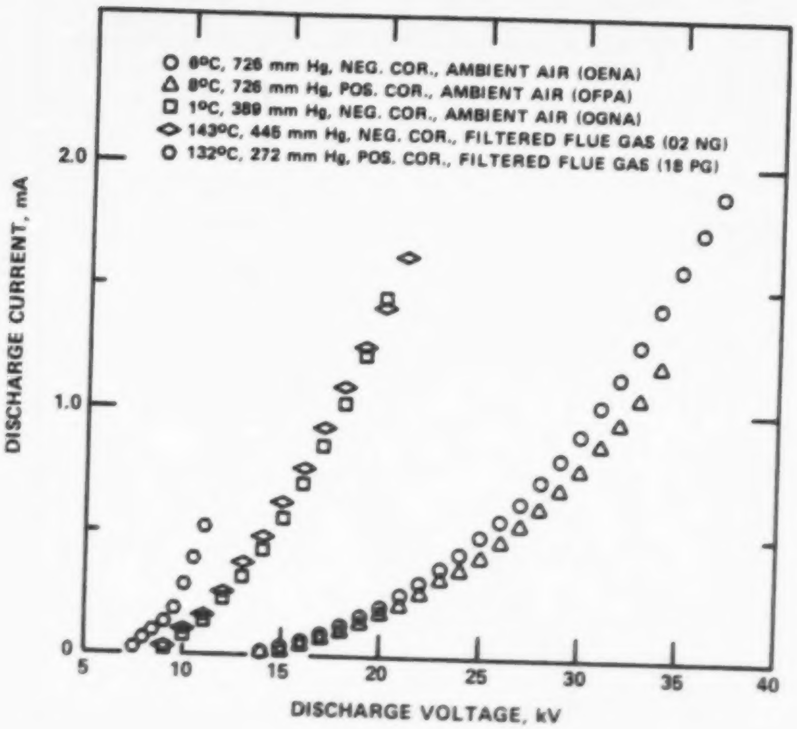

Figure 4. Typical voltage-current characteristics obtained with the probe at Plant C.

Table 1. ION MOBILITY FIELD TEST DATA

Test Site And Date	Run ID[1]	Temp. In °C	Absolute Pressure mm Hg	Effective Mobility K_e cm^2/v-s	Reduced Effective Mobility K_r cm^2/v-s	Multiple Correlation Coefficient	Average Reduced Effective Mobility $\bar{K}_r$	Volume Percent H_2O	Volume Percent O_2	Volume Percent CO_2	PPM SO_2	PPM SO_3	Maximum Voltage kV	Maximum Current Density µA/cm^2	Maximum Average E/p V/cm-Torr
PLANT A															
9/28/77	00NA	21	351	11.38	4.88	0.991		(Ambient Air Outside Flue)					20	4.00	13.2
9/28/77	0ANA	21	732	3.38	3.02	0.983		(Ambient Air Outside Flue)					37	4.83	11.7
9/28/77	01NG	88	300	7.16	2.14	0.998		9.5	6.7	12.9	711	0.9	22	3.19	17.0
9/28/77	04NG	101	338	7.27	2.36	0.992		9.5	6.7	12.9	711	0.9	19	2.42	13.0
9/28/77	02PG	90	338	12.81	4.29	0.913	3.97	9.5	6.7	12.9	711	0.9	13	1.59	8.9
9/28/77	03PG	99	338	11.19	3.65	0.967		9.5	6.7	12.9	711	0.9	13	1.15	8.9
9/28/77	06PG	103	269	19.06	4.90	0.978	5.31	9.5	6.7	12.9	711	0.9	11	1.08	9.5
9/28/77	07PG	107	262	22.80	5.65	0.970		9.5	6.7	12.9	711	0.9	11	0.13	9.7
9/28/77	08PG	107	262	21.78	5.39	0.976		9.5	6.7	12.9	711	0.9	10	0.85	8.8
9/28/77	09NG	107	262	11.57	2.87	0.996	2.91	9.5	6.7	12.9	711	0.9	14	1.82	12.4
9/28/77	10NG	110	254	11.27	2.69	0.992		9.5	6.7	12.9	711	0.9	15	2.08	13.7
9/28/77	11NG	111	254	13.21	3.14	0.996		9.5	6.7	12.9	711	0.9	14	2.05	12.8
9/28/77	12NG	111	254	12.38	2.94	0.994		9.5	6.7	12.9	711	0.9	14	1.89	12.8
9/28/77	13PG	111	254	22.29	5.30	0.931	5.81	9.5	6.7	12.9	711	0.9	10	1.14	9.1
9/28/77	14PG	112	254	26.26	6.22	0.966		9.5	6.7	12.9	711	0.9	10	1.05	9.1
9/28/77	15PG	114	254	25.08	5.91	0.978		9.5	6.7	12.9	711	0.9	10	0.99	9.1
9/28/77	17NP	107	702	3.31	2.20	0.995	2.23	9.5	6.7	12.9	711	0.9	36	4.13	11.9
9/28/77	19NP	121	702	3.45	2.21	0.997		9.5	6.7	12.9	711	0.9	36	4.29	11.9
9/28/77	20NP	121	702	3.55	2.27	0.997		9.5	6.7	12.9	711	0.9	36	4.24	11.9
9/28/77	18PP	112	702	7.26	4.76	0.993	4.81	9.5	6.7	12.9	711	0.9	22	1.83	7.3
9/28/77	21PP	121	702	7.60	4.86	0.999		9.5	6.7	12.9	711	0.9	22	1.80	7.3
PLANT B															
10/18/77	0ANA	21	348	12.32	5.24	0.992	5.17	(Ambient Air Outside Flue)					20	4.34	13.3
10/18/77	0BNA	22	348	12.03	5.10	0.995		(Ambient Air Outside Flue)					18	3.11	12.0
10/18/77	0CPA	22	348	5.02	2.13	0.994		(Ambient Air Outside Flue)					17	1.16	11.3
10/18/77	0DPA	22	602	2.71	1.99	0.996		(Ambient Air Outside Flue)					23	0.98	8.9
10/18/77	0ENA	23	602	5.04	3.60	0.990		(Ambient Air Outside Flue)					31	4.53	11.9
10/18/77	01NG	113	221	13.31	2.74	0.994	2.87	10.7	6.0	13.6	530	<0.5	14	2.27	16.7
10/18/77	02NG	115	221	15.97	3.27	0.995		10.7	6.0	13.6	530	<0.5	12	1.72	12.6
10/18/77	03NG	116	221	12.74	2.60	0.992		10.7	6.0	13.6	530	<0.5	13	1.64	13.4
10/18/77	04PG	116	221	28.00	5.71	0.853	4.75	10.7	6.0	13.6	530	<0.5	10	1.70	10.5
10/18/77	05PG	115	221	18.12	3.71	0.913		10.7	6.0	13.6	530	<0.5	9	0.75	9.4
10/18/77	06PG	115	221	23.66	4.84	0.986		10.7	6.0	13.6	530	<0.5	10	1.23	10.5
10/18/77	08NP	110	559	3.50	1.88	0.991	1.98	10.7	6.0	13.6	530	<0.5	30	3.26	12.4
10/18/77	09NP	116	559	3.99	2.06	0.997		10.7	6.0	13.6	530	<0.5	30	3.38	12.4
10/18/77	10NP	119	559	3.91	2.00	0.997		10.7	6.0	13.6	530	<0.5	30	3.31	12.4
10/18/77	11PP	120	559	7.55	3.86	0.981	4.03	10.7	6.0	13.6	530	<0.5	19	1.62	7.9
10/18/77	12PP	120	559	7.98	4.08	0.971		10.7	6.0	13.6	530	<0.5	15	1.35	6.2
10/18/77	13PP	118	559	8.11	4.16	0.974		10.7	6.0	13.6	530	<0.5	18	1.27	7.5
10/19/77	0FNA	7	348	11.20	5.00	0.997		(Ambient Air Outside Flue)					19	3.27	12.6
10/19/77	0GPA	7	348	5.29	2.36	0.998		(Ambient Air Outside Flue)					18	1.36	12.0
10/19/77	0HPA	9	602	2.61	2.00	0.995		(Ambient Air Outside Flue)					25	1.13	9.6
10/19/77	0INA	10	602	4.66	3.56	0.995		(Ambient Air Outside Flue)					33	4.69	12.7
10/19/77	14NG	107	348	6.30	2.10	0.999	2.13	(No Gas Analysis)					19	1.98	12.6
10/19/77	15NG	109	334	6.72	2.11	0.997		(No Gas Analysis)					20	2.65	13.9
10/19/77	16NG	112	334	6.91	2.15	0.996		(No Gas Analysis)					19	2.12	13.2
10/19/77	17NG	114	334	6.90	2.14	0.996		(No Gas Analysis)					17	1.88	11.8
10/19/77	18PG	115	334	15.43	4.77	0.990	4.97	(No Gas Analysis)					13	1.51	9.0
10/19/77	19PG	116	334	17.07	5.27	0.991		(No Gas Analysis)					13	1.52	9.0
10/19/77	20PG	117	334	15.84	4.87	0.983		(No Gas Analysis)					13	1.55	9.0
10/19/77	22NP	111	557	3.43	1.79	0.994	1.87	(No Gas Analysis)					29	3.01	11.1
10/19/77	23NP	114	557	3.71	1.92	0.988		(No Gas Analysis)					28	2.66	11.0
10/19/77	24NP	116	557	3.70	1.90	0.985		(No Gas Analysis)					27	2.53	11.2
10/19/77	25PP	118	557	7.03	3.60	0.957	3.61	(No Gas Analysis)					18	1.61	7.5
10/19/77	26PP	118	557	7.30	3.74	0.988		(No Gas Analysis)					18	1.35	7.5
10/19/77	27PP	117	557	6.79	3.40	0.959		(No Gas Analysis)					18	1.35	7.5
10/19/77	28NP	121	557	3.96	2.01	0.992	1.98	(No Gas Analysis)					26	2.30	10.8
10/19/77	29NP	121	557	3.84	1.95	0.993		(No Gas Analysis)					26	2.22	10.8
10/19/77	30PP	121	557	5.60	2.00	0.991		(No Gas Analysis)					19	1.17	7.9

---

[1] The Run ID's are coded in the following manner: Digits 1 and 2 are the run number for that test location. If they are letters, it is a test outside the flue. The third digit indicates the polarity of the corona (P or N). The fourth digit indicates gas only (G), gas and particulate (P), or ambient air (A).

Test Site And Date	Run ID[1]	Temp. In °C	Absolute Pressure mm Hg	Effective Mobility K_e cm²/v-s	Reduced Effective Mobility K_0 cm²/v-s	Multiple Correlation Coefficient	Average Reduced Effective Mobility $\bar{K}_0$	Volume Percent H_2O	Volume Percent O_2	Volume Percent CO_2	PPM SO_2	PPM SO_3	Maximum Voltage kV	Maximum Current Density µA/cm²	Maximum Average E/p V/cm-Torr
10/20/77	0JNA	32	343	9.97	4.03	0.994		(Ambient Air Outside Flue)					18	2.53	12.2
10/20/77	0KPA	29	343	5.11	2.08	0.994		(Ambient Air Outside Flue)					17	1.23	11.5
10/20/77	0LPA	26	597	2.63	1.89	0.999		(Ambient Air Outside Flue)					28	1.61	10.9
10/20/77	0MNA	22	597	3.49	2.54	0.988		(Ambient Air Outside Flue)					30	2.87	11.6
10/20/77	31NG	124	243	11.05	2.43	0.993	2.40	10.5	3.5	15.5	570	0.6	14	1.81	13.3
10/20/77	32NG	126	243	10.82	2.37	0.996		10.5	3.5	15.5	570	0.6	14	1.68	13.3
10/20/77	33NG	127	243	10.95	2.39	0.993		10.5	3.5	15.5	570	0.6	14	1.69	13.3
10/20/77	34PG	128	243	27.06	5.89	0.982	6.36	10.5	3.5	15.5	570	0.6	10.5	1.66	10.0
10/20/77	35PG	129	243	30.08	6.53	0.974		10.5	3.5	15.5	570	0.6	10	1.60	9.5
10/20/77	36PG	130	243	30.70	6.65	0.981		10.5	3.5	15.5	570	0.6	10	1.60	9.5
10/20/77	38NP	121	556	3.59	1.82	0.992		10.5	3.5	15.5	570	0.6	30	3.24	12.5
10/20/77	39PP	126	556	8.33	4.17	0.976		10.5	3.5	15.5	570	0.6	18	1.50	7.5
10/20/77	40NP	139	556	4.07	1.97	0.993	1.97	10.5	3.5	15.5	570	0.6	31	4.00	12.9
10/20/77	41NP	134	556	4.00	1.96	0.995		10.5	3.5	15.5	570	0.6	32	4.17	13.3
10/20/77	42PP	134	556	8.64	4.24	0.975	4.12	10.5	3.5	15.5	570	0.6	17.5	1.30	7.3
10/20/77	43PP	135	556	8.15	3.99	0.953		10.5	3.5	15.5	570	0.6	17	1.28	7.1
10/20/77	44NP	140	556	3.89	1.88	0.994	1.81	10.5	3.5	15.5	570	0.6	32	4.06	13.3
10/20/77	45NP	140	556	3.59	1.74	0.988		10.5	3.5	15.5	570	0.6	32	4.00	13.3
10/20/77	46NP	153	556	3.94	1.85	0.992	1.86	10.5	3.5	15.5	570	0.6	32	4.09	13.3
10/20/77	47NP	150	556	3.95	1.87	0.989		10.5	3.5	15.5	570	0.6	31	3.91	12.9
10/20/77	48PP	149	556	6.82	3.23	0.944		10.5	3.5	15.5	570	0.6	18	1.46	7.5
PLANT C															
12/6/77	0ANA	12	719	3.55	3.22	0.988		(Ambient Air Outside Flue)					36	4.40	11.6
12/6/77	0BPA	17	719	2.67	2.38	0.997		(Ambient Air Outside Flue)					36	3.15	11.6
12/6/77	0CNA	18	376	9.20	4.27	0.995		(Ambient Air Outside Flue)					22	3.97	13.6
12/6/77	0DPA	19	376	6.02	2.78	0.985		(Ambient Air Outside Flue)					23	2.78	14.2
12/7/77	0ENA	6	726	3.52	3.29	0.988		(Ambient Air Outside Flue)					37	4.71	11.8
12/7/77	0FPA	8	726	2.63	2.44	0.993		(Ambient Air Outside Flue)					39	3.86	12.4
12/7/77	0GNA	1	389	8.95	4.56	0.992		(Ambient Air Outside Flue)					23	4.24	13.7
12/7/77	0HPA	2	389	5.54	2.81	0.989		(Ambient Air Outside Flue)					24	3.18	14.3
12/7/77	01NG	139	445	7.10	2.75	0.989	3.09	8.3	6.2	13.8	687	0.8	15	1.21	7.8
12/7/77	02NG	143	445	7.04	3.01	0.992		8.3	6.2	13.8	687	0.8	21	3.05	10.9
12/7/77	03NG	145	445	9.15	3.50	0.996		8.3	6.2	13.8	687	0.8	21	3.28	10.9
12/7/77	04PG	143	439	17.05	6.47	0.959	5.59	8.3	6.2	13.8	687	0.8	11.5	0.41	6.1
12/7/77	05PG	141	448	11.99	4.70	0.934		8.3	6.2	13.8	687	0.8	11.75	0.53	6.0
12/9/77	0INA	21	724	3.21	2.84	0.992		(Ambient Air Outside Flue)					32	2.72	10.2
12/9/77	0JPA	22	724	2.37	2.09	0.999		(Ambient Air Outside Flue)					26	1.08	8.3
12/9/77	0KNA	24	368	12.79	5.70	0.990		(Ambient Air Outside Flue)					21	4.74	13.2
12/9/77	0LPA	26	368	5.15	2.28	0.996		(Ambient Air Outside Flue)					17	1.18	10.7
12/9/77	07NG	135	391	9.07	3.12	0.973	3.38	7.8	5.2	14.1	917	2.0	18	2.57	10.7
12/9/77	08NG	138	391	10.70	3.66	0.998		7.8	5.2	14.1	917	2.0	17.5	2.46	10.4
12/9/77	09NG	139	389	9.91	3.36	0.988		7.8	5.2	14.1	917	2.0	18	2.60	10.7
12/9/77	10PG	139	386	12.13	4.08	0.933		7.8	5.2	14.1	917	2.0	11	0.58	6.6
12/9/77	13NG	129	297	17.99	4.78	0.989	4.51	7.8	5.2	14.1	917	2.0	10	0.63	7.8
12/9/77	14NG	132	300	16.76	4.46	0.996		7.8	5.2	14.1	917	2.0	13	1.62	10.0
12/9/77	15NG	133	300	16.14	4.28	0.992		7.8	5.2	14.1	917	2.0	13	1.50	10.0
12/9/77	16PG	135	300	14.14	3.73	0.981	4.21	7.8	5.2	14.1	917	2.0	11	0.68	8.5
12/9/77	17PG	135	300	18.27	4.82	0.977		7.8	5.2	14.1	917	2.0	12	1.31	9.3
12/9/77	18PG	132	272	16.95	4.09	0.981		7.8	5.2	14.1	917	2.0	11	0.98	9.4

(1) K = 2.1-2.3 cm²/V-sec for measurement with negative corona in laboratory air at ambient conditions for applied voltages less than approximately 31 kV.

(2) K = 1.6-1.7 cm²/V-sec for measurement with positive corona in laboratory air at ambient conditions for all applied voltages before sparkover.

(3) K and K_0 are independent of gas flow for both negative and positive corona within the scatter of the data.

(4) K_0 shows strong pressure dependence for negative corona in laboratory air and ambient air outside flue (due to free electron contribution to the current).

(5) K_0 is relatively independent of pressure for positive corona in laboratory air and ambient air outside flue.

(6) K_0 shows strong pressure dependence for negative corona in filtered flue gas (attributable to free electron contribution to the current).

(7) Limited data indicate that K_0 may show a strong pressure dependence for positive corona in filtered flue gas.

(8) Measurements of K_0 for positive corona in filtered flue gas generally yield values which are 1.5-2.5 times as large as those for negative corona under the same conditions.

The technique described in this paper for making _in situ_ effective ion mobility measurements is capable of providing mobility data which are sufficiently accurate for use in modeling the electrostatic precipitation process. Reliable and reproducible data can be easily obtained with the ion mobility probe. The problems associated with the free electron contribution to the negative corona current could be alleviated to a large extent if larger sampling ports were generally available so that the measurement chamber could be larger. If larger sampling ports were available, the effects due to reduced pressures which exist in precipitators operating at high altitudes could be analyzed in a similar geometry. As a further consideration, this technique can be utilized in an extractive system if it proved easier to implement.

ACKNOWLEDGMENTS

This work was supported by the Industrial Environmental Research Laboratory, U.S. Environmental Protection Agency, Research Triangle Park, North Carolina, under Contract No. 68-02-2193, Leslie E. Sparks, Project Officer. The assistance of Herbert W. Spencer, III in the development of this technique is greatly appreciated.

REFERENCES

1. Spencer, H. W. Experimental Determination of the Effective Ion Mobility of Simulated Flue Gas. In: Proceedings of 1975 IEEE-IAS Conference, Atlanta, Georgia, 1975.

2. Tassicker, O. J. Experience with an Electrostatic Precipitation Analyzer in the Evaluation of Difficult Dusts. In: Proceedings of International Clean Air Conference, Melbourne, Australia, May 1972.

3. Marquardt, D. W. An Algorithm for Least-Squares Estimation of Non-Linear Parameters. J. Soc. Ind. Appl. Math., 11:431, 1963.

4. Loeb, L. B. Fundamental Processes of Electrical Discharge in Gases. John Wiley & Sons, Inc., New York, 1939. p. 33.

5. Thomson, J. J. and G. P. Thomson. Conduction of Electricity Through Gases. Vol. I, 3rd ed., Dover Publications, Inc., New York, 1969. p. 123.

6. Bricard, J., M. Cabane, G. Modelaine, and D. Vigla. Aerosols and Atmospheric Chemistry. Edited by G. M. Hidy, New York, 1972. p. 27.

7. Brenchley, D., C. Turley, and R. Yarmac. Industrial Source Sampling. Ann Arbor Science Publishers, Inc., Ann Arbor, Michigan, 1973. pp. 132-138.

8. Brenchley, D., C. Turley, and R. Yarmac, Ref. 7, pp. 138-144.

9. Lisle, E. and J. Sensenbaugh. The Determination of Sulfur Trioxide and Acid Dew Point in Flue Gases. Combustion, 36(7):12-16, 1965.

PILOT SCALE ELECTROSTATIC PRECIPITATORS AND THE ELECTRICAL PERFORMANCE DIAGRAM

Kenneth J. McLean
Ronald B. Kahane
University of Wollongong
P.O. Box 1144, Wollongong,
N.S.W. Australia.

ABSTRACT

The paper develops mathematical relationships which model the electrical characteristics of a pilot scale electrostatic precipitator for a full range of resistivities. These equations are summarised in a convenient form by the Electrical Performance Diagram which relates the back corona onset current and voltage, and the sparkover voltage to the deposited layer operational resistivity. The analysis is based on the dimensions and characteristics of an actual pilot electrostatic precipitator rig, and the usefulness of the Electrical Performance Diagram is demonstrated by using results from tests made on this unit[1].

INTRODUCTION

One important method which is often used to investigate the electrostatic precipitation characteristics of a fly ash is to measure its collection efficiency with a pilot scale electrostatic precipitator.

In order to interpret the results obtained from a pilot electrostatic precipitator, whether for research or commercial purposes, it is desirable to understand how the precipitator's performance with different fly ashes is reflected in its electrical characteristics. In recent years, there has been an increase of interest in these characteristics and in correlating them with the collection performance of both pilot and full sized units.

(This paper is an abbreviated form of the one presented to the International Clean Air Conference, May 15-19, 1978, Brisbane, Australia.)

Preceding page blank

The purpose of this paper is to develop simple mathematical equations which model the main electrical characteristics of a pilot electrostatic precipitator, which are summarised in a convenient form by the Electrical Performance Diagram. This Diagram can be used to interpret the electrical measurements made during actual test runs and relate them to the electrical properties of the precipitated ash on the collecting plates.

PILOT ELECTROSTATIC PRECIPITATOR

The following analysis is based on the CSIRO pulverised-coal-fired furnace and electrostatic precipitator rig. The furance is of horizontal and cylindrical construction which burns 60 kg h^{-1} of coal corresponding to a heat release rate of 1.7×10^5 W m^{-3}. The pilot electrostatic precipitator, powered by fullwave rectifier units, has three identical stages in series, each stage comprising two parallel tubular precipitators. The tubes are 0.76 m long and 0.16 m diameter with a central discharge wire of 2.5 mm diameter.

Voltage Current Characteristics

Before any useful progress can be made in interpreting the measured electrical characteristics of an electrostatic precipitator or constructing the Electrical Performance Diagram, it is necessary to determine the relationship between the applied voltage and corona current of the interelectrode gas gap for dust free conditions.

The actual voltage and current are not steady values but are periodic functions which vary over a cycle. It is convenient however, to use average values when these parameters are measured. The mathematical model used in this paper is based on the simple equivalent circuit shown in Figure 1. The interelectrode gap is represented by the strongly non-linear resistance R_g and the effective resistance of the deposited layer by R_d.

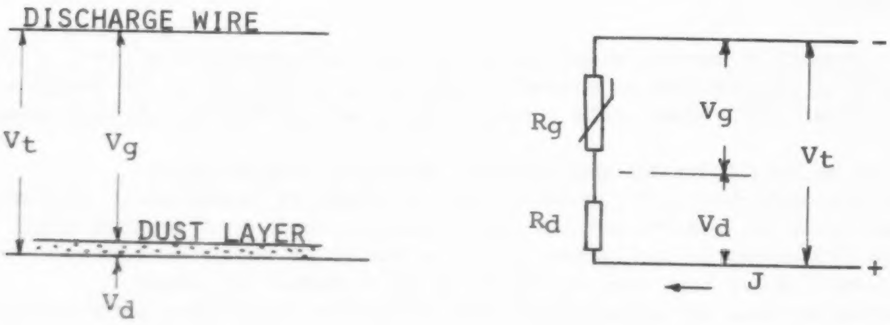

Figure 1: Equivalent Circuit Representation of Interelectrode Gas Gap and Deposited Dust Layer

Dust Free Characteristics

In order to find R_g for the pilot electrostatic precipitator, the V-J characteristic was measured by passing dust free flue gas at the appropriate temperature through the precipitator after it had been thoroughly cleaned. This experimental curve, shown in Figure 2 was then checked with that calculated from the solution of Poisson's Equation and excellent agreement was obtained.

Effect of the Dust Layer

As it is only possible to measure the terminal or external electrical characteristics of a precipitator during operation, it is useful to know from theoretical considerations the manner in which these characteristics are modified by dust build up on the collecting plates. From the equivalent circuit, the terminal voltage is given by,

$$V_t = V_g(J) + \rho Jd \qquad (1)$$

where $V_g(J)$ is the gap voltage and is a function of the current density; ρJd is the voltage drop, V_d, across the dust layer. The effect of the deposited layer is to displace the V-J characteristic as shown in Figure 2, the extent of which depends on the product of ρ and d for a given current density.

The curves in Figure 2 are based on the assumption that ρ is constant. It is however well known that the resistivity of the dust layer decreases with increasing electric field and is consequently a function of corona current density J. As J increases, the operational (or effective) resistivity of the dust layer decreases. Figure 2 shows how the V-J characteristic is modified for a dust layer with an initial field resistivity of 3×10^9 ohm-m and which is reduced by a factor of 3 at high current densities.

SPARKOVER EQUATIONS

For maximum efficiency of precipitator performance, it is normally desirable to set the terminal voltage to the highest value obtainable, which is limited by either the interelectrode sparking intensity or maximum desirable current. In the pilot precipitator, sparking is the usual limiting factor. This may be caused by either one of two distinct mechanisms.

Normal Breakdown

This is the breakdown that occurs with low resistivity dusts and is approximately equal to the gap sparkover voltage, V_{gb}, with dust free electrodes. Its magnitude is determined by the electrode geometry, gas composition, temperature and the polarity of the corona on the discharge wires. For the pilot precipitator investigated in this paper, V_{gb} is approximately 33 kV.

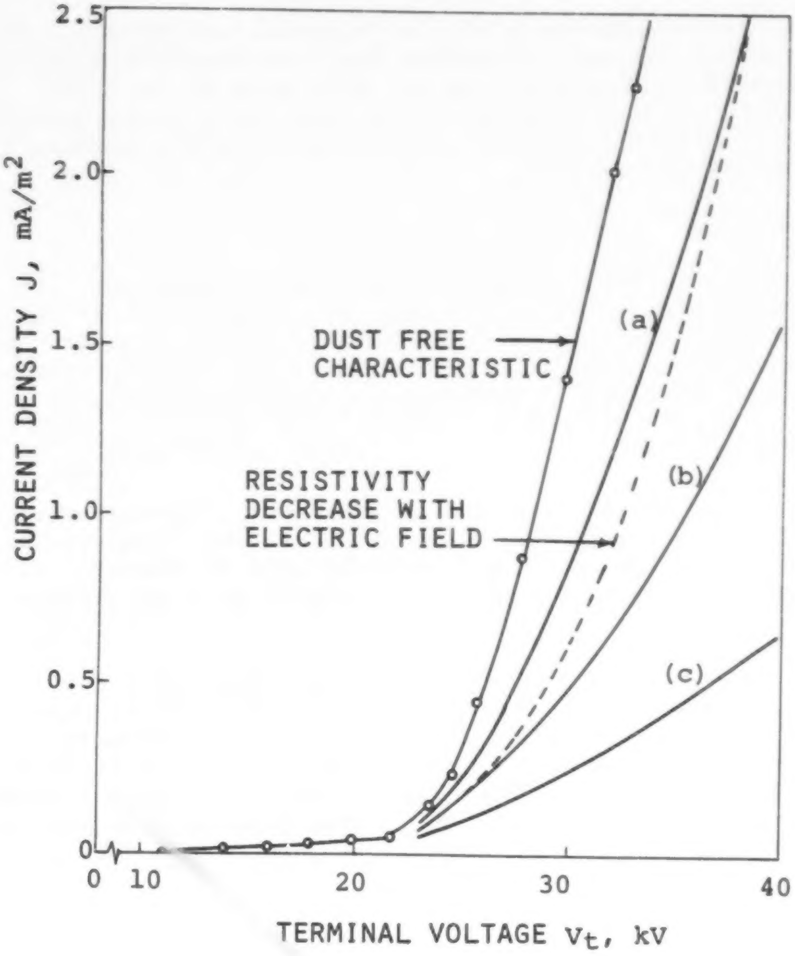

Figure 2: V-J Gas Gap Characteristics Showing the Effect of the Deposited Layer Resistivity. Dust Layer thickness, d = 2.0 mm.

Curve: (a) Resistivity 10^9 Ohm-m
(b) Resistivity 3×10^9 Ohm-m
(c) Resistivity 10^{10} Ohm-m

The terminal voltage at breakdown, V_{tb}, is given by the sum of the gap voltage at breakdown and the voltage drop across the deposited dust layer of thickness d. Hence,

$$V_{tb} = V_{gb} + J_b\rho d$$

$$= 33{,}000 + J_b\rho d \qquad (2)$$

The current density at breakdown, J_b, is determined from the clean V-J characteristics and has a value of 2.3 mA/m^2.

These results are plotted in Figure 3 and form part of the Electrical Performance Diagram for the pilot electrostatic precipitator. In this region, V_{gb} and J_b are constant and the terminal voltage, V_{tb}, increases with increasing values of ρ and d as given by (2).

All electrostatic precipitators have a mode of operation in which the maximum allowable voltage is limited by some design feature of the equipment. This may be the maximum voltage or the current rating of the power supply.

Back Corona Onset

For dust layer operational resistivities above a critical value, back corona will occur before the gap voltage has reached its normal breakdown value. Once back corona is established, sparking is imminent. Its onset represents a critical factor in a precipitator's operation and is responsible for the low sparkover voltages obtained with some of the Australian low sulphur coals.

The current density at the onset of back corona, J_c, is given by the equation,

$$J_c = \frac{E_c}{\rho} \qquad (3)$$

where E_c is the electric field across the dust layer at which breakdown occurs and back corona is established, and ρ is the operational resistivity at this electric field. If it is assumed that $E_c = 3.0 \times 10^6$ V/m, the variation of current density at the onset of back corona may be determined as a function of the resistivity as shown in Figure 3.

If J_c is calculated from (3) for a given resistivity, then by using the dust free V-J characteristic given in Figure 2, the gap voltage, V_{gc}, may be found at back corona onset. The terminal voltage, V_{tc}, is then determined by adding to V_{gc} the voltage drop across the dust layer.

$$V_{tc} = V_{gc} + dE_c \qquad (4)$$

Variation of V_{gc} and V_{tc} with the resistivity for the condition given above and dust thickness of 2 mm are shown in Figure 3. Similar curves may also be drawn for other values of d.

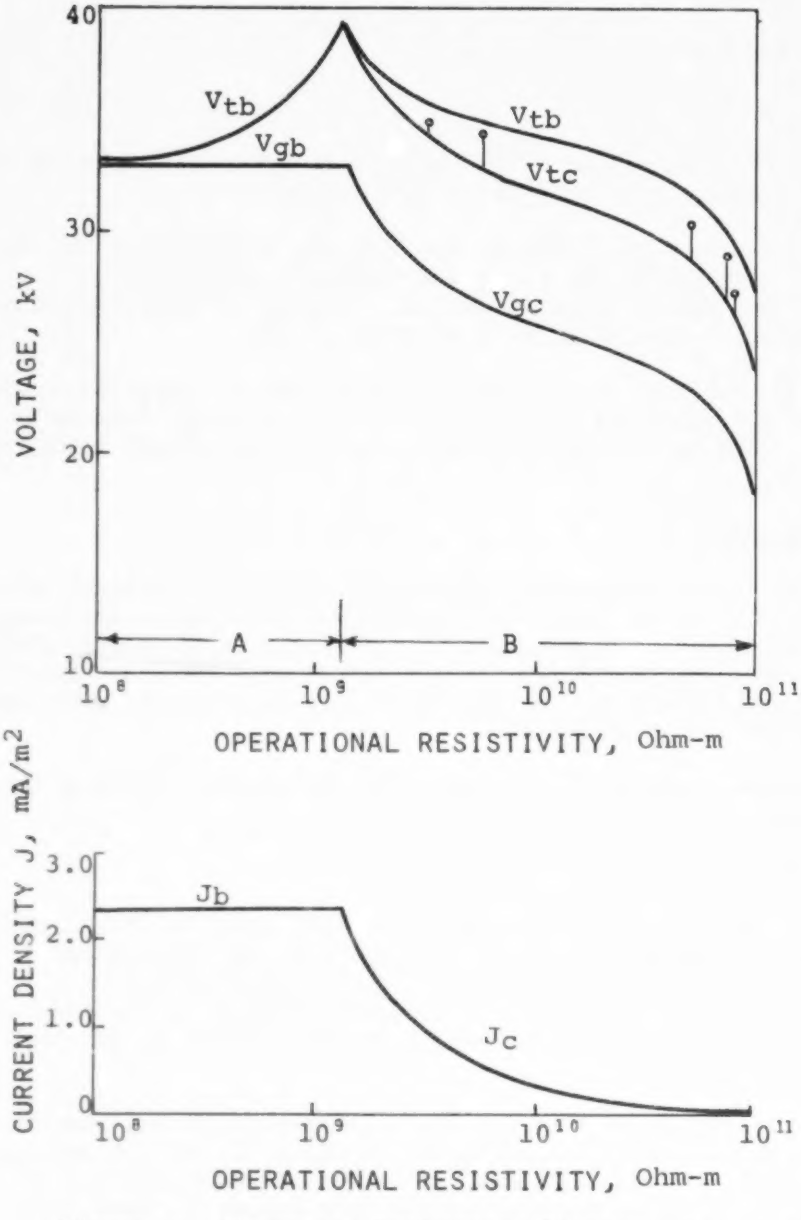

Figure 3: Electrical Performance Diagram. $E_c = 3 \times 10^6$V/m, d = 2 mm. ⫯ measured values of V_x

A Range for normal breakdown
B Range for breakdown due to back corona

The onset of back corona is one of the critical factors which determines the operation of an electrostatic precipitator and the construction of the Electrical Performance Diagram. It can often be detected by the abrupt change in the gradient of the measured V-J characteristic which results from the increase in current due to the positive ion flow from the collecting plate to the discharge electrode.

Sparkover Caused by Back Corona

Sparkover usually occurs at a voltage slightly above the value at which back corona is initiated. This may be expressed as,

$$V_{tb} = V_{tc} + V_x \qquad (5)$$

V_x is the additional voltage required above V_{tc} to cause sparking and is usually in the order of 1-3 kV, but under special conditions it may be higher.

The magnitude of the additional voltage, V_x, depends on several factors and one of the most important appears to be the intensity of the back corona discharge. This has to be sufficiently vigorous to enable it to propagate streamers into the gap and initiate the spark. Values from 1-3 kV appear to be sufficient to do this in the CSIRO pilot electrostatic precipitator although it need not be the same for other units.

Some typical magnitudes of V_x were determined from a number of V-J characteristics measured during actual test runs for coals producing fly ashes with quite different characteristics. These were then added to the appropriate value of V_{tc} and are shown plotted in Figure 3. The resultant terminal voltage, V_{tb}, curve has been drawn assuming $V_x = 3$ kV.

ELECTRICAL PERFORMANCE DIAGRAM

Discussion

The most critical assumption made in constructing the Electrical Performance Diagram is that associated with evaluating the shape of the J-ρ curve in Figure 3. J_b is a measured value, and although it fluctuates slightly with time, its average value is easily measured and is reasonably accurate. The shape of the J_c curve depends on the assumed value of E_c, the electric field at which corona is established (3). The Electrical Performance Diagram is constructed on the basis that $E_c = 3 \times 10^6$ V/m, which is the generally accepted value. It is not expected that this will vary by more than ±30% and, hence, the J-ρ curve must be reasonably accurate.

The voltage between the surface of the dust layer and the discharge wire cannot be measured but its magnitude may be estimated from the clean electrode V-J characteristics if the current density is known. In practice, this characteristic may need to be modified because of contamination of the discharge electrode and the space change effects due to the presence of charged suspended particles. The influence of the particulate space charge can be reduced to a minimum by carrying out the analysis on either the second or third stages of a multistage electrostatic precipitator.

Method of Use

Once the Electrical Performance Diagram is constructed, it may be used to determine the electrostatic precipitator's mode of operation for the different fly ash samples being tested.

The first step, is to measure the V-J characteristic of the outlet stage of the precipitator for normal operation, preferably during or at the end of a test run. The results for four different fly ashes are shown in Figure 4; the maximum voltage for each curve being the value at which sparking occurred. From the shape of these characteristics it is possible to identify the terminal voltage, V_{tc}, and current density, J_c, at which back corona is established for each of the ashes, and the terminal voltage, V_{tb}, and current density, J_b, at breakdown.

By projecting the measured value of J_c to the J-ρ curve in Figure 3 an approximate value of the operational resistivity of the dust layer on the collecting plate may be determined. The gap voltage at the onset of back corona is then found by projecting vertically to the V_{gc} line. This voltage must be reasonably accurate as it is determined from the measured gap characteristics.

The difference between the measured terminal voltage, V_{tc}, and the estimated gap voltage, V_{gc}, depends on the thickness of the dust layer on the plate (4) and this may be roughly estimated from the diagram.

The increase in the terminal voltage from that at back corona onset to the sparkover value is easily determined from the measured V-J characteristics and will result in a corresponding increase in the gap voltage.

If the resistivity of the fly ash is sufficiently low so that back corona is not formed, the precipitator will operate in the normal breakdown mode. This will be obvious from V-J characteristic, which will be slightly displaced from, but will follow the same general shape of the dust free characteristic. The discontinuity of the onset of back corona will be absent.

Interpretation

Some representative V-J characteristics for the second stage of the pilot electrostatic precipitator are shown plotted in Figure 4, together with the clean electrode characteristic. The broken curves show the probable shape of the V-J characteristic if back corona had not occurred. All the ashes come from the combustion of low sulphur coals.

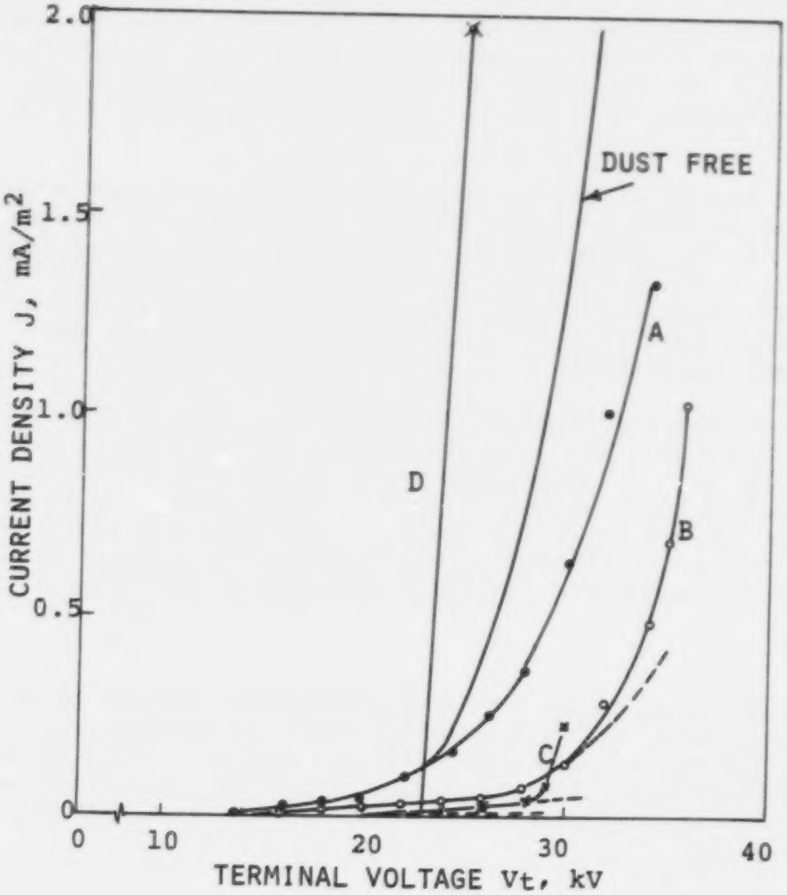

Figure 4: The Measured Corona V-J Characteristics of Different Fly Ashes Compared with the Dust Free Gap Characteristic.

Curve A is for a conditioned fly ash and has all the characteristics of a relatively low resistivity fly ash; it does not exhibit the presence of any back corona and follows very closely the dust free gap characteristic. The displacement to the right is due to the voltage drop across the deposited dust layer together with a possible slight change in the gap V-J characteristics because of the conditioning agent in the flue gas and some contamination of the discharge electrode. Normal gap breakdown has occurred. The operational resistivity is approximately 3×10^8 ohm-m.

Curve B is that of a relatively easy Australian fly ash to collect in commercial electrostatic precipitators. For a marginal fly ash such as this one, it is difficult to know exactly the point of back corona onset, but it probably occurs at about 33 kV. The slope of the V-J characteristic while operating in the main corona mode has been reduced. The operational resistivity is approximately 10^{10} ohm-m and the effective dust layer thickness is in the order of 2.0 mm.

Curves C and D represent the characteristics of very high resistivity fly ashes. For both these ashes the precipitator is operating with very low current densities. The fly ash represented by C, has resistivity in the order of 6×10^{10} ohm-m and a dust layer thickness less than 2.0 mm. Fly ash D has an even higher resistivity, going into the back corona mode at current densities of $J_C = .004$ mA/m^2. Its operational resistivity must be in the order of 10^{12} ohm-m.

CONCLUSIONS

The main purpose of the Electrical Performance Diagram is to determine in general terms the pilot electrostatic precipitator's mode of operation while collecting different fly ash samples. It provides valuable qualitative information concerning how the precipitator is responding electrically and assists in interpretating the efficiency measurements.

ACKNOWLEDGMENTS

One of the authors (McLean), wishes to thank the CSIRO and Dr. E.C. Potter for providing the opportunity to participate in part of their research programme.

REFERENCES

1. McLean, K.J. and Kahane, R.B. "Electrical Performance Diagram for a Pilot Scale Electrostatic Precipitator". In International Clean Air Conference, Brisbane, 1978: White, Hetherington and Thiele, Eds., Ann Arbor Science, U.S.A., 1978.

2. McLean, K.J., "Factors Affecting The Electrical Characteristics of Electrostatic Precipitators," Proc. IEE, 122: 672-674, June 1975.

3. Tassicker, O.J., "Measurement of Corona Current Density at an Electrical Boundary, Electron. Lett., 5:285-286, June 1969.

APPENDIX: RELATIONSHIP OF OPERATIONAL RESISTIVITY TO ACTUAL LAYER RESISTIVITY

In the preceding analysis, average values of voltage and current are used. In order to evaluate the actual layer resistivity from the average current reading, it is necessary to take into account the periodic variation of the corona current[2], and the spacial variation of current density along the discharge wires and in the transverse direction.[3] As a result of this temporal and spacial variation of current density, the actual current density at some points on the dust layer during times of peak voltage is considerably greater than the average value. This maximum current density is related to the average value by,

$$J_m = KJ \qquad (6)$$

where K is a factor, which is a function of the electrode geometry, corona current wave shape and the dust layer resistivity. Back corona will first be initiated in these areas of maximum current density.

The significance of this can be illustrated by considering curve B in Figure 4. Based on average values, the operational resistivity is 10^{-10} ohm-m. If K in Eqn (6) is assumed to be 10, then the actual resistance of the dust layer is,

$$\rho_d = \frac{E}{J_c K} = 3 \times 10^6/0.3 \times 10^{-3} \times 10 = 10^9 \text{ ohm-m}$$

THEORETICAL STUDY OF PARTICLE CHARGING BY UNIPOLAR IONS

D. H. Pontius
W. B. Smith
Southern Research Institute
Birmingham, Alabama 35205

and

J. H. Abbott
U.S. Environmental Protection Agency
Industrial Environmental Research Laboratory
Research Triangle Park, North Carolina 27711

ABSTRACT

Basic concepts of diffusion and electric field effects on particle charging are discussed, and some results of recent theoretical work are presented, with emphasis on applications to electrostatic precipitators. Nonideal effects are treated, including inhomogeneous charging conditions, space charge effects and ultrafine particle charging.

BACKGROUND

Particle charging in an electrostatic precipitator is accomplished by exposing the particulate material to an environment containing a large numerical density of unipolar ions in a strong electric field. Since the electrical force ultimately responsible for removing particles from a gas stream depends on the product of the field strength and the total charge per particle, the effectiveness of particle charging in an electrostatic precipitator is an important factor in the overall collection efficiency of such a system.

The source of ions in a conventional precipitator is a high voltage corona discharge. The ions drift in the electric field from the vicinity of the discharge electrode (typically, a wire) toward a passive electrode. The gas to be cleaned moves through the system in a direction approximately perpendicular to the motion of the ions, and charging results from the interactions between particles and ions. It is easy to see that a simple collision between an ion and an uncharged particle can result in ion attachment. But if the particle has a charge with polarity the same as that of the ions, then there is a repulsive force between the particle and any ion that approaches. The nature of the force between a particle and a neighboring ion is illustrated in Figure 1. It can be seen that there is a repulsive barrier between a charged particle and an ion, but if the ion can be brought close enough to the particle, the direction of the force reverses, providing the attraction necessary for ion attachment.[1] The attractive force results from rearrangement of the electrical charge on the particle (image charge) due to the presence of the nearby ion. It is clear that in order to add charge to a particle it is necessary for an ion to approach with sufficient energy to overcome the repulsive barrier. The source of that energy may be either the thermal energy of the ions or the applied electric field.

CHARGING THEORIES

The early particle charging theories treated the effects of the electric field and the thermal motion of the ions separately. Because of the distinct nature of the two effects, each predominates over a different range of particle diameters. For particles less than approximately 0.1 μm diameter the thermal energy of the ions has the most important effect on particle charging. Electric field effects generally dominate the charging process for particles of the order of 1.0 μm diameter and larger. These are not sharp cut-off values, but depend on the charging conditions.

Diffusion Charging

When only the random thermal motion of the ions is considered, the resulting theory of particle charging is independent of any externally applied fields. In this "diffusion charging" theory the temperature of the gas is the dominant factor. The ions, which are in thermal equilibrium with the gas molecules, move randomly at speeds of several hundred meters per second. But collisions between ions and molecules are so frequent that the mean free path traversed by an ion between successive collisions is less than 0.1 μm.

The electrostatic repulsion between a particle and an ion is a strong force only within a distance of 1 or 2 times the diameter of the particle. Thus, for small particles the distance an ion travels between collisions with molecules may be great enough to span the repulsive barrier. As the charge on a particle increases more energy is required for an ion to penetrate the repulsive barrier. The thermal energy is distributed among the ions such that only a small fraction of them have speeds much greater than the mean value. However, for any required value of energy, there is a non-zero probability that an ion in the system has a greater amount of energy. Thus, there is no limiting value to the total charge that can be accumulated by a particle, but the rate of

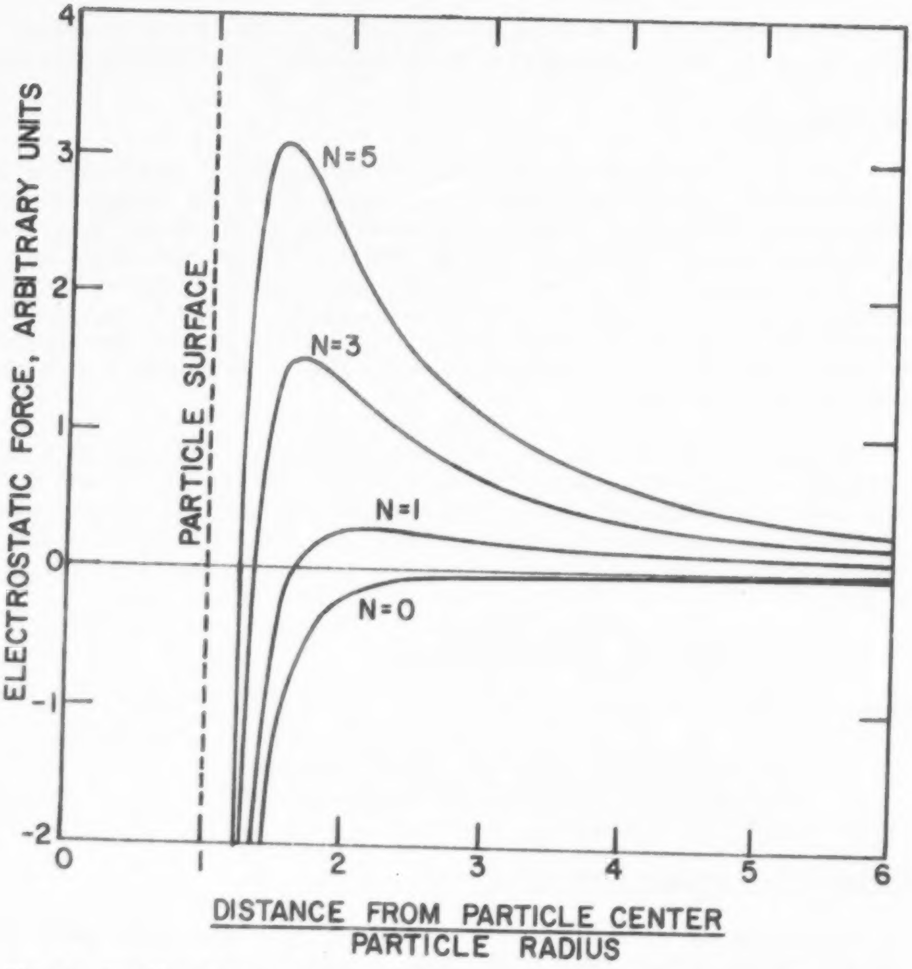

Figure 1. Electrostatic force between an ion and its image charge as a function of the distance between the particle and the ion. A positive value of force indicates repulsion. N is the number of elementary charges on the particle.

charging by the diffusion process decreases as the total charge on a particle increases.

The result of the diffusion charging theory can be expressed by the following equation for the total charge q accumulated by a particle having radius a, where the local ion concentration is N and the absolute temperature is T:

$$q = \frac{akT}{e^2} \ell n \frac{1 + a\overline{v}\pi e^2 Nt}{2kT} \tag{1}$$

In this equation, k is Boltzmann's constant, $\overline{v}$ is the mean molecular velocity, t is the charging time interval, and e is the electron charge.[2]

Field Charging

Ions in an electric field have, in addition to their random microscopic motion, a macroscopic drift velocity along the direction of the field lines. The drift velocity is generally much slower than the average random thermal velocity, but the motion is directed along the electric field lines. Thus, the field charging theory is based upon the interception of a stream of ions by a particle. This theory provides the most accurate description of particle charging when the length of the mean free path of the ions is negligible in comparison with the diameter of the particle.

Unlike the diffusion charging process, field charging is limited by the magnitude of the externally applied electric field. Thus, for a given particle diameter and applied field strength, there is a saturation level beyond which no further field charging can occur. The total charge q on a particle of radius a as a result of the field charging process is[3]

$$q = \left(1 + 2\,\frac{K-1}{K+2}\right) Ea^2 \left(\frac{\pi Nte\mu}{1+\pi Nte\mu}\right) \tag{2}$$

where

K = dielectric constant of the particle
E = applied electric field strength, and
μ = ion mobility.

Comprehensive Charging Theories

Since the field and diffusion charging theories each apply to a restricted range of physical conditions, attempts have been made to develop a unified theory of particle charging applicable to particles of arbitrary size. Murphy, et al.[4] formulated a combined theory in 1959, but the resulting equations were intractable. A simpler theory, by Liu and Yeh[5] provided a useful approach, which was further developed by Smith and McDonald.[6] In this latter theory the effects of the external electric field and the thermal motion of the ions are taken into account simultaneously. The electric field in the vicinity of a particle is computed by application of classical electrodynamics. An ion probability distribution, determined from the field calculation, provides a basis for computing the probability of ion attachment.

Because the local electric field depends upon the state of charge on a particle, as well as the applied field, the changes in the field as charging proceeds must be taken into account. In the theory of Smith and McDonald, an expression is derived for the charging rate for each of three zones on the surface of a particle, each zone defined by specific boundary conditions applied to the electric field at the surface. The sum of the three charging rates is an integral expression which is evaluated numerically by a computer.

Figures 2 through 5 show comparisons between the simple field and diffusion theories, their sum, and the Smith-McDonald theory.

In Figure 2, large values for both applied electric field strength and ion density-residence time product (Nt) are illustrated. The diffusion and field charging results cross at a particle radius of about 0.3 µm. Although the sum of the field and diffusion charging theories agrees well with the Smith-McDonald theory for particles up to 0.2 to 0.5 µm radius, the latter is as much as a factor of 3 greater than the former for particles of the order of 1.0 µm radius or greater.

Figure 3 shows similar results for large Nt and relatively small electric field strengths. In this case the discrepancy between the sum of diffusion and field charging compared with the Smith-McDonald theory is even greater for large particles than in the previous case.

When a low value for Nt is combined with a high electric field strength the sum of field and diffusion theories is nearly identical with the Smith-McDonald theory (Figure 4).

Finally, for small values of Nt and electric field strength, diffusion charging dominates for particle radii up to nearly 1.0 µm, as shown in Figure 5. There is only a 20% maximum difference between the Smith-McDonald theory and the field-diffusion charging sum.

The classical field and diffusion charging calculations involve relatively simple algebraic expressions. It is often advantageous to use such an approach to estimate particle charging. In some cases, however, the results may entail quite large errors, and consequently a more sophisticated method would be justified.

NON-IDEAL EFFECTS

A theoretical model of particle charging requires descriptions of the physical conditions surrounding the particle. But in virtually all applications of such a theory, the electric field strength, the ion density and other charging parameters may be broadly variable functions of

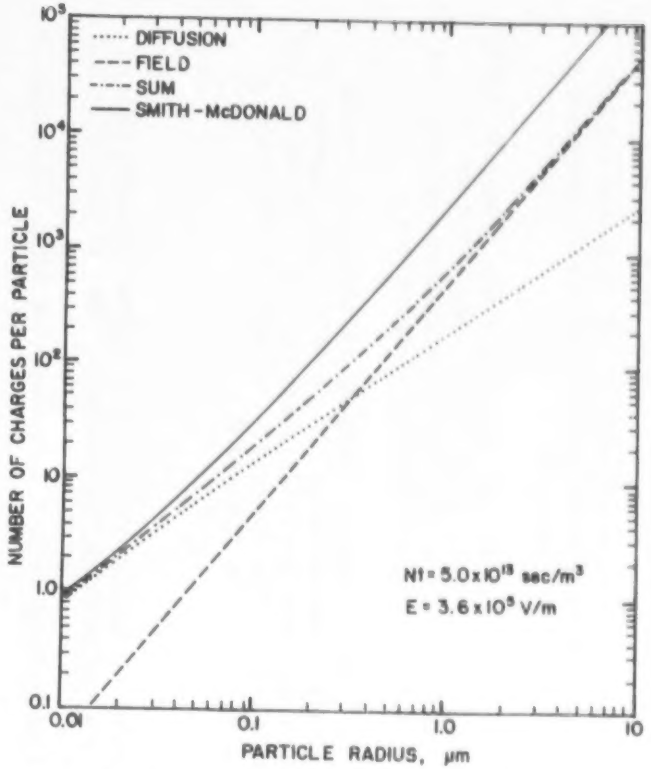

Figure 2. Average charge per particle as a function of particle radius for moderately high values of electric field strength E and ion density-residence time product Nt.

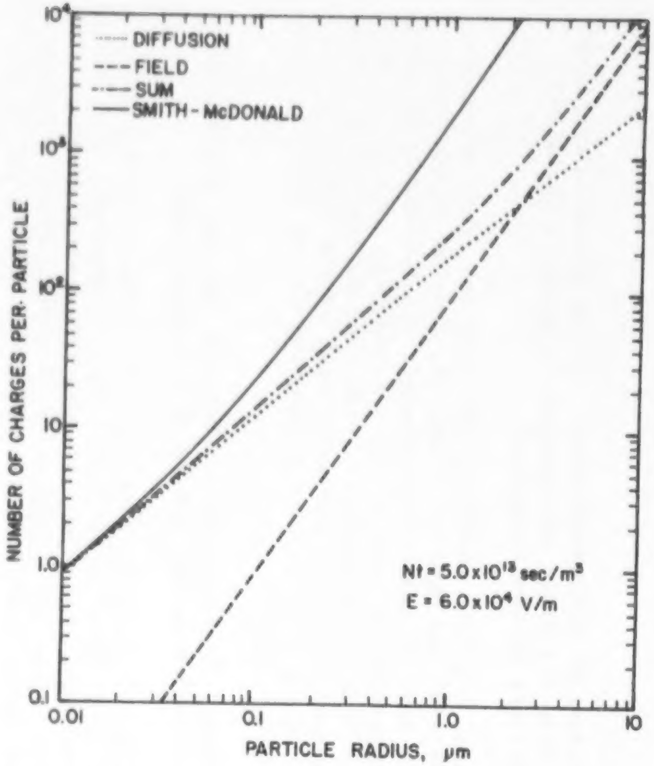

Figure 3. Average charge per particle as a function of particle radius for high value of Nt and reduced electric field strength.

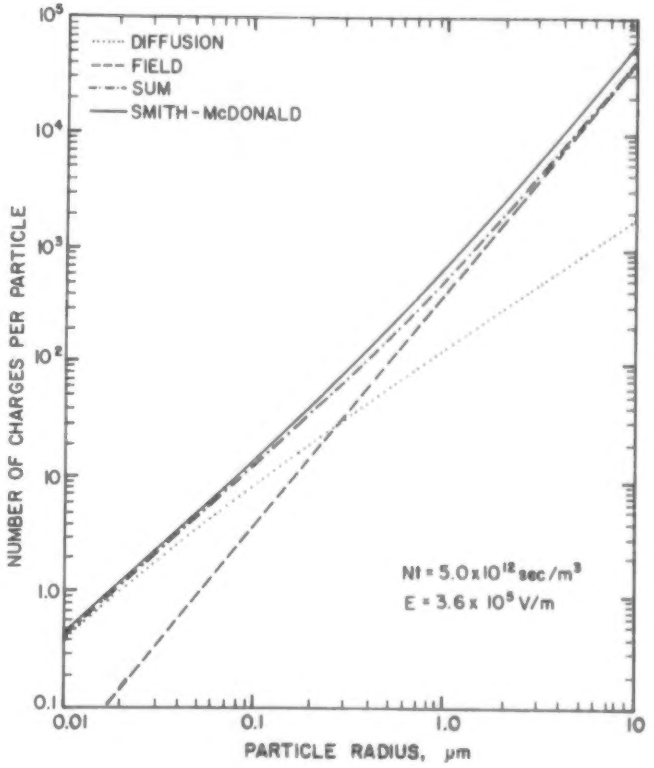

Figure 4. Average charge per particle as a function of particle radius for reduced value of Nt and relatively high electric field strength.

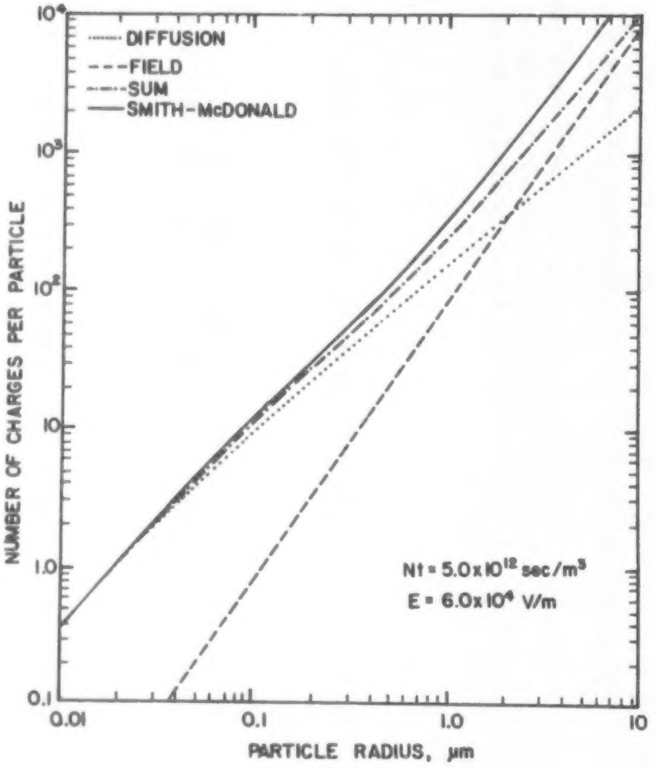

Figure 5. Average charge per particle as a function of particle radius for low values of Nt and electric field strength.

position within the charging region. Thus, the usual practice is to find some meaningful average value for each of the charging parameters.

To illustrate the nature of the problem, consider a single particle passing through a wire-plate precipitator as shown by path AB in Figure 6. The ion density-residence time product $\overline{Nt}$ may be evaluated by means of an integral taken along the path:

$$\overline{Nt} = \int_{t(A)}^{t(B)} N(t)dt$$

or, using $ds = vdt$, where s is a measure of distance along the path,

$$\overline{Nt} = \int_{A}^{B} \frac{N(s)}{v(s)} ds$$

Now, from elementary electrodynamics, the local ion density N(s) is related to the electric field strength E(s) and the current density j(s) by

$$N(s) = \frac{j(s)}{\mu eE(s)}$$

where μ is the ion mobility and e is the elementary unit of charge. Substituting into the above equation, we have

$$\overline{Nt} = \int_{A}^{B} \frac{j(s)ds}{e\mu E(s)v(s)}$$

At this point it is necessary either to establish functional forms for j(s), E(s) and v(s), or to make some simplifying assumptions. Since there are infinitely many paths AB through the system, we cannot define the functions of s in general. A simple result can be obtained by assuming that

(1) v(s) is constant and equal to v_g, the gas velocity through the system, and
(2) E(s) may be represented by some mean value E_{ave} along the path of integration.

As a result,

$$\overline{Nt} = \frac{1}{e\mu E_{ave} v_g} \int_{A}^{B} j(s)ds.$$

Now, the integral expression is simply half of the total current per unit length of corona wire --

$$\int_{A}^{B} j(s)ds = \frac{i}{2L},$$

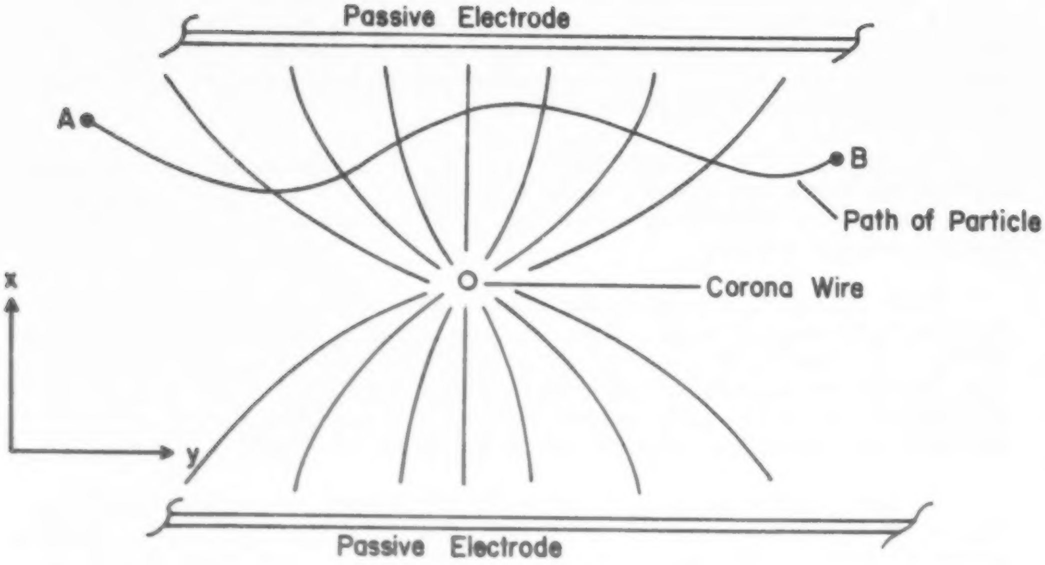
Passive Electrode
A
B
Path of Particle
x
Corona Wire
y
Passive Electrode

Figure 6. Sketch of a plane cross-section of a wire-plate corona system containing a possible nonlinear path of a particle through the system.

where i is the total corona current and L is the length of the corona wire. The expression for $\overline{Nt}$ thus becomes

$$\overline{Nt} = \frac{i}{2Le\mu E_{ave}v_g} ,$$

in which it is clear that $\overline{Nt}$ does not depend upon the detailed configuration of the passive electrode. It depends strongly, however, upon the value of E_{ave}. In this development the average value of the electric field strength is taken along the path of a particle through the field. Where there are many particles passing through the system on arbitrary paths, a charging calculation would require some mean value of E over the entire charging volume.

In addition to nonidealities arising from inhomogeneous charging conditions there are other phenomena which affect particle charging. Among these are reentrainment of collected particles, space charge effects and back corona.

Back corona is a well-known phenomenon generally associated with the precipitation of particulate material having high electrical resistivity. It occurs as a result of electrical breakdown in the collected dust layer, which sets up localized corona discharge regions near the surface of the collecting electrode. As a consequence, ions of both positive and negative polarity are present in the charging region.

A space charge problem is often associated with large number densities of fine particles in an electrostatic precipitator. The problem arises from the fact that charged particles drift much more slowly in an electric field than do the ions. Conduction in a corona system depends upon the movement of ions across the gas-filled space between the electrodes. Where no particles are present a steady-state condition develops in which the ions are distributed throughout the conduction region in such a manner as to balance the processes of ion production and transport. Now if a significant fraction of the total charge in the conduction region is attached to particles the charge transport mechanism is modified, since the particles are virtually stationary in comparison with the velocity of the ions. Consequently, the charge distribution in the system is changed, resulting in a modification in the electric field profile.

In some instances the build-up of a space charge near a corona wire can suppress the field sufficiently to quench the corona discharge. When that happens, no further particle charging can occur until the charged particles are swept out of the area and the field increases sufficiently to support a corona discharge. Thus fluctuations in the behavior of the system can occur, resulting in very inefficient particle charging.

Space charge problems are usually associated with fine particles because the ratio of charge to mass for a given set of charging conditions

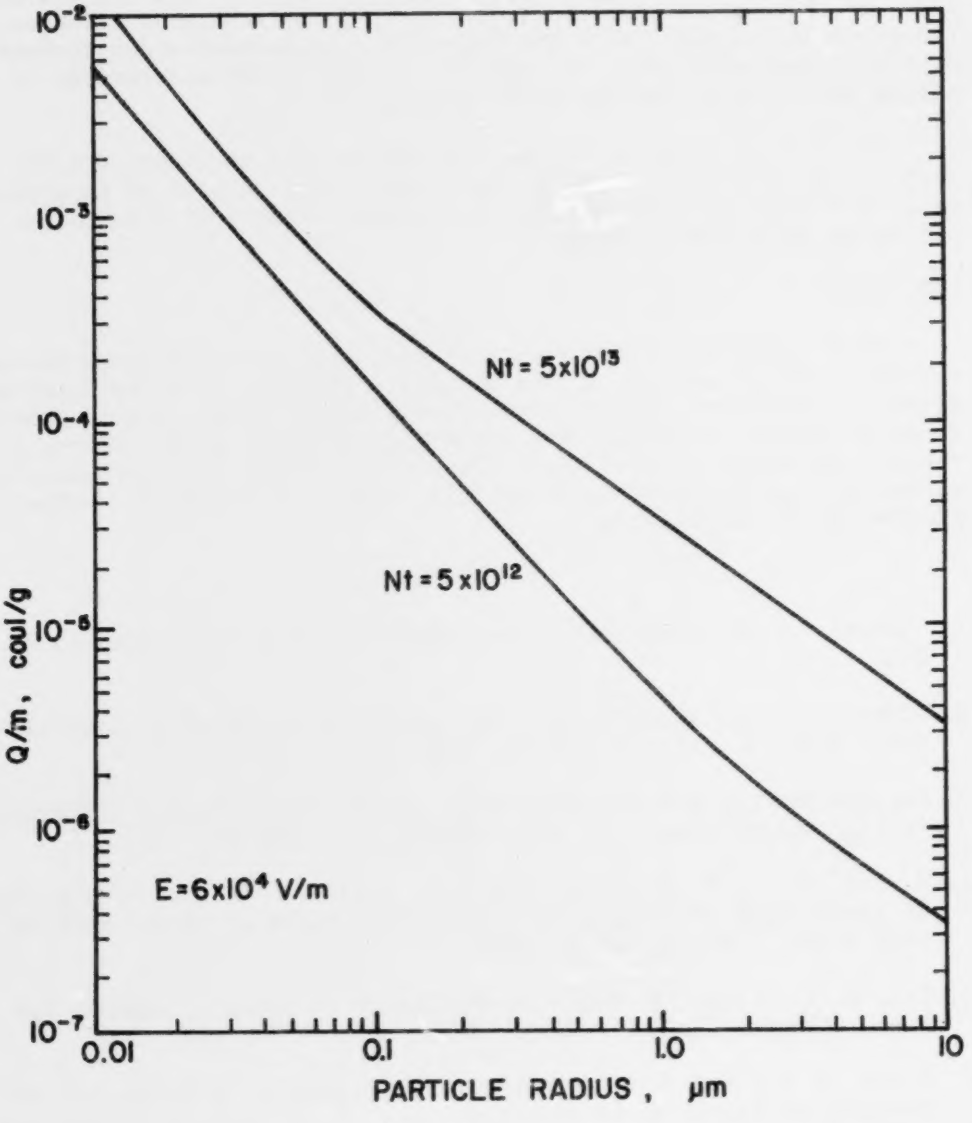

Figure 7. Ratio of charge to mass as a function of particle radius for two different sets of charging conditions.

is an inverse function of particle diameter, as indicated by the graph in Figure 7. It is assumed, in calculating the average charge per particle, that the charge residing on the particles makes a negligible contribution to the current in the system. The ion density is computed from the current density, the electric field strength and the ion mobility. If, however, a significant fraction of the charge is attached to the particles in the system the number of ions available for further particle charging is reduced, and the conduction characteristics of the system are changed from the clean condition.

In practice there is little that can be done to counteract the effects of space charge due to a large number density of fine particles, other than providing for as high as possible density of ions in the inlet fields of a precipitator.

CONCLUSION

Under controlled conditions particle charging can be predicted with a good degree of accuracy by the available theories. But nonideal conditions in practical electrostatic precipitators require that approximations be imposed which may weaken the effectiveness of the theory in charge prediction. The effects of space charge due to large number densities of fine particles is a specific subject toward which further studies should be directed.

REFERENCES

1. Jackson, J. D. Classical Electrodynamics. New York, Wiley, 1962. 641 p.

2. Arendt, P., and H. Kallmann. The Mechanism of Charging of Cloud Particles. Z. Phys. 35:836-97, 1935.

3. Pauthenier, M., and M. Moreau-Hanot. Charging of Spherical Particles in an Ionizing Field. J. Phys. Radium (7)3:590-613, 1932.

4. Murphy, A. T., F. T. Adler, and G. W. Penney. A Theoretical Analysis of the Effects of an Electric Field on Charging of Fine Particles. AIEE Trans. 318-326, Sept., 1959.

5. Liu, B. Y. H., and H. Yeh. On the Theory of Charging Aerosol Particles in an Electric Field. J. Appl. Phys. 39(3):1396-1402, 1968.

6. Smith, W. B., and J. R. McDonald. Development of a Theory for the Charging of Particles by Unipolar Ions. J. Aerosol Sci. 7:151-166, 1976.

AGING CAUSED INCREASE OF RESISTIVITY OF A BARRIER FILM AROUND GLASSY FLY ASH PARTICLES

William J. Culbertson
University of Denver
Denver Research Institute
Denver, Colorado 80208

ABSTRACT

There is evidence for growth of an electrical barrier film similar to perlite around glassy fly ash particles, which are similar to obsidian. This layer is supposed to be due to chemical reaction of the surface of the particles with the flue gas environment. Advantages of separating glassy fly ash particles from other interfering particles before elemental chemical analyses on fly ash are performed are suggested. The film is believed to be important to resistivity and cohesion of ash layers on the collection plate of an electrostatic precipitator.

INTRODUCTION

An importance of gross resistivity of the ash layer deposited on the collection plates of the electrostatic precipitator has long been recognized. This resistivity is commonly said to be important in determining the onset of back ionization as well as determining the "clamping" force on the ash layer.

In the laboratory measurement of gross ash resistivity as a function of temperature at Denver Research Institute we generally make a practice of determining the resistivities at progressively increasing temperatures rather than by first heating the ash and then determining the resistivities at decreasing temperatures.

Moreover, generally, we never re-use a once well heated fly ash sample for resistivity measurement.

The reason for these rules is that during considerable work with glassy fly ash such as Four Corners ash and Cherokee ash generally an increase in resistivity has been noted on cooling the ash after heating as shown in Figure 1. This effect has previously been pointed out by White.[1]

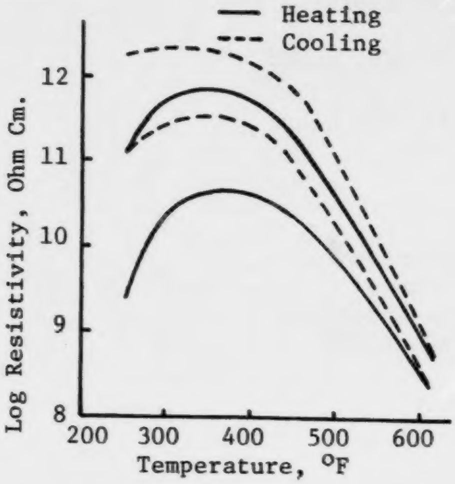

Fig. 1. Effect of Heating on Resistivity of Typical Ash

Several possible reasons for the increase in resistivity on cooling after heating come to mind. One is that sulfuric acid type natural conditioning agent has been driven from the surface of the ash on heating. Another is that such sulfuric acid reacts with oxides or carbonates with the ash to form isolated metal sulfates. Another is that sulfuric acid might promote egress of sodium ions from the surface of the glassy ash hence causing lowered glass conductivity after it has reacted with the sodium to give isolated crystals of sodium sulfate. Electron microscopy of fly ash showing such sodium sulfate crystals does not refute the latter two views.

All of these views might be true to more or less degree for a given glassy fly ash. An additional possibility that can be superimposed on the other views is here presented. This is that a hydration of the obsidian-like glassy fly ash particles may occur at their outer surface that causes formation of a skin of perlite-like material around them of high resistivity.

SIMILARITY OF GLASSY FLY ASH AND OBSIDIAN

Fly ash from many coals has an elemental analysis showing somewhat higher aluminum and somewhat lower silicon than obsidian rock which is a glass of similar composition to rhyolite rock.[2] Such fly ash, on microscopic and x-ray examination, often is seen to consist primarily of glassy spheres or glassy hollow spheres (containing spheres) and is suspected to be close to obsidian in elemental composition and perhaps in other properties, if the other phases such as mullite, calcium oxide, calcium sulfate, etc., were to be removed. The glassy particles are derived from clays in the coal.[3,4]

HYDRATION OF OBSIDIAN

In nature entire obsidian deposits have often been found to alter, primarily by hydration, to perlite around the periphery and extending deeply towards the core. Some perlite has been attributed to weathering at relatively low temperatures while other perlite is thought to have reapidly been formed through exposure of perlite to steam.

The rate of hydration of obsidian is high enough to it can be used for archeological dating of once freshly chipped arrowheads, etc.[5,6] Through several thousand years these will acquire a "patina" or coating of perlite. The thickness of the sharply boundaried perlite layer, along with knowledge of the rate of formation of the perlite, allows calculation of the age of the obsidian tool starting from the time it was fabricated. Much study of the hydration rate of obsidian as influenced by temperature, humidity, and obsidian density and composition has been accomplished.[7,8]

Ericson, Mackenzie and Berger[9] have considered the structure of glass as related to the perlite formation problem and have suggested correlation of the rate of rhyolitic obsidian hydration to perlite with a chemical structural factor, zeta, Z, which is defined to be

$$Z = 100 \frac{A - B}{A + B} \qquad (1)$$

where A = mole % Al_2O_3

B = mole % ($CaO + Na_2O + K_2O$).

A correlation of the rate of hydration with a physical structural factor, omega, Ω, has also been suggested:

$$\Omega = 100 \left[1 + \frac{(\rho_c - \rho_m)}{\rho_c}\right] \qquad (2)$$

where ρ_c = calculated density[10]

ρ_m = measured density

Ambrose[11] has measured in the laboratory the weight uptake of powdered obsidian at various temperatures as have others for glass powders in determining relative durability of glass in various media. Weight uptake is presumed to be proportional to perlite formation. In general, as is to be expected from rate limiting protective film theory, the growing perlite film's weight gain follows a parabolic law in Δ wt. vs time of exposure:

$$\Delta \text{ weight} = kt^{\frac{1}{2}}.$$

Other significant items resulting from studies directed toward hydration of obsidian glass[7,9] are:

1. In alumino silicate glass as Al increases the proton diffusion in the electric field increases. In sodium aluminosilicate the Na diffusion and conductivity increase as Al increases.
2. During chemical attack of the glass surface H^+ ions replace Na^+ ions. Na^+ ions migrate to the surface below the softening range. When Na^+ is removed from glass in water at high temperatures the silica network may be disrupted by OH^- ions.
3. Charles[12] found the activation energy of the attack of a glass surface corresponded to that for the migration of sodium ions to the glass-corrosion layer interface.

SUPERFICIAL DEPLETION OF SODIUM FROM COMMON GLASS AND OBSIDIAN

Manufactured common glass has been found to superficially lose sodium ions through diffusion from the interior to the surface of the glass[13] In the formation of perlite films around obsidian glass the sodium is also found to leave the structure, for the perlite contains little sodium. The sodium lean perlite film was thought to have a higher electrical resistivity than the pristine ash and to possibly be an important cause of the irreversible increase of electrical resistivity we have seen in glassy fly ash during heating.

We have measured the resistivity of some pure obsidians and perlites and also the resistivities of a matched pair from Ruby Mountain near Salida, Colorado. The resistivity of the perlites is nearly an order of magnitude higher than that of the obsidians. We are collecting other matched pairs of perlite and obsidian (Apache tears embedded in perlite). Not only is the resistivity of the perlites higher than that of the obsidians but the field dependency of their resistivity is higher.

HIGHER CONTAINED WATER IN PERLITE COMPARED TO OBSIDIAN

Perlite, which contains up to around 5% water, contains water partly as "free" OH groups, partly as bonded OH groups, and partly as molecular water. The free and bonded OH groups can be distinguished by infra red absorptivity studies and perhaps by TGA. Not only is the rate of hydration influenced by the elemental composition of the obsidian but it is auto catalyzed with respect to water to the extent of resulting in a sharp perlite-obsidian interface. Possibly some degree of ferroelectric phenomena results from the free OH groups and molecular water.

NEEDED IMPROVEMENTS IN ROUTINE CHEMICAL ANALYSIS OF FLY ASH

In order to avoid the confusion caused by minor "impurities" in the glassy fraction such as aluminum rich mullite, calcium rich anhydrite, lime, magnetite, and hematite the ash should be separated into fractions varying in density to obtain a major glassy fraction. This perhaps could be done by the mineralogical technique using heavy liquids.[14] Elemental analyses could then be made of the fractions and in particular of the glassy fraction.

The following properties of the main glassy fraction of the ash determined could be reported:

1. Elemental analysis

2. Specific gravity or density, ρ

3. Z determined from equation (1)

4. Ω determined from equation (2)

These might allow rational study of the rate of ash hydration to perlite.

Thin sections of the ash could be made by conventional petrographic methods[14] for examination of particulates and the thickness of any perlite rinds estimated by microscopic examination of the grain cross sections.

POSSIBLE RESULTS TO A PRECIPITATOR OF PERLITE FORMATION THROUGH ASH AGING

The ash in the deposit closest to the plates of an electrostatic precipitator might develop a thicker film of perlite around each glassy particle resulting in that ash resistivity being relatively high and a greater clamping force developing for this ash than in the ash on top of the deposit.

Ash newly arriving on top of the old ash might not have so thick a perlite film or so high a resistivity and hence might be less cohesive and could be rapped off even though the old ash might be quite tenaceously held. This might be the case at some power plants where too much ash stickiness is suspicioned.

The possibility of a dipole mosaic as well as an overall induced dipole associated with each glassy ash particle complicates the above simple picture to the extent that a plane of weakness in the ash on the plate may occur where induced dipole to dipole forces neutralize clamping current dipole forces. The plane of weakness would be in the ash at some distance from the plate hence rapping might not rap cleanly clear to the plate.

Before a difference in efficiency of one electrostatic precipitator compared with another can be attributed to some factor such as a difference in altitude other factors must also be shown to be comparable or explained. One factor of possible importance is a possible difference in the ash due to differences in coal supply and/or furnace and duct operating conditions causing different perlite formation rates.

REFERENCES

1. White, H.J. Industrial Electrostatic Precipitation. Reading, Massachusetts. Addison-Wesley Publishing Company, Inc. 1963. 376 p.

2. Nockolds, S.R. Average Chemical Composition of Some Ignious Rocks. Bulletin of The Geological Society of America. 65:1007-32, October 1954.

3. Watt, J.D., and D.J. Thorne. Composition and Pozzolanic Properties of Pulverized Fuel Ashes, I. Composition of Fly Ahses from Some British Power Stations and Properties of Their Component Particles. Journal of Applied Chemistry, 15:585-594, December 1965.

4. Mazza, M.H., and J.S. Wilson. X-Ray Diffraction Examination of Coal Combustion Products Related to Boiler Tube Fouling and Slagging. Advances in X-Ray Analysis, Vol 20, Eds. H.F. McMurdie, C.S. Barrett, J.B. Newkirk, and C.O. Ruud. Proceedings of 25th Av. Conf. on Applications of X-Ray Analysis, Denver, Aug. 4-6, 1976. (Sponsored by University of Denver Dept. of Chemistry and Denver Research Institute Dept. of Metallurgy and Materials Sciences.)

5. Friedman, I., and F.W. Trembour. Obsidian: The Dating Stone. American Scientist, 68:44-51, 1978.

6. Friedman, I., and W. Long. Hydration Rate of Obsidian. Science, 191:347-352, 1976).

7. Taylor, R.E., Editor. Advances in Obsidian Glass Studies, Archaeological and Geochemical Perspectives. Park Ridge, New Jersey, Noyes Press, 1976.

8. Friedman, I., R.L. Smith, and W.D. Long. Hydration of Natural Glass and Formation of Perlite. Bulletin of the Geological Society of America 77:323-328, March 1966.

9. Ericson, J.E., J.D. Mackenzie, and R. Berger. Physics and Chemistry of the Hydration Process in Obsidian I: Theoretical Implications, in Ref. 7.

10. Huggins, M.L. Journal of the Optical Society of America. 3:420, 1940.

11. Ambrose, N. Intrinsic Hydration Rate Dating of Obsidian, in Ref. 7.

12. Charles, R.J. Journal of Applied Physics 11:1549, 1958.

13. Douglas, R.W. and J.O. Izard. Journ. Soc. Glass Technol. 33:289, 1949.

14. Wahlstrom, E.E. Petrographic Mineralogy. New York. John Wiley & Sons, Inc., 1955.

ELECTROSTATIC PRECIPITATORS: THE RELATIONSHIP OF ASH RESISTIVITY AND PRECIPITATOR ELECTRICAL OPERATING PARAMETERS

H.W. Spencer, III
Western Precipitation Division
Joy Manufacturing Company
Los Angeles, California 90039

INTRODUCTION

The migration velocities, and hence, the collection efficiencies of electrostatic precipitators, can be increased by either increasing the electric field at the collection plate or by increasing the charge on the particles. The electric field can be increased by increasing the operating voltage and the particle charge by increasing both the operating voltage and current density. In the absence of particulate matter the maximum average voltage and corresponding current are controlled by the electrode geometry, power supply components and configuration, and gas composition. Introducing particulate matter into the system introduces other variables that affect electrical operation.[1] This paper gives the results of a laboratory study of the relationship of electrical resistivity and particle size of the particulate matter to the electrical characteristics of electrostatic precipitators (ESP's).[2] It ignores the effects of particle space charge and the effects of layers collected on the cathode, as well as the effect of electric wind. The results showed that the peak current density for the formation of back corona depends on the resistivity of the dust layer covering the positive electrode and that back corona onset is dependent on particle size.

Included are electrical data as function of ash resistivity for full scale units and recent results from a large scale pilot study. A method for detecting back corona based on the secondary voltage is discussed, which was previously described by White.[1]

APPARATUS AND PROCEDURES FOR LABORATORY MEASUREMENTS

The laboratory study of the influence of dust layers on the electrical behavior of a wire-plate corona discharge was conducted in a closely controlled environment. The wire-plate corona discharge device shown in Figure 1 was used for the study along with an American Society of Mechanical Engineers Power Test Code 28 conductivity cell for measuring ash resistivity. The corona current to any one of the five insulated plate segments of the corona discharge device or the current to the outer plate was measured by selectively connecting the desired element to the current measuring circuit. The current measuring circuit included both picoammeter and oscilloscope outputs. Additional details of the test apparatus and the procedures are contained in a report to the Environmental Protection Agency.[2]

The current-voltage characteristics of the test device were measured with a clean plate and with a 3 mm layer of dust on the plate at temperatures from 60°C to 180°C and at humidities in the range of one percent to fifteen percent water vapor by volume. Simultaneously, resistivity and dielectric strengths of layers were measured.[2] Ashes having mass median diameters of 2.3 μm, 8.2 μm, 14.5 μm, and 40 μm were used for the study. These particles size fractions were obtained by mechanically separating fly ash from the Gaston Power Station into the following size fractions: 0-3 μm, 3-5 μm, 5-7 μm, 15-25 μm, and > 25 μm.

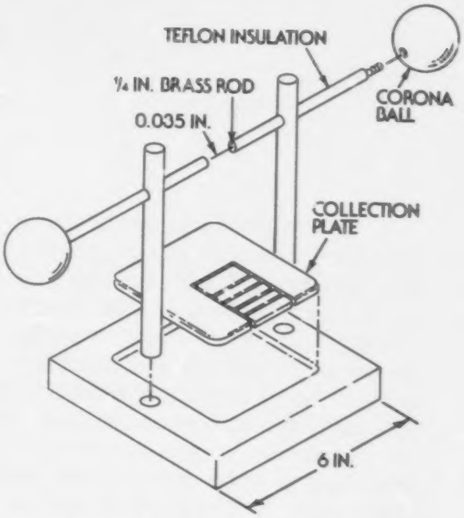

Figure 1. Wire plate corona discharge device.

RESULTS OF LABORATORY MEASUREMENTS

The current density at which back corona forms theoretically depends on the ratio of the dielectric strength and the resistivity of the ash. The dielectric strengths of the different fractions are tabulated in Table 1. For the tabulated values the applied D.C. voltage was increased at the rate of 0.5 kV/sec.

Table 1. DIELECTRIC STRENGTHS OF ASH LAYERS*

Particle Sizes μm	Dielectric Strength, kV/cm
0-3	25.0
3-7	24.2
7-15	21.7
15-25	26.8
>25	20.2

* 3mm layer, temperature 160°C, moisture 4% by volume.

The average dielectric strength of the 3 mm dust layers is 22.7 kV/cm, with a standard deviation of 2.3 kV/cm. The average dielectric strength of the 3 mm air gap was 36.9 kV/cm with a standard deviation of 0.5 kV/cm. (According to Paschen's Law for a 3 mm gap with a uniform field the dielectric strength of air at p = 720 Torr and T = 293°C is 35.23 kV/cm.) The data indicated no correlation of the dust dielectric strength with temperature, resistivity, or particle size.[2]

The physical properties of the dust layers studies in this investigation are tabulated in Table 2 and the resistivities are shown in in Figure 2. The resistivities in the surface conduction region increased with increasing particle size. Bickelhaupt has previously discussed the relationship of resistivity to particle size and surface area.[3] For the different particle size fractions, the estimated diameter of voids in the dust layer ranged from 3 to 29 µm and the surface area per unit volume changed by an order of magnitude.

Table 2. PHYSICAL PROPERTIES OF DUST LAYERS FORMED FROM THE GASTON ASH PARTICLE SIZE FRACTIONS

Size Range of Fraction, µm	Median Diameter, µm	Average Measured Porosity %	Calculated area of voids µm^2	Surface per cm^3 of dust µm^2
0-3	2.3	76.7	6.15	.608
3-7	3.6	69.9	10.6	.502
7-15	8.2	62.4	39.2	.274
15-25	14.5	57.3	98.9	.177
>25	40	54.7	676.5	.068

Changes in the physical properties of the collected ash layer in a precipitator appear to change the ash resistivity and not significantly alter the dielectric strength of the ash layer. The chemical compositions of the size fractions were similar.[2] The results of a comparison of V-I characteristics of the different particle size fractions are shown in Table 3. These show that back corona onset voltages, current densities, and sparkover voltages decreased with increasing particle size and a corresponding increase in ash resistivity. This indicates that the particle size fractionation inherent in normal precipitator operation would tend to improve electrical conditions for dust collection in the downstream fields of a precipitator.

EROSION AND DUST LAYER SURFACES

The surfaces of large-particle dust layers at low resistivities are eroded when current is applied. A combination of electrostatic and mechanical forces due to "electric wind" scatters the dust, thins the layer, and creates surface irregularities. This phenomenon complicates the study of dust layers.

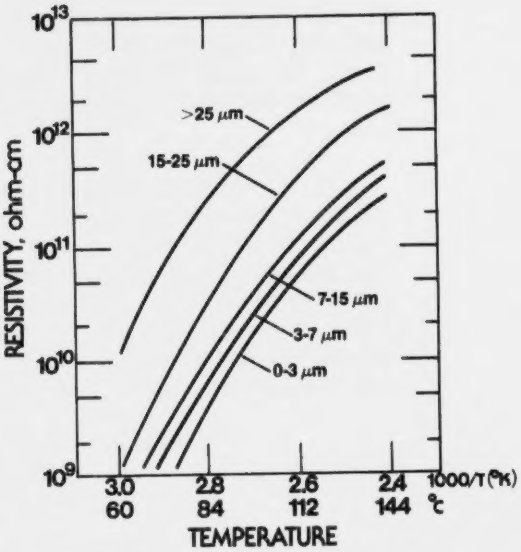

Figure 2. Resistivity vs. temperature for different particle size fractions.

The largest particle fraction studied, with particle diameters greater than 25 microns, was blown from the plate under all conditions. A 3 millimeter layer was removed in about three minutes at room conditions with 30 kV applied. Higher temperature and moistures reduced this effect. The 0-3 μm and 3-7 μm fractions were not significantly disturbed by corona wind under any of the conditions investigated. Penny also experienced problems with erosion.[4] In our tests sparking normally occurred at locations on the anode plate where a crack was present in the dust layer. However, these effects appeared to be slight compared to changes in resistivity.

Table 3. SPARKOVER AND BACK CORONA VOLTAGES FOR SIZE FRACTION

Particle Size Fraction, μm	Sparkover Voltage, kV	Back Corona Voltage, kV	Back Corona Current Density, μA/cm2	Resistivity, Ω-cm
0-3	52	52	1.7	1.0×10^{9}
3-7	48	44	.99	1.9×10^{10}
7-15	46	42	.76	2.4×10^{10}
15-25	42	42	.71	3.6×10^{10}
25	42	34	.25	1.5×10^{11}

Average temperature 90°C, moisture 12.6 % by volume.

V-I CHARACTERISTICS AND BACK CORONA

The series of graphs in Figure 3 show changes in the voltage-current characteristics that occur with an increase in ash resistivity from 3x 10^9 Ω-cm to 1 x 10^{12} Ω -cm. The solid line in each of these plots is the characteristic obtained without an ash layer, circles indicate an ash layer was present. The dashed line is the clean plate characteristic shifted according to the voltage drop across the ash layer, where the voltage drop is calculated by Ohm's Law from the measured resistivity and the measured thickness of the dust layer for a given current density. Current to the center segment of the wire-plate discharge device is shown. Note that the V-I characteristics are plotted on semi-log scales. The curves have a familiar appearance when plotted on linear scales.

The shift in the V-I characteristic with a 10^9 Ω -cm resistivity ash is shown in graph 1 of Figure 3. The difference between these two curves is masked in practice by variations in moisture, temperature, and corona wire characteristics between measurements with and without ash layers.

For a 10^{10} Ω -cm resistivity ash, the shift is several kilovolts and is easily observed as shown in graph 2 of Figure 3. The data points are near the shifted curve until back corona occurs. With the formation of back corona, there is a sharp increase in current, which is clearly observed on a semi-log plot. This break in the characteristic occurs at the onset of back corona.

Clean plate currents at corona onset were observed several times to be less than those for dust layers with 10^{11} Ω -cm resistivities as shown in Graph 3 of Figure 3. A satisfactory explanation for this behavior has not been developed.

In graph 4, the V-I characteristic for a 10^{12} Ω -cm ash layer is plotted. Back corona formed near corona onset as shown by the sharp increase in current.

The influence of ash resistivity on the formation of back corona is displayed in Figures 4 and 5. In Figure 4 the voltages at which back corona or sparkover occurred as determined from the measured V-I characteristics are plotted as function of resistivity. The horizontal lines at the top of the graph indicate the voltages at which sparkover occurred for various temperatures and show a decrease in sparkover potential with increasing temperature. The dashed curve indicates the potential between the outer surface of the dust layer and the corona wire at the formation of back corona or sparkover for a 3 mm dust layer with a dielectric strength of 24 kV/cm. The solid curve is an estimate of the average voltage at the formation of back corona.

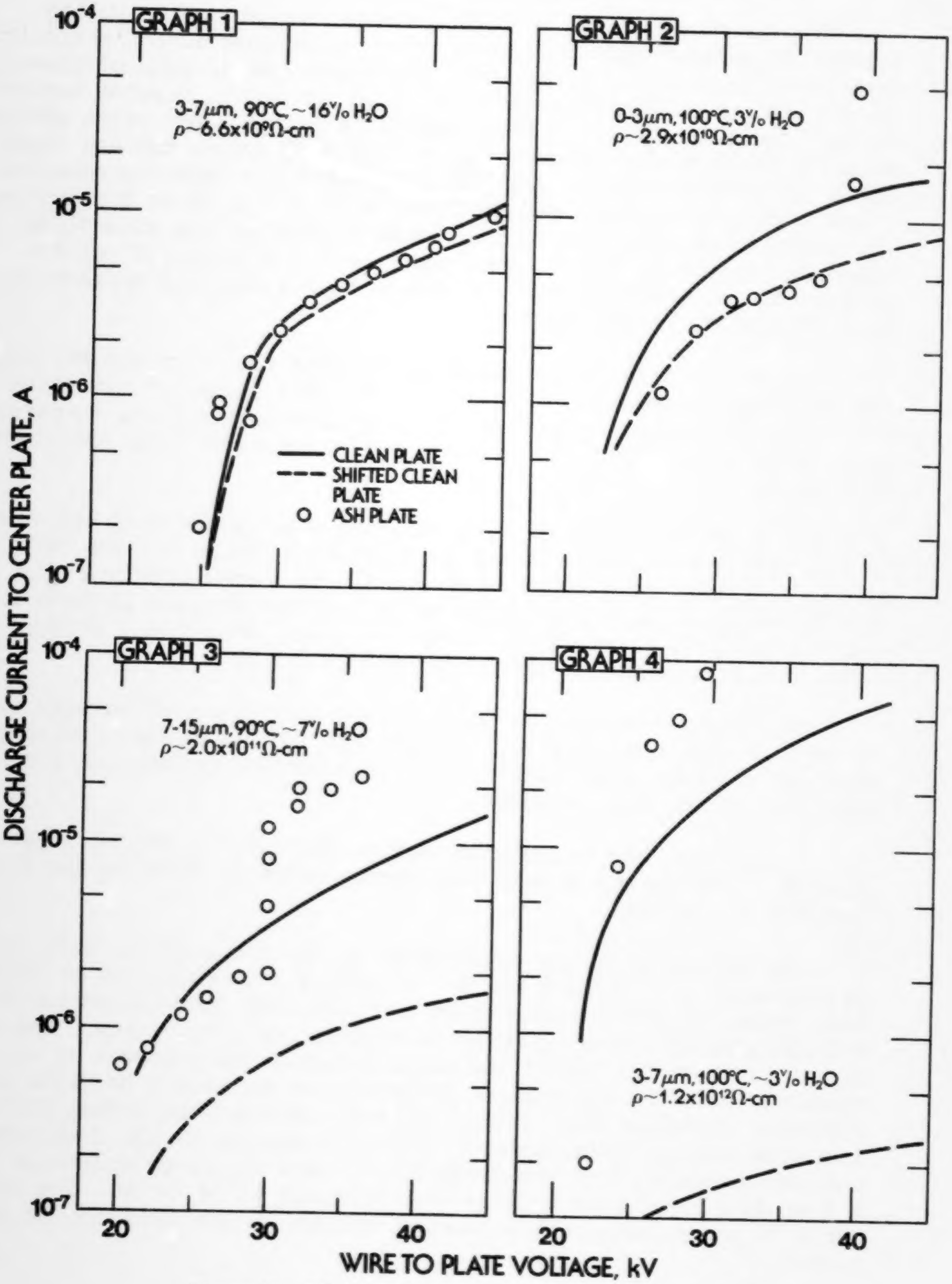

Figure 3. Voltage-current characteristics for wire plate discharge device, 3 mm dust layer.

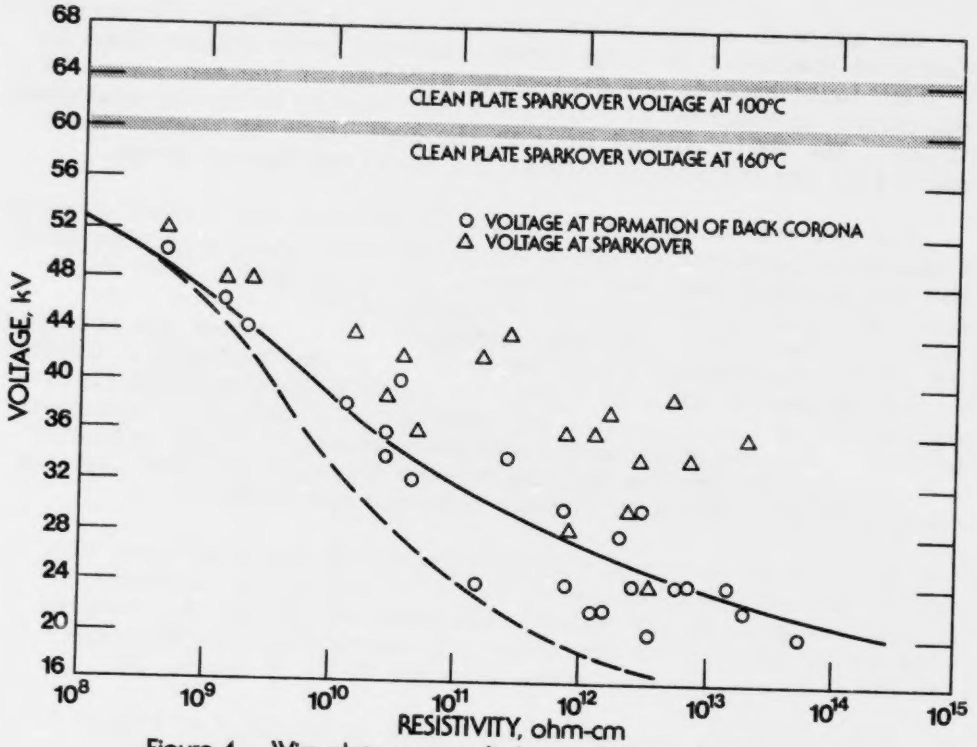

Figure 4. Wire plate corona discharge device voltages for sparkover and for formation of back corona.

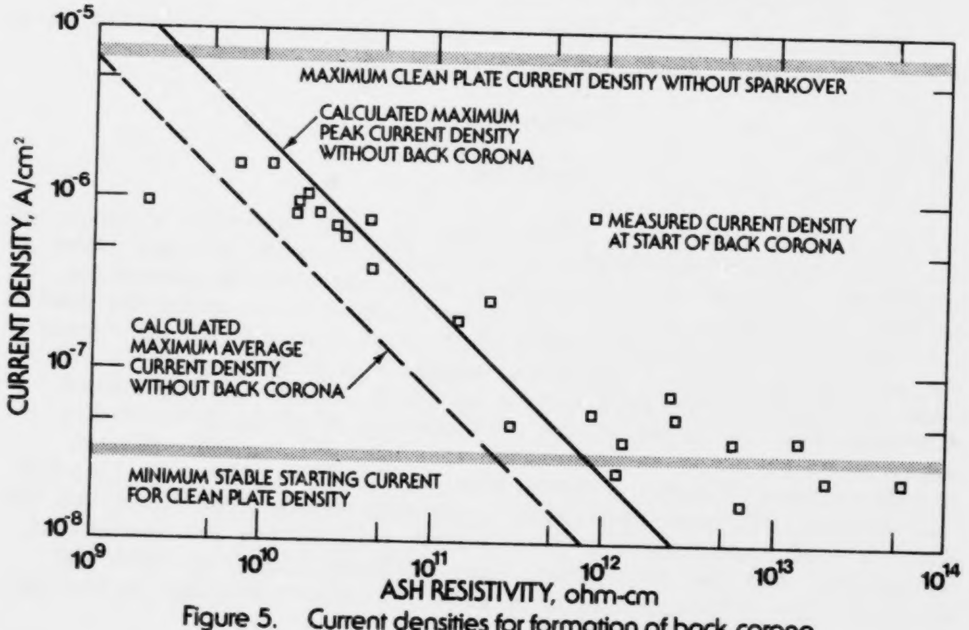

Figure 5. Current densities for formation of back corona in the wire plate corona discharge.

For ash with a resistivity greater than $2\times10^{10}\,\Omega$-cm, the current density at sparkover is large enough that the ohmic voltage drop in the dust layer exceeds the dielectric strength of the ash layer and back corona is observed at voltages significantly below the sparkover voltage. The ohmic voltage drop in the dust layer is represented in Figure 4 by the difference between the solid and dashed curves.

For ash with a resistivity below $2\times10^{10}\,\Omega$-cm, the current density at sparkover produced voltage drops in the dust layer that were less than the measured breakdown voltage of the dust layer. However, as shown in Figure 4, the voltages at sparkover were substantially below the clean plate sparkover voltages and back corona was observed just before sparkover. A full explanation is not available. Cracks and distortions in the dust layers can produce high electric field regions that probably account for some of the reduction in sparkover voltages. The reduction in the sparkover voltage is also partially the result of the smaller spacing between the wire and dust layer as compared to the separation between the wire and plate.

In a precipitator the voltage drop across the dust layer will vary in time as the thickness of the dust varies and, depending on the dust resistivity and operating current densities, the changing voltage drop can account for changes in precipitator performance with time, especially when a precipitator is first turned on.

Although there is considerable scatter, the data in Figure 4 show that the potential difference between sparkover and the formation of back corona increases with increasing resistivity.

The solid diagonal line in Figure 5 represents the current density at the formation of back corona given by the expression:

$$J = \frac{E_{\text{breakdown}}}{\rho_{\text{breakdown}}}$$

for $E_{\text{breakdown}}$ = 24 kV/cm. $E_{\text{breakdown}}$ is the dielectric strength of the dust layer and $\rho_{\text{breakdown}}$ is the resistivity of the ash layer at breakdown. The dotted horizontal line represents the respective maximum and minimum current densities which are the operating limits for the wire-plate corona device used in this series of experiments. The squares in Figure 5 represent either the minimum peak current density obtained when back corona occurred as soon as the corona discharge was initiated or the peak current density at which the back corona occurred as determined from the V-I curves and back corona current pulses. A comparison of the solid diagonal line and the squares indicates reasonable agreement between the theory of the formation of back corona as function of resistivity and the actual processes. The two data points near $10^{11}\,\Omega$-cm that lie above the diagonal line correspond to data from V-I curves similar to the one shown in graph 3 of Figure 3.

CURRENT DENSITY VARIATIONS

The average current density for the total plate area of the wire-plate discharge device was 0.3 to 0.5 times the peak current density. Hence, the dashed diagonal line in Figure 5 represents the maximum average current density at which the device could be operated without the formation of back corona. Likewise, the average operating current density of precipitators is below the theoretical peak current density. The ratio of the average to peak current density depends on wire to plate spacing. In a poorly aligned electrostatic precipitator this effect can lead to back corona formation at a lower average current density than the resistivity of the ash would indicate, greatly reducing operating voltages and collection efficiency.

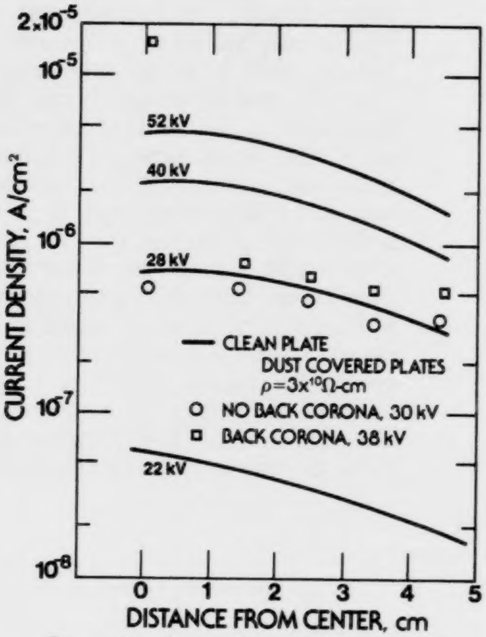

Figure 6. Current density distributions with and without back corona

The current densities of small rectangular areas on the corona discharge device plate, parallel to the corona wire plotted in Figure 6 represent the clean plate current density distributions and the current density distributions for a dust layer with and without back corona. This data shows that the effect of back corona is localized.

ELECTRICAL CHARACTERISTICS
OF A PILOT PRECIPITATOR

In Figure 7 electrical characteristics for the outlet field of a 35,000 ACFM pilot precipitator are plotted with a corresponding plot of the outlet optical density. The voltage-current density characteristic plotted in this figure shows a very definite break similar to the break observed in the laboratory when back corona occurred. The corresponding optical density traces show that no improvement in emissions is obtained by increasing precipitator currents beyond the break. It should be noted that the break in the curves occurred without any sparking. Time traces of the secondary voltage obtained at various points are given in Figure 8 and corresponds to the numbered points in Figure 7.

These traces show a very interesting phenomena. Below the break in the V-I characteristic both the minimum and maximum levels of the voltage trace increase with increasing input power. Above the break in the V-I characteristic the minimum decreases with increased input power. This reversal appears to correspond with onset of back corona indicated by the break in the V-I characteristic and by the increase in emissions that occur when the input power is above the reversal point. This phenomena has also been observed in a large hotside precipitator. It appears that back corona decreases the discharge time for the system, allowing the corona voltage to decrease to a lower voltage between charging pulses than is the case without back corona. The data from the hotside unit indicated that when back corona occurred the discharge

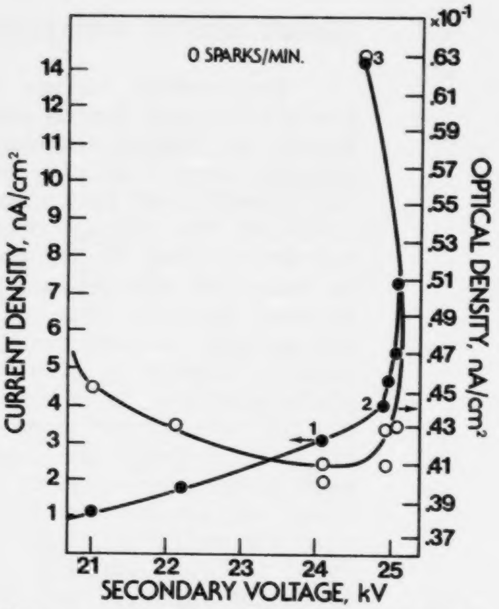

Figure 7. Current density and optical density versus secondary voltage for pilot precipitator.

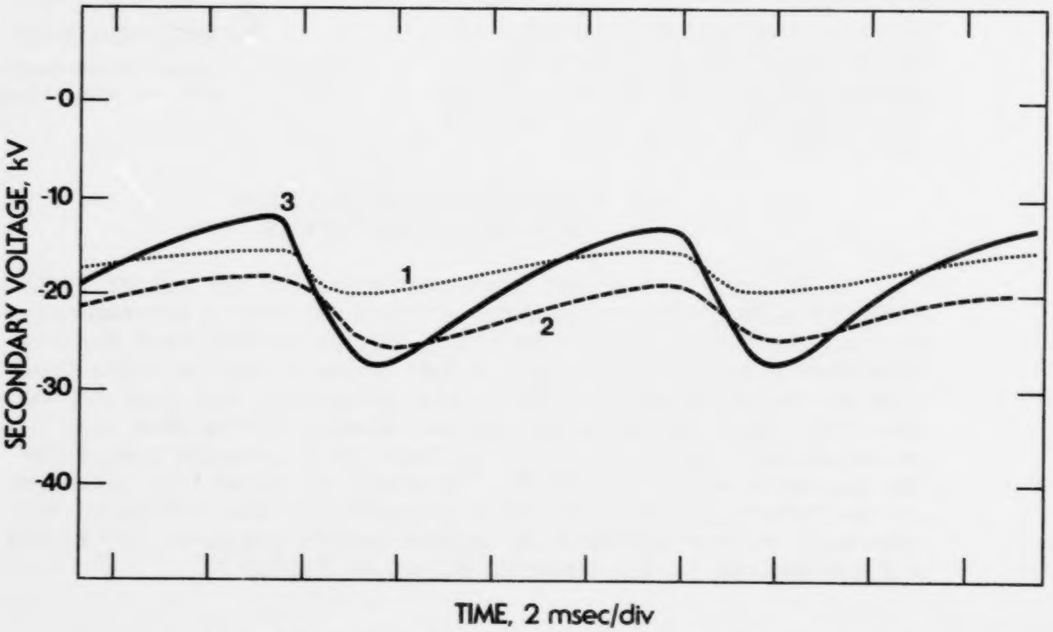

Figure 8. Secondary voltage waveforms for pilot precipitator.

lasted for several milliseconds and that the minimum in the secondary voltage trace could drop below the corona onset voltage. Normally, a precipitator will not discharge below the corona onset voltage because at this point there is no longer a substained discharge to provide a conductive path between the electrodes.

The above observations indicate that time traces of the secondary voltage as a function of precipitator input power provide a useful diagnostic tool for establishing optimum electrical operating points for full scale electrostatic precipitators. Present investigations of this phenomena have been very cursory and additional investigation appears to be warranted.

FULL-SCALE PRECIPITATOR MEASUREMENTS

Operating current densities versus resistivity for several full-scale precipitators are plotted in Figure 9. Resistivities were measured in-situ using a point-to-plane resistivity probe. The operating current densities are the typical spatial and time average current densities that existed during efficiency tests. A large portion of the data in this plot came from studies by Southern Research Institute.[5,6]

Data in Figure 9 indicates only a rough agreement between actual operating current densities for precipitators and the classical theory of back corona illustrated by the laboratory results presented in this paper.

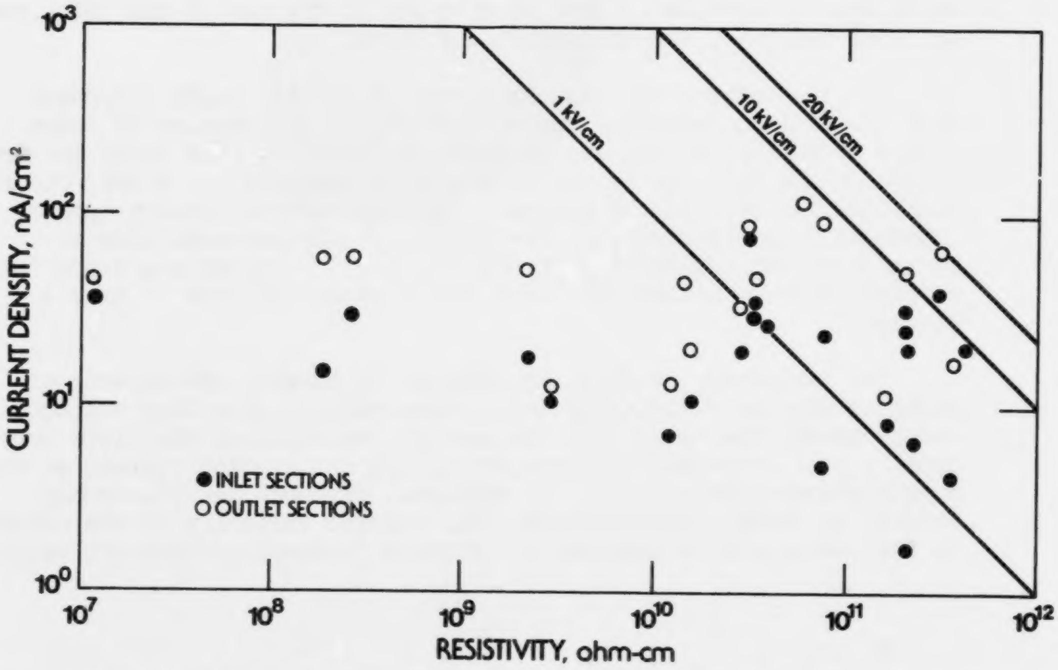

Figure 9. Operating current densities as a function of resistivity for various plants.

For resistivities less than $10^9 \Omega$-cm, direct current densities larger than 1 $\mu A/cm^2$ are feasible without exceeding the dielectric strength of the collected dust layer. However, current densities in field units did not exceed 0.1 $\mu A/cm^2$ even for these low resistivities.

There are several reasons for this, one of which is that several of the units are equipped with power supplies that are inadequate. A second reason is the large size of field units. It is not unusual for a power supply to handle a plate area in excess of 300 m^2 (3000 ft^2) which is much larger than the 100 cm^2 of our laboratory device. This increased area, and the impracticality of machining rounded edges on all parts of a field unit, greatly increase probability of sparkover. Our laboratory measurements also indicate that clean plate sparkover voltage and current density are reduced to some degree even by low resistivity dust layers.

Calculations for cylindrical geometry indicate that the space charge in the precipitator increases the electric field at the passive electrode[7]. For negative corona the field strengths at the anode would be increased and this effect could lead to lower sparkover potentials than those obtained without a dust loading.

A comparison of the inlet and outlet data shown in Figure 9 indicates that in most cases the outlet current density exceeds the inlet current density. Correspondingly, inlet voltages were found to exceed outlet voltages[2]. Explanations for the variations in the voltage-current characteristics from the inlet to outlet attribute the variations to changes in dust loading and to changes in the thickness and resistivity of the collected dust layer.

The laboratory work discussed earlier in this paper indicates that the maximum operating current density in the absence of space charge effects will increase in coldside units from the inlet to the outlet of the unit due to particle size fractionation. A half order magnitude increase of the maximum operating current density appears reasonable, considering that the laboratory measurements show a decrease in ash resistivity of nearly one (1) order of magnitude for particle size fractions with mass median diameters from 40 to 2.3 microns.

The laboratory results, in addition to showing the effects of particle size on resistivity and correspondingly operating voltages and currents, also show that the spatial variation of the plate current density must be considered when predicting the average current at which a precipitator can operate. In addition, although not thoroughly studied in these investigations, the temporal variation of the current to the plate must be considered. Typical temporal and spatial variations indicate that the average current may typically equal 50% of the peak current. The data in Figure 9 shows that precipitators operate with average current densities at least a factor of two less than the current density predicted on the basis of a dielectric strength of 20 kV/cm and an insitu measurement of the dust resitivity at the precipitator inlet.

Other factors that must be considered in attempting to predict electrical operating points for precipitators beyond the scope of the laboratory work reported in this paper include space charge effects, dust layer thickness effects, and the design of the transformer-rectifier system and associated controls.

SUMMARY

Laboratory experiments have shown resistivity to vary as a function of particle size. A corresponding electrical limitation related to the resistivity of an ash layer collected on the positive electrode of a negative corona discharge system is imposed. Maximum operating current density, dust layer dielectric strength, and dust layer resistivity were observed to be related according to the classical relationship developed by White.[8] Upper and lower current limits were also noted. The lower limit is a function of the corona onset voltage and the upper a function of the sparkover voltage in the presence of a dust layer. Back corona was also seen to occur where the spatial variation in current density reached a peak.

A method for detecting the presence of back corona in a full scale unit has been discussed. The method depends upon a change in the conduction characteristics of the flue gas in the presence of the back corona and the pulsed nature of the current supply to full scale precipitators. Data from full scale precipitators has been presented that showed considerable scatter, a significant variation in inlet and outlet operating conditions, and only rough agreement with the classical relationship of maximum operating current density and resistivity.

ACKNOWLEDGEMENTS

The laboratory work discussed in this report was sponsored by the Environmental Protection Agency under contract 68-02-1303 for which Dr. L.E. Sparks was the IERL-RTP project officer. The work was conducted at the Southern Research Institute under the direction of Grady B. Nichols. The field and pilot plant data was obtained from investigations by both the Environmental Protection Agency and the Electric Power Research Institute.

REFERENCES

1. White, H.J. Resistivity Problems in Electrostatic Precipitation. J. Air Pollut. Contr. Assoc. 24:314-338, April, 1974.

2. Spencer, H.W. Electrostatic Precipitators: Relationship Between Resistivity, Particle Size, and Sparkover. Environmental Protection Agency, Research Triangle Park, N.C. Report Number EPA-600/2-76-144. May 1976

3. Bickelhaupt, R.E. Surface Resistivity and the Chemical Composition of Fly Ash. J. Air Pollut. Contr. Assoc. 25:148-152, February, 1975.

4. Penney, G.W., and T.E. Alverson. Influence of Mechanical Collection on Electrostatic Precipitator Sparkover Voltage—A Laboratory Simulation. IEEE Trans. Ind. Gen. Appl. 7 (3): 433-438, May-June 1971.

5. Dismukes, E.B. Conditioning of Fly Ash with Sulfur Trioxide and Ammonia. Joint report, Environmental Protection Agency, Research Triangle Park, N.C. Report Number EPA-600/2-75-015, Tennessee Valley Authority, Chattanooga TN. Report Number TVA/F75 PRS-5. August 1975.

6. Gooch, J.P. and Marchant G.H. Electrostatic Precipitator Rapping Reentrainment and Computer Model Studies. Electric Power Research Institute, Palo Alto, CA. Draft report EPRI Contract RP413-1. August 1977.

7. Lowe, H.J. and D.H. Lucas. The Physics of Electrostatic Precipitation. Brit. J. Appl. Physics, (London), Suppl. 2:540-47, 1953.

8. White, H.J. Characteristics and Fundamentals of the 'Back Corona' Discharge. (Presented at Gas Discharge Conference, Brookhaven National Laboratory, Upton, N.Y., 1948.)

A TECHNIQUE FOR PREDICTING FLY ASH RESISTIVITY

Roy E. Bickelhaupt
Southern Research Institute
2000 Ninth Avenue South
Birmingham, Alabama 35205

ABSTRACT

A technique for predicting fly ash resistivity from an ultimate coal analysis and a chemical analysis of coal ash produced by simple laboratory ignition was attempted. Using a large number of fly ashes, relationships were developed between resistivity and ash composition, temperature, ash layer field strength, and the concentration of water and sulfuric acid vapor in the environment. These relationships were used to form an expression to calculate resistivity versus temperature as a function of the other variables listed above. For purposes of predicting resistivity, the environmental conditions were obtained from a stoichiometric calculation of the combustion products, and the atomic percentage of chemical constituents of interest was obtained from the coal ash analysis. Although this predictive technique is generally applicable to the entire conventional temperature range for dry electrostatic precipitation, the paper defines the procedure for a single temperature.

INTRODUCTION

A research objective that has been pursued for several years is to predict fly ash resistivity as a function of temperature based on a coal ash compositional analysis and the stoichiometrically calculated flue gas. Reaching this goal has been painfully slow principally because one must be reasonably certain that the laboratory resistivity data utilized in developing a predictive technique agrees with the resistivity values that the precipitator will experience. This has been a difficult problem that is magnified when the sulfur oxides are introduced into the experimental environment.

The research program is approaching a conclusion, and in the near future a report will be prepared to offer at least an initial model of a technique to predict resistivity as a function of temperature and environment. This paper will illustrate the type of laboratory resistivity data that has been obtained, the manner in which the data are utilized, and the steps used to predict resistivity at a specific temperature.

EXPERIMENTAL SCOPE AND APPROACH

A large number of commercially produced fly ashes were chemically and physically characterized for this work. By having a large data base, all ranks of coal were represented, and one can assume that the effect of factors such as specific surface and ash layer porosity will be minimized.

Resistivity as a function of temperature for a given set of electrical and environmental conditions was determined using all the available fly ash specimens. From these data, one can relate fly ash resistivity to fly ash chemical composition for one set of experimental conditions and selected temperatures. From the original group, 16 ashes were selected to investigate the effect of the variation in environmental water concentration and applied voltage gradient on resistivity. Eight of these ashes were further utilized in experiments to determine the effect of sulfur trioxide on resistivity. These experiments provided a series of expressions which when successively applied yield a resistivity value for a given temperature, water concentration, sulfur trioxide concentration and applied electrical stress.

EXPERIMENTAL PROCEDURES

The equipment and experimental technique have been previously illustrated and discussed[1] in detail and will be only briefly mentioned here. When the effect of sulfur trioxide was not under consideration, ASME, PTC-28 test cells[2] were used in a stainless steel environmental chamber. Resistivity was determined under an applied voltage gradient of 2 kV/cm from 460°C to 85°C in an environment of nitrogen, 5% oxygen, 13% carbon dioxide, 500 ppm sulfur dioxide and 9% water by volume. In other similar experiments the water concentrations were 5% and 14%. When the effect of applied voltage gradient was of interest, the test temperature was maintained at 162°C.

A special test cell and environmental chamber were developed with which the effect of sulfur trioxide on resistivity was evaluated. The tests were conducted isothermally at several temperatures using sulfur trioxide concentrations of 2, 5 and 10 ppm in an environment of air and water vapor. A radial-flow, concentric-electrode test cell allowed the determination of resistivity for an ash layer one mm thick. This thin layer of ash can be equilibrated with the environment containing sulfuric acid vapor in a reasonable length of time.

EXPERIMENTAL RESULTS

Effect of Ash Composition

Figure 1 shows the relationship between the measured resistivity and the combined atomic concentrations of lithium and sodium for 33 fly ashes. Eastern and Western ashes are indicated by closed and open symbols, respectively. These data were obtained from resistivity versus reciprocal absolute temperature plots for the individual ashes at 1000/T(°K) = 2.4 (144°C, 291°F). Prevailing test conditions included the previously described simulated flue gas containing 9% water, applied electrical stress of 2 kV/cm, and no sulfur trioxide added.

In the upper, right corner of Figure 1, the expressions defining the curve produced by linear regression analysis are shown. One can either calculate the resistivity for the specific set of experimental conditions prevailing using these equations or read the resistivity value from the figure. The slope of approximately -2 indicates a two order of magnitude decrease in resistivity for a one order of magnitude increase in the atomic percentage of lithium plus sodium. A coefficient of correlation of -0.97 was determined. This coefficient defines the degree of fit between the data and the linear regression curve, and a value of 1.00 would define perfect correlation between the two factors.

The high coefficient of correlation suggests that it is improbable that the relationship can be improved by examining these data as a function of the concentration of other chemical species appearing in the ash composition. Of course this statement may not be true if one subjectively selects a specific group of ashes from the larger universe of ashes shown in Figure 1. Since it has been shown[3] that lithium and sodium are principal charge carriers in experimental environments excluding sulfuric acid vapor, the relationship shown in Figure 1 was expected.

Effect of Water Concentration

Figure 2 illustrates the effect of changes in water concentration for one of the sixteen ashes picked for additional evaluation. The water concentrations used were selected based on the data sheets completed by the ash-supplying power stations which showed a range of 6 to 13 volume percent. These curves were generated using the previously defined baseline test conditions with of course the exception of water concentration and are similar to those found by other investigators.[4] The attenuation of resistivity due to increased water concentration is observable at about 230°C and becomes very significant at the lower temperatures.

One way of displaying these data in a form suitable for use in the prediction of resistivity is shown in Figure 3. In this interpretation, the resistivity data of the previous figure have been plotted as a function of water concentration for several isotherms. Expressions developed from data such as these can be used to correct the resistivity value predicted for a given set of baseline conditions to a value for some other

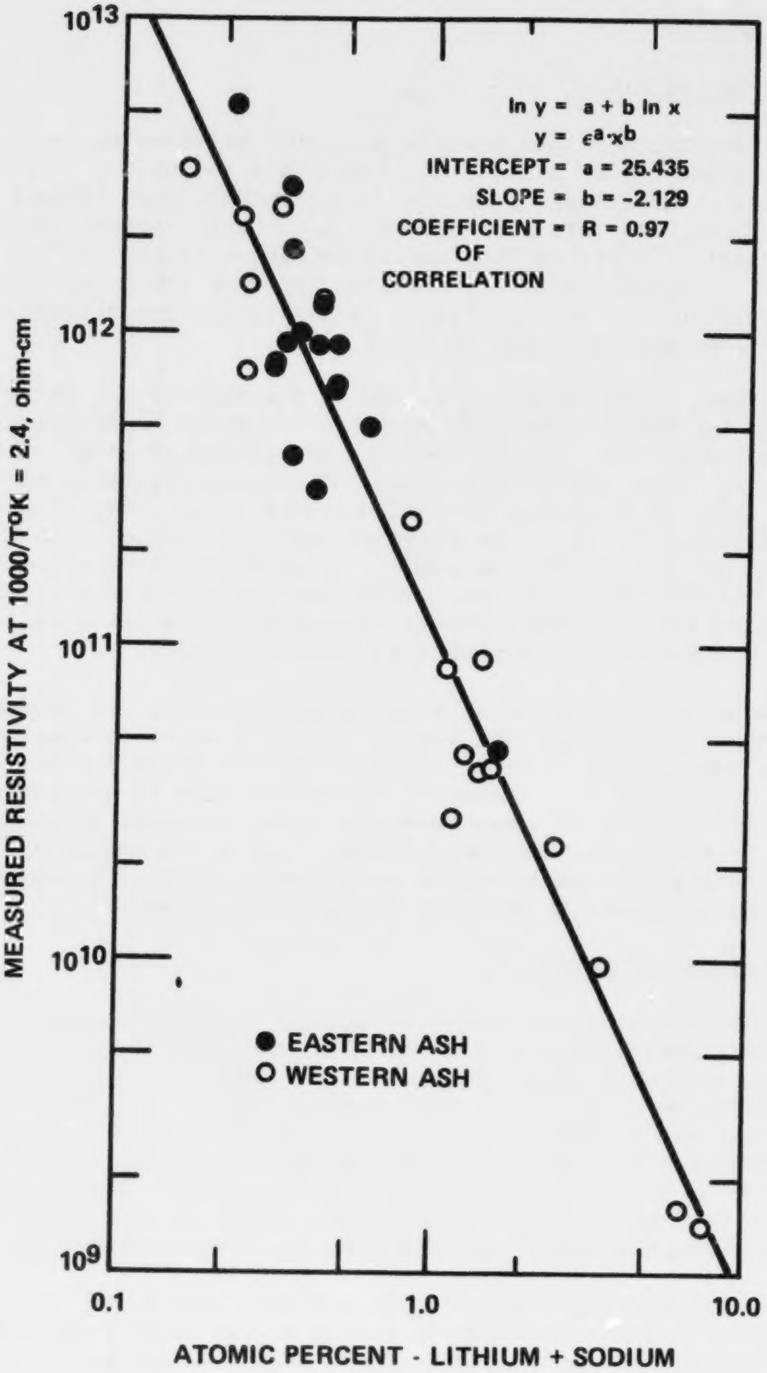

Figure 1. Resistivity as a function of combined lithium and sodium concentrations for a specific set of test conditions.

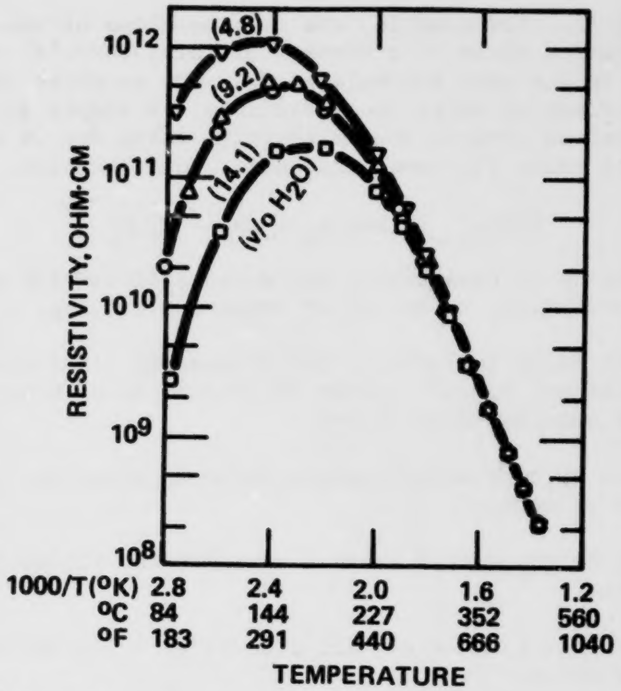

Figure 2. Typical resistivity-temperature data showing the influence of environmental water concentration.

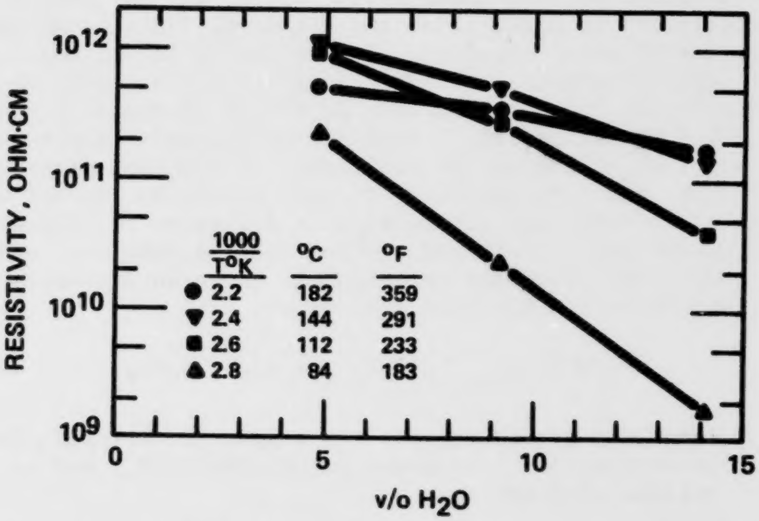

Figure 3. Resistivity as a function of environmental water concentration for various test temperatures.

set of conditions. For example, the average slope of the resistivity-water concentration curve at a temperature of $1000/T(°K) = 2.4$ was -0.085. This is based on the data accumulated from the selected 16 ashes used to evaluate the effect of water concentrations. A simple algebraic expression can be used to convert the resistivity value for 9% water shown in Figure 1 to the value for some other water concentration.

$$\log \rho_{c,w} = \log \rho_c + (W_w - W_c)S_w \qquad (1)$$

$\log \rho_{c,w}$: logarithm of resistivity for a specific lithium plus sodium concentration, c, and water concentration, W_w.

$\log \rho_c$: logarithm of resistivity for a specific lithium plus sodium concentration, c, and a water concentration of 9 volume percent. Value obtained from Figure 1.

W_w: volume percent water concentration to which the resistivity is to be corrected.

W_c: water concentration used in establishing Figure 1, nine volume percent.

S_w: $\Delta \log \rho / \Delta\% \ H_2O$; -0.085 for $1000/T(°K) = 2.4$ and water concentrations between 5% and 15%.

Effect of Applied Electrical Stress

Figure 4 shows the effect of increasing the ash layer voltage gradient on resistivity. The upper curve illustrates the almost neglibible effect experienced by a few ashes and the lower curve shows the average effect for the 16 ashes examined. The variation in the magnitude of the effect of applied voltage gradient on resistivity has been observed during *in situ* testing by Southern Research Institute personnel and in laboratory tests by other investigators.[5] ASME PTC-28 suggests determining resistivity just prior to dielectric breakdown. A research program involving dozens of ashes and a multiplicity of test conditions cannot afford to do this. Therefore tests are conducted on a few ashes to establish a relationship between resistivity and applied voltage gradient, and other data are then calculated from this relationship using an expression similar to that given above for the effect of water.

$$\log \rho_{c,w,e} = \log \rho_{c,w} + (E_e - E_c)S_e \qquad (2)$$

$\log \rho_{c,w,e}$: logarithm of resistivity for a specific lithium plus sodium concentration, c, a water concentration W_w, and an applied voltage gradient E_e.

$\log \rho_{c,w}$: previously defined.

E_e: applied voltage gradient to which $\log \rho_{c,w}$ is to be corrected.

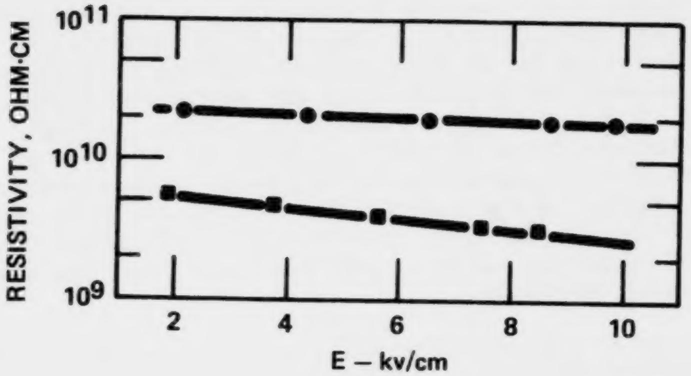

Figure 4. Typcial resistivity values as a function of applied ash layer voltage gradient.

E_C: applied voltage gradient used in establishing Figure 1, 2 kV/cm.

S_e: $\Delta \log \rho/\Delta E$;-0.030 for 1000/T(°K) = 2.4 and an applied voltage gradient range of 2 to 10 kV/cm.

Effect of Sulfur Trioxide

The effect on resistivity of incorporating sulfur trioxide in an environment of water and air was examined using a limited number of ashes and tests. Figure 5 shows the data generated for a specific test and compares the data obtained using the recently described test cell with that of a conventional test cell. Figure 6 shows the results for six tests conducted on one ash to demonstrate the combined effect of sulfur trioxide concentration and temperature on resistivity.

All data thus far obtained at 147-149°C using 2 kV/cm voltage gradient and a baseline environment of air containing 9 volume percent water is shown in Figure 7. Eight ashes were used in conjunction with sulfur trioxide concentrations of nominally 2, 5 and 10 ppm. At this time, it is believed that the data base is too small to make other than guarded statements regarding the quantitative effect of sulfur trioxide on resistivity. It is obvious that the effect can be dramatic in that the presence of 10 ppm of sulfuric acid can reduce the resistivity two or more orders of magnitude.

The initial evidence suggests that the presence of sulfuric acid in the environment provides an alternate conduction mechanism. Therefore, other than the effect of various ashes having different affinities for sulfuric acid vapor, there would seem to be no relationship between the acid and the ash composition with respect to conduction. Presently it is suggested that the effect of sulfuric acid can be combined with the other factors that influence resistivity by considering them as two conduction mechanisms and determining a resultant resistivity from the equation for parallel resistances.

$$\rho_r = \frac{\rho_s \times \rho_{c,w,e}}{\rho_s + \rho_{c,w,e}} \qquad (3)$$

ρ_r: resultant resistivity combining the effects of composition, water concentration, applied voltage gradient, and sulfuric acid concentration.

ρ_s: resistivity resulting from the effect of environmental sulfuric acid concentration taken from Figure 7.

$\rho_{c,w,e}$: previously defined, equation (2).

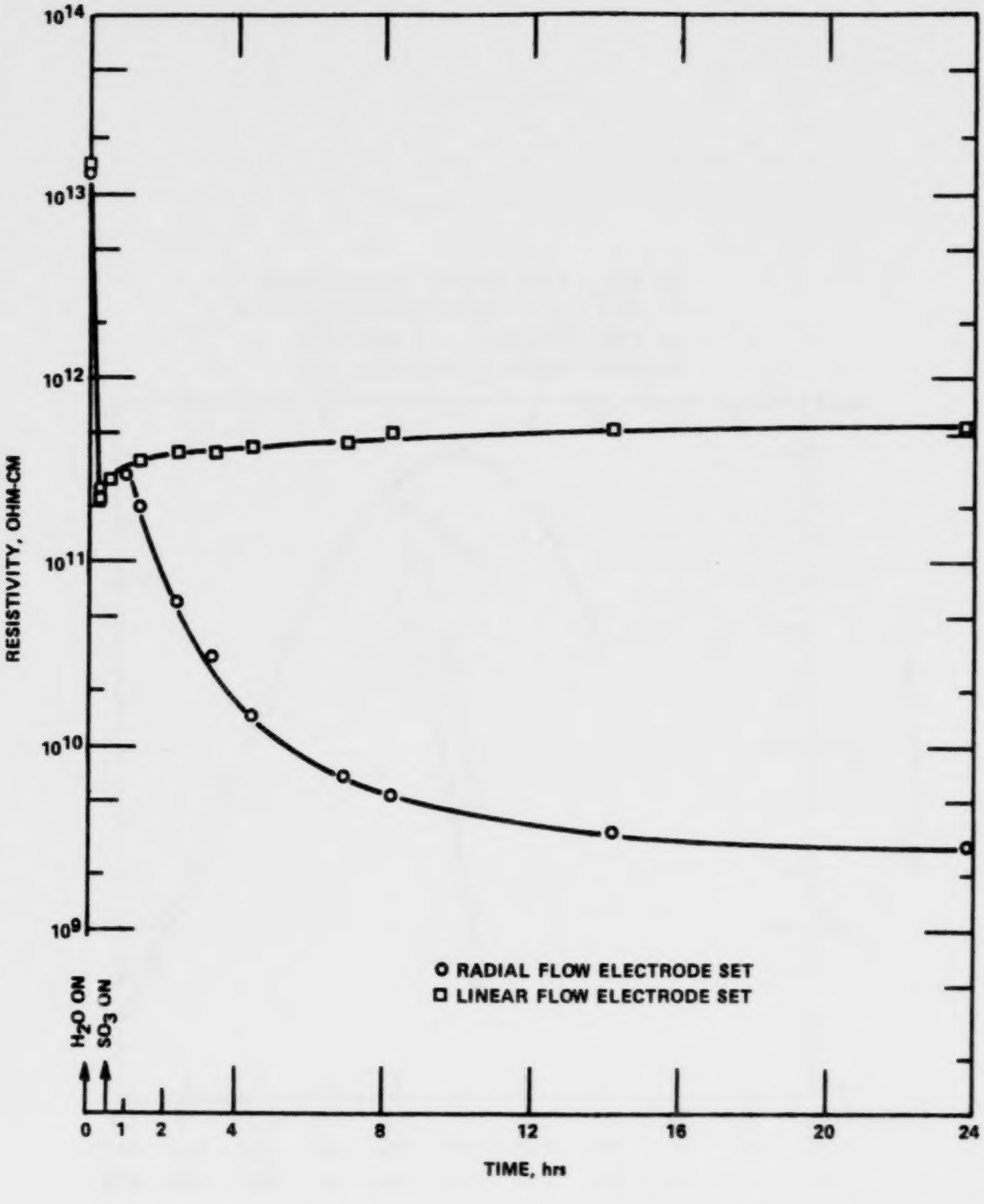

Figure 5. Ash resistivity versus time of exposure to an environment containing sulfuric acid vapor, for reference 1.

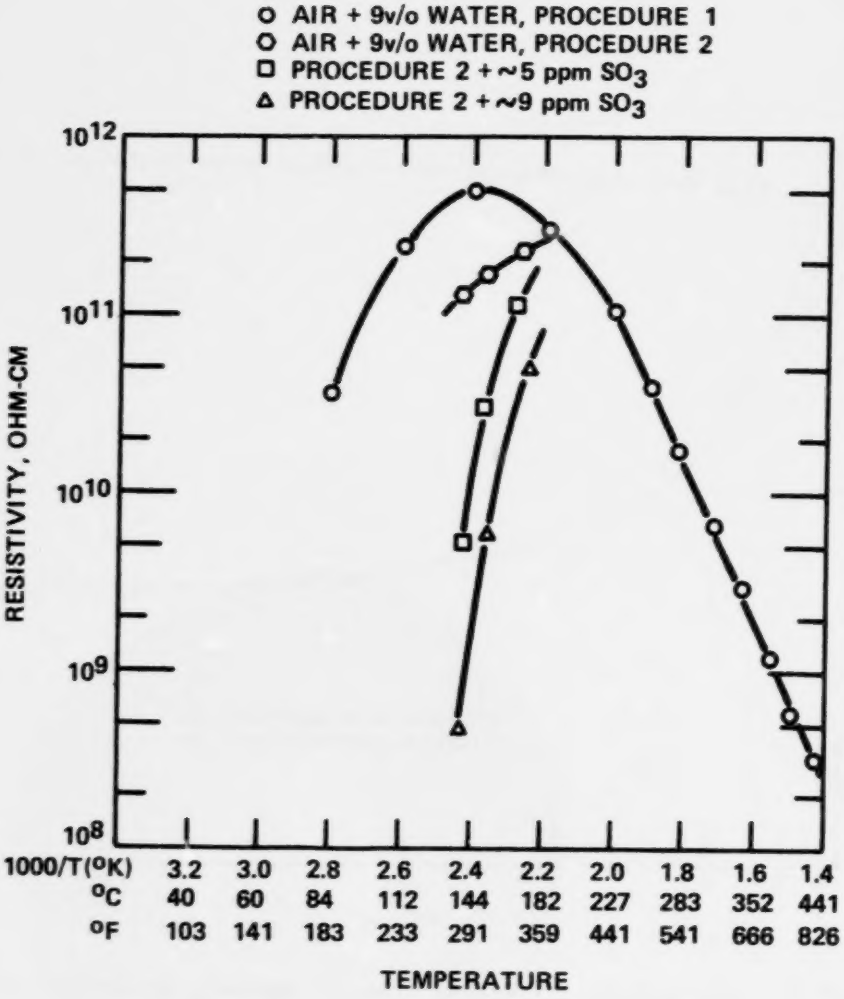

Figure 6. Typical resistivity versus reciprocal absolute temperature data showing the effect of injected sulfur trioxide.

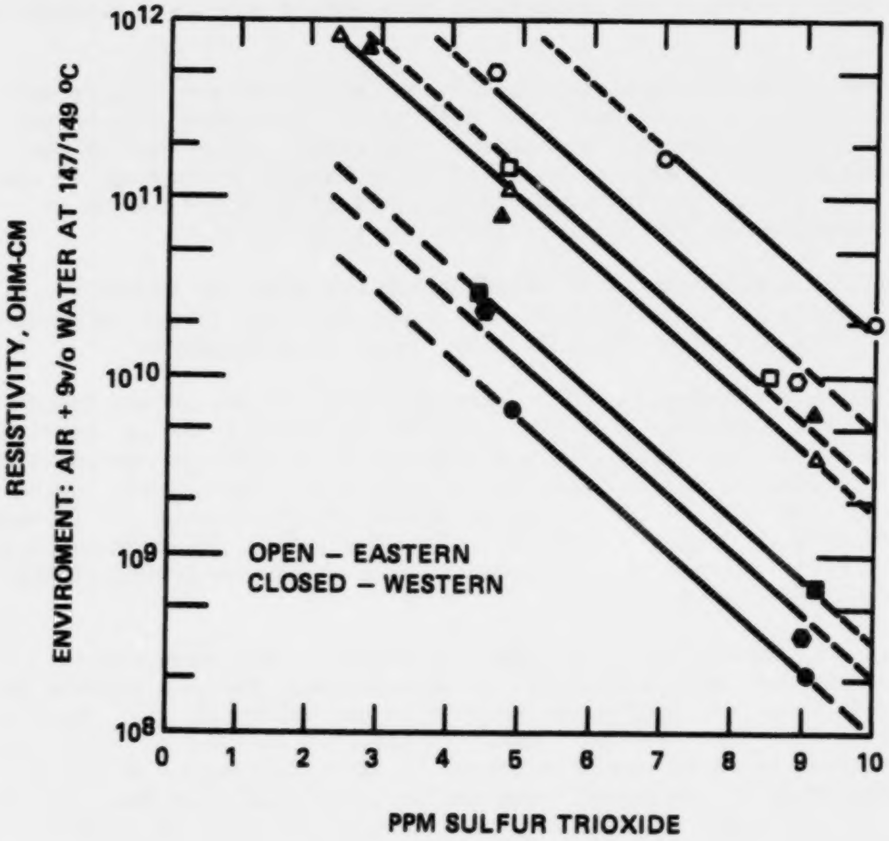

Figure 7. Resistivity as a function of environmental sulfur trioxide concentration for eight fly ashes.

ILLUSTRATION OF RESISTIVITY PREDICTION

The information required to utilize the proposed technique for predicting resistivity is the as-received, ultimate coal analysis and the chemical composition of the coal ash. A stoichiometric calculation of the combustion products is made using 30% excess air to determine the concentration of sulfur dioxide and water. The quantity of excess air used in the calculation was established by comparing stoichiometrically calculated flue gas analyses with *in situ* analyses for those coals involved in this research program. The coal ash is prepared by first igniting the coal at 750°C in air, passing the ash through a 100-mesh screen, and then igniting the ash a second time at 1050°C ± 10°C in air for a period of 16 hours. Good agreement in chemical analysis has been obtained between coal ashes produced in this manner and their respective fly ashes.

The usual chemical analysis of the coal ash in weight percent expressed as oxides is performed. The analysis is converted from weight percent to molecular percent as oxides. The atomic percentage of the lithium and sodium is taken as 66.6% of the molecular percentage of the oxides. The sum of the atomic percentages of lithium and sodium is used to determine the resistivity value, ρ_c, from Figure 1.

Using the concentration of water determined from the combustion products calculation and equation (1), the predicted resistivity in terms of ash composition and water concentration, $\rho_{c,w}$, is determined.

For the ash thickness used in this research, ∿5 mm, it was found that dielectric breakdown generally occurred at applied voltage gradients of 8 to 12 kV/cm. Therefore, it was arbitrarily decided to use 10 kV/cm as the electrical stress at which the resistivity is predicted. Using equation (2) and E_e = 10 kV/cm, the predicted resistivity is put in terms of ash composition, water concentration and dielectric breakdown stress, $\rho_{c,w,e}$. This value then is the predicted resistivity exclusive of the effect of sulfuric acid.

Using the information from a variety of field test programs for which flue gas data were available, it was observed that the average sulfur trioxide value was approximately 0.4% of the sulfur dioxide value at the inlet to cold-side precipitators. This factor is used to calculate the anticipated level of sulfur trioxide based on the amount of sulfur dioxide appearing in the stoichiometrically calculated flue gas. For example, a typical Eastern coal can produce a flue gas containing 2000 ppm of sulfur dioxide which it is anticipated would yield 8 ppm of sulfur trioxide. Referring to Figure 7, a reasonable estimate of the resistivity, ρ_s, resulting from this sulfur trioxide concentration might be 2×10^{10} ohm·cm. One then determines the resultant resistivity, ρ_r, from equation (3) and the values for ρ_s and $\rho_{c,w,e}$.

ACKNOWLEDGMENT

This research was sponsored by the Environmental Protection Agency under Contract No. 68-02-2114, Dr. Leslie E. Sparks, Project Officer. The author is grateful for the financial support and the patience shown by the sponsor while experimental problems were overcome.

REFERENCES

1. Bickelhaupt, R.E.,"Measurement of Fly Ash Resistivity Using Simulated Flue Gas Environments", Environmental Protection Agency, Research Triangle Park, N.C. Report EPA 600/7-78/035, March 1978, 29 pages.

2. ASME PTC-28, "Determining the Properties of Fine Particulate Matter, Section 4.05, Method for Determination of Bulk Electrical Resistivity", pp 15-17, 1965.

3. a) Bickelhaupt, R.E., "Surface Resistivity and the Chemical Composition of Fly Ash", APCA Journal 25 (2) 148-152, 1975.

   b) Selle, S.J., et al, "A Study of the Electrical Resistivity of Fly Ash from Low-sulfur Western Coals Using Various Methods, "Paper 72-107 presented at the 65th Annual Meeting of the APCA, Miami Beach, Fla. 1972.

4. a) Maartmann, Sten, "The Effect of Gas Temperature and Dew Point on Dust Resistivity - and Thus the Collecting Efficiency of Electrostatic Precipitators", Second International Clean Air Congress of the International Union of Air Pollution Prevention Association, December 6-11, 1970, Washington, D. C.

   b) White, H.J., "Chemical and Physical Particle Conductivity Factors in Electrical Precipitation", Chemical Engineering Progress 52 244-248, June 1956.

   c) McLean, K.J., "Factors Affecting the Resistivity of a Particulate Layer in Electrostatic Precipitators", APCA, Journal 26 (9) 866-870, 1976.

5. Baker, J.W. and K. M. Sullivan, "Reproducibility of Ash Resistivity Determinations", presented at the Joint Power Generation Conference, Long Beach, California, September 18-21, 1977.

ELECTRICAL PROPERTIES OF THE DEPOSITED DUST LAYER WHICH ARISE BECAUSE OF ITS PARTICULATE STRUCTURE

Kenneth J. McLean
University of Wollongong
P.O. Box 1144, Wollongong N.S.W.
2500 Australia.

ABSTRACT

The paper outlines the progress made in understanding the effect the particulate structure of a deposited or compacted dust layer has on its overall electrical characteristics. The need to use a simplified idealised model is discussed, and it is shown that the layer's particulate structure is important in considering its effective resistivity, cohesion forces, dielectric properties and the formation of back corona.

INTRODUCTION

It has been recognised for many years that the dust layer deposited on the collecting plates and discharge wires of an electrostatic precipitator can have a significant effect on the precipitator's electrical characteristics and collection performance. One of the basic aims of modern research has been to identify and quantify these effects and to integrate them into a general mathematical model of electrostatic precipitation. In most cases, this is usually done by treating the deposited particulates as homogeneous layers with a given overall characteristic.

While this approach is satisfactory for the purpose of developing a general theoretical approach to characterise precipitator operation, it is important to recognise that the overall characteristics take the form they do because of the hetrogeneous nature of the dust layers. The deposited particulate layer is actually a random compaction of generally spherical particles having a wide size distribution, and a

Preceding page blank

porosity of approximately 50 per cent. It is the particulate nature of the deposited layer which gives it many of its unique characteristics and which plays such an important part in determining the electrostatic precipitator's operation.

The first person to attempt to relate the overall characteristics of a dust layer to its microscopic properties was Masuda[1] in his early papers on resistivity. The importance of this approach was recognised by the electrostatic precipitation research group at the University of Wollongong and the group has sought to develop these ideas further. This microscopic approach has not only been applied to special problems associated with volume and surface resistivity but has been extended to a study of the cohesion forces, measurement of capacitance and the formation of back corona.

The purpose of this paper is to identify those characteristics of a deposited dust layer which result because of its particulate nature and to give a summary of recent progress in this aspect of electrostatic precipitation research.

IDEALIZED MODEL

Suspended particles found in the flue gas after combustion are invariably non-uniform in size and when deposited are randomly packed together. This makes mathematical analysis very difficult. In order to evaluate what geometrical factors are important and to obtain an estimate of the order of magnitude of various variables and unknowns, it is sufficient to consider an idealized dust layer in which the particles are assumed to be spherical, uniform in size and compacted together in a regular array. It is most convenient to assume that the particle radius equals the average value of the particles and that they are compacted in a simple cubic array as shown in Figure 1.

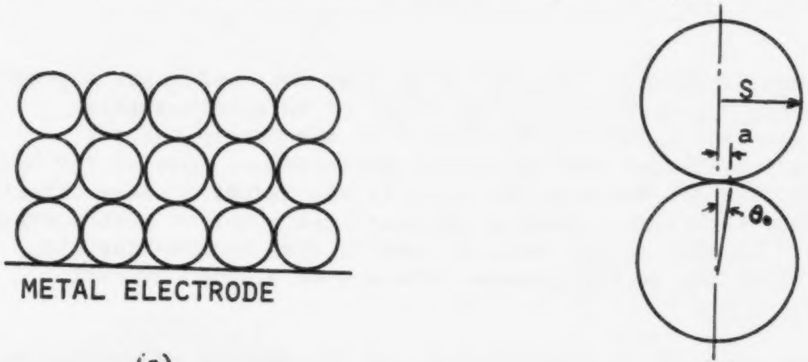

(a) (b)

Figure 1: Arrangement of Ideal Particles. (a) Simple Packing of Layer. (b) Two Particles in Contact.

Current conduction in most industrial situations takes place over the particle surface and this is assumed in the following analysis. The current can only flow from one particle to another via their common points of contact. This causes the current flow to be constricted, and very high microscopic electric fields are developed in the particle itself and in the inter-particle air space in this constriction region. It is this microscopic electric field pattern produced by the current flow which is primarily responsible for many of the overall characteristics of the deposited layer.

The electric field in the airgap between two adjacent particles may be calculated by making several simplifying assumptions. This gives,[2,3]

$$E_z(\theta) = E_a \frac{\ln\,(\tan\,\theta/2/\tan\,\theta_0/2)}{(\cos\theta_0 - \cos\theta)\,\ln\,(1/\tan\,\theta_0/2)} \qquad (1)$$

where E_a is the average electric field across the dust layer. Figure 2 shows the variation of this electric field normalised to E_a and the particle radius S.

If E_a is 10^6V/m, it may be seen that very high electric fields are established in the airgap and are in the order of 10^8V/m and greater for radii less than 0.1S. These high electric fields cannot be sustained and it must be assumed that some kind of stable breakdown occurs across this region.

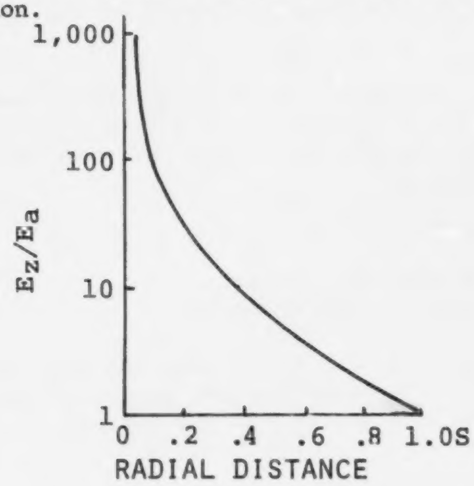

Figure 2: Variation of Electric Field in Airgap Between Adjacent Particles.

In most of the problems that arise, it is necessary to relate the microscopic behaviour of each particle to the macroscopic characteristics of the dust layer. For the idealized model assumed, this can be done by noting that the number of series particles (or contacts) which form one column is

$$n_s = d/S \qquad (2)$$

and the number of parallel paths is equal to the number of columns and is given by

$$n_p = A/4S^2 \qquad (3)$$

where d is the sample thickness and A its cross-section area.

The other important factor in this model is the radius of contact between two adjacent spherical particles. If the particles are compressed together, as shown in Figure 1(b), by either a mechanical or electrical force F, the radius of their common area of contact is given by,[2,4]

$$a = \left(\frac{3}{4}\,\frac{S(1-\nu^2)\ F}{Y}\right)^{1/3}$$

$$= B(SF)^{1/3} \qquad (4)$$

where Y = Young's modules
ν = Poisson's ratio
B = constant

RESISTIVITY

The effective resistivity of a layer will depend on the path the current flows through each particle. It is usual to consider the two extreme cases where current conduction is either predominantly through the volume of the particle or over the particle surface. In the latter case, it is also important to distinguish between the surface and skin conduction modes. The effective resistivity of the layer is dependent on the mode of conduction and on the effective resistance of the contact region between adjacent particles.

In the volume conduction mode, current flows through the volume of the particle and is influenced by the bulk properties of the particle material and temperature. The bulk resistivity of the particle material is given by the well known relationship

$$\rho v = A\varepsilon^{\frac{E}{kT}} \qquad (5)$$

where A = constant   k = Boltzmann's constant
E = activation energy   T = absolute temperature

For the surface conduction mode, current flows over the surface of the particle and is very sensitive to the conditioning agents in the environment and to temperature. One expression for the surface resistivity is given by,[4,5]

$$\rho s = B\varepsilon^{-Lp\varepsilon^{Q/RT}} \qquad (6)$$

here L, B = constants   Q = binding energy of adsorbed water molecules
p = water vapour pressure   R = molecular gas constant

In the skin conduction mode, the main conduction current flows in the thin outer skin of the particle. The conduction mechanism is controlled by the general impurities which are strongly bound into this layer. It has a temperature relationship similar to Eqn.(5) and consequently cannot always be easily distinguished from volume resistivity.

In order to find the theoretical resistivity of the idealized layer of particles, it is necessary to calculate the effective resistance of each particle when compressed together with another. This mainly depends on the effective resistance R_c at their common points of contact and the relationships have already been determined[2,4]. The results are reproduced in Table 1.

Table 1. RESISTIVITY RELATIONSHIPS

	Volume	Surface and Skin
Contact resistance R_c	$\rho_v/2a$	$\frac{\rho_s}{2\pi} \ln 2S/a$
Resistivity ρ_e (i)	$\rho_v/D^3\sqrt{4P}$	$\frac{2\rho_s S}{\pi} \ln \frac{2}{D^3\sqrt{4P}}$
(ii)	$\frac{A}{D^3\sqrt{4P}} \varepsilon^{E/kT}$	$\frac{2S}{\pi} \ln \frac{2}{D^3\sqrt{4P}} B\varepsilon^{-Lp\varepsilon^{Q/RT}}$ *

* Applicable to surface conduction.

Since the particles are connected in series in any single column, the contact resistances must be added to find the resistance of a single column. The columns however, are connected in parallel with one another and this reduces the effective resistance. If the number of parallel paths is N_p per unit area and series contacts is N_s in a unit depth, the effective resistivity becomes

$$\rho = R_c N_s / N_p$$

For a simple cubic array, $N_s = 1/2S$ and $N_p = 1/4S$. Hence:

$$\rho = R_c 2S \tag{7}$$

If two spheres are compressed together with a pressure P, Eqn.(4) may be modified to give the radius of contact,

$$a = DS(4P)^{1/3} \tag{8}$$

The effective resistivity as a function of pressure is found by combining the expressions for R_c with Eqns.(7) and (8) to give the result shown in Table 1, row (i). If Eqns.(5) and (6) are substituted for ρ_v and ρ_s, the complete expression for the effective resistivities may be found as shown in row (ii) of the Table.

These theoretical results are significant as they show the relative importance of the different parameters and variables. This may be illustrated by considering the effect of pressure.

If pressure is first applied to an uncompacted layer of particulates, the reduction of resistivity is primarily due to the rearrangement of the particles in the layer so as to increase N_s and particularly N_p. The effect is similar for both surface and volume conduction modes. Once the layer is compacted so that there is no significant change in the arrangement of the particles with pressure, any additional pressure increases the contact area between the particles. For the volume conduction mode, the resistivity will be proportional to $(P)^{-1/3}$. Since P is in the argument of the logarithm term, the resistivity component due to surface conduction will be much less sensitive to pressure.

In a similar manner, the significance of temperature, environmental conditions, particle size and other parameters may be evaluated.

COHESION

One approach which has been used to calculate the cohesive force F of a particulate layer is to treat it as a parallel plate capacitor with a homogeneous dielectric. This gives the well known expression,

$$F = \frac{\varepsilon_o \varepsilon_r E_a^2}{2} \qquad (9)$$

where E_a is the average electric field across the layer.

A calculated curve based on this equation is shown in Figure 3 together with some experimental results measured by a mechanical balance[3].

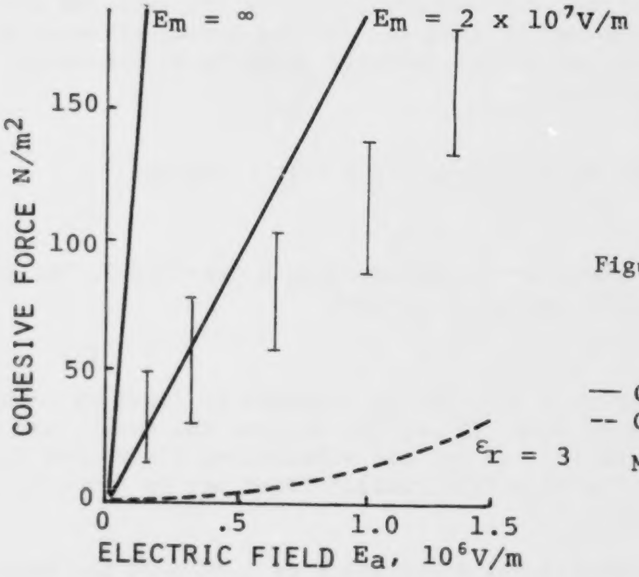

Figure 3: Variation of Cohesive Force With Applied Electric Field.

— Calculated by Eqn(10).
-- Calculated by Eqn(9).
Measured values.

If consideration is given to the particulate nature of the layer, it may be seen that the main electric field holding the layer together is that which exists in the airgap between adjacent particles that go to make up the layer.

By calculating the magnitude of this electric field for the idealized model and integrating the incremental force over the cross-sectional area, it may be shown that an approximate expression for the total cohesive force is,[3]

$$F = KE_a^{\beta} \tag{10}$$

where K and β are constants.

In order to arrive at a reasonable value for F, it is necessary to assume that the electric field is limited to some maximum value for the region in the airgap close to the contact circle of two adjacent particles. Figure 3 shows two theoretical curves based on the assumption that the maximum field is ∞ and 2 x 10^7V/m. The experimental curve can be closely approximated by assuming E_m is between 1 and 2 x 10^7V/m.

The total force per unit area on a dust layer in an electrostatic precipitator is

$$F = KE_a^{\beta} - \varepsilon_o E_f^2/2 \tag{11}$$

The second term on the right hand side is the force due to the electric field E_f in the airspace which tends to pull the dust layer into the gas stream.

CAPACITANCE

The magnitude of the relative dielectric constant of the particulate material is one of the factors which affects the maximum charge a particle can receive in a corona field. Because of this, there has been a general interest in measuring the relative dielectric constant ε_r of different fly ash particles.[7]

If the capacitance of a fly ash layer is measured over the frequency range 1 to 10,000 Hz, there is an apparent change in its value at the low frequency end of the spectrum[6] as shown in Figure 4.

The capacitance at low frequencies may be 5-10 times greater than that at higher values.

This phenomena can be explained by taking into account the particulate nature of the dust layer. By considering the distribution of the flux in the particles and in the airgap between adjacent particles set up by the current flow around the particle surface, it may be shown that the dust layer can be represented by the equivalent circuit shown in Figure 5. The frequency response of this circuit has the same general shape as that measured for the dust layer shown in Figure 4.

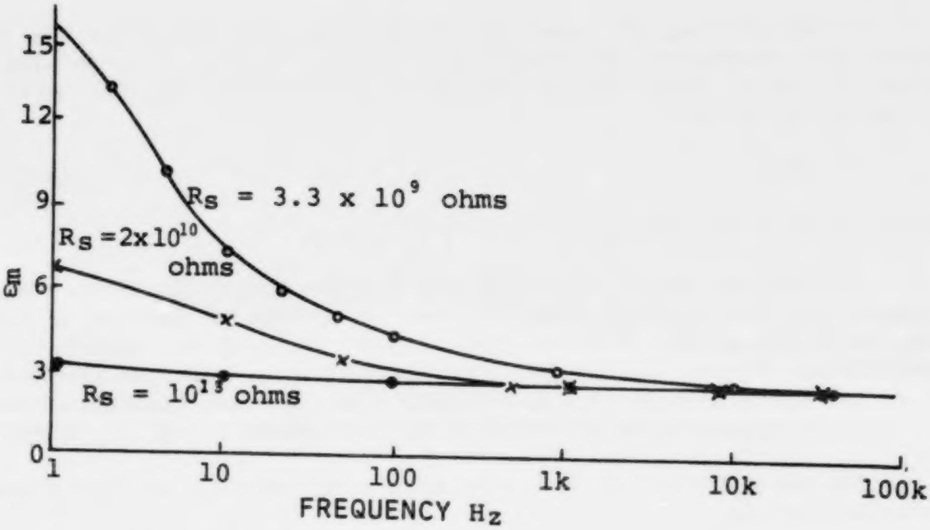

Figure 4: Variation of Relative Dielectric Constant of the Layer with Frequency and Surface Conductivity.

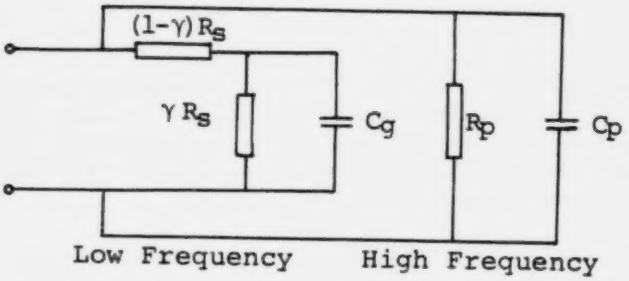

Figure 5: Equivalent Circuit for Dust Layer.

R_s = effective d.c. resistance
R_p = effective a.c. resistance of particles
C_g = airgap capacitance
C_p = effective capacitance due to flux lines in the particles
γ = constant.

It may be concluded that the low frequency response and the d.c. capacitance of the layer is dominated by the surface conductivity and the inter-particle airgap capacitance. At higher frequencies (i.e., >1,000Hz), the characteristic is dominated by the particle shape, material and voltage gradient around the particle surface. The relative dielectric constant of the layer ε_m at these higher frequencies, is related to the relative dielectric constant of the particle material, ε_r by the following expression,

$$\varepsilon_r = K \varepsilon_m \tag{12}$$

where K is an empirical constant. The expression is independent of density, but it does assume all particles are touching one another so that current flows over their surfaces. A research project is to be initiated to determine more accurately the value of K.

The Bottcher equation[8] is sometimes used to calculate ε_r from measured values of ε_m and porosity. This equation cannot be applicable in most practical cases of fly ash samples, as it is based on the assumption that the particles comprise a pure dielectric material and that the field pattern is determined by the geometrical shape of the particles and the layer's porosity.

BACK CORONA

One of the most important phenomena limiting the performance of electrostatic precipitators collecting high resistivity fly ash is back corona. Many aspects of the physics of this discharge have been extensively studied by Herceg[9], Thanh[10] and Masuda, et al[11], and its effect on an electrostatic precipitator's operating variables by Herceg and McLean[12], and McLean and Kahane[13].

The formation of back corona is completely dependent on the fact that the layer is porous and this results from its particulate structure. A qualitative description of the main events that occur during the formation of back corona are given below:

(a) The main corona current flowing through the deposited dust layer will establish an average electric field given by:

$$E_a = J\rho \tag{13}$$

Much higher microscopic electric fields will exist in the air voids between the surfaces of adjacent particles as given by Eqn.(1).

(b) The initial breakdown will probably occur within the layer in these regions of higher electric field. This most likely accounts for the relatively low average electric fields at which back corona onset sometimes appears to occur.

(c) The initial method of ionisation is probably the usual Townsend mechanism. The ionisation process quickly spreads axially through the dust layer. The positive ions will move to the surface and the electrons to the metal electrode. This "explosion" will cause some of the particles to be removed and if an intensive back discharge is established, a small channel will be formed through the layer.

There are a number of additional factors which are necessary in order to maintain the back corona discharge and these are being currently investigated at the University of Wollongong. Their discussion is beyond the scope of this paper.

DISCUSSION

A much deeper insight into the factors affecting the electrical characteristics of a compacted dust layer is obtained by developing mathematical equations based on a simple model of its particulate structure. Since particle size, shape and packing have all been idealized, not all the equations developed can be used for accurate quantitative calculations but they are invaluable in determining the general effects of different parameters in calculating orders of magnitude of the variables, and in writing semi-empirical equations.

ACKNOWLEDGMENTS

The author wishes to thank the Electricity Commission of New South Wales for the financial suport of the projects discussed in this paper.

REFERENCES

1. Masuda, S., Effects of Temperature and Humidity on the Apparent Conductivity of High Resistivity Dust. Electrotech. J. Japan, 7:108-113, February 1962. (English)

2. McLean, K.J. and Huey, R.M., Influence of Electric Field on the Resistivity of a Particulate Layer. Proc. IEE, 122:76-80, January 1974.

3. McLean, K.J. Cohesion of Precipitated Dust Layer in Electrostatic Precipitators. J. Air Poll. Control Assoc. 27:1100-1103, November 1977.

4. McLean K.J., Factors Affecting the Resistivity of a Particulate Layer in Electrostatic Precipitators. J. Air Poll. Control Assoc. 26:866-870, September 1976.

5. Martin, A.D. and McLean, K.J., The Effect of Adsorbed Gases on the Surface Conductivity of Quartz. J. Appl. Phys., 48:2950-2954, July 1977.

6. McLean, K.J. and Pohl, H.K., Dielectric Properties of a Compacted High Resistivity Particulate Layer. (To be published.)

7. Tassicker, O.J., Über die Temperatur - und Frequenzabhängigkeit der Dielektrizitätskonstante von Kraftwerksstaub. Staub-Reinhalt, Luft, 31:331-335, August 1971.

8. Bottcher, C.J.F., The Theory of Electric Polarisation. Elsevier Publishing Company, Amsterdam, 1952 p.415.

9. Herceg, Z., Electrical Characteristics of Contaminated Corona Systems. Ph.D Thesis, University of N.S.W., 1970.

10. Thanh, L.C., Effects of Negative Pulsed Voltage on the Characteristics of an Electrode System with Clean and Contaminated Anode. Ph.D Thesis University of N.S.W., 1976.

11. Masuda, S. and Mizundo, A., Initiation Condition and Mode of Back Discharge. J. Electrostatics, 4:35-52, 1977/1978.

12. Herceg, Z. and McLean, K.J., Efficiency of Electrostatic Precipitators and Relationships to Corona Voltage-Current Characteristics. (Presented at the APCA Annual Meeting, Atlantic City, N.J., 1971.)

13. McLean, K.J. and Kahane, R., Electrical Performance Diagram for a Pilot Scale Electrostatic Precipitator. In International Clean Air Conference, White, Hetherington and Thiele (Eds.), Ann Arbor Science Publishers Inc., 1978. p.207-221.

VOLTAGE AND CURRENT RELATIONSHIPS IN HOT SIDE ELECTROSTATIC PRECIPITATORS*

Donald E. Rugg
Whitney Patten
University of Denver
Denver Research Institute
Denver, Colorado 80210

ABSTRACT

The secondary voltage and current waveforms of the high voltage power supplies of several hot-side electrostatic precipitators have been recorded. Different recorded forms of the time varying voltage-current relationships are shown. In addition to the voltage-current waveforms, dynamic voltage-current curves and average voltage-current curves are presented. The data are interpreted in terms of the electrical characteristics within inlet and outlet sections. Means of changing the electrical characteristics of outlet sections and the possible effects upon particle charging and collection are discussed.

INTRODUCTION

To contend with the problems in collecting high resistivity ash from coal-fired power plants utilizing low-sulfur coal, electrostatic precipitators have been installed on upstream side of the combustion air pre-heaters. In these hot side electrostatic precipitators, the flue gas temperature is typically greater than 300°C. The ash resistivity decreases at these higher temperatures where volume conduction rather than surface conduction prevails and typical values are 10^9-10^{10} ohm-cm. Problems caused by high resistivity ash should not exist in hot side electrostatic precipitators. However, the performance of several hot

---

* This work was supported under Grant R-805324-01 by the Industrial Environmental Research Laboratory, U.S. Environmental Protection Agency, Research Triangle Park, NC.

Preceding page blank

side precipitators located in the western United States are not as good as some of the ones operating in the eastern states.

One of several reasons which could explain the difference in the performance of hot side precipitators located near the east coast and in the west is the difference in altitudes and the corresponding difference in relative air densities. For example, at a given temperature, the relative air density in Denver compared to sea level is 0.82. Several corona characteristics are affected by a decrease in air density. The voltage and electric fields at corona onset are reduced [1]. The ion mobility increases which reduces the ion space charge density for a specified current density [2]. The electrical characteristics of particles within the precipitator are also altered. The rate at which the particles acquire charge decreases because of the lower ion density and field charging is not as effective because the electric fields are lower [3]. Also, spark-over voltages and the breakdown field strength of the ash layer would be reduced. All of these factors tend to degrade precipitator performance.

The voltage and current waveforms for a hot side electrostatic precipitator located at low altitude (750 mm Hg) and hot side electrostatic precipitators located at high altitudes (650 mm Hg) have been measured. A significant difference between the waveforms recorded at the low and high altitude sites existed in both the inlet and outlet sections of the precipitators. It has not been shown that these differences are directly or indirectly related to altitude. However, some possible explanations of the waveforms are discussed.

DESCRIPTION OF THREE HOT SIDE ELECTROSTATIC PRECIPITATORS

The waveforms which are presented were recorded at three coal-fired power plants. A brief summary of design specifications and general information about the electrical sectionalization of the precipitators are presented in Table I. The plate-to-plate spacing, type of collection plates, wire-to-wire spacing and wire diameter are the same. However, the electrical sections vary in size and this should be realized when interpreting waveforms.

Voltage dividers were installed on the secondary of the high voltage power supplies which energized the inlet and outlet sections of each precipitator. The voltage waveform and power supply current waveform for the electrical section under test was recorded on an oscilloscope. By using the x and y oscilloscope inputs for the voltage and current respectively, "dynamic voltage-current curves" were recorded. The average values of the secondary current and voltage were also recorded except at Allen where the average high voltage was not measured.

TABLE I

Brief Description of Three Hot-Side Electrostatic Precipitators

General Information and Design Specifications	Allen Unit 3 Charlotte, NC MFG: Research Cottrell	San Juan Unit 1 Waterflow, NM MFG: Western	Navajo Unit 1 Page, AZ MFG: Western
Electrical Sections from Inlet to Outlet	4	9	6
Length/Electrical Sect.	2.74m	1.37m	1.83m
Area/Electrical Sect.	3913m^2	1990m^2	2341m^2
Specific Collection Area	53m^2/m^3/sec	73m^2/m^3/sec	60.4m^2/m^3/sec
Collection Efficiency	99.2%	99.8%	99.5%
Temperature	350°C	350°C	350°C
Atmospheric Pressure	750mm Hg	650mm Hg	650mm Hg

DISCUSSION OF DATA

Voltage and current waveforms of an inlet section at Allen Unit 3 and San Juan Unit 1 are shown in Figure 1. The corona onset voltage, V_c, was determined by reducing the current to a minimum which was 1.4 na/cm^2 at Allen and not measurable at San Juan. The resulting voltages for corona onset, as shown in Figure 1, were 21KV at Allen and 18.5KV at San Juan. The higher corona onset voltage at Allen could be due to the higher gas density. A typical inlet average current density at Allen was 25 na/cm^2 and for San Juan it was spark limited at 6.5 na/cm^2. Figure 1(a) shows the inlet peak voltage was 45KV and the minimum voltage was 31KV. The peak and minimum voltages in Figure 1(b) were 42KV and 30KV respectively. The most significant difference in the inlet electrical characteristics was the current densities that could be obtained. Two possible reasons for the differences in inlet current densities are: (1) the particle space charge density was less at Allen; (2) the voltage drop across the dust layer was larger at San Juan even though measured dust resistivities are comparable.

A comparison of Allen and San Juan outlet voltage and current waveforms is shown in Figure 2. The Allen outlet corona onset voltage was 21KV, the same as the inlet section. V_c at the San Juan outlet was 15KV which is 3KV to 4KV lower than at the inlet. In Figure 2(a), the peak voltage was 44KV, the minimum voltage was 27KV and the average current density was 41 na/cm^2. For an average current density of 45 na/cm^2 at San Juan, Figure 2(b) shows the peak and minimum voltages were 37KV and 5KV, respectively. The most significant difference in the Figure 2 waveforms is the minimum voltages. The minimum voltage at Allen was 27KV which is 6KV above corona onset while at San Juan the minimum voltage of 5KV is 10KV lower than corona onset. This is an indication of back-ionization at San Juan since the minimum voltage is less than corona onset voltage.

Another presentation of the voltage and current relationship is in the form of dynamic V-1 curves as shown in Figure 3. The arrows denote the direction of increasing time. The dynamic V-1 curves show the maximum and minimum voltage and current values and also the phase relationship. The curves for the Allen inlet, the Allen outlet and the San Juan inlet show the power supply loads are similar to lossy capacitors. At the San Juan outlet, the maximum current occurs after the peak voltage which results in the figure eight appearing curve indicating severe back-ionization. For some purposes, the dynamic V-1 curves are easier to interpret than the two separate waveforms.

Since the voltage fluctuation between the peak and the minimum values appears to show the significant waveform characteristics, peak and minimum voltages were plotted as a function of average current density in Figure 4 and in Figure 5. In the inlet, the voltage at San Juan is higher than at Allen for current densities less than 6 to 8 na/cm^2. The inlet current density at San Juan is spark limited at this density while at Allen the inlet current density can be increased to 35 to 40 na/cm^2 before sparking occurs.

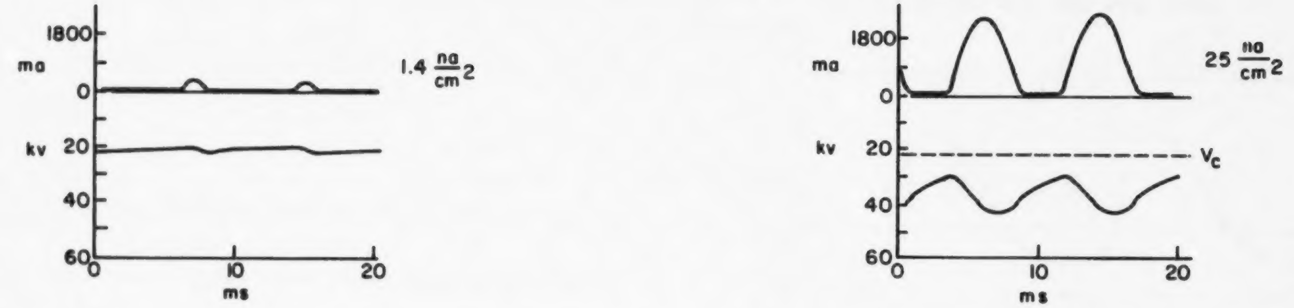

(a) ALLEN INLET

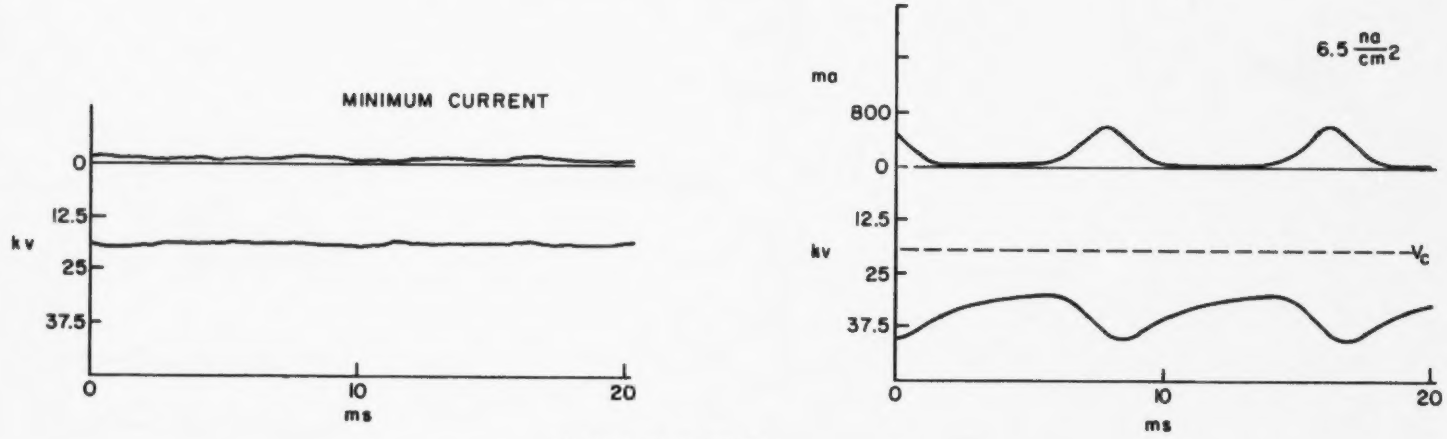

(b) SAN JUAN INLET

FIGURE 1. VOLTAGE AND CURRENT WAVEFORMS AT INLET OF ALLEN AND SAN JUAN

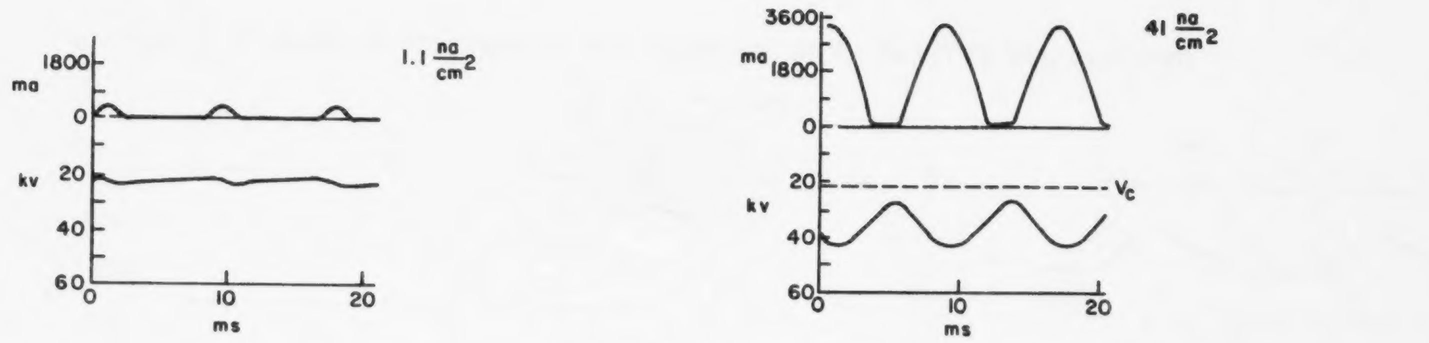

(a) ALLEN OUTLET

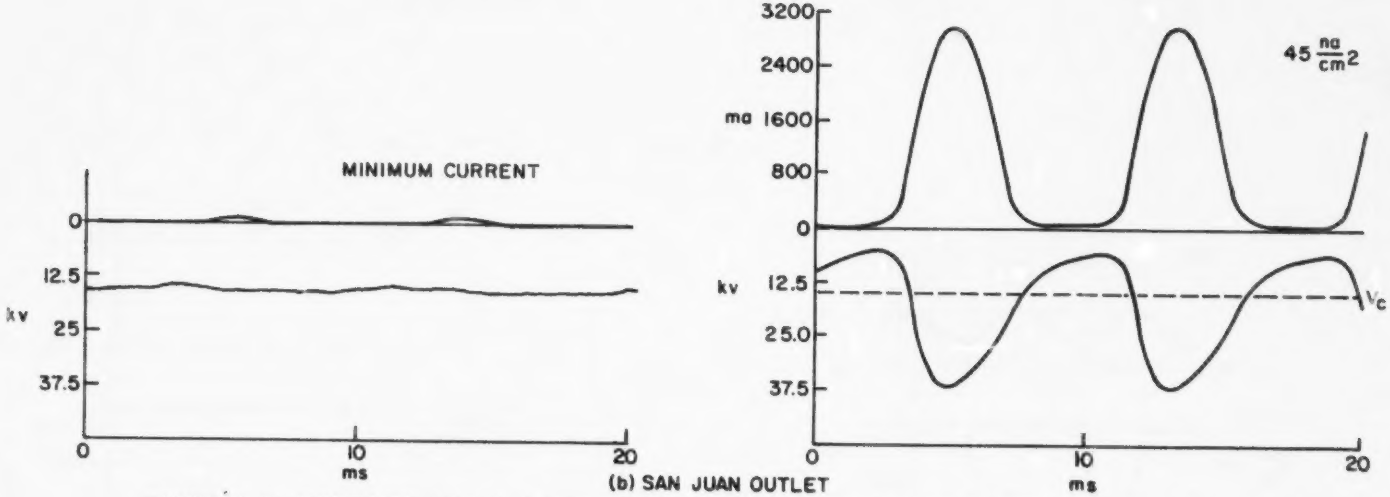

(b) SAN JUAN OUTLET

FIGURE 2. VOLTAGE AND CURRENT WAVEFORMS AT OUTLET OF ALLEN AND SAN JUAN

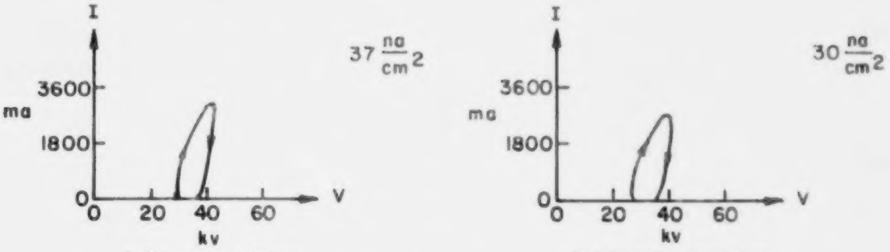

(a) ALLEN INLET

(b) ALLEN OUTLET

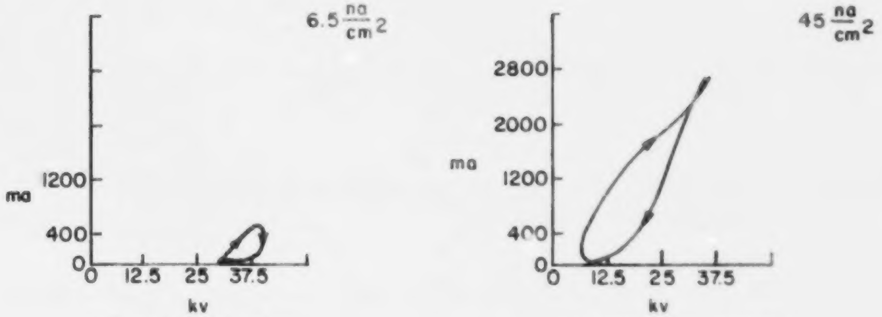

(c) SAN JUAN INLET

(d) SAN JUAN OUTLET

FIGURE 3. DYNAMIC V-I CURVES

Figure 5 shows that the Allen outlet voltage curves are similar to the inlet curves except the voltages are 2KV to 4KV lower for the same current densities. The San Juan minimum voltage curve in Figure 5 increases until a current density of about 5 na/cm^2 is reached and then the minimum voltage decreases. This indicates that back-ionization starts at current densities of about 5 na/cm^2. This is also the same current density range which produced sparking at the inlet. If the dust layer breaks down at 5 na/cm^2, the higher inlet voltage could produce sparking and the lower outlet voltage could lead to stable back-ionization. There is no indication of back-ionization at Allen.

The outlet peak and minimum voltage curves for Navajo Unit 3 were similar to the San Juan outlet curves. The minimum voltage decreased for average current densities larger than 10 na/cm^2 which was also the spark limited inlet current density. This indicates that back-ionization starts at about 10 na/cm^2 at Navajo. The difference in the voltage and current relationships in the three hot side electrostatic precipitators is due to the apparent dust layer breakdown at low current densities at the two plants located in the western United States.

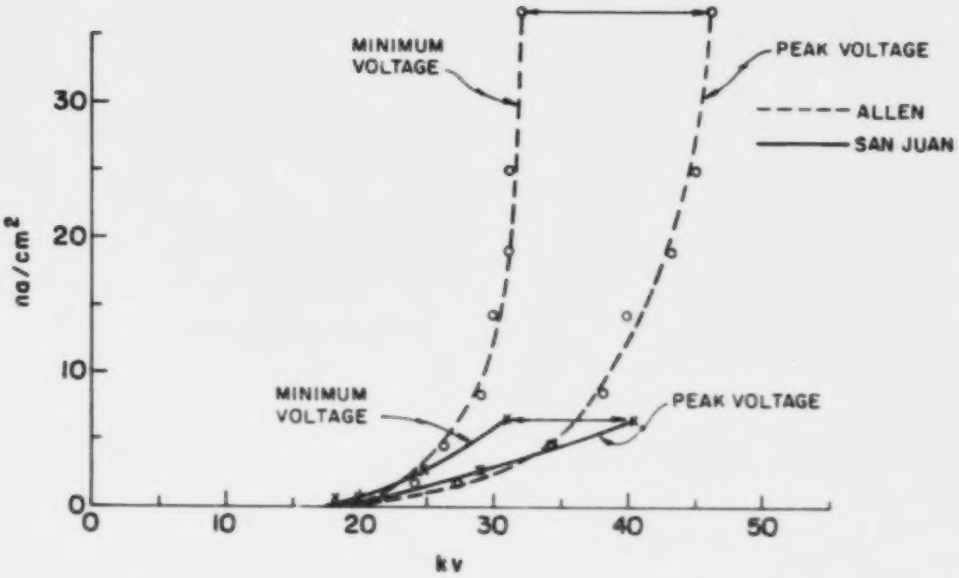

FIGURE 4. COMPARISON OF INLET VOLTAGE FLUCTUATIONS AT ALLEN AND SAN JUAN

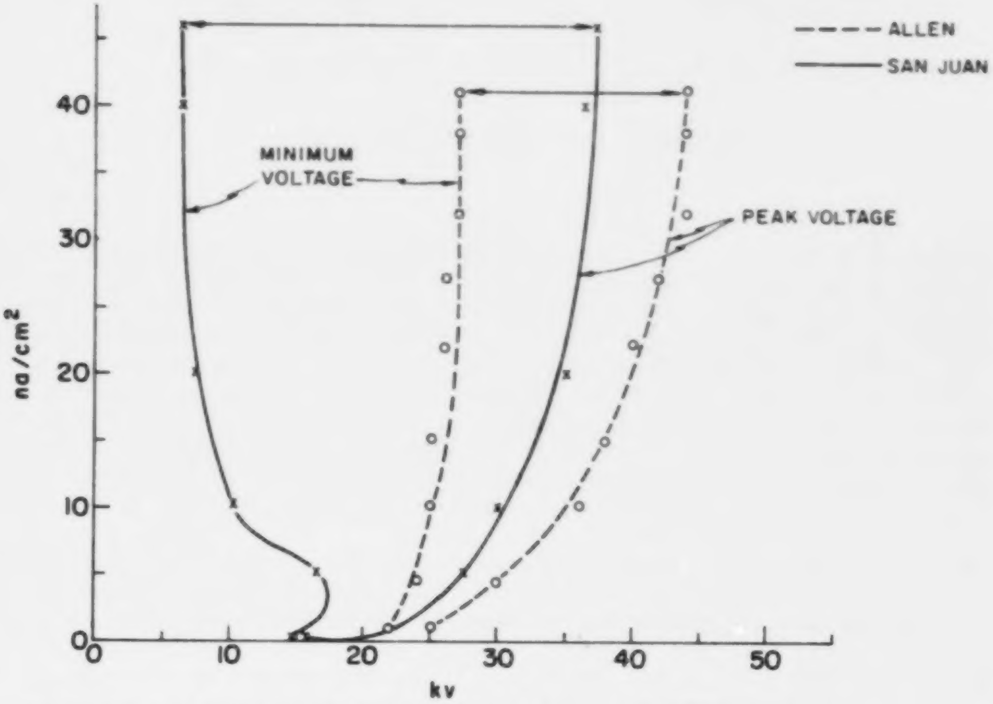

FIGURE 5. COMPARISON OF OUTLET VOLTAGE FLUCTUATIONS AT ALLEN AND SAN JUAN

Methods of detecting the onset of back-ionization have been investigated. One means of determining if back-ionization exists in a precipitator has been to increase and then decrease the current density and plot the average V-I measurements. If the measurements show a hysteresis effect as in Figure 6, then back-ionization is assumed to exist [4]. In an attempt to understand the reasons for the difference between the increasing and decreasing current measurements, which took at least five minutes to run, voltage waveforms were recorded (Figure 7). The voltage waveforms indicate the corona onset voltage decreased about 1.5KV during the test. However, this could be due to a change in dust conditions on the wires and plates between the start and end of the measurements rather than back-ionization.

Another means of detecting back-ionization at the time it occurs involves measuring changes in the delay between the voltage and current waveform peaks. Real time detection of back-ionization onset is necessary if it is to be controlled by changing the electrical operating conditions. Therefore, the investigation of voltage and current relationships will be continued.

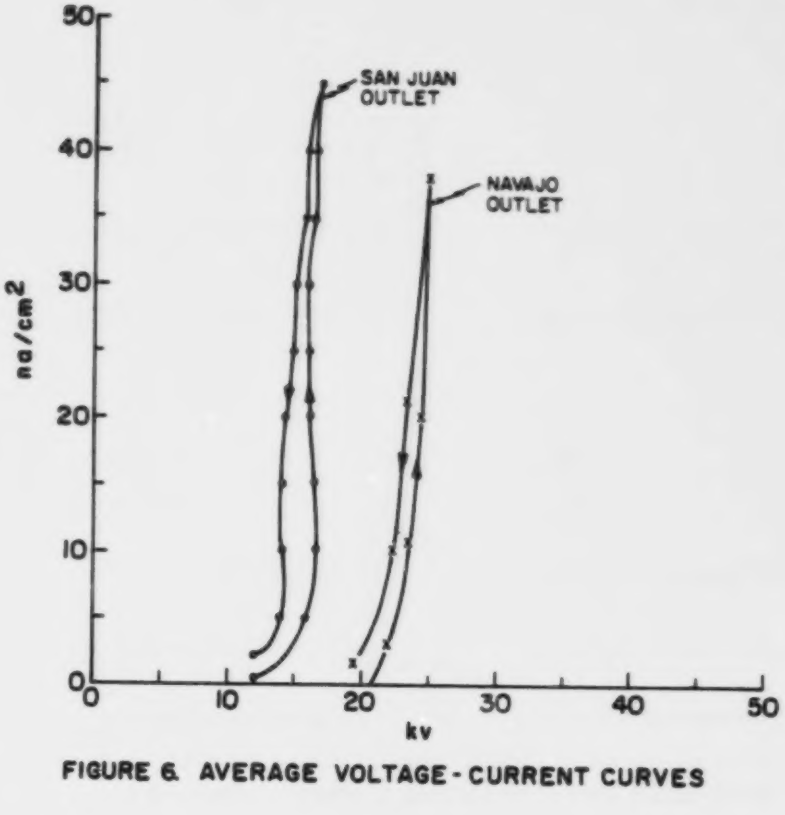

FIGURE 6. AVERAGE VOLTAGE-CURRENT CURVES

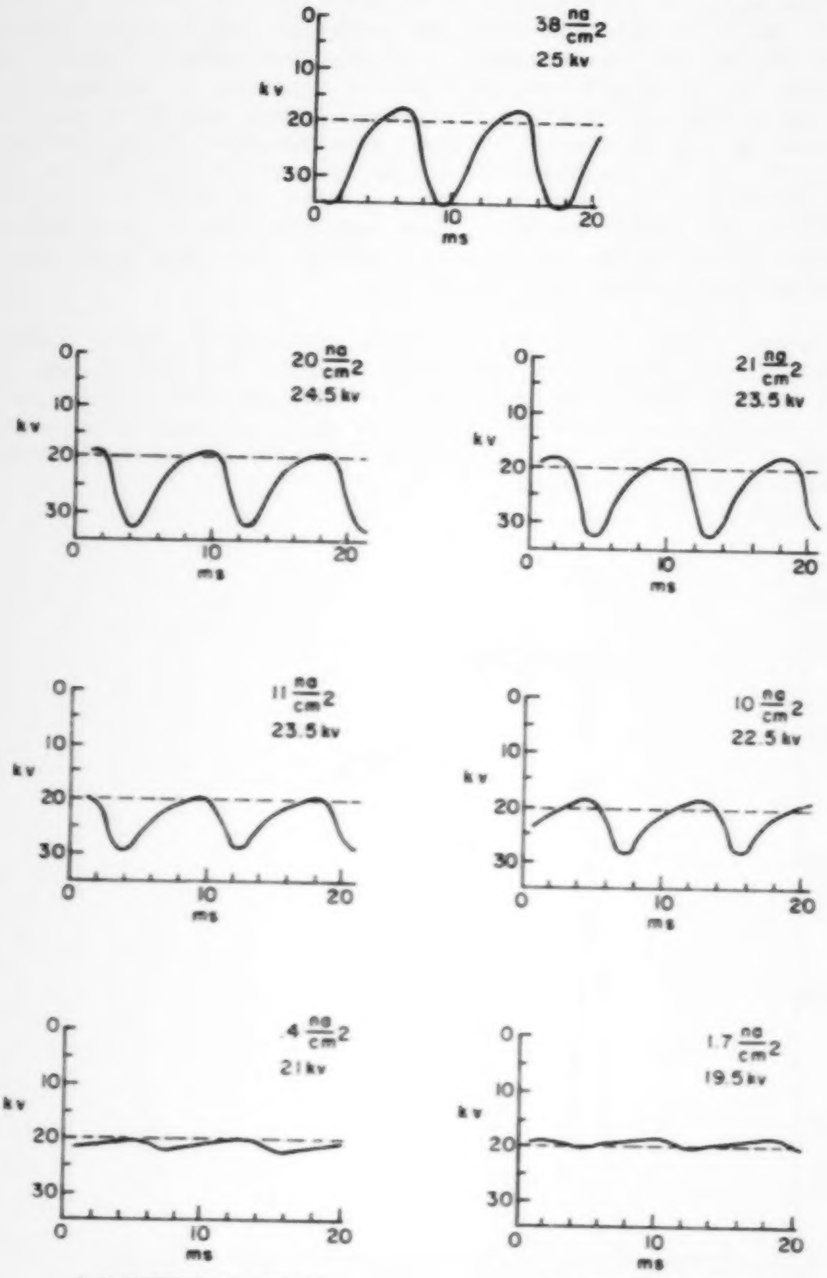

(a) INCREASING CURRENT

(b) DECREASING CURRENT

FIGURE 7. OUTLET VOLTAGE WAVEFORMS AT NAVAJO UNIT 1 FOR INCREASING AND DECREASING CURRENT DENSITIES.

CONCLUDING REMARKS

The voltage and current relationships that have been presented indicate that back-ionization occurs at Navajo and San Juan but not Allen. The measured ash resistivities at the three plants are in the order of 10^9-10^{10} ohm-cm. Although altitude may be one factor, other possible reasons for the breakdown of the ash layer at average current densities of 5-10 na/cm^2 must be investigated.

Back-ionization appears to be the reason that the performance of some hot side precipitators in the west is lower than similar units in the eastern states. However, there is disagreement as to the extent that back-ionization degrades precipitator efficiency. The reduction in efficiency as a result of the lower voltages is not questioned. The extent that the negatively charged particles are discharged is questionable. If the positive ions are uniformly dispersed in the gas and the positive ion current is only 10 percent of the total current, then the particle charge would be reduced by 50 percent [5]. If the positive ions flow in discrete narrow channels instead of being dispersed, then the discharging of the particles would not be significant [6]. In any case, excessive back-ionization is detrimental. Practical means of detecting and controlling the level of back-ionization without reducing the voltage have not been developed.

ACKNOWLEDGMENTS

We wish to thank Dr. Leslie E. Sparks for his suggestions, support and encouragement and for providing data concerning the units which were discussed.

REFERENCES

[1] Peek, F., Dielectric Phenomena in High-Voltage Engineering, McGraw-Hill Book Co., N.Y., 1929.

[2] Thomson, J., and G. Thomson, Conduction of Electricity through Gasses, Cambridge Press, London, 1928.

[3] White, H., Industrial Electrostatic Precipitation, Addison-Wesley Pub. Co., Reading, Mass., 1963.

[4] Gooding, C. H., J. D. McCain and D. K. Sommers, Comparative US/USSR Tests of a Hot-Side Electrostatic Precipitator, EPA-600/2-77-002, January 1977.

[5] Robinson, M., Electrostatic Precipitation, In: Air Pollution Control, Part 1, Strauss, W. (ed.), Wiley-Interscience, N.Y., 1971.

[6] Lowe, H. J., J. Dalmon and E. T. Hignett, Colloq. Electrostatic Precipitators, I.E.E., London, 1965.

PRECIPITATOR EFFICIENCY FOR LOG-NORMAL DISTRIBUTIONS

Philip Cooperman
Fairleigh Dickinson University, Teaneck, N.J.

Gene D. Cooperman
Brown University, Providence, R.I.
Research-Cottrell, Inc., Bound Brook, N.J.

ABSTRACT

The work of Allander and Matts with its subsequent continuation by Matts and Ohnfeldt, on the efficiency of electrostatic precipitation for polydispersed particles, has attracted a certain amount of interest in recent years because of its actual and potential usefulness. In this paper, we look at the same problem, beginning with a straightforward integration of the Deutsch formula for log-normal distributions and obtain a simple result, the m-factor method, for estimating efficiency in this case. The Allander-Matts results are shown to be equivalent to this work if the geometric standard deviation is replaced by a fractional power of itself. We then go on to show that the Matts-Ohnfeldt formula is an apporximation to a formula which one of us published some years ago. We feel that our own theory has a firmer physical basis, and accounts for many other phenomena. However, the pioneering effort of our Swedish predecessors was the starting point of this paper.

INTRODUCTION

The Deutsch formula for the efficiency of electrostatic precipitators, is the basis for sizing them in the design stage, and for testing them when they have been erected.

Preceding page blank

For both of these purposes, the quantity that takes the center of the stage is the effective migration velocity, w_e. Most physical theories, however, deal with a different quantity, the electrostatic migration velocity, w, which is greater than w_e by a factor usually lying in the range 2-10. Accounting for this difference has been one of the major goals of workers in the field of precipitation, and many reasons have been given for it, for example, re-entrainment. About twenty years ago, a further step in this direction was taken by the Swedish workers, Allander and Matts (A-M), who considered the apparent loss of efficiency due to the fact that practically every dust treated by precipitators is not monodisperse as the Deutsch formula assumes.[1] By the words "apparent loss", we mean that the collection efficiency for a distribution of particle sizes is less than for a distribution in which all particles are of a single size equal to the mean of the original distribution. Starting from the results of A-M, Matts and Ohnfeldt (M-O), subsequently obtained via plausibility considerations, a formula in which the exponent appearing in the Deutsch formula is replaced by a fractional power of the exponent[2].

In this paper, we accept the insight of A-M and M-O that the efficiency of a precipitator for a polydisperse distribution is less than that for a monodisperse distribution with the same mean particle size, but go on to new results with a firmer physical foundation.

THE LOG-NORMAL DISTRIBUTION

The log-normal distribution differs from the ordinary normal distribution in that it is the logarithms of the particle sizes which are normally distributed, rather than the sizes themselves. The arithmetic mean of the logarithms is a number , $\ln x_g$, where x_g is called the geometric mean particle size. The arithmetric standard deviation of the logarithms is a number, $\ln \sigma_g$, where σ_g is called the geometric standard deviation. If the values of these two parameters are given, the distribution is completely specified.

If x stands for particle diameter in general, it is convenient to refer the distribution back to the standard normal distribution, about which a great deal is known, by the introduction of a variable, t, defined by

$$t = \frac{\ln(x/x_g)}{\ln \sigma_g} \qquad (1)$$

Multiplying this equation by ln σ_g and taking advantage of the properties of the logarithm function gives the equation below.

(2) $$x = x_g \sigma_g^{\,t}$$

These equations are relations between the particle size variable, x and the standard normal variable, t. We see from them that when $x = x_g$, $t = 0$; when $x > x_g$, t is positive; when $x < x_g$, t is negative.

In terms of the standard variable, the probability density, f(t), is given by

(3) $$f(t) = \frac{1}{(2\pi)^{\frac{1}{2}}} \exp(-\frac{t^2}{2})$$

where exp stands for the exponential function based on the number e. To find the fraction by weight of the distribution lying below a particle size, x_o, one uses Eq. (1) to find the corresponding valus of t, designated here by t_o, and evaluates the integral $\int_{-\infty}^{t_o} f(t)dt$. Some typical values of the integral are: 0.8413 for $t_o = 1$, 0.9773 for $t_o = 2$, and 0.9987 for $t_o = 3$. 99.99993% of the wieght of the distribution lies in the range $t = \pm 5$, a fact which we shall utilize in the numerical integrations to come later.

THE DEUTSCH FORMULA

If F is the fraction of entering particles which escape capture in a precipitator, and if the distribution is monodisperse, the Deutsch formula may be written

(4) $$F = \exp(-wA/Q).$$

Here A is the area of the collecting electrodes, and Q, the actual volume flow rate of the gas in the precipitator. The w which appears in this equation is the electrostatic migration velocity although, in practice, the effective migration velocity is used. However, we shall be assuming for the moment, that w is proportional to particle size, and this assumption is not true for w_e. Under this assumption, we may write the Deutsch formula in the form

(5) $$F = \exp(-Kx),$$

where K contains everything in the exponent of Eq. (4) except particle size.

In order to simplify the treatment of the polydisperse distribution, we need to introduce the variable t. This is easily accomplished with the help of Eq. (2) and we get

(6) $$F = \exp\left(-Kx_g\sigma_g{}^t\right).$$

Let F_g represent the fractional loss for a monodisperse distribution of particle size x_g. By the Deutsch formula,

(7) $$F_g = \exp\left(-Kx_g\right).$$

Hence, F(t) for any particle size can be written

(8) $$F(t) = F_g{}^{(\sigma_g{}^t)} .$$

The fractional loss for a polydisperse distribution can be obtained by integration over the range of particle sizes with a weight factor given by the probability density function, f(t). Thus, if F_p represents the fractional loss in this case, the formula for F_p is

(9) $$\begin{aligned} F_p &= \int_{-\infty}^{\infty} f(t)F(t)dt \\ &= \frac{1}{(2\pi)^{\frac{1}{2}}}\int_{-\infty}^{\infty} \exp\left(-t^2/2\right)F_g{}^{(\sigma_g{}^t)}dt. \end{aligned}$$

The mean value theorem of the integral calculus asserts that there is a value of t, say T, such that $F_p = F_g(T)$. Let

(10) $$m = \sigma_g{}^T$$

Then Eq. (9) can be written

(11) $$F_p = F_g{}^m.$$

This equation does not allow the calculation of F_p. F_p must be calculated by carrying out the integration in Eq. (9). Then m can be found by the use of Eq. (11) in the form

(12) $$m = \frac{\ln F_p}{\ln F_g} .$$

In a similar fashion, the value of T can be computed from Eq. (10) giving

(13) $$T = \frac{\ln m}{\ln \sigma_g} .$$

We shall offer an easy and direct method for computing m later on. Nevertheless, we can make some general remarks about the values of m and T from the physics of the situation. The Deutsch formula predicts that precipitators collect small particles less efficiently than large. Hence, small particles make a larger contribution in the integral for F_p than do the large. It follows that the value of T must be biased toward the small particle sizes, and by our earlier remarks, must be negative. Since the geometric standard deviation is never less than unity, and T is negative, Eq. (10) shows that m is a number lying between 0 and 1.

The last statement has interesting physical meaning. By combining Eqs. (7) and (11), we can get

$$F_p = \exp\ (-Km\ x_g) = \exp\ (-K\ x_p) \tag{14}$$

where $x_p = mx_g$. It is clear that x_p is the particle size such that the precipitation of a monodisperse distribution of that size would be equal in efficiency to the collection of the original polydisperse particles. The fact that m is a proper fraction means that x_p is smaller than x_g and that therefore, the collection of a log-normal distribution of particles is less efficient than one would expect from consideration of x_g. While m has this interesting meaning, its use in practice depends on how easy it is to evaluate it. If T were to depend only on F_g which in turn depends only on x_g, it would be possible to evaluate m from a knowledge of the geometric mean size and the geometric standard deviation of the distribution. We shall see that while these conjectures do not hold exactly, they are approximately true.

NUMERICAL RESULTS

We were able to evaluate the integral appearing in Eq. (9) rapidly and accurately on a programmable pocket calculator, the Texas Instrument SR 52. The accuracy is shown by the fact that for the case of a monodisperse distribution for which $F_p = F_g$, our program agreed with the values of the exponential function for the same exponents to about a unit in the eighth decimal place. The program itself consisted of a twenty interval Simpson's Rule intergration carried out over the range $t = \pm 5$. As was mentioned previously, this range contains $99.9999\bar{3}\%$ by weight of the particles of the distribution.

In Fig. 1, we have poltted F_p against F_g for various values of σ_g. Since the curves are drawn on log-log paper, their physical slope is m. By physical slope, we mean that if the vertical and horizontal distances between two points on the same curve are measured with an ordinary ruler, the ratio of the measurements will be the average value of m for that stretch of the curve. Along each curve σ_g is constant; hence, the variation of m is due entirely to the variation of T with F_g. Actually, T is a function of both F_g and σ_g. but we might hope that it does not vary rapidly with σ_g since m already containes σ_g explicitly. To test this conjecture, the curves in Fig 2 showing T as a function of F_g for various values of σ_g were drawn. It can be seen that the spread between the curves is not great, and that the curvatures are quite small. This led us to hope that a straight line approximation to the entire set of curves would be accurate enough to be useful. We therefore averaged the four curves and fitted a straight line by the method of least squares. The result is shown as the dashed line in Fig. 2. The corresponding equation is:

$$T = 0.0822 \ln F_g - 0.159 \tag{15}$$

This, in turn, provides the following expression for m by use of Eq. (10).

$$m = \exp\left[(0.0822 \ln F_g - 0.159) \ln \sigma_g\right] \tag{16}$$

We have tested this equation against the values obtained by use of Eq. (12), which if the Deutsch formula were valid, would be exact. In the nine cases we tried, the worst error was 4.5% and the average, 2.7%. This accuracy is quite satisfactory for practical use. Further calculations for values of σ_g up to 5.0, indicated that this method would give equally good accuracy for these values. However, as with any approximation, one should be cautious about extrapolation to values of the parameters outside the original range.

We can summarize the m factor method as follows. Suppose we are given a log-normal distribution specified by certain values of x_g and σ_g. Suppose, also, we can estimate the fractional loss, F_g, for monodisperse particles of size x_g. Then, a value of T can be calculated by means of Eq. (15), and when this is substituted in Eq. (10), the corresponding value of m is found. Alternately, m can be obtained from Eq. (16). The loss, F_p, for the log-normal distribution is then estimated by Eq. (11).

It has been frequently noted that, in designing precipitators for a given application, a lower value of migration velocity must be used for the more efficient precipitators. The m factor method clearly shows this effect. Higher efficiencies are equivalent to lower values of F_g and the ln F_g term in Eq. (16) therefore becomes more negative. Hence the m factor itself becomes smaller. Thus, the equivalent particle size, x_p, given by mx_g, is also smaller, a fact which reduces the corresponding migration velocity. This is what would be expected to happen from intuitive considerations, but the fact that the m factor method makes the correct prediction automatically is a useful feature of the method.

THE ALLANDER-MATTS RESULTS

Up to the point reached at Eq. (9), our work and the work of A-M have run parallel courses, with the major difference consisting of the assumption by A-M, that the migration velocity in the Deutsch formula is proportional to a fractional power, n, of the particle size. In our notation, this assumption may be written

$$w/w_g = (x/x_g)^n \tag{17}$$

where w_g is the value of the migration velocity for particles of size x_g. The reason given for the use of this equation is that the charge on submicron particles does not vary with particle size as rapidly as it does for larger particles, and that one may try to take this fact into account by means of the assumption embodied in Eq. (17). We shall show later that for n = 0.5, the assumption is valid even for particles above one micron in size, provided, however, that effective migration velocity is used, not electrostatic.

Since F_g is given by

$$F_g = \exp\ (-w_g A/Q) \tag{18}$$

and

$$(x/x_g)^n = \sigma_g^{nt} = (\sigma_g^n)^t \tag{19}$$

every previously developed formula and every curve in Figs. 1 and 2, retain their validlty if σ_g is replaced by σ_g^n. Thus, our curves, previously computed for the range 1-3 in σ_g, can, if n = 0.5, now cover the range 2.25 - 9 instead. This result was also found by A-M in terms of the arithmetic standard deviation, a.

If the standard deviation, σ_g, is replaced in Eq. (16) by $\sigma_g{}^n$, the equation turns into

$$m = \exp\left[n(0.0822 \ln F_g - 0.159) \ln\sigma_g\right] \tag{20}$$

Suppose m_1 denotes the value of m when n = 1 and $m_{\frac{1}{2}}$, the value for the same case when n = 0.5. Note that m_1 is the m we have been using preciously. Then,

$$m_{\frac{1}{2}} = (m_1)^{\frac{1}{2}} \tag{21}$$

Since m is always a proper fraction, $m_{\frac{1}{2}}$ is always greater than m_1. As an example, let us take $m_1 = 0.64$. Then, $m_{\frac{1}{2}} = 0.8$. Thus we have the odd situation that a basic A-M assumption leads to a value of x_p which is larger than the value that would be produced without it. Because of this fact, the value of w that the A-M formula predicts for a polydisperse distribution is larger than one would obtain from the Deutsch formula handled straightforwardly as in the first page of this paper.

We shall show later that the effective migration velocity is approximately proportional to the square root pf particle size. This will be true, however, even in the case of a monodisperse distribution and, furthermore, this fact will itself arise from the assumption that the electrostatic migration velocity is proportional to the first power of particle size. Nevertheless, whether by the A-M approach or by our, we find that while the increase in the loss from a precipitator over what one would expect from the mean size is real and significant, it is not as great as the simple application of the Deutsch formula predicts.

In 1963, a paper by Matts and Ohnfeldt continued the earlier work, and proposed in place of the integral appearing there, a new and simpler expression. The M-O formula is given below, in our notation.

$$F_p = \exp\left[-(w_k A/Q)^{\frac{1}{2}}\right] \tag{22}$$

To obtain this result, M-O argued that there are many factors in precipitation which involve statistics in addition to particle size. These could be taken into account by generalizing the standard deviation of all the factors. In addition, there were certain phenomena of a non-statistical character that the Deutsch formula neglected. These were that the value of the migration velocity decreased when the gas flow rate decreased, and that the migration velocity decreased also when the precipitation efficiency increased. In order to include these phenomena in precipitator sizing, M-O proposed that the exponent in the Deutsch formula be raised to a power k. The best fit to the results of the A-M work was obtained for k = 0.5. The number w_k seems to be an empirical migration velocity. Because of its simplicity and because it makes an adjustment in sizing precipitators to take account of the non-statistical factors mentioned above, the M-O formula is undoubtedly useful. Nevertheless, it is basically empirical in character, and seems to lack contact with the physical processes taking place in a precipitator.

THE COOPERMAN FORMULA FOR LOG-NORMAL DISTRIBUTIONS

About ten years ago, one of us (P.C.) incorporated the idea into efficiency theory, that the electric wind and gas flow turbulence give rise to a mixing action which by smoothing the differences in particle concentrations, opposes the collecting force. The details are given in several publications[3,4]. We mention only that it has given explanations, without the use of ad-hoc assumptions, of such non-deutschian phenomena as the variation of effective migration velocity with gas velocity, the high migration velocity of wide precipitators, the unexpectedly slow variation of efficiency with particle size, and other matters.

The theory employs two new parameters, D and f, but in return, uses the electrostatic migration velocity which can be calculated by well-known methods, in contrast to the empirical migration velocities used in other formulas. The parameter D is a measure of the strength of mixing and has the dimensions of a diffusion coefficient. The dimensionless parameter, f, is the ratio of the backflow of particles to the flow of particles towards the collecting surface. This is not necessarily due to re-entrainment or rapping losses; we feel that even without these factors, there are forces, possibly electrostatic in nature, which oppose contact between the incoming particles and the collecting surface.

Before giving the formula itself, we must construct two dimensionless quantities which will appear in it. Let

$$(23) \qquad \alpha = \frac{b\,v}{2D}, \qquad \beta = \frac{(1-f)\,bw}{2D}$$

where b is the half-width of a precipitator duct, v is the gas velocity through the precipitator , and w is the electrostatic migration velocity. The best way to write the formula for the present purpose is to use it to determine the effective migration velocity. Thus,

$$w_e = v\left[(\alpha^2 + 2\beta)^{\frac{1}{2}} - \alpha\right] \quad (24)$$

Notice that while the electrostatic migration velocity, w appears in the equation above, the effective migration velocity is influenced by other factors, such as the duct width, the gas velocity, the losses of particles at the electrodes, and the mixing coefficient, D. Fig. 3 shows a typical relation between the effective and electrostatic migration velocities. It is valid for the data listed in Fig. 4, but should not be taken as a universal curve. Eq. (24) can be used for numerical calculations with the help of a simple, nonprogrammable calculator, but its meaning becomes easier to comprehend by consideration of two limiting cases. The first case occurs when $\alpha^2 > 2\beta$. Then, using the first two terms in the power series for the square root functions, Eq. (24) gives approximation

$$w_e = (1-f)\ w. \quad (25)$$

When this result is substituted in Eq. (1), we get a formula almost the same as the original Deutsch formula, the difference being that because of the factor (1-f), particle losses at or near the collecting surfaces are taken into account.

Although little data is available, what there is suggests that representative values of D are 1, 10, and 30 sq. ft./sec., for bench, pilot plant, and full scale precipitators respectively. The reasons for this are not clearly understood, but the work of Robinson suggests that the vertical scale of eddies under precipitator conditions may be responsible[5]. The values of f are a little more uncertain, but we have used f = 0.5 with good success. Our calculations show that the modified Deutsch formula

$$F = \exp\left[\frac{-\ (1-f)\ w\ A}{Q}\right] \quad (26)$$

is valid only for some laboratory scale equipment operated at relatively high gas velocities.

The other limiting case occurs when $2\beta > \alpha^2$. The corresponding approximation is given by Eq. (27) below.

$$F = \exp - \left[(2\beta)^{\frac{1}{2}} L/b\right] \quad (27)$$

This formula applies with fair accuracy to full scale precipitators. Since β contains w, the formula shows that the effective migration velocity is proportional to the square root of the electrostatic migration velocity, and does so without need of questionable assumptions. To see how the approximation applies to the M-O formula, we rewrite Eq. (27) in the following form:

$$(28)\qquad F = \exp\left[-\left(C\frac{w\ L}{v\ b}\right)^{\frac{1}{2}}\right]$$

where

$$(29)\qquad C = \left[\frac{(1-f)\ L\ v}{D}\right]$$

In the style of our treatment of the Deutsch formula, let us write

$$(30)\qquad \left(\frac{w\ L}{v\ b}\right)^{\frac{1}{2}} = (Kx)^{\frac{1}{2}} = (Kx_g\sigma_g{}^t)^{\frac{1}{2}}$$

$$= (Kx_g)^{\frac{1}{2}}\sigma_g{}^{\frac{1}{2}t}$$

$$= \left(\frac{w_gL}{bv}\right)^{\frac{1}{2}}\sigma_g{}^{\frac{1}{2}t} = \left(\frac{w_gL}{bv}\right)^{\frac{1}{2}}(\sigma_g{}^{\frac{1}{2}})t$$

If the last expression is substituted in Eq. (28) and integrated for a log-normal distribution, the end result will be similar to our earlier one. More precisely, we will obtain

$$(31)\qquad F_p = \exp\left[-(mC)^{\frac{1}{2}}\left(\frac{w_gL}{vb}\right)^{\frac{1}{2}}\right]$$

This equation gives an approximation to the fractional loss which our efficiency theory would predict and it also resembles the M-O formula. It would be exactly the M-O formula if the value of $(mC)^{\frac{1}{2}}$ were unity. For the precipitator data given in Fig. 4, and a more or less typical value of 0.64 for m, $(mC)^{\frac{1}{2}}$ turns out to have the value 1.07. We consider the difference of this value from unity to be insignificant.

Although the agreement is excellent and although the M-O formula, undoubtedly works will in many cases, we have certain objections to it. In the first place, it stems from a good, but not excellent, approximation to the exact theory. See, for example, Fig. 1 where the curve for $\sigma_g = 1.5$ represents the predictions of the A-M formula for $\sigma_g^2 = 2.25$. The dashed curve labelled $\sigma_g = 2.25$ in that figure represents the results of the exact theory and is noticeably different. More importantly, since m is a function of F_g and σ_g while C depends on f, L, v, and D, the value of $(mC)^{\frac{1}{2}}$ will be close to unity only if all of these factors combine to give this result. While this seems to happen rather more frequently than one would expect, it requires an element of luck which might not be present under all circumstances

CONCLUSION

With modern electronic calculation generally available, we believe that it is just as easy to use the full expression for w_e given by Eq. (24) as to use either approximation. The calculations for Fig. 4 made for eight points on each curve, took only a few hours on an SR 52, and could be done in a matter of minutes on a computer. At first glance, the curves of Fig. 4 seem quite different from those of Fig. 1, lying lower, and hence predicting lower losses, i.e., higher efficiencies. The curves of Fig. 1, however, were computed by the Deutsch formula. To use them for the A-M formula with n = 0.5, the standard deviations of Fig. 1 correspond to their square in Fig. 4. Thus, the curve for which $\sigma_g = 1.5$ on Fig. 1 should lie between the curves for which the values of this quantity are 2.0 and 2.5 on Fig. 4. We have chosen to show the same fact in another way by plotting the curve for $\sigma_g = 2.25$ by our theory, on Fig. 1, where it lies between the Deutsch curves for $\sigma_g = 1.5$ and $\sigma_g = 2.0$.

An additional and even more important reason for the curves of Fig. 4 to lie below those of Fig. 1, is that these curves reflect only the effect on efficiency of having to deal with a log-normal distribution (F_p) instead of a monodisperse distribution (F_g). Thus, all our theory is doing is to compare the effective migration velocities for log-normal and monodisperse distributions, and to say that the loss of efficiency for the log-normal case is not as great as would be predicted by the Deutsch formula. This is also the significance of fractional powers in both the A-M and M-O formulas. In contrast, the curves of Fig. 1 give the effect of particle size distribution on the electrostatic migration velocity and show that this effect is large. Our theory agrees with both statements.

The A-M formula, and its simpler version, the M-O formula, differ mathematically from the Deutsch formula for log-normal distributions mainly in that a fractional power of the geometric standard deviation takes the place of the deviation itself. The M-O formula turns out to be an approximate version of an efficiency formula proposed by one of us.

The Deutsch formula, at least in modified form, is another approximation to our theory. We have shown that the A-M formula is the Deutsch formula for log-normal distributions with the difference for the value of the standard deviation noted previously. Thus, all four efficiency formulas are interrelated.

ACKNOWLEDGMENTS

We should like to thank Dr. Paul Feldman whose interest in these matters stirred our own.

REFERENCES

1. Allander, C. and S. Matts, Staub, 303, (1957).
2. Matts, S. and P. O. Ohnfeldt, Flakten, 93, (1963-4).
3. Cooperman, P., Atmosph. Environ., (1971).
4. Cooperman, P., Proc. Int. Clean Air Congress, Tokyo, (1977).
5. Robinson, Myron, Ph. D. thesis, Cooper Union, 1976.

LIST OF SYMBOLS

Symbol	Meaning	Units
a	arithmetic standard deviation	μm
A	surface area of precipitator electrodes	sq. ft.
b	half-width of precipitator duct	ft.
C	parameter defined by Eq. (30)	none
D	coefficient measuring intensity of mixing due to turbulence and electric wind	sq.ft./sec.
e	the number 2.71......	none
exp	the exponential function based on e. Thus, exp Z = e^Z.	none
f(t)	the normal probability density function exp $(-t^2/2)$	none
f	the ratio of particle flow due to mixing action to the flow of particles toward the electrode	none
F	the fractional loss of particles from a precipitator. F is the ratio of the outlet particle flux to the inlet flux.	none
F_g	the value of F for monodisperse particles	none
F_p	the value of F for log-normal distributions	none
k	the power appearing in the M-O formula, usually 0.5	none
K	the value of all factors except particle size appearing in the Deutsch exponent, including a conversion factor to allow compatibility with units	$(\mu m)^{-1}$
ln	natural logarithm	none
L	precipitator length in direction of gas flow	ft.
m	ratio of particle size to geometric mean size, for monodisperse distribution having efficiency equal to that of a log-normal distribution with the given geometric mean size	none
m_1	same as m. Subscript distinguishes it from $m_{\frac{1}{2}}$	none
$m_{\frac{1}{2}}$	value of m for $\sigma_g^{0.5}$. $m_{\frac{1}{2}} = (m)^{\frac{1}{2}}$	none
n	fractional power in A-M formula	none
Q	actual rate of gas flow through a precipitator	cu.ft./sec.
t	standardized variable for normal distributions	none
t_o	value of t corresponding to x_o. See below.	none

Symbol	Meaning	Units
T	average value of t in computation of F_p	none
v	mean velocity of gas flow	ft./sec.
w	electrostatic migration velocity	ft./sec.
w_e	effective migration velocity	ft./sec.
w_g	value of either w or w_e for monodisperse distribution. Choice of meaning depends on whether Deutsch or Cooperman theory is used.	ft./sec.
w_k	value of migration velocity appearing in M-O formula	ft./sec.
x	particle size	μm
x_g	geometric mean particle size	μm
x_p	size giving same efficiency as distribution with mean size x_g. Note: $x_p = mx_g$	μm
x_o	a value of x for which the fraction of sizes lying below it, contain a given percentage of the total weight. t_o is the standardized normal variable which corresponds to x_o.	μm
α	quantity appearing in Cooperman theory. $\alpha = bv/2D$	none
β	quantity appearing in Cooperman theory. $\beta = (1-f)\ bw/2D$	none
σ_g	geometric standard deviation	none

Figure I. Deutsch Loss, F_p, for Log-Normal Distributions as a Function of Monodisperse Loss F_g

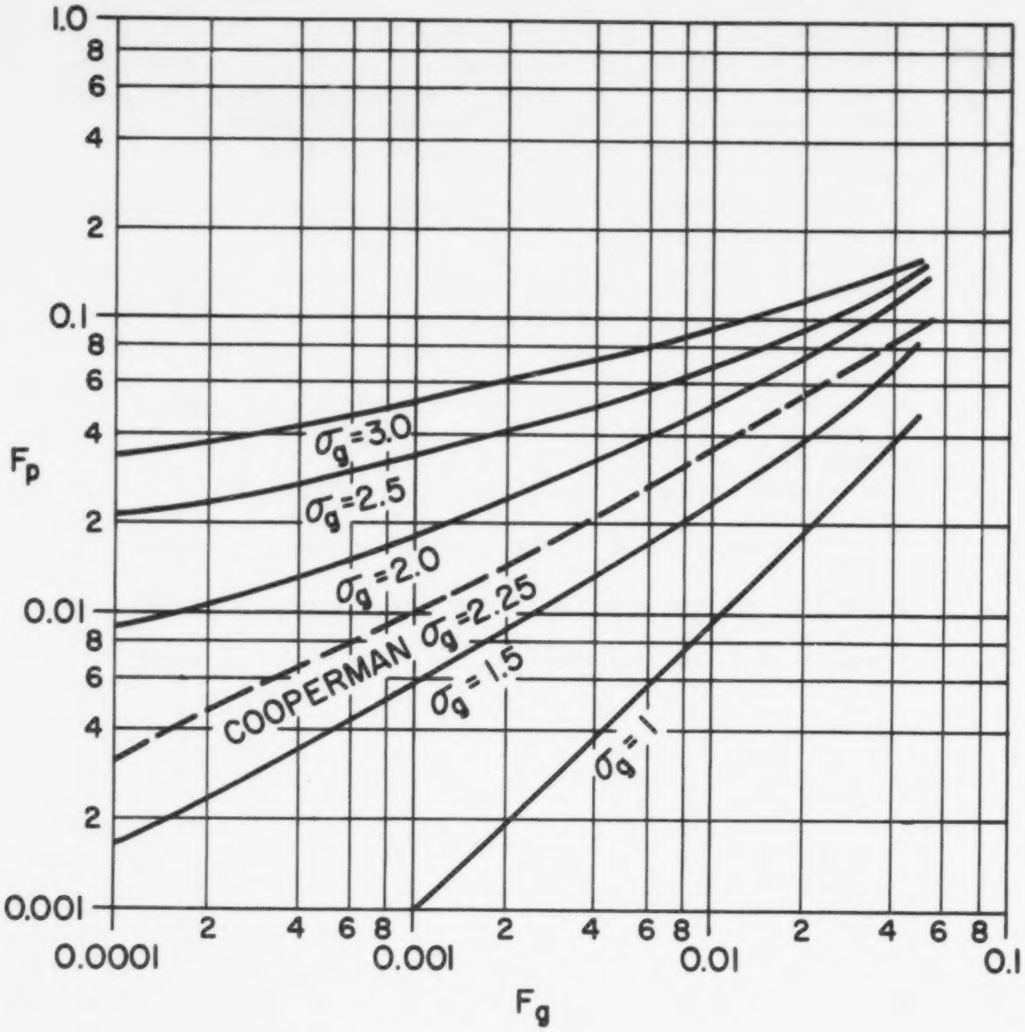

Figure 2. T as a Function of Fractional Loss F_g

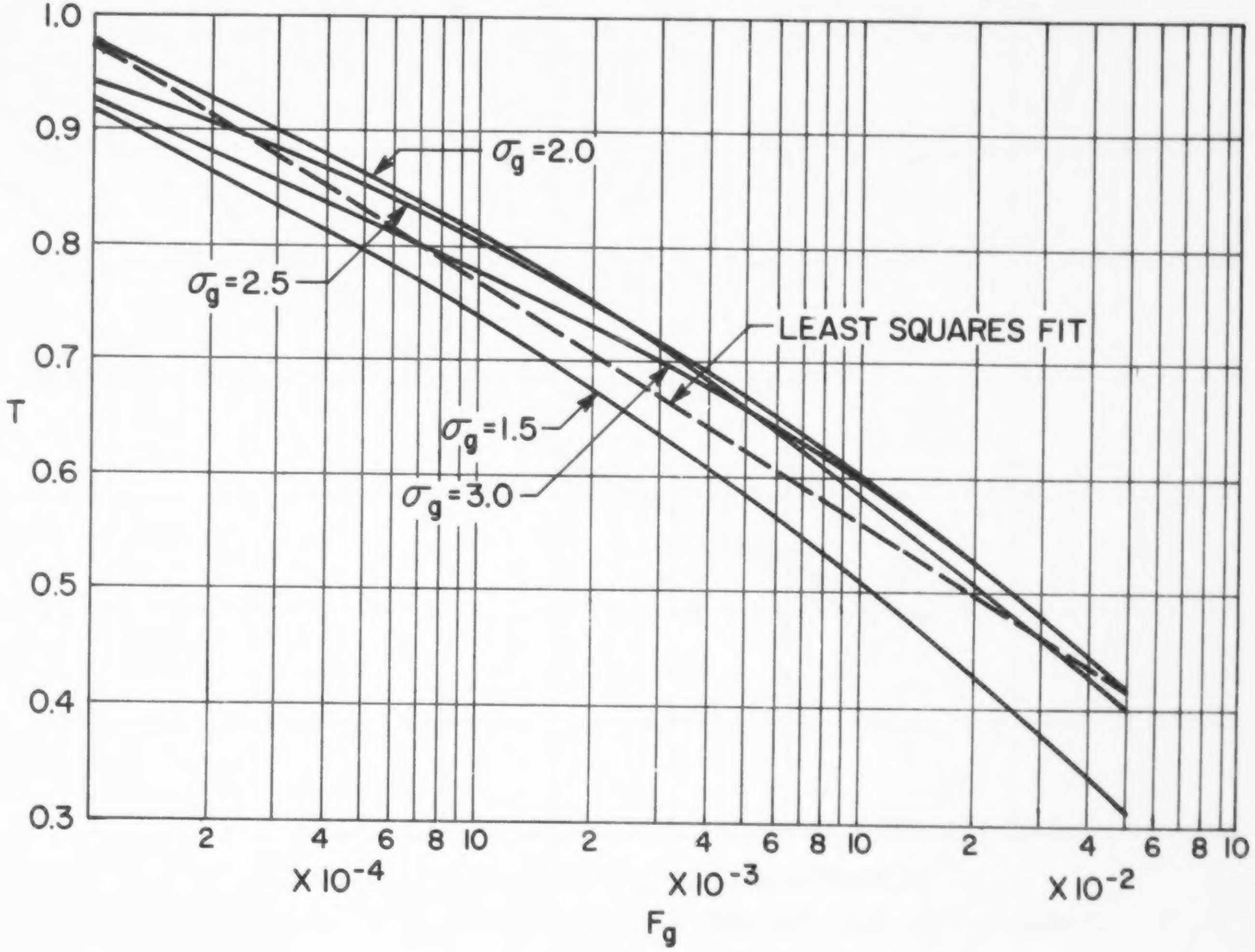

Figure 3. Variation of Effective Migration Velocity with Electrostatic Migration Velocity for a Typical Precipitator

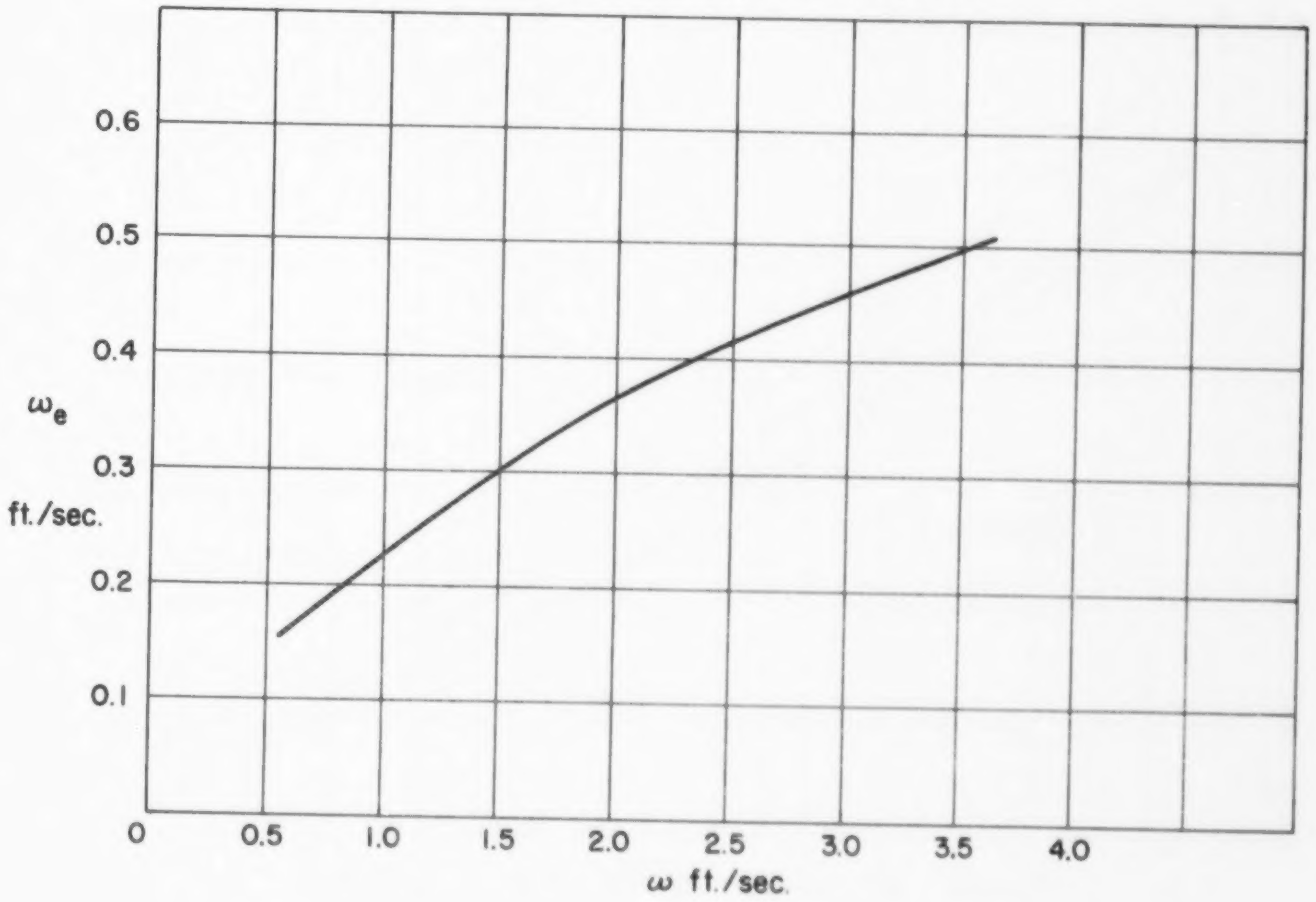

Figure 4. Cooperman Loss, F_p, for Log-Normal Distributions as a Function of the Monodisperse Loss, F_g

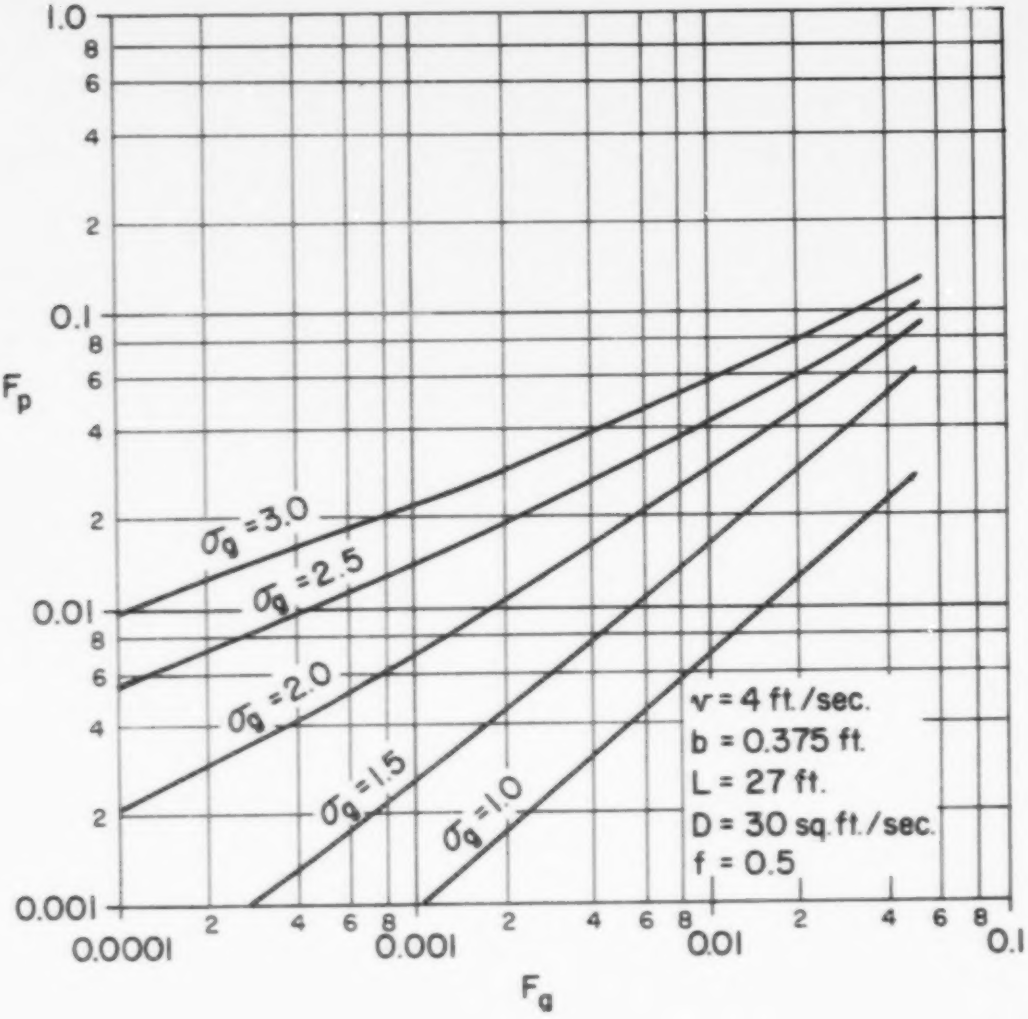

ELECTROSTATIC PRECIPITATOR USING IONIC WIND FOR VERY LOW RESISTIVITY DUSTS FROM HIGH TEMPERATURE FLUE GAS OF PETROLEUM-COKES CALCINING KILN

Fumio Isahaya
Koyo Iron Works & Construction Co., Ltd.
Tokyo, Japan

ABSTRACT

It has been difficult to collect low resistivity dusts such as $10^2 \sim 10^3$ Ω-cm at 270°C by a dry type ESP, because of electrostatic repulsion action. In order to solve such problem, at first, the measurement of relationship between the corona current density distribution and ionic wind velocity for an wire-plate type model electrode, as well as the field test using a pilot-scale ESP having the collecting electrode height of 2m on the calcining kiln for petroleum-cokes production process was carried out. From these experiments, it became clear that the cokes dusts are, under continuous electrostatic repulsion acting motion are blown together by an ionic wind in the stagnant zone which is provided on the collecting electrode and that the scale-up correction formula for migration velocity was given. Finally, depending on these results, the full-scale ESP having the collecting electrode height of 12m and gas flow rate of 167,000 Nm^3/h (270°C) was constructed and the good agreement for the migration velocity between the predicted value from the correction formula and measured one, as well as a satisfactory performance collecting efficiency was obtained.

INTRODUCTION

It is generally difficult to collect low resistivity dusts of approximately 10^4 Ω-cm or less by a dry type ESP due to the generation of electrostatic repulsion phenomenon, therefore, such a system which is composed of a dry type ESP to be utilized as an electrostatic pre-coagulator and an after cyclone unit or fabric filter to be installed after the ESP has been conventionally carried out for collecting such dusts.

Preceding page blank

However, this system causes a sharp drop in pressure and it tends to detract the feature of ESP system which is low in power consumption. As alternate system, there is a method utilizing a wet type ESP which is capable of easily collecting such low resistivity dusts, but this system has such a drawback that its cost of waste-water treatment tends to become expensive and it cannot be economically operated. As a new system which eliminates the necessity for an after mechanical collector and waste-water treatment, we have recently developed a new system for collecting low resistivity dusts with a dry type ESP by the utilization of ionic wind to be induced by corona discharge. Although it has long been known that ionic wind is induced by corona discharge inside an electrostatic precipitator(1), many points have not been made clear yet as to the industrial dimensions of wire-plate type electrodes being widely utilized in industrial fields. Due to this, we, first of all, conducted laboratory tests on wire-plate type electrodes being utilized in industrial scale and measured corona current density distribution. ionic wind velocity and static pressure distribution to find out the relationship between them(2). Further we observed the behavior of low resistivity petroleum-cokes dusts on the collecting plate electrode within corona field being affected by electrostatic repulsion force and ionic wind since such behavior had not been made clear yet. As a result of these tests, the following possibility was successfully made clear: Low resistivity dusts can be captured by the blow-together effect of ionic wind on a collecting electrode where a stagnant zone is caused to form by providing an adequate barrier on the electrode.

Based on such principles, a pilot-scale ESP equipped with a collecting electrode having a height of 2m was then manufactured and it was field tested on a calcining kiln for petroleum cokes-production process.

As a result of these field tests, the collecting performance efficiency of the pilot-scale ESP was proved to be sufficiently satisfactory which would be suitable for practical utilization, and a formula for correcting migration velocity which was required to scale up this ESP for industrial use was also given. At last, based on the result of these tests, a full-scale ESP having a gas flow rate of 167,000 Nm^3/h (270°C) and a collecting electrode of 12m in height were designed. So far they have been continuously operated for about 6 months and they have achieved successful results which are sufficiently lower than the requirement of 0.03 g/Nm^3 of outlet dust concentration. A description about their details is now given below:

IONIC WIND AND MOTION BEHAVIOR OF LOW RESISTIVITY DUST FOR INDUSTRIAL SCALE WIRE-PLATE TYPE MODEL ELECTRODE

As shown in Fig. 1 and Fig. 2, the relationship between corona current density distribution and ionic wind to be induced by corona current and static pressure distribution by using a wire-plate type model electrode was measured. Fig. 3 and Fig. 4 show examples of results of such measurements, and the pattern of ionic wind velocity distribution is similar to that of corona current density distribution. That is, ionic wind velocity becomes a maximum value in the vicinity of the front part of the discharge electrode and becomes a minimum value in the vicinity of the middle between discharge electrodes. Fig. 5 is a plotted diagram showing the relationship between ionic wind velocity v_i and ionic current density i at respective measuring points and they show that v_i is in the approximate proportional relationship against $\sqrt{i}$. Assuming that ionic wind velocity is proportional to the velocity of gas molecule ion v_i, this can also be verified by the followings(2),(3):

$$v_i = EK_i$$

$$= \sqrt{\frac{i}{AK_i}} \cdot K_i \qquad (1)$$

Where E : corona field intensity
K_i: mobility of gas molecule ion
A : constant

Also, in the industrial ESP, its practical corona current density is within the range of the following:

$$i = 0.1 \sim 1.0 \text{ mA/m}^2$$
$$= 0.01 \sim 0.1 \text{ μA/cm}^2$$

The ionic wind velocity corresponding to the above can be assumed from Fig. 5 to be within the range between about 0.1 and 1 m/s. This is equivalent to the same order against migration velocity or a value several times larger than that of migration velocity, and this is considered to be interesting in reviewing the physical meaning of migration velocity. Fig. 6 shows a prediction of flow pattern of ionic wind regarding a wire-plate type electrode which has been obtained from the above experimental results. Next an observation was made on how low resistivity petroleum cokes dust having a resistivity as shown in Fig. 8 mounted on a wire plate type electrode as shown in Fig. 7 behave in response to corona discharge which takes place in an atmosphere of high temperatures between 200 and 300°C. As a result of this observation, it was made clear that such dust particles repeated electrostatic repulsion motion and at the same time dust particles in part were captured by the blow-together effect of ionic wind in the stagnant zone formed inside the barriers provided at the both ends of the plate electrode as shown in Fig. 7.

FIELD TEST USING PILOT-SCALE ESP

Field tests of a pilot-scale ESP equipped with a collecting electrode of 2 m in height as shown in Fig. 9 were carried out on a calcining kiln for petroleum cokes production process for making feasibility study. The temperature of this treating flue gas was 270°C. Fig. 10 shows an example of deposition distribution of cokes dusts accumulated on the dust bunker of this pilot-scale ESP and as clearly seen from this, the amount of dust deposition is considerably large immediately under the barriers provided on the collecting electrode. This is considered to further prove the fact made clear by the aforementioned laboratory tests that low resistivity dusts can be effectively collected by the blow-together effect of ionic wind by this pilot-scale ESP. Fig. 11 shows an example of performance characteristics of this pilot-scale ESP obtained by these field tests and it was confirmed that a high collecting efficiency which would satisfactorily meet the requirement for practical industrial utilization could be obtained.

Based on the above test results, a project for developing a full-scale ESP was carried out and a collecting electrode of 12 m in height was required due to the relationship between the allowable installation space and treating gas flow rate. In the case of low resistivity cokes dusts of which adhesive force to a collecting electrode is weak and which is affected by electrostatic repulsion force, it is necessary to give consideration to the effect of L/H ratio of collecting electrode which affects migration velocity of re-entrainment. Now, a correction formula for migration velocity ω which can be used in such a case has been given as follows:

$$\omega = \omega_o \left(1 - e - \frac{V_G}{V_g}\frac{L}{H}\right) \qquad (2)$$

Where ω_o: Migration velocity at a very low treating gas velocity
V_G: Apparent gravity settling velocity
V_g: Treating gas velocity

In this case, ω_o is used as a function of the size of dust particle and corona current, and V_G as a function of the bulk density of precipitated dusts in coagulation condition and their apparent size and they experimental constants mainly representing such factors. Based on Formula (2), the migration velocity of the full-scale ESP was predicted and further the sizing of its electrode was performed.

PERFORMANCE TEST RESULTS FOR FULL-SCALE ESP

From the aforementioned investigation results, a full-scale ESP with a collecting electrode of 12 m in height of which treating gas flow rate is 167,000 Nm^3/h and gas temperature is 280°C was installed on a calcining kiln for petroleum cokes production process for the purpose of cleaning its flue gas. Fig. 12 shows an example of performance test results of this ESP. That is, the measured value of migration velocity shows approximate proportional relationship against the 1/2 power of corona current, and in this case it is considered that the migration velocity is strongly affected by ionic wind. The calculated value of migration velocity to be obtained from Fig. 11, the experimental results of a pilot-scale ESP and Formula (2) was confirmed to agree with the measured value of the full-scale ESP. The full-scale ESP has so far been continuously operated for about 6 months in stable condition without generating sparking-over and it successfully maintains a high collection efficiency which easily satisfies the requirement of 0.03 g/Nm^3 of outlet dust concentration. Also, fine cokes dusts being collected by this ESP are recovered as finished goods.

CONCLUSION

Although it has been generally considered to be difficult to collect low resistivity dusts of about 10^2 to 10^3 Ω-cm by a dry type electrostatic precipitator alone with a high collection efficiency due to its electrostatic repulsion action, it has been made clear that it is possible to collect such dusts at an adequately high collecting efficiency by the utilization of blow-together effect of ionic wind to be induced by corona discharge if a suitable configuration of electrode and reasonable sizing of electrode [based on Formula (2)] are adopted. The results of our researches are not limited to the utilization for low resistivity dusts alone, but there is a possibility that these results can also be utilized for the clarification of electrostatic precipitation of high resistivity dusts and improvement of their performance.

ACKNOWLEDGMENTS

We express our sincere thanks to those staff members of Petro-cokes Co., Ltd. of Japan and Continental Oil Co., of Far east for their decisive judgement to adopt this dry type ESP in their petroleum cokes production process for the first time.

REFERENCE

(1) W. Deutsh : Ann. d. Physik, 9 (1931) 249
(2) F. Isahaya : Doctor Thesis of Tokyo Univ., [Analysis of Corona Field Intensity Distribution for ESP and its Industrial Applications] (1961), 105 ∿ 127
(3) M. Robinson: AIEE Trans., 80 (1961), 143

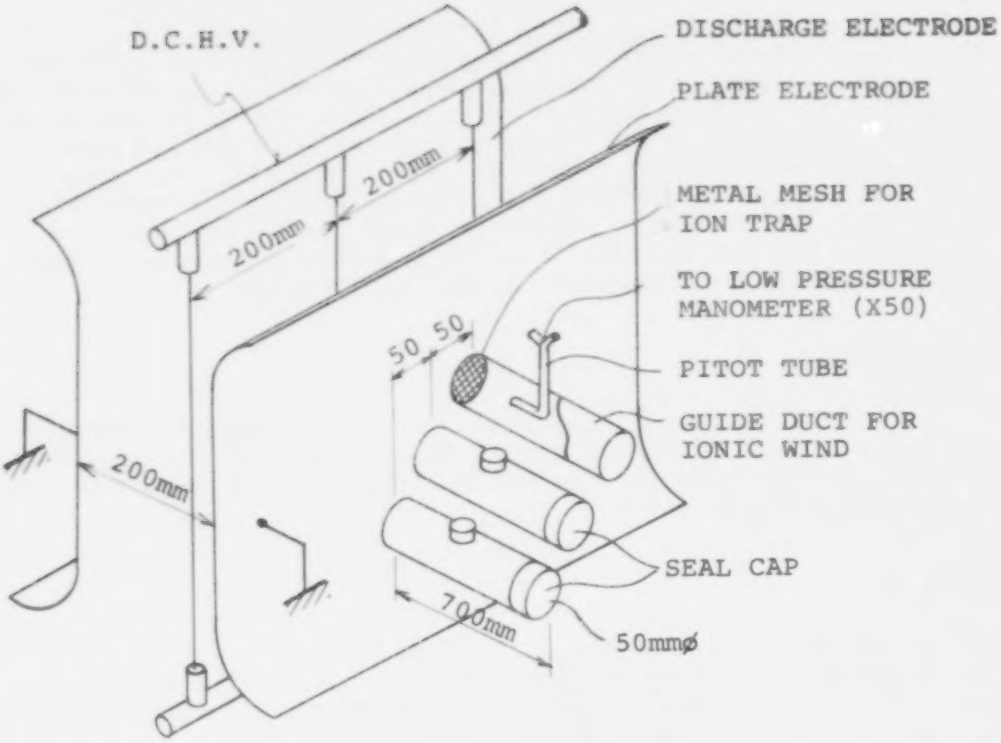
D.C.H.V.
DISCHARGE ELECTRODE
PLATE ELECTRODE
200mm
200mm
METAL MESH FOR ION TRAP
TO LOW PRESSURE MANOMETER (X50)
50
50
PITOT TUBE
GUIDE DUCT FOR IONIC WIND
200mm
SEAL CAP
700mm
50mmø

Fig. 1 Measurement apparatus for ionic wind velocity and static pressure distribution of wire-plate type electrode

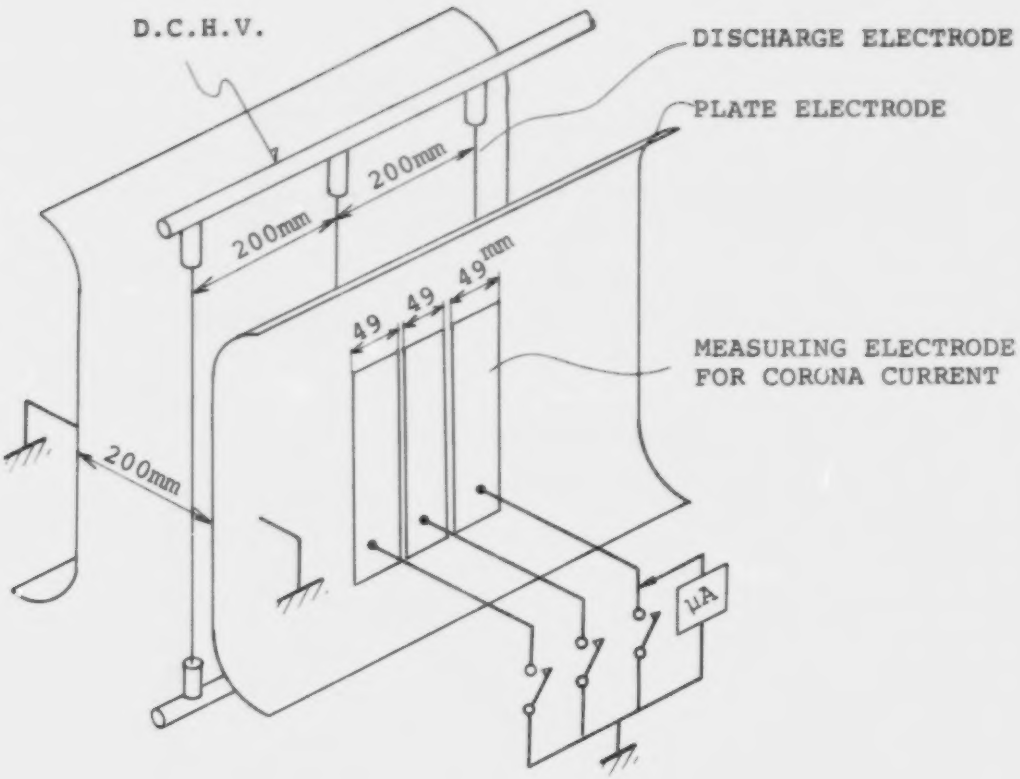
D.C.H.V.
DISCHARGE ELECTRODE
PLATE ELECTRODE
200mm
200mm
49
49
49mm
MEASURING ELECTRODE
FOR CORONA CURRENT
200mm
μA

Fig. 2 Measurement apparatus for corona current distribution of wire-plate type electrode

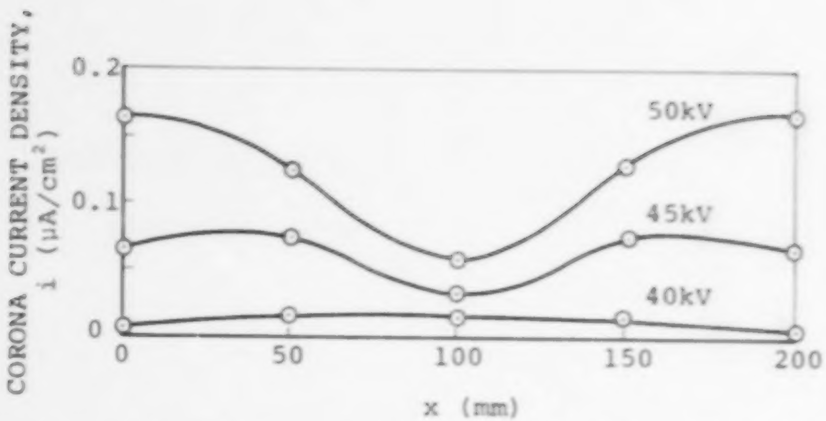

Fig. 3 Corona current distribution for wire-plate type electrode

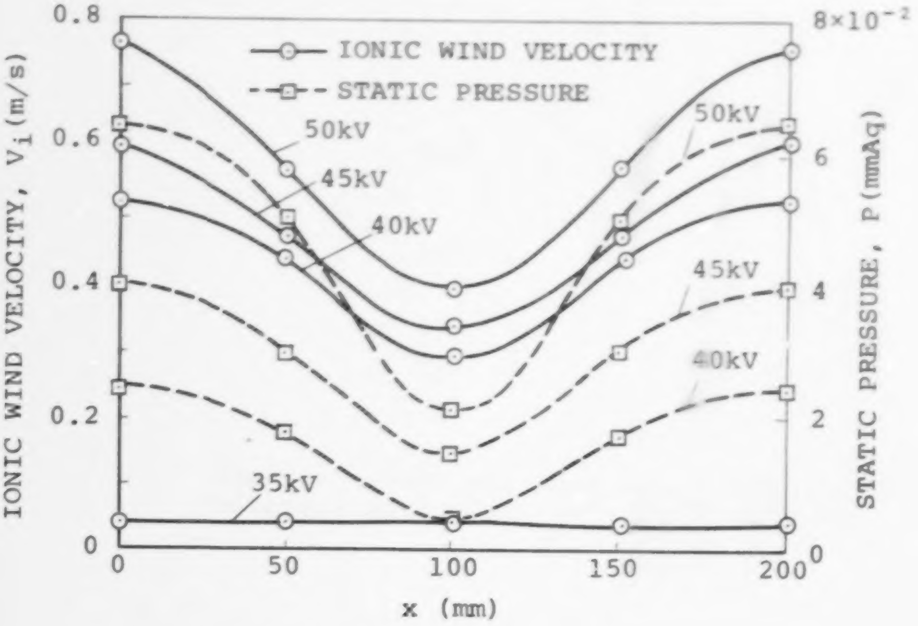

Fig. 4 Ionic wind velocity and static pressure distribution for wire-plate type electrode

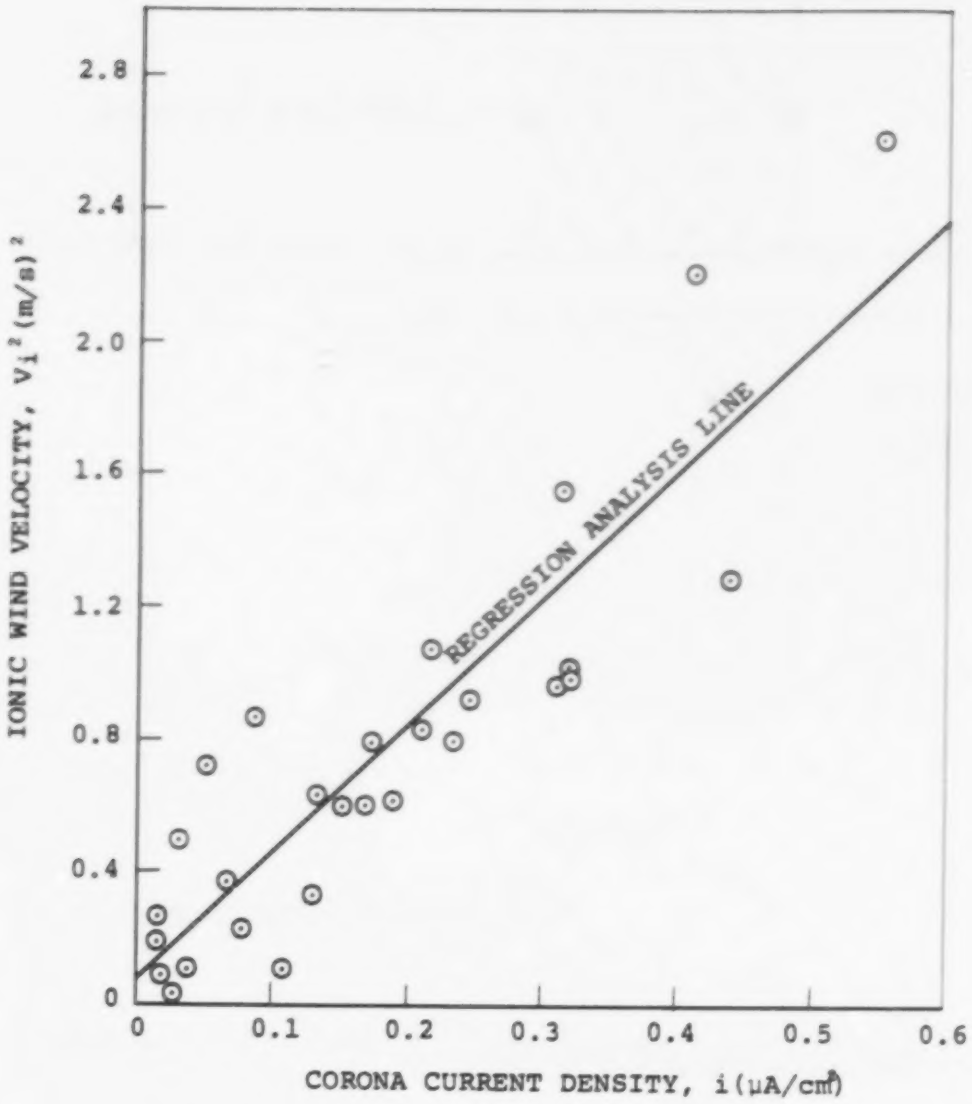

Fig. 5 Relationship between ionic wind velocity and corona current density

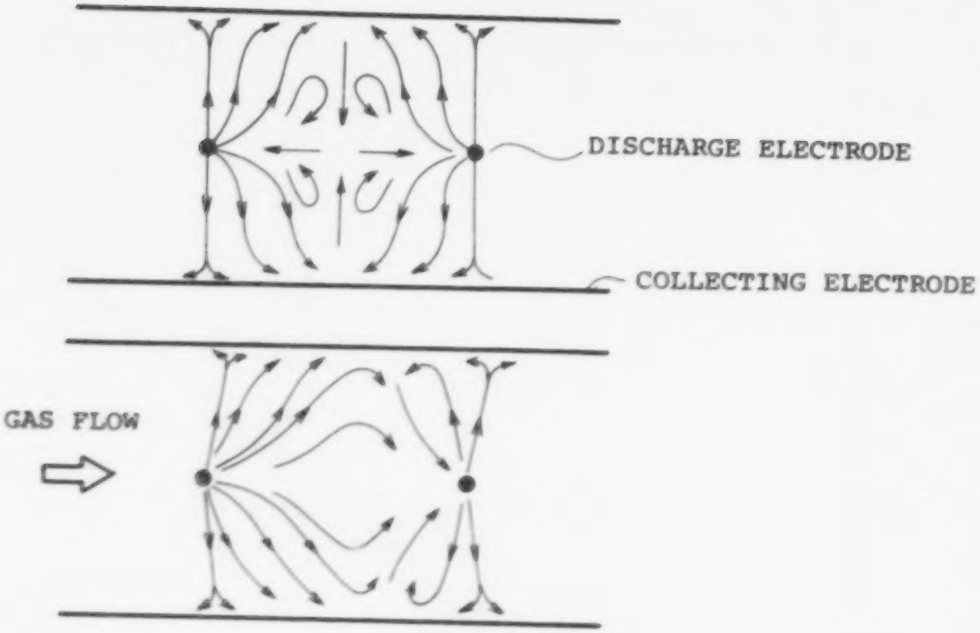
DISCHARGE ELECTRODE
COLLECTING ELECTRODE
GAS FLOW

Fig. 6 Flow pattern of ionic wind for wire-plate type electrode

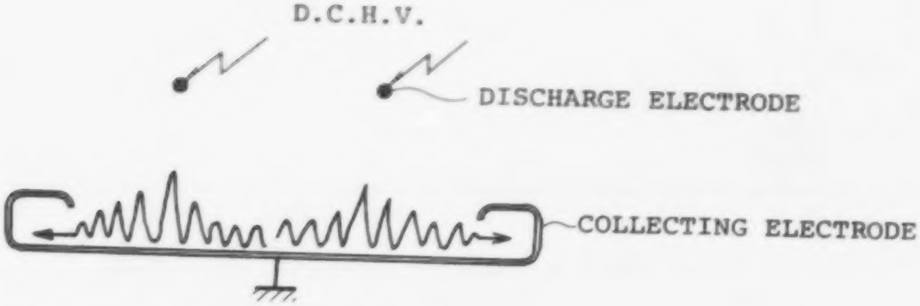
D.C.H.V.
DISCHARGE ELECTRODE
COLLECTING ELECTRODE

Fig. 7 Behavior motion under ionic wind and electrostatic repulsion for low resistivity cokes-dusts

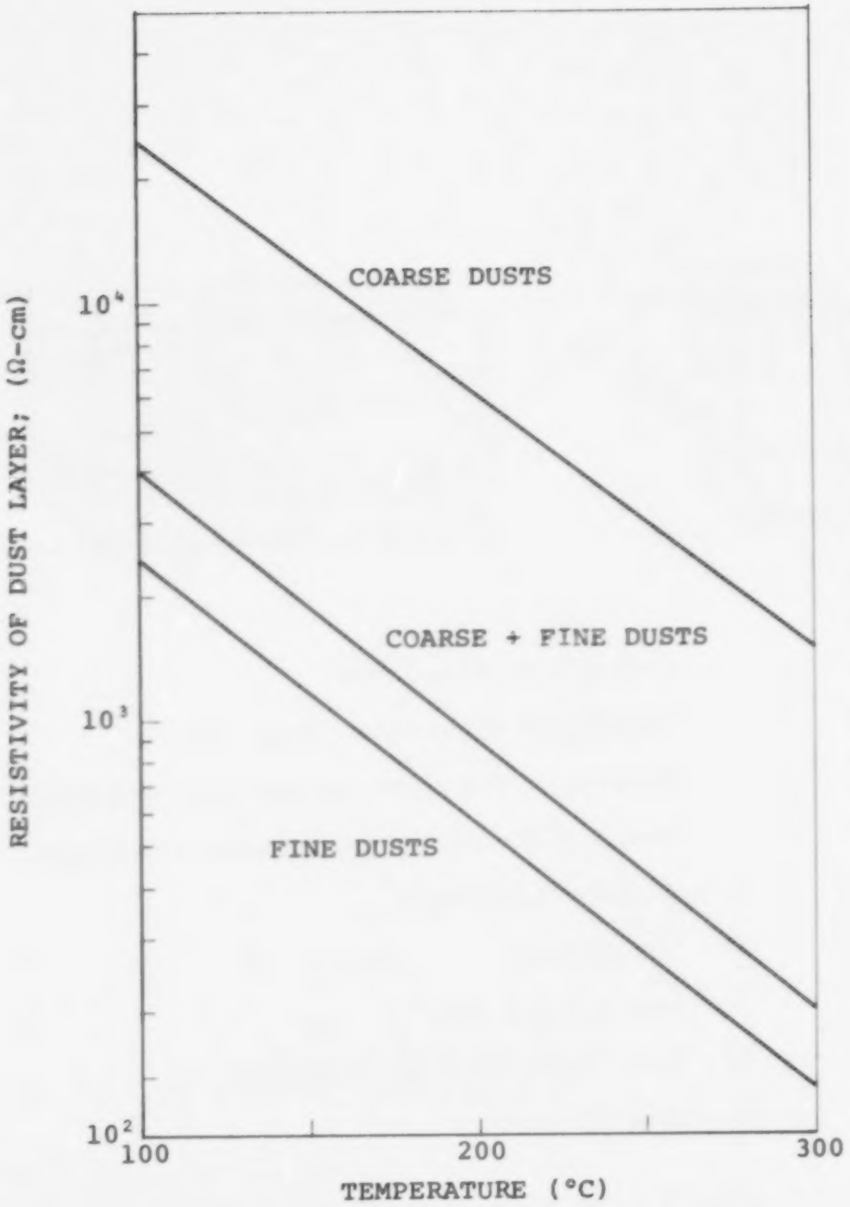

Fig. 8 Resistivity-temperature characteristics for petroleum-cokes dusts

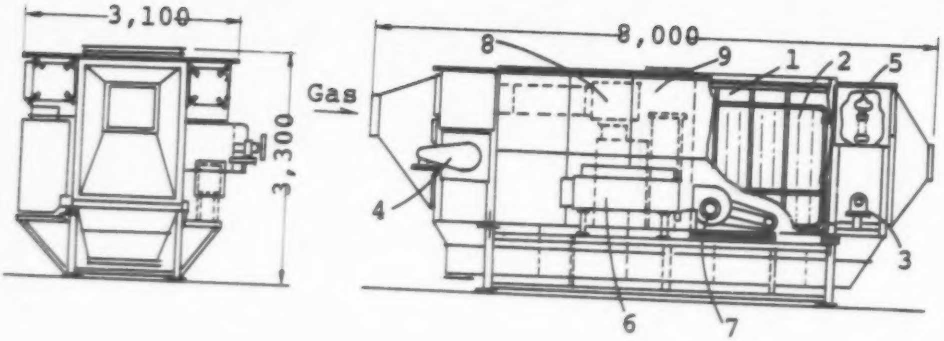

1. Collecting electrode
2. Discharge electrode (frame type)
3. Rapping device for collecting electrode
4. Rapping device for discharge electrode
5. Support insulator
6. Air heater
7. Sealing air fan
8. D.C. high voltage generator
9. Control panel

Fig. 9 Out side view of pilot-scale ESP

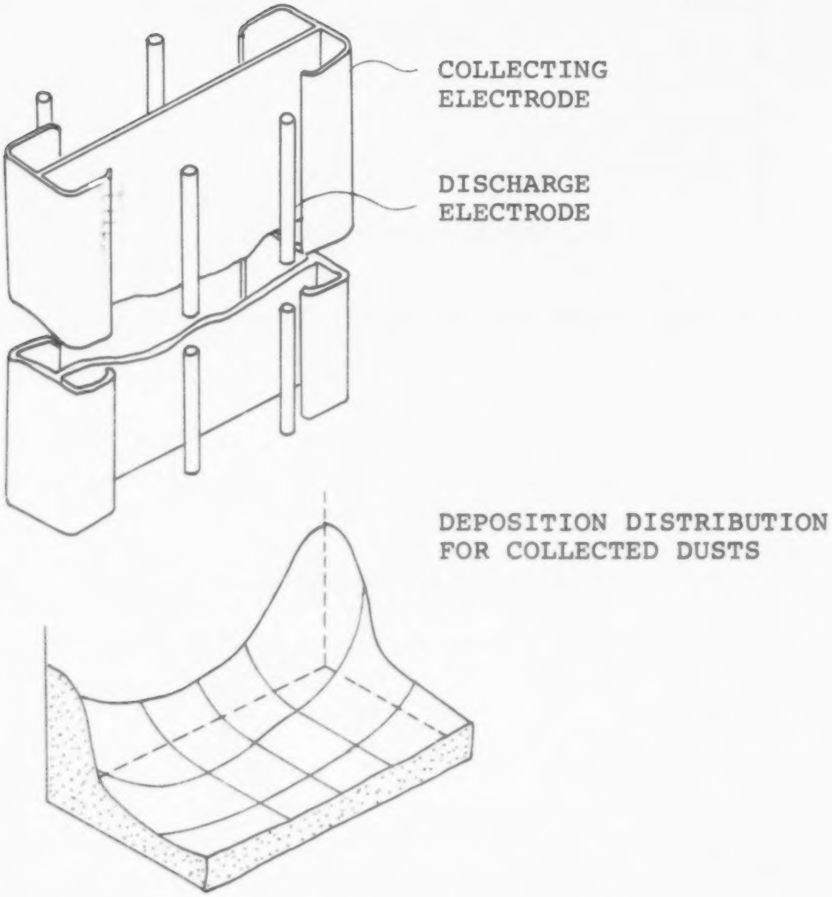
COLLECTING ELECTRODE
DISCHARGE ELECTRODE
DEPOSITION DISTRIBUTION FOR COLLECTED DUSTS

Fig. 10 Collected dusts deposition distribution directly under collecting electrode

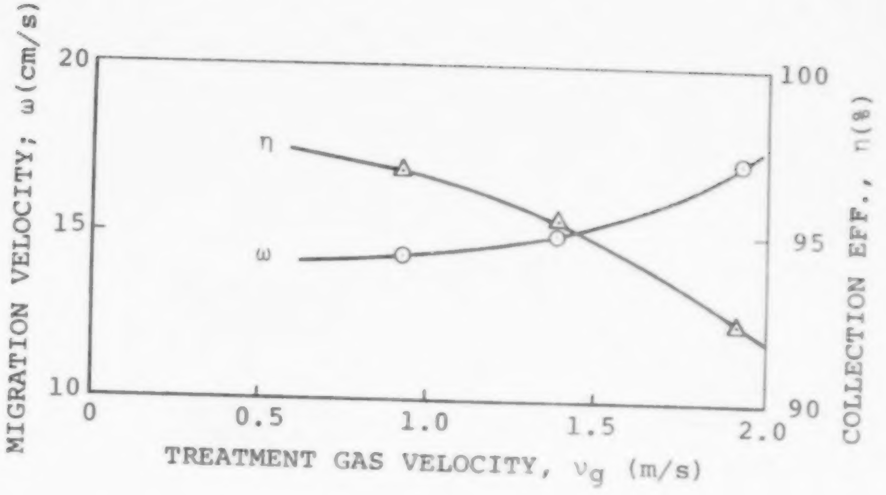

Fig. 11 Performance test results for pilot-scale ESP

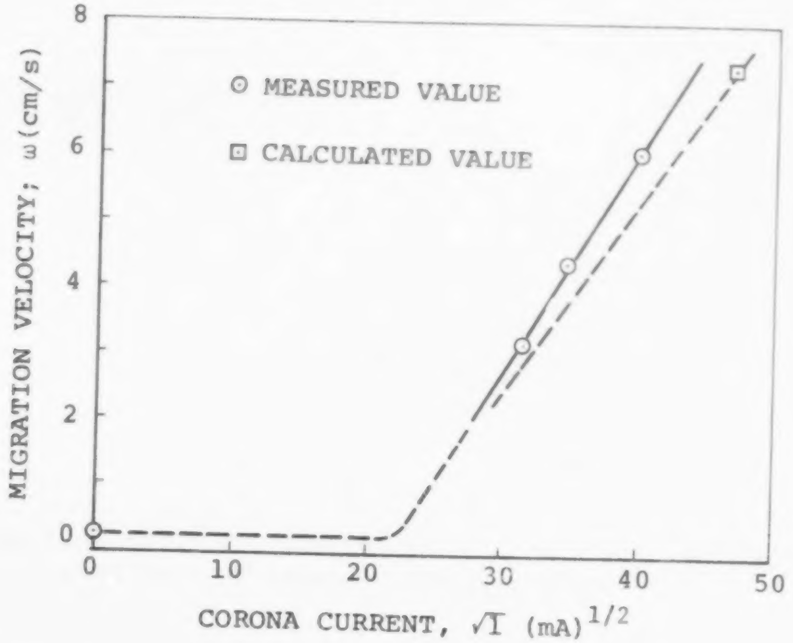

Fig. 12 Performance test results for full-scale ESP

THE USE OF ELECTROSTATIC PRECIPITATORS FOR COLLECTION OF PARTICULATE MATTER FROM BARK AND WASTE WOOD FIRED BOILERS IN THE PAPER INDUSTRY

Robert L. Bump
Product Manager
Industrial Precipitator Division
Research-Cottrell, Inc.
Bound Brook, New Jersey

The fundamental process by which particulate matter is removed from a gas stream by an electrostatic precipitator is well known at this point in time. Referring to Figure I, it consists simply of grounded collecting surfaces placed in juxtaposition to high voltage discharge electrodes which are energized by a low current, high voltage unidirectional power supply. An electrical field is created due to ionization of the gas and the dust particles are propelled toward the electrode of opposite polarity. Removal of the material is accomplished by imparting a shock to the electrodes by electrical or mechanical means.

The historical formula for the efficiency of a precipitator is the Deutsch-Anderson equation shown on Figure 2. Although modified somewhat in recent years, it remains essentially correct. It is to be noted that the efficiency is derived from consideration of the volumetric flow rate, the total area of the collecting surfaces and selection of the precipitation rate parameter, referred to as "drift velocity." This value varies with the specific application and is derived from the charging and collecting field characteristics, the mass mean particule radius and the gas viscosity. It becomes obvious that one of the major determinates of drift velocity lies in the electrical characteristics. These are established largely by the resistivity (or conductivity) of the particle being collected. This characteristic may be a function of temperature above 600°F wherein the chemistry of the particle itself accounts for the degree of conductivity or a surface conduction mechanism in lower temperature ranges (300 - 600°F). In the latter case, constituents in the gas such as water or sulphur trioxide are absorbed on the surface of the dust particle and this controls the conductivity.

Summarizing those factors which are taken into consideration when applying a precipitator to collection of bark ash, we find (Figure 3):

Gas Volume -- A precipitator is a volumetric device and increased flow results in a decrease in efficiency.

Temperature-- Can effect gas volume and resistivity as described above.

Dust Composition and Gas Analysis -- Primarily as related to resistivity. Also has some impact on method of rapping electrodes and dust removal system.

Dust Loading -- Since a precipitator is sized to yield a certain percentage efficiency by weight (inlet - outlet/inlet), it is obvious that increasing the quantity at the inlet will also result in an increase at the outlet.

Particle Size -- All things being equal, a decrease in particle size necessitates a larger precipitator.

Efficiency Required -- The higher the required efficiency, the larger the precipitator.

It can be seen that on a given process where the gas volume, temperature, particulate loading, gas and particulate analysis, and particle size are either known or predictable, the application of a precipitator boils down simply to a knowledge of how the material will react mechanically and electrically. It must be understood that the precipitator recognizes only these properties. It does not know the difference between sodium sulphate from a recovery furnace and ash from bark burning, except as manifested by electrical and mechanical behavior. How, then, are these properties established?

The apparatus for measuring the electrical resistivity of a given dust is shown on Figure 4. This is basically a mini-precipitator which can be inserted in a flue. A layer of dust one (1) centimeter thick is precipitated and the resistance of the layer is measured and expressed in ohms per centimeter. A typical resistivity curve is shown on Figure 5. It has been established that values above 10^{10}

ohms/centimeter herald the "danger zone" for precipitator operation, i.e., the dust is too good an insulator. Values in the 10^{12} and 10^{13} range signal an almost imposible application unless some means is used to reduce the resistivity such as gas conditioning or a temperature change. On the other end of the scale is a low resistivity situation. Materials in the 10^3-10^5 ohm/cm range accept an electrical charge readily, but, upon reaching the collecting surface, give up their charge very readily. It had been thought in the past that this condition results in excessive reentrainment of material and poor precipitator performance. Our experience has been contrary to this belief. Figure 6 indicates the resistivity levels found at several plants. Note that plants A and B are producing a very low resistivity particulate due to the high combustible content of the ash. Despite this, the precipitators are operating at a high level of efficiency. This same experience was found in collecting the particulate from burning rubbish in large municipal incinerators. The ash has a high percentage of large carbonaceous (paper char) particles but there are dozens of precipitators in successful operation.

Our first activity in evaluating the use of a precipitator on the ash from bark burning consisted of a pilot precipitator on a hog fuel fired boiler. A brief description of the process and the results may be found on Figure 7. In summary, the pilot work established that a precipitator is a viable method of controlling this problem. Outlet loadings of 0.023 gr/acf (average) were obtained with a treatment length of 18'-0". The sizing parameters derived from the study indicated no problems with the collection of this material.

Subsequent to the pilot work, two (2) contracts were obtained and a brief case history of each may be found on Figures 8 and 9. One of the installations may be seen on Figure 10. In the first case, the system consists of three (3) boilers, two (2) coal fired and one (1) bark fired; the other comprises four (4) boilers, three (3) coal fired, and one (1) bark fired. Of interest is the fact that the resistivity of the ash from the bark fired boiler was 8.74×10^9 whereas from the coal fired units it reached 8.5×10^{10}. This merely says that the bark ash is easier to collect than the coal ash. This has been our consistent experience with combination firing systems whether oil or coal. The bark ash is not the determinant of precipitator size; in fact, it usually has an overall beneficial effect on the other, more highly resistive materials.

A few considerations in applying a precipitator to a bark ash application:

1) If auxiliary fuel is to be used, oil or coal, give a complete analysis of the fuel and ash, particularly in the case of coal.

2) A mechanical collector is recommended ahead of the precipitator in the case of bark ash. It removes the large, carbonaceous particles and results in a smaller, hence less expensive, precipitator. Figures 11 and 12 are photomicrographs (300 x magnification) showing the type of material one might expect from a low efficiency (60-70%) mechanical and that entering a precipitator.

3) If the bark is derived from salt water borne logs, resistivity measurements, either in-situ or laboratory, should be made since chlorides can cause a high resistivity condition at temperatures below 450-500°F if the moisture content is not above 10 percent by volume.

A few of the important design considerations in applying a precipitator to bark ash (or any highly carbonaceous, conductive material) would be:

1) Careful selection of the face velocity. Too high a velocity can cause scouring of the dust from the collecting surfaces, reentrainment and loss of efficiency.

2) The collecting surface design must be such that a quiescent zone exists in order to minimize the aforementioned reentrainment.

3) For efficiency requirements above 98%, the aspect ratio (length/height) of the precipitator should be no less than 1. This also affects reentrainment.

4) Care must be exercised in the selection and application of the precipitator rappers. The intensity must be adjustable or reentrainment will definitely be a problem. Our rappers are easily adjustable from 0 to 24 foot pounds.

Summarizing, our experience based on pilot study, laboratory and in-situ resistivity measurements, and full scale installations indicates that electrostatic precipitation is a viable solution to the collection of particulate matter from firing bark and hog fuel.

Figure 1

PLAN VIEW OF PRECIPITATOR LANE

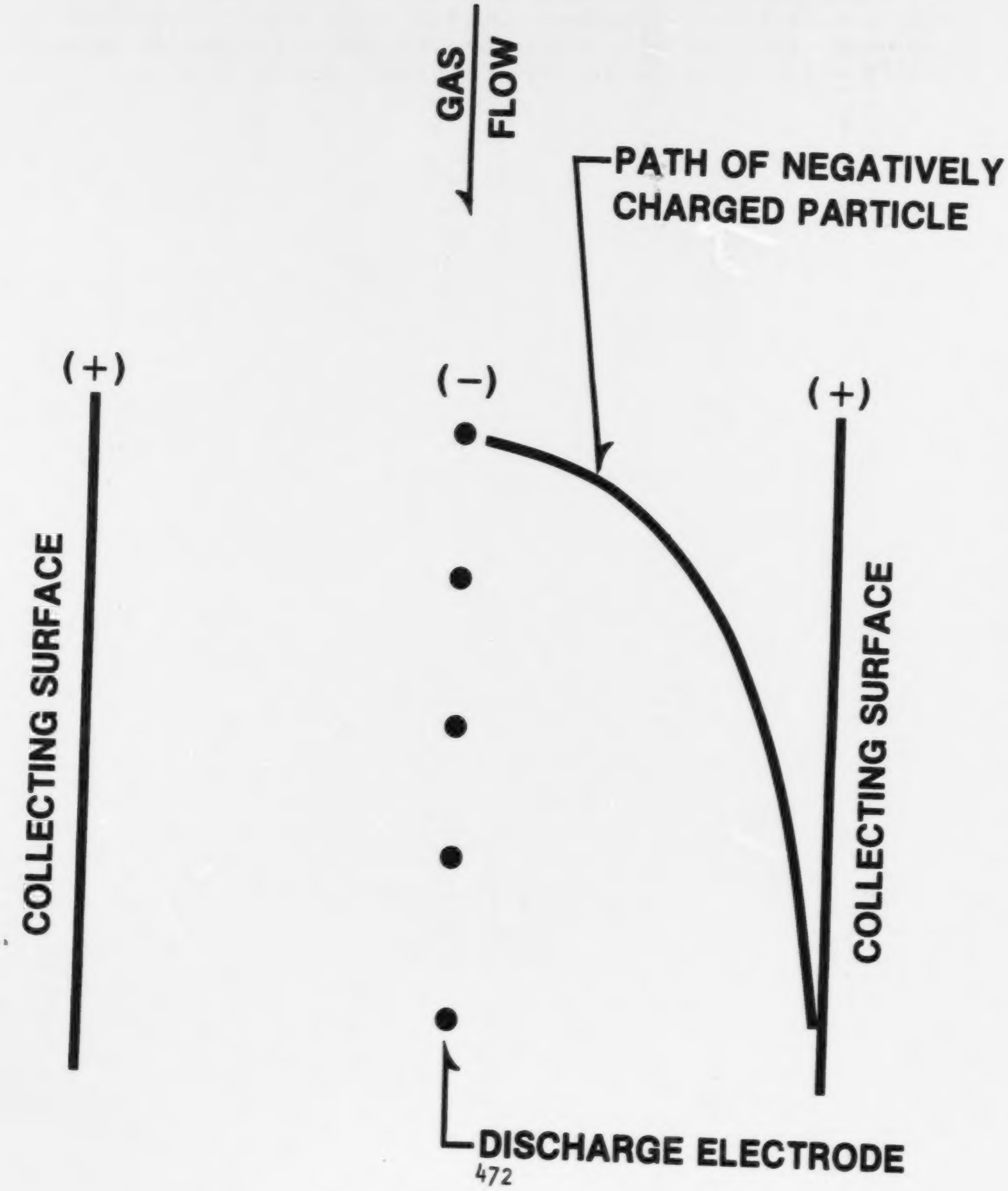
GAS FLOW
PATH OF NEGATIVELY CHARGED PARTICLE
(+)
(−)
(+)
COLLECTING SURFACE
COLLECTING SURFACE
DISCHARGE ELECTRODE

Figure 2

ELECTROSTATIC PRECIPITATORS

$$EFF = 1 - e^{\frac{-A}{V} w}$$

$$w = \frac{Eo\ Ep\ a}{2 \pi \eta}$$

EFF = Fractional % Collected

A = Surface Area Collecting Electrodes

V = Volumetric Flow Rate

w = Particle Drift Velocity or PPTN Rate Parameter

Eo = Charging Fields $\frac{\text{Volts}}{\text{Distance}}$

Ep = Collecting Field $\frac{\text{Volts}}{\text{Distance}}$

a = Particle Radius

η = Gas Viscosity

Figure 3

FACTORS CONSIDERED IN SIZING

A. GAS VOLUME

B. TEMPERATURE

C. DUST LOADING

D. DUST COMPOSITION

E. GAS ANALYSIS

F. PARTICLE SIZE

G. EFFICIENCY REQUIRED

Figure 4

COMPLETE FIELD RESISTIVITY APPARATUS

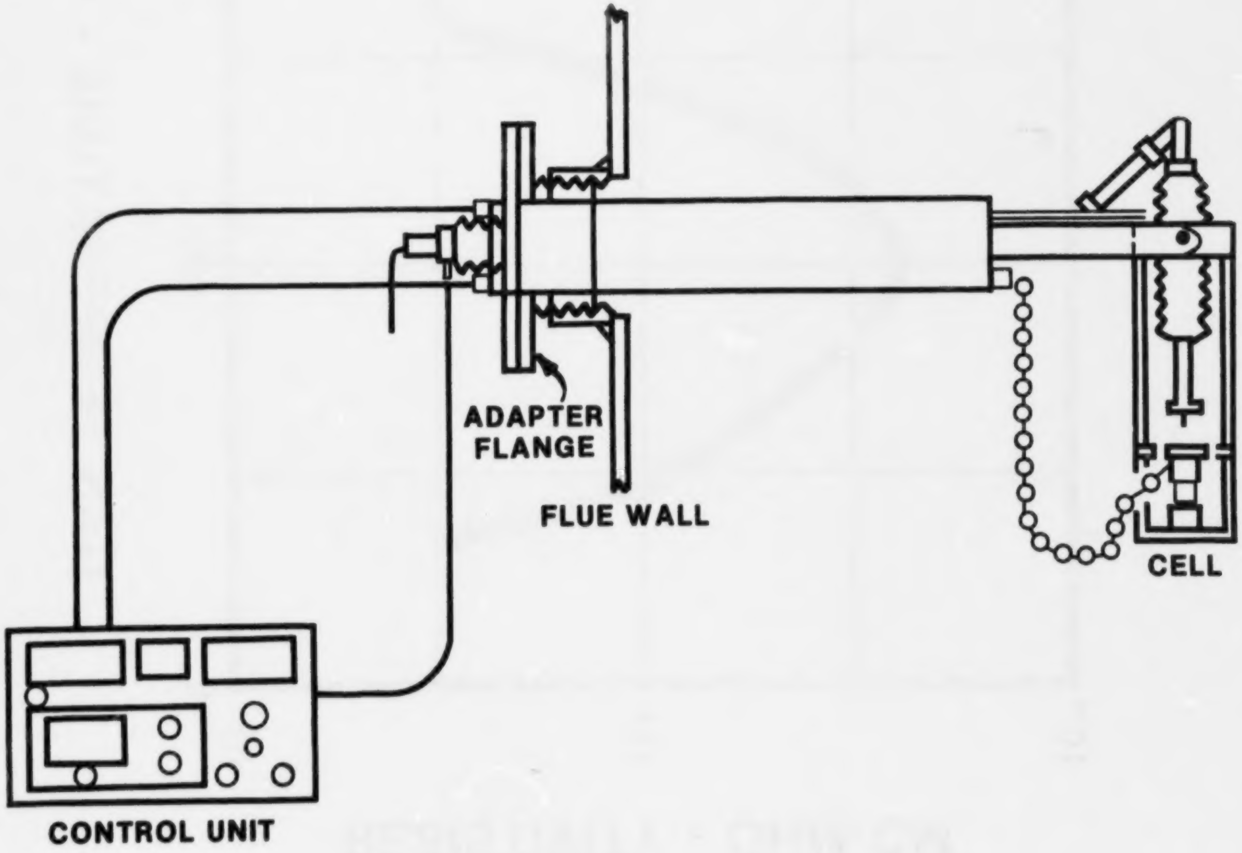
ADAPTER FLANGE
FLUE WALL
CELL
CONTROL UNIT

Figure 5

TYPICAL RESISTIVITY CURVE

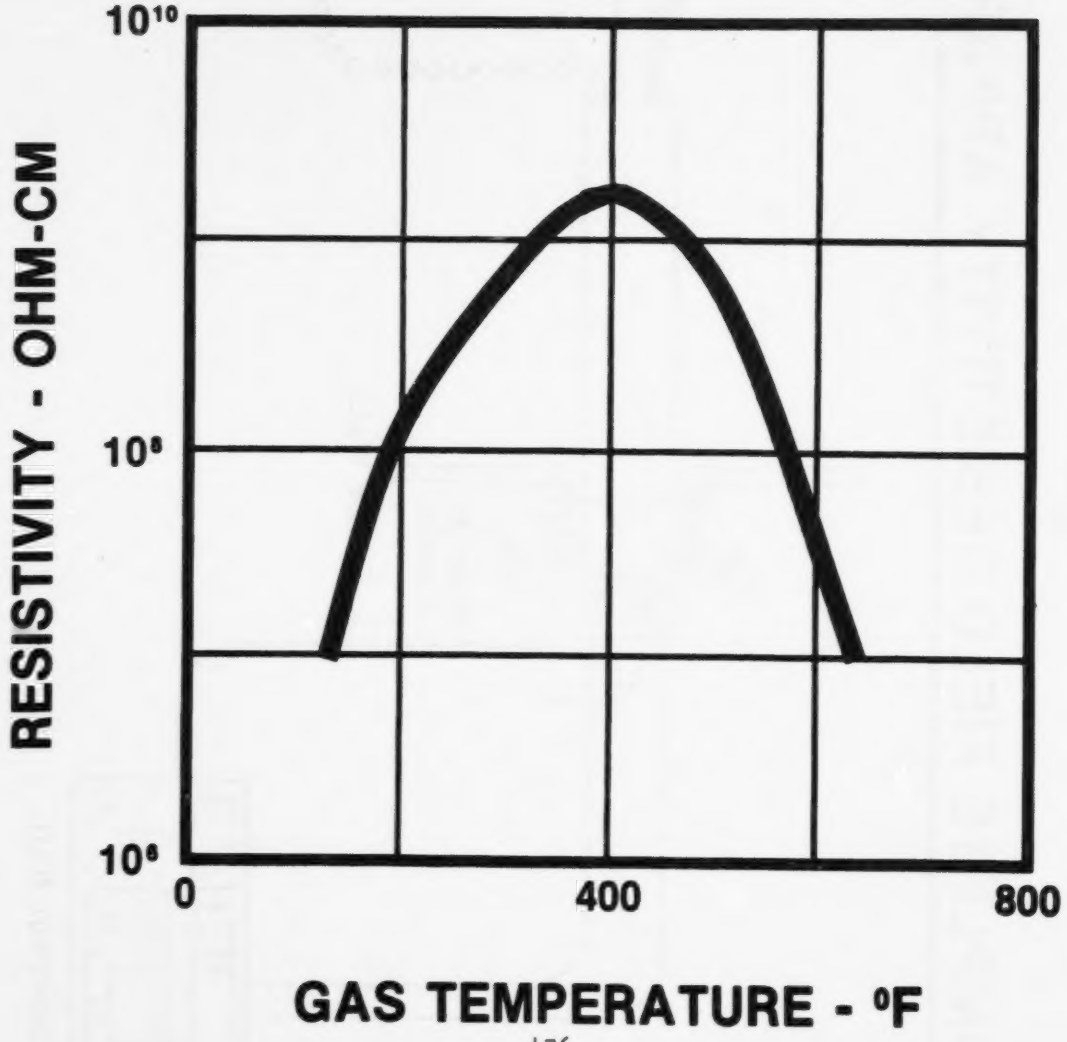

Figure 6

RESISTIVITY MEASUREMENTS

PLANT	MATERIAL	RESISTIVITY	ESP PERFORMANCE
A	PETROLEUM COKE (85% COMBUSTIBLE)	5×10^3 ohm/cm.	99% (0.004 GR/ACF)
B	COKING BOILERS (65% COMBUSTIBLE)	3×10^4	0.0087 GR/ACF (vs .025 GUARANTEE)
C	BARK & COAL (13.7% COMBUSTIBLE)	8.7×10^9	0.011 GR/ACF (vs .023 GUARANTEE)
D	BARK ONLY (3 BOILERS)	1.4×10^6 9.6×10^5 8.4×10^7	— — —
E	BARK & COAL (27% COMBUSTIBLE)	8.4×10^6	99.38% 0.0085 GR/ACF

Figure 7

B.C. FOREST PRODUCTS
VICTORIA, B.C.

PILOT PLANT TESTS

PROCESS: 50,000 LB./HR. HOG FUEL FIRED, DUTCH OVEN TYPE, LOW PRESSURE STEAM GENERATOR. FURNACE FUELED BY A MIXTURE OF BARK, CHIPS, AND SHAVINGS. NO AUXILIARY FIRING DURING TESTS.

PILOT PRECIPITATOR: FOUR (4) GAS PASSAGES, 6' HIGH, TWO (2) 9'-0'' ELECTRICAL FIELDS, ENERGIZED BY TWO (2) 250 MA T-R SETS.

TEST RESULTS: (AVG. OF 6 RUNS)

GAS VOLUME ------ 4320 ACFM
TEMPERATURE ------ 548°F
INLET LOADING ------ 0.452 GR/SCFD
OUTLET LOADING ------ 0.043 GR/SCFD
EFFICIENCY ------ 90.6%

Figure 8

P.H. GLATFELTER PAPER COMPANY
SPRING GROVE, PENNSYLVANIA

SPECIFICATION

Precipitator Design Conditions:

GAS VOLUME -- 325,000 ACFM
TEMPERATURE -- 285-485°F
PRESSURE -- ±15'' H_2
INLET LOADING -- 0.23-0.37 GR/ACF
OUTLET LOADING -- 0.023 GR/ACF
EFFICIENCY -- 90%

Precipitator Data:

NO. OF UNITS -- 1 (FOR 3 BOILERS)
NO. OF CHAMBERS -- 2
GAS PASSAGES -- 33 PER CHAMBER
NO. OF FIELDS -- 3 PER CHAMBER
TREATMENT LENGTH -- 21'-0''
FIELD HEIGHT -- 24'-0''
ENERGIZING SETS -- 3 AT 1500 MA, 45 KV
RAPPING -- 40 MAGNETIC IMPULSE FOR PLATES
18 ELECTRIC VIBRATORS FOR WIRES

Test Data:

ONE CHAMBER

GAS VOLUME -- 292,210 ACFM (vs. 162,500 DESIGN)
OUTLET LOADING -- 0.025 GR/ACF
EMISSIONS -- 62.6 LB./HR. (vs. 104.5 ALLOWABLE)

TWO CHAMBERS

GAS VOLUME, ACFM --	268,300	246,013
OUTLET LOADING, GR/ACF --	.012	.0095
EMISSIONS, LB./HR. --	27.13 (92.4 ALLOWABLE)	20.03 (89.8 ALLOWABLE)

Figure 9

GEORGIA KRAFT COMPANY
ROME, GEORGIA

SPECIFICATION

Precipitator Design Conditions:

GAS VOLUME -- 550,000 ACFM
TEMPERATURE -- 300-485°F
PRESSURE -- ± 15'' H_2O
INLET LOADING -- .8-1.0 GR/ACF
OUTLET LOADING -- 0.005 GR/ACF
EFFICIENCY -- 99.5%

Precipitator Data:

NO. OF UNITS -- 1 (FOR 4 BOILERS)
NO. OF CHAMBERS -- 2
GAS PASSAGES -- 43 PER CHAMBER
NO. OF FIELDS -- 4 PER CHAMBER
TREATMENT LENGTH -- 36'-0''
FIELD HEIGHT -- 30'-0''
ENERGIZING SETS -- 8 AT 1000 MA, 45 KV

Test Data: (Avg. of 3 Tests)

GAS VOLUME -- 517,000 ACFM
INLET LOADING -- 1.38 GR/ACF
OUTLET LOADING -- 0.0085 GR/ACF
EFFICIENCY -- 99.38%

Figure 10

P.H. GLATFELTER PAPER CO.
SPRING GROVE, PENNA.

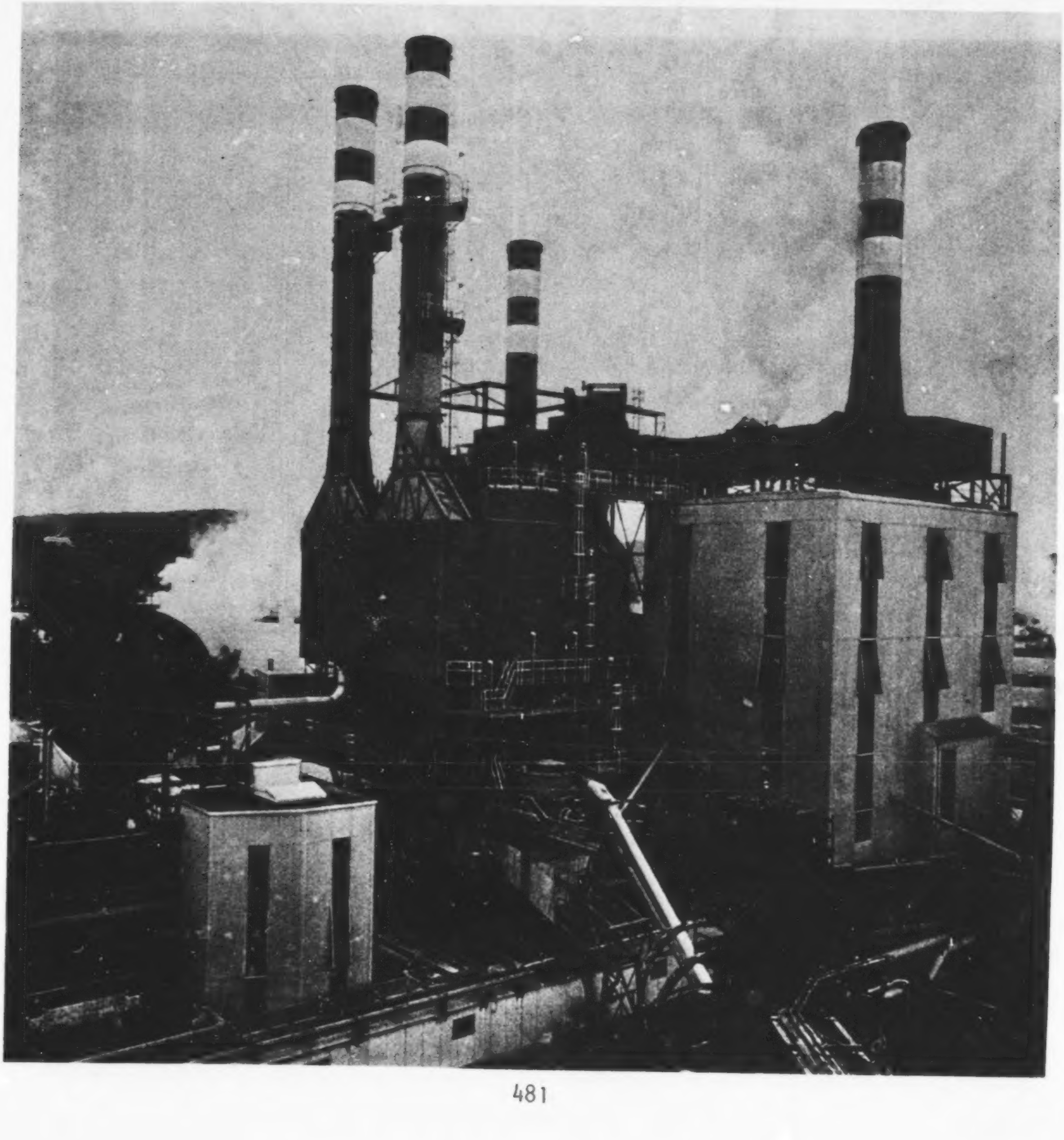

Figure 11

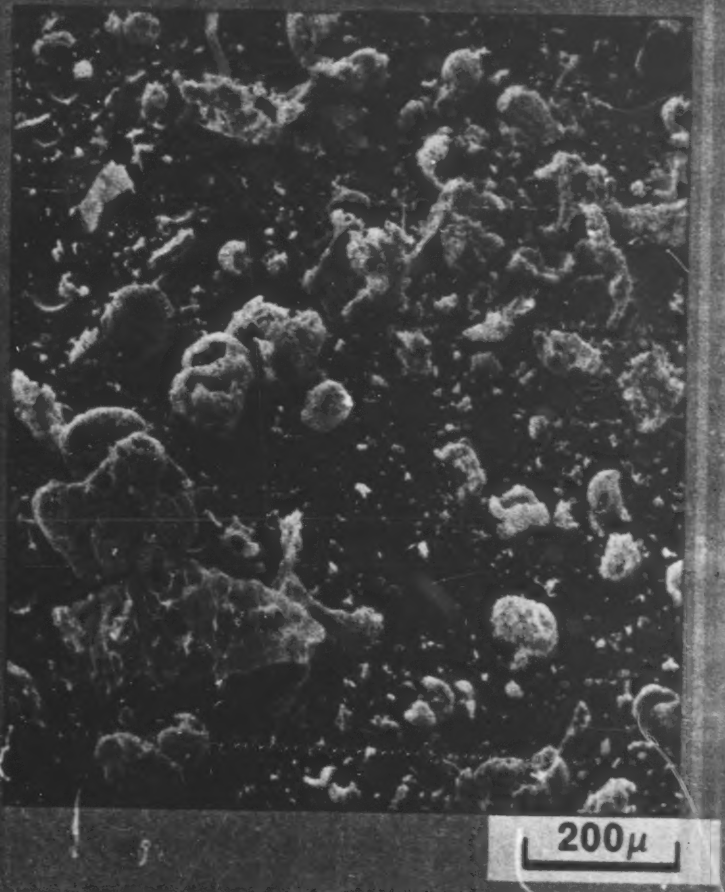

MECHANICAL COLLECTOR

Figure 12

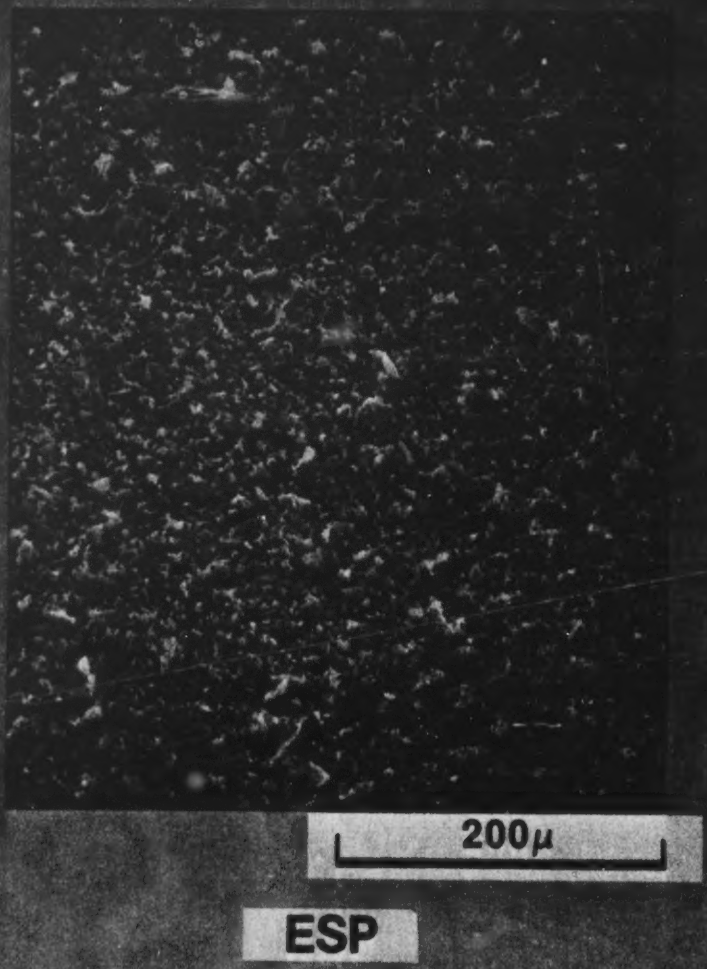

ROOF-MOUNTED ELECTROSTATIC PRECIPITATOR

Shoji Ito
Shigeyuki Noso
Masakazu Sakai
Kiyoshi Sakai
SUMITOMO HEAVY INDUSTRIES, LTD.

INTRODUCTION

There are several methods of supprressing the plume to be discharged into the air from dust-generating sources like steel making plants, the most common being the dust collector.

For various reasons, these collectors may not be as effective as desired, and this creates a big problem in some factories. For example, near high-temperature plant such as converters, electric furnaces, and casting floors of blast furnaces for steel making, it is not feasible to handle all the plume the plant generates. Dust which is not trapped by the collector stays in the work environment until it is discharged into the air, which causes pollution in the neighborhood.

In order to avoid the above-mentioned air pollution and the deterioration of the atmosphere in the factory, dust collectors have been developed which, after the building has been made air-tight, collect the plume and hot air and pass them through the dust collector so only dust-free air is discharged from the plant.

There are two types of collector like this. One type uses a suction hood on the roof to intake the plume and send it to the dust collector. The other type utilizes the factory's natural ventilation, by means of which the plume passes through an electrostatic precipitator on the roof. The suction type has to draw in not only the plume but also a great volume of air from its periphery. Dust collectors of this type usually make use of a baghouse, the operation of which requires high electricity consumption, thus they are not very economical.

To overcome the demerits these conventional dust collectors, we have developed the "Roof-mounted Electrostatic Precipitator" (hereafter

Preceding page blank

referred to as R-EP) for industrial workshops. This system relies on the upward convection of the plume, due to its higher temperature, and the natural draft force in the workshop to carry the plume into the R-EP. This R-EP is particularly remarkable from the energy saving standpoint. It has already been installed in four converter plants, eleven electric furnace plants and the casting floor of a blast furnace.

An explanation and description of R-EP and its energy saving features are given below.

WORKSHOP DUST COLLECTION SYSTEMS

Methods of eliminating dust from the plume generated in workshops are classified as either forced suction or natural ventilation type. Most dust collection systems presently in use are of the former type and employ baghouses, e.g. the Canopy Hood, Closed Workshop, Closed Workshop with Opening-Closing type Monitor (Illustrated in Figure 1, and Canopy Hood and Closed Workshop Combined System. The problem common to all of them is high energy consumption.

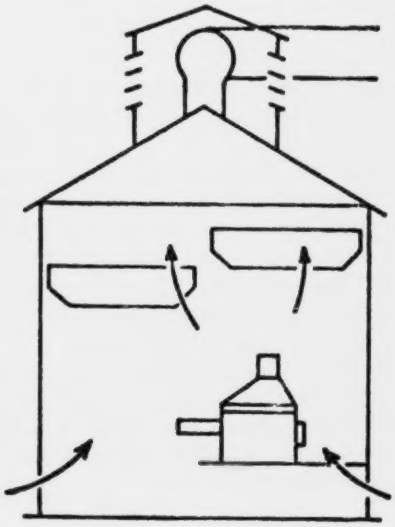

Fig.1 Closed workshop system with opening closing type monitor

R-EP is the only natural ventilation type system. It is illustrated in Figure 2.

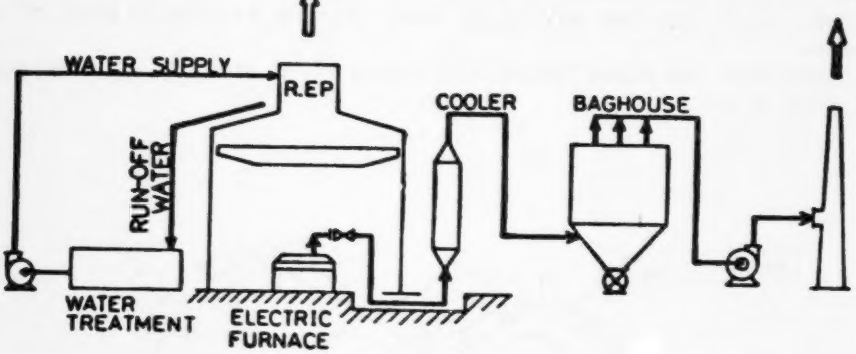

Fig. 2 R.EP System

The plume from high temperature workshops in buoyant, and rises by convection; in its upward flow it is diluted by the surrounding air to become a large volume of dirty gas. Therefore suction type dust collecting systems cannot selectively collect the hot plume as it is generated in the workshop; they have to intake a large volume of air with the plume. The intake of the dust collector is as much as 1.5 to 2.5 times the volume of the plume generated, and their power consumption is very high. Furthermore, with forced suction a half-effective dust collector sometimes acts as a brake to the rising plume, giving rise to short-circuited current and dead stock, which worsens working conditions in the workshop.

In the natural ventilation type, the plume reaches the R-EP by its buoyancy and the building's upward draft force only. That is, R-EP works on the hot plume selectively, and the power required for gas is zero. Accordingly it is the best method in use from the energy saving standpoints.

THE DEVELOPMENT OF R-EP

R-EP was originally conceived as a dust collector that needed no floor space for its installation. A steel mill of Kobe Steel, Ltd., Japan urgently needed to install a dust collector to control the emissions from its converter shop, but had no space in which to put such a collector.

To meet this demand, it was proposed to put an Electrostatic Precipitator on the roof of the workshop, and the feasibility of this idea was investigated. First, a light prototype Electrostatic Precipitator was designed. By relying on convection and natural upward draft, the need for a main blower was eliminated. Further, intermitted of the collecting electrode by a water spray was adopted in place of dry tapping, which has the advantage that serious re-entrainment of dust is avoided.

This was the first practical apprecation of R-EP, in conjunction with Kobe Steel, Ltd.

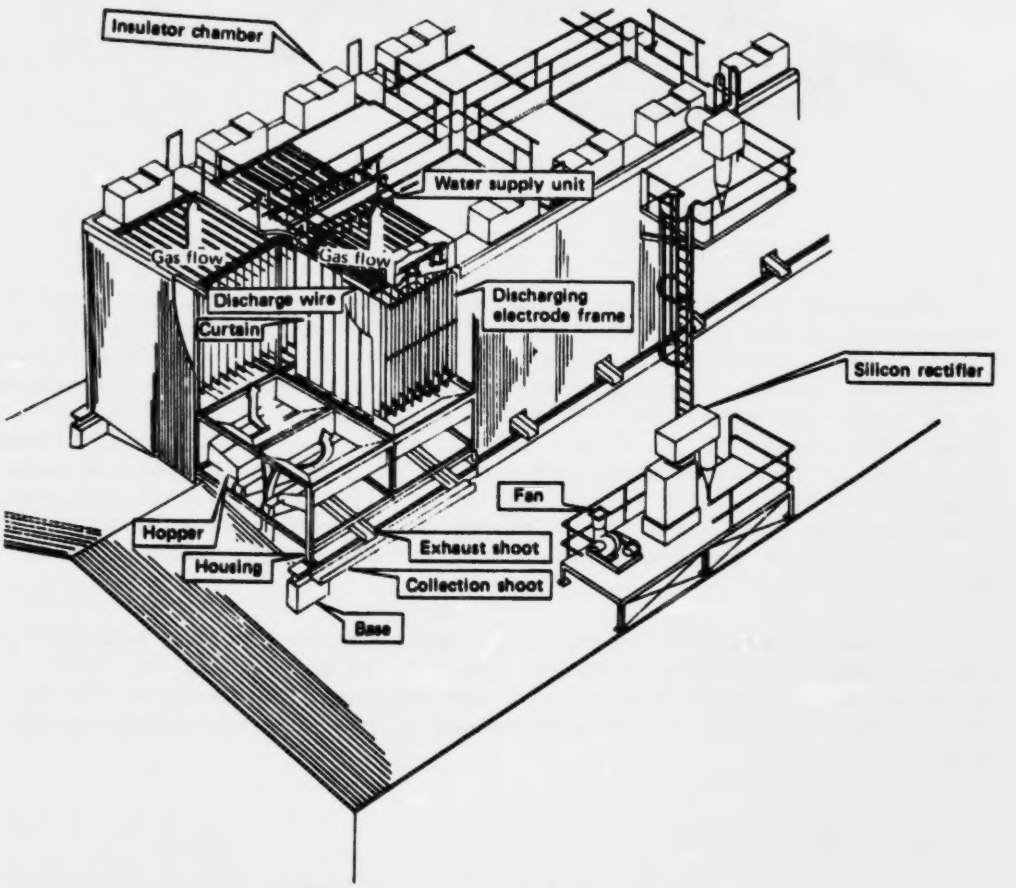
Insulator chamber
Water supply unit
Gas flow
Gas flow
Discharge wire
Curtain
Discharging electrode frame
Silicon rectifier
Fan
Hopper
Exhaust shoot
Housing
Collection shoot
Base

Fig. 3 Construction of R-EP

OUTLINE OF R-EP

R-EP's mechanism is as follows. Based on the electrostatic precipitator principle, R-EP has discharge electrodes and collecting electrodes and a corona discharge is developed between them. The corona discharge negatively charges dust particles in the upward gas flow and they precipitate to the collecting electrodes by coulomb force.

The dust that collects on the collecting electrodes is washed off once a day by a water spray of 10 minutes duration. The dusty run-off water is collected, cleaned and re-cycled. By washing the R-EP one block at a time in sequence, the total water flow rate is only 400 ℓ/min.

Construction and functions of R-EP

Construction diagram of R-EP is shown in Figure 3, in which:
Gas flow: vertical upward flow
Collecting electrode: flat plate, corrosion-resistant, electricity conducting synthetic resin for lightness.
Discharge electrode: stainless steel wires or round piano wires attached to a frame.
Hopper: for collecting the run-off water and controlling the upward gas flow.
Dust removal: intermittent water spray washing for about 10 minutes a day for each block. (R-EP is separated into small blocks)
High voltage wiring: bus duct or Cottrell cable type.
Voltage control: rapidly, accurately and continuously detects fluctuations in loading, and selects the most suitable voltage according to the dust load, thus operating R-EP at high efficiency.

ACTUAL APPLICATION OF R-EP

Items which must be taken into account for acutal application of R-EP are:

Gas flow due to heat convection

The theoretical gas volume of hot gas due to heat convection is given by the following expressions:

$$q_Z = 1.95\, Z^{3/2}\, (H')^{1/3} \quad \ldots\ldots \ (1)$$

$$H' = \frac{1.45}{60}\, A_s\, (\Delta t)^{4/3} \quad \ldots\ldots. \ (2)$$

where; Z: distance from provisional point of heat source to hood opening (m)
q_Z: gas flow rate at the distance Z from the point of heat source (m3/min)

H': Heat transmission of convection current from heat source (kcal/min)
A_s: surface area of heat source (m^2)
Δt: temperature difference between hot body and ambient (°C)

The actual volume of gas to be handled by R-EP is determined by multiplying the theoritical value q_z by a coefficient, which is found from pre-installation measurements of the gas volume at the workshop monitor. When R-EP is to be installed in a newly built plant and these measurements cannot be performed, N can only be approximated from experience of similar situations.

Pre-installation measurements

Pre-installation measurements at the workshop monitor of gas flow velocity, gas temperature and dust loading, depending on the type of work and plant.

Observations of gas spread and effect of lateral wind

Chemical analysis, size distribution and electric resistivity of the dust

Ventilation cycle

Weather conditions

Application of R-EP to a steel mill converter shop

Photo 1 R-EP for a 250 ton/ch. converter shop

Using the performance anaryses of tests on a model, a R-EP was designed for use in the above-mentioned conveter shop and was installed in November 1973. It has been working well since that date. Up to the present time, four R-EPs have been installed in converter shops including one in Japan's first bottom-blown oxygan process (Q-BOP) plant.

Photo 1 shows the R-EP on the roof of a 250 ton/ch. converter shops. Table 1 shows the comparison of design conditions and actual performance of R-EP.

Table 1. COMPARISON OF DESIGN CONDITIONS AND ACTUAL PERFORMANCE OF R-EP FOR CONVERTER SHOP

INSTALLAION		TOTAL GAS VOL. m^3/min	GAS VOL. PER CONVERTER m^3/min	GAS VEL. m/sec	INLET DUST LOADING g/Nm^3	OUTLET DUST LOADING g/Nm^3	REMARKS
A	DESIGN	24000	8000	1.77	0.1	0.02	LD
	ACTUAL	13600 - 28600	4500 - 9500	1.0 - 2.1	0.269 (MAX)	0.047	80 t/ch × 3UNITS
B	DESIGN	43800	14600	1.78	0.4	0.03	LD
	ACTUAL	51000	17000	1.9	0.33	0.02	250 t/ch × 3UNITS
C	DESIGN	30900	7700	0.8	0.4	0.02	LD
	ACTUAL	42400	10600	1.1	0.35	0.02	160 t/ch × 3UNITS
D	DESIGN	27000	13500	1.66	0.4	0.03	Q-BOP
	ACTUAL	9800 - 22800	4900 - 11400	0.6 - 1.4	1.09 (MAX)	0.038	230 t/ch × 2UNITS

Application of R-EP to electric furnace shop

Before installing R-EP in the electric furnace shop, measurements were taken of electrical resistivity and collectability of the dust.

As no model test was performed for the electric furnace R-EP, design was based only on the pre-installation measurements of gas velocity, gas temperature, dust loading taken at the monitor.

Photo 2 shows the R-EP for a 100 ton/ch. electric furnace shop. Table 2 shows the comparison of design conditions and actual performance of R-EP.

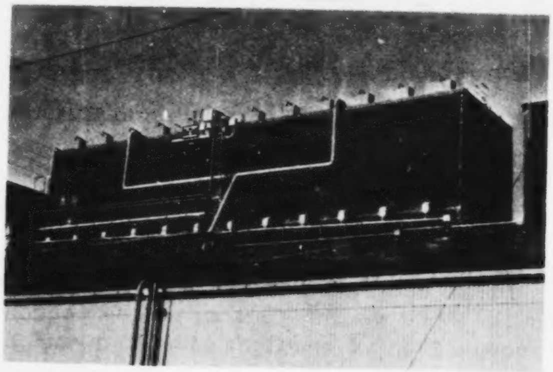

Photo 2 R-EP for a 100 ton/ch electric furnace

Table 2. COMPARISON OF DESIGN CONDITIONS AND ACTUAL PERFORMANCE OF R-EP FOR ELECTRIC FURNACE SHOP

INSTALLAION		TOTAL GAS VOL m³/min	GAS VOL PER EF m³/min	GAS VEL. m/sec	INLET DUST LOADING g/Nm³	OUTLET DUST LOADING g/Nm³	REMARKS
A	DESIGN	8200	8200	1.0	0.2	0.02	100T/ch × 1UNIT
	ACTUAL	10700	10700	1.3	0.2-0.4	0.01 0.03	
B	DESIGN	4900	4900	1.0	0.3	0.03	30T/ch × 1UNIT
	ACTUAL	4600	4600	0.94	0.15-0.29	0.01-0.02	
C	DESIGN	5600	2800	1.0	0.3	0.03	18T/ch × 2UNITS
	ACTUAL	6800-9000	3400-4500	1.2-1.6	0.16-0.42	0.01-0.03	
D	DESIGN	4000	2000	1.0	0.3	0.03	8T/ch × 2UNITS
	ACTUAL	3700	1950	0.92	0.1-0.16	0.01-0.015	

Application of R-EP to casting floor of blast furnace

Photo 3 shows the R-EP for the casting floor of a blast furnace.

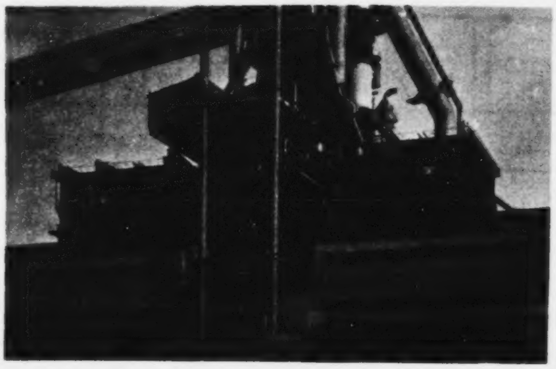

Photo 3 R-EP for the casting floor of a blast furnace

COMPARISON OF ELECTRIC POWER CONSUMPTION OF BAGHOUSE SYSTEMS & R-EP

R-EP relies on natural ventilation and therefore unlike baghouse type dust collectors, uses no blowers. This makes its electric power consumption very small.

The amount of water needed for washing the collecting electrodes is 400 l/min, and used water can be recycled after the cleaning treatment. The water needed for replenishment, to make up for water lost in dehydrated dust cakes and by evaporation, is very little.

The low power consumption R-EP contributes immensely to energy saving. (See Table 3 to Table 5)

Table 3. COMPARISON OF ELECTRICITY CONSUMPTION (CONVERTER SHOP)

INSTALLATION	GAS VOL. m^3/min	ELECTRICITY CONSUMPTION, KW	
		BAGHOUSE	R-EP
A	24000	2800	60
B	43800	5100	150
C	30900	3600	170
D	27000	3100	90

Table 4. COMPARISON OF ELECTRICITY CONSUMPTION
(ELECTRIC FURNACE SHOP)

INSTALLATION	GAS VOL. m^3/min	ELECTRICITY CONSUMPTION, KW	
		BAG HOUSE	R-EP
A	8200	1900	101
B	4900	1120	63
C	5600	1290	65
D	4000	930	50

Table 5. COMPARISON OF ELECTRICITY CONSUMPTION
(BLAST FURNACE SHOP)

	BAG HOUSE	R-EP
RATING PUT OUT POWER, KW	3500	240

GAS VOL. : 25000 m^3/min

The above comparison are based on the assumption that the gas volumes handled are same in both R-EP and beghouses. However, as mentioned above, the gas volume handled in the latter is about 1.5 to 2.5 times that of R-EP, for comparable dust collecting. Therefore, the difference in the power consumption becomes for larger than the tables show.

CONCLUSION

The R-EP developed by Sumitoto Heavy Industries, Ltd. is used for many converter shops, electric furnace shops and casting floors of blast furnaces etc., owing to its energy and space saving characteristics. We believe that R-EP will further serve for anti-airpollution purposes.

REFERENCES

1. The Improvement and its Technique of Labor Atmosphere. Labor Standards Bureau, Ministry of Labor, Japan, 1948.

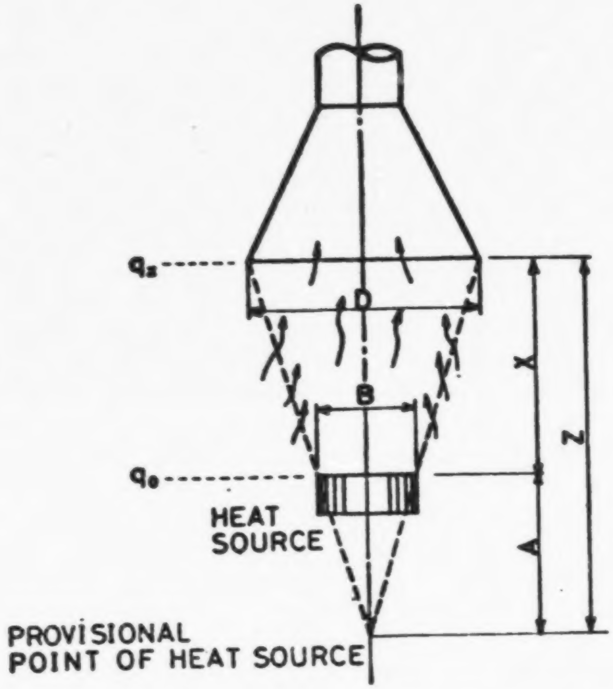
q_z
D
X
Z
B
q_0
HEAT SOURCE
A
PROVISIONAL POINT OF HEAT SOURCE

Fig.4 Plume from a heat source

POM EMISSIONS FROM COKE OVEN DOOR LEAKAGE AND THEIR CONTROL BY A WET ELECTROSTATIC PRECIPITATOR

Richard E. Barrett and Paul R. Webb
Battelle-Columbus Laboratories
Columbus, Ohio

Clyde E. Riley and Andrew R. Trenholm
U.S. Environmental Protection Agency
Research Triangle Park, North Carolina

ABSTRACT

Measurements of POM emissions were made upstream and downstream of a wet electrostatic precipitator being used to control emissions from coke oven doors. The measurements were intended to obtain data on POM emissions from door leakage and, thus, were made during periods when no coke pushing was occurring. Determinations were made of (1) POM emission levels and (2) the effectiveness of the wet ESP for controlling POM emissions. Sampling was conducted using an EPA Method 5 type sampling train with a Tenax adsorbent column added between the filter and impingers. Separate analyses were made for "particulate" POM (probe wash and filter catch) and "gaseous" POM (adsorbent column catch). Emission values are reported for 18 POM species. The wet ESP was ineffective in controlling emissions of naphthalene, 93 to 94 percent effective in controlling emissions of fluoranthrene and pyrene, and 96 to 100 percent effective in controlling emissions of the remaining POM species.

Preceding page blank

INTRODUCTION

Air pollutant emissions from coke ovens have long been recognized as significant. Although oven charging and pushing operations have received most of the attention, coke-oven door leakage has been identified as a contributor to overall coke-oven emissions[1]. Unpublished data suggest that there are significant emissions of polycyclic organic materials (POM) due to door leakage during the coking cycle.

Recently, efforts have been made to collect coke-side emissions with sheds or hoods, and to reduce pollutant emissions by using emission control devices to remove the pollutants from the gas stream[2,3]. One device used to remove the pollutants from the gas stream is the wet electrostatic precipitator (WESP).

This paper describes results of a coke-oven emission measurement program which was conducted as part of the U.S. Environmental Protection Agency's overall program to develop emission factors and emission standards for various industrial processes. The prime objective of this program was the measurement of emissions arising from door leakage during the coking cycle; it did not include measurements during coke-pushing operations. POM concentrations were measured at the inlet and outlet of a WESP used to remove pollutants from a coke-oven shed exhaust stream, and control device efficiency was determined for total POM, and for 18 specific POM species.

It should be pointed out that this paper is not a comprehensive survey and evaluation of all coke-oven door leakage emissions data. Rather it reports on one field measurement program which included certain unique features (such as determining emissions and control device efficiency for a number of separate POM species). Also, there is substantial scatter in the unpublished POM emissions data concerning samples collected in different locations, and collected using different sampling and analysis procedures. EPA is currently conducting an evaluation of all available coke-oven POM emissions data.

DESCRIPTION OF COKE OVEN AND SHED

The Wisconsin Steel Works coke plant consists of a battery of 45 coke ovens. The capacity of each oven is about 15.4 metric tons (17 tons) of coke per coking cycle.

The coke oven includes an emission control system that was constructed to remove fumes from the hot coke, or push side, of the coke battery. It consists of a 79 m (260 ft) long shed that serves to collect pushing and coke side door leakage emissions. Inside the shed at the top is a 0.315 m x 0.315 m (80 x 80 inch) duct with openings along the sides and bottom for fumes to enter. The single exhaust duct connects to two wet electrostatic precipitators. The shed is fitted with an emergency door in the shed roof that can be opened to vent fume in case of induced draft fan failure.

DESCRIPTION OF THE EMISSION CONTROL DEVICE

The emission control device at the Wisconsin Steel Works is a MikroPul™ wet electrostatic precipitator[4]. This device incorporates the continuous spraying of finely divided liquid droplets into the gas stream. The water droplets become electrically charged and are attracted to the collecting plates. The precipitated water droplets create an evenly distributed water film over the collector surface. The solid particulates also become charged and migrate to the collected surfaces where they are captured by the continuously downward moving film of water. The water film on each of the collecting plates and discharge electrodes flows, by gravity, into a slurry trough for disposal.

The precipitator collector consists of two parallel units, each designed for a flow rate of 47 m^3/s (100,000 acfm)[5]. The design inlet and outlet temperatures are 73 C (200 F) and 43 C (110 F), respectively. Each precipitator is a two-field unit and provides for about 4.9 m (16 ft) of electrical treatment length.

From each precipitator, the gas flow passes to an induced draft fan. The two fan outlets are connected to a common 2.4 m (8 foot) diameter stack which is 24 m (80 ft) high.

A common water treatment system including pH control tanks and recirculating pumps is located under the precipitators. The design water flow rate is about 0.038 m^3/s (600 gpm).

EMISSION MEASUREMENT PROGRAM

In an effort to determine the efficiency of WESP units for collecting process emissions from leakage of coke oven doors, EPA contracted with Battelle-Columbus Laboratories and Clayton Environmental Consultants to measure the emissions at the inlet and outlet of the WESP units at the Wisconsin Steel Works coke oven plant, Chicago, Illinois.

Battelle-Columbus Laboratory personnel were responsible for sampling and analyzing the WESP inlet and outlet gas streams to determine the concentrations of 18 POM compounds in these streams. POM samples were collected using a modified Method 5 sampling train; gas chromatography-mass spectrometry (GC-MS) analyses were conducted to determine quantity of each POM species present in each sample. Battelle also collected gas samples in Tedlar™ bags during the entire sampling period (about 8 hours) and analyzed those for benzene and acetylene.

Clayton Environmental Consultants personnel were responsible for the measurement of particulate and benzene soluble organic concentrations in the WESP inlet and outlet gas streams, and for determination of CO_2, O_2, and CO concentrations in gas samples collected in Tedlar^{TM} bags.

This paper is limited to reporting of POM emissions as measured at the WESP inlet and outlet.

Table 1 lists the POM species of interest for this program together with an indication of the reported carcinogenicity of each[6]. Twenty-one species are listed. In several cases two nearly identical species had the same reported carcinogenicity; where this was observed, no effort was made to determine the quantity of each species present and the reported values are for the sum of the two species. Because of the difficulty and cost of the analysis, beta-naphthylamine was only analyzed for samples from one run.

Sampling Schedule

The operation of the coke oven during the field test was on a two-shift basis; that is, coke was pushed and charged between 3 p.m. and 7 a.m. No pushing and charging occurred during the 7 a.m. to 3 p.m. shift.

Sampling Runs 1, 2, and 3 were conducted between about 10 a.m. and 8 p.m. on 3 separate days; the purpose of these runs was to sample during a period of expected low door leakage. Since coke pushing was not begun before 3 p.m., at least 5 hours of sampling occurred when there was no pushing activity. The last 3 hours of sampling (which required 5 hours of time) occurred during the period when the first ovens were being pushed. Sampling was stopped prior to each push and not resumed until pushing emissions had cleared from the shed area (about 5 minutes).

Run 4 was conducted from 8 p.m. to 7 a.m. and was intended to include a period of high door leakage. Door leakage is greatest during the early part of the cycle and more ovens were operating in this part of the cycle during the Run 4 test period.

Location of Sampling Points

Sampling was conducted using existing sample ports; sampling point locations were determined as outlined in EPA Method 1.

Precipitator inlet stack gases were sampled from 0.315 m x 0.315 m (80 x 8C inch) horizontal duct at the location shown in Figure 1; the probe was inserted into the duct vertically from above through six existing ports. The stack geometry was such that 48 sample points were required for representative sampling. Sample ports were located 2.8

Table 1. POM species of interest.

POM Species	Carcinogenicity[a]
Naphthalene	-
Fluoranthrene	-
Pyrene	-
Benz(c)phenanthrene	+++
Chrysene	±
Benz(a)anthracene	+
7,12-Dimentylbenz(a)anthracene	++++
Benz fluoranthrenes:	
benz(b)fluoranthrene	++
benz(j)fluoranthrene	++
Benz(a)pyrene	+++
Benz(e)pyrene	-
Cholanthrene	++
Indeno(1,2,3-cd)pyrene	+
Dibenz(a,h)anthracene	+++
Dibenz acridines:	
dibenz(a,j)acridine	++
dibenz(a,h)acridine	++
Dibenz(c,g)carbazole	+++
Dibenz pyrenes:	
dibenz(a,h)pyrene	+++
dibenz(a,i)pyrene	+++
3-Methyl cholanthrene	++++
Benz(j)aceanthrylene	++
Beta-naphthylamine	+
Triphenylene	±

(a) Reported carcinogenicity by Public Health Services[6] where

++++, +++, ++	Strong carcinogenic
+	Carcinogenic
±	Uncertain or weakly carcinogenic
-	Not carcinogenic.

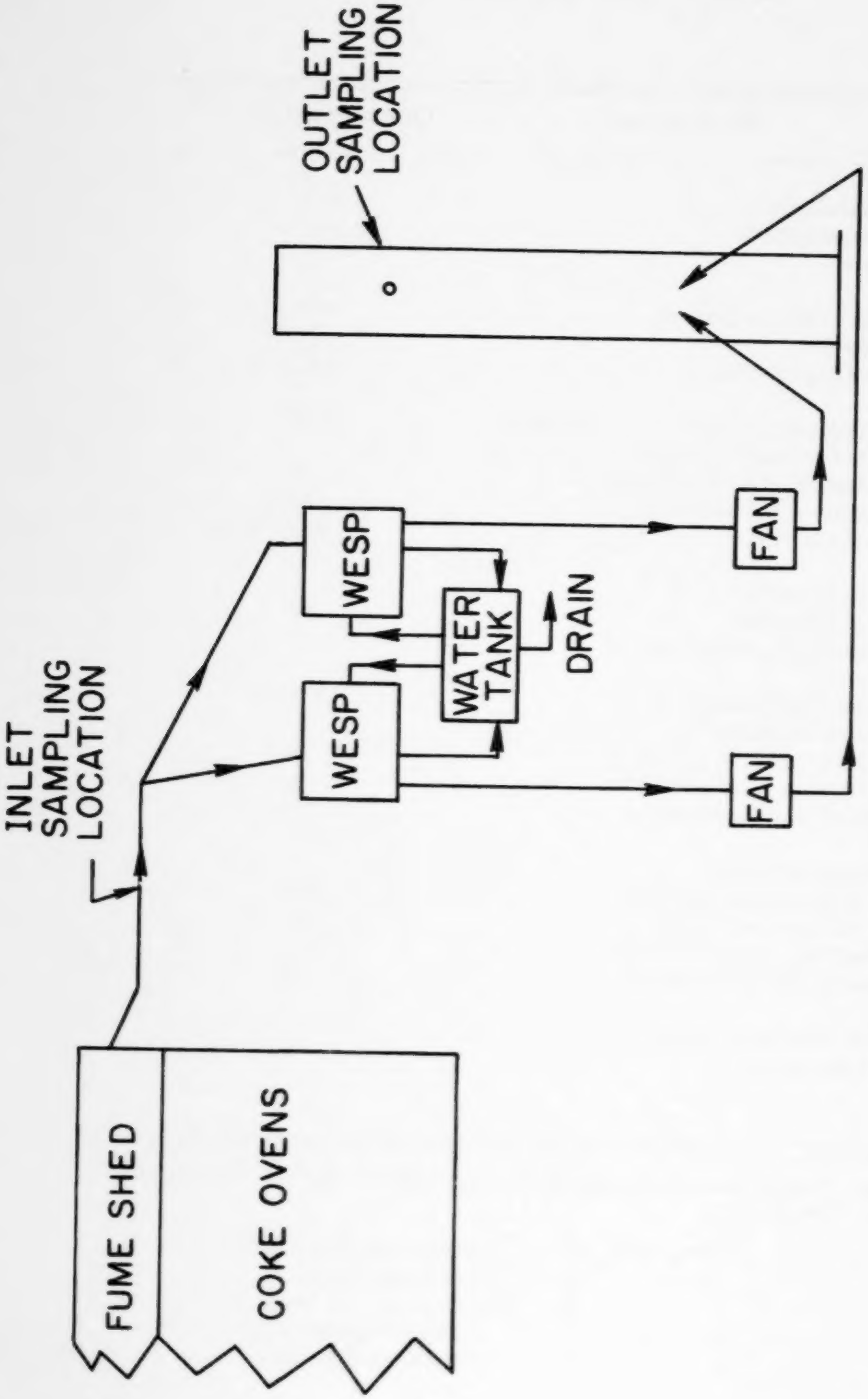
FUME SHED
COKE OVENS
INLET SAMPLING LOCATION
WESP
WESP
WATER TANK
DRAIN
FAN
FAN
OUTLET SAMPLING LOCATION

Figure 1. Schematic of emission control system

duct diameters downstream and 2.0 duct diameters upstream from flow disturbances.

Outlet stack sampling was from a 24 m (80 foot) high, 2.4 m (80 foot) diameter, vertical stack. The stack geometry, as presented in Figure 1, shows the sample port location relative to the nearest upstream and downstream flow disturbance. Straight, unobstructed distances upstream and downstream of the sampling position were 5.5 and 2.0 stack diameters, respectively. Accordingly, 24 sample points were required.

POM Sampling Procedures

An established methodology to sample organic and POM compounds is not yet available as an EPA method. The state of the art, to date, is to incorporate a special organic adsorbent material (which is enclosed in a temperature-controlled column) within the conventional particulate sampling train. To accomplish this, an EPA Method 5 sampling train is modified to insert the adsorbent (Tenax^{TM}) column between the filter and the impingers. The adsorbent column collects POM that is not collected on the filter, nor collected by adsorption on probe and glassware surfaces. Schematic drawings of the trains used for sampling at the inlet and outlet of the wet electrostatic precipitators at Wisconsin Steel Works coke oven plant are given in Figure 2. Details of the construction and operation of the column are given in Reference 7.

At the inlet location, where sampling was conducted vertically from above, the filter and adsorbent column were attached directly to the end of the glass-lined sample probe. An umbilical line comprised of a flexible polyethylene hose with the associated thermocouple and electric lines was attached between the adsorbent column outlet and the Method 5 impinger box, which in turn was connected to the meter box (Figure 2). As the inlet probe had to be repositioned in the vertical plane for traversing, this sampling configuration both avoided line losses of organic material and kept the probe assembly weight to a minimum.

The precipitator outlet gases were sampled simultaneously with the inlet in order to determine precipitator efficiency. The sampling train used at the outlet was similar to the train used at the inlet (see Figure 2). The outlet sampling location was a vertical stack and, thus, impinger box support could be provided. Hence, the impinger box was connected directly to the adsorbent column outlet.

The filters that were used were 2500 QAST quartz tissue filters manufactured by the Pallfex Products Corporation.

Some past data show collection efficiency of the column is temperature dependent[8]; therefore, the gas temperature entering the column was

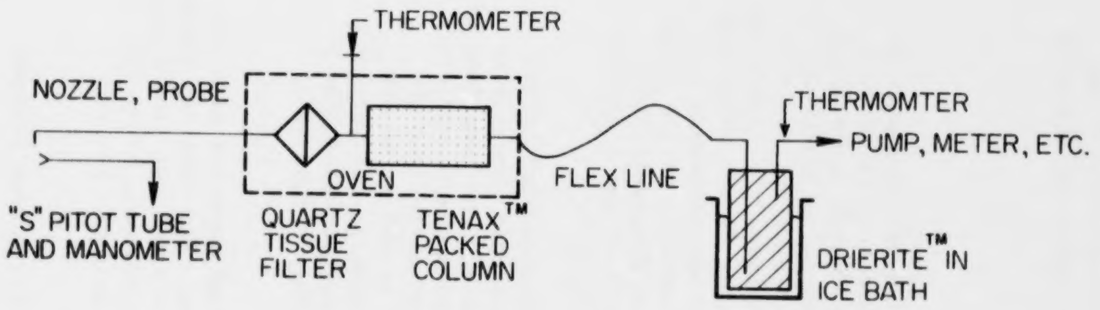
THERMOMETER
NOZZLE, PROBE
"S" PITOT TUBE AND MANOMETER
OVEN
QUARTZ TISSUE FILTER
TENAX™ PACKED COLUMN
FLEX LINE
THERMOMTER
PUMP, METER, ETC.
DRIERITE™ IN ICE BATH

a. INLET SAMPLING TRAIN CONFIGURATION

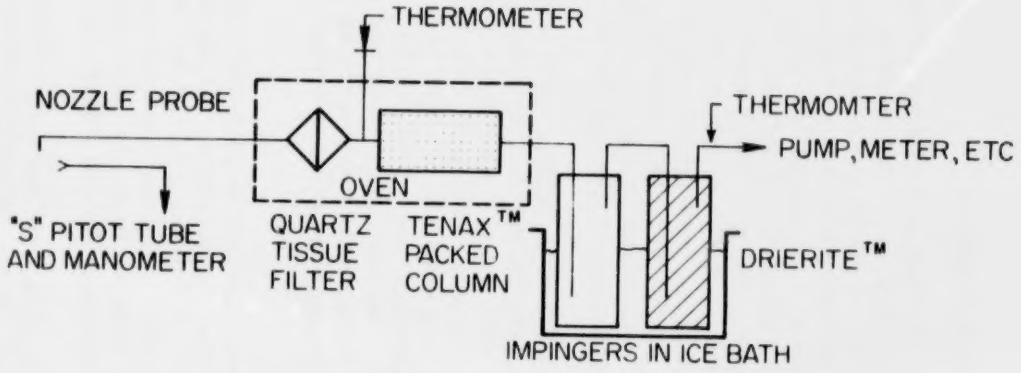
THERMOMETER
NOZZLE PROBE
"S" PITOT TUBE AND MANOMETER
OVEN
QUARTZ TISSUE FILTER
TENAX™ PACKED COLUMN
THERMOMTER
PUMP, METER, ETC
DRIERITE™
IMPINGERS IN ICE BATH

b. OUTLET SAMPLING TRAIN CONFIGURATION

Figure 2. Configuration of POM sampling trains

monitored and the oven temperature was adjusted to maintain a gas temperature of 52 C ± 3 C (125 F ± 5 F).

Because of the light sensitive nature of polycyclic organic matter, it is necessary to keep all samples in the dark during sampling, cleanup, and during shipment to the laboratory.

POM Sample Cleanup Procedures

After the sample was collected, the sample trains were removed to an onsite mobile laboratory. Each probe and all glassware through the front half of the filter holder was rinsed with about 200 ml of methylene chloride and 100 ml of acetone and the rinses were stored in separate amber bottles. The filter was sealed in a glass petri dish and stored in the dark. The back half of the filter holder and all glassware up to the POM column were rinsed with about 50 ml of methylene chloride and 25 ml of acetone and the rinses were placed in the amber bottles containing the front half rinses. The POM columns were capped and were stored in light-tight containers. The POM columns, the amber bottles containing the rinses, and the filters were taken to Battelle labs to be analyzed for POM.

To establish background data from solvents and sample train contamination, a pre-cleanup wash of all glass components upstream of the absorbent column was made.

The Drierite™ was weighed before and after the run and was discarded following the run.

POM Analysis

The POM analysis was conducted using standard Battelle POM analysis procedures. Basically, the analysis procedure includes extracting the filter and adsorbent column with methylene chloride and pentane, respectively. Then the solvent solutions (probe washes, filter extract, and absorbent column extract) are analyzed separately, or in various combinations, by gas chromatography-mass spectroscopy (GC-MS) techniques. Details regarding these procedures are described in Reference 7.

For this study, the methylene chloride and acetone rinses of the probe and glassware were combined with the filter extract to determine a single POM value representing all sampling train components upstream of the column; the adsorbent column was analyzed separately. Also of interest would be the POM value for the probe rinses and filter, but not including rinses of glassware between the filter and column; this is often referred to as "filterable" catch, or in this case "filterable" POM. Due to the low gas temperatures at the sampling points and the small surface area of sampling train glassware between the filter and column, it is unlikely that significant POM was collected on these surfaces. Hence, POM values for the rinse-plus-filter samples can be assumed to be nearly identical to filterable POM. For convenience, POM values for the rinse-plus-filter samples are labeled filterable POM in the tables of results. Blanks of rinse materials and rinses from the pre-cleanup were analyzed for POM and all POM values reported have been corrected for blanks.

Comments on POM Sampling and Analysis Procedures

The POM sampling and analysis procedures described above have been used by Battelle in the collection of hundreds of POM samples. Laboratory validation runs, where sampling of gases doped with specific POM compounds is conducted, have shown good accuracy for these procedures[7,9] POM emission measurements on residual oil fired boilers in the laboratory have shown results that are consistent and that follow expected trends as combustion variables are altered[10]. Further, EPA has incorporated virtually the same sampling procedures as part of their Level I source assessment sampling system (SASS) methodology. Thus, although these procedures have not been fully verified in field use, they are state of the art and we have reason to believe that they are reliable.

RESULTS

The inlet and outlet gas sampling flow rates and temperatures are summarized in Table 2. Flow rates at the WESP outlet are consistently higher than at the inlet; the outlet flow averages about 5 percent greater than the inlet flow. Remembering that these WESP are upstream of induced draft fans, any leakage in the WESP would result in increased outlet flow rates.

Tables 3 and 4 present the results showing the quantities of selected POM species present in the gas streams at the WESP inlet and outlet in terms of concentrations and emission rates, respectively. (Benz (j) aceanthrylene and triphenylene were not detected in any sample and, thus, are not included in Tables 3 and 4.) In Tables 3 and 4, two values are presented for each sample; one represents the probe and glassware rinses and the filter, and other represents the adsorbent column.

Examination of Tables 3 and 4 shows that both the concentrations of specific POM compounds in the gas stream and the ratio of specific POM compounds to total POM varied considerably from one run to another. Considering the complex chemistry of POM compounds, and the undefined variables related to details of coke-oven operation (time-temperature profiles, temperature-space profiles, door sealing, etc.), it is likely that these variations are real and are not due to analytical inaccuracies.

Table 2. General sampling conditions.

Run	Stack Flow m^3/min	Stack Flow Nm^3/min	Temperature, C
Inlet			
1	5305	5110	23
2	5411	5068	32
3	5518	5102	35
4	5425	5010	34
Average	5415	5073	31
Outlet			
1	5455	5366	16
2	5552	5359	22
3	5582	5318	26
4	5584	5277	25
Average	5543	5330	22

Table 4 also presents results on the effectiveness of the WESP for controlling emissions of individual POM species. The WESP was relatively effective (over 93 percent) in reducing POM emissions of all species except naphthalene. Only 3 POM species (naphthalene, fluoranthrene, and pyrene - all non-carcinogens) were emitted from the WESP in quantities greater than 2.2 mg/hr.

Table 5 summarizes the effectiveness of the WESP for controlling total POM emissions from the coke oven. In Table 5, the sum of the POM emissions in the inlet and outlet streams are reported, along with the control device efficiency. For three runs, the control device efficiency on total POM ranged from 80.7 to 92.4 percent and averaged 86.3 percent. The low efficiency for Run 4 of 17.2 percent (attributed to a high naphthalene value for the outlet adsorbent column sample) reduced the average efficiency for the four runs to 69.0 percent. Neglecting naphthalene, WESP efficiencies for the four runs were 93.5, 95.5, 98.8, and 94.5; an average of 95.6.

Preliminary results of the particulate emission measurements show that the WESP collection efficiency was about 54, 85, 92, and 92 percent for Runs 1 through 4, respectively. Thus, the average collection efficiency was 81 percent. Neglecting the unexplained low value for Run 1, the average efficiency was 90 percent.

Table 3. POM concentrations in inlet and outlet gas streams (ng/Nm^3)

	Sample Fraction	Run 1		Run 2		Run 3		Run 4		Averages		Total of Both Fractions	
		Inlet	Outlet	Inlet	Outlet	Inlet	Outlet	Inlet	Outlet	Inlet	Outlet	Inlet	Outlet
Naphthalene	Filter.	2.24	2.68	600.	0.416	525.	0.057	576.	0.056	426.	0.77		
	Ad.Col.	49.2	35.8	2450.	1090.	883.	1120.	9.45	2210.	848.	1110.	1270.	1110.
Fluoranthrene	Filter.	560.	7.54	613.	8.67	3120.	6.84	587.	9.79	1220.	8.21		
	Ad.Col.	17.1	116.	419.	81.2	310.	38.7	1.73	49.3	187.	71.3	1410.	79.5
Pyrene	Filter.	377.	4.31	393.	5.20	798.	3.76	357.	2.81	481.	4.02		
	Ad.Col.	10.6	50.3	291.	35.0	180.	21.2	0.974	32.4	121.	34.8	602.	38.8
Benz(c)phenanthrene	Filter.	51.8	0.108	30.3	0.590	38.1	0.034	29.6	2.09	37.5	0.710		
	Ad.Col.	0.229	0.539	17.0	0.925	25.2	0.205	18.8	0.675	15.3	0.586	52.8	1.30
Chrysene	Filter.	535.	0.503	297.	6.96	322.	0.593	263.	0.584	354.	2.16		
	Ad.Col.	1.64	5.16	93.3	3.25	40.5	4.46	73.0	5.52	52.1	4.60	406.	6.76
Benz(a)anthracene	Filter.	535.	1.68	286.	3.58	284.	0.570	223.	0.787	332.	1.65		
	Ad.Col.	2.97	6.47	81.5	3.01	27.9	4.33	52.5	5.29	41.2	4.78	373.	6.43
7,12-Dimethylbenz(a)anthracene	Filter	<0.05	<0.06	9.53	<0.06	3.81	<0.06	<0.05	<0.06	3.35	<0.06		
	Ad.Col.	0.345	0.06	<0.05	<0.06	<0.05	<0.06	<0.05	<0.06	0.105	<0.06	3.46	<0.12
Benz fluoranthrenes	Filter	497.	1.86	469.	2.60	755.	C.969	291.	1.97	503.	1.85		
	Ad.Col.	0.585	3.25	1.19	1.63	3.93	1.49	0.877	2.04	1.65	2.10	505.	3.95
Benz(a)pyrene	Filter.	150.	1.34	129.	n.d.	195.	0.741	89.0	3.37	141.	1.36		
	Ad.Col.	0.221	n.d.	0.343	0.486	0.286	0.422	0.758	0.922	0.402	0.458	141.	1.82
Benz(e)pyrene	Filter.	246.	0.383	227.	2.29	625.	0.148	146.	0.315	311.	0.784		
	Ad.Col.	n.d.	1.77	0.064	n.d.	0.011	0.011	n.d.	0.067	0.019	0.462	311.	1.25
Cholanthrene	Filter.	<0.05	<0.06	<0.05	<0.06	<0.05	<0.06	<0.05	<0.06	<0.05	<0.06		
	Ad.Col.	<0.05	<0.06	<0.05	<0.06	<0.05	<0.06	<0.05	<0.06	<0.05	<0.06	<0.10	<0.12
Indeno(1,2,3-cd)pyrene	Filter.	135.	2.04	143.	1.85	242.	1.48	84.1	1.91	151.	1.82		
	Ad.Col.	<0.05	<0.06	0.107	<0.06	<0.05	<0.06	<0.05	0.911	0.45	0.251	151.	2.07
Dibenz(a,h)anthracene	Filter.	108.	1.92	158.	1.85	272.	<0.06	84.6	2.02	156.	1.46		
	Ad.Col.	<0.05	<0.06	<0.05	<0.06	<0.05	<0.06	<0.05	<0.06	<0.05	<0.06	156.	1.49
Dibenz acridines	Filter.	<0.05	<0.06	<0.05	<0.06	n.d.	<0.06	<0.05	<0.06	<0.05	<0.06		
	Ad.Col.	<0.05	<0.06	<0.05	<0.06	<0.05	<0.06	<0.05	<0.06	<0.05	<0.06	<0.10	<0.12
Dibenz(c,g)carbazole	Filter.	<0.05	<0.06	<0.05	<0.06	n.d.	<0.06	<0.05	<0.06	<0.05	<0.06		
	Ad.Col.	<0.05	<0.06	<0.05	<0.06	<0.05	<0.06	<0.05	<0.06	<0.05	<0.06	<0.10	<0.12
Dibenz pyrenes	Filter.	137.	1.80	131.	1.85	217.	1.25	82.1	1.69	142.	1.65		
	Ad.Col.	<0.05	<0.06	<0.05	<0.06	<0.05	<0.06	<0.05	<0.06	<0.05	<0.06	142.	1.68
3-Methyl cholanthrene	Filter.	<0.05	<0.06	<0.05	<0.06	n.d.	<0.06	<0.05	<0.06	<0.05	<0.06		
	Ad.Col.	<0.05	<0.06	<0.05	<0.06	<0.05	<0.06	<0.05	<0.06	<0.05	<0.06	<0.10	<0.12
Beta-napthylamine	Filter					0.42	<0.09						
	Ad.Col					<0.08	<0.09					0.42-0.50	<0.18

Notes: Solvent, filter and adsorbent column blanks were subtracted from POM mass before concentrations were calculated.
n.d. = none detected

Table 4. POM emission rates (mg/hr)

	Sample Fraction	Run 1		Run 2		Run 3		Run 4		Averages		Total of Both Fractions		Control Device Efficiency, percent (Inlet-Outlet / Inlet x 100)
		Inlet	Outlet	Inlet	Outlet	Inlet	Outlet	Inlet	Outlet	Inlet	Outlet	Inlet	Outlet	
Naphthalene	Filter.	0.687	0.863	183.	0.134	161.	0.017	173.	0.017	129.	0.258	387.	355.	8.3 or 47.6(a)
	Ad.Col.	15.1	11.5	744.	350.	270.	357.	2.84	699.	258.	354.			
Fluoranthrene	Filter.	171.	2.43	186.	2.79	952.	2.18	176.	3.10	371.	2.63	428.	25.5	94.0
	Ad.Col.	5.24	37.4	127.	26.1	95.2	12.4	0.520	15.6	57.	22.9			
Pyrene	Filter.	116.	1.39	120.	1.67	244.	1.20	107.	0.889	147.	1.29	184.	12.4	93.0
	Ad.Col.	3.25	16.2	88.5	11.3	55.1	6.76	0.293	10.3	36.8	11.1			
Benz(c)phenanthrene	Filter.	15.9	0.034	9.22	0.190	11.7	0.010	8.89	0.662	11.4	0.224	17.1	0.412	97.6
	Ad.Col.	-	0.173	5.17	0.297	7.71	0.066	5.65	0.216	4.63	0.188			
Chrysene	Filter.	164.	0.164	90.3	2.24	98.9	0.190	79.1	0.185	108.	0.695	124.	2.17	98.3
	Ad.Col.	0.503	1.66	28.4	1.04	12.4	1.42	22.0	1.75	15.8	1.47			
Benz(a)anthracene	Filter.	164.	0.541	87.0	1.15	86.9	0.182	67.0	0.249	101.	0.531	114.	2.05	98.2
	Ad.Col.	0.910	2.06	24.8	0.965	8.54	1.38	15.8	1.67	12.5	1.52			
7,12-Dimethylbenz(a)anthracene	Filter.	<0.02	<0.02	2.89	<0.02	1.17	<0.02	<0.02	<0.02	1.03	<0.02	1.06	<0.04	>96.2
	Ad.Col.	0.106	<0.02	<0.02	<0.02	<0.02	<0.02	<0.02	<0.02	0.036	<0.02			
Benz fluoranthrenes	Filter.	152.	0.599	142.	0.836	231.	0.310	87.5	0.624	153.	0.592	154.	1.26	99.2
	Ad.Col.	0.179	1.04	0.362	0.524	1.20	0.475	0.263	0.645	0.501	0.671			
Benz(a)pyrene	Filter.	45.9	0.432	39.2	-	59.7	0.236	26.8	1.07	42.9	0.435	43.0	0.581	98.6
	Ad.Col.	0.067	-	0.104	0.156	0.088	0.134	0.228	0.292	0.122	0.146			
Benz(e)pyrene	Filter.	75.4	0.123	69.0	0.736	191.	0.048	43.9	0.100	94.8	0.252	94.8	0.399	99.6
	Ad.Col.	-	0.570	0.020	-	0.004	0.004	-	0.021	0.006	0.149			
Cholanthrene	Filter.	<0.02	<0.02	<0.02	<0.02	<0.02	<0.02	<0.02	<0.02	<0.02	<0.02	<0.04	<0.04	-
	Ad.Col.	<0.02	<0.02	<0.02	<0.02	<0.02	<0.02	<0.02	<0.02	<0.02	<0.02			
Indeno(1,2,3-cd)pyrene	Filter.	41.4	0.657	43.5	0.595	74.1	0.473	25.3	0.605	46.1	0.583	46.1	0.663	98.6
	Ad.Col.	<0.02	<0.02	0.033	<0.02	<0.02	<0.02	<0.02	0.288	0.016	0.080			
Dibenz(a,h)anthracene	Filter.	33.1	0.618	48.0	0.595	83.3	<0.02	25.4	0.640	47.5	0.466	47.5	0.49	99.0
	Ad.Col.	<0.02	<0.02	<0.02	<0.02	<0.02	<0.02	<0.02	<0.02	<0.02	<0.02			
Dibenz acridines	Filter.	<0.02	<0.02	<0.02	<0.02	-	<0.02	<0.02	<0.02	<0.02	<0.02	<0.04	<0.04	-
	Ad.Col.	<0.02	<0.02	<0.02	<0.02	<0.02	<0.02	<0.02	<0.02	<0.02	<0.02			
Dibenz(c,g)carbazole	Filter.	<0.02	<0.02	<0.02	<0.02	-	<0.02	<0.02	<0.02	<0.02	<0.02	<0.04	<0.04	-
	Ad.Col.	<0.02	<0.02	<0.02	<0.02	<0.02	<0.02	<0.02	<0.02	<0.02	<0.02			
Dibenz pyrenes	Filter.	42.0	0.579	39.8	0.595	66.4	0.399	24.7	0.535	43.2	0.527	43.2	0.54	98.8
	Ad.Col.	<0.02	<0.02	<0.02	<0.02	<0.02	<0.02	<0.02	<0.02	<0.02	<0.02			
3-Methyl cholanthrene	Filter.	<0.02	<0.02	<0.02	<0.02	-	<0.02	<0.02	<0.02	<0.02	<0.02	<0.04	<0.04	-
	Ad.Col.	<0.02	<0.02	<0.02	<0.02	<0.02	<0.02	<0.02	<0.02	<0.02	<0.02			
Beta-napthylamine	Filter					0.13	<0.03					0.13-0.15	<0.06	-
	Ad. Col.					<0.02	<0.03							

a. Neglecting Run 4 where outlet > inlet.

Table 5. WESP effectiveness for controlling POM emissions

	Inlet[a]		Outlet(a)		
Run No.	Sample	Total POM Emissions, mg/hr	Sample	Total POM Emissions, mg/hr	$\frac{\text{Inlet-Outlet}}{\text{Inlet}} \times 100$
Including Naphthalene					
1	Filterable	1,021.39	Filterable	8.43	
	Ads. Column	25.36	Ads. Column	70.60	
	Total	1,046.75	Total	79.03	92.4
2	Filterable	1,059.91	Filterable	11.53	
	Ads. Column	1,018.30	Ads. Column	390.38	
	Total	2,078.30	Total	401.91	80.7
3	Filterable	2,261.30	Filterable	5.23	
	Ads. Column	450.24	Ads. Column	379.64	
	Total	2,711.54	Total	384.87	85.8
4	Filterable	844.59	Filterable	8.66	
	Ads. Column	47.59	Ads. Column	729.78	
	Total	892.18	Total	738.44	17.2
				Average	69.0
Excluding Naphthalene					
1	Filterable	1,020.70	Filterable	7.57	
	Ads. Column	10.26	Ads. Column	59.10	
	Total	1,030.96	Total	66.67	93.5
2	Filterable	876.91	Filterable	11.40	
	Ads. Column	274.39	Ads. Column	40.38	
	Total	1,151.30	Total	51.78	95.5
3	Filterable	2,100.30	Filterable	5.23	
	Ads. Column	180.24	Ads. Column	22.64	
	Total	2,280.54	Total	27.87	98.8
4	Filterable	671.59	Filterable	8.66	
	Ads. Column	44.75	Ads. Column	30.78	
	Total	716.34	Total	39.44	94.5
				Average	95.6

(a) Inlet and outlet values for total POM were obtained by summation of values for individual POM species.

Uncontrolled (inlet) emission rates of filterable particulate (Method 5 front half) ranged from 3520 to 9080 g/hr; about 2100 to 5400 times the uncontrolled (inlet) POM emission rates.

CONCLUSIONS

Recently developed techniques for sampling and analysis of POM compounds, developed for combustion emission sources, appear to have been successfully applied to measurement of POM emissions from coke oven door leakage. As a consequence of utilizing these procedures, data are now available relating to a specific control device for limiting total POM emissions from coke-oven door leakage. In addition, data are available on the emissions and the effectivenss of the control device for 18 individual POM species.

The collected data show that the wet electrostatic precipitator applied to the coke ov[illegible] examined in this program was relatively effective in reducing emissions of all POM species that were reported, except for naphthalene. The collection efficiency was 93 to 94 percent for fluoranthrene and pyrene, and was 98 percent or greater for all other POM species. It was determined that the efficienct of the WESP for controlling emissions of the various species related to molecular weight of the species. Table 6 tabulates and Figure 3 shows graphically the collection efficiency for various POM species and molecular weight.

The large quantity of naphthalene present in the gas stream, together with the low effeciency of collection for this compound, resulted in collection efficiency for total POM averaging only 69 percent. When naphthalene is not included, the collection efficiency for total POM was 95.6 percent.

A good collection-efficiency for most POM species would be expected due to the low operating temperature of the WESP control device. At temperatures below 38 C (100 F), it would be expected that the majority of the POM would be present as droplets, particles, or condensed on particles and, thus, would be susceptable to collection in an electrostatic precipitator.

It was somewhat surprising to find the WESP only about 90 percent efficient for controlling particulate emissions and in excess of 96 percent efficient for controlling emissions of most POM species. This difference in observed collection efficiency may be due to differences in the nature of carbon particles and POM droplets. However, it would be expected that the collection efficiency for the reportedly smaller condensed hydrocarbon droplets would be less than for the larger carbon particles[4].

The low particulate collection efficiency observed during their runs may be explained by the relatively low inlet loadings resulting

Table 6. WESP control device efficiency as related to molecular weight of various POM species.

Species	Molecular Weight	WESP Efficiency, percent
Naphthalene	128	8.3 or 47.6
Fluoranthrene	202	94.0
Pyrene	202	93.0
Benz(c)phenanthrene	228	97.6
Chrysene	228	98.3
Benz(a)anthracene	228	98.2
Benz fluoranthrenes	252	99.2
Benz(a)pyrene	252	98.6
Benz(e)pyrene	252	99.6
7,12-Dimethylbenz(a)anthracene	256	>96.2
Indeno (1,2,3-cd)pyrene	276	98.6
Dibenz (a,h)anthracene	278	99.0
Dibenz pyrenes	302	98.8

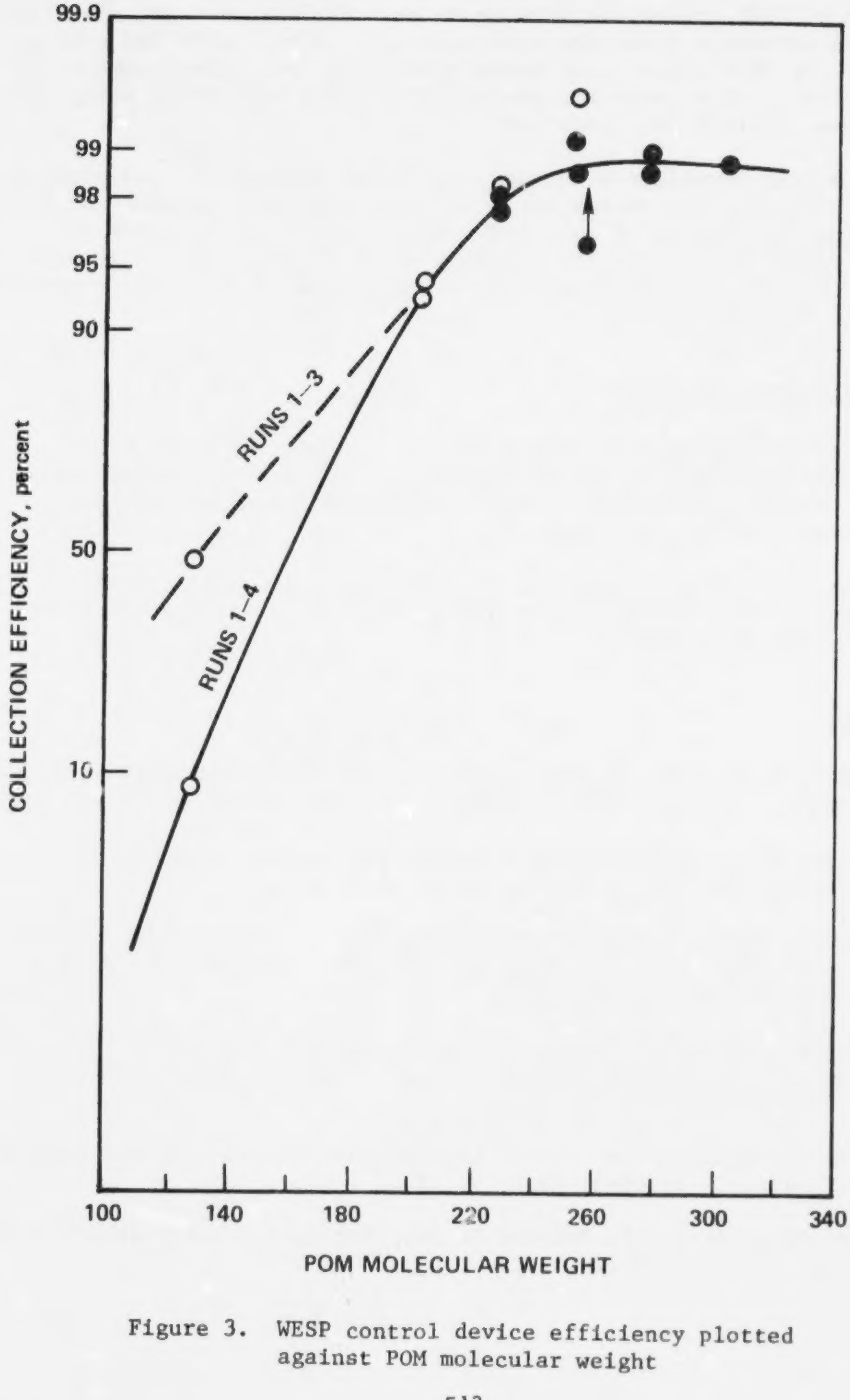

Figure 3. WESP control device efficiency plotted against POM molecular weight

from door leakage; collection efficiency would possibly be higher during the coke pushing periods when inlet loadings would be much higher. Others report WESP control devices to be over 98.5 percent efficient for collecting emissions from coke oven pushing[4]. Also, there had been an outage of the WESP units a few weeks before the test; readjustments to obtain balanced flow rates for the two WESP units were still being made at the time the test was conducted.

For as yet unexplained reasons, the inlet loading of both particulate and POM was lower during Run 4 (the intended maximum emission run) than during the average of Runs 1 through 3 (the intended minimum emission runs). Also, the BaP emission rates determined by this test are less than the BaP emission rates as determined from tests on several other coke oven batteries[11].

ACKNOWLEDGEMENTS AND NOTES

The study described in this paper was conducted for the U.S. Environmental Protection Agency, Emission Standards and Engineering Division, Emission Measurement Branch, Research Triangle Park, N.C. under Contract 68-02-1409, Task 50.

Mention of specific products or trade names does not constitute endorsement or recommendation for use by the U.S. Environmental Protection Agency or Battelle.

REFERENCES

1. Voelker, F. C., Jr. A contemporary Survey of Coke-Oven Air Emissions Abatement. Iron and Steel Engineer. 52 (2): 57-64, February, 1975.

2. Steiner, B. A. Ferrous Metallurgical Operations. Chapter 21 in Air Pollution. Vol. IV, Academic Press, 1977, p 897.

3. Hamilton, W. M. Construction and Operation of a Coke Side Shed at Dofasco. Ironmaking Proceedings. Vol. 36: 344-350. The Metallurgical Society of AIME, 1977.

4. Bakke, E. Wet Electrostatic Precipitators for Control of Submicron Particles. Journal of the Air Pollution Control Association. 25 (2): 163-167, February, 1975.

5. Personal communication from D. Parikh, United States Filter Corporation, MikroPul Division, March 9, 1978.

6. Particulate Polycyclic Organic Matter, National Academy of Sciences, Washington, D. C., 5-12, 1972.

7. Jones, P. W., R. D. Giammar, P. E. Strup, and T. B. Stanford. Efficient Collection of Polycyclic Organic Compounds from Combustion Effluents. Environmental Science & Technology. 10: 806-810, August, 1976.

8. Barrett, R. E., P. R. Webb, W. C. Baytos, S. E. Miller, and E. L. Merryman. Source Testing Methodology for the Asphalt Roofing Industry. U.S. Environmental Protection Agency. EPA Project No. 75-ARM-10. January 10, 1977, 47-52.

9. Unpublished report on Battelle program conducted for an industrial sponsor.

10. Giammar, R. D., A. E. Weller, D. W. Locklin, and H. H. Krause. Experimental Evaluation of Fuel Oil Additives for Reducing Emissions and Increasing Efficiency of Boilers. U.S. Environmental Protection Agency. EPA Publication EPA-600/2-77-0086. January, 1977.

11. Trenholm, A. R., and L. L. Beck. Assessment of Hazardous Organic Emissions from Slot Type Oven Batteries. Internal U. S. Environmental Protection Agency Report. March 16, 1978.